

REPORT DOCUMENTATION PAGE				<i>Form Approved OMB No. 0704-0188</i>	
<small>The public reporting burden for this collection of information is estimated to average 1 hour per response, including the time for reviewing instructions, searching existing data sources, gathering and maintaining the data needed, and completing and reviewing the collection of information. Send comments regarding this burden estimate or any other aspect of this collection of information, including suggestions for reducing the burden, to Department of Defense, Washington Headquarters Services, Directorate for Information Operations and Reports (0704-0188), 1215 Jefferson Davis Highway, Suite 1204, Arlington, VA 22202-4302. Respondents should be aware that notwithstanding any other provision of law, no person shall be subject to any penalty for failing to comply with a collection of information if it does not display a currently valid OMB control number.</small>					
PLEASE DO NOT RETURN YOUR FORM TO THE ABOVE ADDRESS.					
1. REPORT DATE (DD-MM-YYYY)		2. REPORT TYPE		3. DATES COVERED (From - To)	
4. TITLE AND SUBTITLE				5a. CONTRACT NUMBER	
				5b. GRANT NUMBER	
				5c. PROGRAM ELEMENT NUMBER	
6. AUTHOR(S)				5d. PROJECT NUMBER	
				5e. TASK NUMBER	
				5f. WORK UNIT NUMBER	
7. PERFORMING ORGANIZATION NAME(S) AND ADDRESS(ES)				8. PERFORMING ORGANIZATION REPORT NUMBER	
9. SPONSORING/MONITORING AGENCY NAME(S) AND ADDRESS(ES)				10. SPONSOR/MONITOR'S ACRONYM(S)	
				11. SPONSOR/MONITOR'S REPORT NUMBER(S)	
12. DISTRIBUTION/AVAILABILITY STATEMENT					
13. SUPPLEMENTARY NOTES					
14. ABSTRACT					
15. SUBJECT TERMS					
16. SECURITY CLASSIFICATION OF:			17. LIMITATION OF ABSTRACT	18. NUMBER OF PAGES	19a. NAME OF RESPONSIBLE PERSON
a. REPORT	b. ABSTRACT	c. THIS PAGE			19b. TELEPHONE NUMBER (Include area code)

Final Report
Contract Number N00014-00-1-0415
Period of Performance 04/01/00 – 09/30/03

Richard D. Hale
Associate Professor
Aerospace Engineering
University of Kansas
785-864-2949
785-864-3597 (FAX)
rhale@ku.edu
www.engr.ku.edu/~rhale

Richard Moon -- Graduate Research Assistant, Aerospace Engineering
KokSiong Lim -- Graduate Research Assistant, Aerospace Engineering
Kurt Schueler -- Graduate Research Assistant, Computer Science
Andrew Yoder -- Graduate Research Assistant, Aerospace Engineering
Harshinder Singh -- Graduate Research Assistant, Aerospace Engineering

TABLE OF CONTENTS

1.0 SUMMARY OF OBJECTIVES & APPROACH.....	2
1.1 ADVANCED MANUFACTURING TECHNIQUES AND PROJECT OVERVIEW	4
1.1.1. <i>What is Fiber Placement?</i>	4
1.1.2 <i>Machine Description</i>	5
1.2. WHAT IS STEERED FIBER COMPOSITE?	9
1.3. OVERVIEW OF SCADS PROJECT	10
2.0 APPROXIMATE GEOMETRIC METHODS FOR THE MODELING OF OFFSET CURVES AND LAMINATE FAMILY CURVES IN APPLICATION TO FIBER PLACED COMPOSITE STRUCTURE.....	12
2.1.0. INTRODUCTION.....	12
2.1.1 <i>Organization</i>	16
2.2.0. RELATED WORK.....	17
2.2.1. <i>Offset Curves on a Surface</i>	17
2.2.2 <i>Design and Analysis of Composite Structures</i>	21
2.3.0 THE METHODS	24
2.3.1 <i>Geometric Description of Offset Curve Generation on an Arbitrarily Curved Surface</i>	24
2.3.2. <i>Offset Curve Generation Algorithm</i>	28
2.3.3. <i>Geometric Description of Generation of a Laminate Family Curve</i>	29
2.3.4. <i>Laminate Family Curve Generation Algorithm</i>	31
2.4.0. THE ERROR	33
2.4.1. <i>Resulting Error of Method to Generate Offset Curves on a Surface</i>	33
2.4.2. <i>Resulting Error of Method to Place Laminate Family Curve on Surface</i>	40
2.5.0 IMPLEMENTATION	41
2.5.1. <i>Object Structure of Self Positioning Tows</i>	41
2.5.2. <i>Design Process</i>	44
2.5.3. <i>Analysis Capabilities</i>	53
2.6.0. ERROR VERIFICATION	55
2.6.1 <i>Surface with Circular Arc Cross Section</i>	55
2.6.2. <i>Surface with Arbitrarily Curved Cross Section</i>	58
2.6.3. <i>Laminate Family Curve</i>	61
2.7.0. CONCLUSIONS	67
2.7.1. <i>Future Directions</i>	68
3.0 STRUCTURAL OPTIMIZATIONS OF STEERED-FIBER COMPOSITE STRUCTURES.....	71
3.1.0. INTRODUCTION TO FIBER STEERING CONCEPTUAL DESIGN.....	73
3.1.1 <i>Motivations to Fiber Steering Conceptual Design</i>	73
3.1.2 <i>Motivations to FS Conceptual Design</i>	80
3.1.3 <i>FP Design Process Flow using FS Conceptual Design</i>	85
3.1.4 <i>Technical Objectives of FS Conceptual Design</i>	86
3.1.5 <i>Brief Outlines of the Sections</i>	87
3.2.0.LITERATURE REVIEW	88

3.3.1. Structural Optimization of Composite Laminates.....	91
3.3.2 Structural Optimization Program: MBB-LAGRANGE.....	92
3.3.3 Optimization Algorithm.....	107
3.3.4 Selection of Optimization Algorithms	110
3.3.5 FEA Package: MSC/PATRAN and MSC/NASTRAN.....	111
3.3.6 Flight Data Simulation Tool: VORSTAB	114
3.4.0. PRELIMINARY STUDIES	115
3.4.1 A Glance on the Literature.....	115
3.4.2 Preliminary Studies: Four Simple Models	117
3.4.2.4 Cantilever Cylindrical Tube subjected to Combined Loadings	130
3.4.3 Results and Discussion of Preliminary Studies.....	131
3.4.4 Brief Conclusion for Preliminary Studies	167
3.5.0. REPRESENTATIVE AIRCRAFT PRIMARY AND SECONDARY STRUCTURES USING FIBER STEERING CONCEPTUAL DESIGN.....	169
3.5.1 A Representative Wing of a Regional Jet.	171
3.5.2 A Representative Aft Pressure Bulkhead of a General Aviation Aircraft.	178
3.5.3 A Representative Horizontal Stabilator of a Tactical Fighter.	182
3.5.4 Results and Discussion.....	187
3.5.5 Brief Conclusion.....	210
3.6.0. CONCLUSIONS AND RECOMMENDATIONS	212
3.6.1 Conclusion of Fiber Steering Conceptual Design.....	212
3.6.2. Recommendations for Future Works.....	214
3.6.3. Recommendations for MBB-LAGRANGE Improvements	218
3.7 APPENDIX A: MATERIAL PROPERTIES	219
3.8 APPENDIX B: SAMPLE MBB-LAGRANGE INPUT FILE	222
3.9 APPENDIX C: FIBER STEERING CONCEPTUAL DESIGN OF PRELIMINARY STUDIES	227
3.9.1 Plate with a hole, $W/D = 3.33$, under bi-axial tensile loads.....	227
3.9.2 Plate with a hole, $W/D = 3.0$, under bi-axial tensile loads.....	234
3.9.3 Cantilever rectangular panel under transverse loads.	241
3.9.4 Cantilever cylindrical tube under combined loads.	248
3.10 APPENDIX D: FIBER STEERING CONCEPTUAL DESIGN OF PRELIMINARY STUDIES USING MSC/NASTRAN SOL 200.....	251
3.10.1 Cantilever panel under transverse loads	253
3.10.2 Plate-with-a-hole model, $W/D = 5.0$, under bi-axial tensile loads.....	255
3.11 APPENDIX E: FIBER STEERING CONCEPTUAL DESIGN FOR REPRESENTATIVE AIRCRAFT STRUCTURAL COMPONENTS	256
3.11.1 Fiber steering conceptual designs for a representative general-aviation's pressure bulkhead, subjected to cabin pressures.....	256
3.11.2 Fiber steering conceptual designs for a representative military horizontal stabilator, subjected to aerodynamic loads.	262
4.0 NONDESTRUCTIVE EVALUATION AND MECHANICAL TESTING OF STEERED FIBER COMPOSITES.....	273
4.1.0. INTRODUCTION.....	275
4.2.0. REVIEW OF LITERATURE.....	276
4.2.1 Fiber Placement	276
4.2.2. Steering Effect, Steering Radius Investigation.....	276

4.2.3. Tow Waviness.....	277
4.2.4. Fiber Misalignment Effect.....	278
4.2.5. Nondestructive Evaluation.....	278
4.2.6. Specimen Size Effect.....	279
4.3. PREVIOUS DATA AND METHODS REVIEW.....	280
4.3.1 Review Data	280
4.3.2. Review Previous Methods	280
4.4 RESEARCH FACILITIES.....	281
4.4.1. NDE (Dolphin) Machine	281
4.4.2. Diamond Cutter.....	283
4.4.3. Specimen Grinder and Polisher	284
4.4.4. Photomicroscopy and Camera System.....	284
4.4.5. Mechanical Test Machine (Instron).....	285
4.4.6 Compression Test Fixtures.....	286
4.5 PANEL AND SPECIMEN IDENTIFICATION	287
4.5.1 Panel Fiber Orientation.....	287
4.5.2 Centerline and Radius Identification	289
4.5.3 Minimum Steering Radius Investigation	293
4.5.4 Tow Layout Identification	293
4.6.0. NON-DESTRUCTIVE EVALUATION AND MECHANICAL TESTING	297
4.6.1. Non-Destructive Evaluation (NDE).....	297
4.6.2 Preparation for Mechanical Testing.....	305
4.6.3 Test Matrix Identification.....	308
4.6.4 Specimen Preparation.....	311
4.6.5 Test Procedures.....	313
4.6.6 Results and Analysis.....	317
4.6.7 Theoretical Model and Analysis.....	322
4.7.0. CONCLUSIONS AND RECOMMENDATIONS	325
5.0 EFFECT OF COMMON TOW FEATURES ON COMPRESSIVE PROPERTIES OF UNIDIRECTIONAL COMPOSITE	326
5.1 INTRODUCTION.....	326
5.1.1 Feature types.....	326
5.1.2 Literature Review	328
5.2 EXPERIMENTAL APPROACH.....	332
5.2.1 Fabrication.....	332
5.2.2 Non-Destructive Evaluation.....	340
5.2.3 Tabbings.....	340
5.2.4 Microscopy Study.....	342
5.2.5 Sectioning and Gauging	344
5.2.6 Data Acquisition System	347
5.2.7 Fixtures and Machinery	350
5.2.8 Experimental Procedure	353
5.3 ANALYSIS AND DISCUSSION	360
5.3.1 Finite Element Analysis.....	360
5.3.2 Nondestructive Evaluation.....	372
5.3.3 Photomicroscopy Studies	376

5.3.4 Mechanical Testing	377
5.4 GENERAL CONCLUSIONS	396
5.4.1 Conclusions	396
5.4.2 Recommendations for Future Research	396
5.5 APPENDIX A – NDE SCANS	399
5.6 APPENDIX B – INITIAL STIFFNESS PLOTS	406
5.7 APPENDIX C – ONSET OF NONLINEARITY PLOTS	416
5.8 APPENDIX D – COUPON MEASUREMENTS	422
5.9 APPENDIX E – RAW AND NORMALIZED DATA	434
6.0. DESIGN OF A LOW COST TAPE PLACEMENT HEAD FOR AUTOMATED FIBER STEERING (LOW COST FIBER PLACEMENT/COMPOSITE PANEL MANUFACTURING).....	445
6.1. MOTION CONTROL	445
6.2. ACCURACY TESTS	447
6.3. INITIAL HEAD DESIGN.....	449
6.4. DESIGN OF A LOW COST PLACEMENT HEAD FOR AUTOMATED FIBER STEERING	452
6.4.1. Customer Requirements	452
6.4.2. Head Configuration.....	453
6.4.3 Integration with robotic facilities at University of Kansas, composites lab	463
7.0 SUMMARY AND CONCLUSIONS.....	466
7.1 CONCLUSIONS FOR INTEGRATED DESIGN AND ANALYSIS TOOLS	467
7.2 CONCLUSIONS FOR STRUCTURAL OPTIMIZATIONS OF STEERED-FIBER COMPOSITE STRUCTURES	468
7.3 CONCLUSIONS FOR NONDESTRUCTIVE EVALUATION AND MECHANICAL TESTING OF STEERED FIBER COMPOSITES	471
7.4 CONCLUSIONS FOR THE EFFECT OF COMMON TOW FEATURES ON COMPRESSIVE PROPERTIES OF UNIDIRECTIONAL COMPOSITE	471
7.4.1 Effect on Initial Stiffness	471
7.4.2 Effect on the Point of Nonlinearity.....	472
7.4.3 Effect on the Axial strength.....	472
7.5 CONCLUSIONS FOR THE DESIGN OF A LOW COST TAPE PLACEMENT HEAD FOR AUTOMATED FIBER STEERING	472
8.0 REFERENCES.....	473

List Of Figures

Figure 1.1	The Schematics of Viper FPS-3000 and Axis Definition [37].....	6
Figure 1.2	Viper(FPS-300) Fiber Placement Machine Head [37]	8
Figure 1.3	Results from Tape Minimum Radius of Curvature Steering Tests [9].	9
Figure 1.4	Schematics of SCADS Project	11
Figure 2.1.1	Fiber Placement Head Delivers Multiple Tows in a Course	13
Figure 2.1.2	Steered Course Illustrates Difference in Feed Rate Across Tows in the Course ..	14
Figure 2.2.1	CNC Milling Parameters	18
Figure 2.3.1	Initial Input to the Method	25
Figure 2.3.2	The Fiber Axis Definition is Swept in the Direction of \vec{V}	26
Figure 2.3.3	The Reference Curve is a Surface-Surface Intersection.....	27
Figure 2.3.4	Cross Section of Placement Surface Showing Calculation of Offset Point	27
Figure 2.3.5	Algorithm to generate array of offset curves	28
Figure 2.3.6	Algorithm to Divide Curve into Segments and Generate Additional Segment Points.....	29
Figure 2.3.7	Algorithm to Generate Additional Defining Points on a Curve Segment.....	29
Figure 2.3.8	A Laminate Family Curve Angle θ to Offset Curves	30
Figure 2.3.9	P' is Found by Orienting a Plane at P and Intersecting with the Next Curve	31
Figure 2.3.10	Algorithm to Generate a Laminate Family Curve.....	32
Figure 2.4.1	Error Associated with Placing a Point on a Surface with Circular Arc Cross Section.....	34
Figure 2.4.2	Fiber Placed Raytheon Premier Fuselage Section.....	39
Figure 2.5.1	Object Relationships in Fiber Placed Structure.....	42
Figure 2.5.2	Class Inheritance at Ply, Course and Tow Levels	43
Figure 2.5.3	Tool Surface, Ply Boundary and Fiber-Axis are Initially Defined	44
Figure 2.5.4	Initial Ply Generation Creates Enough Courses to Completely Cover Ply Boundary	45
Figure 2.5.5	Tow Paths are Trimmed (only undropped segments are shown here)	46
Figure 2.5.6	Magnified View of Band Offset Ply Showing Individual Tow Path Representations	47
Figure 2.5.7	Laminate Family Ply Generation with Full Paths	48
Figure 2.5.8	Laminate Family Ply Generation with Full Paths	49
Figure 2.5.9	Laminate Family Ply after Trimming.....	50
Figure 2.5.10	Magnified View of Laminate Family Ply After Trimming of Tows	51
Figure 2.5.11	View of Overlap and Gap Regions (gap regions are shaded black).....	52
Figure 2.5.12	Analysis Examples (tow gap and overlap regions of three laminate family plies are shown)	53
Figure 2.5.13	Finite Element Mesh (60 x 10 elements) of Test Coupon.....	54
Figure 2.6.1	Curves are Based on the Initial Curve on the Placement Surface	56
Figure 2.6.2	Points are Placed on Cross Section of Placement Surface	56
Figure 2.6.3	Offset Curves are Placed on an Arbitrarily Curved Surface	59
Figure 2.6.4	Cross Section of Figure 2.6.3 Surface Shows Defining Points	59
Figure 2.6.5	Offset Curves are Placed on Representative Wing Surface	60
Figure 2.6.6	Cross Section of Figure 6.5 Surface Shows Defining Points.....	61
Figure 2.6.7	Example of a 40° Laminate Family Curve.....	62
Figure 2.6.8	Angle of Intersection Error for Offset $d = 0.100$	63

Figure 2.6.9	Angle of Intersection Error for Offset $d = 0.150$	64
Figure 2.6.10	Angle of Intersection Error for Offset $d = 0.200$	64
Figure 2.6.11	Angle of Intersection Error for Offset $d = 0.250$	65
Figure 2.6.12	Angle of Intersection Error for Laminate Family Angle of 40° and Varying Offset Distance, d	66
Figure 2.7.1	Fiber Orientation Direction is Optimized at Discrete Locations.....	69
Figure 3.1:	Schematics of (a) fiber placement system and (b) fiber placement head (copied from Ref. 1).....	74
Figure 3.2:	Successful utilization of fiber placement technology for fabricating representative aerospace structures ⁷	77
Figure 3.3:	Fiber steering of 0° , $+45^\circ$, and 90° courses on a mandrel ¹	78
Figure 3.4:	Fiber steering at different radii of curvatures on a flat surface ³	79
Figure 3.5:	Screen dumps of FIBERSIM showing (a) critical fiber path regions in yellow and red contours, and (b) modification of those regions with darting and draping theories ⁹	79
Figure 3.6:	Simulations of fiber path on complex-curvature parts with ACRAPLACE ^{11,12}	80
Figure 3.7:	A structural component with ply dropoff variable stiffness laminates.	81
Figure 3.8:	A laminate with variable fiber spacing.	81
Figure 3.9:	Schematics of conventional laminate family with 0° , $\pm 45^\circ$, and 90°	83
Figure 3.10:	Schematics of curvilinear laminate family with $(\theta_2/\pm\theta_1/\theta_3)$ in percentage, balanced based on local coordinate system.....	83
Figure 3.11:	A structural component with constant-rangewise fiber orientation and layer thickness. .	84
Figure 3.12:	A structural component with continuous-topological fiber orientation and layer thickness.	84
Figure 3.13:	Process flow or CAD/CAM/CAE for FP technology with the implementations of Fiber Steering Conceptual Design.....	86
Figure 3.3.1:	Definition of design variables for a symmetric laminate.	90
Figure 3.3.2:	MBB-LAGRANGE software architecture, “Three Column Concept” ⁴¹	96
Figure 3.3.3:	Coordinate system transformations of composite laminates.....	98
Figure 3.3.4:	Schematics of flat rectangular laminates subjected to (a) bi-axial compression and (b) in-plane shear loads.	103
Figure 3.3.5:	Schematics of design variable linking (a) linking over several layers, and (b) linking over several elements (copied from Ref. 45).	106
Figure 3.3.6:	Optimization algorithms of MBB-LAGRANGE.	108
Figure 3.3.7:	Classifications of Mathematical Programming Methods ⁴¹	108
Figure 3.3.8:	Comparisons of number of iterations and CPU time at optimum design with different optimization algorithms for preliminary studies (design configuration defined in Table 3.4.1).	112
Figure 3.3.9:	Comparisons of normalized structural weight at optimum design with different optimization algorithms for preliminary studies (design configuration defined in Table 3.4.1).	113
Figure 3.4.1:	Curvilinear fiber format of a plate with a hole of $W/D = 3.0$ under uniaxial tensile loads (copied from Ref. 20).....	115
Figure 3.4.2:	Optimum layer thickness and fiber orientation mappings for a cantilever panel under a vertical nodal load (copied from Ref. 23)	116
Figure 3.4.3:	Fiber arrangement of a hollow pipe with a circular hole under axial tension	

(copied from Ref. 51).....	116
Figure 3.4.4: Optimal layer thickness and orientation distributions of a fin (copied from Ref. 45).....	117
Figure 3.4.5: Schematics of a symmetric laminate, $[\pm\theta_1, \theta_2, \theta_3]_s$	119
Figure 3.4.6: Schematics of an oblique-symmetric laminate, $[\pm\theta_1, \theta_2, \theta_3]_{os}$	119
Figure 3.4.7: Schematics of laminate family rosettes for different configurations.	121
Figure 3.4.8: Nomenclature of square plates with a central circular hole.	123
Figure 3.4.9: Finite element discretization of plates with a hole of $W/D = 5.0$ under (a) bi-axial tensile loads, (b) uniaxial tensile loads, (c) in-plane shear loads.	124
Figure 3.4.10: Finite element discretization of plates with a hole of (a) $W/D = 3.33$, and (b) $W/D = 2.5$ under bi-axial tensile loads.	124
Figure 3.4.11: Schematics of laminate family rosettes for plate model in close-up view.	124
Figure 3.4.12: Schematics of ICW finite element discretization without upper skins.	126
Figure 3.4.13: Rangewise DV-linking definitions for ICW models (same-color elements carry identical material properties).....	127
Figure 3.4.14: Schematics of laminate family rosettes for ICW model.	127
Figure 3.4.15: Nomenclature of ICW model subjected to aerodynamic loads.....	128
Figure 3.4.16: Schematics of (a) finite element discretization of a cantilever panel under transverse loads and (b) laminate family rosettes in close-up view.....	129
Figure 3.4.17: Nomenclature of a cantilever panel under transverse loads.....	129
Figure 3.4.18: Schematics of finite element discretization of a cantilever tube under combined loads along with laminate family rosettes in close-up view.....	130
Figure 3.4.19: Nomenclature of a cantilever cylindrical tube under combined loads.	131
Figure 3.4.20: Specific location labeling for the plate-with-a-hole models.	133
Figure 3.4.21: Layer-thickness contours for pl16L013.	135
Figure 3.4.22: Layer-thickness contours for pl16L113.	136
Figure 3.4.23: Layer-angle mappings for pl16L113.....	137
Figure 3.4.24 Layer Thickness Contours for pl16L213.	139
Figure 3.4.25: Layer-angle mappings for pl16L213.....	140
Figure 3.4.26: Layer-thickness contours and layer-angle mappings for pl16L313.	141
Figure 3.4.27: Layer-thickness contours for pl16L023.	143
Figure 3.4.28: Layer-thickness contours for pl16L123.	144
Figure 3.4.29: Layer-angle mappings for pl16L123.....	145
Figure 3.4.30: Layer-thickness contours for pl16L223.	146
Figure 3.4.31: Layer-angle mappings for pl16L223.....	147
Figure 3.4.32: Layer-thickness contours and layer-angle mappings for pl16L323.	148
Figure 3.4.33: Layer-thickness contours for pl16L033.	150
Figure 3.4.34: Layer-thickness contours for pl16L133.	151
Figure 3.4.35: Layer-angle mappings for pl16L133.....	152
Figure 3.4.36: Layer-thickness contours for pl16L233.	153
Figure 3.4.37: Layer-angle mappings for pl16L233.....	154
Figure 3.4.38: Layer-thickness contours and layer-angle mappings for pl16L333.	155
Figure 3.4.39: Specific location labeling for the ICW model.....	157
Figure 3.4.40: Layer-thickness contours for ICW2L013, total (top contour) and 1 st (bottom contour) layers.....	158
Figure 3.4.40 (contd.):Layer-thickness contours for ICW2L013, 2 nd (top contour) and 3 rd (bottom contour) layers.....	158

contour) layers.....	159
Figure 3.4.41: Layer-thickness contours for ICW2L213, total (top contour) and 1 st (bottom contour) layers.....	161
Figure 3.4.41 (contd.): Layer-thickness contours for ICW2L213, 2 nd (top contour) and 3 rd (bottom contour) layers.....	162
Figure 3.4.42: Layer-angle mappings for ICW2L213 upper skin.	163
Figure 3.4.43: Layer-angle mappings for ICW2L213 lower skin.	163
Figure 3.4.44: Layer-thickness contours for ICW2L313, total (top contour) and 1 st (bottom contour) layers.....	164
Figure 3.4.44 (contd.): Layer-thickness contours for ICW2L313, 2 nd (top contour) and 3 rd (bottom contour) layers.....	165
Figure 3.4.45: 1 st and 2 nd layer-angle mappings for ICW2L313 upper skin.	166
Figure 3.4.46: 1 st and 2 nd layer-angle mappings for ICW2L313 lower skin.	166
Figure 3.5.1: Coefficients of pressure distribution over BGE wing models at various flight conditions.	173
Figure 3.5.1(contd.): Coefficients of pressure distribution over BGE wing models at various flight conditions.....	174
Figure 3.5.2: Finite element discretization of a representative general aviation wing subjected to aerodynamic and internal fuel loads.....	174
Figure 3.5.3: Schematics of (a) rangewise DV definitions (same-color ranges of elements carry identical material properties) and (b) laminate family rosettes of BGE wing. ...	176
Figure 3.5.4: Nomenclature of a representative regional jet wing.....	177
Figure 3.5.5: FIBERSIM screen dump showing darts and splices added to the virtual plies of an aft pressure bulkhead of Raytheon Premier I (copied from Ref. 55).	179
Figure 3.5.6 Finite element discretization of a representative pressure bulkhead under cabin pressure in (a) planar, (b) side, and (c) isometric views.	180
Figure 3.5.7: Layer-angle mappings for baseline design of pb2 model.	181
Figure 3.5.8: Nomenclature of a representative aft pressure bulkhead.	182
Figure 3.5.9 Finite element discretization of a representative military horizontal stabilator subjected to aerodynamic loads at high speed and altitude.....	183
Figure 3.5.10: Coefficients of pressure distribution over F22 horizontal stabilator at various flight conditions.....	184
Figure 3.5.11: Layer-angle mappings for baseline design of F22 model.	185
Figure 3.5.12: Schematics of rangewise DV definitions for F22 model (same-color ranges of elements carry identical material properties).	186
Figure 3.5.13: Nomenclature of a representative horizontal stabilator.....	187
Figure 3.5.14: Layer-thickness contours for bge11L013 lower skin.....	190
Figure 3.5.15: Layer-thickness contours for bge11L013 upper skin.....	191
Figure 3.5.16: Layer-thickness contours for bge12L013 lower skin.....	193
Figure 3.5.17: Layer-thickness contours for bge12L013 upper skin.....	194
Figure 3.5.18: Layer-thickness contours for bge11L213 lower skin.....	195
Figure 3.5.19: 1 st and 2 nd layer-angle mappings for bge11L213 lower skin.	196
Figure 3.5.19 (contd.): 3 rd and 4 th layer-angle mappings for bge11L213 lower skin.	197
Figure 3.5.20: Layer-thickness contours for bge11L213 upper skin.....	198
Figure 3.5.21: 1 st and 2 nd layer-angle mappings for bge11L213 upper skin.	199
Figure 3.5.21 (contd.): 3 rd and 4 th layer-angle mappings for bge11L213 upper skin.	200

Figure 3.5.22: Layer-thickness contours for bge11L313 lower skin.....	202
Figure 3.5.23: 1 st and 2 nd layer-angle mappings for bge11L313 lower skin.	203
Figure 3.5.24: Layer-thickness contours for bge11L313 upper skin.....	204
Figure 3.5.25: 1 st and 2 nd layer-angle mappings for bge11L313 upper skin.	205
Figure 3.5.26: Layer-thickness contours for bge12L313 lower skin.....	206
Figure 3.5.27: 1 st and 2 nd layer-angle mappings for bge12L313 lower skin.	207
Figure 3.5.28: Layer-thickness contours for bge12L313 upper skin.....	208
Figure 3.5.29: 1 st and 2 nd layer-angle mappings for bge12L313 upper skin.	209
Figure 3.6.1: Schematics of constructive design models for (a) topological ply distribution and (b) topological prepreg courses (taken from Ref. 27)	216
Figure 3.6.2: Schematics of fiber steering configurations for buckling panels.	216
Figure 3.6.3: Schematics of baseline and steering configurations for vibration panels in exploded view.	217
Figure C1: Layer-thickness contours for pl25L013.	228
Figure C2: Layer-thickness contours for pl25L113.	229
Figure C3: Layer-angle mappings for pl25L113.....	230
Figure C4: Layer-thickness contours for pl25L213.	231
Figure C5: Layer-angle mappings for pl25L213.....	232
Figure C6: Layer-thickness contours and layer-angle mappings for pl25L313.	233
Figure C7: Layer-thickness contours for pl34L013.	235
Figure C8: Layer-thickness contours for pl34L113.	236
Figure C9: Layer-angle mappings for pl34L113.....	237
Figure C10: Layer-thickness contours for pl34L213.	238
Figure C11: Layer-angle mappings for pl34L213.....	239
Figure C12: Layer-thickness contours and layer-angle mappings for pl34L313.....	240
Figure C13: Specific location labeling for the cantilever panel.	241
Figure C14: Layer-thickness contours for cb1L013.....	242
Figure C15: Layer-thickness contours for cb1L113.....	243
Figure C16: Layer-angle mappings for cb1L113.	244
Figure C17: Layer-thickness contours for cb1L213.....	245
Figure C18: Layer-angle mappings for cb1L213.	246
Figure C19: Layer-thickness contours for cb1L313.....	247
Figure C20: Layer-angle mappings for cb1L313.	248
Figure C21: Layer-thickness contours for tb1L073 (front and aft views).....	249
Figure C22: Layer-thickness contours for tb1L173 (front and aft views).....	249
Figure C22 (contd.):Layer-thickness contours for tb1L173 (front and aft views).....	250
Figure C23: Layer-angle mappings for tb1L173 (front and aft views).	250
Figure D1: Schematics of coordinate systems, fiber and principal stress orientations.	252
Figure D2: Layer-thickness contours for cb1N011, baseline configuration.....	253
Figure D3: Layer-thickness contours for cb1N111, Steering I configuration.	253
Figure D3 (contd.):Layer-thickness contours for cb1N111, Steering I configuration.	254
Figure D4: Layer-angle mappings for cb1N111, Steering I configuration.	254
Figure D5: Layer-thickness contours for pl16N011, baseline configuration.	255
Figure E1: Layer-thickness contours for pb2L013.	257
Figure E2: Layer-thickness contours for pb2L213.	258
Figure E3: Layer-angle mappings for pb2L213.....	259

Figure E4:	Layer-thickness contours for pb2L313.	260
Figure E5:	Layer-angle mappings for pb2L313.	261
Figure E6:	Layer-thickness contours for F22L013 lower skin.	263
Figure E7:	Layer-thickness contours for F22L013 upper skin.	264
Figure E8:	Layer-thickness contours for F22L213 lower skin.	265
Figure E9:	Layer-angle mappings for F22L213 lower skin.	266
Figure E10:	Layer-thickness contours for F22L213 upper skin.	267
Figure E11:	Layer-angle mappings for F22L213 upper skin.	268
Figure E12:	Layer-thickness contours for F22L313 lower skin.	269
Figure E12	(contd.):Layer-thickness contours for F22L313 lower skin.	270
Figure E13:	Layer-angle mappings for F22L313 lower and upper skins.	270
Figure E13	(contd.):Layer-angle mappings for F22L313 lower and upper skins.	271
Figure E14:	Layer-thickness contours for F22L313 upper skin.	272
Figure E14	(contd.):Layer-thickness contours for F22L313 upper skin.	272
Figure 4.3.1	Longitudinal Compression Strength and Modulus Data from Boeing Company	280
Figure 4.3.2	Compression Load Path for Baseline and Steered Fiber Composite	281
Figure 4.4.1	KU_NDE (Dolphin), SONIX 6D CSF 1000-3X.....	282
Figure 4.4.2	NDE Test Fixture	283
Figure 4.4.3	The Diamond Section Saw	Figure 4.4.4 ISOMET 1000..... 284
Figure 4.4.5	Specimen Grinder	Figure 4.4.6 Ecomet V Polisher 284
Figure 4.4.7	Photomicroscopy System	Figure 4.4.8 Camera System 285
Figure 4.4.9	MTS-Upgraded Instron Mechanical Testing Machine.....	285
Figure 4.5.1	Centerline Identification of Samples for Existing Fiber Steering Tests Are Incorrectly Located.	289
Figure 4.5.2	Cross Sectional Surface of Tow Illustrates Angular Orientation of Individual Fibers	290
Figure 4.5.3	Schematics of Steered Fiber Radius Determination.....	291
Figure 4.5.4	Layer 5 (0°) of a Representative Steered Fiber Panel (A3D3) Illustrates Local Tow Waviness Common in Fiber Steering and Fiber Placement.	292
Figure 4.5.5	Steering Radius and Center Identification for N3E6_2 Panel.....	293
Figure 4.5.6	Cross sectional view of a sample panel (A3D3, inboard, upper side, left section)	295
Figure 4.5.7	Tow Buckling in a Sample Panel Fiber Steered Panel (A3D3, inboard, upper side, center section)	295
Figure 4.6.1	Summary of Research Plan	298
Figure 4.6.2	Flaw Detection with Ultrasonic C-Scan.....	300
Figure 4.6.3	Example of 10-Layer Unidirectional Panel (N3E5_1).....	301
Figure 4.6.4	Example Scanning Results for a 10-Layer Unidirectional Panel (N3E5_1).....	302
Figure 4.6.6	C-scan Images for Baseline (A3C4_B) and Steered (A3C3) Panels Illustrate Local Orientation of Tows and Courses Through features such as Overlaps and Gaps.	303
Figure 4.6.5	Fiber Orientation Identification with Interface Ultrasonic C-Scan	304
Figure 4.6.7	Specimen Layout for Boeing Panels	306
Figure 4.6.8	Specimen Layout for Northrop Grumman Panels.....	307
Figure 4.6.9	Coupons with Strain Gage and Tab.....	312
Figure 4.6.10	Mechanical Test for Calibration using AL 6061-T6.....	314

Figure 4.6.12.	Corrected Stress-Strain Curve of N3E4_1_23_2_LCS_0_3 [5].....	318
Figure 4.6.13.	Experimental Data of Failure Stress and Modulus in Width and Radius Variation	320
Figure 4.6.14.	Experimental Data of Failure Stress and Modulus in Fiber Misalignment and Radius Variation.....	321
Figure 4.6.15	Theoretical Test Data of Normalized Peak Stress in Misalignment and Radius Variation.....	324
Figure 5.1	Gap Flaw Created by Fiber Placement.....	327
Figure 5.2	Overlap Flaw Created by Fiber Placement	327
Figure 5.3	Twisted Tow Flaw Created by Fiber Placement	328
Figure 5.4	Layer Waviness Example of 2-D Woven Laminates	329
Figure 5.5	Idealized Representation of a Wavy Fiber	330
Figure 5.2.1	Coupon Lay-Out for Square 9 inch Panel	333
Figure 5.2.2	Drawing of Well and Plunger.....	335
Figure 5.2.3	Bottom Plate of Well and Plunger Showing Tape Pattern	335
Figure 5.2.4	First Spacer Location	336
Figure 5.2.5	Location of Subsequent Spacers	337
Figure 5.2.6	Release Film with Alignment Lines for Laying Up Tow Plies.....	338
Figure 5.2.7	Single Ply of Tow Prepreg	338
Figure 5.2.8	50% and 100% Gap Tow Flaws for a Single Ply.....	339
Figure 5.2.9	50% Overlap and Twist Tow Flaws for a Single Ply.....	339
Figure 5.2.10	Ultra Sonic NDE Machine and Controller	340
Figure 5.2.11	Glass/Epoxy Tabbing with 45 Degree Bevel	341
Figure 5.2.12	Tabbed Panel Showing Positions of Tabbing	342
Figure 5.2.13	Diamond Cutter	343
Figure 5.2.14	Grinding/Polishing Stations	343
Figure 5.2.15	Idealized Gap Flaw Location Viewed On Axis	344
Figure 5.2.16	Coupon Label Nomenclature	345
Figure 5.2.17	Label Location on Coupons	345
Figure 5.2.18	Exaggerated Examples of Problems Due to Grinding	346
Figure 5.2.19	Centerline Marks for Gage Placement	346
Figure 5.2.20	Schematic of MTS Data Acquisition and Control Systems	348
Figure 5.2.21	Schematic of Riehle Data Acquisition and Control Systems.....	349
Figure 5.2.22	Data Acquisition Computer and 8 Channel Terminal Block	349
Figure 5.2.23	Front Panel of Data Acquisition Program For MTS Setup	350
Figure 5.2.24	Front Panel of Data Acquisition Program for Riehle Setup.....	350
Figure 5.2.25	Mechanical Testing Machinery	351
Figure 5.2.26	ASTM D 3410 Compression Fixture	352
Figure 5.2.27	Load Cell Synchronization Curve	354
Figure 5.2.28	Riehle Calibration Curves	355
Figure 5.2.29	Alignment Jig Set Up	356
Figure 5.2.30	Specimen Gripped and Ready with Tighten Pattern	356
Figure 5.2.31	Test Fixture Preparations	357
Figure 5.2.32	Load Rate Adjustment Knob for the Riehle Test Machine	358
Figure 5.3.1	Specimen Illustration Showing Flaw Location for On-Axis Model	360
Figure 5.3.2	Specimen Illustration Showing Flaw Location for Off-Axis Model.....	361

Figure 5.3.3	Specimen Illustration Showing Flaw Location for Combination Model.....	361
Figure 5.3.4	On-Axis Loads and Boundary Conditions	362
Figure 5.3.5	On-End Representation of 100% Gap Sample.....	363
Figure 5.3.6	On-End Representation of 50% Gap Sample.....	363
Figure 5.3.7	On-End Representation of 50% Overlap Sample.....	363
Figure 5.3.9	Off-Axis Loads and Boundary Conditions	366
Figure 5.3.10	Nastran Analysis Results for Off-Axis Flaws	368
Figure 5.3.11	Representation of 100% Gap Sample.....	369
Figure 5.3.12	Representation of 50% Gap Sample.....	370
Figure 5.3.13	Representation of 50% Overlap Sample	370
Figure 5.3.15	Peak Energy and TOF for Panel without Flaws (Tape Panel)	373
Figure 5.3.16	Histogram for Panel without Flaws (Tape Panel)	374
Figure 5.3.17	Gap Flaw from Photomicroscopy 10X.....	376
Figure 5.3.18	Gap Flaw from Photomicroscopy 20X.....	376
Figure 5.3.19	Fiber Fracture Examples 20X	377
Figure 5.3.20	Raw Stress-Strain Curve Example	378
Figure 5.3.21	Illustration for Normalizing for Bending	379
Figure 5.3.22	Representative Plot of Bending Normalized Data	381
Figure 5.3.23	Initial Axial Compression Stiffness for Twist Tape Specimens	384
Figure 5.3.24	Thickness Measurements at the Tabs.....	384
Figure 5.3.25	Initial Axial Compression Stiffness for Twist Tape Specimens Normalized to Bending	385
Figure 5.3.26	Axial Compression Stiffness Comparison Between the Tow Families	386
Figure 5.3.27	Axial Compression Stiffness Comparison Between the Tape Families.....	387
Figure 5.3.28	Curve Fit Example	388
Figure 5.3.29	Onset of Nonlinearity for 50% Overlap Tow Specimens	390
Figure 5.3.30	Nonlinearity Onset Comparison Between the Tow Families.....	391
Figure 5.3.31	Nonlinearity Onset Comparison Between the Tape Families	392
Figure 5.3.32	Strength Comparison Between the Tape Families	394
Figure 5.3.33	Strength Comparison Between the Tow Families.....	395
Figure 5.4.1	Finite element Twist.....	398
Figure 5.5.1	Peak Energy and TOF for Panel with 100% Tow Gap Flaws (Tape Panel)	400
Figure 5.5.2	Peak Energy and TOF for Panel with 50% Tow Gap Flaws (Tape Panel)	400
Figure 5.5.3	Peak Energy and TOF for Panel with 50% Tow Overlap Flaws (Tape Panel)...	400
Figure 5.5.4	Peak Energy and TOF for Panel with Tow Twist Flaws (Tape Panel).....	400
Figure 5.5.5	Peak Energy and TOF for Panel without Flaws (Tow Panel)	401
Figure 5.5.6	Peak Energy and TOF for Panel with 100% Tow Gap Flaws (Tow Panel).....	401
Figure 5.5.7	Peak Energy and TOF for Panel with 50% Tow Gap Flaws (Tow Panel).....	401
Figure 5.5.8	Peak Energy and TOF for Panel with 50% Tow Overlap Flaws (Tow Panel)....	401
Figure 5.5.9	Peak Energy and TOF for Panel with Tow Twist Flaws (Tow Panel).....	402
Figure 5.5.10	Histogram for Panel with 100% Tow Gap Flaws (Tape Panel).....	402
Figure 5.5.11	Histogram for Panel with 50% Tow Gap Flaws (Tape Panel).....	402
Figure 5.5.12	Histogram for Panel with 50% Tow Overlap Flaws (Tape Panel).....	403
Figure 5.5.13	Histogram for Panel with Tow Twist Flaws (Tape Panel).....	403
Figure 5.5.14	Histogram for Panel without Flaws (Tow Panel).....	403
Figure 5.5.15	Histogram for Panel with 100% Tow Gap Flaws (Tow Panel).....	404

Figure 5.5.16	Histogram for Panel with 50% Tow Gap Flaws (Tow Panel)	404
Figure 5.5.17	Histogram for Panel with 50% Overlap Flaws (Tow Panel).....	404
Figure 5.5.18	Histogram for Panel with Tow Twist Flaws (Tow Panel)	405
Figure 5.6.1	Initial Stiffness for Non-Flawed Tape Specimens	407
Figure 5.6.2	Initial Stiffness for 100% Gap Tape Specimens	407
Figure 5.6.3	Initial Stiffness for 50% Gap Tape Specimens	408
Figure 5.6.4	Initial Stiffness for 50% Overlap Tape Specimens	408
Figure 5.6.5	Initial Stiffness for Non-Flawed Tow Specimens	409
Figure 5.6.6	Initial Stiffness for 100% Gap Tow Specimens	409
Figure 5.6.7	Initial Stiffness for 50% Gap Tow Specimens	410
Figure 5.6.8	Initial Stiffness for 50% Overlap Tow Specimens.....	410
Figure 5.6.9	Initial Stiffness for Twist Tow Specimens.....	411
Figure 5.6.10	Initial Stiffness for Non-Flawed Tape Specimens Normalized to Bending.....	411
Figure 5.6.11	Initial Stiffness for 100% Gap Tape Specimens Normalized to Bending.....	412
Figure 5.6.12	Initial Stiffness for 50% Gap Tape Specimens Normalized to Bending.....	412
Figure 5.6.13	Initial Stiffness for 50% Overlap Tape Specimens Normalized to Bending.....	413
Figure 5.6.14	Initial Stiffness for Non-Flawed Tow Specimens Normalized to Bending	413
Figure 5.6.15	Initial Stiffness for 100% Gap Tow Specimens Normalized to Bending	414
Figure 5.6.16	Initial Stiffness for 50% Gap Tow Specimens Normalized to Bending	414
Figure 5.6.17	Initial Stiffness for 50% Overlap Tow Specimens Normalized to Bending	415
Figure 5.6.18	Initial Stiffness for Twist Tow Specimens Normalized to Bending	415
Figure 5.7.1	Onset of Nonlinearity for Non-Flawed Tape Specimens	417
Figure 5.7.2	Onset of Nonlinearity for 100% Gap Tape Specimens	417
Figure 5.7.3	Onset of Nonlinearity for 50% Gap Tape Specimens	418
Figure 5.7.4	Onset of Nonlinearity for 50% Overlap Tape Specimens.....	418
Figure 5.7.5	Onset of Nonlinearity for Twist Tape Specimens	419
Figure 5.7.6	Onset of Nonlinearity for Non-Flawed Tow Specimens.....	419
Figure 5.7.7	Onset of Nonlinearity for 100% Gap Tow Specimens.....	420
Figure 5.7.8	Onset of Nonlinearity for 50% Gap Tow Specimens.....	420
Figure 5.7.9	Onset of Nonlinearity for Twist Tow Specimens.....	421
Figure 5.8.1	Location of Tab Section Thickness Measurements.....	423
Figure 5.8.2	Location of Gage Section Thickness Measurements	423
Figure 5.8.3	Location of Coupon Width and Length Measurements	423
Figure 6.1	Intellex 605 Robotic Arm.....	446
Figure 6.2	ASEA 6L Robotic Arm	447
Figure 6.3	Accuracy Test Path Curves with Theoretical Curve Overlay	448
Figure 6.4	Accuracy Test with Head Rotation	449
Figure 6.5	Fiber Placement Head (Front View)	450
Figure 6.6	Fiber Placement Head (Side View).....	451
Figure 6.7	Spear Exacto Blade	451
Figure 6.8	The Tow placement head configuration.....	454
Figure 6.9	The Tow placement head side view	454
Figure 6.10	The symbolic representation of the Control System	455
Figure 6.11	Iwatsu optical Encoder.....	456
Figure 6.12	BASIC Stamp 2p 24-Pin Module.....	456
Figure 6.13	Motorola HC-11 Micro-controller chip	457

Figure 6.14	Motorola HC-11 Micro-controller chip mounted on board	457
Figure 6.15	12 Volt / 90 Ohm Unipolar Stepper Motor	458
Figure 6.16	Stepper board mounted on the head	459
Figure 6.17	Tow cutting principle with a flat edged blade.....	460
Figure 6.18	Tow cutting principle with a spear type blade	460
Figure 6.19	Tow cutting principle with angled blade.....	461
Figure 6.20	The Xacto cutting blade profile.....	461
Figure 6.21	The cut system assembly.....	462
Figure 6.22	The feed system assembly	462
Figure 6.23	Prototype placement head mounted on KU Intelledex Robot.....	463
Figure 6.24	Prototype placement head – Roller and Linear Actuator	464
Figure 6.25	Prototype placement head – Controller Board and Swing Assembly	465

List of Tables

Table 1.1	The Fiber Placement Application in Modern Vehicles [1]	5
Table 1.2	The detail specification of Viper, FPS-3000 [37]	7
Table 1.3	Advanced Fiber Placement Machine Capacity Comparisons	8
Table 3.1	Comparisons of Fiber Placement Machine with Filament Winding and Tape Laying Machines. ^{1,2,3,4}	75
Table 3.2:	Comparisons of Constant-Rangewise FS Design with Continuous-Topological FS Design.....	84
Table 3.3.1	Comparisons of Structural Optimization Capabilities between DASA/MBB-LAGRANGE with MSC/NASTRAN, and GENESIS based on Fiber Steering Conceptual Design. ^{41 to 49}	93
Table 3.4.1	Configurations of test models based on conventional and fiber steering conceptual designs.....	122
Table 3.4.2	Finite Element and Design Optimization Attributes for Preliminary Studies.....	125
Table 3.4.3	Lists of Number of Layer-Angle Design Variables for Preliminary Studies in Steering I, II, and III Configurations.....	125
Table 3.4.4:	Summary of structural weight savings for preliminary studies using FS conceptual design.	133
Table 3.5.1:	Basic wing geometry of a representative regional jet wing or BGE wing.....	171
Table 3.5.2:	Parameters required for VORSTAB computations of pressure coefficient distributions.....	172
Table 3.5.3:	Attributes of BGE wing substructures.	175
Table 3.5.4:	Finite element and design optimization attributes for representative aircraft structural components.	177
Table 3.5.5:	Lists of number of layer-angle design variables for representative aircraft structural components in Steering II, and III configurations.	178
Table 3.5.6:	Attributes of F22 horizontal stabilator substructures.	183
Table 3.5.7:	Summary of structural weight savings for representative aircraft structural components using FS conceptual design.....	188
Table A1:	Material properties for IM7/8551-7A or Graphite/Epoxy tape.....	219
Table A2:	Material properties for IM7/5260 or Graphite/BMI tape.....	219
Table A3:	Material properties for 2024T3 aluminum alloy sheet.....	220
Table A4:	Material properties for 2024T3 aluminum alloy extrusion.....	220
Table A5:	Material properties for 7075T6 aluminum alloy sheet.....	221
Table A6:	Material properties for 5056 aluminum alloy hexagonal honeycomb.	221
Table 4.5.1	Identification of Available Boeing and Northrop-Grumman Panels	287
Table 4.5.2	Composite Panel and Mechanical Test Specimen Description.....	288
Table 4.5.3	Summary of Radius Identification using Microscopic Method	291
Table 4.6.1	Available Test Specimens for Three Boeing Panels and Six NG Panels.....	309
Table 4.6.2	Test Matrix for Mechanical Test.....	310
Table 4.6.3	Area Ratio for Tabbing Material Samples	312
Table 5.2.1	Material Properties for Tape and Tow Prepreg.....	332
Table 5.2.2	ASTM D 3410 Method B Recommendations [5.4]	352
Table 5.2.3	Recommended Specimen Dimensions [5.4]	352
Table 5.3.1	Critical Stress for Common Tow Flaw Compressive Analyses.....	364
Table 5.3.2	Critical Stress for Common Tow Flaw Compressive Analyses.....	367

Table 5.3.3	Critical Stress for Common Tow Flaw Compressive Analyses.....	371
Table 5.3.4	Attenuation Data	375
Table 5.3.5	Initial Axial Compression Stiffness Raw Data for Tape Specimens	382
Table 5.3.6	Initial Axial Compression Stiffness Normalized Data for Tow Specimens.....	382
Table 5.3.7	Initial Axial Compression Stiffness Normalized Data for Tape Specimens.....	382
Table 5.3.8	Mean Tow Axial Compression Stress for Onset of Nonlinearity	389
Table 5.3.9	Mean Tape Axial Compression Stress for Onset of Nonlinearity.....	389
Table 5.3.10	Mean Tape Values for Laminate Strength	393
Table 5.3.11	Mean Tow Values for Laminate Strength	393
Table 5.8.1	Tape Coupon's Gage Section Thickness Measurements	424
Table 5.8.2	Tape Coupon's Width Measurements.....	425
Table 5.8.3	Tape Coupon's Length Measurements	426
Table 5.8.4	Tape Coupon's Top Tab Section Thickness Measurements.....	427
Table 5.8.5	Tape Coupon's Bottom Tab Section Thickness Measurements	428
Table 5.8.6	Tow Coupon's Gage Section Thickness Measurements.....	429
Table 5.8.7	Tow Coupon's Width Measurements	430
Table 5.8.8	Tow Coupon's Length Measurements	431
Table 5.8.9	Tow Coupon's Top Tab Section Thickness Measurements	432
Table 5.8.10	Tow Coupon's Bottom Tab Section Thickness Measurements	433

1.0 Summary of Objectives & Approach

Fiber placement technology is a modern, automated method of manufacturing composite structure. This manufacturing method has received significant attention recently due to well-documented success in producing complex composite structures in a cost-effective manner. What is not well documented is that the capabilities of existing fiber placement hardware far exceed the capabilities of current design engineering tools, particularly with respect to the ability to fabricate structures exhibiting steered or curvilinear fiber paths. Steered fiber architecture has the potential to offer significant weight savings by improving tailoring of local fiber orientation to the specific internal load path of the structure. However, the lack of robust analytical tools and design environments capable of modeling the complexity of steered fibers in the preliminary design phase are prohibiting optimal design solutions. In fact, the current design approach in industry is to neglect the fact that fiber placement is the chosen manufacturing method, and to design and analyze the structure as though it will be fabricated by conventional hand-layup methods. With this approach, the concept of fiber steering can not be addressed and thus the potential weight advantages can not be realized.

This program enabled development of the basis for an integrated design for manufacturing/fiber steering capability for fiber placement that will achieve optimum structural efficiency while producing affordable primary composite structures. This report describes geometric design tools which encompass the overall process flow and which allow parallel considerations for manufacturability and mechanical performance, thus allowing optimization for cost as well as weight. The modeling of individual tows in a fiber placed part constitutes the challenge addressed by methods presented herein. One method is presented to approximate offset curves on a free form surface using the geometric constraints of the fiber placement process. A second method is presented to approximate a curve on a free form surface that can be used to generate a laminate family ply. We demonstrate that these approximation methods are sufficient for the accuracy of the fiber placement machine. The implemented design system represents the first step towards an integrated design and analysis system that can be used to realize the potential performance enhancements of fiber placed structures.

Analytical methodologies for steered fiber composites are explored through trade study exercises on numerous aerospace structural examples and by experimentally characterizing mechanical performance of such composites. In this paper, the fiber steering (FS) conceptual design has been applied to four test models and three representative aircraft structural components. FS conceptual design, derived from the tow-placed variable-stiffness laminate concepts, calls for the tailorability of curvilinear-family laminates, which involves simultaneous optimizations of both layer thickness and orientation. A curvilinear-family laminate consists of four layers or $[\pm\theta_1, \theta_2, \theta_3]_s$, where each layer is composed of a collective of several plies. Structures exhibiting steered-fiber architecture have been shown to improve load capability and ultimately weight reductions. Optimal structural efficiency in FS promises fabrications of affordable composite structures due to no increase in manufacturing cost.

To demonstrate FS conceptual design, MBB-LAGRANGE, a finite-element and gradient-based optimization routine, is adopted as the analysis tool throughout the project. It has the capability to allow variations of both layer thickness and fiber orientation with respect to the primary load paths. It is configured solely on $[A]$ matrix or composite membrane formulations with several mathematical programming algorithms available for structural optimization.

Although only fiber-related failure modes (longitudinal tension and compression) are granted, MBB-LAGRANGE has proven to be a robust and effective tool in the structural optimization for FS conceptual design. New effective plate elements available with MSC/NASTRAN should be able to duplicate the desired response described within.

Four design configurations, namely Baseline, Steering I, II and III, have been analyzed. All four configurations are composed of symmetric laminates, but each has different balance properties. The objective function is minimum structural weight, while maximum strain failure criterion, upper and lower layer thickness, and $\pm 45^\circ$ angle thresholds are design constraints under different loading cases. Displacement or maximum wing-tip deflection and critical-buckling constraints are also included in some of the models. Weight savings of FS-related configurations (Steering I, II and III) are compared with the baseline conventional design.

The optimal results of FS conceptual design show that weight savings of up to 30% for linear static analysis is attainable, which is primarily based on Steering II configuration. In addition, weight savings associated with Steering I and III configurations are about 25% and 20%, respectively. In most cases, rangewise continuous layer-angle mappings and layer-thickness contours are clearly demonstrated, where the layer thickness and fiber orientation are very load-path sensitive. Although such trade studies are admittedly extreme (generally responding to limited load cases), it is also shown that weight savings on the order of 7% may be realizable on representative in-service structures with multiple loading scenarios. With controllable variable stiffness, these laminates can be made useful in many military and civilian related applications. Incorporated into state-of-the-art fiber placement technology, FS conceptual design will provide a new horizon to composite structural designs at no additional cost. Successful utilization of this concept will benefit both civilian and military related applications.

Mechanical testing illustrates that fiber placed and fiber steered components follow predictable trends for mechanical performance. In particular, trade studies examining fiber steering effects on compression performance illustrate no statistically significant variation in stiffness or strength to steering radii of 46cm. Destructive and nondestructive evaluation experiments reveal higher density occurrences of tow and course edge features, such as overlaps, twists, gaps and fiber waviness. The mechanical response of the effects of these defects is still under investigation. Finally, low-cost benchtop systems for fiber placement manufacturing are described. These have yet to be validated in service, but are necessary to enable fundamental research in the mechanical response of fiber steering, and the effects of defects.

Research activities outlined offer significant increases in design and analysis capability for the fiber placement process. This increased capability has the potential to offer significant weight savings in composite structural applications, at no additional cost. Results from specific research in this activity will serve the greater good by identifying a real potential for expected weight savings on representative aerospace structure, and by providing useful design and analysis tools and methodologies. Other industries will realize the benefits of this research program as they explore the advantages of composite materials and begin to become involved with fiber placement.

1.1 Advanced Manufacturing Techniques And Project Overview

1.1.1. What is Fiber Placement?

Modern aerospace industries are facing the great challenge of affordability. Fiber placement provides the potential to reduce material waste and labor costs in comparison to conventional part fabrication methods. As an example, the material utilization for the Affordable Composite for Propulsion (ACP) engine-cowling program shows 2.5 % to 6.2 % of scrap factor with the fiber placement method [36]. The scrap factor shows the great improvement of material savings comparing with 50%-100% of scrap factor in conventional fabrication methods. In addition, fiber placement offers an opportunity to optimize structural efficiency and to manufacture large and complex parts.

Fiber placement automates the application of numerous pre-impregnated fiber “tows” directly to the tool surface. The tows are fed from the creel, which stores the spools of tow material, to a processing head where the tows are collimated into a continuous band and applied to the tool surface under heat, pressure, and low tension. Fiber placement can fabricate both concave and convex structure. The use of multiple narrow tows and the ability to stop and restart individual tows allows fiber placement to lay-up parts with significant changes in part contour and size and to steer material along a complex surface without buckling the material.

In comparison to fiber placement, tape laying machines are characterized as large NC gantry machines that have a tape laying head and a cassette or roll of material carried on the head. The material is typically 7.62 to 15.24 cm wide. The material is fed off the spool and compacted to the tool surface with a roller. The tape laying machine cuts and restarts the material under preprogrammed control. Since the material is 7.62 to 15.24 cm wide, tape laying is restricted to flat or slightly contoured parts. Parts of moderate to high contour will cause severe wrinkles in the tape. Filament winding machines wind filaments onto a convex mandrel under high tension. The process is restricted to convex shapes because of fiber tension.

The fiber placement machine consists of the spindle, the fiber placement delivery system (head, redirects, and creel), and the off-line programming system. The machine is used to position the fiber placement head. The machine is usually a gantry or side carriage machine with a rotary axis to rotate the collation tool. The machine controller coordinates motion between the machine, collation tool, and the material. The fiber placement delivery system is the specialized hardware that stores and delivers the composite tow. It consists of the creel, which stores the material, the tow, redirects, which guide the material from the creel to the head, and the delivery head, which stops, restarts, and applies the individual tows to the lay-up surface. The off-line programming system provides the means to program a part.

There are many aircraft programs using fiber placement technology to fabricate their structural components. Fiber placement applications in current and in future can be summarized in Table 1.1.

Table 1.1 The Fiber Placement Application in Modern Vehicles [1]

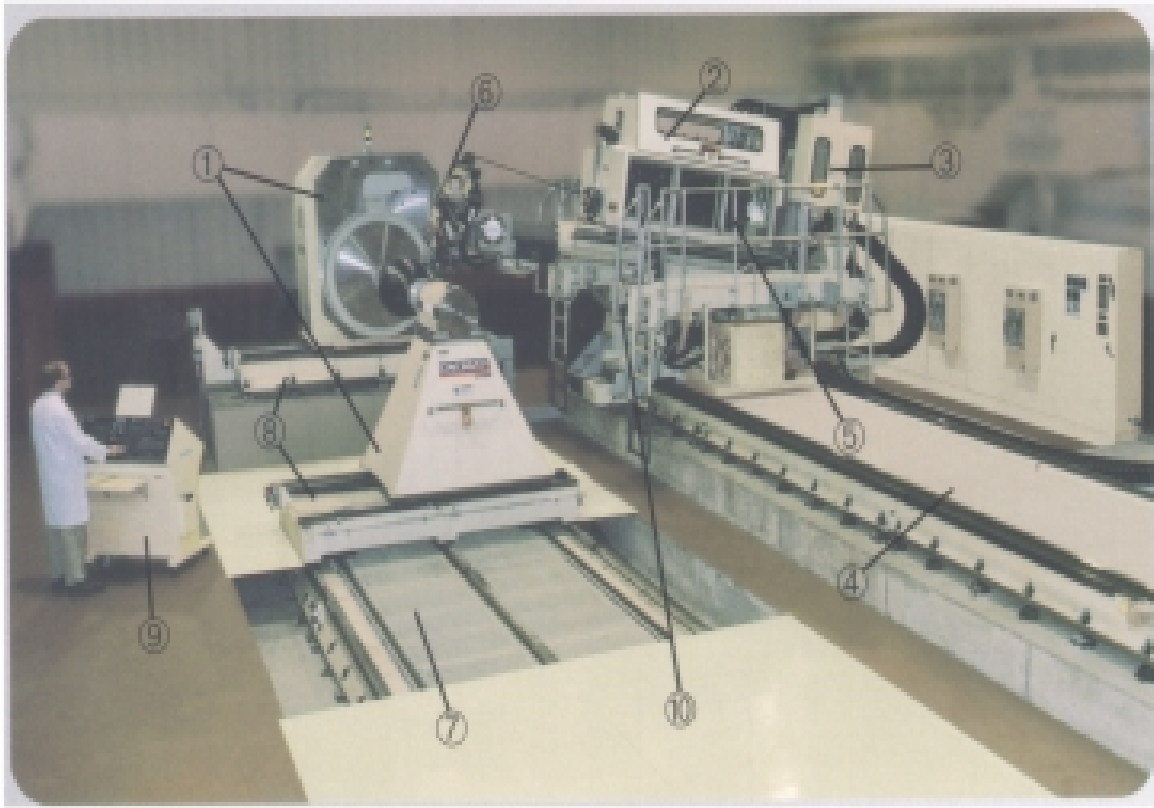
Vehicles	Structural Component	Manufacturer
F/A-18 E/F	Inlet Duct Skins	Alliant Techsystems
	Side Skins	
	Horizontal Stabilator Skins	Alliant Techsystems
C-17	Main Landing Gear Pod Fairing	
T-45A	Horizontal Stabilator Skins	
F-22	Horizontal Spindle Shaft	
V-22 Osprey	Aft Fuselage	Alliant Techsystems
	Side Skins	
	Drag Angle	
	Sponsons	Alliant Techsystems
	Refuel Probe	
Premier 1	Fuselage	Raytheon
	Nose Cone	Raytheon
Airbus	Integrated Inlet Fuselage Duct	Alliant Techsystems
JSF	Intake Duct, Fuselage Skin	
Airbus A3XX	Nacelle	Airbus
	Rear Fuselage Skin	
	Pressure Bulkhead	
X-33	Liquid Oxygen Tank	Alliant Techsystems
CH-47	Fuel Tank Shell	Alliant Techsystems

1.1.2 Machine Description

In this section, two different fiber placement machines manufactured by Cincinnati Milacron and Ingersoll will be described.

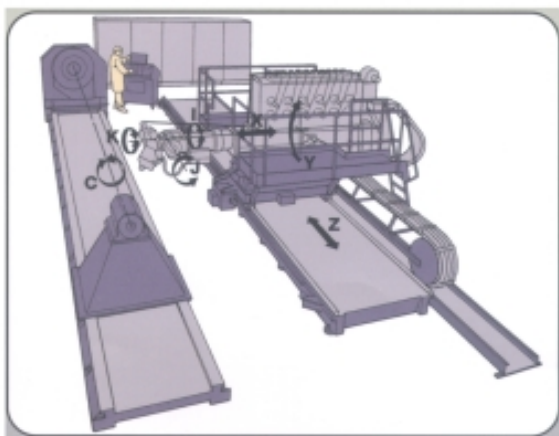
1.1.2.1 Cincinnati Milacron Fiber Placement Machine

The fiber placement machine used by Northrop Grumman is designed and manufactured by Cincinnati Milacron and called “Viper FPS-3000” The Viper is a seven-axis machine that uses six axes to position the fiber placement head and the seventh axis rotates the lay-up mandrel. The FPS-3000 has two work stations with independent headstocks allowing two mandrels to be loaded and processed. The two work station configuration prevents manual operations or lengthy inspection operations from impacting the utilization of the machine. Figure 1.1 shows the schematics of Viper FPS-3000 and the definition of seven axes. The Cincinnati Milacron machine can hold mandrels 78 cm long and 365 cm in diameter. With two mandrels in the machine, the maximum combined length of the mandrels is 1148 cm. Each individual mandrel can weight 18,000 kg with an inertia of 230.424 cm-kg/sec. The FPS-3000 is designed for twenty-four or thirty-two 0.318 cm wide tows. The main axis of the machine along the length of the mandrels has 860 cm of travel. The position of the headstock and tailstock can be automatically adjusted up to 120 cm perpendicular to the mandrel axis to accommodate different mandrel diameters. The detail specification of the Viper can be seen in Table 1.2. [37].



1. Heavy-Duty Headstock and Tailstock, 2. Creel Enclosure, 3. Backing Film Recovery System, 4. Modular Machine Beds, 5. Programmable Electronic Bi-Directional Tensioner, 6. Computer-Controlled Placement Head, 7. Tailstock Beds, 8. X-Prime Axis, 9. Advanced Computer Control, 10. Pendant

A) The Schematic of Viper, FPS-3000



- Crossfeed (X-axis): 34000 mm/min, 150cm travel
- Arm Tilt (Y-axis): 2.2 rpm, 30° travel
- Carriage (Z-axis): 50800 mm/min, 860cm travel
- First Head Axis(Yaw: I): 8800°/min, 210° travel
- Second Head Axis (Pitch: J): 6300°/min, 100° travel
- Third Head Axis (Roll: K):

B) The Definition of 7-axes

Figure 1.1 The Schematics of Viper FPS-3000 and Axis Definition [37]

Table 1.2 The detail specification of Viper, FPS-3000 [37]

Section	Categories	Specification
Crossfeed	Acceleration Repeatability Accuracy	0.76 m/sec^2 0.05 mm $\pm 0.17 \text{ mm/m}$
Arm Tilt	Acceleration Repeatability Accuracy	$15^\circ/\text{sec}^2$ 20 arc sec $\pm 40 \text{ arc sec}$
Carriage	Acceleration Repeatability Accuracy	1.00 m/sec^2 0.05 mm $\pm 0.17 \text{ mm/m}$
Mandrel	Repeatability Accuracy	18 arc sec $\pm 36 \text{ arc sec}$
Application	Number of Tows Fiber Bandwidth Fiber Placement Speed Ply Orientation Accuracy	24, 32 10 cm 5000 to 30000 mm/min $\pm 0.5 \text{ deg}$
Material	Form Width Thickness, uncured Core Inside Diameter Diameter of Spool (max) Weight of Spool (max)	Tow/tape impregnated with thermoset resin $3.175 \text{ mm} \pm 0.254 \text{ mm}$ 0.152 to 0.254 mm 23cm to 28cm 20cm w/ 7.6cm core I/D or 25.4cm w/15cm core I/D 11 kg

The fiber delivery system is attached to a large tilt-crossfeed (horizontal gantry) robot and consists of the creel, the cut-clamp-restart head, and the tow redirects. The refrigerated creel holds twenty-four or thirty-two spools of composite tow and maintains a constant temperature of 35°F . The creel is located on the top of the machine behind the head. The fiber placement head (Figure 1.2) is a complex mechanism that applies the tows to the collation tool. The tow redirect determines the path of the tows between the creel and head preventing the tows from becoming tangled. The tension control system is the most critical component in preventing the tows from angling during machine motion. The tensioning system has hi-directional tensioning motors and tension sensors.

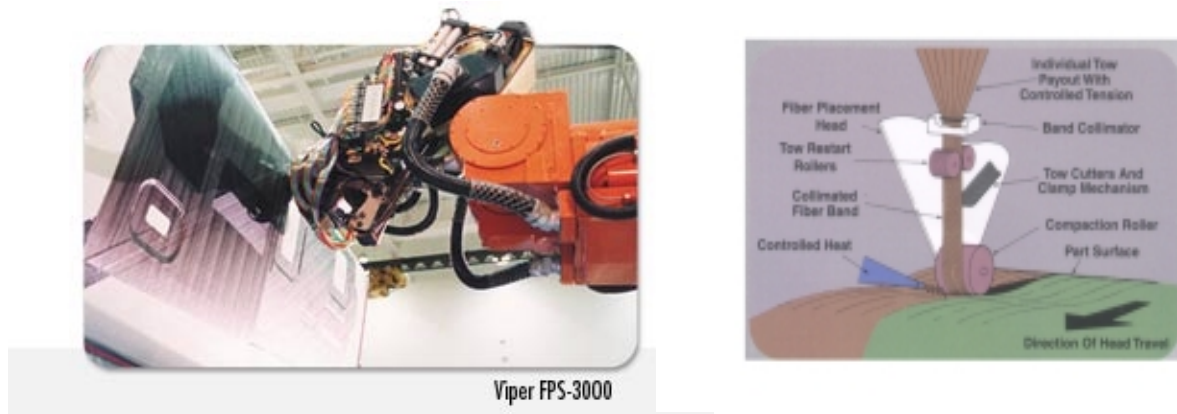


Figure 1.2 Viper(FPS-300) Fiber Placement Machine Head [37]

1.1.2.2 Ingersoll Fiber Placement Machine

Another fiber placement used in many industries like Boeing is designed and manufactured by Ingersoll Milling Machine Company. The Ingersoll multi-axis fiber placement machine utilizes seven axes, six machine axes to properly position the fiber placement head and one axis to rotate the lay-up tool.

The headstock and tailstock on the Ingersoll machine are used to secure and rotate the lay-up tool. Their housings mount to a supporting bedway that runs the length of the Z-axis. The headstock is fixed in position and contains the motor and gearbox to rotate the lay-up tool. It is equipped with a low gear to handle high inertia parts. The tailstock can be driven along the bedway to adjust for different length tools and then manually clamped once it is positioned. The head and tailstock can support an 36,363 kg tool with a maximum inertia of 576,059 cm. kg/sec. A list of Cincinnati-Milacron and Ingersoll fiber placement machines currently in use and their capacities is shown in the following Table 1.3.

Table 1.3 Advanced Fiber Placement Machine Capacity Comparisons

Owner	Manufacturer	Max Diameter (cm)	Max Length (cm)	No of Tows	Tow Width (cm)
Boeing— Seattle	IMMC	50.8	190.5	32	0.318
Boeing— Auburn	IMMC	50.8	95.3	24	0.318
Boeing—St. Louis	IMMC	50.8	96.5	12 or 32	0.462
Boeing— Philadelphia	CMI	30.5	72.39	24	0.318
Bell— Fort Worth	CMI	10.2	38.1	12	0.318
CMI— Cincinnati	CMI	33.0	88.9	24	0.318
Raytheon—Wichita	CMI	33.0	163.8	24	0.318
Northrop— LA	CMI	31.8	78.7	20	0.399
Northrop— Milledgeville	CMI	38.1	101.6	24/20	0.318/0.399
Thiokol — Huntsville	CMI	17.8	76.2	12	0.318
Alliant – West Virginia	CMI	24.5	132.8	12	0.318

1.2. What is Steered Fiber Composite?

Fiber steering is a modern composite manufacturing technique. Steered fiber architecture has the potential to offer significant weight savings by tailoring the local fiber orientation to the specific internal load path of the structure. The shape of modern aircraft structure needs highly nonlinear curvature in order to achieve better aerodynamic characteristics. The higher curvature in the laminate makes more misalignments of fiber orientation from the force axis. This is the cause of the higher safety factor requirement in composite structural design. The fiber steering technique provides a preferred solution in this problem since the steered fiber orientation can be designed along the local force axis.

Although the steered fiber architecture is a reasonable technique for fabrication it needs more design development and more testing to demonstrate material properties because of the complexity of steering characteristics. The initial investigation of fiber steering technique shows great improvement in feasibility and affordability compared with conventional fabrication methods. As discussed already, the fiber placement technique shows an improvement in material saving compared to the conventional fabrication method. The fiber steering technique provides approximately 3 % additional weight savings compared to the fiber placement technique in analytical models. [38]

The fiber placement machine can tow steer due to its capability to feed out individual tows at unique speeds. The machine moves over the entire width of the path in the same amount of time and the tows on the outside of the curve must feed out faster than the tow on the inside to prevent the band from wrinkling or buckling because the inside and outside edges of a curved path have different lengths. The capability of tow steering depends not on machine capability, but on acceptable deformation of tow material. The buckling or wrinkling of the laminate may be a function of lay-up speed, compaction force, temperature, tow width, and steering radius. All these possible factors must be investigated to determine the mechanical property of the laminate. The effect of tow width variation was investigated by Draper Laboratory [9]. The result shows the minimum allowable material width to avoid wrinkling was found to be 1.27 cm. Figure 1.3 shows the results from tape minimum radius of curvature steering tests.

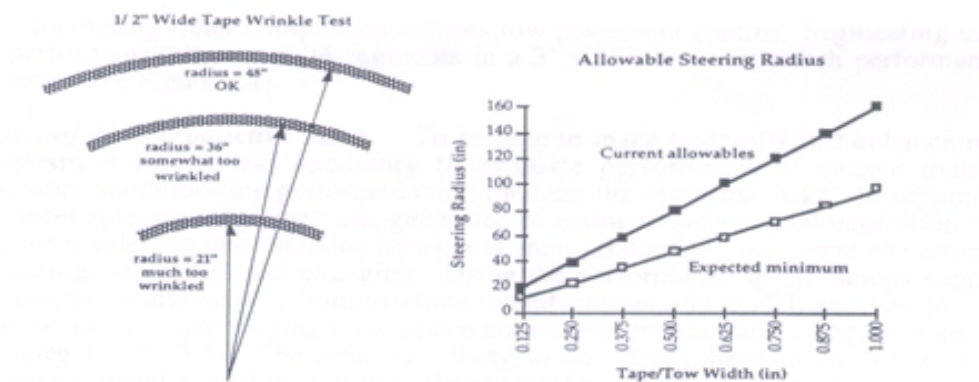


Figure 1.3 Results from Tape Minimum Radius of Curvature Steering Tests [9].

1.3. Overview of SCADS Project

The main objective of SCADS project is to develop an integrated design for manufacturing/fiber steering capability for fiber placement that will achieve optimum structural efficiency while producing affordable primary composite structures. This will be achieved by developing analytical methodologies for steered fiber composites, and by experimentally characterizing mechanical performance of such composites. Design tools which encompass the overall process flow and which allow parallel considerations for manufacturability and mechanical performance will be developed, thus allowing optimization for cost as well as weight.

Research activities outlined offer significant increases in design and analysis capability for the fiber placement process. This increased capability has the potential to offer significant weight savings in composite structural applications, at no additional cost. Results from specific research in this activity will serve the greater good by identifying a real potential for expected weight savings on representative aerospace structure, and by providing useful design and analysis tools and methodologies.

The research activities in this SCADS project consists of four main tasks, described in subsequent sections: Development of Object-Oriented Design Software and Integration, Structural Design and Analysis tool development, Feature Identification, Nondestructive Evaluation (NDE) and Mechanical Testing and Low Cost Fiber Placement/Composite Panel Manufacturing. Figure 1.4 shows the schematics of SCADS project.

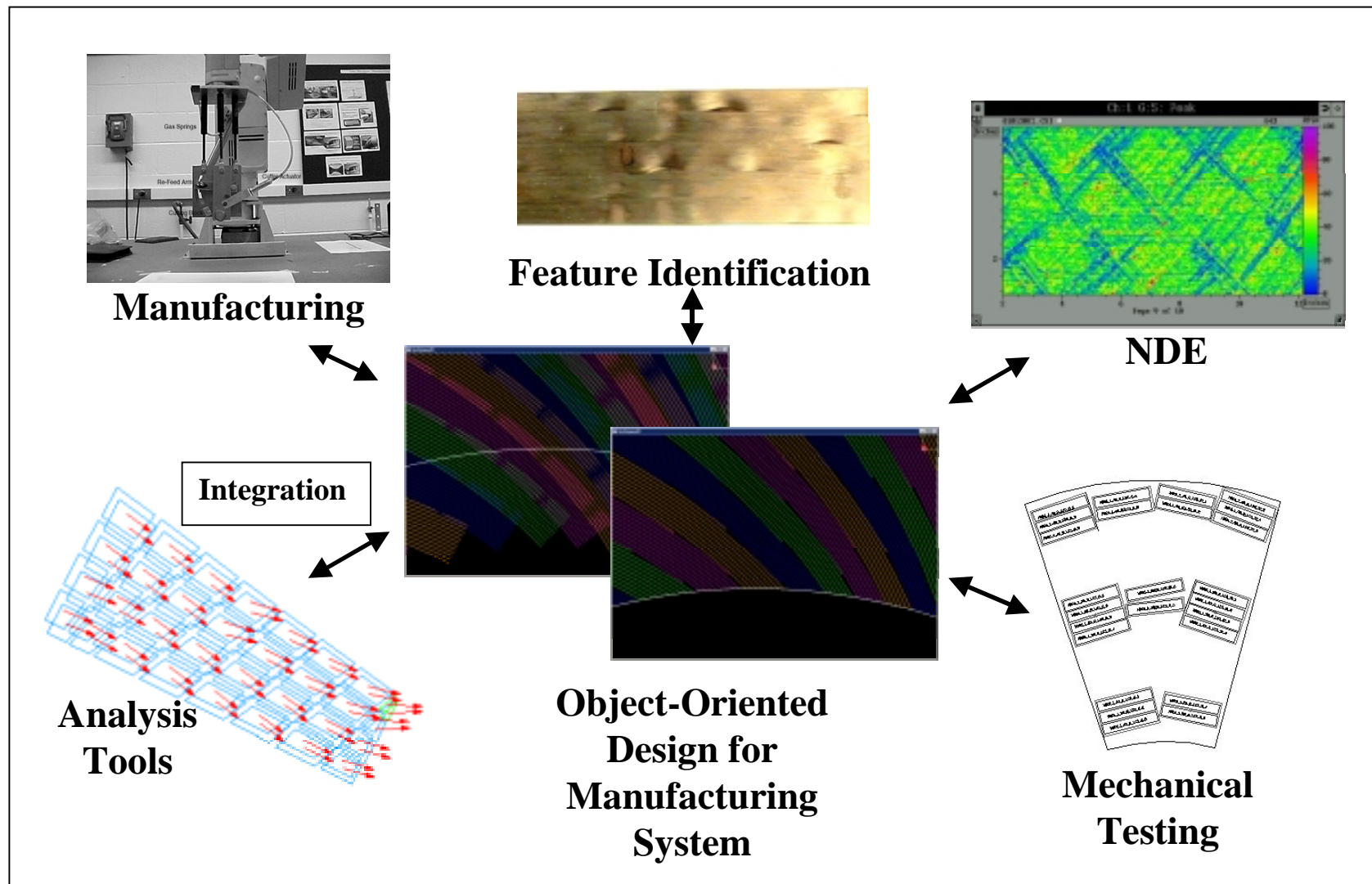


Figure 1.4 Schematics of SCADS Project

2.0 Approximate Geometric Methods for the Modeling of Offset Curves and Laminate Family Curves in Application to Fiber Placed Composite Structure

2.1.0. Introduction

A composite structural material is constructed from two or more materials combined on a macroscopic level, as opposed to the microscopic combination of metal alloys. In many structural applications, composite materials offer higher strength to weight and stiffness to weight ratios than conventional materials, and thus have been used widely in aerospace applications since the 1970's. Composite materials are used to increase strength and save weight in airplane types ranging from remotely piloted micro air vehicles, to high performance military fighters, to the newest designs for jumbo passenger jets. While more and more composite materials are used in aerospace and other engineering applications, new materials and manufacturing techniques continue to be developed, oftentimes ahead of a full understanding of the resulting material properties.

One such composite manufacturing technique is fiber placement. The basic component of a fiber placed part is the tow. The tow consists of a long and narrow (~0.125 inch) strip of resin impregnated fiber, about 0.01 inches in thickness. The minimum length of the tow is limited by the fiber placement machine- usually 4.0 inches. The maximum length of a tow is limited only by the amount wound on the supply spool- typically in excess of 10,000 feet. The tow itself consists of thousands of hair-like fibers aligned along the length of the tow and impregnated with resin. When cured with heat and pressure, the resin impregnated tow imparts strength and stiffness along its length. A fiber placement machine delivers from one up to approximately 30 adjacent tows in a single pass of the machine head. The tackiness of the tows allows them to be compacted onto a surface, which can contain concave or convex features, although concavity is limited by the head geometry. The adjacent tows placed by the fiber placement machine in a single pass are known as a course. Figure 2.1.1 shows a schematic of the fiber placement machine head placing a single course. Multiple courses placed alongside each other form a single layer, known as a ply, of the composite tow material. Multiple plies are placed atop each other to impart thickness to the shell-like structure.

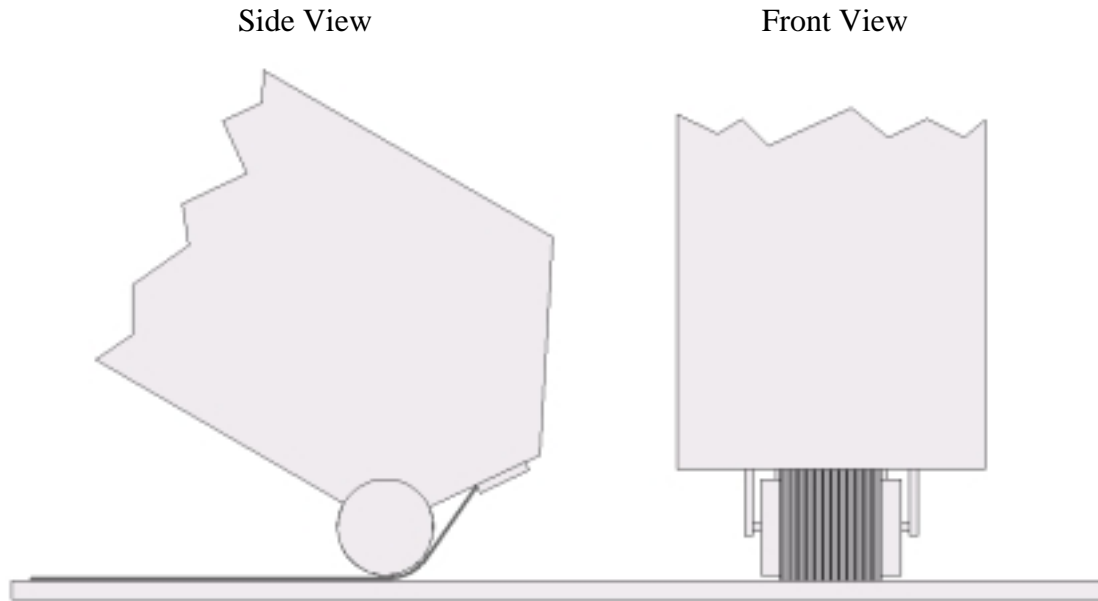


Figure 2.1.1 Fiber Placement Head Delivers Multiple Tows in a Course

Each tow in a course can be independently cut (dropped) or restarted (added). This capability allows precise control over the amount of material placed on the structure, and hence can be used to precisely manufacture differing thickness regions on the part. In addition to drop and add capabilities, the feed rate of each tow is individually controlled, allowing a curved course with tows at the outside of the curve to be fed faster than those on the inside of the curve (see Figure 2.1.2). The ability to feed tows at differential rates allows the fibers of the tow material to be steered in a relatively tight radius without buckling the tow material. Steered fibers can thus be aligned with the calculated loads of the entire structure, allowing continuous orientation of fibers along the load paths of the structure.

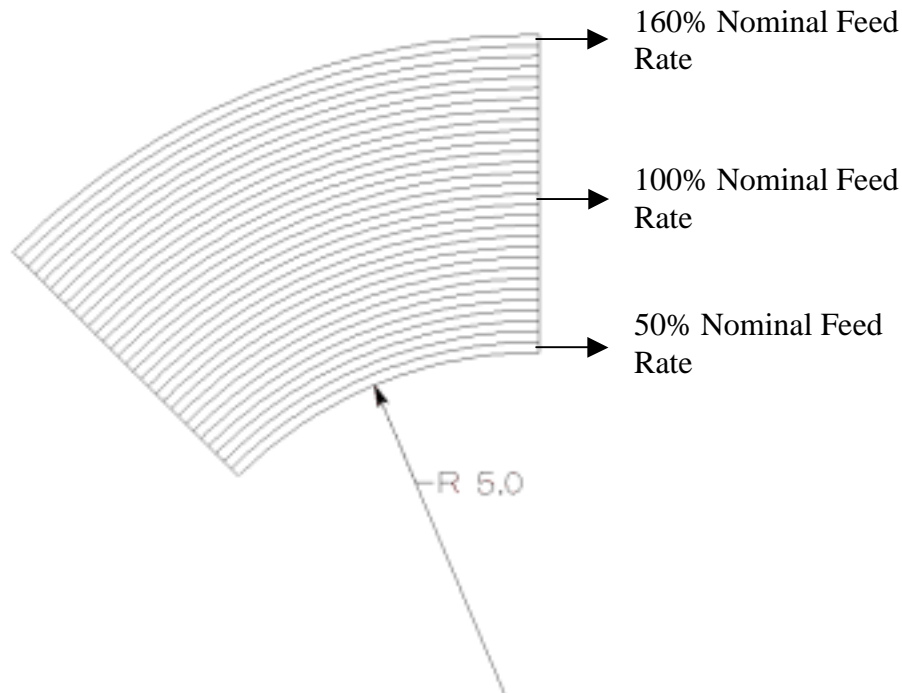


Figure 2.1.2 Steered Course Illustrates Difference in Feed Rate Across Tows in the Course

Fiber placement manufacturing techniques offer the capability of precise fiber orientation control, and hence strength tailoring, that had not been available previously. Although the prospect of structural weight savings is very attractive to the aerospace industry, fiber placement's potential cost savings over other manufacturing techniques is perhaps the more powerful force driving its use at this time. Fiber placement manufacturing typically produces 2% to 15% scrap, as compared to 50% to 100% scrap for the traditional technique of draping resin impregnated cloth by hand layup [¹]. Where hand layup techniques trim away excess material, the drop and add capability of fiber placement avoids much of the excess material altogether. Additionally, the mechanized process of fiber placement offers the assurance of repeatability that is not possible with hand layup techniques on free form surfaces. Thus, costs associated with part inspection are greatly reduced.

The cost savings associated with scrap rates and process repeatability represent manufacturing cost savings that currently motivate the use of fiber placement manufacturing technologies. In addition to these manufacturing cost savings, the potential weight savings associated with curvilinear fiber paths represent operational cost savings much greater than those of manufacturing. Currently, those potential operational savings cannot be realized because of a lack of engineering design tools allowing the consideration, during the preliminary design phase, of curvilinear fiber paths in a fiber placed part. Fiber placed designs are generated assuming that they will be constructed using conventional hand layup methods. Details of tow geometry are

¹. Hale, R. D. *Excerpts From the Technical Proposal for Integrated Design and Analysis Tools for Reduced Weight, Affordable Fiber Steered Composites*. University of Kansas Flight Research Laboratory, KU-FRL-22480-1. 1 September, 1999.

currently obtained, after component design release, using the offline programming system of the fiber placement machine.

In a similar manner to Computer Numerical Control (CNC) machining, a fiber placement machine includes a programming system to plan the motions of the machine. Given a surface on which to place tows, a curve representing ideal fiber orientation, and specification of orientation control method; the offline programming system computes the path that the machine will take as it lays down each course. Currently, design capability for fiber placed parts resides within the offline programming system of the machine. Because the offline programming system only computes course paths, individual tow path information is not available during design. A need exists for a design tool that models the fiber placed part down to the level of the tow. Such a tool, when coupled with current finite element analysis (FEA) capabilities, will allow the engineer to generate multiple design solutions for a single part, evaluate those solutions, and choose the best one for production.

Modeling individual tows in a fiber placed part constitutes the first of the challenges addressed by the methods presented in this thesis. The only modeling tool currently available is the offline programming system of the fiber placement machine itself. As mentioned above, the offline programming system computes paths representing courses, but not individual tows. In addition, current offline programming systems convert free form surfaces to a discretized mesh on which the course paths are calculated. Meshing accuracy (the distance between a mesh element surface and the free form surface) has been found to be as loose as 0.050 inch [²], which translates to similar errors when calculating course paths. These errors result in unanticipated gaps or overlaps in tow material that must be detected *after* the part is manufactured.

One method presented in this thesis uses the free form surface, as produced by a CAD system, to approximate curves representing individual tows in the fiber placed part. Given the free form surface on which tows will be placed and a curve representing an initial fiber path, a method is presented that approximates a series of offset curves on the surface. The method is used to represent the position of individual tows in the fiber placed part. By approximating curves on the actual design surface, our method avoids unanticipated gaps and overlaps associated with a discretized surface. It should be noted that the method is specifically motivated by, and limited to, a domain where the offset distance between curves is no more than half the local radius of curvature of features on the surface.

A second challenge addressed by this thesis is that of fiber orientation in the offset load direction. As mentioned previously, a frequent design goal is to orient tows in a continuous manner along the primary load path of the structure. In addition, there will generally be loads in directions other than those of the primary load path. In composite design, the fibers in each ply can be oriented along the primary load path, or at a fixed angle to the primary load path. A ply where fibers are aligned along the primary load path is known as a 0° ply. A common practice is to orient additional plies at 90°, 45° and -45° to the primary load path. Local loads can always be resolved to principal components of axial, transverse and shear loads. 0° is best for axial

². The Boeing Company. *Fiber Placement Benchmark and Technology Roadmap*. Report 99P0028. 15 July, 1999.

load, 90° for transverse, and $\pm 45^\circ$ for shear. A ply containing tows aligned at a fixed angle to the primary load path is known as a laminate family ply. The goal of the composite designer is to design a through-the-thickness sequence of 0° and laminate family plies that meets the strength requirements of the part. In a fiber placed part, where tows of the 0° ply are placed along a curved primary load path, a challenge is to model a ply to the definition of a laminate family ply.

The second method presented in this thesis is used to approximate a laminate family curve. The method uses each tow representation in the 0° ply to calculate a piecewise linear curve that preserves a fixed angle of intersection between the laminate family curve and each tow in the 0° ply. By preserving the angle of intersection between the laminate family curve and tows in the 0° ply, the fiber orientation of the laminate family ply can be kept constant.

Fiber placement manufacturing techniques present an unrealized potential for increased performance and reduced cost through weight savings due to tailoring of fiber orientations to loads within a structure. To realize this potential, design engineers must be able to model and analyze the fiber placed part down to the level of the tow. A need exists for a system that allows the design engineer to perform such modeling independent of the fiber placement machine itself. The modeling of individual tows in a fiber placed part constitutes the challenge addressed by methods presented in this thesis. One method is presented to approximate offset curves on a free form surface using the geometric constraints of the fiber placement process. A second method is presented to approximate a curve on a free form surface that can be used to generate a laminate family ply. These methods have been implemented in a design system that enables the design, to the tow level, of fiber placed structures. We demonstrate that these approximation methods are sufficient for the accuracy of the fiber placement machine. The implemented design system represents the first step towards an integrated design and analysis system that can be used to realize the potential cost savings and performance enhancements of fiber placed structures.

2.1.1 Organization

The remainder of this chapter is organized into six sections. Section 2.2 presents a summary of previous work in the areas of offset curves on surfaces, and modeling systems for the domain of composite fabrication. We formally define the offset curve on surface and the laminate family curve in Section 2.3. Methods to calculate piecewise linear approximations of both offset curves and laminate family curves are also presented in Section 2.3. The error of our approximation methods is addressed in Section 2.4. A closed form solution is derived for the error of placing offset curves on a surface with circular arc cross section. For a surface with arbitrarily curved cross section, we present an approximate method of calculating offset error.

The approximation methods of Section 2.3 have been implemented in SCADS, a design and analysis system for fiber placement. In Section 2.5, the SCADS system is described and an example of ply design is presented. Section 2.6 presents a verification of the offset curve and laminate family curve approximation methods, and confirms the error associated with them. Finally, work related to design tool development is summarized in Section 2.7, and recommendations for further work are proposed.

2.2.0. Related Work

The development of a system to aid in the design of fiber placed structures has involved effort in two broad areas: development of geometric methods to approximate the position of individual tows within a fiber placed structure, and implementation of those methods into a software package providing an integrated design and analysis capability. The approximation of tows placed on the tool surface of a fiber placed part is a similar problem to offset curve generation problems generally, and specifically to offset curve generation on a surface. The generation of general offset curves has received a considerable amount of research effort. Section 2.2.1 concentrates on the area of offset curves on a surface. The development of integrated design and analysis software in the domain of composite structures is presented in Section 2.2.2.

2.2.1. Offset Curves on a Surface

The calculation of a piecewise linear approximation of a fiber placed tow on a placement surface is a problem similar to the generation of tool paths for a 5-axis Computer Numerical Control (CNC) milling machine. 5-axis CNC milling is used to machine free-form surfaces. The 5-axis CNC machine allows the machining tool to be positioned anywhere on the free-form surface, in a similar manner to the fiber placement machine head. Using a CAD/CAM package, curves are calculated on the free form surface, and points are generated corresponding to cutter location (CL points). The CNC machine recreates the curve on the surface by interpolating the points with the cutting tool. Because the machining tool can only mill a narrow band on the surface, multiple tool paths are required. It is desired that the tool ‘work’ (i.e. grind, cut, etc) over its entire path, avoiding paths that pass over previously machined areas. This leads to the desire to use offset curves on the surface to generate tool paths.

This section presents four methods that have been used to generate approximate offset curves on a design surface:

- Iso-parameter offsets
- Iso-planar offsets
- Iso-scallop offsets
- Machining strip width offsets

Figure 2.2.1 shows a cross section of a design surface under CNC machining. The design surface is a simple circular cross section. A ball end milling tool is represented by a half circle. Other tools, with non spherical shapes, are possible. Figure 2.2.1 shows the ball end tool at the same cross section in two adjacent paths. The straight line distance between adjacent paths is the side-step distance. The CNC milling process removes material on each path, approximating the shape of the design surface. The excess material remaining between two adjacent tool paths is

known as a scallop. The height of the scallop is shown as 'h' in Figure 2.2.1. The scallop height is affected by both the side-step distance and the curvature of the design surface.

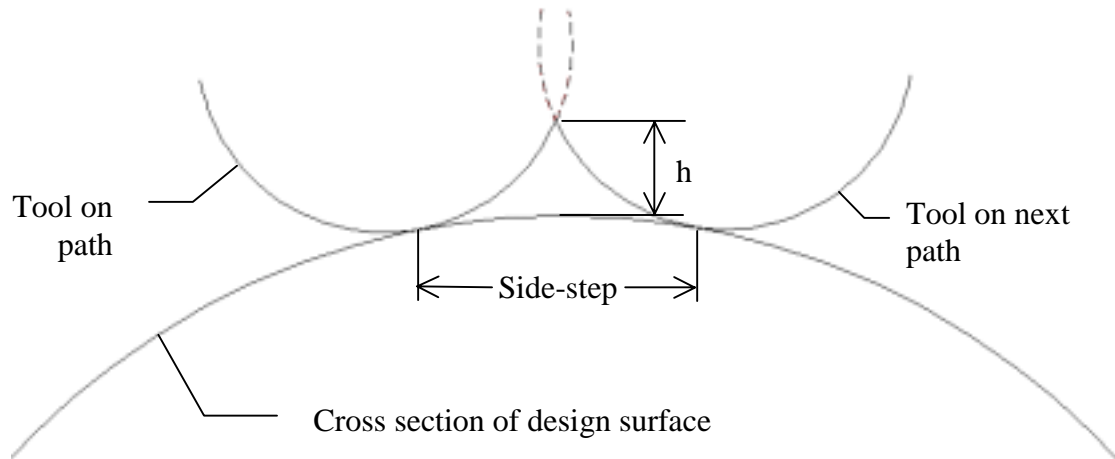


Figure 2.2.1 CNC Milling Parameters

The first methods used to calculate offset paths utilized iso-parameter lines of parametric surfaces. Given a surface $S(u, v)$, where a Cartesian point on the surface is expressed by $(X(u, v), Y(u, v), Z(u, v))$, an iso-parameter curve corresponds to a constant value of one of the parameterization variables. For purposes of this discussion, we will assume that the iso-parameter curve results from holding the parameter v constant. An offset curve results by adding a constant value to v : $(v + \Delta v)$. Two early examples of Computer Aided Design/Computer Aided Manufacturing (CAD/CAM) systems use iso-parameter offset curves for tool path generation. An unnamed system was developed by Broomhead and Edkins at the University of Manchester Institute of Science and Technology [3]. Computer Interactive Surfaces Pre-APT (CISPA) was developed at Lehigh University by Loney and Ozsoy [4]. The challenge for both systems was to generate offset curves in parameter space that did not violate constraints in Cartesian space.

Broomhead and Edkins recognized that scallop height between adjacent tool paths varies with surface curvature, and that scallop height cannot be kept constant while tracing iso-parameter curves. It was also recognized that the distance, on the surface, between two iso-parameter curves varies along the curves. Both systems considered a single iso-parameter curve for each pass of the CNC tool. Therefore, the authors developed a method of iteratively considering points on an existing tool path to find a parameter space side-step (Δv) that results in a bounded scallop height between that tool path and the next candidate. On surfaces where the

³. Broomhead, P. and Edkins, M. Generating NC Data at the Machine Tool for the Manufacture of Free-form surfaces. *International Journal of Production Research*. Vol 24. Jan/Feb, 1986. ns 1.1-14

⁴. Loney, G. C. and Ozsoy, T. M. NC machining of free form surfaces, *Computer Aided Design*. Vol 19, n 2. March, 1987. pp 85-90

distance between iso-parameter lines varies, this method results in over machining where the distance decreases between iso-parameter lines on the surface.

The CISP system utilizes bicubic Coons patches to represent the design surface. As with Broomhead and Edkins' system, CISP calculates side-step in parameter space such that the scallop height is bounded. CISP assumes that the surface patch cross section between adjacent tool paths is approximated by a circular arc. The method samples the iso-parameter curve at $u = 0.0, 0.25, 0.5, 0.75$ and 1.0 (where $u \in [0.0, 1.0]$) to calculate the side-step distance (Δv) resulting in an acceptable scallop height. It is assumed that the patches are "not so severely deformed" that the above five samples will not produce the correct result.

A more recent use of iso-parametric curves for offset tool path generation is developed by Xia and Ge [5]. The method uses kinematics fundamentals to create an analytic representation of the swept section of the tool as it traverses a tool path. The analytic representation of the swept section is based on previous work [6]. That representation is then used to exactly determine the side-step in parameter space that will result in a scallop height that does not exceed the maximum allowable.

Two drawbacks of using iso-parameter curves to generate offset curves on the design surface are: the distance between iso-parameter curves in Cartesian space can vary significantly, which can result in 'over machining' areas of the surface where iso-parameter curves get closer in Cartesian space; and the choice of tool path direction is limited to the directions of the two parameterization variables. Huang and Oliver attempt to overcome these drawbacks by using surface-surface intersections, between the design surface and a plane, as the curves from which CL points are generated [7]. The method is called iso-planar tool path generation. In a manner similar to Broomhead and Edkins', the plane intersection method considers points on an existing tool path to generate candidate offset planes. The method chooses the plane that results in a generated tool path with a bounded scallop height. It can be seen from inspection of Figure 2.1 that, to keep the scallop height constant, increased curvature of the design surface cross section results in decreased side-step distance. Thus, if the plane offset is sized by an area of the surface with high curvature, over-machining may still occur on areas with little curvature. In addition, Huang and Oliver admit that their offset plane method is more computationally intensive than the iso-parameter curve methods, but consider that drawback to be outweighed by the added flexibility in tool-path direction and more efficient use of the machining tool. Another problem is that the original tool path can't be adapted to the design surface- it must be a plane-surface intersection.

⁵. Xia, J. and Ge, Q.J. An exact representation of effective cutting shapes of 5-axis CNC machining using rational Bezier and B-spline tool motions. *Proceedings - IEEE International Conference on Robotics and Automation*, v 1, 2001. 2001 IEEE International Conference on Robotics and Automation (ICRA), May 21-26 2001. Seoul. pp 342-347

⁶. Ge, Q. J. Kinematics-driven geometric modeling: a framework for simultaneous NC tool-path generation and sculptured surface design. *Proceedings - IEEE International Conference on Robotics and Automation*, v2, 1996, *Proceedings of the 1996 13th IEEE International Conference on Robotics and Automation. Part 2 (of 4)*. Apr 22-28 1996. Minneapolis, MN, USA. pp 1819-1824

⁷. Huang, Y. and Oliver, J. H. Non-constant parameter NC tool path generation on sculptured surfaces. *Computers in Engineering - 1992, Proceedings of the 1992 ASME International Computers in Engineering Conference and Exposition*. Aug 2-6 1992. San Francisco, CA, USA. pp 411-419

Another offset tool path generation method is motivated by a desire to avoid over-machining of parts- or passing the machine tool over areas that have already been machined. This is common with iso-parameter tool path generation when iso-parameter curves become closer together in Cartesian space. This is also a problem with iso-planar tool path generation when plane offset distance is dictated by design surface areas with small radii of curvature. A method of avoiding this type of over-machining was developed by Suresh and Yang [⁸] who attempt to keep the scallop height constant between adjacent tool paths. The method generates CL points on an adjacent tool path using the CL points of a reference path. At each CL point $P_0 = S(u_0, v_0)$, on the reference path, the curvature of the design surface is calculated. Given the cross section of the oriented cutting tool, the method calculates Δu and Δv in the surface parameter space such that a new point $P_1 = S(u_0 + \Delta u, v_0 + \Delta v)$ results in the desired scallop height, and $P_1 - P_0$ is perpendicular to the reference tool path. Thus, the method considers the local properties of the design surface when calculating the local offset to a reference curve. The offset tool path will not generally lie at a constant distance along the surface from the reference tool path unless the curvature of the design surface cross section is constant along the tool paths.

A natural extension to the method of Suresh and Yang is presented by Sarma and Dutta [⁹]. Instead of maintaining a constant scallop height, Sarma and Dutta allow a functional definition of a constantly varying scallop height. Again, though, the offset tool path is generated in a piecewise manner using the individual CL points of the reference tool path and local design surface properties.

The final offset method discussed is similar to the scallop height specified method described above. Instead of considering the scallop height between tool paths, the method considers machining strips- the actual material surface that lies within a specified offset of the design surface after the machine tool has passed. The concept of the machining strip is based on Li and Ji's work [¹⁰]. The machining strip has a defined width at any point on the tool path. The optimal offset distance between two tool paths becomes the sum of the machining widths portions between the tool paths. Lee uses this relationship to generate CL points of an offset tool path from those of a reference tool path [¹¹].

Chiou and Lee combine Lee's machining-width offset method with a method for determining a 'best' initial tool path curve from which offsets are calculated [¹²]. Given the initial tool path, the method generates offset tool paths, using the machining strip offset method, until the machining strip width of an offset tool path falls below a specified minimum. At that time, the method determines another initial tool path for the unmachined portion of the part. It is

⁸. Suresh, K. and Yang, D.C.H. Constant scallop-height machining of free-form surfaces. *Journal of Engineering for Industry, Transactions of the ASME*. Vol 116, n 2. May, 1994. pp 253-259

⁹. Sarma, R. and Dutta, D. Geometry and generation of NC tool paths. *Journal of Mechanical Design, Transactions Of the ASME*. Vol 119, n 2. June, 1997. pp 253-258

¹⁰. Lee, Y. S. and Ji, H. Surface interrogation and machining strip evaluation for 5-axis CNC die and mold machining. *International Journal of Production Research*. v 35, n 1. Jan, 1997. pp 225-252.

¹¹. Lee, Y.S. Adaptive tool path planning by machining strip evaluation for 5-axis complex surface machining. *Transactions of NAMRI/SME*. Vol 26. 1998. pp 141-146.

¹². Chiou, C.J. and Lee, Y.S. A Machining Potential Field Approach to Tool Path Generation for Multi-Axis Sculptured Surface Machining. *Computer-Aided Design*. v 34, n 5. 15 April, 2002. pp 357-371

interesting to note that the method presented by Chiou and Lee is very similar to the method presented in this thesis that generates a fiber placement ply within a ply boundary (see Section 2.5).

All of the methods described in this section address a problem of offset curves on a free form design surface, but none can be applied directly to the domain of fiber placement. In the fiber placement domain, part material is built up as opposed to cut away. The tow material of fiber placement is of constant width, resulting in adjacent offset curves whose minimum distance, as measured on the design surface, remains constant. None of the methods described in this section can be used to approximate offset curves needed for fiber placement. The method that comes closest is that of machining strip offsets, but a constant machining strip width does not necessarily mean a constant distance between tool paths on the surface.

While none of the methods described in this section can be directly applied to the domain of fiber placement, the piecewise manner in which curves are approximated by the iso-scallop height and machining strip methods is utilized by the offset method of this thesis. Both methods use a piecewise linear approximation of a reference curve to generate a piecewise linear approximation of an offset curve. In Section 2.3 we will show how this method is used to generate offset curves that represent the position of individual tows in a fiber placed part.

2.2.2 Design and Analysis of Composite Structures

In this paper, we present methods of placing offset curves on a surface. The offset curves are used to approximate the placement of long, thin strips of composite material (tows) on a fiber placed structure. The position of individual tows in the fiber placed structure is used within a larger design and analysis package described in Section 2.5. Other design and analysis software packages have been developed for different types of composite manufacture. A common goal of these packages is to represent the defining geometry of the components of composite manufacture.

Two design and analysis packages are currently available for the engineering of hand layup composite structures: PACKS is described in Section 2.2.2.1, and FiberSIM is described in Section 2.2.2.2. Techniweaver, described in Section 2.2.2.3, addresses the process of composite textile weaving. In the area of fiber placement, an analysis package has been developed that takes all tow positions as input. This package is described in Section 2.2.2.4, and forms the analysis capability of the SCADS software described in Section 2.5.

2.2.2.1. PACKS

The Parametric Composite Knowledge System, PACKS, was developed at McDonnell Douglas Corporation (currently Boeing Aircraft Company) in St. Louis, Missouri with a goal to reduce the cost of designing hand layup composite parts [¹³, ¹⁴]. Like a fiber placed part, the

¹³. Hale, R.D. and Vasey-Glandon, V.M. PACKS: an Affordable Knowledge-driven Composite Design for Manufacturing Process. *Proceedings of the 46th International SAMPE Symposium and Exhibition - Science of Advanced Materials and Process Engineering Series, Vol. 46, Long Beach, CA, May 6–10, 2001*. Society for the Advancement of Material and Process Engineering, pp 1885-1899

¹⁴. Vasey-Glandon, V.M., Hale, R.D. et al. Knowledge Driven Composite Design Optimization Process and

hand layup composite part consists of composite materials placed on a tool surface. The composite material used in hand layup consists of fibers woven in a flat cloth. The cloth is impregnated with resin, and when the resin cures, the fibers in the cloth impart stiffness to the composite structure. A hand layup part consists of multiple cloth layers stacked such that the fiber directions in each layer are oriented as specified by the designer. The smallest component of manufacture is a single piece of composite cloth- known as a ply. Plies are stacked to result in a specified thickness and fiber orientation distribution. Hand layup has been a traditional method of composite manufacture in the aerospace industry- from homebuilt aircraft to high performance fighters.

PACKS was developed in response to a common separation of the design, analysis and manufacturing phases of hand layup design and manufacturing:

“It became immediately clear that each of these disciplines had their own concept of a “ply”, and each maintained a separate geometric database to represent the concept of a ply. The most significant improvements to affordability and productivity may be attributed to integrating 3D composite definition to the ply level, across disciplines, resulting in a single geometric database and a single concept of a ply.” [13]

PACKS utilizes the Adaptive Modeling Language [¹⁵], an object oriented language incorporating a solid modeling kernel to handle geometric objects. AML is the same development environment used to implement the methods presented in Section 2.3 of this document, and is described further in Section 2.5. The AML language allowed the developers of PACKS to combine geometric representations of the ply with an implementation of the design, analysis and manufacturing process.

PACKS represents all three dimensions of a ply, including its thickness. An input to the program is a description of required material thickness of specific fiber orientations inside discrete regions of the part. The program then calculates potential ply solutions (patterns) that, when stacked, will meet the design intent of thickness and orientation with the least number of plies. This process had previously been done by hand. By incorporating the geometric representation of the ply, the developers of PACKS note a documented 60% savings in engineering labor required to establish ply definitions of a hand layup part [13].

2.2.2.2. FiberSIM

Like PACKS, FiberSIM [¹⁶, ¹⁷] is a package used in hand layup composite manufacture. FiberSIM also incorporates the geometric representation of a ply, but considers the ply to be a surface with no thickness. FiberSIM offsets the surface to impart thickness to the part. The

System Therefor. United States Patent 6,341,261. 22 January, 2002.

¹⁵. TechnoSoft, Inc. *Adaptive Modeling Language Reference Manual: AML Version 3.1.3*. Cincinnati, Ohio. 1999.

¹⁶. Guillermin, O. and Grape, J. Advanced CAD software tools for cost-effective composite engineering. *Proceedings of the 46th International SAMPE Symposium and Exhibition - Science of Advanced Materials and Process Engineering Series, Vol. 46, Long Beach, CA, May 6–10, 2001*. Society for the Advancement of Material and Process Engineering, pp 1899-1911

¹⁷. Vistagy, Inc. *FiberSIM Documentation*. Waltham, Massachusetts. 2001.

strength of FiberSIM lies in its implementation of fabric draping theory to predict what happens when fabric is placed over a free-form surface. This simulation allows the fiber orientation of the draped cloth to be calculated- in turn allowing analysis of different drapings. Then, given a desired ply draped over a free-form surface, FiberSIM calculates the flat pattern that will result in the draped result. Like PACKS, FiberSIM supports analysis by allowing the user to query the part at any point to calculate part thickness (number of plies) and fiber orientations. Unlike PACKS, FiberSIM does not calculate ply definitions to meet thickness and fiber orientation requirements.

In the currently available version of FiberSIM, a fiber placement module is available. As described [17, ¹⁸], the module consists as an interface to AcraPlace, the offline programming system of the fiber placement machine manufactured by Cincinnati Machine. The FiberSIM fiber placement module allows the user to create input files for the offline programming system directly from a CAD system. The current fiber placement module models the fiber placed part to the level of the ply, not to the tow. The FiberSIM fiber placement module can also be used to visualize course information generated by the fiber placement offline programming system.

2.2.2.3. Techniweaver

Techniweaver is a design and analysis tool for three dimensional (3D) woven structures [¹⁹]. The composite construction materials of hand layup and fiber placement impart strength within the thin area of a ply (in-plane). There is no reinforcement between plies. In contrast, 3D woven composites include composite fibers through the thickness planes.

The Techniweaver program models sections of the composite part taken through the thickness. The ‘through the thickness’ model is used to consider different methods of weaving fibers through the thickness of the part. The resulting material properties of the section can be estimated, and instructions can be generated for the weaving machine. Techniweaver does not attempt to model all three dimensions of the textile part, only two dimensional cross sections through the thickness.

2.2.2.4. Fiber Placement Analysis

The Fiber Placement Analysis (FPA) software was developed as an analysis tool to be used in the domain of fiber placed composite construction [²⁰]. The system was motivated by a desire to perform analysis of individual tows of a fiber placed part. Designers of fiber placed parts wanted to know exact fiber orientations, overlaps and gaps between tows and part thickness distributions. They also wanted a system that could export the data to finite element analysis (FEA) packages for that type of analysis. At the time, the capability existed to extract the position of individual tows as piecewise linear curves in space.

¹⁸. Vistagy, Inc. FiberSIM FiberPlacement Interface. Waltham, Massachusetts. May 1, 2001.

¹⁹. Goering, J. Integrated design and analysis tool for 3D woven structures. *AIAA/ASME/ASCE/AHS/ASC Structures, Structural Dynamics, and Materials Conference and Exhibit, 41st*. Atlanta, GA. Apr. 3-6, 2000. AIAA Paper 2000-1376.

²⁰. Hale, R.D. and Vasey-Glandon, V.M.. Fiber Placement and Fiber Steering Systems and Corresponding Software for Composite Structures. Boeing Attorney Docket 99-441, Submitted to U.S. Patent Office July, 2001.

The tow position information used by the FPA software originates from the fiber placement machine as it manufactures a part. The software used to program the fiber placement machine generates machine motion paths only; information of individual tow locations is available only after a part has been built. The FPA software takes tow location data as an array of points in three space. Those points are then projected to a representation of the tool surface along the normal to that surface. The projected points are then interpolated with a spline. The interpolated splines, representing positions of individual tows, are used for analysis of the part.

The FPA software forms the analysis portion of the SCADS software presented in Section 2.5 of this document. The FPA software required the construction of a fiber placed part before analysis could take place. SCADS uses the geometric relationships, defined by the fiber placement process and implemented by the methods described in Section 2.3, to approximate the locations of individual tows, thus avoiding the expensive proposition of building every design iteration of a part.

Of the design *and* analysis packages developed, to date, for composite manufacture, none addresses the domain of fiber placement. The FPA software addresses analysis of a fiber placed part, but not design. To create a useful design tool for fiber placement, a capability of modeling the fiber placed part must be implemented. That design tool requires methods to either approximate or exactly calculate the positions of individual tows within the fiber placed part. In Section 2.3, we present methods to approximate the positions. In Section 2.5, we present the Steered Composites Analysis and Design System (SCADS), a design and analysis package for fiber placement. SCADS uses the methods of Section 2.3 to model the fiber placed part. Additionally, SCADS incorporates the FPA software, thus providing analysis capabilities of the fiber placed part.

2.3.0 The Methods

In this section, we describe our method of generating piecewise linear approximations to offset curves on an arbitrarily curved surface, and our method of generating a piecewise linear approximation to a curve which is defined at a constant angle to a series of our approximate offset curves. Section 2.3.1 gives a geometric description of the methods used to generate offset curves on a surface. Section 2.3.2 presents the algorithms developed to implement the methods described in Section 2.3.1. Section 2.3.3 introduces, motivates and describes the laminate family curve, a curve which is generated at a constant angle to a series of offset curves. Finally, Section 2.3.4 presents the algorithms developed to generate laminate family curves.

2.3.1 Geometric Description of Offset Curve Generation on an Arbitrarily Curved Surface

The purpose of the method is to place points on a surface (the placement surface) that, when interpolated with a curve on the surface, will form a curve that is a constant offset from a reference curve on the surface. An offset curve on the surface is defined:

Given: a surface, $s(u, v)$; two curves on the surface, $r(u(t), v(t))$ and $r_d(u_d(t), v_d(t))$; and a point P on r . Let $D(P)$ be the shortest distance, measured along the surface, from P to r_d . If, $\forall P \in r$, $D(P)=d$, then r_d is an offset curve at distance, d , from r on the surface, s .

The method presented in this section produces an approximation of r_d given r and s . The method generates a piecewise linear approximation of r_d by using points on r to generate points on r_d .

The inputs to the method are a placement surface, fiber axis, projection vector, curve generation tolerance and offset distance. All defining points of the offset curves are generated on the placement surface. The placement surface must be a surface whose partial derivatives are G^1 continuous. Furthermore, it must not intersect itself. The fiber axis is projected along the projection vector to the placement surface to create the first curve from which offsets are generated. The fiber axis is a NURBS space curve that may or may not lie on the placement surface. Finally, the curve generation tolerance is used to generate points on a reference curve. The points on the curve form a piecewise linear approximation, such that the maximum distance between the curve and any line segment defined by two adjacent points will be bounded by the tolerance. Figure 2.3.1 shows the initial input to the method.

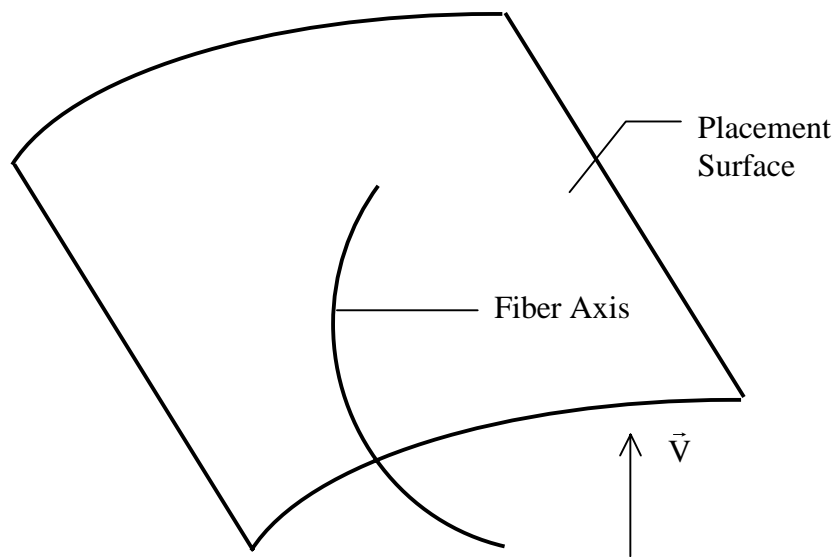


Figure 2.3.1 Initial Input to the Method

Given the input, the method creates a swept surface with cross section defined by the fiber axis definition curve, and axis defined by the projection vector. Figure 2.3.2 shows the swept surface. The method uses the intersection of the placement surface and the swept fiber axis as the initial curve, from which offset curves are approximated.

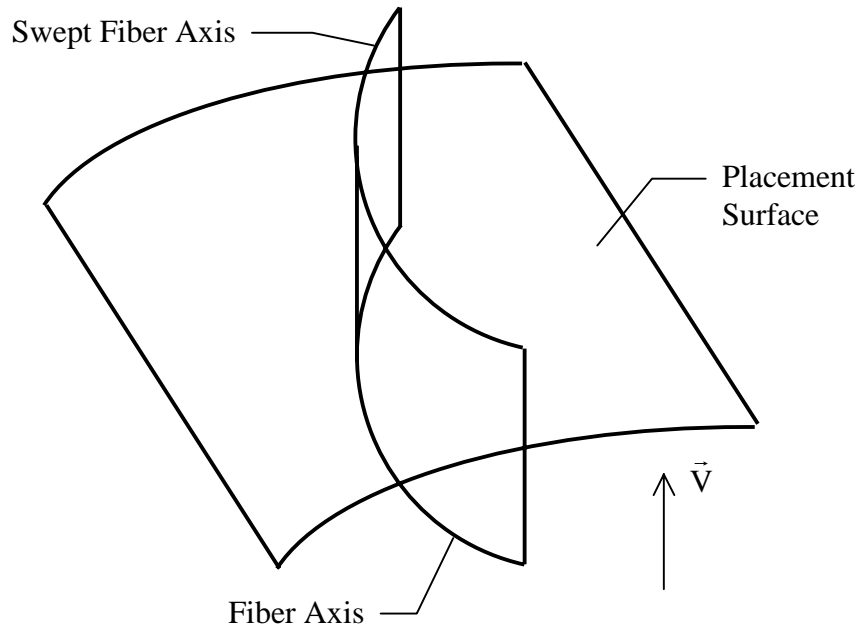


Figure 2.3.2 The Fiber Axis Definition is Swept in the Direction of \vec{V}

An offset curve is approximated from a reference curve by interpolating points that are offset from points on the reference curve. As the initial reference curve is defined by a surface-surface intersection, an initial array of points lying on the reference curve must be generated. The points are generated by a recursive algorithm which constructs a piecewise linear approximation of the curve such that the maximum distance between the curve and any line segment defined by two adjacent points will be less than or equal to the input tolerance. A detailed description of this algorithm is given in Section 2.3.2.

Figure 2.3.3 shows the initial reference curve that is the result of intersecting the placement surface with the fiber axis definition sweep. Defining points are generated on the reference curve. Figure 2.3.3 shows that, at each point, P , generated on the reference curve, we compute the normal vector to the surface, \vec{N} , and the tangent vector to the curve, \vec{T} .

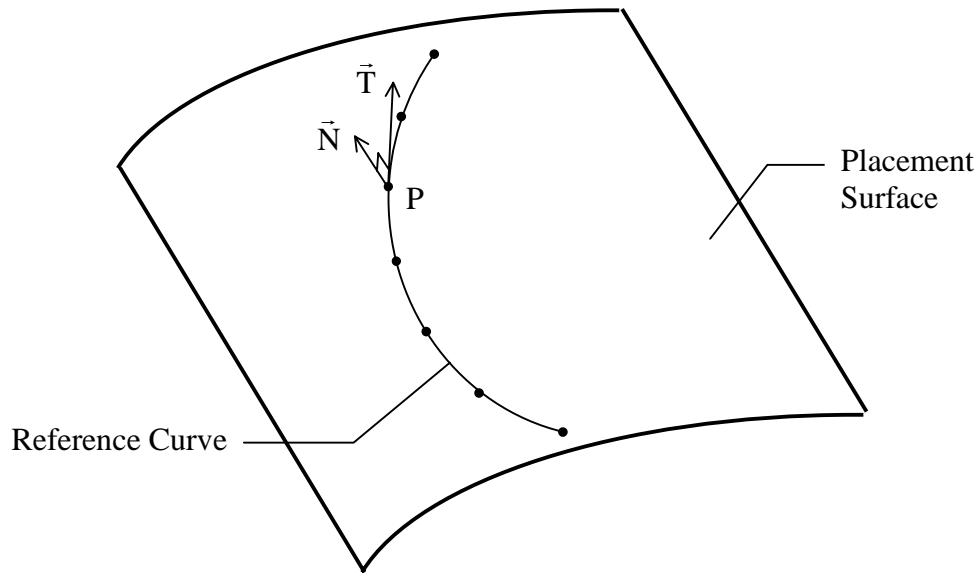


Figure 2.3.3 The Reference Curve is a Surface-Surface Intersection

The curve generation method creates a new curve by offsetting each defining point of the parent curve by a constant distance along the placement surface. This is approximated by calculating, at each defining point in the reference curve, the tangent vector to the curve (\vec{T} in Figure 2.3.3) and the normal vector to the surface at that point (\vec{N} in Figure 2.3.3). Using these vectors, an offset vector is calculated by taking the cross product of the normal vector and the tangent vector. The resulting vector, \vec{O} , is tangent to the surface, and perpendicular to the curve. A new point is calculated by projecting the original point, P, along the offset vector by the offset distance, d. Finally, this point is projected along a surface normal to the nearest point on the surface using a Newton-Raphson technique, resulting in P'. Figure 2.3.4 shows how P' is determined using P and \vec{O} .

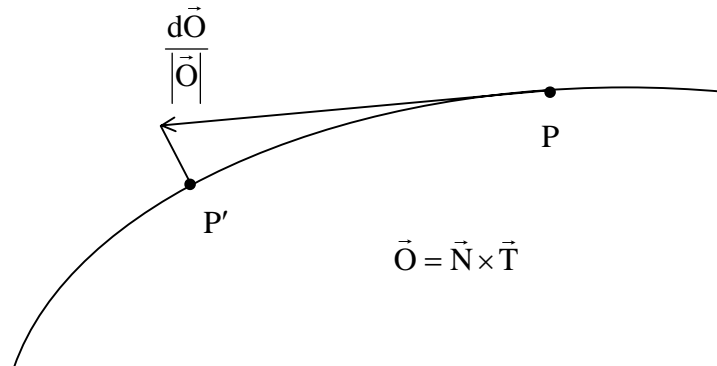


Figure 2.3.4 Cross Section of Placement Surface Showing Calculation of Offset Point

2.3.2. Offset Curve Generation Algorithm

This section presents a description of algorithms developed to implement the methods described in the previous section. The algorithms are presented in pseudo code. Figure 2.3.5 presents the main algorithm used to generate offset curves from initial inputs of a placement surface, fiber axis definition, projection vector, points generation tolerance and offset distance. These inputs were described in the previous section. In addition, the algorithm takes as input the number of offset curves to be generated in negative and positive directions.

```
Alg: generate-offset-curves(fiber-axis, placement-surface,
                           projection-vector,
                           point-generation-tolerance,
                           offset-distance, num-pos-curves,
                           num-neg-curves)
neg-curves[num-neg-curves] ← NULL
pos-curves[num-pos-curves] ← NULL
swept-axis ← swept-surface(fiber-axis, projection-vector)
reference-curve ← surface-surface-intersection(swept-axis,
                                                placement-surface)
;;compute a piecewise linear approximation of the first
;;reference curve
reference-curve.points ← generate-intermediate-points-on-curve
                        (reference-curve,
                         point-generation-tolerance)
first-pos-points ← path-offset-points(reference-curve,
                                     placement-surface,
                                     (offset-distance/2.0))
pos-curves[1] ← three-space-curve(placement-surface,
                                  first-pos-points)
first-neg-points ← path-offset-points(reference-curve,
                                     placement-surface,
                                     -(offset-distance/2.0))
neg-curves[num-neg-curves] ← three-space-curve(placement-surface,
                                              first-neg-points)
for i from 2 to num-neg-curves do
  ref-idx ← (num-neg-curves - (i - 2))
  points ← path-offset-points(neg-curves[ref-idx],
                              placement-surface,
                              (- offset-distance))
  neg-curves[ref-idx - 1] ← three-space-curve(placement-surface,
                                              points)
done
for i from 2 to num-pos-curves do
  points ← path-offset-points(pos-curves[i - 1],
                              placement-surface,
                              offset-distance)
  pos-curves[i] ← three-space-curve (placement-surface,
                                     points)
done
return append(neg-curves, pos-curves);
end (generate-offset-curves)
```

Figure 2.3.5 Algorithm to generate array of offset curves

Figure 2.3.5 shows that the initial reference curve created by the algorithm is not included in the array of offset curves that is returned by the algorithm. To preserve uniform spacing between all of the offset curves, the first curve offset on either side of the initial reference curve is offset by half the offset distance. The procedure ‘path-offset-points’ used in the algorithm

implements the projection process of Figures 2.3.3 and 2.3.4 for each point in the piecewise linear approximation of the reference curve.

Figure 2.3.5 shows an algorithm ‘generate-intermediate-points-on-curve’ that is used to generate additional defining points on the reference curve if needed. Before points for a new curve are calculated, points are added to the reference curve (without changing its shape) such that a piecewise approximation of the curve through its defining points will have a bounded error. In other words, the maximum distance between the curve and any line segment defined by two adjacent defining points will be less than or equal to a given tolerance. Figure 2.3.6 shows the algorithm generate-intermediate-points-on-curve which divides the curve into segments, defined by the original points, and calls a recursive algorithm (see Figure 2.3.7) which generates additional points for that segment.

```
Alg: generate-intermediate-points-on-curve(curve,
                                          point-generation-tolerance)
    new-points ← curve.points[1]
    for i from 1 to (length(curve.points) - 1) do
        new-points ← append(new-points,
                            generate-additional-points-on-curve(curve,
                                                                curve.points[i],
                                                                curve.points[i + 1],
                                                                point-generation-tolerance))
    done
    curve.points ← new-points
    return
end (generate-intermediate-points-on-curve)
```

Figure 2.3.6 Algorithm to Divide Curve into Segments and Generate Additional Segment Points

```
Alg: generate-additional-points-on-curve(curve, point1, point2, tolerance)
    points ← NULL
    mid-point ← (point1 + point2)/2.0 ;;a well defined op per [21]
    new-point ← point-on-geometry(curve, mid-point)
    error ← points-distance(mid-point, new-point)
    if (error > tolerance) then
        points ← append(
                        generate-additional-points-on-curve(curve, point1,
                                                            new-point, tolerance),
                        generate-additional-points-on-curve(curve,
                                                            new-point, point2, tolerance))
    else
        points ← list(point2)
    fi
    return points
end (generate-additional-points-on-curve)
```

Figure 2.3.7 Algorithm to Generate Additional Defining Points on a Curve Segment

2.3.3. Geometric Description of Generation of a Laminate Family Curve

The purpose of the method presented in this section is to construct a curve based on a field of offset curves in an arbitrary surface. The method is a companion to the method

²¹. Miller, J.R. Vector Geometry for Computer Graphics. *IEEE Computer Graphics and Applications*. Vol. 19, No. 3. May/June 1999. pp 66-73.

presented in section 2.3.1. The method is used to construct a laminate family curve. A laminate family curve is defined:

Given: n offset curves, $\{C_1, \dots, C_i, \dots, C_n\}$, generated by the algorithm of Figure 2.3.5; a curve, l , in the surface of the offset curves that does not intersect itself and intersects each C_i exactly once at point S_i ; and a laminate family angle, θ . If, $\forall S_i$, the angle between the tangent to l at S_i and the tangent to C_i at S_i equals θ , then l is a laminate family curve.

The laminate family curve is a curve that intersects each of the offset curves at a specified angle- the laminate family angle. Where the motivation of the offset curves of the previous section is to follow the primary load path in a structure, the laminate family curve is aligned to coincide with offset load directions defined at a constant angle to the primary load path. The method presented here computes a piecewise linear approximation of a laminate family curve. Figure 2.3.8 shows a piecewise linear approximation to a laminate family curve, calculated using a set of offset curves. In keeping with the terminology introduced in Section 2.1, the set of offset curves is called the 0° ply. The detail of Figure 2.3.8 shows that the intersection of each linear segment of the piecewise linear laminate family curve with each of the offset curves occurs at the laminate family angle, θ .

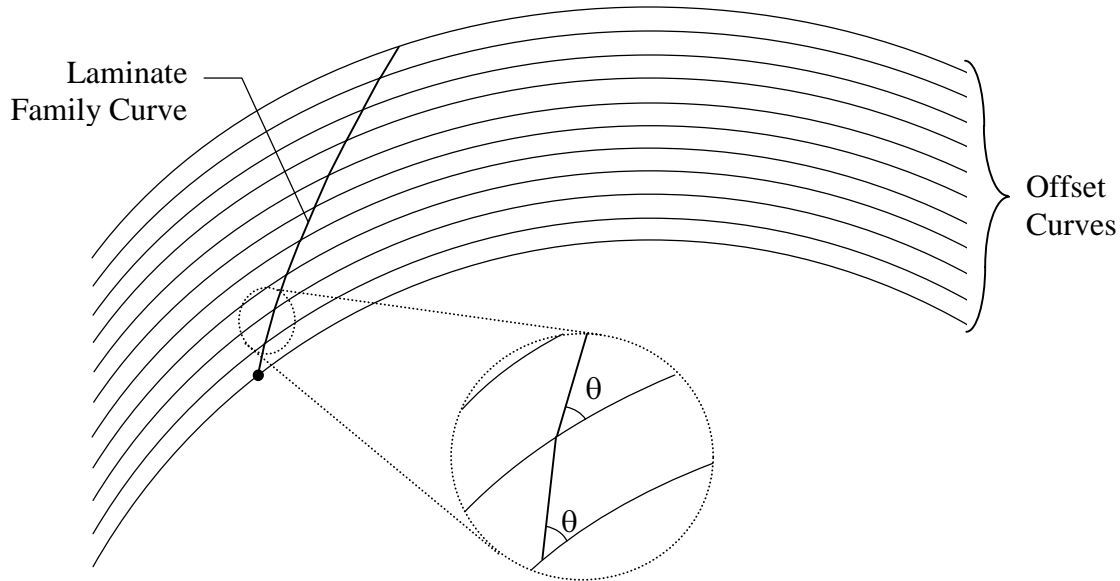


Figure 2.3.8 A Laminate Family Curve Angle θ to Offset Curves

The laminate family curve is constructed from a specified point on one of the offset curves in the 0° ply. To calculate the next point, P' , two vectors are computed at point P ; the tangent vector to the curve, \vec{T} , and the normal vector to the placement surface, \vec{N} . An orientation vector, \vec{O} , is determined by rotating \vec{T} about \vec{N} by the laminate family angle, θ .

The vectors \vec{O} and \vec{N} are used to orient a plane containing those vectors. P' is then found by intersecting the plane with the next offset curve. Figure 2.3.9 shows the vectors used to orient the plane which, in turn, is used to determine P' .

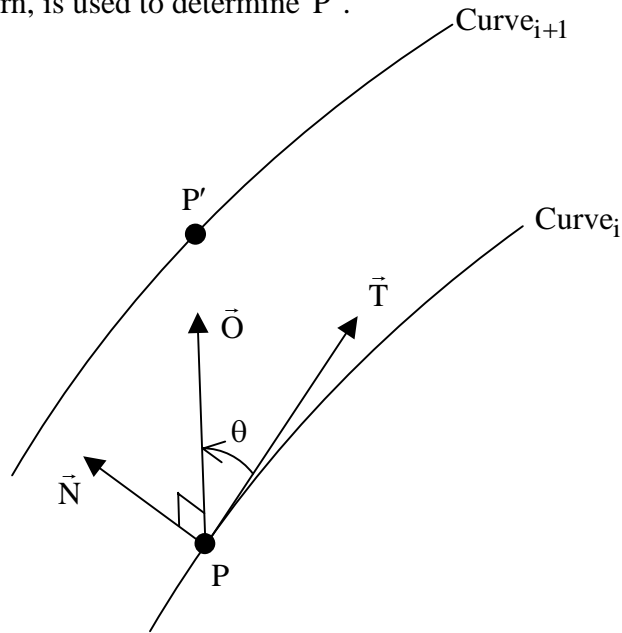


Figure 2.3.9 P' is Found by Orienting a Plane at P and Intersecting with the Next Curve

2.3.4. Laminate Family Curve Generation Algorithm

Figure 2.3.10 shows a pseudo-code implementation of the previous method in an algorithm that calculates the defining points for a laminate family curve based on a collection of offset curves lying in a placement surface. The collection of offset curves is referred to as the zero-degree-ply.

```

Alg: generate-pts-list-from-home-point(home-point, zero-degree-ply,
                                     family-angle, sheet-side-length)
  surface ← get-placement-surface(zero-degree-ply)
  points[1] ← home-point;

  for i from 2 to length(zero-degree-ply.curves) do
    prev-tow ← zero-degree-ply.curves[i - 1]
    prev-point ← points[i - 1]
    sheet-tangent ← normal-to-surface-at-point(surface, prev-point)
    sheet-normal ← rotate-point(tangent-to-curve(prev-tow,
                                                  prev-point),
                               axis( (0, 0, 0), sheet-tangent),
                               family-angle)
    orient-sheet ← align-sheet((new sheet(sheet-side-length,
                                          sheet-side-length)),
                              prev-point, sheet-tangent,
                              sheet-normal)

    points[i] ← intersect-point(zero-degree-ply.curves[i],
                                orient-sheet)
  done

  return points
end (generate-pts-list-from-home-point)

```

Figure 2.3.10 Algorithm to Generate a Laminate Family Curve

2.4.0. The Error

This Section presents the derivation of error inherent in the methods described in Section 2.3. Section 2.4.1 discusses the error arising from the method to place offset curves on a surface. A closed form solution for a surface with circular arc cross section is presented. An approximate method of determining the error on a surface with arbitrarily curved cross section is presented, followed by an approximate method based on the closed form solution for a circular arc cross section. Finally, in Section 2.4.2, the error that can result in the generation of a laminate family curve is discussed.

2.4.1. Resulting Error of Method to Generate Offset Curves on a Surface

The generation of offset curves on a surface attempts to create a curve that is located at a constant offset distance, as measured on the surface, from a reference curve. An approximate method of generating an offset curve is presented in Section 2.3.1. Figure 2.3.4 shows the method used to generate defining points of an offset curve at the offset distance. It can be seen that the offset distance is used to calculate a point that typically does not lie on the surface. That point is then projected back to the surface. On non-planar surfaces the distance between the points along the surface is not equal to the offset distance. This is due to the approximate method which does not attempt to calculate distance on the surface. We can therefore define our error measure as the difference between actual distance between the points and the desired distance. A closed form equation for this error can be derived when the cross section of the placement surface, between the two points shown in Figure 2.3.4, is a circular arc. A derivation of this solution is presented in Subsection 2.4.1.1.

When the surface cross section between the two points of Figure 2.3.4 is not a circular arc, the error of the method can be approximated by computing the distance along the surface, giving a value of the error that is as accurate as the length computation. Subsection 2.4.1.2 presents another approximate method, based on the method of Subsection 2.4.1.1 and appropriate to the domain of fiber placement, that avoids computing length along the surface.

2.4.1.1. Surface with Circular Arc Cross Section

The method used to place points on a surface that, when interpolated with a curve on the surface, will form an offset curve to a reference curve, is an approximate method. Error associated with the method arises when computing a point on a curved surface and in the interpolation of the points. Figure 2.4.1 shows the exact error resulting from placing a point, P' , from an existing point, P , on a surface whose local cross section is a circular arc. Placement of P' uses the method illustrated in Section 2.3.1. It should be noted that the surface cross section shown in Figure 2.4.1 is repeated on the right side of the figure so that normal vectors to the surface can be clearly seen.

The absolute error associated with projecting a single defining point of a curve on a surface with a circular arc cross section can be expressed as:

$$\text{Error} = (d - l) \quad \text{Eqn 2.1}$$

Where d is the offset distance of each defining point of the curve. The quantity l is the actual distance on the arc cross section. This quantity can be expressed as:

$$l = r\psi \quad \text{Eqn 2.2}$$

Where r is the radius of the arc containing l , and ψ is the angle of the arc l . ψ can also be expressed as the angle between the normal vectors on the surface at points P and P' : \vec{N}_i and \vec{N}_{i+1} (see Figure 2.4.1).

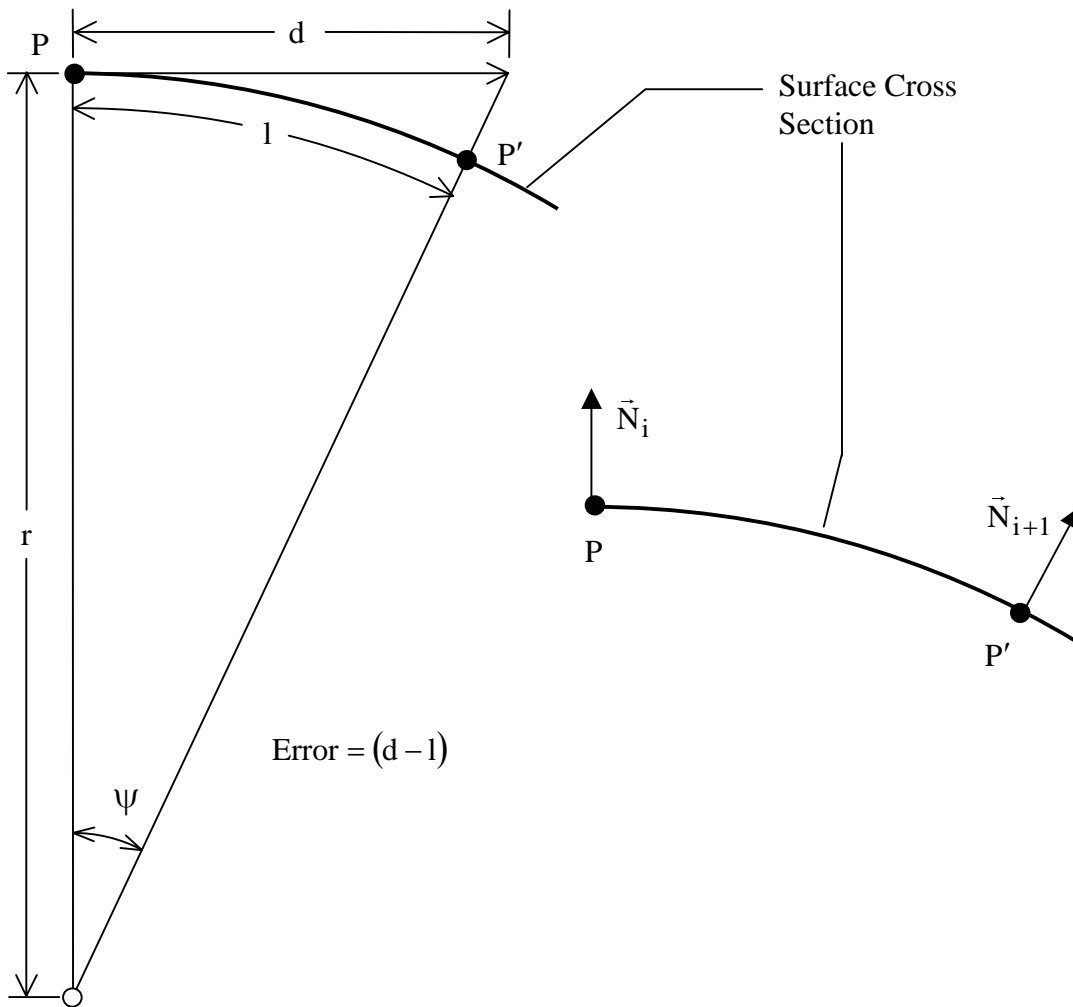


Figure 2.4.1 Error Associated with Placing a Point on a Surface with Circular Arc Cross Section

Using the definition of dot-product [21], ψ can be determined using:

$$\cos \Psi = \frac{\vec{N}_i \cdot \vec{N}_{i+1}}{|\vec{N}_i| |\vec{N}_{i+1}|} \quad \text{Eqn 2.3a}$$

where ψ ($0 \leq \psi \leq \pi$)

$$\Psi = \cos^{-1} \left(\frac{\vec{N}_i \cdot \vec{N}_{i+1}}{|\vec{N}_i| |\vec{N}_{i+1}|} \right) \quad \text{Eqn 2.3b}$$

Also, using the definition of tangent, r can be determined from:

$$\tan \Psi = \frac{d}{r} \quad \text{Eqn 2.4a}$$

$$r = \frac{d}{\tan \Psi} \quad \text{Eqn 2.4b}$$

Therefore, Eqn 2.2 can be rewritten:

$$l = \frac{d * \Psi}{\tan \Psi} \quad \text{Eqn 2.5}$$

Assuming the surface is well approximated locally by a surface with circular cross section, the error defined by Eqn 2.1 can now be expressed as a function of ψ , the angle between normal vectors taken on the surface at two successive points, and the offset distance d :

$$\text{Error} = d \left(1 - \frac{\Psi}{\tan \Psi} \right) \quad \text{Eqn 2.6}$$

Now, the question can be asked: can the error be negative? Again, assuming the surface is well approximated locally by a surface with circular cross section, the answer is no. By definition of offset, the offset distance is greater than zero. By inspection of Figure 2.4.1, as d approaches infinity, ψ approaches $\pi/2$. A Taylor Series expansion of $\tan(\psi)$ where $0 < \psi < \frac{\pi}{2}$ can be written [22]:

²². Beyer, W. H. (editor). *CRC Standard Mathematical Tables*. CRC Press, Inc. Boca Raton, Florida. 1984

$$\tan \psi = \psi + \frac{\psi^3}{3} + \frac{2\psi^5}{15} + \dots + \frac{2^{2n}(2^{2n}-1)B_n \psi^{2n-1}}{(2^n)} + \dots \quad \text{Eqn 2.7}$$

where $|\psi| < \frac{\pi}{2}$ and B_n is the nth Bernoulli number.

Because $0 < \psi < \frac{\pi}{2}$, it can be seen from Eqn 2.7 that $\tan \psi \geq \psi$. Furthermore, if $\tan \psi > \psi$, then $\frac{\Psi}{\tan \Psi} \leq 1$, and $\left(1 - \frac{\Psi}{\tan \Psi}\right) \geq 0$. Finally, if $\left(1 - \frac{\Psi}{\tan \Psi}\right) \geq 0$ and $d \geq 0$, then $\text{Error} \geq 0$.

Using the derivation of error per offset (Eqn 2.6), and the property $\text{Error} \geq 0$, the total error for a series of n offset points on a surface with circular cross section can be calculated:

$$\text{TotalError} = \sum_{i=2}^n d \left(1 - \frac{\Psi_i}{\tan \Psi_i}\right) = (n-1)d - d \sum_{i=2}^n \frac{\Psi_i}{\tan \Psi_i} \quad \text{Eqn 2.8}$$

and for a constant radius cross section and n offset points:

$$\text{TotalError} = d(n-1) \left(1 - \frac{\Psi_i}{\tan \Psi_i}\right) \quad \text{Eqn 2.9}$$

A verification of Eqn 2.9 using an implementation of the method is presented in Section 2.6.

2.4.1.2. Surface with Arbitrarily Curved Cross Section

The desire of the offset curve approximation method is that the distance between curves, *on the placement surface*, be kept constant. However, when the placement surface is curved, error will result, which can be determined exactly when the placement surface cross section between defining points of neighboring curves describes a circular arc. If the cross section is not a circular arc, the error calculation method itself will not be exact, as the arc length, on the surface, between points P and P' will differ from a circular arc length. This section presents two approximate methods that can be used to estimate the error on a surface with arbitrarily curved cross section. One method uses length calculations of a curve constructed on the surface. Another approximate method assumes that the surface cross section is approximated by a circular arc, and that the method of the previous section can be used.

As offset curves are successively placed on the surface, corresponding points on each curve will lie at approximately the offset distance from each other. These corresponding points can be used to construct a parametric curve in the placement surface. The parametric curve will

intersect the offset curves at approximately 90°. The arc length along this parametric curve (with parameterization variable u) between points P and P' is then defined by [²³]:

$$l = \int_P^{P'} \sqrt{\left(\frac{d(x(u))}{du}\right)^2 + \left(\frac{d(y(u))}{du}\right)^2 + \left(\frac{d(z(u))}{du}\right)^2} du \quad \text{Eqn 2.10}$$

The method is approximate because a closed form solution to Eqn 2.10 is not generally available. While methods exist to approximate arc length as a function of the parameterization variable (e.g. [²⁴]), the method of building the curve point-by-point will result in a new curve with every placement of a new point. While an approximate method using length approximations of parametric curves is possible, the cost of such a method may be prohibitive. Assuming that a series of n offset curves has m defining points on each curve, this approximate method requires the construction of $n*m$ parametric curves and a length calculation of each curve. The cost increases further by considering that the cost of constructing each parametric curve is a function of the number of defining points. The high cost of this method motivates an approximate method that uses the calculations initially used to generate the corresponding points on the offset curves.

Theoretically, the cross section of an arbitrarily curved placement surface between two defining points can be of any shape. This would invalidate the use of Eqn 2.6 to calculate error in the offsetting algorithm. In the domain of fiber placement, it can be assumed that the cross section between corresponding defining points of two curves is well approximated by a circular cross section. The assumption thus ignores surface cross sections containing an inflection point. Evidence that the assumption is valid for the domain of fiber placement is:

1. The cross section of the tow is approximated by a rectangle whose width is equal to the offset distance, and a height of less than 1/10 the offset distance. The material properties of the tow do not allow the cross section to bend significantly, or it will split. This limitation allows a bend corresponding to a local surface cross section radius of 0.250 inches [2], or about twice the tow width. The bending properties of the tow allow an inflection, but the radius of curvature on either side of the inflection point must be much larger than the minimum cross section radius mentioned above. Using Eqn 2.6 to estimate error in an offset region where an inflection occurs will not produce an accurate estimate of error, but the large radii of curvature on either side of the inflection makes the inaccuracy negligible. Section 2.6 will show that, even when a placement surface has multiple curvature inflections, error estimation using Eqn 2.8 is 'very close' to error approximated by constructing a parametric curve on the surface and approximating its length.
2. While curvature inflections may occur on the surface of a fiber placed part, they are relatively rare (between zero and five curvature inflections). The number of tows, and hence offset curves, placed on the surface is of the order of 10^3 to 10^4 . So, inaccuracies in

²³. Farin, G. *Curves and Surfaces for Computer Aided Geometric Design- A Practical Guide*. Academic Press. San Diego, California. 1997

²⁴. Walter, M. and Fournier, A. Approximate Arc Length Parameterization. *Anios do IX SIBGRAPI*. Caxambu, MG, Brazil. 1996. pp. 143-150

error estimation due to inflection points will only occur in about 1/100 to 1/1000 offset points.

With the assumption of circular cross section, the error calculation method of the previous sub-section can be used. As shown in Eqn 2.6, the error can be estimated as a function of the constant construction offset distance, d , and the angle between normal vectors, ψ , measured at the two points. As shown in Section 2.3, the method of placing the defining points of a new curve based on a reference curve requires the calculation of the surface normal at each defining point of the reference curve. Therefore, the estimation of error requires only a constant time calculation of the error at each point using Eqn 2.6.

A comparison of error approximation methods for two placement surfaces with non-circular arc cross section is presented in Section 2.6. One case uses a cross section with multiple curvature inflections, while the other uses a cross section of an airfoil shape. The comparison shows that, for the test cases, the estimate is of the same order as the value obtained by creating a curve from offset points and calculating its length.

2.4.1.3. Theoretical and Practical Error Buildup

The demonstration of error associated with the method of placing offset curves on a curved surface presents the following concern: Consider a surface with circular cross section r on which a point is placed at offset distance d . As the ratio of d/r gets larger, ψ increases, and the error increases. For example, when $d=r$, ψ is $\pi/4$, and error is $d\left(1 - \frac{\pi}{4}\right)$. This is 21.4% of the offset distance between curves. In this section, we demonstrate that the magnitude of d/r used in the domain of fiber placement is such that the error buildup remains within acceptable limits.

We begin by deriving the maximum value of d/r in the application domain of fiber placement. As mentioned in the previous section, the minimum radius of curvature of the surface cross section is 0.250 inches for an offset distance (tow width) of 0.125 inches. This results in d/r bounded by 0.5. Eqn 2.4a shows that ψ for that case is 0.46 radians per tow width. Eqn 2.6 then shows an error of 7% per offset. This is not an insignificant error, but must be viewed in its context of fiber placement.

A fiber placed part is built up on a tool surface which sometimes, but not always, forms a closed shape such as a cylinder. So, a conceivable part is a cylinder with a circular cross section of radius 0.250. The cross section would require about 12.7 offset curves around its circumference, but since fractional tows cannot be laid, we round up to 13. The total error after 13 offsets, at 7% per offset, is 91% of the offset distance.

While a cylinder of 0.250 inch radius is theoretically possible given the minimum feature radius of 0.25 inches, it is not practically possible. The tool²⁵ of such a part would not have the structural integrity needed to withstand the pressure of the fiber placement head. A more practical instance of a feature with radius of 0.25 inches is a corner, with a total turn angle of

²⁵ The tool refers to a structure with a surface on which layers of the part are built up. The part is separated from the tool before or after curing.

$\pi/2$ radians. In such a case, about 3.4 offsets are required around the feature. The total error after 3 offsets is 21% of one offset.

A more realistic case of error buildup on a cylinder is a cross section with radius of 12 inches, and a tow width of 0.15 inches. The 12 inch radius represents a structurally sound tool. Eqn 2.4a shows that ψ for that case is about 0.01250 radians per tow width. So, a total turn of 2π radians requires 503 points. Total error is $502 \cdot 0.15(1 - 0.99995) = 0.0039$ inches, or 2.6% of a tow width.

A real-world example is the fuselage of the Raytheon Premier I Business Jet (Figure 2.4.2). The fuselage of this airplane is a fiber-placement manufactured cylindrical shell, with a maximum inner width of 5 ft, 6 inches [26]. This corresponds to a cross sectional radius of 33 inches. Again, assuming a tow width of 0.15 inches, Eqn 2.4a shows that ψ for that case is about 0.00455 radians per tow width. So, a total turn of 2π radians requires 1382 points. Total error is: $1381 \cdot 0.15(1 - 0.99999) = 0.014$ inches, or 0.95% of a tow width.

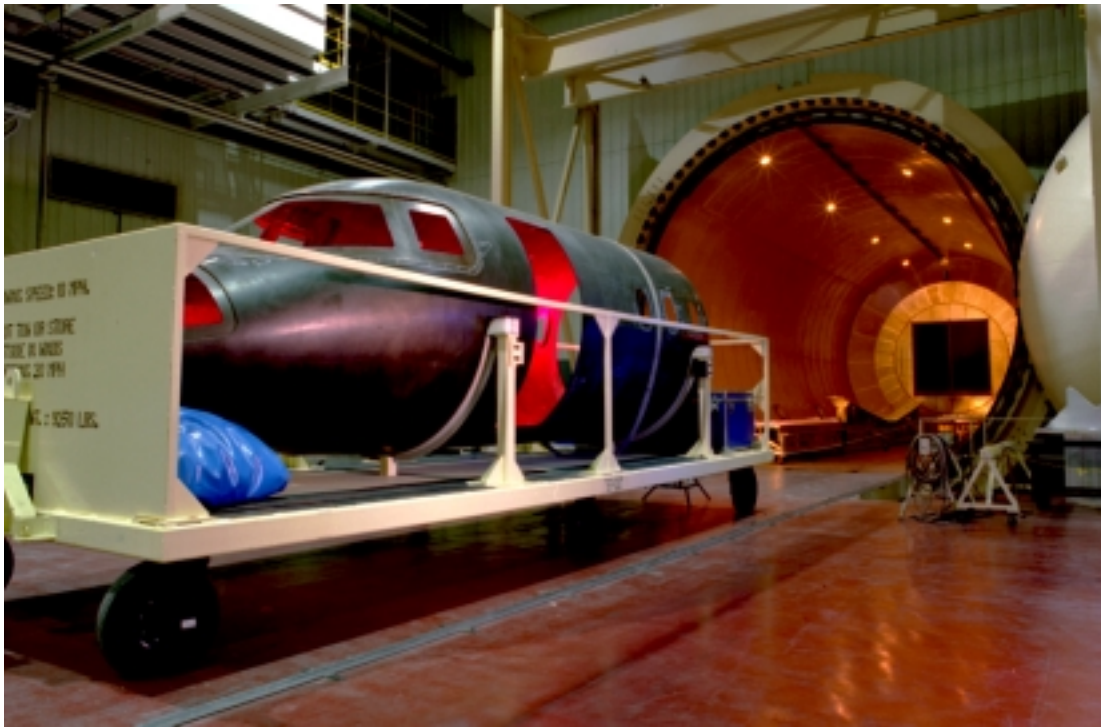


Figure 2.4.2 Fiber Placed Raytheon Premier Fuselage Section

Each of the previous examples uses a placement surface with circular cross section. While some parts are cylindrical, most are not. In Section 2.6, we consider two placement surfaces with non-circular cross sections. In both cases, where the radius of curved features on the surface is much greater than the offset distance, the total error after placing all offset curves is less than one offset width.

²⁶. Jackson, P. Editor. *Jane's All the World's Aircraft 2001-2002*. Jane's Information Group, Ltd. Surrey, England. 2001

It is useful to compare the error of the approximate method to place offset curves on a surface to the actual error observed in tow position on a fiber placed part. We have found that, in the domain of fiber placement, the cumulative error in placing offset curves on a surface is on the order of the offset distance itself. This error accumulates after placing a number of curves on the order of 1000. Current acceptable practice in design for fiber placement allows a cumulative error of 0.25 inches over a total distance of 12 inches [2]. This represents a cumulative error of twice the offset distance after about 100 curves. Additionally, upon inspection of fiber placed panels manufactured for mechanical testing purposes, tow position error has been found that is much greater than the error of the offset curve approximation method presented in this thesis [²⁷].

2.4.2. Resulting Error of Method to Place Laminate Family Curve on Surface

The purpose of this section is to discuss the potential for error when placing a laminate family curve. Briefly, the purpose of the method is to construct a curve that demonstrates a fixed angle of intersection with every curve in a series of offset curves on a surface. The previous chapter showed how this is done in a piecewise manner. Error occurs when the piecewise points are interpolated in a smooth curve. A verification of this error is presented in Section 2.6.

²⁷. Hale, R. D., et al. *Integrated Design and Analysis Tools for Reduced Weight Affordable Fiber Steered Composites, Year 1 Annual Summary Report*. University of Kansas Flight Research Laboratory, KU-FRL-22480-2. 15 September, 2001.

2.5.0 Implementation

The Steered Composite Analysis and Design System (SCADS) represents an integrated design system for the fiber placement process. Preliminary through detailed design is enabled by modeling theoretical paths of individual tows using the methods of Section 2.3. Paths are approximated for a set of user-defined manufacturing criteria; including tool surface geometry, tow material and desired path parameters. Historically, design of fiber placed structures has utilized the offline programming system of the fiber placement machine. Representation of individual tow paths is not available with the offline programming system.

Development of SCADS has focused on two areas. The first is the development of software components that implement the approximation of offset curves and laminate family curves that simulate the position of individual tow paths in a fiber placed part. Initial user-required parameters include tool surface definition, and one or more initial fiber orientation curves. Object classes for two fiber angle control methods, corresponding to the two piecewise linear approximation methods of Section 2.3, are implemented and are presented in this Section.

The implementation has utilized object-oriented programming techniques via the object oriented language and development environment, Adaptive Modeling Language (AML) [15]. AML offers an adaptive object-oriented geometric modeling paradigm that can be used to model a wide variety of engineering process domains. The language incorporates a class library of geometric objects based on the Parasolid solid modeling geometry kernel [28]. The geometric classes of AML (e.g. interpolating spline and NURBS surface) can be inherited by user defined classes that define parametric relationships between objects and features in the modeled domain- in this case, fiber placement.

A second focus of SCADS development is the integration of tow positioning methods with existing Fiber Placement Analysis software (see Section 2.2.2.4). Previously developed Fiber Placement Analysis (FPA) software has the capability of analyzing properties, to the tow level, of a fiber-placed part. Analysis capabilities include area analyses, tow orientation and radius of curvature analyses. Features that can be quantified include discontinuation of single tows, restart of single tows, gaps between tows in a ply and overlaps between tows in a ply. Also, automated geometric analyses can be performed at points defined by finite element meshes. The previously developed FPA software requires an input file of tow definitions created by the fiber placement machine as a part is manufactured. Thus the FPA software is useful only as a tool to be used after a part has been manufactured. Integration of tow curve objects that include positioning methods (self positioning tows) now allows SCADS to act as a stand-alone design and analysis package.

2.5.1. Object Structure of Self Positioning Tows

Section 2.1 describes a fiber placed structure in terms of tow, course and ply relationships. The part consists of a collection of plies, corresponding to a single layer of material. The ply consists of a collection of courses, each of which corresponds to a single pass

²⁸. Unigraphics Solutions, Inc. *Parasolid Online Documentation Web, Parasolid V11.1.167*. Maryland Heights, MO. November, 1999.

of the fiber placement machine head as it lays down material. The course consists of a collection of tows laid down in parallel by the fiber placement head. This object relationship structure is shown in Figure 2.5.1 with the added objects of tow-curve and points; the geometric abstractions used to represent the position of the physical tow. The tow curve is a piecewise linear approximation of the tow curve produced by one of the methods of Section 2.3.

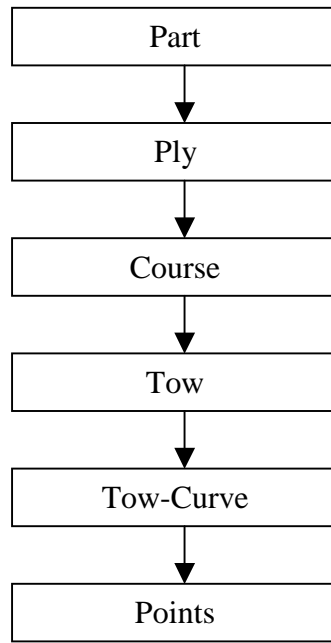


Figure 2.5.1 Object Relationships in Fiber Placed Structure

The physical structure shown in Figure 2.5.1 suggests that most classes will consist of a collection of sub-objects of the next class (lower) on the figure. Hence, the ply class consists of course sub-objects, and methods used to locate those courses. The course class consists of tow sub-objects, and methods used to locate the tows.

While Figure 2.5.1 indicates a logical structure based on the part's physical structure, it does not address the different fiber angle control methods required to design fiber placed parts, which suggest an inheritance hierarchy shown in Figure 2.5.2. The fiber angle control methods are based on the methods of Section 2.3:

- **Band Offset:** an initial fiber path is specified. This fiber-path serves as the reference curve for a series of offset curves on the surface. The offset distance between courses can be specified so that gaps or overlaps occur between courses. On a curved surface, significant variation from the initial fiber path can occur as offsets are approximated farther from the initial fiber path.

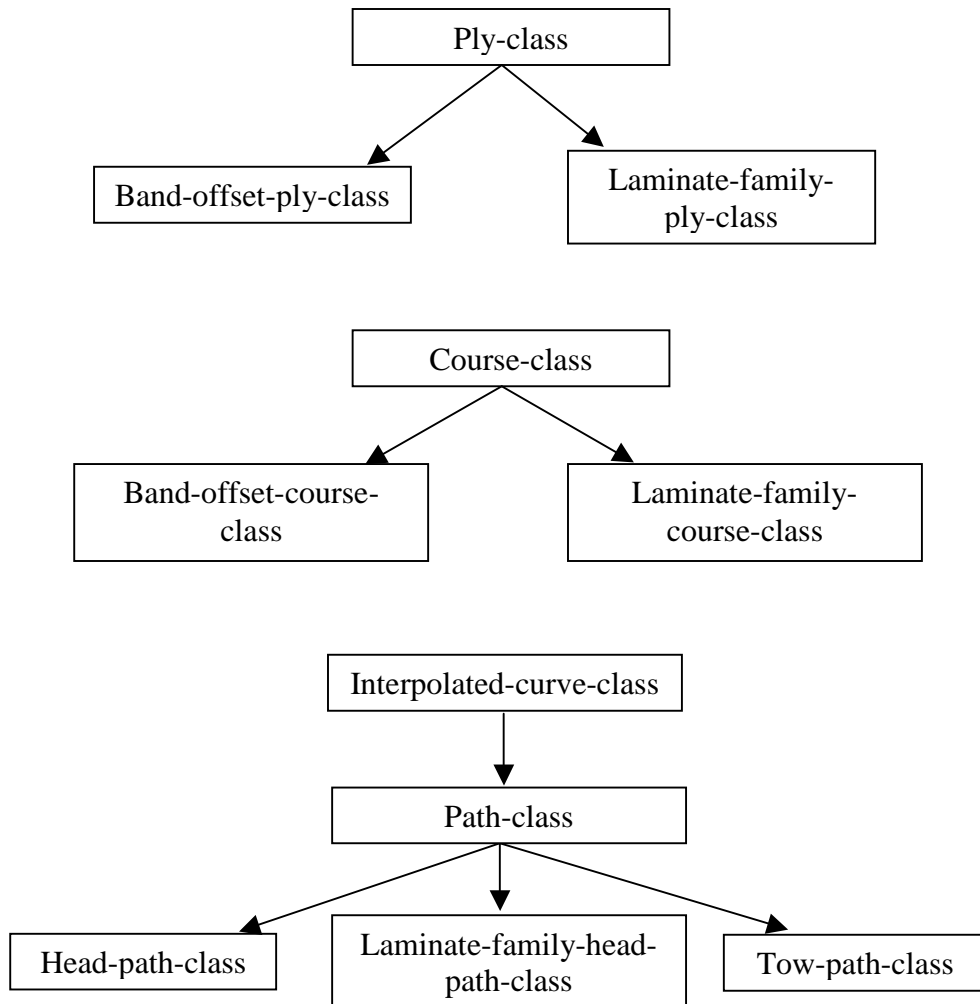


Figure 2.5.2 Class Inheritance at Ply, Course and Tow Levels

- **Laminate Family:** given a guiding ply (0° ply), course paths are generated such that the angle between the course path and the closest tow in the 0° ply is a constant. This method is used to generate laminate family plies (e.g. 45° ply, 90° ply) as described in Section 2.1.

The bottom portion of Figure 2.5.2 depicts two types of paths implemented in SCADS; the head-path-class and the tow-path-class. The head path is a curve representation of the path of the fiber placement machine head as it lays down a single course. The tow path is a curve representation of individual tows in the part. The head path implements the band offset and laminate family fiber angle control methods, while the tow path implements the method of placing an offset curve on the surface.

Self positioning tow classes can be inherited by other class definitions, adding self positioning capabilities to those other classes. Like SCADS, development of the Fiber Placement Analysis (FPA) software also utilized the object oriented AML language and development environment. Because both systems are object oriented, the self positioning classes described here can be directly inherited by the FPA classes, which have already implemented analysis methods. Other than an inheritance statement, very few changes are required in the FPA software classes.

2.5.2. Design Process

This section presents screen shots and descriptions of the process of designing two plies of a fiber placed part: a band offset ply, and a laminate family ply created using band offset ply. The part is a simple panel with the primary fiber path combining an arc portion and two straight line portions extending both sides of the arc (Figure 2.5.3).

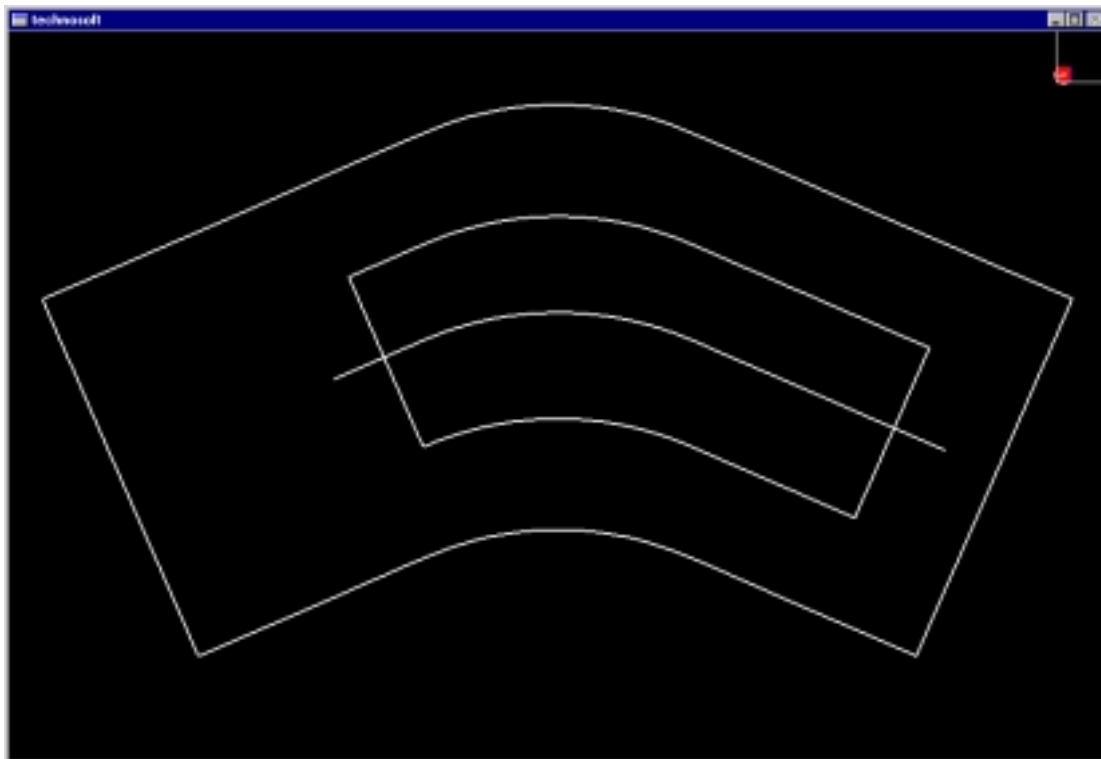


Figure 2.5.3 Tool Surface, Ply Boundary and Fiber-Axis are Initially Defined

Figure 2.5.3 shows the tool surface, ply boundary and fiber axis definition for the flat panel part. The tool surface is the initial surface on which the part will be built. The outer closed boundary represents the boundary of the tool surface. The inner closed boundary represents the ply boundary, outside which tows will not be placed. The single, non-closed curve represents the fiber axis. All tows in the band offset ply will be created as offsets to the fiber axis curve.

After specifying the required input for a band offset ply, the system generates tows and courses such that the ply boundary is completely covered by tows (see Figure 2.5.4). Figure 2.5.4 shows the band offset ply before tows are trimmed to the ply boundary. Individual courses are colored and can be seen as the 11 bands in Figure 2.5.4. Each course consists of 12 tow paths. Individual tow paths are not clearly visible in the figure.

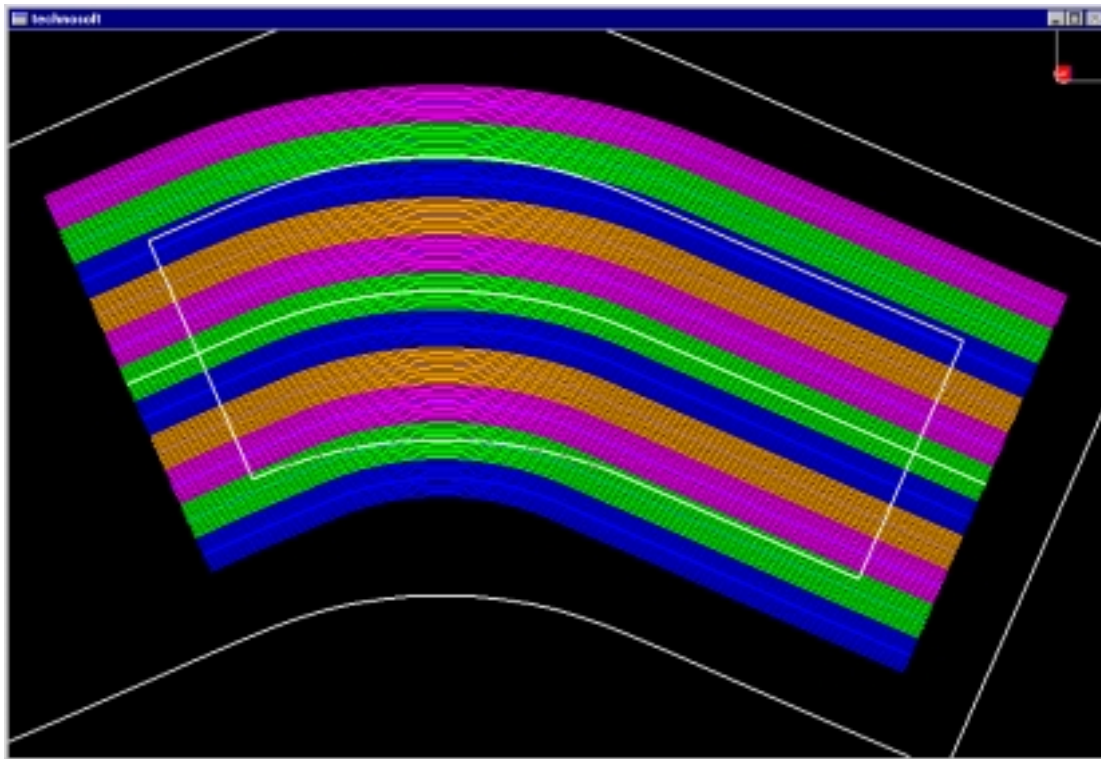


Figure 2.5.4 Initial Ply Generation Creates Enough Courses to Completely Cover Ply Boundary

After the initial generation of courses, which completely cover the ply boundary, the system divides each tow path into segments lying inside (undropped) or outside (dropped) of the boundary. This is called trimming and corresponds to the fiber placement machine's ability to drop and add individual tows in a course. Figure 2.5.5 shows courses remaining inside the ply boundary after trimming. It can be seen in Figure 2.5.4 that two courses lie completely outside of the ply boundary. These courses are completely trimmed away and ignored by any operations involving undropped tows.

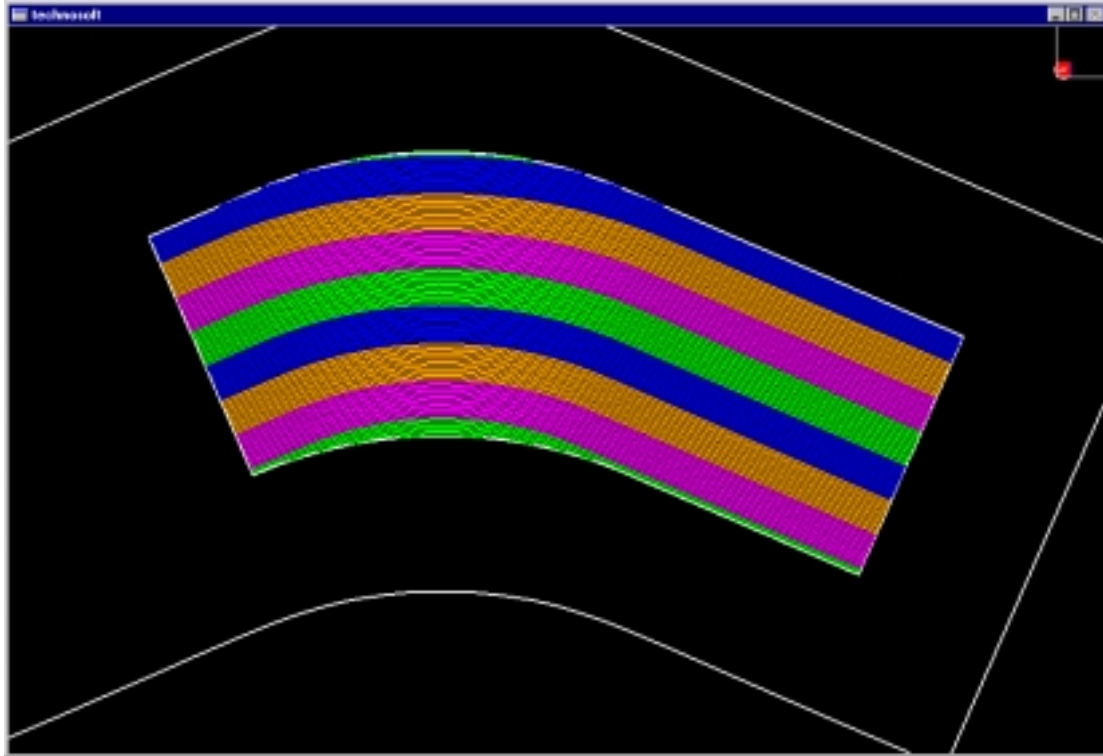


Figure 2.5.5 Tow Paths are Trimmed (only undropped segments are shown here)

Figure 2.5.5 shows the band offset ply after trimming of tows to the ply boundary. The differently shaded bands in Figure 2.5.5 represent individual courses in the ply. Figure 2.5.6 shows an enlarged view of the detail of the lower left corner of the band offset ply. In Figure 2.5.6, individual tow paths can be discerned. The curves shown in Figure 2.5.6 represent the centerline of each tow, from which a surface or solid (given a tow cross section) can be constructed by the design program.

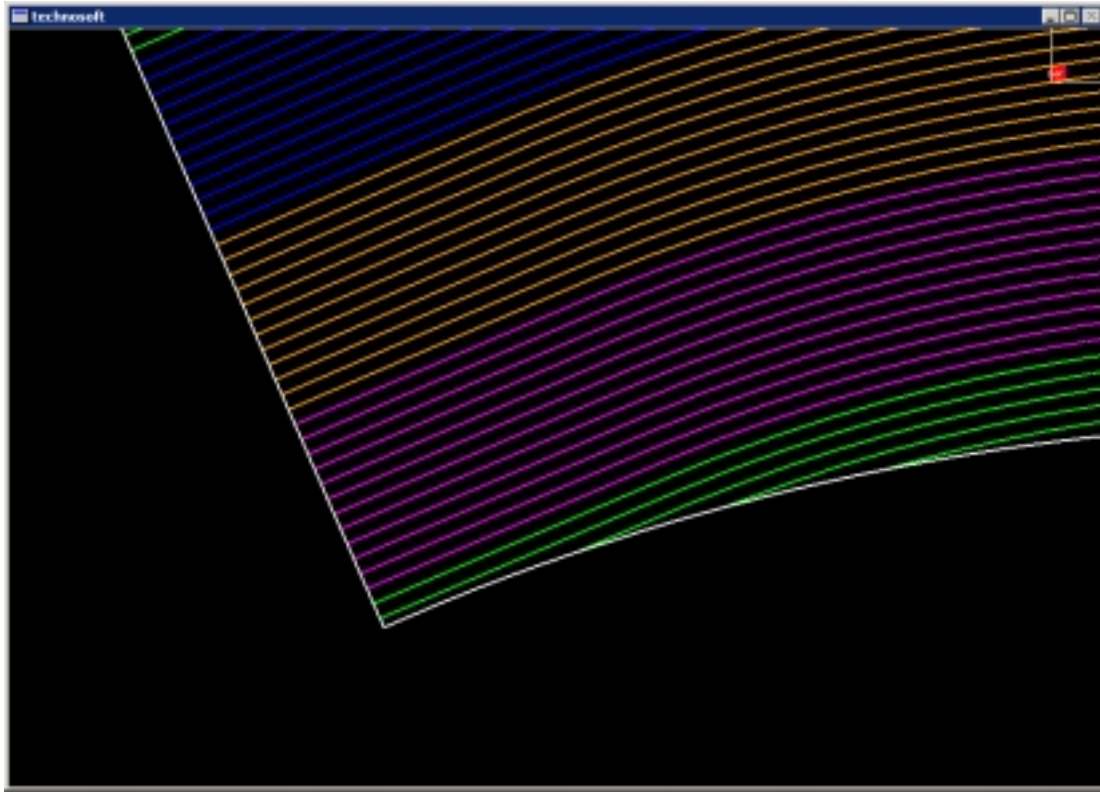


Figure 2.5.6 Magnified View of Band Offset Ply Showing Individual Tow Path Representations

After a band offset ply has been generated, a laminate family ply can be generated. The laminate-family ply is created by generating course paths using the band offset ply of Figure 2.5.4. Each course path is generated as a laminate family curve, oriented at 45° to the band offset ply. The tow path curves in each course are offset curves from the laminate family head path curve. Figure 2.5.7 shows the laminate family ply created so that courses completely cover the ply boundary. The tows are not trimmed to the ply boundary, and courses converge onto one another as they are steered towards the center of curvature of the band offset ply. This convergence of the courses requires that tows be dropped to avoid excessive overlap and additional material thickness.

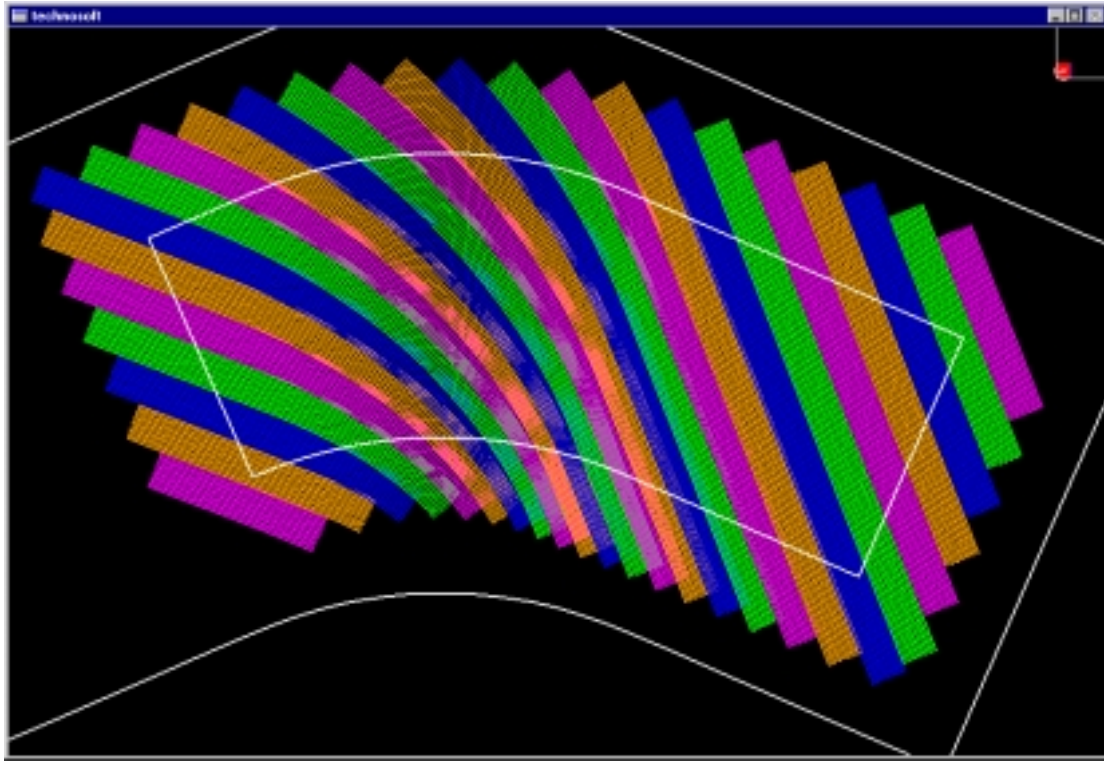


Figure 2.5.7 Laminate Family Ply Generation with Full Paths

The differently shaded bands of Figure 2.5.7 represent individual courses in the laminate family ply. It can be seen that the courses converge upon one another as they are steered toward the center of curvature of the band offset ply. Figure 2.5.8 shows an enlarged view of the converging courses, where it can be seen that individual tows from neighboring courses are overlapping.

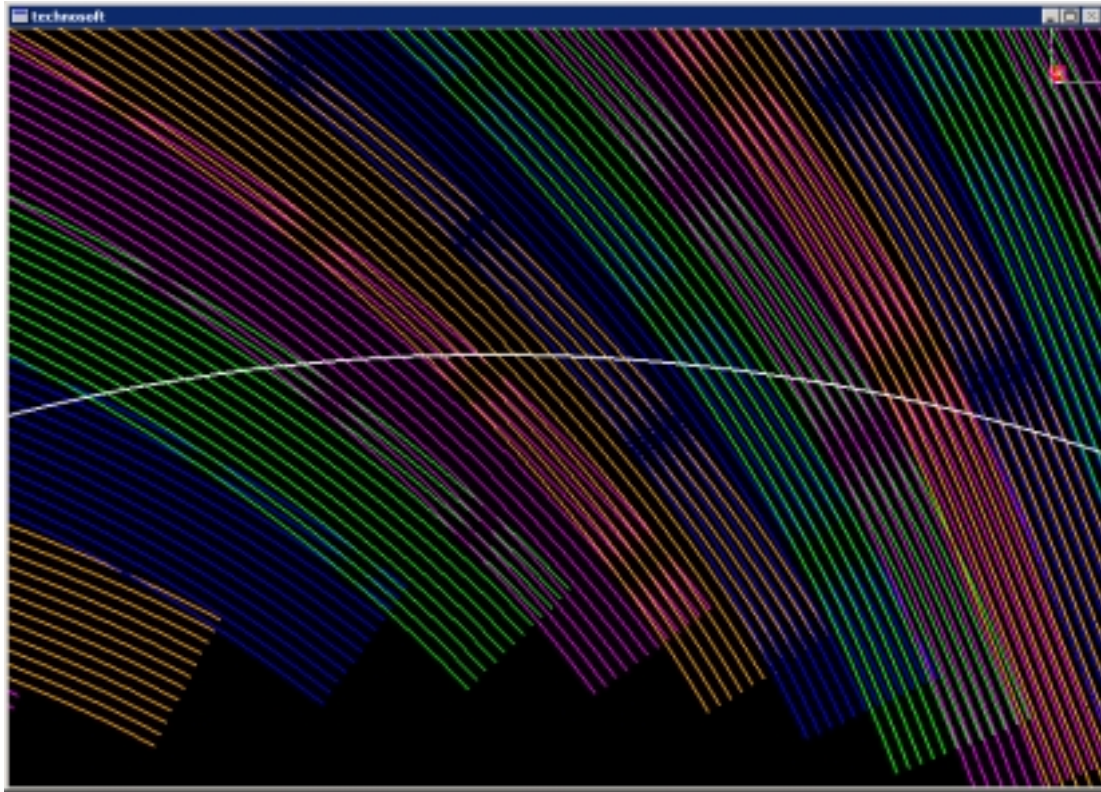


Figure 2.5.8 Laminate Family Ply Generation with Full Paths

Finally, the full tow paths of Figures 2.5.7 and 2.5.8 are trimmed to the ply boundary, and tows are dropped as the courses converge. Figure 2.5.9 shows the tow paths of Figure 2.5.8 after trimming of tow paths to the ply boundary and to overlapping courses.

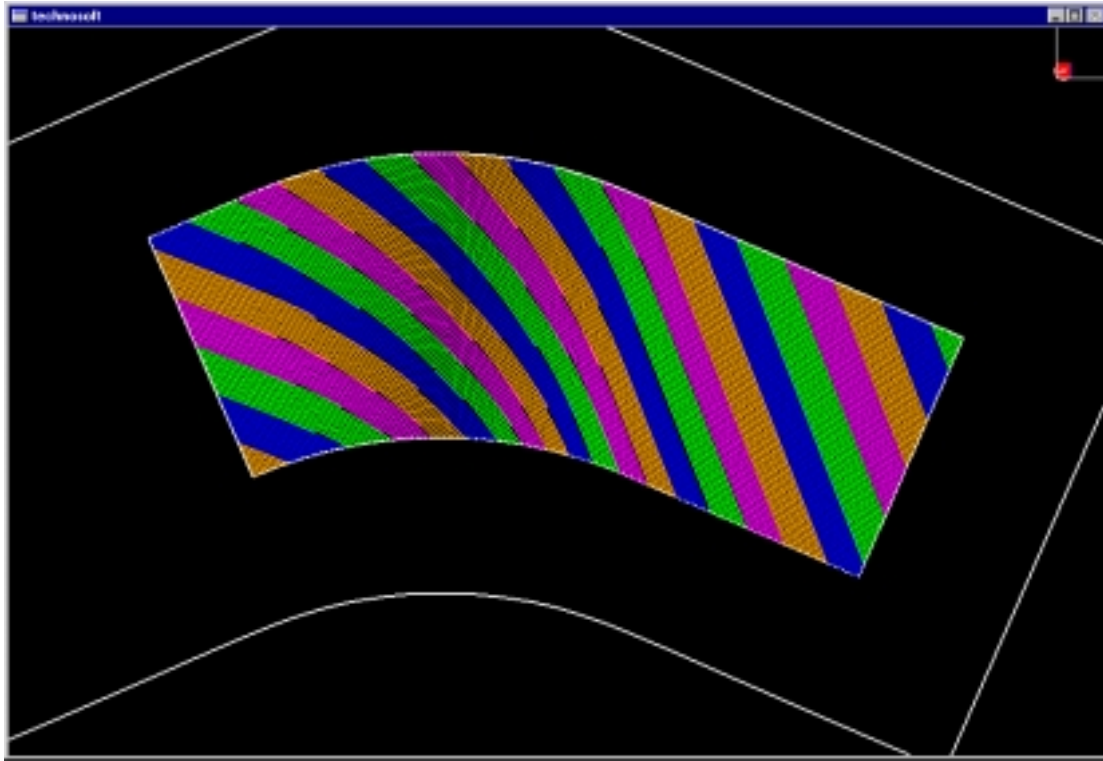


Figure 2.5.9 Laminate Family Ply after Trimming

The differently shaded bands of Figure 2.5.9 represent individual courses. It can be seen that the courses have been trimmed to the ply boundary. As courses converge towards one another, tows are trimmed (dropped) from alternating courses. The amount of overlap that can occur before a tow is dropped is specified by the user. In Figure 2.5.9, overlap of 50% is specified. In this case, when the distance between two tow paths becomes less than one half of one tow width, one of the tows is dropped. If less than 100% overlap is specified, gaps in tow material develop from the point where a tow is dropped until the overlapping tow completely takes its place. The specification of allowed overlap results in a controllable ratio of overlap to gap regions. Figure 2.5.10 shows a depiction of tow curves that result with the 50% overlap specification, resulting in equal overlap and gap areas.

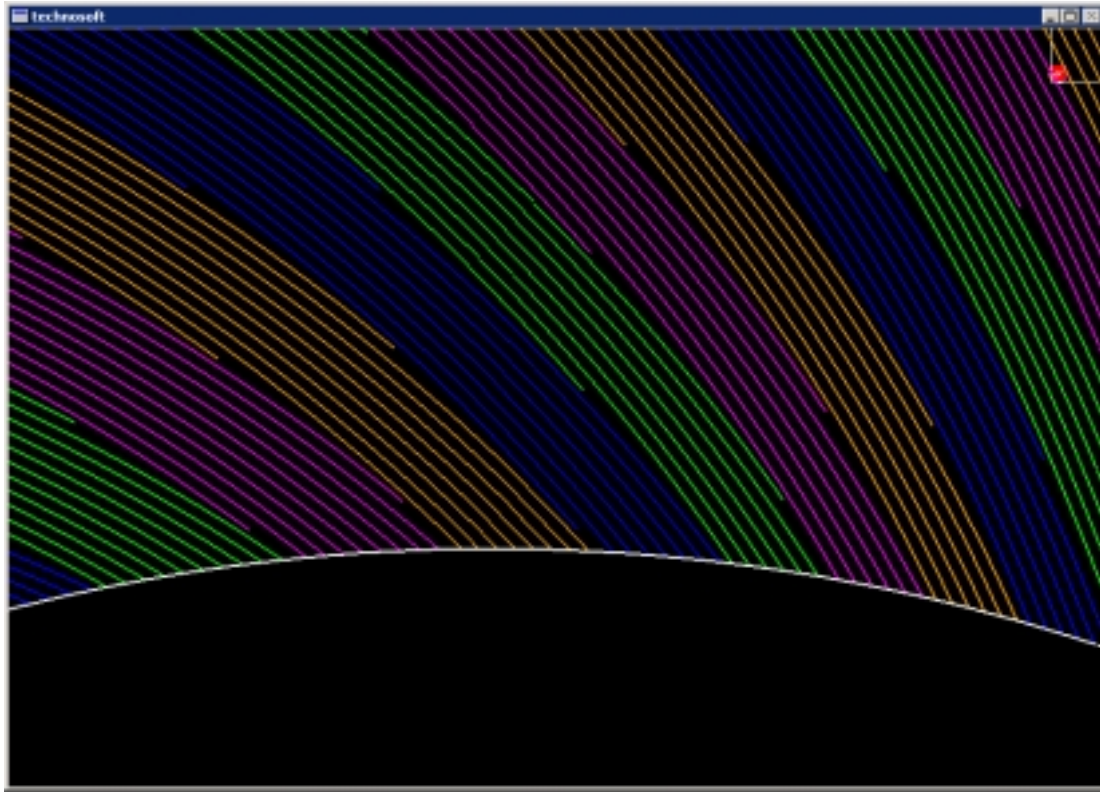


Figure 2.5.10 Magnified View of Laminate Family Ply After Trimming of Tows

Figure 2.5.11 shows detail of tows in a laminate family ply after tow trimming has taken place. The full tow outline is displayed, as opposed to the tow path (centerline) of previous figures. The step boundary occurs when a tow is dropped. The figure shows that a tow is dropped when it overlaps a neighboring tow by 50%. Gaps in tow material are represented by black shaded regions in Figure 2.5.11, and result from the point of tow drop until the next tow meets the neighboring course.

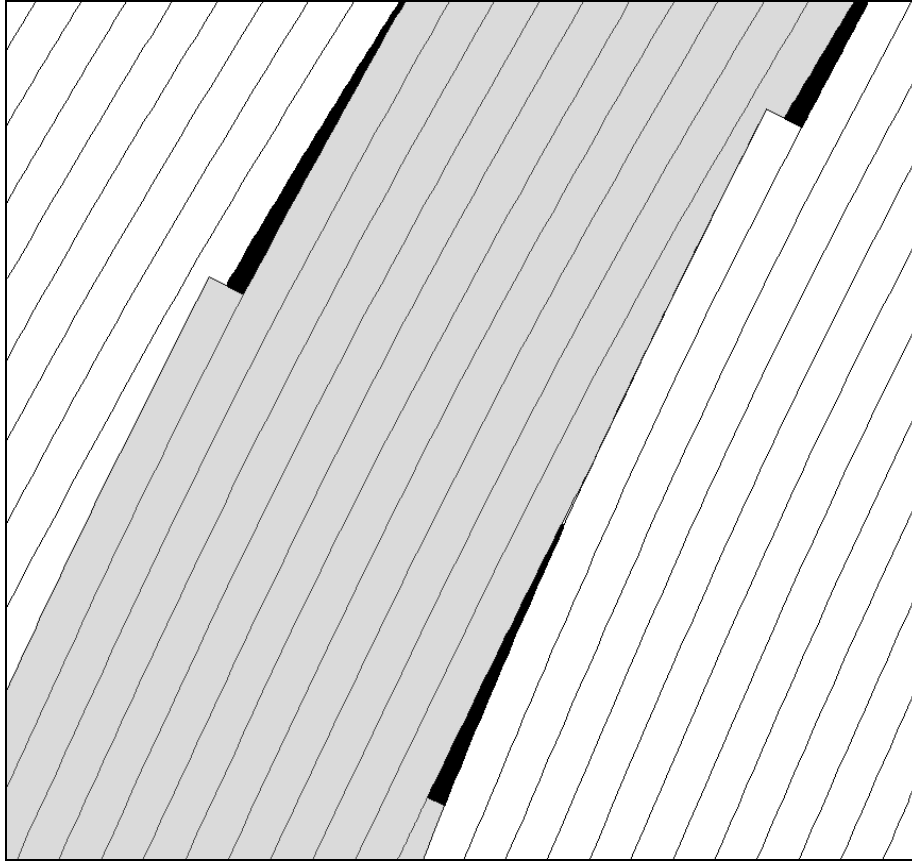


Figure 2.5.11 View of Overlap and Gap Regions (gap regions are shaded black)

Figures 2.5.3 through 2.5.11 show the design sequence for a band offset ply and a laminate family ply. In the design of a fiber placed part, multiple plies would be specified in the same manner to create the desired distribution of fiber orientations and part thickness.

After generation of the plies, the analysis tools of the software can be used. Analysis capabilities include area analyses, orientation and radius of curvature analyses, quantification of drops, adds, gaps and overlaps, and automated geometric analyses at points defined by finite element meshes.

2.5.3. Analysis Capabilities

Figure 2.5.12 shows an example of gap, overlap, and ply-level analyses in the SCADS software. Gaps and overlaps in three plies of a fiber placed part are depicted visually on the left of Figure 2.5.12. The number and position of gap and overlap regions are important to the designer, as they can greatly affect the strength properties of the part. In the system, gaps and overlaps are differentiated by color; gaps are white and overlaps are yellow in Figure 2.5.12. The two dialog boxes at the center of the figure depict a query of gaps and overlaps in a 6 inch by 6 inch area of the part.

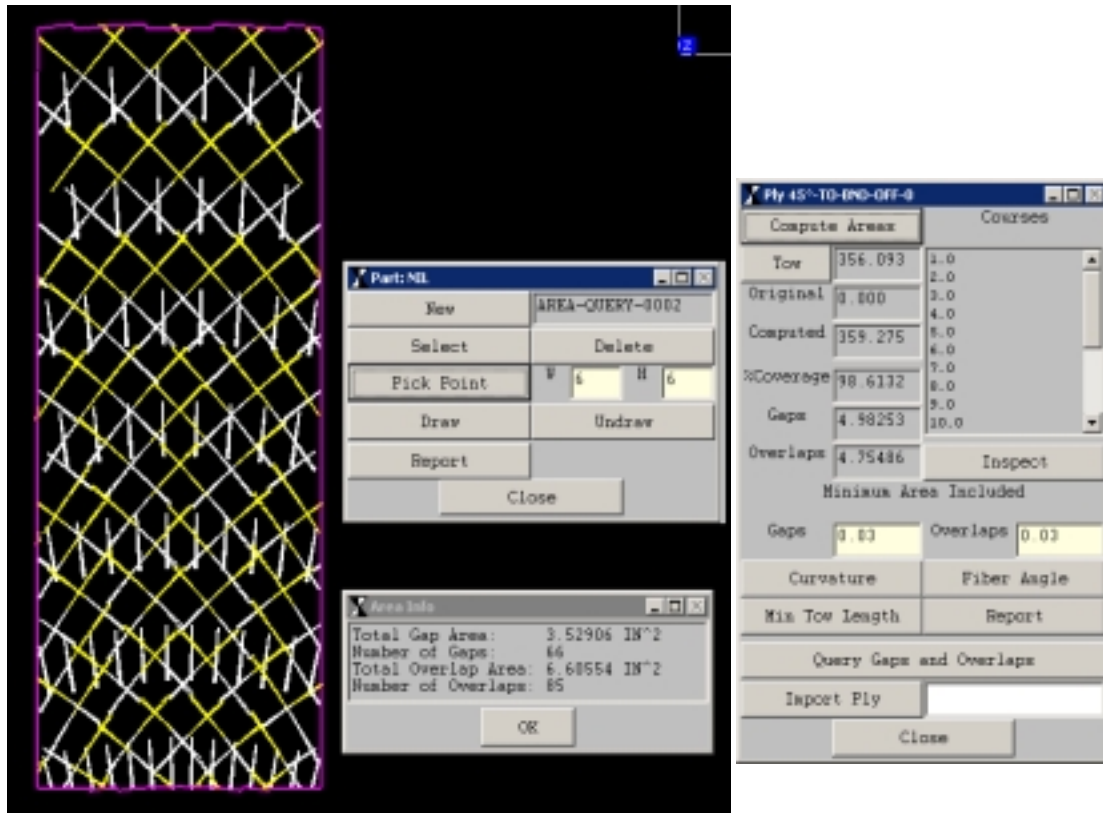


Figure 2.5.12 Analysis Examples (tow gap and overlap regions of three laminate family plies are shown)

The right side of the figure shows a dialog box depicting area analyses of a 45° laminate family ply.

An additional analysis capability is implemented by finite element node and mesh generation and export to FEA analysis packages. Classes are implemented for simple parallelogram quad meshes. The previously implemented Fiber Placement Analysis (FPA) software implemented geometric queries at node points as specified by an input file. The FPA software required two input files generated by a finite element analysis package such as

NASTRAN [²⁹] or ANSYS [³⁰]. An update to the FEA capabilities of the FPA software allows generation of nodes and meshes without input files. The nodes and meshes are then used to generate finite element analysis (e.g. NASTRAN) files for coupon type elements located anywhere on the part (see Figure 2.5.13).

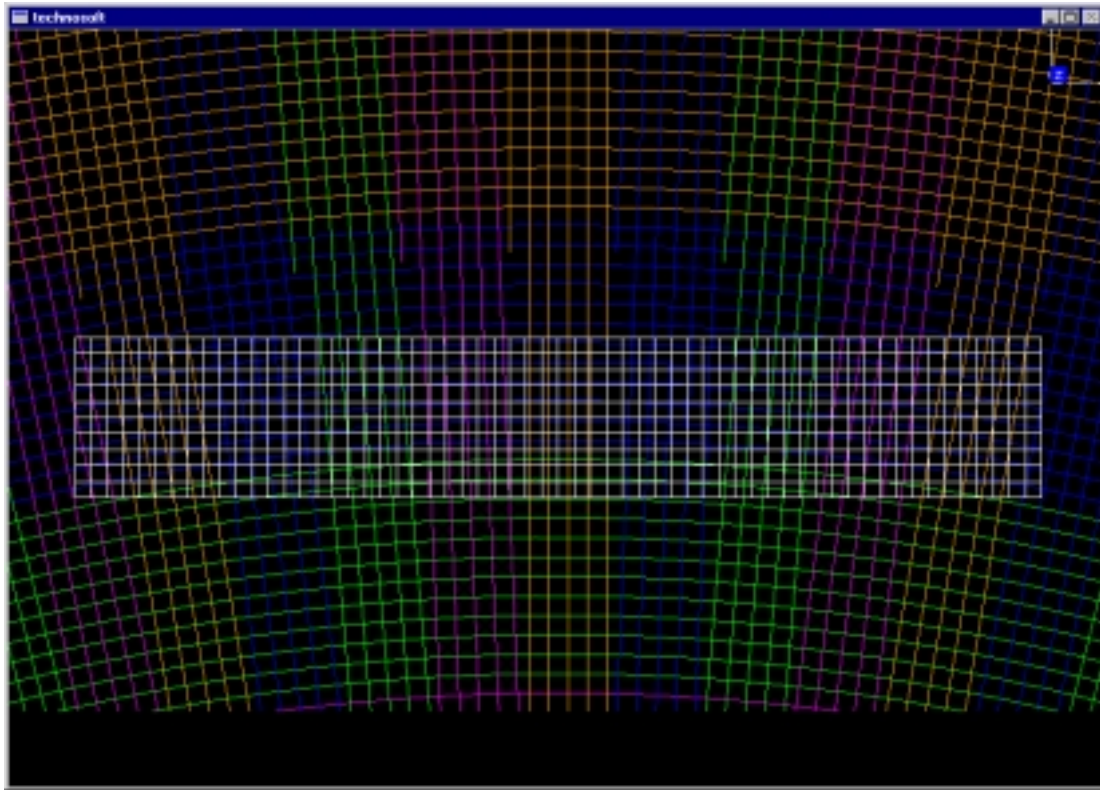


Figure 2.5.13 Finite Element Mesh (60 x 10 elements) of Test Coupon

²⁹. MSC.Software Corporation. *MSC.Patran User's Guide, MSC.Patran 2001 r2a*. Santa Ana, CA. 2001.
³⁰. Ansys Incorporated. *ANSYS 6.0 Documentation*. Canonsburg, PA. 2001.

2.6.0. Error Verification

The purpose of this section is to present verification of the error calculation methods presented in the Section 2.4. Sections 2.6.1 and 2.6.2 present verification of the estimation of error in placing offset points on a surface with circular cross section, and on a surface with non-circular cross section, respectively. Section 2.6.3 shows an experimental verification of the error in creating a laminate family curve oriented to a series of offset curves.

2.6.1 Surface with Circular Arc Cross Section

Section 2.4.1 showed that the potential error buildup of approximating offset curves on a surface with circular cross section. When a defining point on a reference curve is used to calculate a defining point on an offset curve, error accumulates. The error can be expressed as a function of the offset distance between corresponding defining points on two adjacent curves, d , the angle between surface normal vectors at these points, ψ , and the total number of curves, n . The equation is repeated here:

$$\text{TotalError} = (n - 1)d \left(1 - \frac{\Psi_i}{\tan \Psi_i} \right) \quad \text{Eqn 2.1}$$

To verify the error prediction of Eqn 2.1, the SCADS software (see Section 2.5- presentation of SCADS) is used. The SCADS software implements the methods of Section 2.3 for the domain of fiber placement of composite structures (see Section 2.1- Introduction and motivation). The SCADS application is used to create a placement surface describing a half cylinder. Five half-cylinder surfaces are considered- with radii equal to equal to 1.0, 2.0, 4.0, 8.0 and 16.0 length units. In all cases, the distance between curves is 0.15 length units. The initial curve, from which subsequent curves are placed, is a straight line corresponding to the axis of the cylinder projected onto the surface at $\theta = 90^\circ$ (see Figure 2.6.1). The defining points on the initial curve are used to place defining points for additional curves (on either side of the initial curve) that cover most of the half cylinder surface. Figure 2.6.2 shows a cross section of the placement surface.

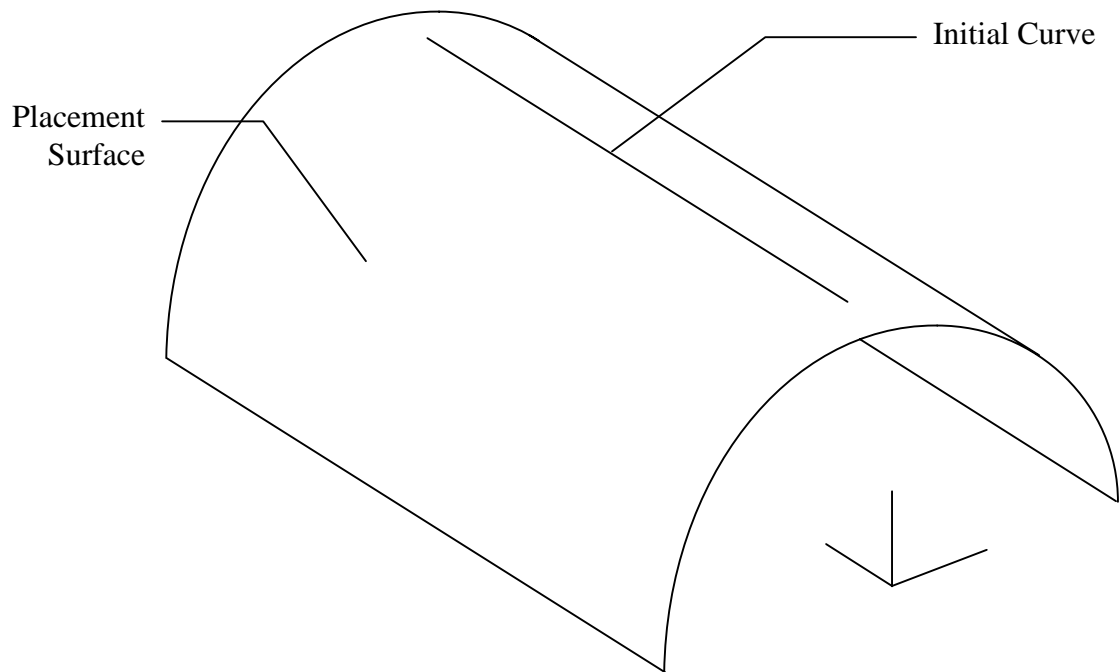


Figure 2.6.1 Curves are Based on the Initial Curve on the Placement Surface

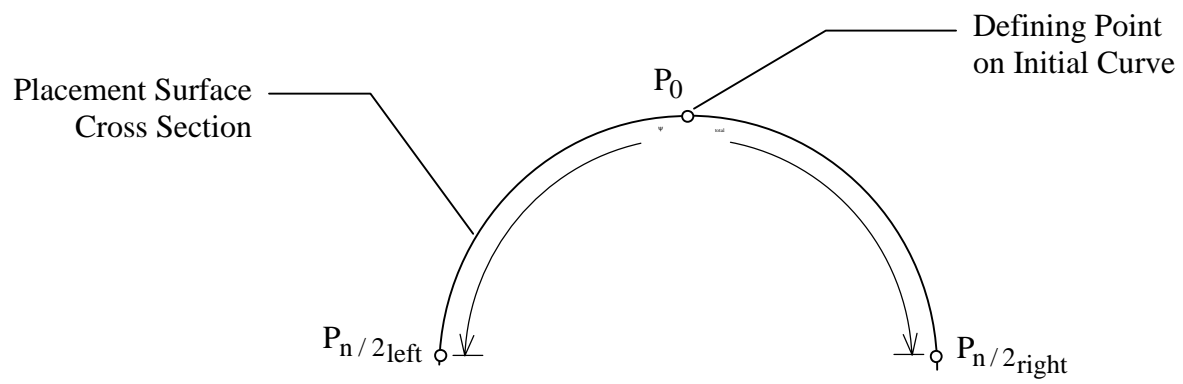


Figure 2.6.2 Points are Placed on Cross Section of Placement Surface

Figure 2.6.2 indicates that points are located on either side of P_0 , the defining point on the initial curve. $\frac{n}{2}$ points are placed to the left, and $\frac{n}{2}$ to the right. Because the first point on either side of P_0 is placed at half the offset distance (see Section 2.3.1), the total error to one side of P_0 becomes $\left(\frac{n}{2} - \frac{1}{2}\right)d \left(1 - \frac{\Psi_i}{\tan \Psi_i}\right)$. The total error on both sides of P_0 remains $(n-1)d \left(1 - \frac{\Psi_i}{\tan \Psi_i}\right)$.

Table 2.6.1 shows a buildup of the total error accumulated in placing n points as demonstrated by the SCADS application using the method of Section 2.3. Five cylinders with increasing radii are considered. In each case, the offset distance is 0.15. The nominal length along the cross section of the cylinder is calculated from $(n-1)d$.

Table 2.6.1 Placement Error Measured from Model

r_{cyl}	n	$(n-1)d$	Measured Ψ_{total} (rad)	$r\Psi_{total}$	Measured Error	Ψ_i (rad)	Calculated Error (Eqn 1)	Dif- ference
1.0	22	3.1500	3.1275	3.1275	0.0225	0.14889	0.0233	0.0008
2.0	42	6.1500	3.0693	6.1387	0.0113	0.07486	0.0115	0.0002
4.0	84	12.4500	3.1111	12.4442	0.0058	0.03748	0.0058	0.0000
8.0	168	25.0500	3.1309	25.0471	0.0029	0.01875	0.0029	0.0000
16.0	336	50.2500	3.1405	50.2485	0.0015	0.00937	0.0015	0.0000

Ψ_{total} is found by calculating the angle between surface normals at $P_{n/2left}$ and $P_{n/2right}$. Ψ_{total} is multiplied by r_{cyl} to arrive at the length from $P_{n/2left}$ to $P_{n/2right}$ on the placement surface. Because of the fixed value of d , Ψ_{total} will be close to, but not exactly equal to π radians. The measured error is the difference between the nominal distance $(n-1)d$ and $r\Psi_{total}$. The error is also calculated using Eqn 2.1. Ψ_i is calculated from Eqn 2.4a of Section 2.4: $\tan \Psi = \frac{d}{r}$. The last column of Table 2.6.1 shows the difference between the measured error, and the error calculated using Eqn 2.1.

Table 2.6.1 shows that there is a difference between the measured and calculated error when the radius of the cylinder is 1.0 or 2.0 and the offset distance is 0.15. When the radius of the cylinder is greater than 4.0, the measured and calculated errors are found to be the same within the accuracy of the computation.

Table 2.6.1 also shows that as the ratio of offset distance to cylinder radius decreases, the total error also decreases, even though the number of curves placed on the surface increases. This confirms that the method to approximate an offset curve on a surface is more accurate when the offset distance is very small when compared to the local radius of curvature on the surface.

2.6.2. Surface with Arbitrarily Curved Cross Section

We only have a closed form solution for the error of the method when the cross section of the placement surface is a circular arc. Section 2.4.1.2 proposes two methods of approximating error for arbitrarily curved cross sections. One method constructs an interpolating curve from corresponding defining points on a series of offset curves. The length of the interpolating curve can then be approximated and compared to the nominal length of the curve. We proposed a second approximate method that assumes that the arc between corresponding defining points of two curves can be approximated with one circular cross section. With this assumption, the error can be estimated as a function of the constant construction offset distance, d , and the angle between normal vectors, Ψ , measured at the two points. The quantities used to calculate this approximation were initially used to create the offset curves. The cumulative error can then be estimated from:

$$\text{TotalError} = \sum_{i=2}^n d \left(1 - \frac{\Psi_i}{\tan \Psi_i} \right) \quad \text{Eqn 2.2}$$

where d is the distance between corresponding defining points on adjacent curves, P_i and P_{i-1} , and Ψ_i is calculated from:

$$\Psi_i = \cos^{-1} \left(\frac{|\vec{N}_i \cdot \vec{N}_{i-1}|}{|\vec{N}_i| |\vec{N}_{i-1}|} \right) \quad \text{Eqn 2.3}$$

where \vec{N}_i and \vec{N}_{i-1} are normal vectors to the placement surface at points P_i and P_{i-1} respectively.

Both approximation methods are used to estimate the cumulative error of placing offset curves on an arbitrarily curved surface, and the results compared. Where the cross section of the placement surface of the previous section was a circular arc, the cross section in this case is a wave-like form created by interpolating points (see Figure 2.6.3). Figure 2.6.3 shows the placement surface with offset curves placed by the SCADS application using the method of Section 2.3. Figure 2.6.4 shows a cross section of defining points.

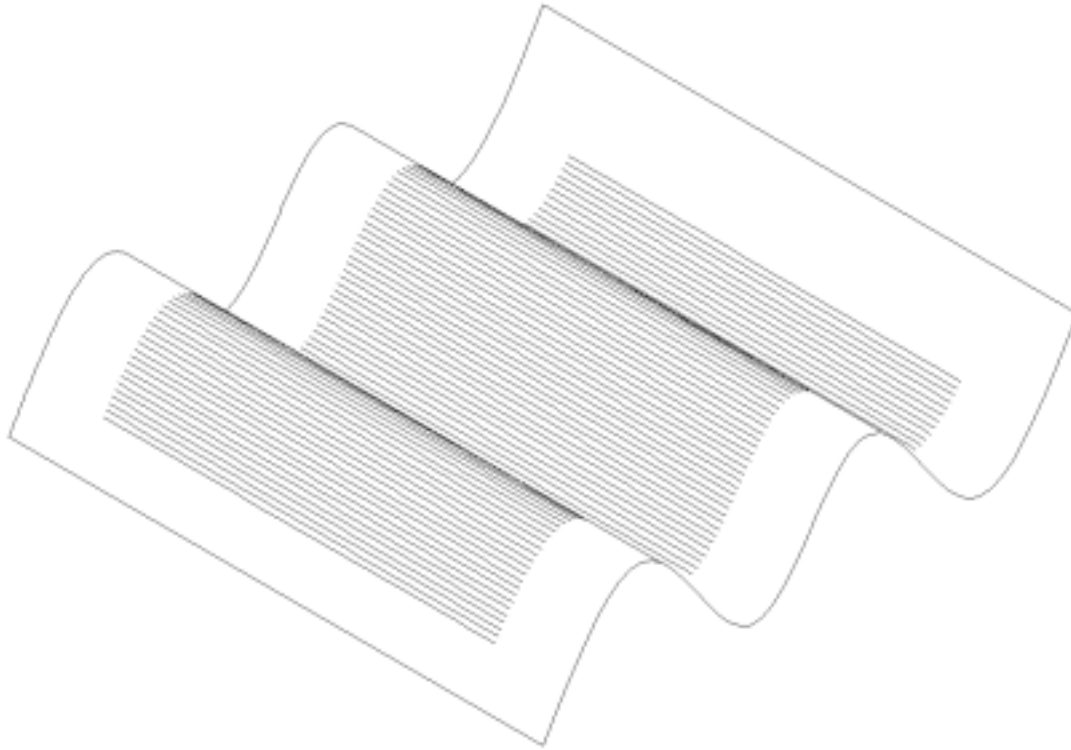


Figure 2.6.3 Offset Curves are Placed on an Arbitrarily Curved Surface

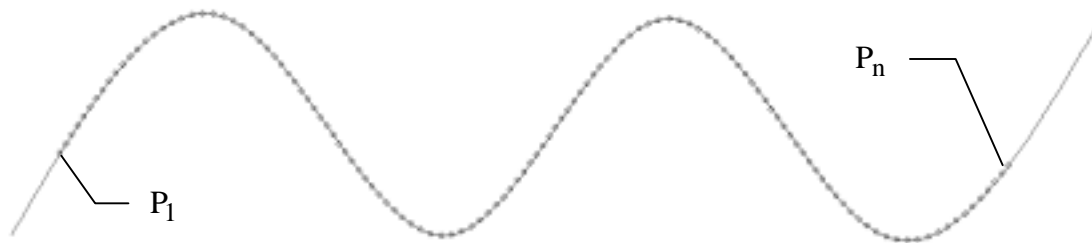


Figure 2.6.4 Cross Section of Figure 2.6.3 Surface Shows Defining Points

The method described above is used to estimate the placement error in locating the 124 points shown in Figure 2.6.4. The nominal length measured along the surface between P_1 and P_n is calculated from $d(n-1)$. With an offset distance, d , of 0.1500, the nominal length is 18.4500. Two approximations of error are calculated- one using surface normal vectors, and one using a spline interpolating the points P_1 through P_n . Using the SCADS application, the surface normal vector is queried at each of the points shown in Figure 2.6.4. Using Eqn 2.2, the total error is estimated to be 0.0508 length units, or 33.9% of the offset distance. As a comparison, an interpolating spline is constructed that passes through points P_1 through P_n . The length of the interpolating spline is approximated using a query to the SCADS geometry engine. The length calculation is accurate to 10^{-8} for a length less than 1000 [28]. The length of the interpolating spline is approximated to be 18.4002. The difference between the approximated length of the interpolating spline (18.4002) and the nominal length (18.4500) is the approximated error:

0.0498, or 33.2% of the offset distance. We can see that the two approximation methods produce an error estimate that is of the same magnitude.

Another example of a placement surface with a non-circular cross section is the outer surface of an airplane wing. For this example, a wing surface, based on the Raytheon Premier I small business jet [26], is constructed. One half of the wing (to the left of the fuselage) is constructed with a root chord length of 88.9 inches, tip chord length of 44.5 inches and a root to tip span of 287.8 inches. Because the airfoil shapes of the Raytheon Premier I remain proprietary, representative airfoil shapes are chosen from publicly available literature. The assumed root airfoil shape is of the NACA 23014 profile [31], while the tip airfoil is of the NACA 23012 profile [31]. The surface is created as a ruled surface between the root and the tip airfoil. Figure 2.6.5 shows a wireframe representation of the placement surface. Figure 2.6.5 also shows the region of the surface on which offset curves are generated. This region is represented as the shaded portion of Figure 2.6.5. Using an initial curve that coincides with the leading edge of the wing, 790 offset curves are placed within the shaded region shown in Figure 2.6.5, and correspond to a single ply of a theoretical wing skin panel fabricated using fiber placement techniques.

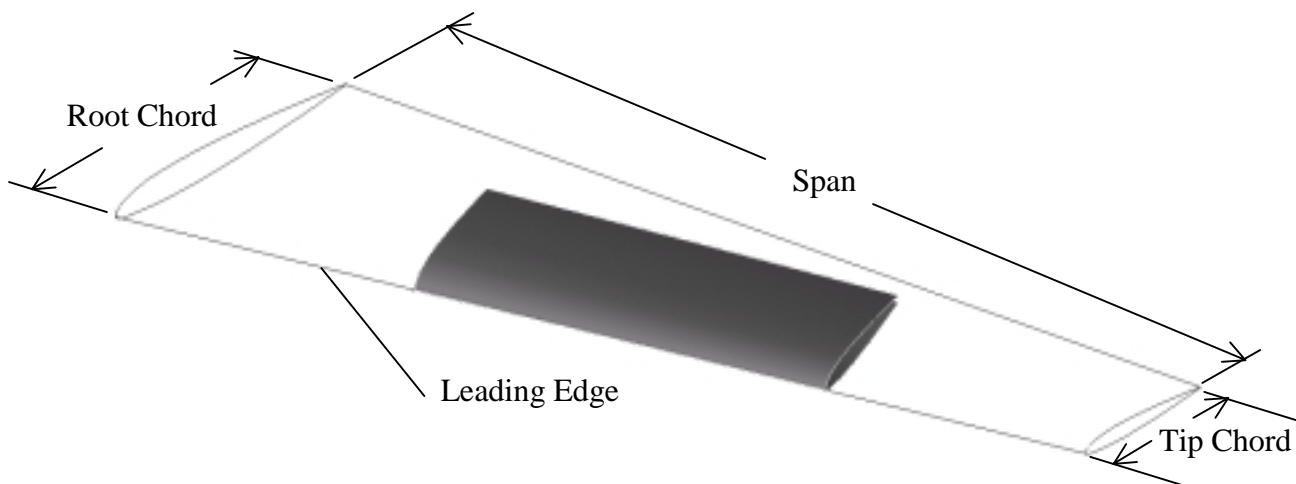


Figure 2.6.5 Offset Curves are Placed on Representative Wing Surface

Figure 2.6.6 shows a cross section (taken by aligning the normal of a cutting plane with the leading edge) of offset curve defining points corresponding to the point of each offset curve that is closest to the root of the wing surface.

³¹. Abbott, I. H. and Von Doenhoff, A. E. *Theory of Wing Sections*. Dover Publications, Inc. New York, New York. 1959.

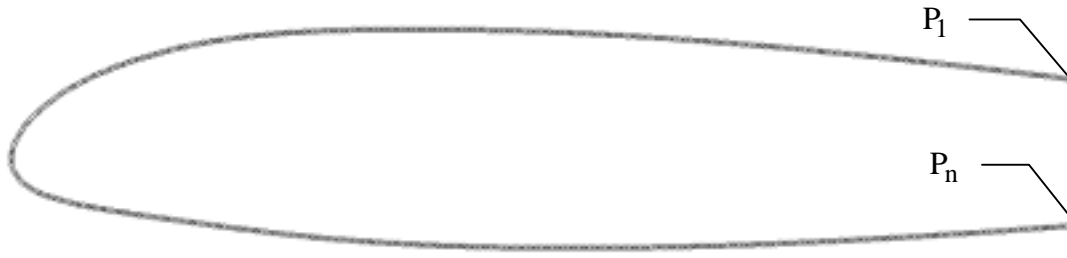


Figure 2.6.6 Cross Section of Figure 6.5 Surface Shows Defining Points

The method of the previous example is used to estimate the placement error in locating the 790 points shown in Figure 2.6.6. The error is first approximated by constructing an interpolating spline that passes through points P_1 through P_n , approximating its length (using a query to the SCADS geometry engine), and comparing that length to the nominal length of $d(n-1)$. The length of the curve constructed through points P_1 through P_n is approximated as 118.3428 inches. For the offset distance, d , of 0.1500 inches, the nominal length is 118.3500 inches. Therefore, the error approximated by constructing an interpolating spline is 0.0072 inches, or 4.8% of the offset distance. Using the SCADS application, the surface normal vector is queried at each of the points shown in Figure 2.6.6. Using Eqn 2.2, the total error is estimated to be 0.0093 inches, or 6.2% of the offset distance. The difference between the two error approximations is 0.0021 inches. Again, the two approximation methods predict error of the same order. It should be noted that the approximated placement error, after placing 790 points is just 4.8% of the offset distance. As mentioned in Section 2.4, current practice in the domain of fiber placement allows a cumulative error of 0.25 inches over a total offset distance of 12 inches [2]. This represents a cumulative error of 200% of the offset distance after about 100 points. So, the error of our approximation method is significantly better than current allowables.

2.6.3. Laminate Family Curve

The objective of the method to create a laminate family curve is to construct a curve that demonstrates a fixed angle of intersection with every curve in a series of offset curves on a surface. The fixed angle of intersection is known as the laminate family angle. Section 2.3.4 describes a piecewise method of constructing a laminate family curve. As stated in Section 2.4.2, when the points generated by the method of Section 2.3.4 are interpolated by a spline, error can develop for the angle of intersection between the laminate family curve and an offset curve. This section presents a study that records the angle of intersection error with changes in offset distance, radius of curvature of the offset curves and laminate family angle.

The study is performed using offset curves defining arcs in a plane. The offset curve arcs vary in radius from about 16 length units (r_{\min}) to about 52 length units (r_{\max}), depending on the offset distance. A laminate family curve is then constructed using the offset curves. Figure 2.6.7 shows an example of a 40° laminate family curve constructed using a series of offset curves.

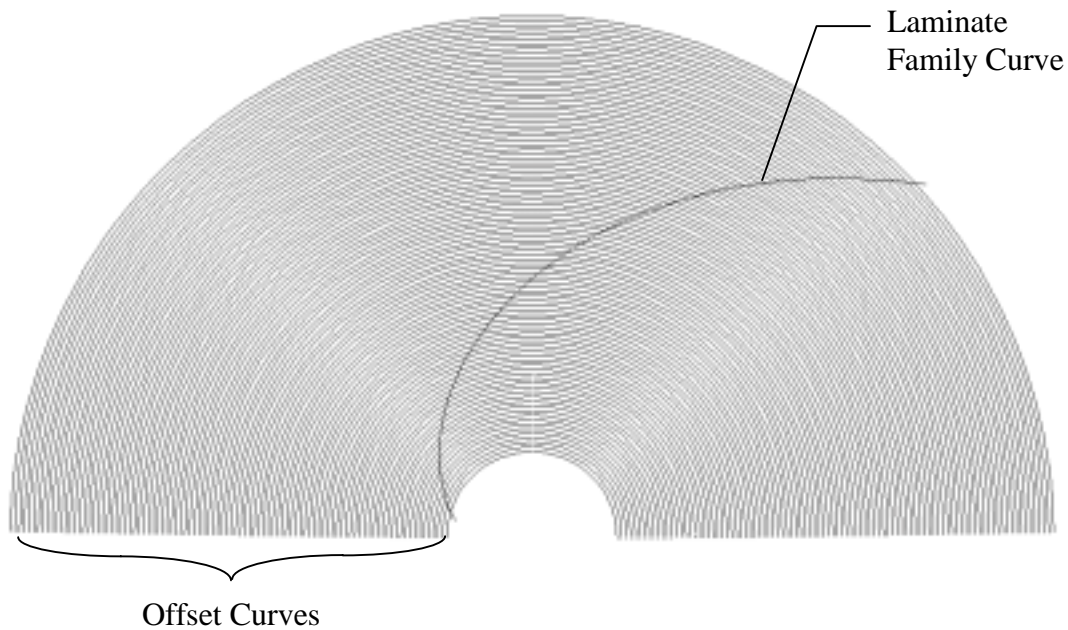


Figure 2.6.7 Example of a 40° Laminate Family Curve

The study evaluates the error of the laminate family curve orientation halfway between two offset curves. To evaluate this error, a series of offset curves is approximated at the given offset distance and used to approximate the laminate family curve. Then, an additional series of offset curves is approximated so that one new offset curve is placed between each of the original offsets. The angle of intersection between the laminate family curve and each of the new offset curves is calculated. The error is calculated as the actual angle of intersection subtracted from the desired laminate family angle. For the study, the laminate family angle and the offset distance are varied, and the error is recorded as a function of the radius of curvature of the offset curve. Table 2.6.2 shows the study parameters.

Table 2.6.2 Laminate Family Curve Error Study Parameters

Offset Distance	r_{\min}	r_{\max}	n_{curves}
0.100	18.950	51.8500	330
0.125	17.6875	52.8125	282
0.150	17.0250	51.9750	234
0.175	16.9625	53.5375	210
0.200	17.5000	52.1000	174
0.225	15.9375	52.1625	162
0.250	17.3750	54.6250	150

Although presented as non-specific length units, the offset distances shown in Table 2.6.2 correspond to ‘typical’ values, in inches, used in the domain of fiber placement [2]. The minimum radius value, r_{\min} , is somewhat less than the accepted minimum radius of curvature,

in inches, used in the fiber placement process. While the maximum radius of curvature, r_{\max} , can obviously go to infinity (i.e. zero curvature), the value of about 50 inches is considered large enough to establish the behavior of error with increasing radius of curvature.

Results of the study are presented graphically. Each figure corresponds to a case presented in Table 2.6.2, but only figures for the cases of $d = 0.100$, $d = 0.150$, $d = 0.200$ and $d = 0.250$ are presented in this section. The cases are presented in Figures 2.6.8, 2.6.9, 2.6.10 and 2.6.11, respectively. For each of the cases, the laminate family angle is varied from 10° to 80° by 10° increments. It should be noted that, for a laminate family angle of 90° , the error in the angle of intersection is zero, as the laminate family curve describes a radial line on the offset arcs.

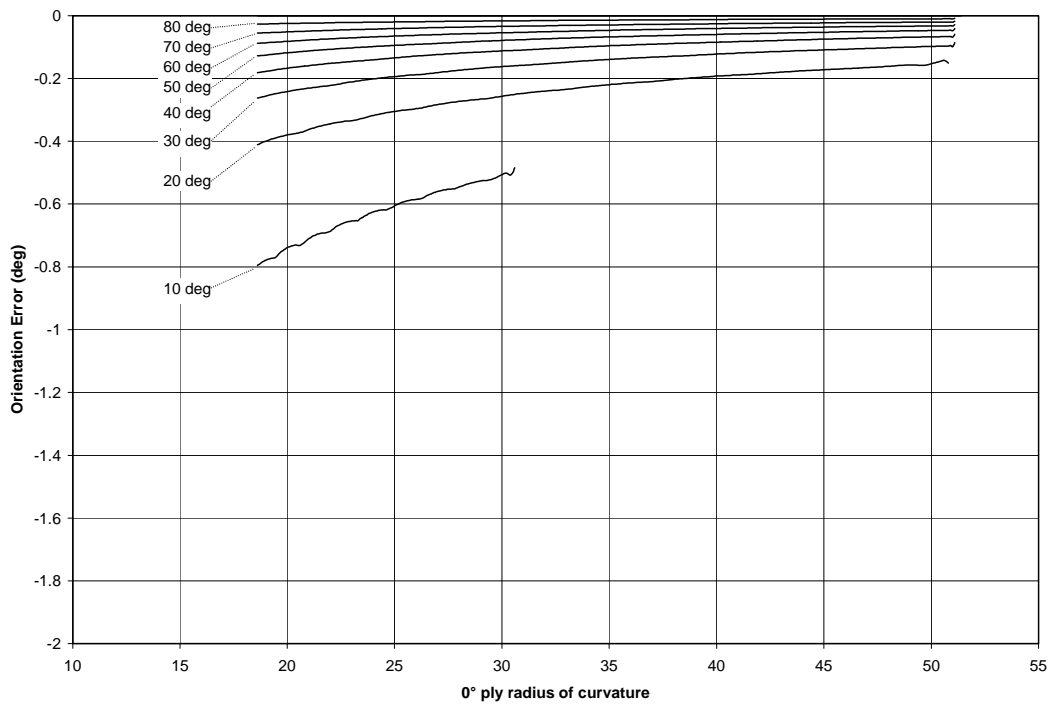


Figure 2.6.8 Angle of Intersection Error for Offset $d = 0.100$

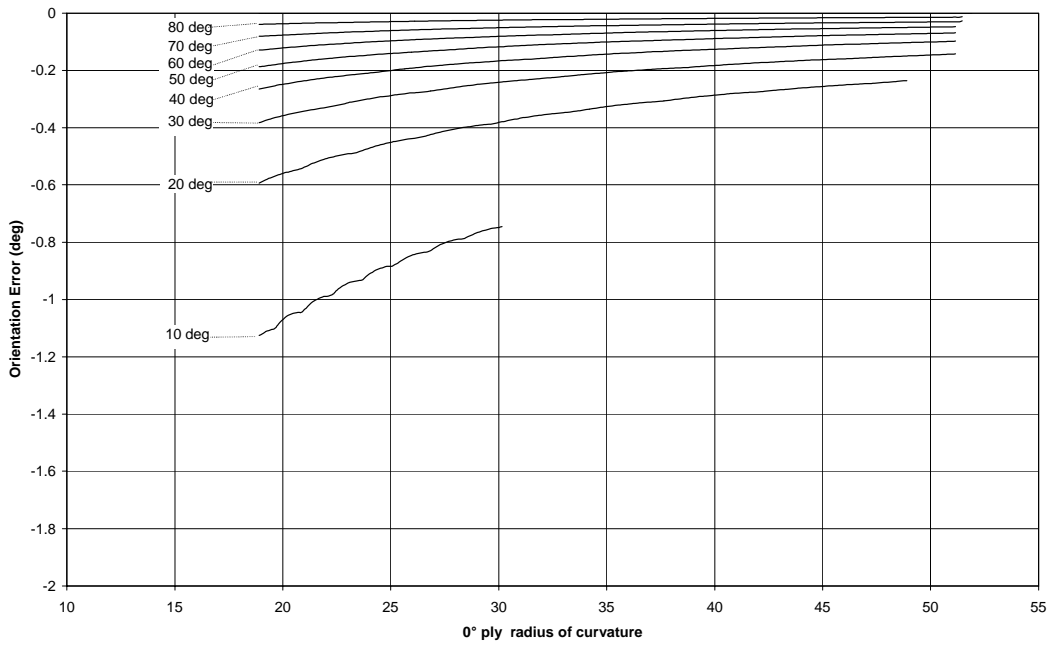


Figure 2.6.9 Angle of Intersection Error for Offset $d = 0.150$

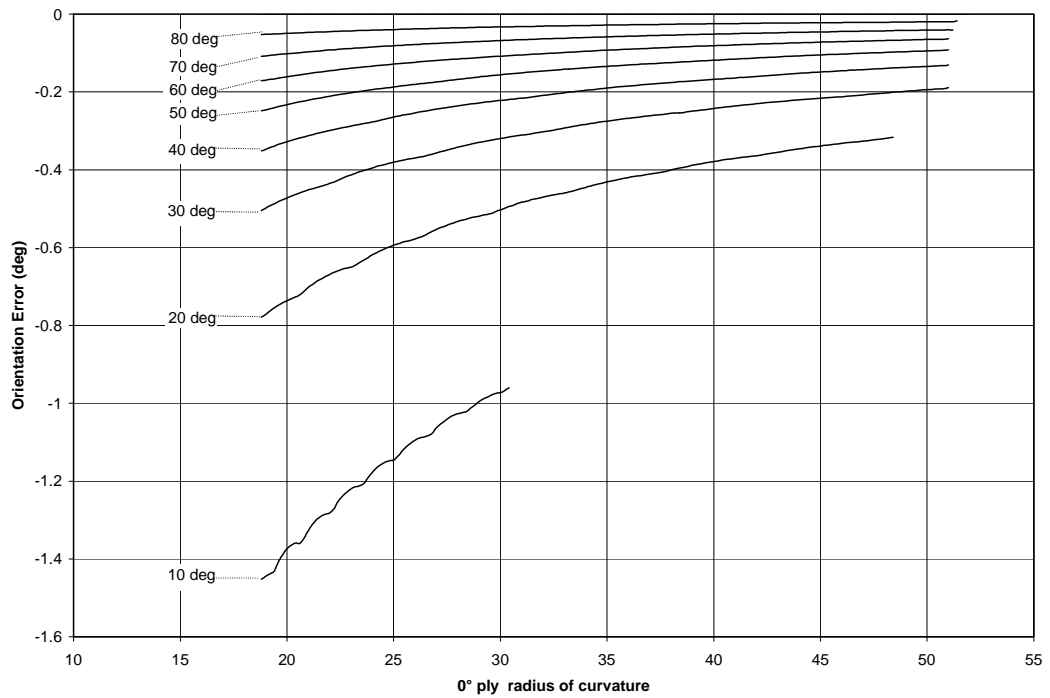


Figure 2.6.10 Angle of Intersection Error for Offset $d = 0.200$

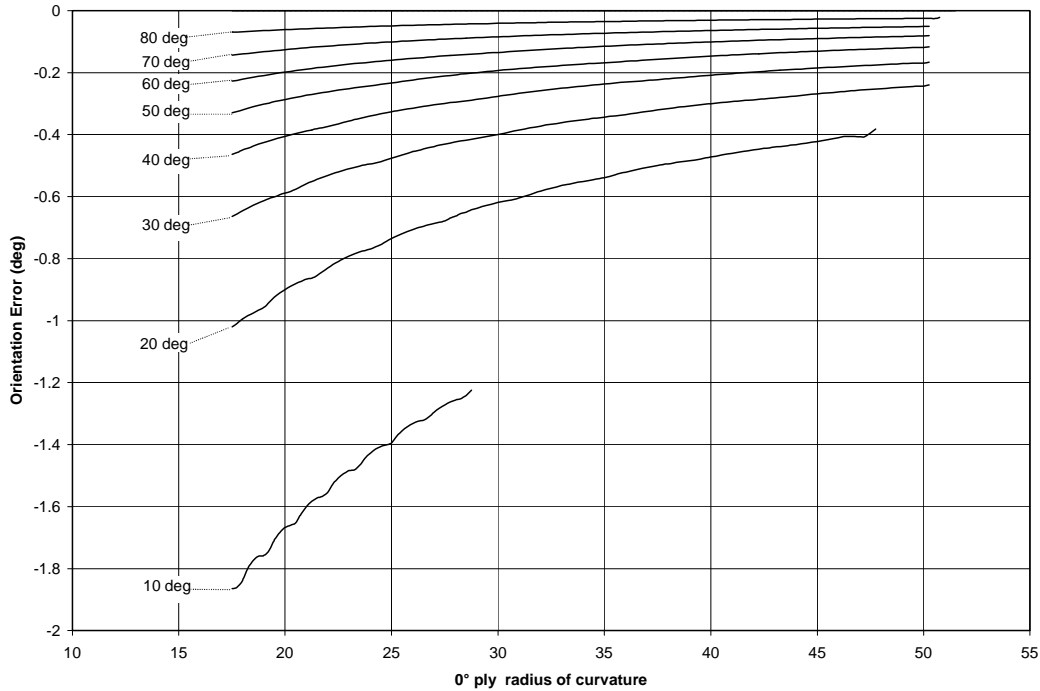


Figure 2.6.11 Angle of Intersection Error for Offset $d = 0.250$

Figures 2.6.8 through 2.6.11 show the error in the actual angle of intersection between a laminate family curve, and an offset curve used to construct it. The figures show the following trends:

- The greatest absolute error occurs with the smallest value of laminate family angle, and goes to zero as the laminate family angle goes to 90° .
- As the radius of curvature gets larger, the error decreases. In all cases, as the radius of curvature goes to infinity, the error will go to zero.
- As the offset distance increases, the absolute value of the error also increases (see Figure 2.6.12).

Figure 2.6.12 shows the variation of the error for each of the offset distance cases listed in Table 2.6.4.

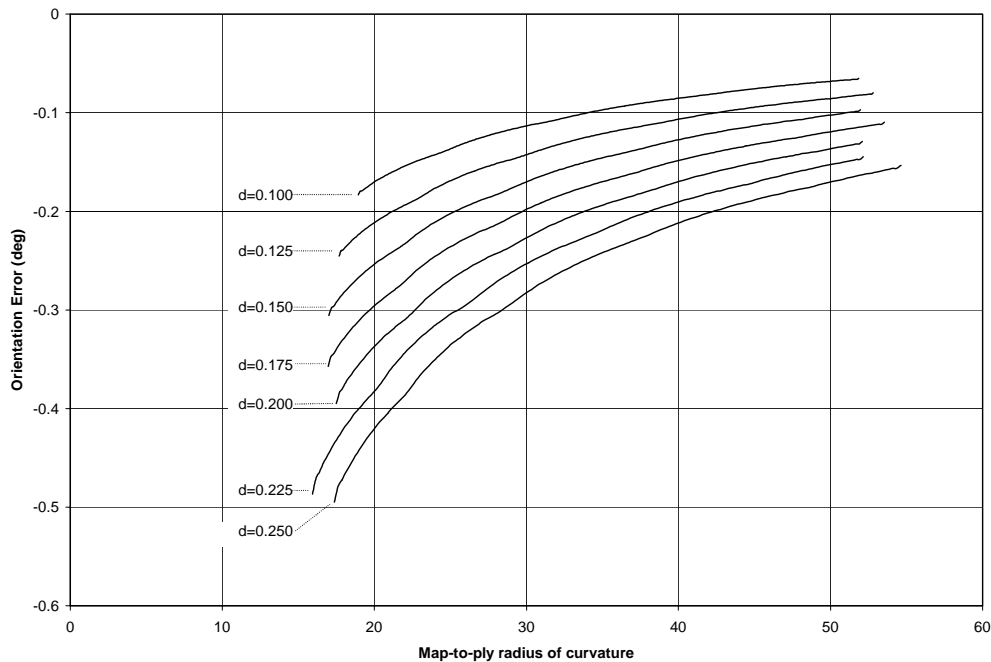


Figure 2.6.12 Angle of Intersection Error for Laminate Family Angle of 40° and Varying Offset Distance, d

It should be noted that, in the domain of fiber placement, laminate family angles vary between $+90^\circ$ and -90° . Figures 2.6.8 through 2.6.11 show the error of the methods for laminate family angles between $+10^\circ$ and $+90^\circ$. For all of these cases, the error (measured angle of intersection subtracted from laminate family angle) is less than or equal to zero. For laminate family angles between -10° and -90° , the same trends in error are seen, except the sign of the error becomes positive.

The study presented in this section shows that the error of the method used to create a laminate family curve exhibits predictable trends with laminate family angle. The error also exhibits predictable trends with variation of the radius of curvature and offset distance of curves used to construct the laminate family curve. Figure 2.6.11 shows a maximum error magnitude of about 1.9° for a laminate family angle of 10° , offset distance of 0.250 and 0° ply radius of 16. This case represents extreme values for all values in the domain of fiber placement. More typical values are laminate family angle of 45° , offset distance of 0.125, and 0° ply radius of greater than 25. For such a case, Figure 2.6.9 shows an error magnitude of about 0.3° .

It is useful to compare the orientation error to allowable error in composite parts. The United States Federal Aviation Administration allows for an orientation error of 0.25 inches in one foot when fabricating parts to be used for mechanical testing [³²]. This is equivalent to a 1.2°

³². Tomblin, J. et al. *Material Qualification Methodology for Epoxy-Based Prepreg Composite Material Systems*. United States Department of Transportation, Federal Aviation Administration Report DOT/FAA/AR-00/47. Washington, DC. April, 2001.

variation if straight, and a higher variation if the fiber curves over and then back across the nominal orientation. The error is allowed in specimens that are fabricated for the purpose of establishing material properties. This allowable represents a lower bound for the error that can be accepted in a manufactured part. Common practice allows for 2.0° variation in manufactured parts. Thus, the 1.8° orientation error observed in Figure 2.6.11 is still within the acceptable error of a manufactured part.

2.7.0. Conclusions

Fiber placement of composite structures promises reduced cost in the form of production waste savings, and increased structural strength-to-weight ratios that can be realized with tailored fiber orientations. To date, reduced production costs have been realized with fiber placement, but a lack of robust design and analysis tools prevents designers from fully exploring weight saving design solutions in the preliminary design phase. A design and analysis tool for fiber placed composites must be capable of modeling the part down to the level of the tow, in turn requiring a method to represent the position of individual tows on the design surface. In this thesis, we have formally defined two types of curves required to represent individual tows in a fiber placed part; the offset curve on a surface, and the laminate family curve; and present approximate methods to compute both types.

Offset curves on a surface are used to represent the positions of individual tows that lie next to one another with no gaps or overlaps of tow material. The curves are used to represent a group of tows laid by a single pass of the fiber placement machine head (a course), and can be used to orient multiple courses along the primary load path of the part. We present a method to calculate piecewise linear approximations of offset curves on the surface. We also present a closed form expression which bounds the error of our approximation when the cross section of our design surface is well approximated by a circular arc. We report no such closed form expression for a design surface with arbitrarily curved cross section. However, we propose an alternative method of bounding the error that does not involve additional geometric constructions or queries. It is verified that the results of this approximation are of the same order as a much more computationally intensive method involving the construction and length calculation of additional curves on the surface. It is found that, in the domain of fiber placement, the cumulative error in offset distance after placing 10^3 to 10^4 curves is of the order of a single offset. This error is well within current allowable error for a manufactured part.

To handle loads that are offset from the primary load path of a part, a different fiber (curve) orientation method is needed. Such a curve must exhibit a constant angle of intersection with each curve in a series of offset curves. This curve is known as a laminate family curve. A method is presented that calculates a piecewise linear approximation of a laminate family curve, given a series of offset curves. We have shown that the approximate laminate family curve exhibits error (variation from the desired angle of intersection) that directly proportional to the offset distance and indirectly proportional to the local radius of curvature of the offset curves.

The approximation methods for offset curves and laminate family curves are implemented in the Steered Composites Analysis and Design System, SCADS. SCADS uses the approximation methods to model the tows, courses and plies of a fiber placed part. The analysis methods of a previously implemented system are incorporated into SCADS- allowing the

quantification of gaps, overlaps, and tow level properties; and the generation of files for use by Finite Element Analysis packages.

2.7.1. Future Directions

The SCADS system represents a first step towards a robust design and analysis system for the design of fiber placed composite structures. Enhancements to the system can be grouped into two areas: development of additional geometric methods to model the fiber placed parts and further development of SCADS itself. In addition, while verification of the approximation methods of this thesis has been performed in a computer environment, integration of the methods into a fiber placement machine programming system would allow verification using actual parts.

At this point in the development of SCADS, two immediate geometric modeling challenges exist. The first challenge involves the computation of one or more continuous fiber orientation curves from an array of points on the design surface, with an optimal fiber orientation direction at each point. Such an array of points and directions is the result of structural optimization using finite element analysis. Figure 2.7.1 shows an example fiber orientation angles optimized for a part with a hole at the center. Only one quarter of the part is shown in Figure 2.7.1. A need exists for a method to find a best solution of fiber axis curve(s) that most closely match optimal fiber orientation at discrete points while not violating the physical constraints of manufacture and without producing excessive tow gaps and overlaps. Because a number of potential solutions may exist, heuristics must be developed to evaluate solutions against each other.

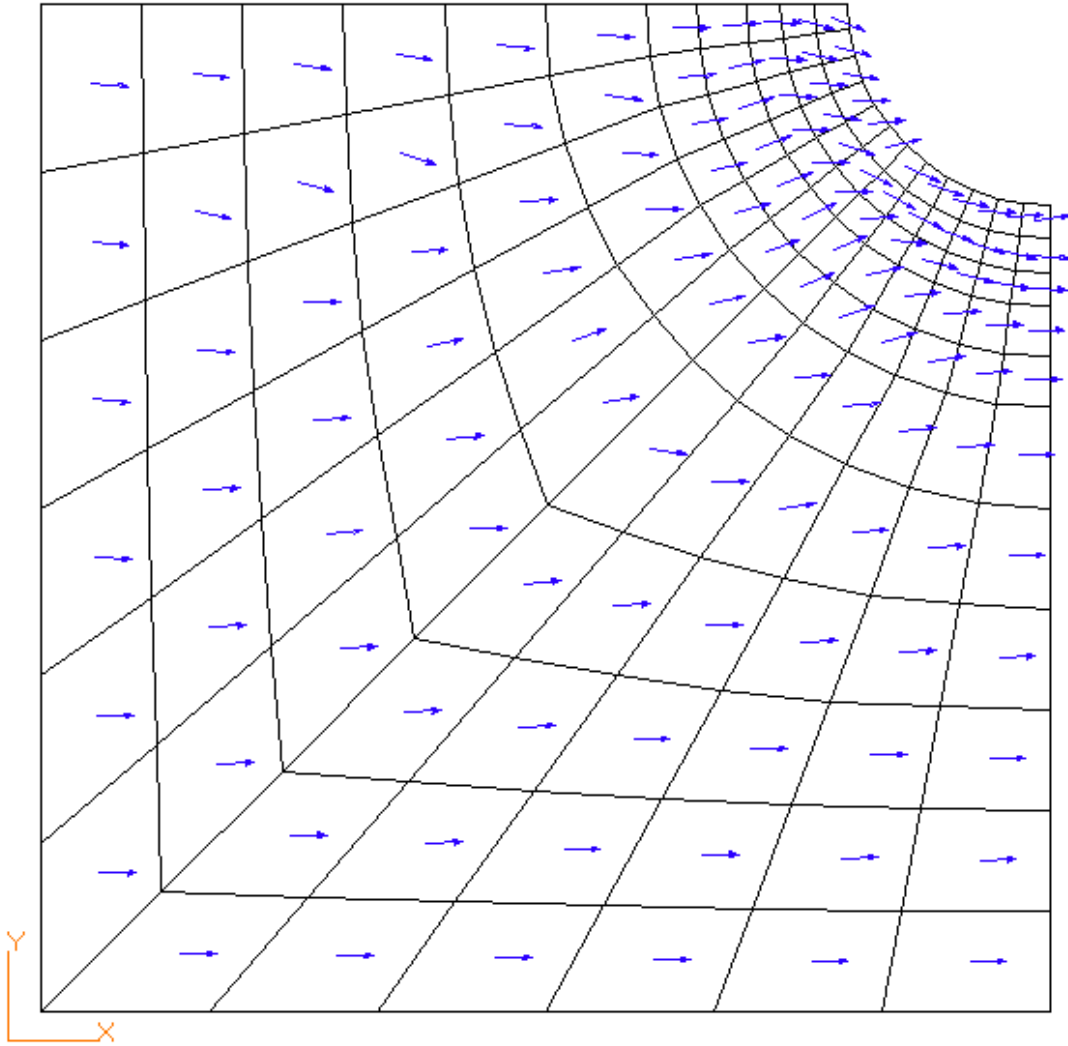


Figure 2.7.1 Fiber Orientation Direction is Optimized at Discrete Locations

A second geometric challenge of modeling is the update of the design surface with each ply of tow material. With each layer of material, the design surface changes. While many methods exist for the approximation of offset surfaces, the fiber placement domain introduces the challenge of multiple surfaces because a single ply seldom covers the design surface entirely. Thus, the next design surface is a combination of the original design surface and an offset of part of that surface. As multiple plies are placed by the machine, more and different combinations of surfaces can result. In addition, it is not uncommon for a layer of core material (e.g. honeycomb) to be placed between plies of a fiber placed part, introducing an additional surface. So, a need exists for a robust method to represent the design surface as a combination of multiple surfaces in the part.

In addition to geometric methods, several areas of development are needed for the SCADS software. One needed enhancement, the ability to define the tool surface as a combination of surfaces, would be enabled by the geometric methods mentioned above. A

second enhancement involves the user interface of the system. The SCADS system, to date, has not been thoroughly tested by users. Thus, the user interface should be evaluated with user testing and changed as needed. In addition, the modeling capability of SCADS should enable it to exchange geometric data with the offline programming systems of fiber placement machines. Current offline programming systems use a discretized representation of the design surface, and machine head positioning error can result. Because the SCADS system models individual courses on the curved surface, a piecewise linear approximation of a head path can be calculated and exported to the offline programming system.

In Section 2.5, we describe the incorporation of an existing analysis capability into the SCADS system. Another previously developed system contains capabilities that are useful to SCADS. The Parametric Composite Knowledge System, PACKS, was developed for hand layup composite structural design, but its ply calculation methods are also applicable to the domain of fiber placement. Thus, these methods should be incorporated into SCADS. As with any CAD/CAM system, development of SCADS should be ongoing. The enhancements presented here by no means represent a complete list of needed development for SCADS. Rather, these enhancement represent the next step in the development of the system.

Finally, a need exists to evaluate the methods presented herein, and the overall modeling of the SCADS system, using structures that are physically built by a fiber placement machine. Current research in the Aerospace Engineering Department at the University of Kansas includes the design and fabrication of a fiber placement machine. The KU fiber placement machine utilizes a 6-axis light industrial robot. The SCADS system can currently export head position files that can be interpreted by the robot's motion control program. To date, development of the KU fiber placement machine head continues, and a part has yet to be built. When a part can be built with the KU machine, verification of SCADS and its methods can begin. As mentioned previously, a future direction of the SCADS system is the capability to calculate machine head location data for the offline programming systems of commercial fiber placement machines. At that point, verification can be performed using parts built with commercial fiber placement machines.

Many challenges exist for a fiber placement CAD/CAM system in the areas of geometric methods, enhancements to the SCADS system, and verification using actual parts. By meeting these challenges, and the many others that will appear along the way, a robust design and analysis tool for fiber placed composite structure design can be realized. Such a system will allow designers to take advantage of machine capability to steer structural fibers, and hence realize weight savings associated with this capability. In the aerospace industry, with its constant push towards lighter, stronger structures, the promise of weight savings in fiber placed structures should drive the development of SCADS to a widely used design and analysis tool.

3.0 Structural Optimizations of Steered-Fiber Composite Structures

Nomenclature

[A]	Extensional stiffness matrix
[B]	Coupling stiffness matrix
[D]	Bending stiffness matrix
[K]	Elastic stiffness matrix
[K_G]	Differential/geometric stiffness matrix
{N}	Force per unit length vector
{M}	Moment per unit length vector
[Q]	Reduced stiffness matrix
[T]	Transformation matrix
E	Young's modulus
F(x)	Objective functions
G	Shear modulus
L(x,λ)	Lagrangian functions
R_F	Composite laminate failure indices
a	Long-side length in buckling field
b	Short-side length in buckling field
c	Aspect ratio of buckling field
g_j(x)	Inequality constraint functions
h_k(x)	Equality constraint functions
{p}	Load vector
r(y(x))	State variables
s	Downhill search direction
t_i	i th -layer thickness
{u}	Displacement vector
x_i	Design variables
y(x)	Structural variables

Greek

α	Step size in search direction
α_{mn}	Coefficient of Fourier Series

$\{\gamma\}$	Shear strain vector
ϵ_G	Small positive constant for numerical accuracy in finite difference method
ϵ_f	Termination parameter for relative change in objective function
ϵ_{res}	Termination parameter for maximum violation of constraints
ϵ_x	Termination parameter for relative change in design variable
$\{\epsilon\}$	Strain vector
$\{\kappa\}$	Midplane curvature vector
λ_i	eigenvalues
ν	Poisson's ratio
$\{\sigma\}$	Stress vector
$\{\tau\}$	Shear stress vector
θ_i	i^{th} -layer angle

Superscript

o	Initial design; also, laminate midplane property
*	Optimal design
c	Constant parameter

Subscript

i	i^{th} -number of design variable
j	j^{th} -number of inequality constraint
k	k^{th} -number of equality constraint; also k^{th} -ply number
x	x direction in element coordinate system
y	y direction in element coordinate system
xy	xy-plane direction in element coordinate system
1	Longitudinal or axial direction in local material coordinate system
2	Transverse direction in local material coordinate system
12	In-plane direction in local material coordinate system
s	Symmetric laminate
os	Oblique symmetric laminate

3.1.0. Introduction to Fiber Steering Conceptual Design

Composite materials have attracted significant attention in the civil and military arena due to their high specific strength, specific stiffness, and directionality of properties. They have been designed to meet specific applications, where various fiber orientation, material properties, or ply thickness are combined to construct a laminate that is tailored favorably to a prescribed loading condition. Traditionally, composite structures are configured based on the constant-stiffness laminate design, where lamina elastic properties remain constant throughout the entire ply. This traditional design method generally yields quite satisfactory performance. Both designers and manufacturers favor this method because most composite structures can be easily designed and fabricated. However, with the advent of fiber placement (FP) technology, it is now possible to vary the lamina property over a range or continuously over the entire ply. In fact, the capabilities of this hardware far exceed current design practices especially in the placement of tow preregs onto structures with complex curvature. Therefore, it is desirable to further explore the design concept of composite materials so that better designs may be realized and the resulting structures may offer improved structural efficiency over existing methodologies. One concept that arrives at these hypotheses is the idea of fiber steering (FS) conceptual design.

3.1.1 Motivations to Fiber Steering Conceptual Design

Fiber placement, as shown in Figure 3.1, is an automated manufacturing technology for fabricating affordable composite structures with complex curvatures using multiple tows of composite materials. Initially introduced in the 1980s, FP is a technology incorporating features of filament winding and tape-laying machines^{1,2}. Comparisons of these machines' capabilities are listed in Table 3.1. The main features of FP technology are highlighted as follows:

- Wide FS capability
- Precise towpreg deposition on complex geometry
- Better quality control over void content, scrap rate, gaps and overlaps
- Superior control over individual tow delivery or differential tow payout
- Affordable composite-structure fabrication technique with lower part counts.

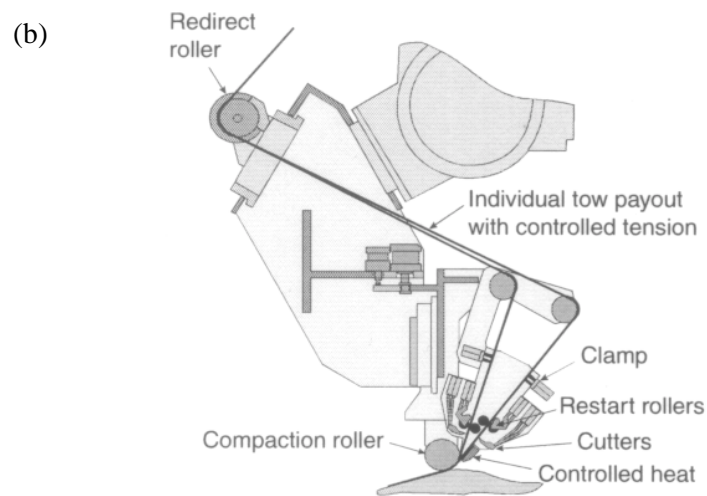
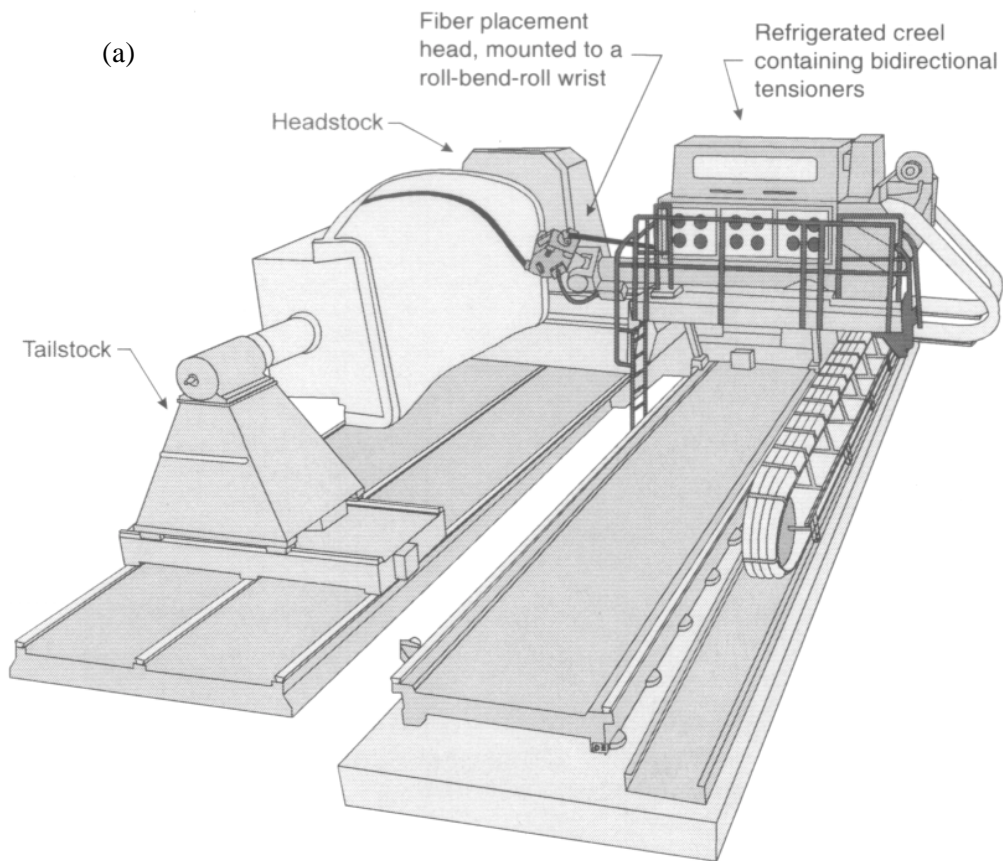


Figure 3.1: Schematics of (a) fiber placement system and (b) fiber placement head (copied from Ref. 1).

Table 3.1 Comparisons of Fiber Placement Machine with Filament Winding and Tape Laying Machines.^{1,2,3,4}

Attributes	Fiber Placement	Tape Laying	Filament Winding
Part Geometry	Complex, convex/concave surfaces, open and closed section	Flat or nearly-flat surface with large aspect ratio	Best for bodies of revolution
Fiber Path	Complex fiber path	Natural path	Geodesic winding path only
Steering Radius	25-inch radius without buckling the individual tow, for a 0.125-inch fiber band	800-inch radius with small amount of fiber buckling, for a 3-inch fiber band	Data Not Available
Winding Angle [deg]	No Limit (0° to 90°)	N/A	Must be greater than 15° (15° to 90°)
Axes of Motion	7 axes	5 axes	2 axes
Tow Cut and Restart	YES	YES	NO
Differential tow payout	YES	NO	NO
Void Content [%]	Less than 1	Less than 1 *	4 – 8
Scrap Rate [%]	2	>2 *	20 – 40
Accuracy in tow placement	Within 1°	N/A	±7°
Minimum cut/tow length	4 inch/cut	4 inch/cut *	N/A
Typical layout rate [ipm]	Up to 1200 **	Up to 1200 ***	Data Not Available
Delivery tow number per band	Up to 36 tows	One tape ***	Up to 8 tows
Prepreg Thickness	0.005 – 0.015	0.005 – 0.015 *	0.010 – 0.025
Off-line Programming	ACRAPLACE **	Natural Path Programming (NPP) ***	Data Not Available

* estimated based on a typical fiber placement machine
 ** based on a 7-axis Cincinnati fiber placement machine
 *** based on a 5-axis Ingersoll tape laying machine

With its transition from a developmental status to a reliable production stage over the past decades, FP has become a viable option to the costly and labor-intensive hand lay-up method. Both thermoset and thermoplastic matrix systems have been utilized with this technology. FP utilizing thermoplastic matrix systems, which is categorized as “in-situ fiber placed thermoplastic matrix composites”, has the potential to eliminate the post-process autoclave cycle [5]. With the flexibility in the fiber-placed head design, FP has enabled fabrications of relatively small opened and closed section parts. FP technology offers advantages of less than 2% scrap, up to 20% weight reduction compared with conventional metallic configuration, and up to two times part-count reduction [6]. Successful utilization of this method with cost reduction has been well documented in the worldwide aerospace industry, as seen in Figure 3.2 for benchmark cases in many secondary aerospace structures [7]. The promise of affordability, process reliability, and superior fabricating capability of this technology can be realized.

At the current stage, capabilities of existing FP hardware far exceed the capabilities of current design engineering tools, particularly with respect to (w.r.t.) the ability to fabricate structures exhibiting curvilinear fiber paths or FS. FS is defined as “binormal radius of curvature along a fiber path”¹ as illustrated in Figure 3.3 for 0° , $\pm 45^\circ$, and 90° towpreg courses on a cone-shaped mandrel. Some researchers have explored the effect of FS on FP processing parameters (course bandwidth, towpreg feed rate, compaction force, etc.)⁸ and demonstrated a minimum radius of 5 inch. Figure 3.4 represents FS at different radii of curvatures³. By allowing the fiber path to vary spatially either within a region or over a ply, the laminate stiffness and strength can be tailored.

Nevertheless, this concept has not been fully explored and integrated into design, analysis, and manufacturing. Also, drawbacks are seen in the manufacturing practices. Many manufacturers depend on intelligent front-end tools for manufacturing simulations, such as FIBERSIM^{9,10} and ACRAPLACE^{11,12} software, to generate mappings of the tow paths that conform to complex surfaces with acceptable geometrically induced fiber distortion (fabric shifting, wrinkling, and tearing). Unfortunately, these tools require complete definitions of manufacturable ply boundaries, and this cannot be executed until after the completion of detailed design. Although implementations of these tools, which are depicted in Figures 3.5 and 3.6, may reduce time to market and inherit better ply management, courses of tows following these patterns may not constitute the optimal design.

Military	Civilian
<ul style="list-style-type: none"> → F-18 E/F inlet duct, aft center side skins, stabilator skins → C-17 fan cowl doors, landing gear pod fairings → V-22 fuselage skin and sponson → T-45 horizontal stabilator → F-22 pivot shaft → AH-1 helicopter main rotor spars → X-32 JSF intake duct and fuselage skins 	<ul style="list-style-type: none"> → Bell/Agusta 609 fuselage section → Raytheon Premier I fuselage section → Hawker Horizon fuselage section → A3xx Domed pressure bulkhead → Airbus A340-500/600 fan cowl doors → Ariane 5 payload adapters, thrust frame, vehicle equipment bay

Figure 3.2: Successful utilization of fiber placement technology for fabricating representative aerospace structures⁷.

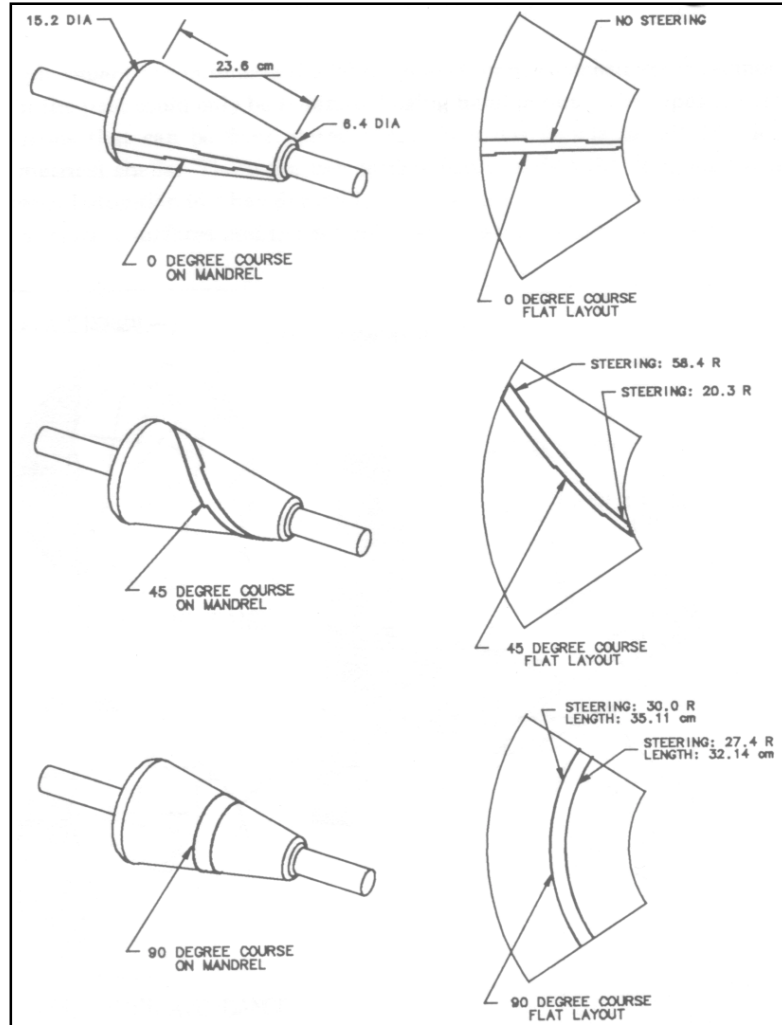


Figure 3.3: Fiber steering of 0°, +45°, and 90° courses on a mandrel¹.

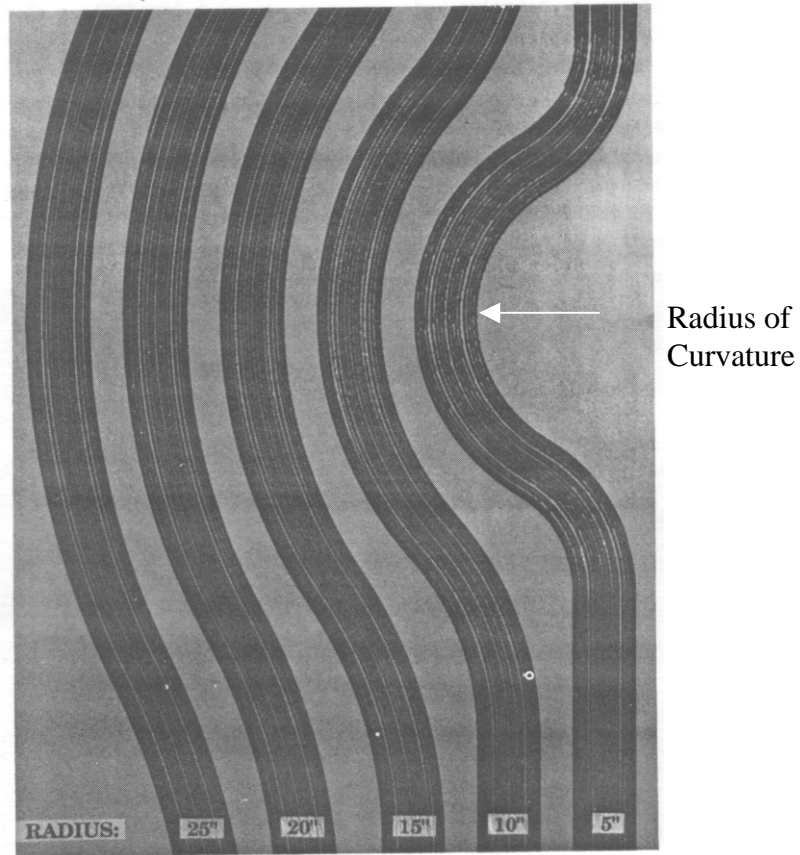


Figure 3.4: Fiber steering at different radii of curvatures on a flat surface³.

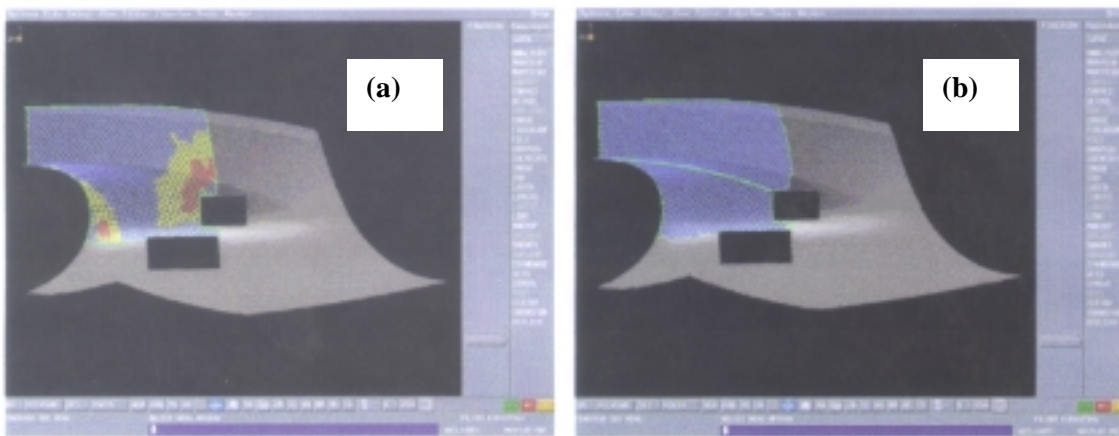


Figure 3.5: Screen dumps of FIBERSIM showing (a) critical fiber path regions in yellow and red contours, and (b) modification of those regions with darting and draping theories⁹.

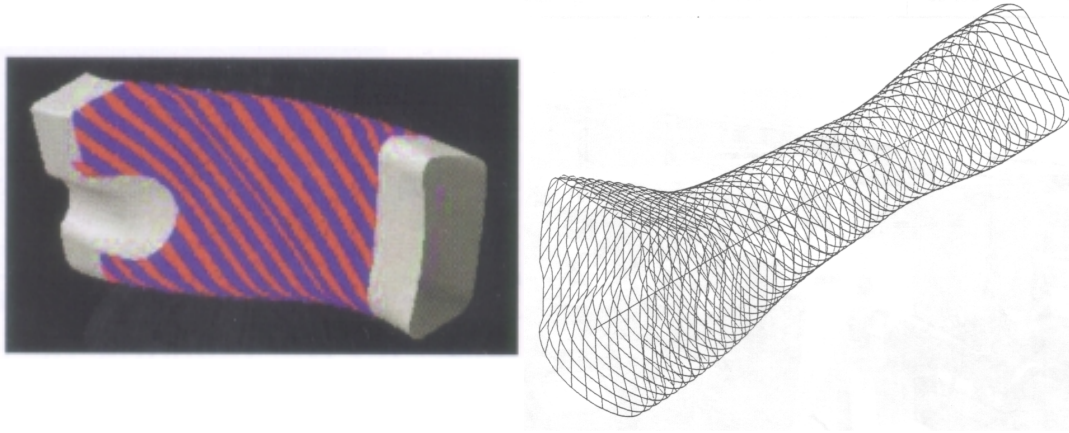


Figure 3.6: Simulations of fiber path on complex-curvature parts with ACRAPLACE^{11,12}.

Apart from the immature engineering and manufacturing practices, military aircraft and spacecraft operate in extreme environments, which can cause concern for the safety of the structures. Essentially, most design practices are cost and performance driven. With the application of FS conceptual design and adoption of state-of-the-art FP technology, not only can structural efficiency be improved, but reductions in weight and ultimately cost can also be attained. If this novel conceptual design process can be proposed to enable structural efficiency while maintaining affordability, such a design process should be implemented in future composite structures.

3.1.2 Motivations to FS Conceptual Design

The design of composite laminates can be grossly categorized as:

- ➔ Constant Stiffness Laminate
- ➔ Variable Stiffness Laminate

Conventional composite parts are made of constant stiffness laminates. However, one should realize that by spatially varying the stiffness properties within each lamina, an even greater use of composite material could be achieved.

There are many ways to design a composite laminate with spatially varying properties, either within a range or over the entire ply. This includes dropping plies or tows, varying the fiber volume fraction or variable fiber spacing, and changing the fiber orientation within a lamina. Figure 3.7 shows an example of lamination with ply dropoffs across the structure. The elastic properties of this structure are changed when dropping a ply. This also introduces an eccentricity of loading, especially when dropping into an adjacent ply with a different fiber orientation. DiNardo¹³ studied the response of several laminated plates with ply dropoffs and concluded reductions of critical buckling loads. An example of a laminate with varying fiber spacing is illustrated in Figure 3.8. The fiber volume fraction is controlled such that stiffness can

be properly tailored in the loaded region. The structural behavior (vibration and buckling) of rectangular composite plates with variable fiber spacing has been investigated by Leissa¹⁴. Numerical solutions predicted substantial increases in the buckling load and the vibration characteristics.

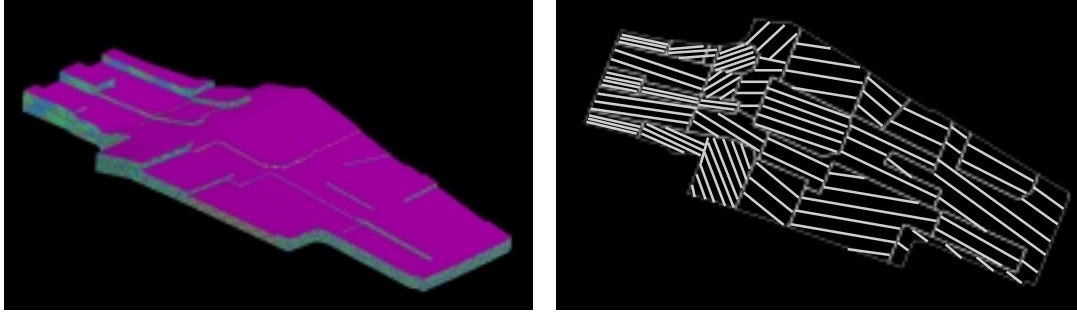


Figure 3.7: A structural component with ply dropoff variable stiffness laminates.

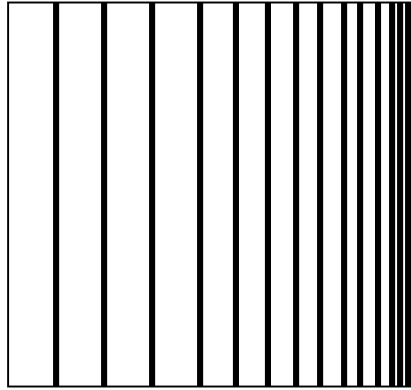


Figure 3.8: A laminate with variable fiber spacing.

FS conceptual design derives from the variable-stiffness laminate concepts as a design of tow-placed variable-stiffness laminates. It calls for the tailorability of the laminate family by the variation of both layer thickness and fiber orientation across the laminate. Structures with steered fiber architecture have the potential to offer significant weight savings by simultaneously tailoring the local fiber orientation and layer thickness to specific internal load paths. Optimum structural efficiency in FS promises fabrications of affordable composite structures due to no increase in manufacturing cost.

Generally, a laminate family has four fiber orientations with different ply thicknesses, which has a convention of $(\theta_2/\pm\theta_1/\theta_3)$ in percentage. Current industrial practice limits the allowable orientation to 0° , $\pm 45^\circ$, and 90° , which is depicted in Figure 3.9 with $\pm\theta_1 = \pm 45^\circ$, $\theta_2 = 0^\circ$, and $\theta_3 = 90^\circ$. Using symmetric and balanced design, the laminate is orthotropic in nature, having three mutually perpendicular planes of elastic symmetry. A $(25/50/25)$ family with $[\pm 45, 0, 90]_s$ governs the load paths of the structure in axial, transverse, and shear w.r.t. the principal material axes. The resultant laminate is a quasi-isotropic laminate. However, a laminate is only

balanced when one of the principal material axes coincides with the primary load paths or the principal stress trajectories. Based on FS conceptual design, one of four arbitrary fiber angles with different layer thickness is tailored to follow the primary axial load trajectory across the laminate. The three remaining angles are aligned and linked w.r.t. the primary load path to define the transverse and shear respectively. The resultant laminate is an orthogonal-curvilinear design, where the local family rosettes follow the curvilinear load path as seen in Figure 3.10. In this case, the laminate is symmetric and balanced w.r.t. the local material axes (or the primary load path), but is unbalanced w.r.t. the global coordinate system.

To implement structural optimization for FS conceptual design, two design definitions can be described:

- ➔ Constant-Rangewise FS Design (Figure 3.11)
- ➔ Continuous-Topological FS Design (Figure 3.12)

For the constant- rangewise FS design, the fiber orientation within a range is constant. These design variables can be easily described at the finite element or discretization level. The fiber orientations can then be mapped continuously from range to range as a function of position using a knowledge-based post-processor or curve-fitting process. On the other hand, continuous-topological design variables consist of tow paths at the geometry level, where individual tows are explicitly defined using geometric representations. One example of these paths is a topological B-spline or curve composed of control points. This method requires an approach to develop all offset tows as a function of a sample spline. The comparisons between these designs are listed in Table 3.2.

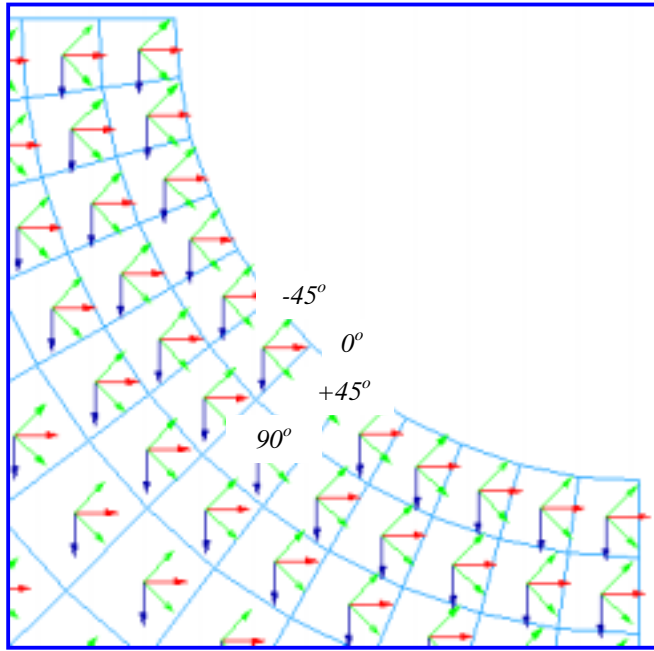


Figure 3.9: Schematics of conventional laminate family with 0° , $\pm 45^\circ$, and 90° .

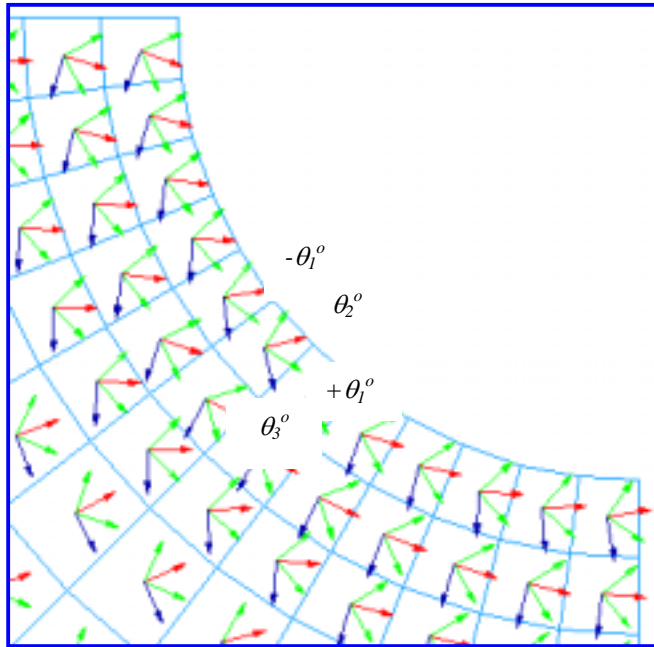


Figure 3.10: Schematics of curvilinear laminate family with $(\theta_2/\pm\theta_1/\theta_3)$ in percentage, balanced based on local coordinate system.

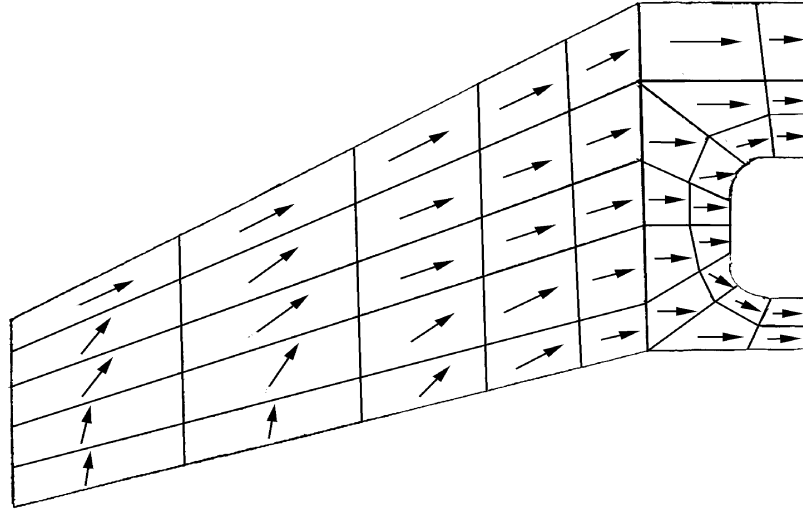


Figure 3.11: A structural component with constant-rangewise fiber orientation and layer thickness.

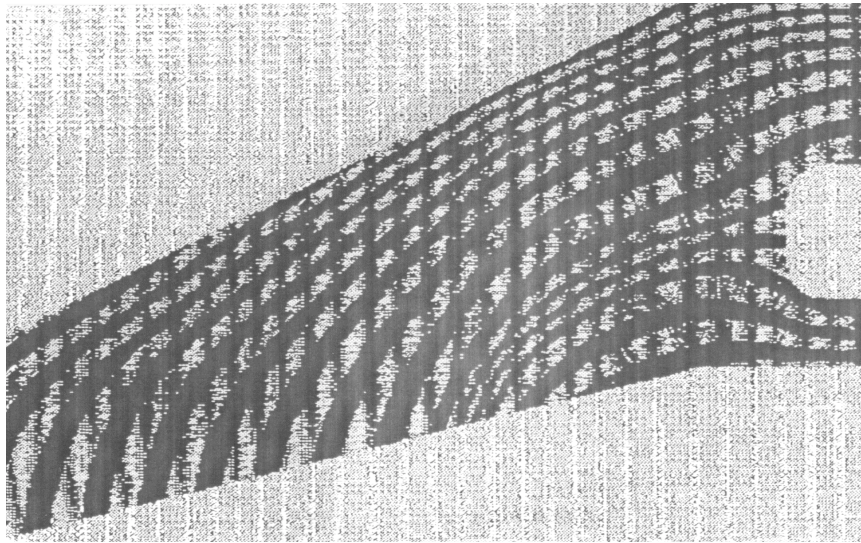


Figure 3.12: A structural component with continuous-topological fiber orientation and layer thickness.

Table 3.2: Comparisons of Constant-Rangewise FS Design with Continuous-Topological FS Design.

Attributes	Constant-Rangewise FS Design	Continuous-Topological FS Design
Design Variable Level	Finite Element	Geometrical/Topological
Design Variable Type	FE-Discretized Ply Thickness & Fiber Orientation	Continuous Ply Thickness & Fiber Orientation
Requirements on Post-Processor	“Smoothing” Process for fiber-path curve fitting	An approach to develop offsets tows
Difficulty in Mathematical Programming (MP)	Relatively simple	Relatively difficult

Several analytical methodologies have been introduced in the design of laminated composites with optimal layer orientations and layer thickness. Reviews of these methodologies are detailed in Chapter Two. A majority of these methodologies rely on constant-rangewise optimization. Others explore and define the fiber path using geometrical or topological optimization. While some of these algorithms use full $[A]$, $[B]$, $[D]$ matrices (extensional, coupling and bending stiffness, respectively) to design a laminate, others concentrate on just the $[A]$ -matrix to decide an optimal laminate with effective bending properties. The former is fully integrated based on Classical Lamination Theory (CLT). Nevertheless, the latter offers simplicity in the design of laminates based on laminate family optimization, neglecting the $[D]$ -matrix computation and stacking sequence effects. Since the design of composite laminates is very challenging mathematically speaking, many existing commercially available software are not keen on describing both layer thickness and fiber orientation as design variables and at the same time taking full CLT matrices to arrive at a feasible design regime. A feasible family-based laminate is usually composed of the layer thickness as primary design variable while making 0° , $\pm 45^\circ$, and 90° constant throughout the laminate. With the complexity in its failure modes due to the directionality in properties, a robust and effective optimization routine has yet to be integrated into design, analysis, and manufacturing tools.

In this paper, FS conceptual design is explored with the aid of MBB-LAGRANGE, a finite-element and gradient-based structural optimization software. MBB-LAGRANGE has the potential to allow both layer thickness and fiber orientation to vary according to the constant-rangewise definition. It is configured solely on $[A]$ matrix computations with several mathematical programming algorithms available for structural optimization. Although only fiber-related failure modes (longitudinal tension and compression) are granted, MBB-LAGRANGE is employed throughout this project due to its robustness and effectiveness in the structural optimization for FS conceptual design. Detailed references for MBB-LAGRANGE are addressed in Section 3.3.

3.1.3 FP Design Process Flow using FS Conceptual Design.

FS conceptual design can be implemented in the process flow or CAD/CAM/CAE for FP technology, as illustrated in Figure 3.13. The geometry (2-D surface or 3-D solid modeling), the corresponding loading and boundary conditions, and the material properties are imported into a global and local finite element solver to define an initial design. Then, MBB-LAGRANGE is employed for constant-rangewise FS design. The results of layer thickness are rounded for best stacking sequence using a stacking sequence realizer (e.g. PACKS¹⁵). With the aid of the knowledge-based composite design package (e.g. PACKS), the manufacturability and design practices are taken into consideration. At this point, the laminate may be altered. The structural optimization loop is performed until a best laminate family design is obtained. The geometry analysis and simulation of fiber paths are performed via intelligent front-end tools, such as SCADS¹⁶ and FIBERSIM^{9,10}. A final detailed finite element analysis (FEA) is carried to ensure design feasibility under prescribed preliminary requirements. Finally, the computer numerical controlled (CNC) code is generated with a FP off-line translator like ACRAPLACE or O.P.S.^{11,12}. This code is fed into the FP machine to fabricate the parts.

3.1.4 Technical Objectives of FS Conceptual Design

In this paper, the design concept of FS has been applied to primary and secondary components of general aviation and military aircraft. MBB-LAGRANGE, a finite-element and gradient-based optimization routine, is adopted as the analysis tool throughout the project. To validate FS conceptual design, four simple test models have been examined. The models are a square plate with a central circular hole subjected to various loading conditions, a cantilever rectangular panel subjected to transverse loads, a cantilever circular tube subjected to combined loadings, and an intermediate complexity wing (ICW) subjected to aerodynamic loads. Significant weight savings have been achieved in preliminary studies, described in Section 3.4.

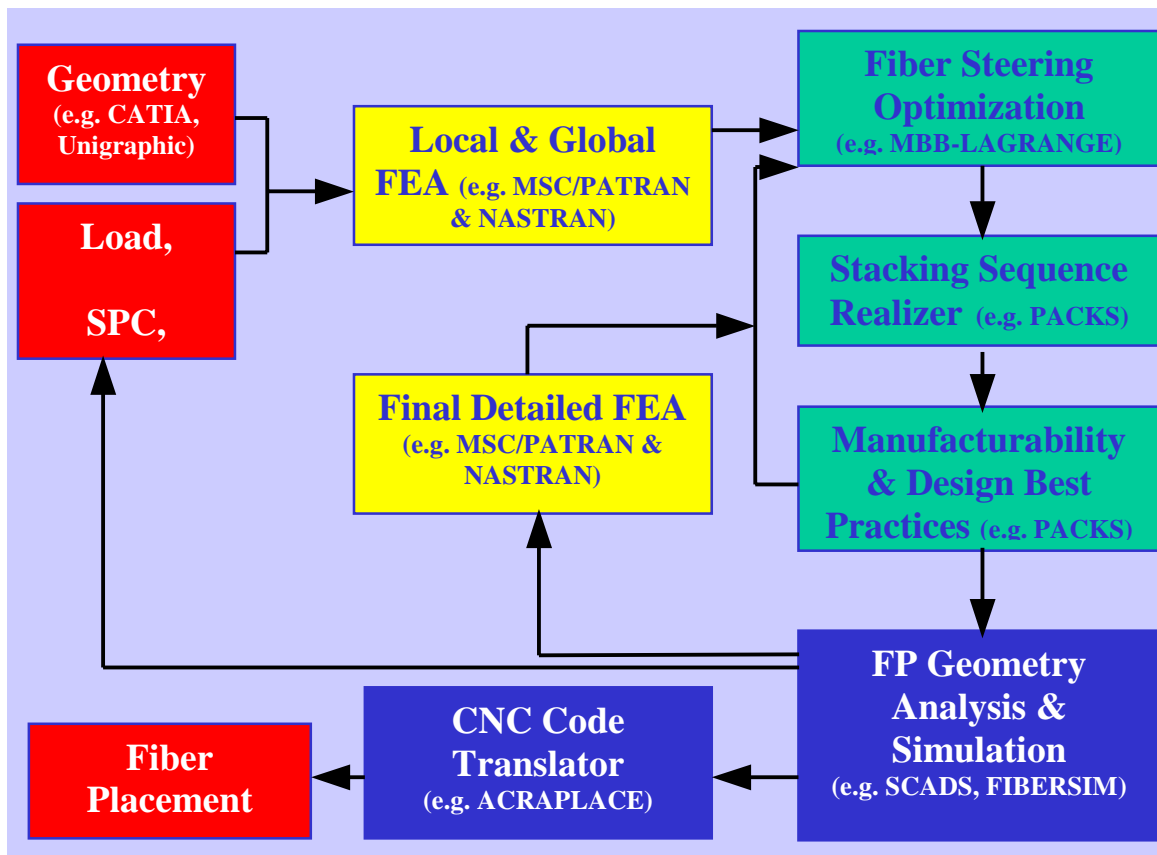


Figure 3.13: Process flow or CAD/CAM/CAE for FP technology with the implementations of Fiber Steering Conceptual Design.

Having investigated and validated the design concept of FS, three representative structural components of existing aircraft are then examined. The models are a representative general-aviation pressure bulkhead subjected to cabin pressure, a representative regional-jet wing subjected to aerodynamic and internal fuel loads, and a representative military horizontal stabilizer subjected to aerodynamic loads. The application of FS conceptual design on these representative aircraft components will exhibit optimum structural efficiency and affordable composite structures. Results of these models are listed in Section 3.5.

The objective of this paper is to document studies for the potential payoffs using FS conceptual design based on constant-rangewise finite-element discretization and gradient-based structural optimization. Optimum design of primary and secondary composite structures can be obtained by allowing layer thickness and fiber orientations to vary across the structures. Significant weight reduction and enhanced load-carrying performance for fiber-steering solutions can be achieved.

In summary, this research explores novel conceptual designs for composite laminates subjected to the static flight envelope. Composite laminates having steered fiber architecture offer improved weight and structural efficiency by tailoring local fiber orientations to specific internal load paths of the structures. Previous research, cited in Section 3.2, has demonstrated potential payoffs within FS conceptual design. With controllable variable stiffness, these laminates can be made useful in many military and civilian related applications. Using state-of-the-art FP technology, FS conceptual design will provide a new horizon to composite structural designs at no additional cost. Successful utilization of this concept will benefit both civilian and military related applications.

3.1.5 Brief Outlines of the Sections

The outlines of subsequent sections within this chapter are summarized as follows:

- ➔ Section 3.2 accounts for the development of variable-stiffness laminates and similar works of FS conceptual design.
- ➔ Section 3.3 deals with the technical approaches to FS conceptual design.
- ➔ Section 3.4 presents the results of preliminary studies upon three simple models
- ➔ Section 3.5 lists the results of three representative aircraft primary and secondary composite structures using FS conceptual design.
- ➔ Section 3.6 concludes the research efforts and recommends future developments.

3.2.0.Literature Review

Many documents have conveyed consistent improvements in structural efficiency for structures following curvilinear or trajectorial fiber reinforcements. By simultaneously tailoring local fiber orientation and layer thickness to follow unique internal load paths, structural efficiency can be enhanced. With different loading conditions, the load carrying capacity of structures using a curvilinear fiber format can be significantly improved.

The design concept of trajectorial fiber reinforcement is not new. In 1885, W. Roux¹⁷ had already investigated the optimum disposition of fibers in the field of biomechanics based on his theory of maximum minimum (maximum strength and minimum materials). His finding, i.e. a trajectorial fiber construction of a bone, was later investigated and supported by F. Pauwells¹⁷ in the 1950s using photoelastic experiments. Michell¹⁷, an Australian scientist, developed a similar approach based on the concept of trajectories of principal stresses in 1904, called Michell's optimum layout theory. This theory was applied in the design of a composite cantilever beam. Makiyama and Platts¹⁷ adapted Michell's approach to tailor the distribution of loads for the optimum topology for a composite cantilever beam.

In the 1970s, Cooper¹⁸ developed a fiber-laying gadget (FLAG) to study the effect of trajectorial fiber reinforcement. He observed that structural efficiency could be increased if fiber directions follow a unique internal load path, which was induced by the boundary conditions. More than ten years later, Katz et. al.¹⁹ explored ply orientation optimization of a plate with a central hole using sequential linearization programming (SLP) and showed that load carrying capacity of curvilinear fiber format is greater than that of unidirectional design. Similarly, Hyer and Charette²⁰, and Hyer and Lee²¹ successfully established a design method using curvilinear fiber format in the design of a plate with a central hole subjected to both tensile and compressive loads. In both cases, significant improvements in structural efficiency (tensile and buckling capacities) were achieved. Jones and Platts²² reconstruct a composite plate with a pin-loaded hole by defining the internal fiber geometry (and thus orientation) in the vicinity of the hole to reduce stress concentrations.

With these firm milestones, Berchtold and Klenner²³ developed an "Integrated Tape Laying System" (ITLS) utilizing a tape steering concept for a tape placement machine and demonstrated it to the design of a cantilever panel and an aircraft vertical fin of carbon fiber skins with an aluminum honeycomb core. Weight savings up to 30% were obtained for the vertical fin when subjected to aeroelastic constraints. Recently, Tosh and Kelly²⁴ revisited the design of a plate with a central hole with the application of trajectorial fiber steering, where the fibers or tows are aligned with respect to the structure's principal stress vectors and load paths. Their investigation concluded an increase of up to 85% specific strength for their specimens. In addition, Duvaut et. al.²⁵ developed a design method that determined both optimal fiber orientations and volume fraction for four cantilever square panels subjected to different boundary conditions. In addition, a computer aided internal optimization routine (CAIO) was developed by Reuschel and Mattheck²⁶ to predict optimal fiber arrangement for minimum shear stress designs. Incorporating with a commercial finite element analysis program (ABAQUS), CAIO determined a "force flow-tailored fiber pattern" by redirecting the orthotropic material axes along the principle stress trajectories.

While above authors investigated the benefits of curvilinear fiber formats within a laminate using constant-rangewise design based on finite element level, Eschenauer et. al.²⁷ developed a “constructive design concept” using geometric or topological parameters as explicit design variables, such as topological ply distribution and pregreg tape courses. Constructive design allows flexibilities in defining manufacturing constraints and establishing interfaces between mathematical modeling and actual layout. Gurdal et. al.²⁸, Olmedo et. al.²⁹, and Waldhart et. al.³⁰ explored another dimension of fiber steering design by applying the variable stiffness concept. Two configurations of variable stiffness were proposed, i.e. “shifted and parallel fiber variable stiffness laminates”. Substantial increases in critical buckling loads were achieved using this design concept. Nagendra et. al.³¹ also launched another design concept similar to Gurdal, called “tow-fiber path shape optimization” using geometrical- or topological-based optimization procedure. Pandey³² studied the variation of buckling strength when composite plates have a pre-described fiber waviness or sinusoidal pattern, and concluded that an 80% increase in the buckling load of a simply supported laminate is obtained. Although these concepts were very appealing, they involved tremendous computational times and efforts.

On the other hand, Pratt, et. al.³³ explored other applications of the variable stiffness concept, where acoustic performance (especially passive damping and acoustic transmission losses) of composite sandwich panels have been enhanced. Up to 102% damping enhancement in composite structures exhibiting “continuous wave geometric patterns” over cross-ply constrained layer damped panels is attainable. Steurer³⁴ shared a common trait in damping enhancement of composite structures with continuous fiber wave patterns, called “continuous wave composite-viscoelastic (CWCV)”. Steurer tested a number of sandwich panels and proved that CWCV panels could provide higher levels of damping and increased stiffness. In addition, Biggerstaff and Kosmatka³⁵ performed tests on “integrally damped composite plates” and concluded that the loss factor of these plates was governed by the directional damping coefficients.

In summary, composite structures exhibiting steered fiber architecture demonstrate potential improvements in structural efficiency and weight reductions. Whether this concept is performed via constant-rangewise design or continuous-topological design, significant benefits can be obtained when allowing the tailoring of fiber orientation and layer thickness to specific load paths. Apart from implementing this concept on static and buckling applications, enhancements in acoustic performance and vibration characteristics can also be achieved. Nonetheless, what is lacking at this stage is the optimization of layer thickness and fiber orientations in terms of curvilinear laminate family format. In addition, few researchers have addressed utilizations of FS conceptual design on aircraft structures. Therefore, it is intended to further investigate FS conceptual design and document potential payoffs to the aerospace community.

3.3.0. Theoretical Considerations and Approaches

Due to the nature of composite materials, the optimization of laminates can be challenging and expensive. Even a simple composite laminate is governed by a rather large number of design variables (DVs)³⁶. As seen in Figure 3.3.1, design constraints or responses associated with these variables are bewilderingly large, especially when considering multiple loading conditions and objective functions (multidisciplinary or multicriteria optimization)³⁷. For instance, the many factors aircraft structures must fulfill in the preliminary design phase are as follow:

- ➔ Static ultimate (and yield) strength
- ➔ Elastic deformations of primary structures
- ➔ Buckling stability (local and global buckling failures)
- ➔ Dynamic properties (natural frequencies, mode shapes)
- ➔ Fatigue life and crack initiation
- ➔ Weight (or cost)

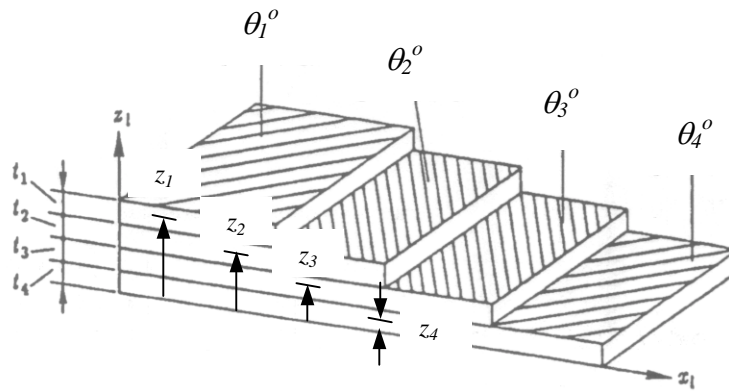


Figure 3.3.1: Definition of design variables for a symmetric laminate.

Furthermore, composite laminates are subjected to various failure modes, including ply longitudinal, transverse, and shear failures, and delamination³⁶. With the implementation of fiber steering conceptual design, a robust and efficient optimization routine should be employed. In this section, a brief introduction to the design optimization of composite laminates is presented, followed by a detailed program description of MBB-LAGRANGE. MSC/PATRAN, MSC/NASTRAN, and VORSTAB will also be discussed briefly.

3.3.1. Structural Optimization of Composite Laminates

The complexities in the design optimization of composite laminates are attributed to current modeling, analysis, and optimization processes³⁸. Today, many researchers use using the finite element analysis (FEA) in the modeling and analysis of composite structures based on Classical Lamination Theory. Complexities in these areas are encountered when defining stiffened composite panels, implementing nonlinear analyses, such as postbuckling, uncertainty in material properties, loading, and geometrical imperfections³⁸. In terms of the optimization complexity, the design of composite laminates becomes expensive with discrete and global optimization problems. The discrete nature of composite structures usually involve large, non-convex, integer programming problem. Recently, the genetic algorithm (GA) has become increasingly popular for integer optimization problems. One advantage associated with integer optimization techniques is that they yield a laminate family of near global optimal design³⁸. When dealing with noisy search spaces, GAs have been proved efficient and robust³⁹. However, recent research and development concludes that continuous optimization problems are relatively lower in computational cost and more robust compared with integer programming techniques because of the unavailability of easy-to-use commercial integer programming software and high computational cost of solving integer programs^{38,39}. The problem associated with continuous algorithms is that the laminate designs often have multiple local optima with comparable performance. Also, current design and manufacturing practices confine the discrete nature of ply thickness (0.0055, 0.010 inches) and a set of ply orientations (0° , 90° , and $\pm 45^\circ$). This has pushed designers to conclude (round off) the final results from the continuous analytical models.

Another difficulty in structural optimization of composite laminates is with failure definitions. In general, two failure definitions have been used⁴⁰:

- ➔ first-ply failure
- ➔ progressive failure

The former can be easily dealt with by numerical optimization because all constraint functions are continuous at this point. However, this approach is somewhat conservative, recognizing that adjacent plies can take additional failure load before the entire structure collapses. The latter requires a stepwise analysis procedure, where the failed-ply and its constraint are rendered ineffective for carrying additional loads. The entire laminate still retains load-carrying capacity at this point. Nevertheless, this creates a rather complex decision process from an optimization viewpoint, because the constraint functions are no longer continuous with respect to DVs.

Owing to the advancement in the fiber placement technique in the past decade, the capability of fabricating complex structural components with continuous variation of tow orientations or fiber steering is made possible. In this chapter, the continuous optimization routine is implemented in the design of composite structures exhibiting steered-fiber architecture. MBB-LAGRANGE v12.0, a gradient- or derivative-based structural optimization program, is selected due to the robustness and efficiency in the optimization procedures for both layer thickness and orientations. Table 3.3.1 describes the differences of optimization capabilities between MBB-LAGRANGE^{41 - 46} with commercially available optimization packages, such as

MSC/NASTRAN^{47,48}, and GENESIS⁴⁹. Note that these software have the capabilities to design composite laminates with both layer thickness and fiber orientations as DVs. These parameters can only be defined as continuous variables, except that discrete variables are now available in the latest version of GENESIS for both parameters and only the discrete thickness in MSC/NASTRAN 2001. Nonetheless, MBB-LAGRANGE has proven to be a more powerful tool when dealing simultaneously with layer-thickness and fiber-angle optimizations.

3.3.2 Structural Optimization Program: MBB-LAGRANGE

To obtain optimal layouts for composite laminates that meet all constraints with a minimal weight, optimal values for layer thickness, fiber orientations, and stacking sequence must be determined. Iterative processes or structural optimization algorithms are necessary, consisting of continuous alterations between structural analysis and successive modifications of the design.

Table 3.3.1 Comparisons of Structural Optimization Capabilities between DASA/MBB-LAGRANGE with MSC/NASTRAN, and GENESIS based on Fiber Steering Conceptual Design.^{41 to 49}

Design Optimization Parameters	DASA/MBB-LAGRANGE 12.0	MSC/NASTRAN Solution 200	GENESIS 7.0
Continuous Design Variables	<ul style="list-style-type: none"> → Sizing: Ply Thickness → Fiber Orientation → Topological: Constructive Design 	<ul style="list-style-type: none"> → Sizing: Ply Thickness → Fiber Orientation → Topological: DVGRID* Shape Optimization 	<ul style="list-style-type: none"> → Sizing: Ply Thickness → Fiber Orientation → Topological: Shape Optimization
Discrete Design Variables	N/A	<ul style="list-style-type: none"> → Discrete ply number 	<ul style="list-style-type: none"> → Discrete ply number → Discrete ply angle
Design Variable Linking	<ul style="list-style-type: none"> → Custom: Balanced lamination → Special: VLAMINAT** 	<ul style="list-style-type: none"> → Custom: Balanced lamination → Special: User defined equations 	<ul style="list-style-type: none"> → Custom: Balanced lamination → Special: User defined equations
Built-in Design Response or Constraint	<ul style="list-style-type: none"> → Failure criteria: MSTN, TSAI*** → Material property lower & upper bounds → Displacement → Membrane buckling → Aeroelastic efficiencies 	<ul style="list-style-type: none"> → Failure criteria: STRN, HOFF, HILL, TSAI† → Material property lower & upper bounds → Displacement → Membrane buckling → Aeroelastic efficiencies 	<ul style="list-style-type: none"> → Failure criteria: STRN, HOFF, HILL, TSAI† → Material property lower & upper bounds → Displacement → Membrane buckling → Aeroelastic efficiencies
Custom Design Response	N/A	<ul style="list-style-type: none"> → User defined equations 	<ul style="list-style-type: none"> → User defined equations → External routine linking
Objective Functions	<ul style="list-style-type: none"> → Standard: minimize weight → Special: minimum distance for crack identification 	<ul style="list-style-type: none"> → Standard: minimize weight → Special: User defined objective function 	<ul style="list-style-type: none"> → Standard: minimize weight → Special: User defined objective function
Optimization Algorithms	<ul style="list-style-type: none"> → IBF, MOM, SLP, SRM, RQP1, RQP2, GRG, CONLIN, QPRLT, SCP† 	<ul style="list-style-type: none"> → MFD, SLP, SQP††† 	<ul style="list-style-type: none"> → Latest Approximation Methods

* DVGRID: Design variable to coordinate relation; define the relationship between design variables and grid coordinates.

** VLAMINATE: Whole laminate orientation is ONE angle DV; i.e., for $[\pm\theta_1, \theta_2, \theta_3]$ laminate the θ_2° ply is the primary angle DV, with $\pm\theta_1^\circ$ and θ_3° plies linked to the local θ_2° DV at orientations of $\pm 45^\circ$ and 90° respectively

*** MSTN: Maximum strain failure, and TSAI: Tsai-Wu failure criteria

† STRN: Maximum strain failure, HOFF: Hoffman failure, HILL: Tsai-Hill failure, and TSAI: Tsai-Wu failure criteria

†† IBF: Inverse Barrier Function, MOM: Method of Multipliers, SLP: Sequential Linear Programming, SRM: Stress Ratio Method, RQP1: Recursive Quadratic Programming after Schittkowski, RQP2: Recursive Quadratic Programming after Powell, GRG: Generalized Reduced Gradient, CONLIN: Convex Linearization, QPRLT: Quadratic Programming with Reduced Line Search Technique, SCP: Sequential Convex Programming

††† MFD: Method of Feasible Direction, SLP: Sequential Linear Programming, SQP: Sequential Quadratic Programming.

MBB-LAGRANGE is a multidisciplinary structural optimization program developed by Messerschmitt-Bolkow-Blohm (MBB) and several university institutes since 1984. It is based on the finite element method (FEM) for structural analysis and panel methods for aerodynamic computations. It uses mathematical programming and derivative to fulfill multidisciplinary constraints, such as failure criteria, maximum displacement, stability requirements, dynamic responses, aeroelastic efficiencies and flutter speeds. MBB-LAGRANGE v12.0 supports ten different optimization algorithms that enable the user to decide the appropriate routine for a given problem. Another feature of MBB-LAGRANGE is the commonality of the structural modeling description with MSC/NASTRAN. This has also enabled the user to obtain the output punch file in the bulk data file format for post processing and verification via MSC/NASTRAN. However, being developed by different companies, there are some differences between these programs as documented in Appendix D. A major difference is that MBB-LAGRANGE supports only isoparametric membrane elements for composite laminates; whereas, plate and shell elements can be used in the modeling of composite structures within MSC/NASTRAN. Therefore, only extensional stiffness properties, $[A]$, are considered in MBB-LAGRANGE along with effective bending stiffness properties, $[D]$. This eliminates the effect of stacking sequence, bending and twisting couplings, as well as the optimization capabilities using stacking sequence as DVs.

Currently, MBB-LAGRANGE supports various structural disciplines with sensitivity analyzes, including modules like:

- ➔ Linear static analysis
- ➔ Linear static stability (or buckling)
- ➔ Linear dynamic analyses, such as modal analysis (eigenvalues and eigenvectors), transient and frequency response with deformation, velocity or acceleration constraints.
- ➔ Flutter speed and damping
- ➔ Linear static aeroelastic quantities (force and moment effectiveness criteria with respect to loads, static aircraft stability criteria, maneuver performance requirements, structural divergence, and control surface reversal).

For composite-laminate optimization, MBB-LAGRANGE adopts the first-ply failure as the design philosophy for fiber-related failure only, i.e. longitudinal tension and compression. One may argue that MBB-LAGRANGE is not conservative because it neglects matrix-related (transverse tension and compression) and in-plane shear failures. However, this scenario can be addressed if designers intend to obtain a best laminate family with optimal layer thickness and orientation via MBB-LAGRANGE. Designers may then rely on a stacking sequence realizer (e.g. PACKS) and a knowledge-based tool incorporating manufacturability and design best practices prior to the design release (please refer to Figure 1.13). Then, a proper multi-ply failure analysis can be performed, where the neglected failure modes can be accounted for.

Two laminate failure criteria, which are usually employed in MBB-LAGRANGE, are maximum strain (MSTN) and Tsai-Wu (TSAI) failure criteria. MSTN computes the failure

indices or strain ratio, R_F , with respect to material allowable strains; whereas, TSAI, a quadratic failure criterion, evaluates composite failure for the interaction of different stresses with respect to material allowable stresses. Throughout this research, only MSTN has been taken into consideration.

Other design constraints currently supported by MBB-LAGRANGE are:

- ➔ Material allowable strain or stress, where MSTN or TSAI are described (CMAT)
- ➔ Displacement constraints (CDIS)
- ➔ Sizing constraints (CGAGE)
- ➔ Ply angle gage constraints (CGANG)
- ➔ Gage constraints for concentrated masses (GACONM)
- ➔ Buckling constraints (BUCK)
- ➔ Frequency constraints (FRECO).

3.3.2.1. Program Architecture

In general, an optimization problem, which is a nonlinear problem, can be expressed mathematically as:

$$\text{minimize} \quad F(\vec{x}) \quad \text{design objective} \quad (3.3.1)$$

$$\text{subject to} \quad g_j(\vec{x}) \leq 0 \quad j = 1, \dots, m \quad \text{inequality constraints} \quad (3.3.2)$$

$$h_k(\vec{x}) = 0 \quad k = 1, \dots, p \quad \text{equality constraints} \quad (3.3.3)$$

$$x_i^l \leq x_i \leq x_i^u \quad i = 1, \dots, n \quad \text{side constraints} \quad (3.3.4)$$

$$\text{where} \quad \vec{x} = \{x_1, x_2, \dots, x_n\} \quad \text{design variables.} \quad (3.3.5)$$

Within MBB-LAGRANGE, the optimization task is divided into three main parts, so-called “three column concept”⁴¹, as illustrated in Figure 3.3.2:

- ➔ structural model
- ➔ optimization model
- ➔ optimization algorithm.

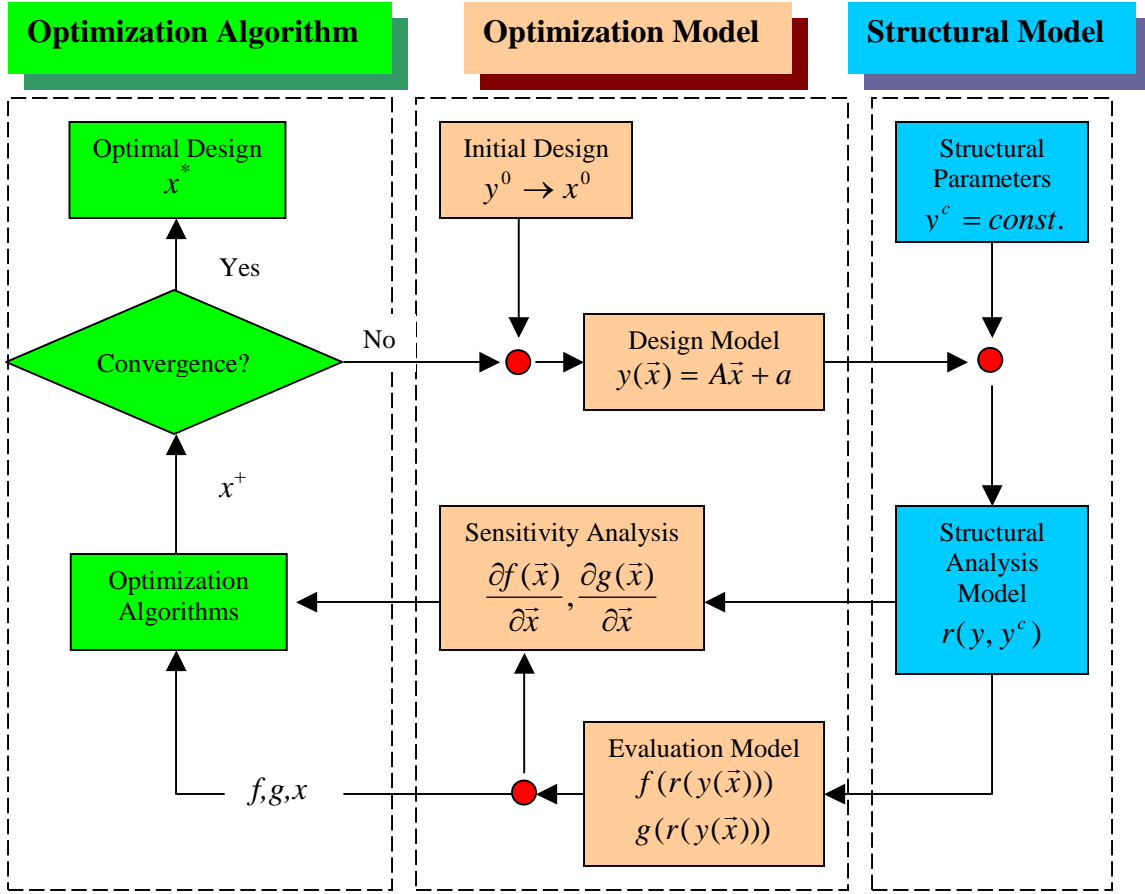


Figure 3.3.2: MBB-LAGRANGE software architecture, “Three Column Concept”⁴¹.

3.3.2.2 Structural Model

In the structural model, the physical behavior of the structure is defined as a mathematical description using appropriate state variables, $r(y(\vec{x}))$, (e.g. deformation, stresses, strains, eigenvalues, etc.), which depend on the structural variable, $y(\vec{x})$, (e.g. cross-section dimensions, layer thickness, fiber angles, etc). The finite element analysis (FEA) takes place here.

Based on the generalized Hooke’s law for composite materials, the stress-strain relation for an orthotropic lamina using a plane stress condition in the principal material coordinate system is:

$$\begin{Bmatrix} \sigma_1 \\ \sigma_2 \\ \tau_{12} \end{Bmatrix} = \begin{bmatrix} Q_{11} & Q_{12} & 0 \\ Q_{12} & Q_{22} & 0 \\ 0 & 0 & Q_{66} \end{bmatrix} \begin{Bmatrix} \varepsilon_1 \\ \varepsilon_2 \\ \gamma_{12} \end{Bmatrix}$$

$$\sigma_3 = 0$$

$$\tau_{23} = \tau_{31} = 0$$
(3.3.6)

$$Q_{11} = \frac{E_1}{1 - \nu_{12}\nu_{21}}, \quad Q_{22} = \frac{E_2}{1 - \nu_{12}\nu_{21}}, \quad Q_{66} = G_{12},$$

where $Q_{12} = \frac{\nu_{12}E_2}{1 - \nu_{12}\nu_{21}} = \frac{\nu_{21}E_1}{1 - \nu_{12}\nu_{21}}$

$$E_1\nu_{21} = E_2\nu_{12}$$
(3.3.7)

Q_{ij} , reduced stiffness matrices, are functions of four engineering constants; i.e., longitudinal modulus, E_1 , transverse modulus, E_2 , in-plane shear modulus, G_{12} , and Poisson's ratio, ν_{12} .

Transforming the stress-strain relation into x-y coordinates (Figure 3.3.3), becomes:

$$\begin{Bmatrix} \sigma_x \\ \sigma_y \\ \tau_{xy} \end{Bmatrix} = [T]^{-1} \begin{Bmatrix} \sigma_1 \\ \sigma_2 \\ \tau_{12} \end{Bmatrix} \quad \text{and} \quad \begin{Bmatrix} \varepsilon_x \\ \varepsilon_y \\ \gamma_{xy}/2 \end{Bmatrix} = [T]^{-1} \begin{Bmatrix} \varepsilon_1 \\ \varepsilon_2 \\ \gamma_{12}/2 \end{Bmatrix}$$
(3.3.8)

where $[T] = \begin{bmatrix} \cos^2 \theta & \sin^2 \theta & 2 \sin \theta \cos \theta \\ \sin^2 \theta & \cos^2 \theta & -2 \sin \theta \cos \theta \\ -\sin \theta \cos \theta & \sin \theta \cos \theta & \cos^2 \theta - \sin^2 \theta \end{bmatrix}$

(3.3.9)

is the transformation matrix and θ is measured counterclockwise with respect to the longitudinal axis.

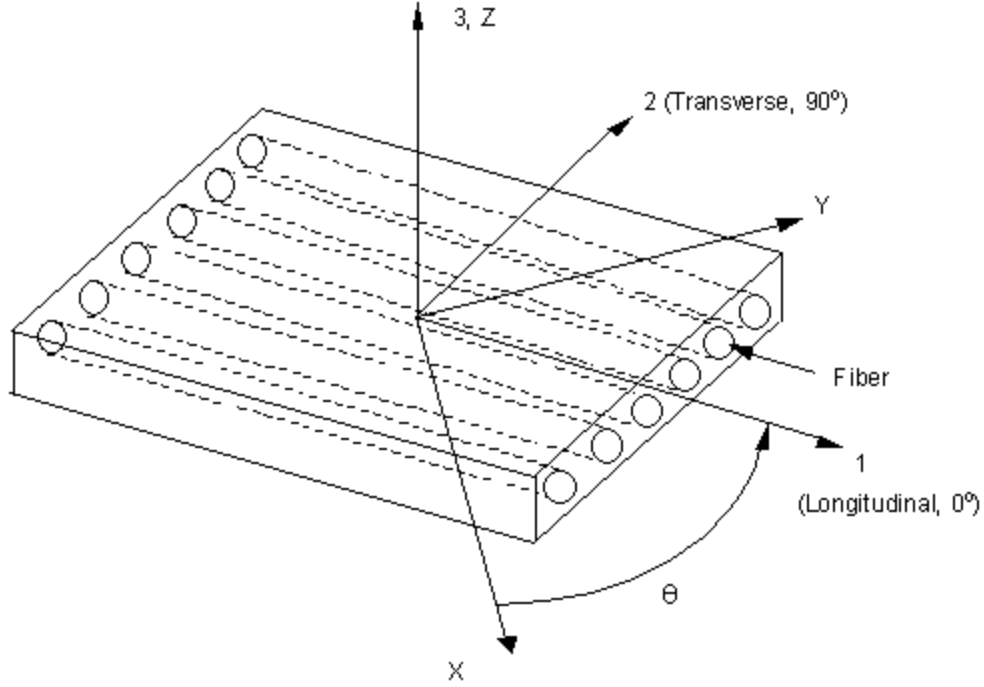


Figure 3.3.3: Coordinate system transformations of composite laminates.

Expanding Equation (3.3.8) into the form of Equation (3.3.6), yields:

$$\begin{Bmatrix} \sigma_x \\ \sigma_y \\ \tau_{xy} \end{Bmatrix} = \begin{bmatrix} \bar{Q}_{11} & \bar{Q}_{12} & \bar{Q}_{16} \\ \bar{Q}_{12} & \bar{Q}_{22} & \bar{Q}_{26} \\ \bar{Q}_{16} & \bar{Q}_{26} & \bar{Q}_{66} \end{bmatrix} \begin{Bmatrix} \varepsilon_x \\ \varepsilon_y \\ \gamma_{xy} \end{Bmatrix} \quad (3.3.10)$$

where \bar{Q}_{ij} matrices are the transformed reduced stiffness matrix based on $[Q]$ and the fiber orientation, θ :

$$\begin{aligned} \bar{Q}_{11} &= Q_{11} \cos^4 \theta + 2(Q_{12} + 2Q_{66}) \sin^2 \theta \cos^2 \theta + Q_{22} \sin^4 \theta \\ \bar{Q}_{12} &= (Q_{11} + Q_{22} - 4Q_{66}) \sin^2 \theta \cos^2 \theta + Q_{12} (\sin^4 \theta + \cos^4 \theta) \\ \bar{Q}_{22} &= Q_{11} \sin^4 \theta + 2(Q_{12} + 2Q_{66}) \sin^2 \theta \cos^2 \theta + Q_{22} \cos^4 \theta \\ \bar{Q}_{16} &= (Q_{11} - Q_{12} - 2Q_{66}) \sin \theta \cos^3 \theta + (Q_{12} - Q_{22} + 2Q_{66}) \sin^3 \theta \cos \theta \\ \bar{Q}_{26} &= (Q_{11} - Q_{12} - 2Q_{66}) \sin^3 \theta \cos \theta + (Q_{12} - Q_{22} + 2Q_{66}) \sin \theta \cos^3 \theta \\ \bar{Q}_{66} &= (Q_{11} + Q_{22} - 2Q_{12} - 2Q_{66}) \sin^2 \theta \cos^2 \theta + Q_{66} (\sin^4 \theta + \cos^4 \theta) \end{aligned} \quad (3.3.11)$$

By stacking several laminae together to make a laminate, the stress-strain relation of each lamina, denoted by a subscript k , satisfies the generalized Hooke's law:

$$\begin{Bmatrix} \sigma_x \\ \sigma_y \\ \tau_{xy} \end{Bmatrix}_k = \begin{bmatrix} \bar{Q}_{11} & \bar{Q}_{12} & \bar{Q}_{16} \\ \bar{Q}_{12} & \bar{Q}_{22} & \bar{Q}_{26} \\ \bar{Q}_{16} & \bar{Q}_{26} & \bar{Q}_{66} \end{bmatrix}_k \begin{Bmatrix} \varepsilon_x \\ \varepsilon_y \\ \gamma_{xy} \end{Bmatrix}_k \quad (3.3.12)$$

The variation of stress and strain through the laminate thickness can be determined from the Classical Lamination Theory (CLT) according to Kirchhoff-Love hypothesis. This hypothesis has several assumptions and approximations:

- ➔ Bonds between adjacent laminae are perfect and infinitesimally thin.
- ➔ The laminate is thin relative to either its length or width.
- ➔ Originally straight and perpendicular to the laminate's midplane, a line is assumed to remain straight and perpendicular to the laminate's midplane after deformation. Thus, the shears in the z-direction are neglected; i.e., $\gamma_{xz} = \gamma_{yz} = 0$.
- ➔ Also, this line has the same length after deformation. Therefore, this implies that the strain in the z-direction is ignored; i.e., $\varepsilon_z = 0$.

As a result, the u and v displacements become linear functions of midplane strains, u^0 and v^0 , the z coordinate or stacking sequence, and the midplane slopes in x and y directions, $\frac{\partial w^0}{\partial x}$ and $\frac{\partial w^0}{\partial y}$, respectively:

$$\begin{aligned} u &= u^0 - z \frac{\partial w^0}{\partial x} \\ v &= v^0 - z \frac{\partial w^0}{\partial y} \end{aligned} \quad (3.3.13)$$

Then, the strains in the x - y plane can be expressed based on strain-displacement relations:

$$\begin{Bmatrix} \varepsilon_x \\ \varepsilon_y \\ \gamma_{xy} \end{Bmatrix} = \begin{Bmatrix} \varepsilon_x^0 \\ \varepsilon_y^0 \\ \gamma_{xy}^0 \end{Bmatrix} + z \begin{Bmatrix} \kappa_x \\ \kappa_y \\ \kappa_{xy} \end{Bmatrix} \quad (3.3.14)$$

where the midplane strains are:

$$\begin{Bmatrix} \varepsilon_x^0 \\ \varepsilon_y^0 \\ \gamma_{xy}^0 \end{Bmatrix} = \begin{Bmatrix} \frac{\partial u^0}{\partial x} \\ \frac{\partial v^0}{\partial y} \\ \frac{\partial u^0}{\partial y} + \frac{\partial v^0}{\partial x} \end{Bmatrix} \quad (3.3.15)$$

and the midplane curvatures are:

$$\begin{Bmatrix} \kappa_x \\ \kappa_y \\ \kappa_{xy} \end{Bmatrix} = - \begin{Bmatrix} \frac{\partial^2 w^0}{\partial x^2} \\ \frac{\partial^2 w^0}{\partial y^2} \\ 2 \frac{\partial^2 w^0}{\partial x \partial y} \end{Bmatrix} \quad (3.3.16)$$

When a laminate is subjected to plane stresses and moments, the equilibrium equations can be obtained by integrating stresses in each lamina through the laminate thickness:

$$\begin{Bmatrix} N_x \\ N_y \\ N_{xy} \end{Bmatrix} = \sum_{k=1}^N \int_{z_{k-1}}^{z_k} \begin{Bmatrix} \sigma_x \\ \sigma_y \\ \tau_{xy} \end{Bmatrix} dz \quad \text{and} \quad \begin{Bmatrix} M_x \\ M_y \\ M_{xy} \end{Bmatrix} = \sum_{k=1}^N \int_{z_{k-1}}^{z_k} \begin{Bmatrix} \sigma_x \\ \sigma_y \\ \tau_{xy} \end{Bmatrix} z dz \quad (3.3.17)$$

Substituting Equations (3.3.12) and (3.3.15) into Equation (3.3.17) while taking the stiffness terms outside the integral in Equation (3.3.17), the stress and moment resultants can be expressed as:

$$\begin{Bmatrix} N_x \\ N_y \\ N_{xy} \end{Bmatrix} = \sum_{k=1}^N [\bar{Q}]_k \left\{ \int_{z_{k-1}}^{z_k} \begin{Bmatrix} \epsilon_x^0 \\ \epsilon_y^0 \\ \gamma_{xy}^0 \end{Bmatrix} dz + \int_{z_{k-1}}^{z_k} \begin{Bmatrix} \kappa_x \\ \kappa_y \\ \kappa_{xy} \end{Bmatrix} z dz \right\} \quad (3.3.18)$$

$$\begin{Bmatrix} M_x \\ M_y \\ M_{xy} \end{Bmatrix} = \sum_{k=1}^N [\bar{Q}]_k \left\{ \int_{z_{k-1}}^{z_k} \begin{Bmatrix} \epsilon_x^0 \\ \epsilon_y^0 \\ \gamma_{xy}^0 \end{Bmatrix} z dz + \int_{z_{k-1}}^{z_k} \begin{Bmatrix} \kappa_x \\ \kappa_y \\ \kappa_{xy} \end{Bmatrix} z^2 dz \right\}$$

Equation (3.3.18) can now be defined by the midplane strains and curvatures, the extensional stiffness matrix, $[A]$, the coupling stiffness matrix, $[B]$, and the bending stiffness matrix, $[D]$, as follows:

$$\begin{Bmatrix} N_x \\ N_y \\ N_{xy} \end{Bmatrix} = \begin{bmatrix} A_{11} & A_{12} & A_{16} \\ A_{12} & A_{22} & A_{26} \\ A_{16} & A_{26} & A_{66} \end{bmatrix} \begin{Bmatrix} \epsilon_x^0 \\ \epsilon_y^0 \\ \gamma_{xy}^0 \end{Bmatrix} + \begin{bmatrix} B_{11} & B_{12} & B_{16} \\ B_{12} & B_{22} & B_{26} \\ B_{16} & B_{26} & B_{66} \end{bmatrix} \begin{Bmatrix} \kappa_x \\ \kappa_y \\ \kappa_{xy} \end{Bmatrix} \quad (3.3.19)$$

$$\begin{Bmatrix} M_x \\ M_y \\ M_{xy} \end{Bmatrix} = \begin{bmatrix} B_{11} & B_{12} & B_{16} \\ B_{12} & B_{22} & B_{26} \\ B_{16} & B_{26} & B_{66} \end{bmatrix} \begin{Bmatrix} \epsilon_x^0 \\ \epsilon_y^0 \\ \gamma_{xy}^0 \end{Bmatrix} + \begin{bmatrix} D_{11} & D_{12} & D_{16} \\ D_{12} & D_{22} & D_{26} \\ D_{16} & D_{26} & D_{66} \end{bmatrix} \begin{Bmatrix} \kappa_x \\ \kappa_y \\ \kappa_{xy} \end{Bmatrix}$$

$$\begin{aligned}
A_{ij} &= \sum_{k=1}^N (\bar{Q}_{ij})_k (z_k - z_{k-1}) \\
\text{where } B_{ij} &= \sum_{k=1}^N (\bar{Q}_{ij})_k (z_k^2 - z_{k-1}^2) \\
D_{ij} &= \sum_{k=1}^N (\bar{Q}_{ij})_k (z_k^3 - z_{k-1}^3)
\end{aligned} \tag{3.3.20}$$

Linear Static Analysis

Using FEA, MBB-LAGRANGE calculates the state variables, $r(y(\vec{x}))$, and their derivatives with respect to structural variables (SV), $y(\vec{x})$, such as layer thickness and fiber orientation, following the assembly of element matrices of all finite elements:

$$\begin{aligned}
K(\vec{x})u(\vec{x}) &= p(\vec{x}) \Leftrightarrow F(\vec{x}, u(\vec{x})) = K(\vec{x})u(\vec{x}) - p(\vec{x}) = 0 \\
K(\vec{x}) \frac{du(\vec{x})}{dx_i} &= \frac{\partial p(\vec{x})}{\partial x_i} - \frac{\partial K(\vec{x})}{\partial x_i} u(\vec{x}) \\
i &= 1, \dots, n
\end{aligned} \tag{3.3.21}$$

where $K(\vec{x})$ is the elastic stiffness matrix

$u(\vec{x})$ is the displacement vector

$p(\vec{x})$ is the load vector.

These first order derivatives or sensitivity analyses with respect to constraint functions can be performed analytically or numerically with the finite difference method:

➔ Analytical

$$\begin{aligned}
\frac{\partial g_j(\vec{x})}{\partial x_i} &= \frac{\partial g_j(\vec{x})}{\partial r_i} \frac{\partial r_i}{\partial x_i} + \frac{\partial g_j(\vec{x})}{\partial r_i} \frac{\partial r_i}{\partial u(\vec{x})} K(\vec{x})^{-1} \left(-\frac{\partial K(\vec{x})}{\partial x_i} u(\vec{x}) + \frac{\partial p(\vec{x})}{\partial x_i} \right) \\
i &= 1, \dots, n \\
j &= 1, \dots, m
\end{aligned} \tag{3.3.22}$$

➔ Numerical based on first order forward difference method:

$$\frac{\partial g_j(\vec{x})}{\partial x_i} \cong \frac{g_j(\vec{x} + \varepsilon_G x_i) - g_j(\vec{x})}{\varepsilon_G x_i}$$

$$i = 1, \dots, n$$

$$j = 1, \dots, m$$
(3.3.23)

where ε_G is a small positive constant for numerical accuracy and stability.

The analytical approach involves a large programming effort due to differentiation of all functional and sensitivity equations, and the inverse of the elastic stiffness matrix, K^{-1} . The solution has a higher numerical efficiency compared with that of the finite difference method. The numerical solution by the finite difference method is characterized by a low programming effort.

Buckling Analysis

In general, the constitutive equation for a buckling analysis is stated as follows:

$$[K(\vec{x}) + \lambda_i K_G(\vec{x})] \{u(\vec{x})\} = 0$$

$$i = 1, \dots, n$$
(3.3.24)

where $K(\vec{x})$ is the elastic stiffness matrix

$K_G(\vec{x})$ is the differential/geometric stiffness matrix.

λ_i are the eigenvalues

$u(\vec{x})$ are the eigenvectors.

For an unstiffened symmetric laminate ($[B] = 0$) subjected to bi-axial compression loads as depicted in Figure 3.3.4(a), the governing buckling differential equation leads to:

$$-D_{11} \frac{\partial^4 v}{\partial x^4} - 4D_{16} \frac{\partial^4 v}{\partial x^3 \partial y} - 2(D_{12} + 2D_{66}) \frac{\partial^4 v}{\partial x^2 \partial y^2} - 4D_{26} \frac{\partial^4 v}{\partial x \partial y^3}$$

$$-D_{22} \frac{\partial^4 v}{\partial y^4} = N_x \frac{\partial^2 v}{\partial x^2} + N_y \frac{\partial^2 v}{\partial y^2}$$
(3.3.25)

At the present stage, MBB-LAGRANGE employs the analytical approach to compute such stability criteria for a specially orthotropic material; i.e., $D_{16} = D_{26} = 0$:

$$v(x, y) = \alpha_{mn} \sin\left(\frac{m\pi}{a} x\right) \sin\left(\frac{n\pi}{b} y\right)$$
(3.3.26)

where α_{mn} is the coefficient of Fourier series

and m, n correspond to numbers of mode shape.

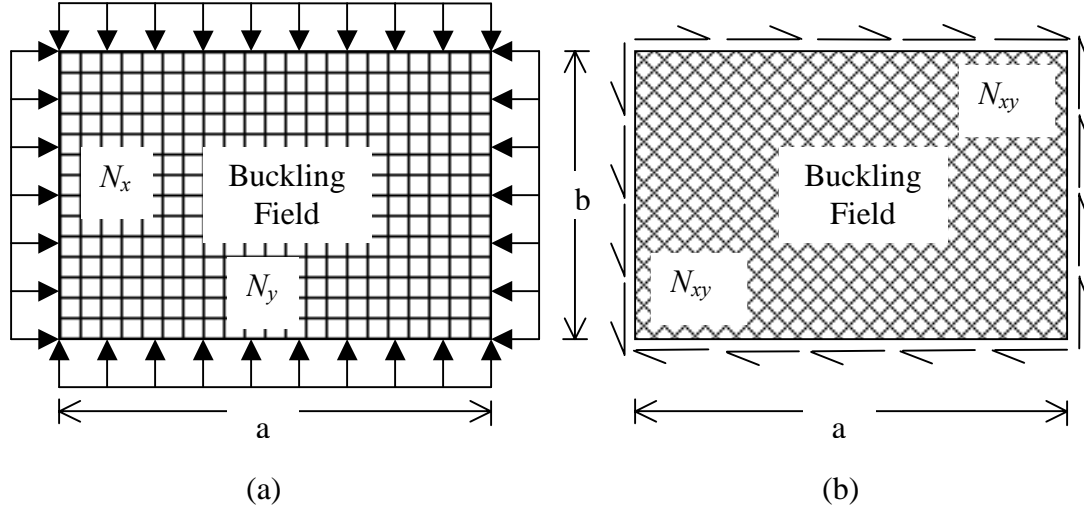


Figure 3.3.4: Schematics of flat rectangular laminates subjected to (a) bi-axial compression and (b) in-plane shear loads.

The following assumptions are also applied to solve the buckling differential equation:

- ➔ Rectangular buckling fields
- ➔ Flat buckling fields
- ➔ Constant thickness of buckling field
- ➔ Orthotropic axis are parallel to the support
- ➔ Simply supported boundary; i.e., for $x = 0$ and $x = a$: $v = 0$, $M_x = 0$ and for $y = 0$ and $y = b$: $v = 0$, $M_y = 0$.
- ➔ $N_x(y) = \text{constant}$, $N_y(x) = \text{constant}$

Then, the critical normal stress for the laminate under bi-axial compression loads is:

$$\sigma_{x-cr} = \frac{\pi^2}{b^2 t \left[1 + \gamma \left(\frac{nc}{m} \right)^2 \right]} \left[D_{11} \left(\frac{m}{c} \right)^2 + 2(D_{12} + 2D_{66})n^2 + D_{22} \left(\frac{c}{m} \right)^2 n^4 \right] \quad (3.3.27)$$

where $\gamma = \frac{N_y}{N_x}$, $c = \frac{a}{b}$, and $D_{ij} = \frac{t^3}{12} \bar{Q}_{ij}$

and t is the plate thickness.

When subjected to in-plane shear loads (Figure 3.3.4(b)), the critical shear stress can be deduced:

$$\tau_{cr} = \begin{cases} \frac{4}{tb^2} \sqrt[4]{(D_{11}D_{22}^3)} \cdot \left(8.12 + \frac{4.05}{\delta}\right) & \text{if } \delta \geq 1 \\ \frac{4}{tb^2} \sqrt{D_{22}(D_{12} + 2D_{66})} \cdot (11.7 + 0.532\delta + 0.938\delta^2) & \text{if } \delta < 1 \end{cases} \quad (3.3.28)$$

where $\delta = \frac{\sqrt{D_{11}D_{22}}}{D_{12} + 2D_{66}}$ and $\frac{a}{b}$ is large.

3.3.2.3 Optimization model

The optimization model is a mathematical description of the structural design task. It provides the linkage between the structural model and the optimization algorithm. It is divided into a design model and an evaluation model. The SV-to-DV relation is defined in the design model with an initial design. On the other hand, the evaluation model describes the quantity of the structural model subjected to the function minimization and design responses of the state variables.

Design Model

A design model dictates the mathematical relationship between DV and SV using a linear transformation:

$$y(\vec{x}) = A\vec{x} + a, \quad A = (\alpha_{ij}) \in \mathfrak{R}^{m \times n}, a = (a_i) \in \mathfrak{R}^m \quad (3.3.29)$$

In the structural optimization of fiber steering conceptual design, the layer thickness and angle are DVs. These variables are related mathematically with the structural properties defined in PCOMP as:

$$\begin{Bmatrix} t \\ \theta \end{Bmatrix} = \begin{bmatrix} A_t & 0 \\ 0 & A_a \end{bmatrix} \begin{Bmatrix} x_1 \\ x_2 \end{Bmatrix} + \begin{Bmatrix} t^o \\ \theta^o \end{Bmatrix} \quad (3.3.30)$$

where t = vector of the layer thicknesses

θ = vector of layer angles

A_t, A_a = linking matrices of layer thicknesses and angles

x = DV vectors

t^o, θ^o = constant portions of the layer thicknesses and angles.

With the adaptation of the finite element mesh, MBB-LAGRANGE enables two DV definitions:

- Single DV
- Range or Regional DV.

These DV can be linked appropriately to:

- reduce number of DV
- define a linear relation between one SV and another
- define symmetric and balanced laminates.

Figure 3.3.5 shows two generic examples of DV linking in MBB-LAGRANGE⁴⁵. Coefficients of linking matrices and vectors of constants are set to a dimensionless value ‘1’ for numerical stability in the optimization algorithm.

Evaluation Model

The evaluation model defines requirements on the structure to be optimized, which are constraint definitions. MBB-LAGRANGE supports multidisciplinary constraints to fulfill the design optimization, as described in the previous pages. For this research, MSTN or CMAT, CDIS, CGAGE, CANG, and BUCK are considered.

MSTN dictates the failure safety factor or index, R_F , of each layer material. MBB-LAGRANGE only calculates R_F based on the fiber failure, i.e., the longitudinal tension and compression failures in the fiber direction:

$R_F = 1$, ultimate strength is reached

$R_F < 1$, ultimate strength is exceeded, design is undersized.

$R_F > 1$, design is oversized.

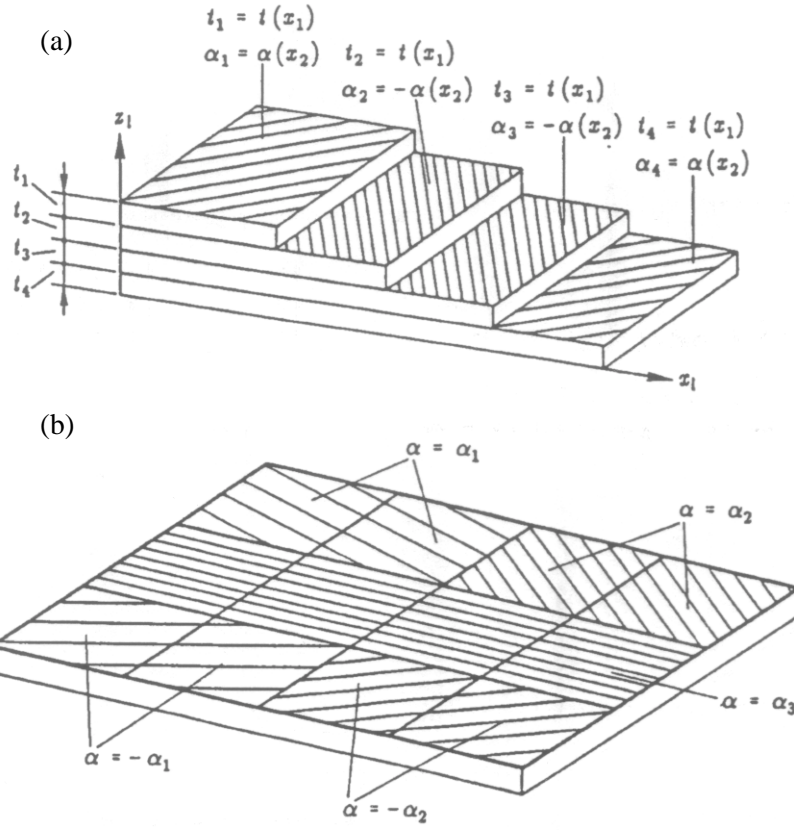


Figure 3.3.5: Schematics of design variable linking (a) linking over several layers, and (b) linking over several elements (copied from Ref. 45).

The normalized constraint function for R_F and its derivative are described as follows:

$$\begin{aligned}
 R_F(\vec{x}) &= \frac{\varepsilon_1^{tu}}{\varepsilon_1^t(\vec{x})} \text{ or } \frac{\varepsilon_1^{cu}}{\varepsilon_1^c(\vec{x})} \\
 g_j(\vec{x}) &= 1 - \frac{1}{R_F(\vec{x})} \geq 0 \\
 \frac{\partial g_j(\vec{x})}{\partial R_F} &= \frac{1}{R_F^2(\vec{x})}.
 \end{aligned} \tag{3.3.31}$$

Displacement constraints (CDIS) of discrete displacements, u , of nodal points based on FEA are defined as:

$$\begin{aligned}
 g_j(\vec{x}) &= 1 - \frac{u(\vec{x})}{u_{\max}} \geq 0 \\
 g_j(\vec{x}) &= \frac{u(\vec{x})}{u_{\min}} - 1 \geq 0.
 \end{aligned} \tag{3.3.32}$$

Gage constraints, such as CGAGE for layer thickness and CGANG for layer angle, are mathematically described as:

$$\begin{aligned} g_j(\vec{x}) &= 1 - \frac{t(\vec{x})}{t_{\max}} \geq 0 \\ \text{CGAGE:} \quad g_j(\vec{x}) &= \frac{t(\vec{x})}{t_{\min}} - 1 \geq 0 \end{aligned} \quad (3.3.33)$$

$$\begin{aligned} g_j(\vec{x}) &= 1 - \frac{\theta(\vec{x})}{\theta_{\max}} \geq 0 \\ \text{CANG:} \quad g_j(\vec{x}) &= \frac{\theta(\vec{x})}{\theta_{\min}} - 1 \geq 0. \end{aligned} \quad (3.3.34)$$

Besides defining these constraints in absolute values, both CGAGE and CGANG can be described in percentage and incremental inputs, respectively. For instance, designers can impose an angle threshold of $\pm 45^\circ$. In this scenario, 0° ply can only be varied within $\pm 45^\circ$ threshold.

In the buckling analysis, only pure thickness optimization is considered. The failure criterion of a simply-supported, rectangular, flat and constant thickness buckling field, specially symmetric orthotropic laminate (see 3.3.2.2 for buckling analysis) is assessed by the constraint:

$$g_B(\vec{x}) = 1 - \frac{|\sigma(\vec{x})|}{\sigma_{cr}} - \left(\frac{\tau(\vec{x})}{\tau_{cr}} \right)^2 \quad (3.3.35)$$

3.3.3 Optimization Algorithm

The optimization algorithm carries out the mathematical procedures for solving an optimization problem statement, which is described in Equations (3.3.1) to (3.3.5). Because of nonlinearity describing the relationships between the behavior functions (objective and constraint functions) and DVs, iterative and numerical processes must be performed. For this purpose, MBB-LAGRANGE supports several mathematical programming (MP) algorithms or strategies (Figures 3.3.6 and 3.3.7) and an optimality criteria procedure, called the Kuhn-Tucker condition. Generally, mathematical programming methods can be classified as:

- ➔ Transformation methods
- ➔ Primal methods
- ➔ Direct methods
- ➔ Dual concepts.

Since optimization algorithms are problem-dependent, no single known algorithm is universally preferred for every optimization problem⁴¹.

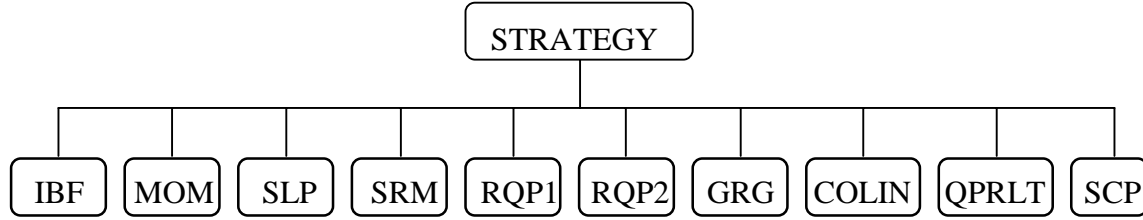


Figure 3.3.6: Optimization algorithms of MBB-LAGRANGE.

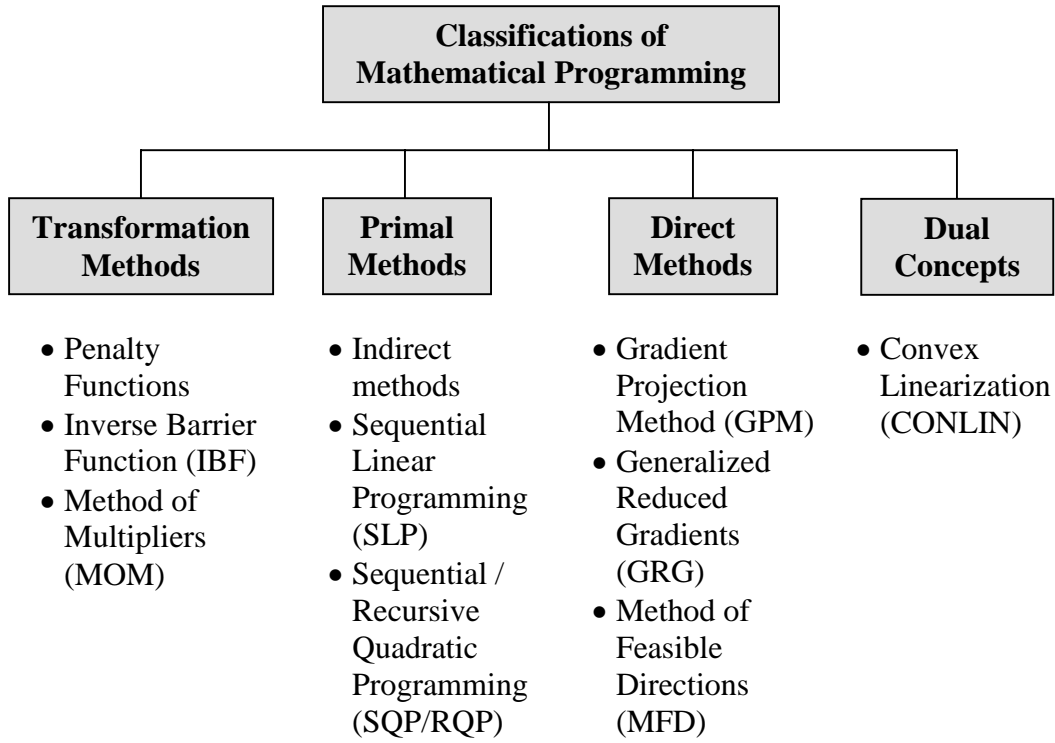


Figure 3.3.7: Classifications of Mathematical Programming Methods⁴¹.

For a structural optimization problem subject to only inequality constraints, $g_j(\vec{x}) \leq 0; j = 1 \text{ to } m$, the constitutive formulation is the optimality conditions or Kuhn-Tucker (K-T) conditions:

$$\nabla_x L(\vec{x}^*, \lambda) = 0 \Leftrightarrow \nabla_x f(\vec{x}^*) = \sum_{j=1}^m \lambda_j \nabla_x g_j(\vec{x}^*), \forall i = 1, \dots, n$$

$$\lambda_j \cdot g_j(\vec{x}^*) = 0; \forall j = 1, \dots, m \text{ (dot product of } \lambda_j \text{ and } g_j(\vec{x}) \text{ equals zero)} \quad (3.3.36)$$

$$\lambda_j \geq 0; \forall j = 1, \dots, m$$

where $L(\vec{x}, \vec{\lambda}) = f(\vec{x}) - \sum_{j=1}^m \lambda_j g_j(\vec{x})$ is the Lagrangian function

\vec{x}^* is the optimal solution vector

λ^* is the Lagrangian multiplier at the optimum

∇_x is the gradient with respect to x .

This means that “the gradient of the objective function at the optimum is a non-negative linear combination of the gradient of active constraints.”⁴¹ Active constraints are those constraints or design responses that influence the design change. Inactive constraints have less influence in the design determination, and are therefore temporarily neglected. MBB-LAGRANGE allows the users to impose a percentage of constraint restriction (POR):

➔ POR = 0.0 means all constraints are considered active

➔ POR = 1.0 means only violated constraints are considered active.

To find the optimal solution vector \vec{x}^* , the following iterative formulation is used:

$$\vec{x}^{n+1} = \vec{x}^n + \alpha^n s^n \quad (3.3.37)$$

where s^n is the downhill search direction

and α^n is the step size.

α^n , a positive scalar, minimizes the function F in the direction of s^n using a one-dimensional line search:

$$f(\vec{x}^{n+1}) = \min_{\alpha} [f(\vec{x}^n + \alpha^n s^n)] \quad (3.3.38)$$

α^n is determined through an evaluation of the structural model. The mathematical definition of a usable search direction is:

$$\text{minimize} \quad \nabla f(\vec{x}) \cdot \vec{S} \quad (3.3.39)$$

$$\begin{aligned} \text{subject to:} \quad & \nabla g_j(\vec{x}) \cdot \vec{S} \leq 0 \quad \text{for } j = 1, \dots, m \\ & \vec{S} \cdot \vec{S} \leq 1 \end{aligned} \quad (3.3.40)$$

The angles between search directions and gradients of constraint functions must be within 90° and 270°.

To terminate the optimization loops for optimum design, MBB-LAGRANGE performs several precision checks based on the relative change of the:

→ Objective function:

$$\frac{|f^n(\vec{x}) - f^{n-1}(\vec{x})|}{|f^n(\vec{x})|} \leq \varepsilon_f \quad (3.3.41)$$

where ε_f is the termination parameter for relative change in objective function

→ Feasibility of design variables:

$$\frac{|x^n - x^{n-1}|}{|x^n|} \leq \varepsilon_x \quad (3.3.42)$$

where ε_x is the termination parameter for relative change in design variables

→ Feasibility of constraints or maximum constraint violation:

$$-\{\min g_j(\vec{x})\} \leq \varepsilon_{res} \quad \forall j = 1, \dots, m \quad (3.3.43)$$

where ε_{res} is the termination parameter for maximum violation of constraints

→ Fulfillment of Kuhn Tucker Conditions in Equation (3.3.36), ε_{KTO} .

3.3.4 Selection of Optimization Algorithms

Studies have been performed to determine the most robust algorithm suitable for fiber steering conceptual design based on the first three preliminary models defined in Section 3.4. Four design variable configurations (Table 3.4.1) are defined for these models. With the application of fiber steering conceptual design, algorithms that showed convergence in the objective function are:

- (a) Quadratic Programming with Reduced Line search Technique (QPRLT)
- (b) Recursive Quadratic Programming by Schittkowski (RQP1)
- (c) Recursive Quadratic Programming by Powell (RQP2).

Optimization jobs are performed using Silicon Graphics Indigo² Impact 10000. The processor of this machine is MIPS R10000 with 195 MHz. It runs on IRIX64 release 6.2 operating system with a memory of 128 MByte.

Figure 3.3.8 shows comparisons of number of iterations and CPU time at optimum design with different optimization algorithms. From the diagrams, the most robust strategy is RQP2. For most configurations, minimal CPU time and iterations (therefore, cost of computational efforts) are required with the RQP2 strategy. QPRLT is not an ideal strategy for fiber steering conceptual

design because the optimum objective function (minimum weight) is not achieved, as shown in Figure 3.3.9. The structural weight is normalized with the optimum result using RQP2 algorithm. In general, optimum designs for RQP1 and RQP2 are relatively close. However, a tremendous difference in CPU time is found between these strategies. As a result, RQP2 is selected for future optimization strategies involving fiber steering conceptual design.

3.3.5 FEA Package: MSC/PATRAN and MSC/NASTRAN

MSC/PATRAN is a pre and post processor to many commercially available finite element packages. MSC/NASTRAN, being one of them, is a general-purpose FEA solver developed by MacNeal Schwendler Corporation (MSC). MSC/NASTRAN supports several disciplines, including static (SOL 101), normal modes (SOL 103), buckling (SOL 105), nonlinear static (SOL 106), design optimization (SOL 200), and other dynamics and thermal analyses. In this research, MSC/NASTRAN is used solely for finite element analysis. The design optimization (SOL 200), which optimization capabilities with respect to the fiber steering conceptual design were described in Table 3.3.1, has been performed at the preliminary stage for the first two models described in Section 3.4. Appendix D lists the fiber steering results with SOL 200 for these models. MSC/NASTRAN SOL 200 has not been an ideal solver for the fiber steering conceptual design. It reached “a best compromise infeasible design”⁴⁸ for those models because it has an apparent limitation in performing optimization with layer thickness and fiber orientation simultaneously.

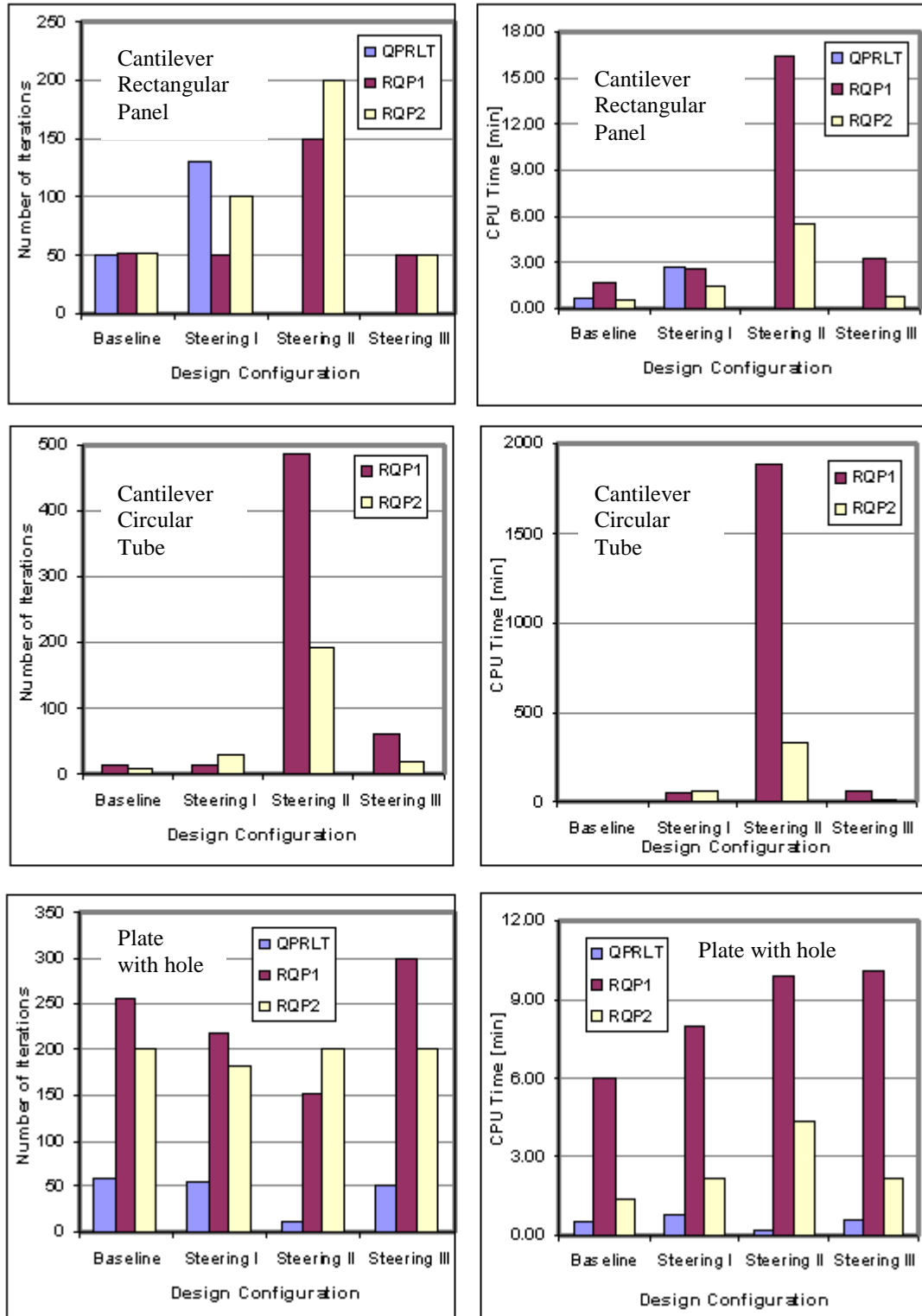
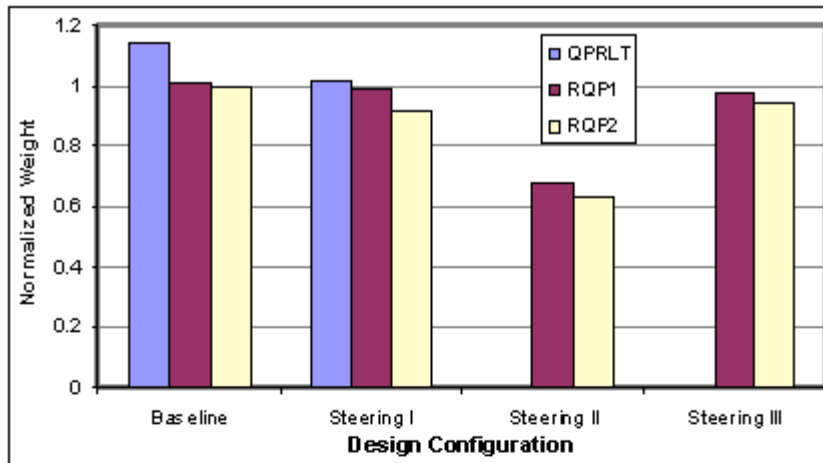
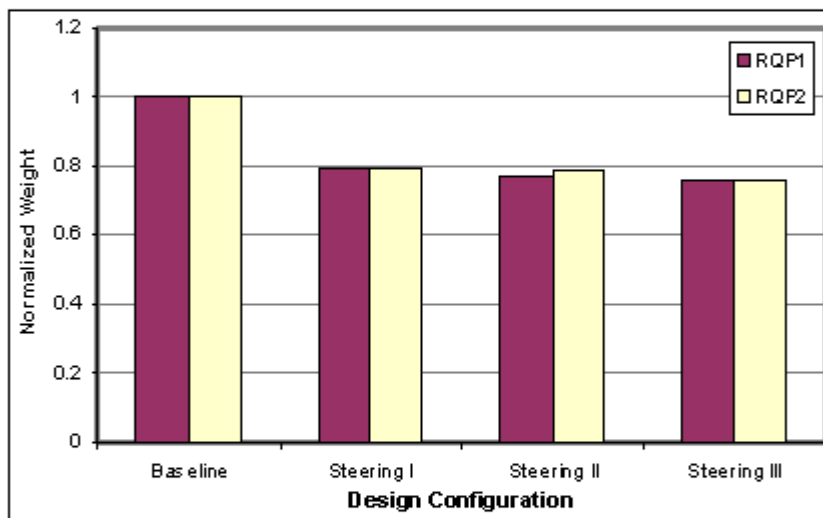


Figure 3.3.8: Comparisons of number of iterations and CPU time at optimum design with different optimization algorithms for preliminary studies (design configuration defined in Table 3.4.1).



Cantilever
Rectangular
Panel



Cantilever
Circular
Tube

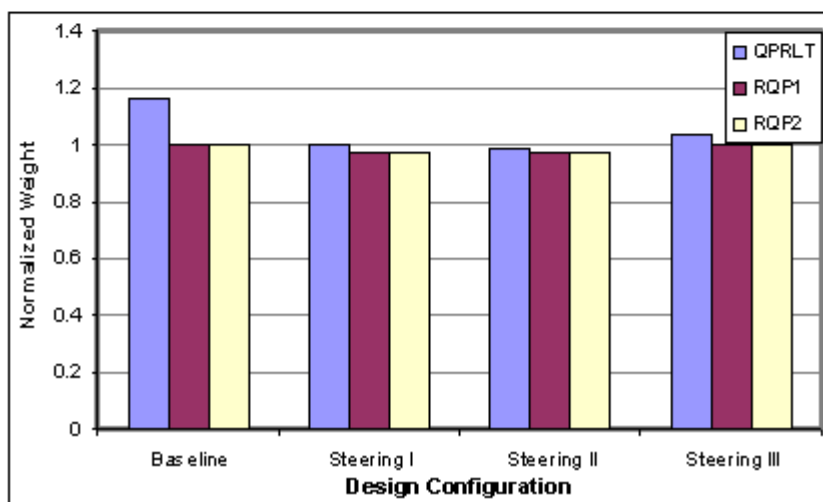


Plate with
hole of
 $W/D = 5.0$

Figure 3.3.9: Comparisons of normalized structural weight at optimum design with different optimization algorithms for preliminary studies (design configuration defined in Table 3.4.1).

3.3.6 Flight Data Simulation Tool: VORSTAB

VORSTAB has been selected to determine the pressure coefficient over the lifting surfaces of two representative aircraft, which are discussed in Section 3.5. It is an advanced aerodynamic code for aircraft flight characteristics and stability evaluations. Initially developed at the University of Kansas by Dr. C. Edward Lan, this code is written based on the quasi-vortex-lattice method, which is similar to the conventional vortex-lattice method in general but far superior in accuracy⁵¹.

VORSTAB is capable of performing aerodynamic calculations upon various kinds of aircraft configurations, as listed:

- ➔ lifting surfaces including wings, vertical tails, horizontal tails, leading-edge flaps, strakes, ailerons, trailing-edge flaps, winglets,
- ➔ fuselage, body of revolution, irregular cross-section shapes,
- ➔ user definable wing cambers, twisting, tapered wings and airfoil thickness distributions.

Another feature of this versatile code is the computation capability that covers both subsonic and supersonic flight regimes. Other computation capabilities of VORSTAB are:

- ➔ longitudinal characteristics and 9 lateral-directional stability parameters
- ➔ pitch damping derivatives at pre- and post-stall conditions
- ➔ high angle-of-attack characteristics
- ➔ in- and out-of-ground effects
- ➔ hinge moment, torsional moment & bending moment distributions on lifting surfaces
- ➔ asymmetric forebody vortex separation
- ➔ vortex breakdown and wake effects
- ➔ interactive input preparation
- ➔ built-in graphical viewing of geometries and computed results.

In summary, MBB-LAGRANGE has been selected as the optimization routine for fiber steering conceptual design. Based on the results in Figures 3.3.8 and 3.3.9, the recursive quadratic programming after Powell (RQP2) is employed for future optimization strategies involving fiber steering conceptual design. MSC/PATRAN and MSC/NASTRAN are used to verify the results obtained from MBB-LAGRANGE. Finally, VORSTAB has been selected to determine the pressure coefficient over the lifting surfaces of two representative aircraft, which are discussed in Section 3.5.

3.4.0. Preliminary Studies

Fiber steering (FS) conceptual design calls for the tailorability of curvilinear-family laminates, which involves simultaneous optimizations of both layer thickness and orientation either within a region or over the entire lamina. Many researchers have explored the optimization of these variables upon simple composite structures. Studies of these structures give insights for further developments of the variable stiffness design. In this section, preliminary studies on four simple models are discussed to evaluate the potential payoffs of the conceptual design based on steered-fiber architecture.

3.4.1 A Glance on the Literature

Hyer, et. al.²⁰ and Katz, et. al.¹⁹ both studied curvilinear fiber trajectories with respect to (w.r.t.) the failure loads for a plate with a hole under uniaxial tensile loads. Substantial improvements in the failure loads were predicted analytically when comparing the curvilinear design with conventional quasi-isotropic laminates. The curvilinear fiber format of the plate model with $W/D = 3.0$ is shown in Figure 3.4.1. Using MBB-LAGRANGE, Berchtold, et. al.²³ investigated the optimal design of a two-ply cantilever beam or panel subjected to a vertical load, as illustrated in Figure 3.4.2. Reuschel, et. al.⁵² examined the fiber arrangement of a hollow pipe with a circular hole under uniaxial tensile loads. The optimal design (Figure 3.4.3) showed a reduction in the maximum principal stresses by 50%. On the other hand, an optimal layer-thickness and fiber-orientation design of a fin was presented by Eschenauer, et. al.⁴⁵ in Figure 3.4.4, showing a possibility of weight savings. The fin is subjected to failure safety; while it's aerodynamic model takes into account of aeroelastic efficiencies and flutter speed. The resultant model had a structural weight that was reduced by 8% to 40%. All of these works shared a similar trend in the improvement of structural efficiency and weight reductions for composite structures exhibiting curvilinear fiber format.

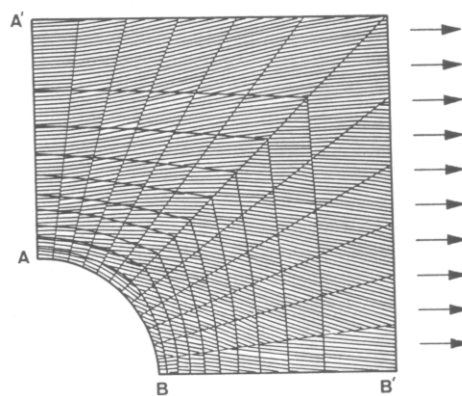


Figure 3.4.1: Curvilinear fiber format of a plate with a hole of $W/D = 3.0$ under uniaxial tensile loads (copied from Ref. 20)

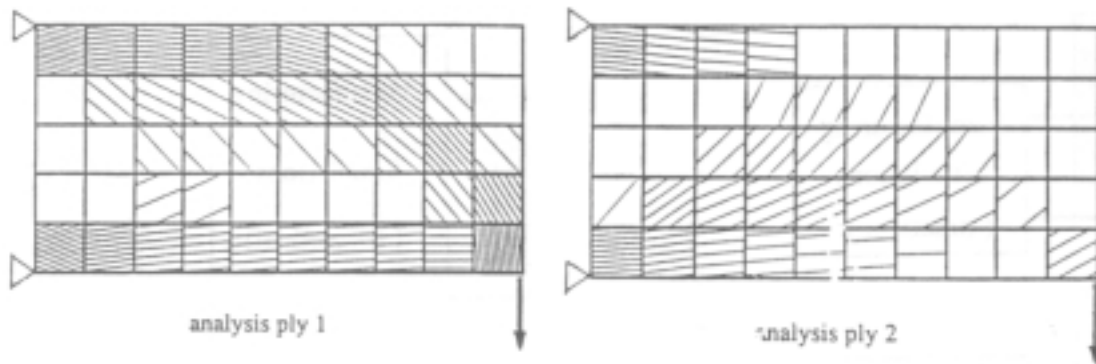


Figure 3.4.2: Optimum layer thickness and fiber orientation mappings for a cantilever panel under a vertical nodal load (copied from Ref. 23)

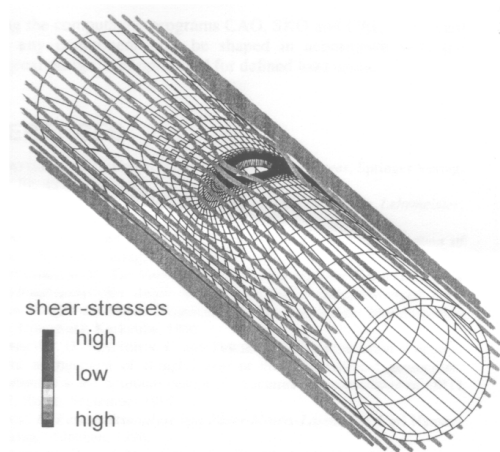


Figure 3.4.3: Fiber arrangement of a hollow pipe with a circular hole under axial tension (copied from Ref. 51)

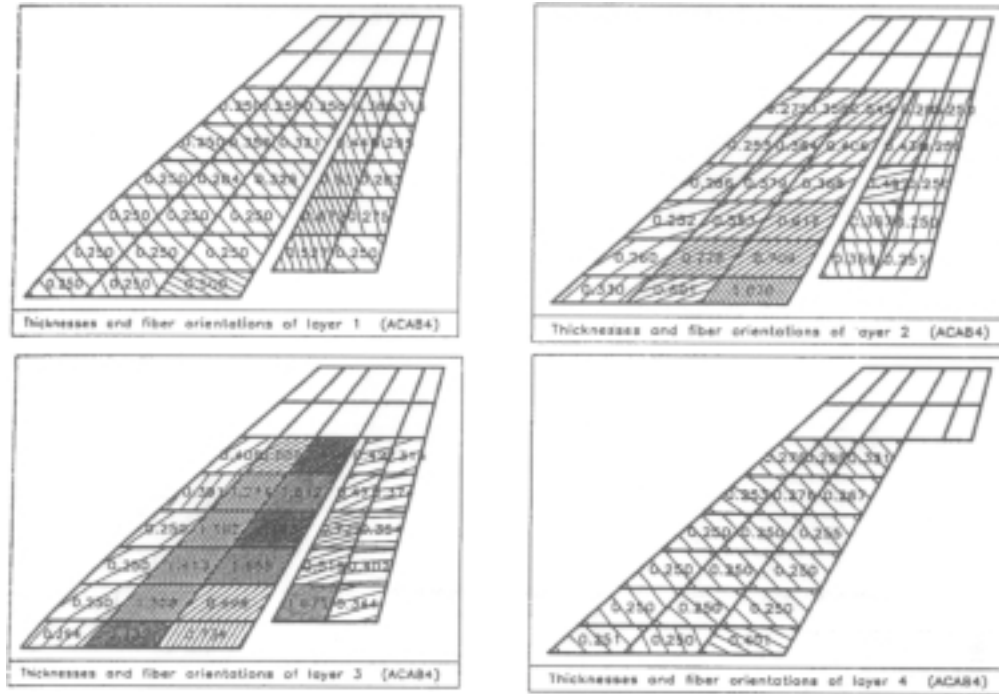


Figure 3.4.4: Optimal layer thickness and orientation distributions of a fin (copied from Ref. 45)

3.4.2 Preliminary Studies: Four Simple Models

In this chapter, four test models have been selected and set up with MSC/PATRAN. They are:

- ➔ Three square plates with central circular holes subjected to various loads
- ➔ An intermediate complexity wing (ICW) subjected to aerodynamic loads
- ➔ A cantilever rectangular panel subjected to transverse loads
- ➔ A cantilever cylindrical tube subjected to combined loads.

IM7/8551-7A, material properties for which are listed in Appendix A, is taken as the primary carbon/epoxy composite material throughout the research. The initial laminate with $[\pm 45, 0, 90]_s$ is analyzed with MSC/NASTRAN based on static analysis and maximum strain failure criterion, STRN, to determine the initial layer thickness for each angle. Each layer consists of a collective of several plies, where each ply has a minimum gage of 0.0055 inch. The initial MSC/NASTRAN analysis, then, support an initial laminate family for an unsteered laminate. The optimal laminate family based on FS conceptual design can be obtained via MBB-LAGRANGE, where optimization jobs are performed with Silicon Graphics Indigo² Impact 10000 machine.

As stated in Section 3.3, Recursive Quadratic Programming by Powell (RQP2) is selected as the primary optimization algorithm. The objective function for these models is the structural weight, while first-ply fiber-related failure based on maximum strain failure criterion (MSTN or CMAT), upper and lower layer thickness (CGAGE) and angle bounds (CGANG) are design constraints:

- CMAT: Longitudinal tensile strain, $\varepsilon_1^t = 12800 \mu\text{in} / \text{in}$
Longitudinal compression strain, $\varepsilon_1^c = 11100 \mu\text{in} / \text{in}$
- CGAGE: Lower bound layer thickness, $t_l = 0.011 \text{ inch}$ (2 plies)
Upper bound layer thickness, $t_u = 0.500 \text{ inch}$ (~91 plies)
- CGANG: Angle threshold of $\pm 45^\circ$ are imposed onto all angle design variables (DV's).

Note that MBB-LAGRANGE calculates $[A]$ matrix with effective $[D]$ matrix only, or in other words it uses membrane composite properties. Therefore, only four layers (collectives of several plies in each layer) are required for each element or range of elements in a laminate family optimization. Each layer thickness of the resultant laminate is divided into two to yield a symmetric laminate according to MSC/NASTRAN definition, $[\pm\theta_l, \theta_2, \theta_3]_s$. Then, the lower bound CGAGE is a 2-ply thickness to ensure laminate symmetry (Figure 3.4.5). The reason CGANG of $\pm 45^\circ$ threshold are imposed onto all angle DV's is to avoid a design with only one angle for all layers. In addition, if a 0° layer wishes to vary by more than 45° , then it is preferred to reduce the thickness of the current 0° layer and increase thickness of the current 45° layer rather than reorienting the 0° layer. Practically, the CGANG constraint is intended to distribute longitudinal, transverse, and in-plane shear loads among four layers with different layer angle for laminate family optimization. However, one may argue that $\pm 45^\circ$ may be appropriate.

For the ICW model, additional constraints are a maximum wing-tip vertical deflection (CDIS) and critical buckling loads on the upper skin (BUCK). Allowable strains for ICW model are modified with an imposed safety factor of 1.5. Also, the fourth layer in the laminate family has a lower bound thickness of 0.0055 inch (or minimum gage). This is intended to allow an oblique-symmetric laminate, $[\pm\theta_l, \theta_2, \theta_3]_{os}$. An oblique-symmetric laminate has a ply ($t = 0.0055 \text{ inch}$) located at the laminate centerline, as illustrated in Figure 3.4.6. Therefore, ICW model is subject to:

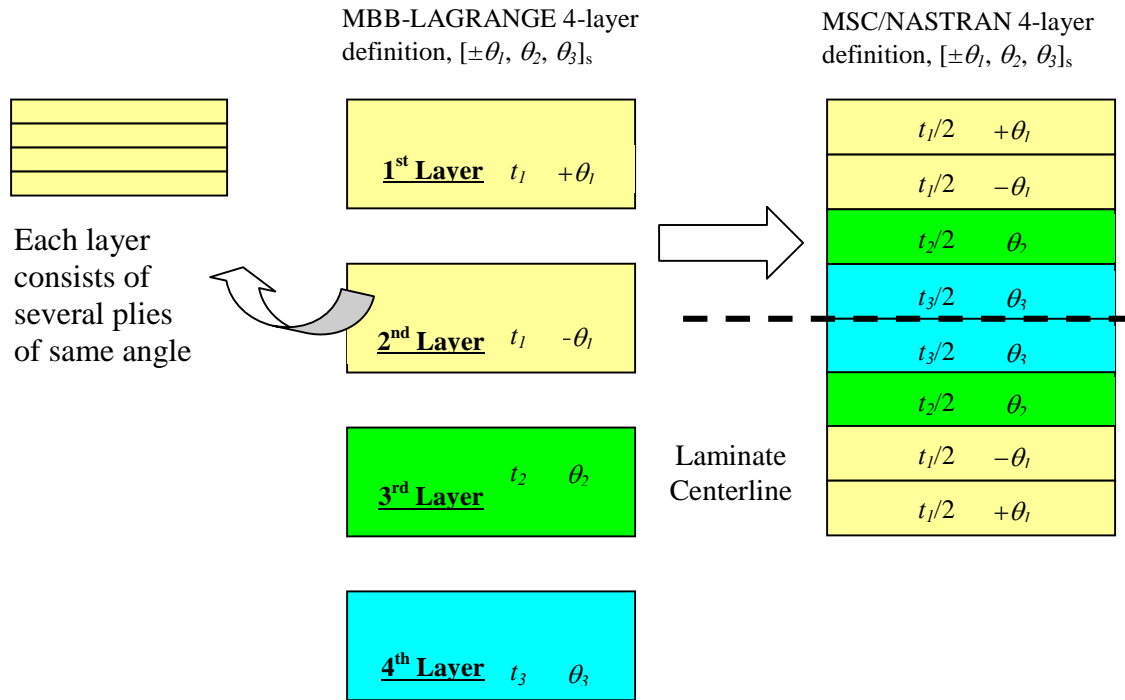


Figure 3.4.5: Schematics of a symmetric laminate, $[\pm\theta_1, \theta_2, \theta_3]_s$

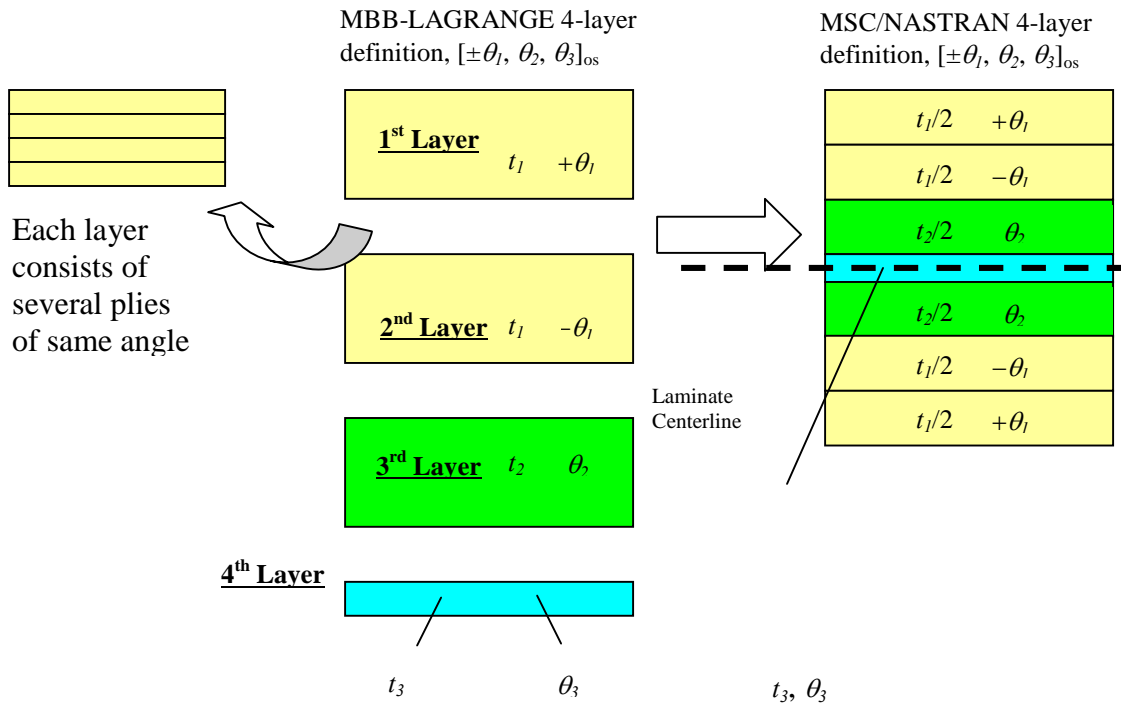


Figure 3.4.6: Schematics of an oblique-symmetric laminate, $[\pm\theta_1, \theta_2, \theta_3]_{os}$.

- MSTN: Longitudinal tensile strain, $\varepsilon_1^{tu} = 8533 \mu\text{in} / \text{in}$
Longitudinal compression strain, $\varepsilon_1^{cu} = 7400 \mu\text{in} / \text{in}$
- CGAGE: For 1st, 2nd, and 3rd layers
Lower layer thickness, $t_l = 0.011 \text{ inch}$ (2 plies)
Upper layer thickness, $t_u = 0.500 \text{ inch}$ (~91 plies)
For 4th layer
Lower layer thickness, $t_l = 0.0055 \text{ inch}$ (1 ply)
Upper layer thickness, $t_u = 0.500 \text{ inch}$ (~91 plies)
- CGANG: Angle threshold of $\pm 45^\circ$ are imposed onto all angle DVs.
- CDIS: Vertical displacement of five inches
- BUCK: Critical buckling loads on the upper skin

The tow steering radius is not considered as a design constraint in this research, although Flory and Bernardon⁸ have examined and proposed that this parameter is one of the active manufacturing constraints.

A sample format of the input file for MBB-LAGRANGE is listed in Appendix B. The termination parameters applied on these models are:

- Relative change in the objective function, $\varepsilon_f = 1.0 \times 10^{-3}$
- Relative change in DV, $\varepsilon_x = 1.0 \times 10^{-3}$
- Termination for Kuhn Tucker Conditions, $\varepsilon_{KTO} = 1.0 \times 10^{-6}$
- Maximum constraint violation, $\varepsilon_{res} = 1.0 \times 10^{-3}$

Also, the ε_G parameter, used for numerical accuracy and stability in the finite difference computation is set to 1.0×10^{-4} .

To compare the results of conventional laminates with FS conceptual designs, four DV configurations have been decided and summarized in Table 3.4.1. Note that all four configurations are composed of symmetric laminates with $[\pm\theta_1, \theta_2, \theta_3]_s$. The baseline configuration is a pure layer thickness optimization design with $[\pm 45, 0, 90]_s$. Layer thicknesses for the first two layers are linked as one DV in order to maintain balanced w.r.t. the principal

material coordinate, as shown in Figure 3.4.7. The Steering I configuration has one angle DV per element or range of elements following VLAMINAT definition; i.e., for $[\pm\theta_1, \theta_2, \theta_3]$ the θ_2° layer is the primary angle DV, with $\pm\theta_1^\circ$ and θ_3° layers linked to the local θ_2° DV at orientations of $\pm 45^\circ$ and 90° respectively:

$$\begin{aligned}\theta_1 &= \theta_2 + 45^\circ \\ -\theta_1 &= \theta_2 - 45^\circ \\ \theta_3 &= \theta_2 + 90^\circ\end{aligned}\tag{3.4.1}$$

Steering I laminate is balanced w.r.t. the local material coordinate, where $\pm\theta_1^\circ$ layers share the same layer thickness. The Steering II configuration has three angle DV per element or range of elements. $\pm\theta_1^\circ$ layers, are linked as one DV each for layer thickness and orientation, respectively. However, Steering II laminate is unbalanced w.r.t. either the local or principal material coordinate. Finally, Steering III configuration takes only one DV by linking $\pm\theta_1^\circ$ layers in $[\pm\theta_1, 0, 90]$. As a result, Steering III is balanced w.r.t. the principal material coordinate.

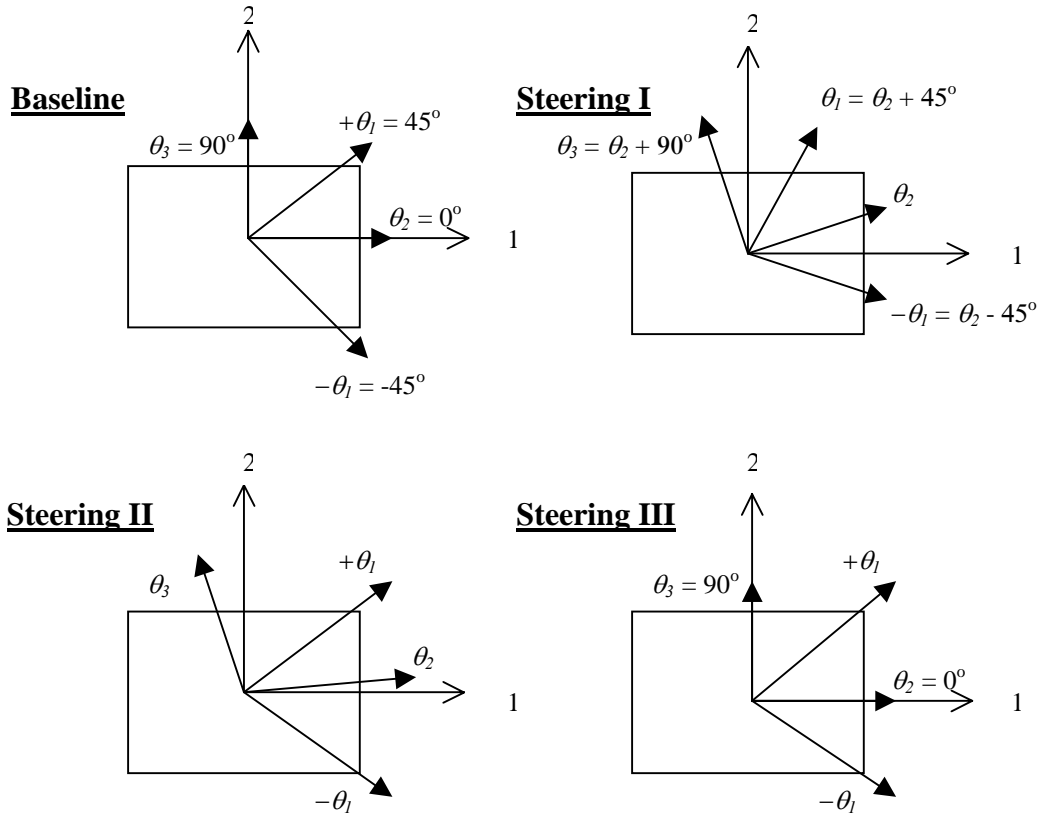


Figure 3.4.7: Schematics of laminate family rosettes for different configurations.

Table 3.4.1 Configurations of test models based on conventional and fiber steering conceptual designs.

Configurations	Conventional Design	Fiber Steering Conceptual Design		
	Baseline	Steering I	Steering II	Steering III
Layer-Thickness Design Variable	<ul style="list-style-type: none"> All layers in $[\pm 45, 0, 90]_s$. $\pm 45^\circ$ layers are linked as ONE design variable. 	<ul style="list-style-type: none"> All layers in $[\pm \theta_l, \theta_2, \theta_3]_s$. $\pm \theta_l^\circ$ layers are linked as ONE design variable. 	<ul style="list-style-type: none"> All layers in $[\pm \theta_l, \theta_2, \theta_3]_s$. $\pm \theta_l^\circ$ layers are linked as ONE design variable. 	<ul style="list-style-type: none"> All layers in $[\pm \theta_l, 0, 90]_s$. $\pm \theta_l^\circ$ layers are linked as ONE design variable.
Layer-Angle Design Variable	<ul style="list-style-type: none"> N/A 	<ul style="list-style-type: none"> Only θ_2° layer or VLAMINAT* θ_3° and $\pm \theta_l^\circ$ layers are tailored with respect to θ_2° layer. 	<ul style="list-style-type: none"> All layer angles in $[\pm \theta_l, \theta_2, \theta_3]_s$. $\pm \theta_l^\circ$ layers are linked as ONE design variable. 	<ul style="list-style-type: none"> Only $\pm \theta_l^\circ$ layers. $\pm \theta_l^\circ$ layers are linked as ONE design variable.
Symmetric Laminate	<ul style="list-style-type: none"> Symmetric laminate 	<ul style="list-style-type: none"> Symmetric laminate 	<ul style="list-style-type: none"> Symmetric laminate 	<ul style="list-style-type: none"> Symmetric laminate
Balanced Laminate	<ul style="list-style-type: none"> Balanced with respect to the principal material coordinate. 	<ul style="list-style-type: none"> Balanced with respect to the local material coordinate Unbalanced with respect to the principal material coordinate. 	<ul style="list-style-type: none"> Unbalanced with respect to either the local or the principal material coordinate. 	<ul style="list-style-type: none"> Balanced with respect to the principal material coordinate.

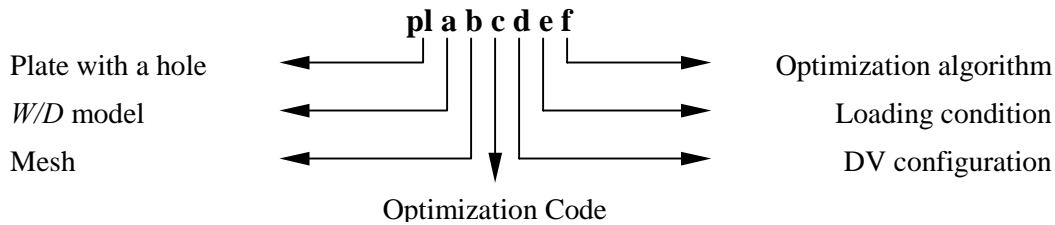
* VLAMINAT: Whole laminate orientation is ONE angle DV; i.e., for $[\pm \theta_l, \theta_2, \theta_3]$ the θ_2° layer is the primary angle DV, with $\pm \theta_l^\circ$ and θ_3° layers linked to the local θ_2° DV at orientations of $\pm 45^\circ$ and 90° respectively.

To study the potential weight savings, comparisons of weight savings are performed for all models between:

- ➔ Baseline and Steering I
- ➔ Baseline and Steering II
- ➔ Baseline and Steering III

3.4.2.1 Square Plate with a Central Circular Hole under Various Loadings.

The plate-with-a-hole models have been categorized based on the plate-width-to-hole-diameter ratio, or $W/D = 5.0, 3.33$, and 2.5 . Figure 3.4.8 defines the nomenclature of these models. Besides looking at the effect of weight savings associated with each configuration, the effect of load paths under different load-cases (bi-axial tensile, uniaxial tensile, and in-plane shear loads) are also studied for $W/D = 5.0$ model. In addition, the sensitivity of fiber steering effect to W/D parameter under bi-axial tensile loads is documented. Figures 3.4.9 and 3.4.10 show the finite element discretizations for $W/D = 5.0, 3.33$ and 2.5 respectively. Due to symmetry in geometry and loadings, only a quarter of the plate is modeled. Each element, a CQUAD4* membrane, carries a layer thickness and angle DV depending on the configuration. The longitudinal axis of the principal material coordinate of these models is the x-axis, where the laminate family rosettes are illustrated in Figure 3.4.11. Attributes of these models can be found in Tables 3.4.2 and 3.4.3. The optimal results for these models will be discussed from Sections 3.4.3.2 to 3.4.3.5.



<u>a</u>	<u>b</u>	<u>c</u>	<u>d</u>	<u>e</u>	<u>f</u>
1: $W/D = 5.0$	6: 132 elements	L: MBB/Lagrang e	0: Baseline	1: Bi-axial tension	3: RQP2
2: $W/D = 3.33$	5: 96 elements		1: Steering I	2: Uniaxial tension	
3: $W/D = 2.5$	4: 84 elements		2: Steering II	3: In-plane shear	
			3: Steering III		

Figure 3.4.8: Nomenclature of square plates with a central circular hole.

* CQUAD4 is an isoparametric membrane-bending or plane strain quadrilateral plate element based on MSC/NASTRAN element libraries.

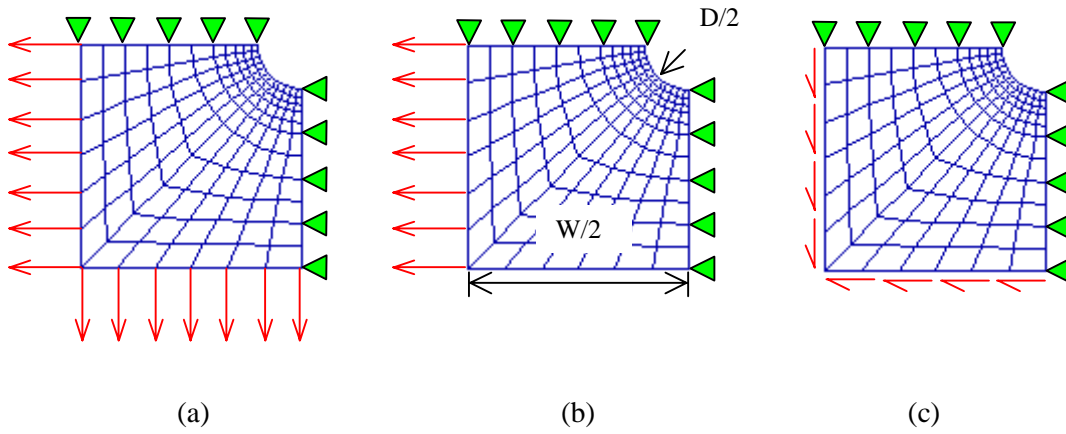


Figure 3.4.9: Finite element discretization of plates with a hole of $W/D = 5.0$ under (a) bi-axial tensile loads, (b) uniaxial tensile loads, (c) in-plane shear loads.

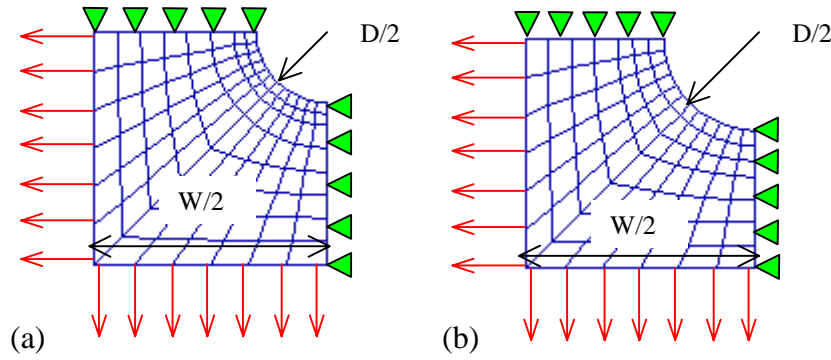


Figure 3.4.10: Finite element discretization of plates with a hole of (a) $W/D = 3.33$, and (b) $W/D = 2.5$ under bi-axial tensile loads.

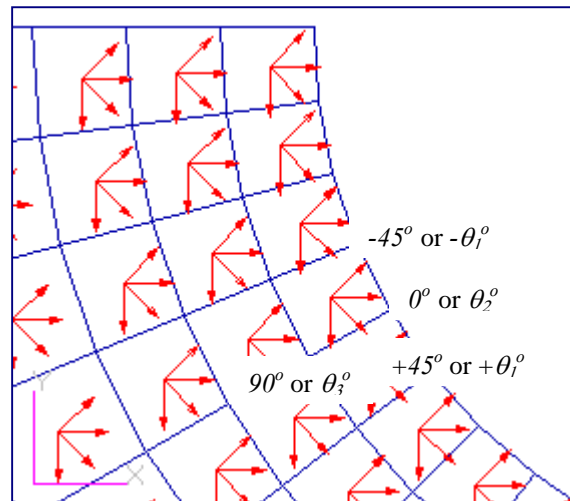


Figure 3.4.11: Schematics of laminate family rosettes for plate model in close-up view.

Table 3.4.2 Finite Element and Design Optimization Attributes for Preliminary Studies.

Attributes	pl16	pl25	pl34	cb1	tb1	ICW1	ICW2
Number of Elements	132	96	84	50	288	158	158
Number of Nodes	156	117	104	66	304	88	88
Number of DOFs	288	216	192	120	864	234	234
Number of Sizing Design Variables	396	288	252	150	864	96	96
Number of Constraints	528	384	336	200	1152	276	290

Table 3.4.3 Lists of Number of Layer-Angle Design Variables for Preliminary Studies in Steering I, II, and III Configurations.

Model	Steering I	Steering II	Steering III
pl16	132	396	132
pl25	96	288	96
pl34	84	252	84
cb1	50	150	50
tb1	288	864	288
ICW1	N/A	96	32

3.4.2.2 Intermediate Complexity Wing (ICW) subjected to Aerodynamic Loads

An intermediate complexity wing (ICW) is modeled based on the geometry and aerodynamic loads (load-case = 1) taken from Ref. 53. The wing is a three-spar torque box with eight bays. Figure 3.4.12 represents the finite element discretization of the wing. It consists of:

- ➔ 2 triangular composite membrane skin elements, CTRIA3^{*}
- ➔ 62 quadrilateral composite membrane skin elements, CQUAD4^{**}

* CTRIA3 defines an isoparametric membrane-bending or plane strain triangular plate element based on MSC/NASTRAN.

** CQUAD4 defines an isoparametric membrane-bending or plane strain quadrilateral plate element based on

- 32 aluminum rib shear panels, CSHEAR[†]
- 23 aluminum spar shear panels, CSHEAR[†]
- 39 aluminum rods, CROD^{††}

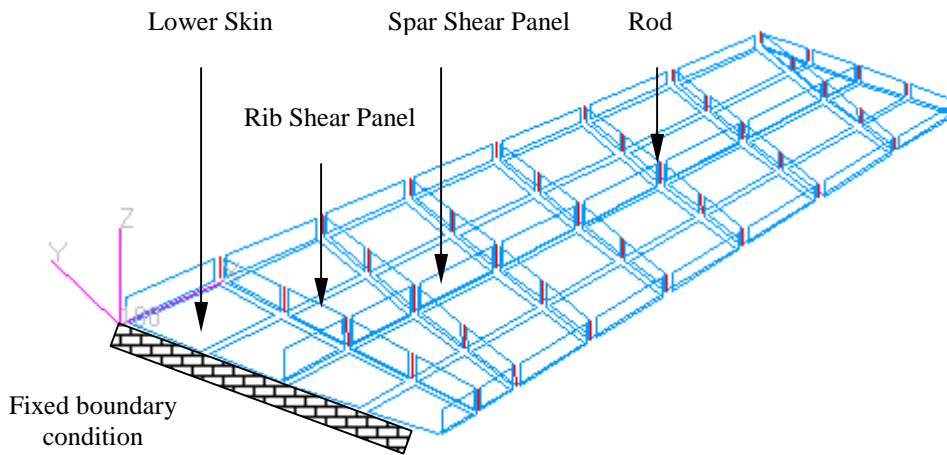


Figure 3.4.12: Schematics of ICW finite element discretization without upper skins.

Only composite membrane skins are the DVs, where the rangewise DV-linking over several elements is shown in Figure 3.4.13. The aluminum substructures (rib and spar shear panels, and rods) are designed via MSC/NASTRAN for a safety factor of 1.5, material properties for which are listed in Appendix A. The longitudinal axis of the principal material coordinate is referred to the mid-spar of the wing, as shown in Figure 3.4.14.

MSC/NASTRAN.

[†] CSHEAR defines a shear panel element based on MSC/NASTRAN.

^{††} CROD defines a tension-compression-torsion element based on MSC/NASTRAN.

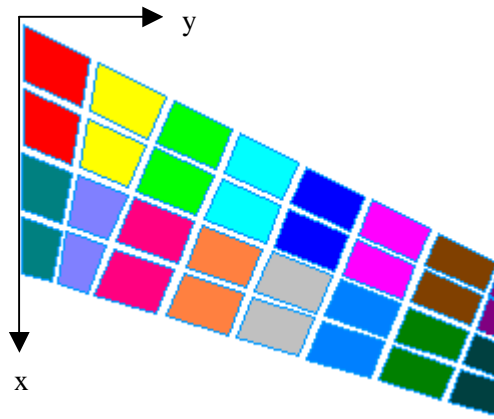


Figure 3.4.13: Rangewise DV-linking definitions for ICW models (same-color elements carry identical material properties).

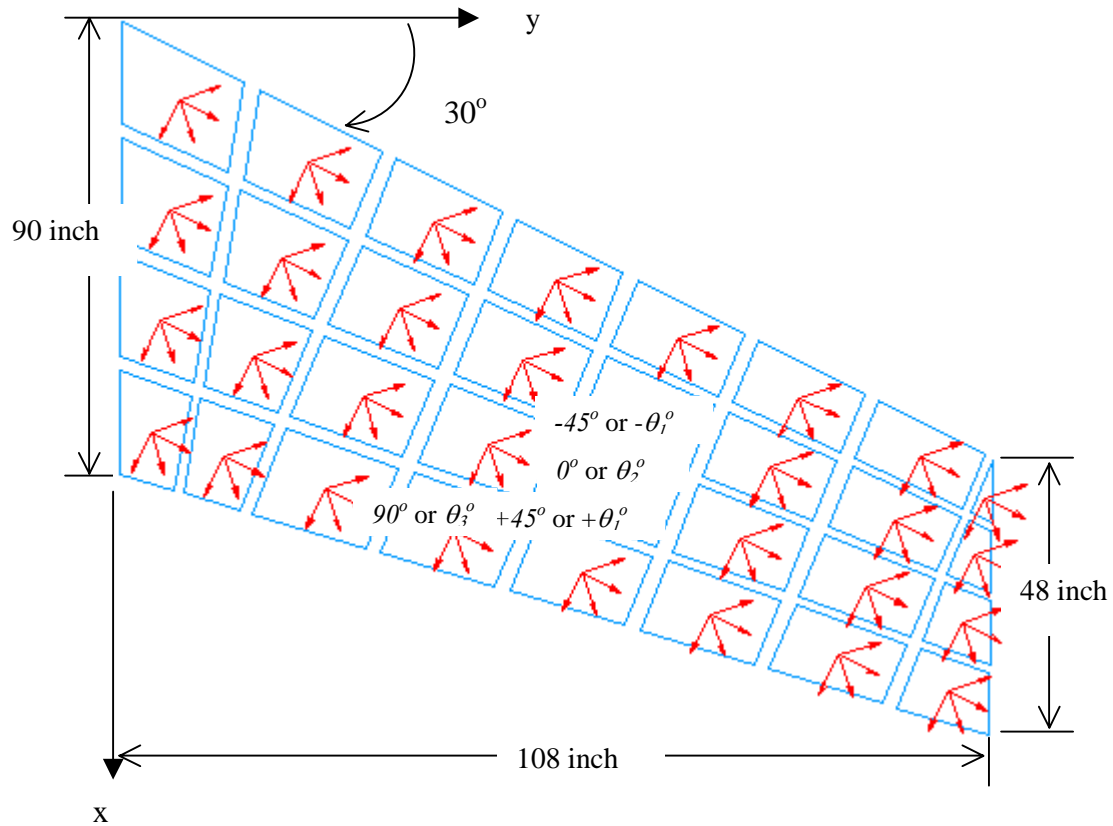


Figure 3.4.14: Schematics of laminate family rosettes for ICW model.

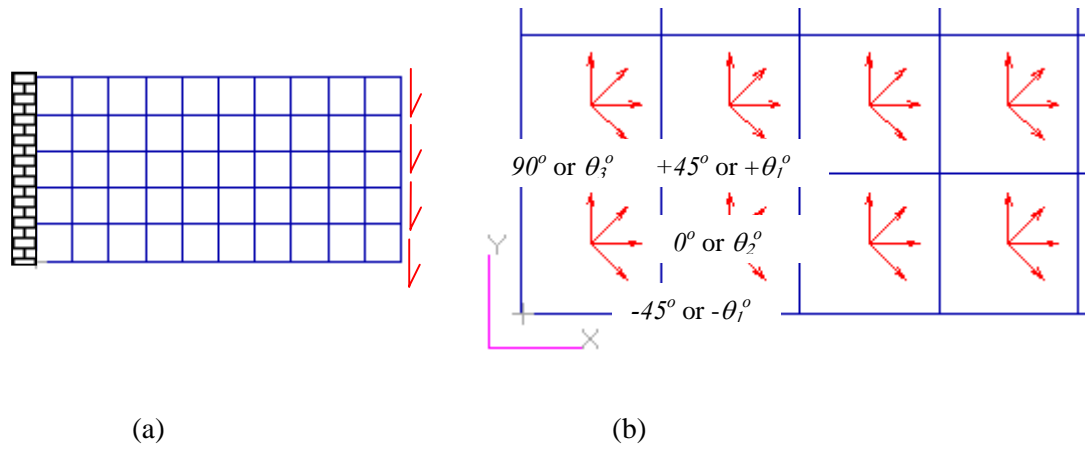
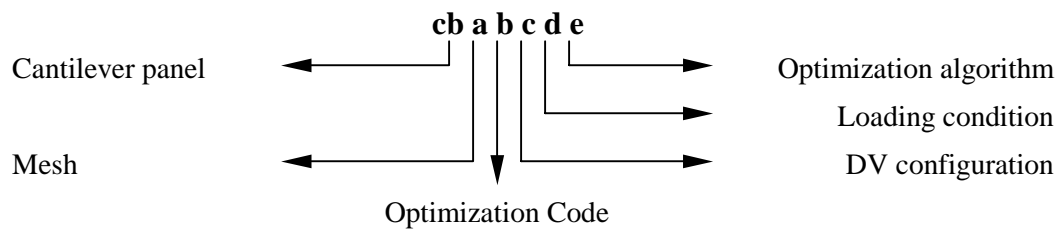


Figure 3.4.16: Schematics of (a) finite element discretization of a cantilever panel under transverse loads and (b) laminate family rosettes in close-up view.



<u>A</u>	<u>b</u>	<u>c</u>	<u>d</u>	<u>e</u>
1: 50 elements	L: MBB/Lagrang e	0: Baseline 1: Steering I 2: Steering II 3: Steering III	1: Transverse loads	3: RQP2

Figure 3.4.17: Nomenclature of a cantilever panel under transverse loads.

3.4.2.4 Cantilever Cylindrical Tube subjected to Combined Loadings

A cantilever circular tube of length-to-diameter ratio, $L/D = 4.5$, subjected to compression, torsion, and bending moments has been studied to determine the potential payoffs based on FS conceptual design. Figure 3.4.18 shows the finite element discretization of the model along with the laminate family rosettes.

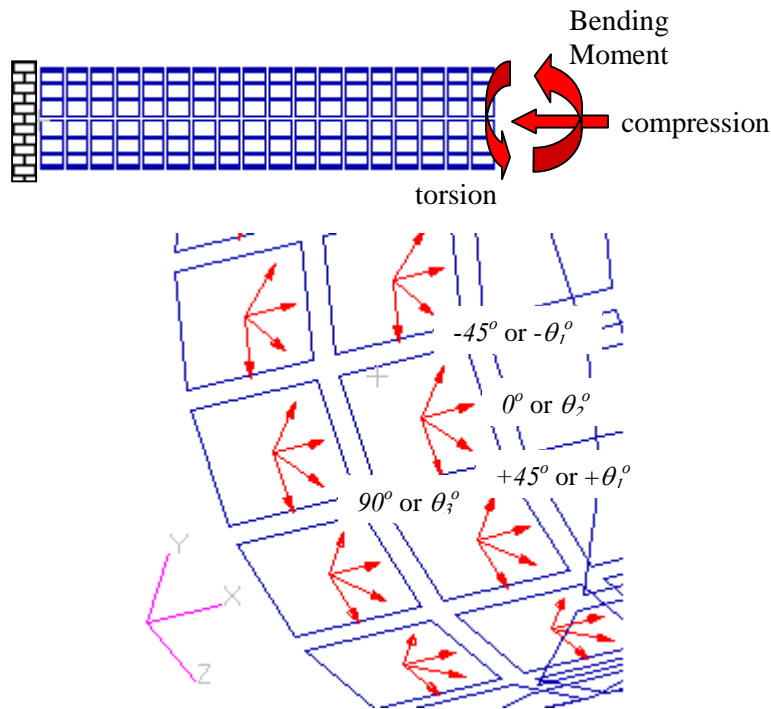


Figure 3.4.18: Schematics of finite element discretization of a cantilever tube under combined loads along with laminate family rosettes in close-up view.

The longitudinal axis of the principal material coordinate is the x-axis and the transverse axis follows the hoop directions. It consists of 288 CQUAD4 membrane elements with each element carrying a layer thickness and angle DV depending on the configuration. The attributes of this model can be found in Tables 3.4.2 and 3.4.3. The model's nomenclature is depicted in Figure 3.4.19. Layer-thickness contour and layer-angle mapping plots are presented in Appendix C.4.

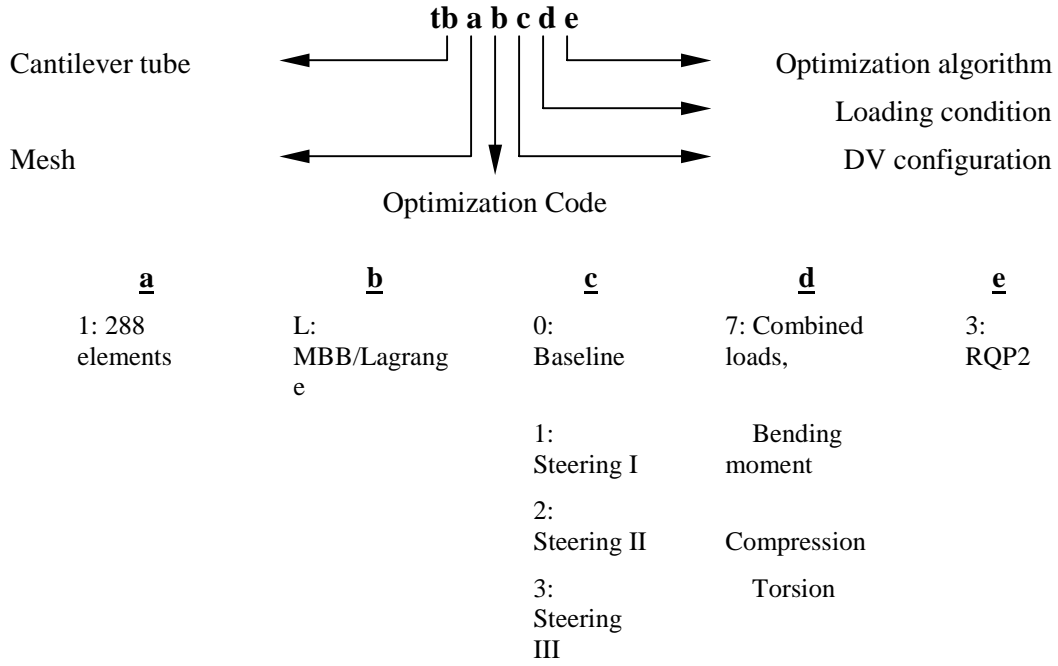


Figure 3.4.19: Nomenclature of a cantilever cylindrical tube under combined loads.

3.4.3 Results and Discussion of Preliminary Studies

Four test models have been studied to determine the potential payoffs of laminates using FS conceptual design. The optimal designs of each model are presented in the following paragraphs and Appendix C as layer-thickness contours and layer-angle mappings. In layer-thickness contours, there are four contour plots:

- ➔ Total layer thickness in inches, t_{all} , at page top left, denoted as (a)
- ➔ 1st and 2nd layer thickness in percentage, $2t_1$, at page top right, denoted as (b)
- ➔ 3rd-layer thickness in percentage, t_2 , at page bottom left, denoted as (c)
- ➔ 4th-layer thickness in percentage, t_3 , at page bottom right, denoted as (d)

On the other hand, four layer-angle mappings are presented respectively as:

- ➔ Curvilinear fiber format of $+\theta_l^\circ$ layer at page top left, denoted as (a)[†]
- ➔ Curvilinear fiber format of $-\theta_l^\circ$ layer at page top right, denoted as (b)^{††}

[†] For plate-with-a hole models in Steering III configuration, this layer is denoted as (e)

- Curvilinear fiber format of θ_2° layer at page bottom left, denoted as (c)
- Curvilinear fiber format of θ_3° layer at page bottom right, denoted as (d)

3.4.3.1 Weight savings of Laminates Exhibiting Steered-Fiber Architecture.

Table 3.4.4 summarizes the weight savings for preliminary studies using FS conceptual design. The greatest weight reduction is seen with Steering II configuration for up to 27% in the static case and 6% in the buckling case. With more layer-angle DVs per element or range compared with Steering I and II, weight savings for this configuration is obviously greater. However, further verifications and sound decisions must be made because of the unbalanced nature of Steering II configuration. Depending on the model description, weight reduction corresponding to Steering III (up to 26%) is potentially greater than that of Steering I (up to 20%). Note that Steering III yields balanced results w.r.t. the primary material coordinate; whereas, the resultant laminates based on Steering I are balanced w.r.t. the local material coordinate. A discrepancy of weight savings occurred in ICW2 model for Steering III configuration during buckling analysis. This is probably due to the limitations of buckling formulations in MBB-LAGRANGE environment. Further investigations should be made by incorporating an improved buckling formulation.

3.4.3.2 Square Plate with a Hole, $W/D = 5.0$, under Biaxial Tensile Loads.

To help explaining the results of FS conceptual design, several locations of the plate-with-a-hole models ($W/D = 5.0$, 3.33, and 2.5) are labeled, as shown in Figure 3.4.20. Weight savings w.r.t. DV configurations for $W/D = 5.0$ plate are listed in Table 3.4.4. A greater weight reduction is seen with Steering II, followed by Steering III and Steering I.

^{††} For plate-with-a hole models in Steering III configuration, this layer is denoted as (f)

Table 3.4.4: Summary of structural weight savings for preliminary studies using FS conceptual design.

Model	Weight saving [%]		
	Steering I	Steering II	Steering III
Plate with a hole, pl16, load case 1	0.1	5.3	1.6
Plate with a hole, pl16, load case 2	2.2	17.8	16.3
Plate with a hole, pl16, load case 3	3.3	19.7	3.8
Plate with a hole, pl25, load case 1	8.2	9.7	0.4
Plate with a hole, pl34, load case 1	4.4	6.4	0.3
Cantilever rectangular panel, cb1	9.7	17.4	3.2
Cantilever cylindrical tube, tb1	20.4	26.7	25.7
Intermediate Complexity Wing, ICW1	N/A	21.0	6.7
Intermediate Complexity Wing, ICW2	N/A	6.6 [†]	-1.3 [†]
Maximum weight savings [%], static	20.4	26.7	25.7
Maximum weight savings [%], buckling	N/A	6.6 [†]	-1.3 [†]

[†] MBB-LAGRANGE returns 3 warning messages:

1. B-FIELD INTERNAL ANGLE IS TOO LARGE OR TOO SMALL
2. MATERIAL AXES NOT PARALLEL TO B-FIELD SUPPORT
3. BUCKLING FORMULA NOT VALID FOR THIS CASE

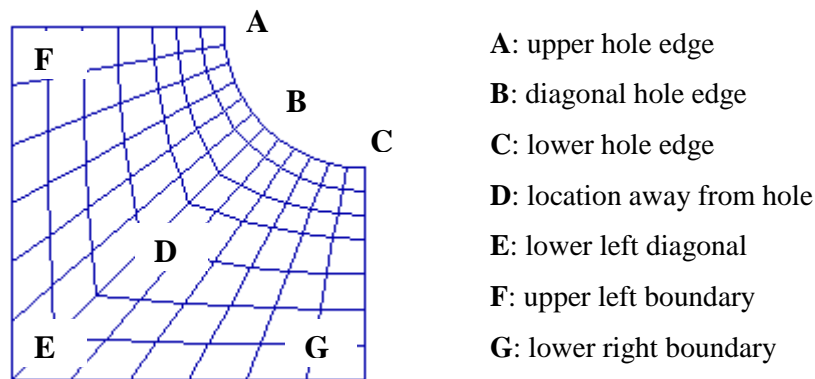
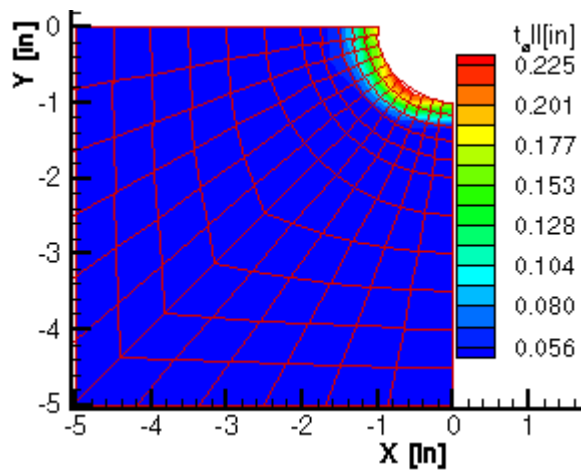


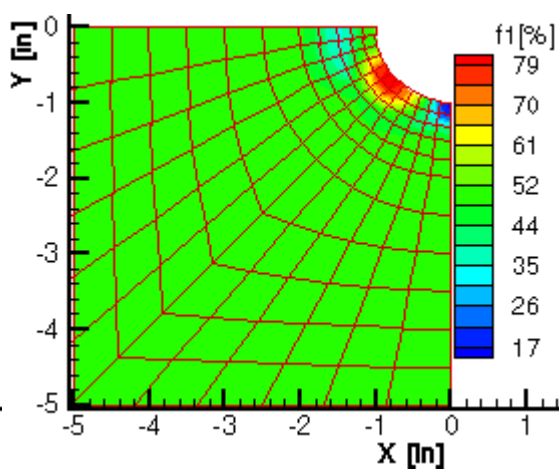
Figure 3.4.20: Specific location labeling for the plate-with-a-hole models.

Layer-thickness contours of the conventional design or baseline (pl16L013) are shown in Figure 3.4.21. The plate is thicker around the hole vicinity, especially at **B**. At this location, $\pm 45^\circ$ layers (Figure 3.4.21(b)) contribute greatly to the plate thickness to take in-plane shear loads. The laminate family is approximately (10/80/10). Both 0° and 90° layer thicknesses are dominant at **C** and **A** due to biaxial tensile loads, with laminate families of about (70/15/15) and (10/40/50), in Figures 3.4.21(c) and 3.4.21(d) respectively. Away from the hole (**D** to **G**), the laminate family becomes a conventional quasi-isotropic laminate, or (25/50/25) family as expected.

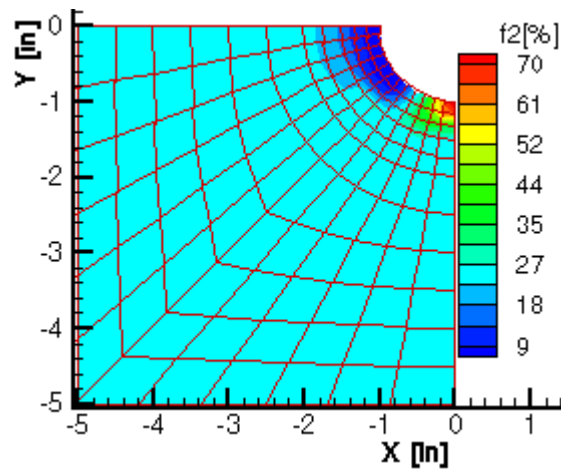
Figures 3.4.22 and 3.4.23 represent optimal laminates of the plate model based on Steering I configuration or pl16L113. Similar to the baseline, the plate is thicker around the hole vicinity as depicted in Figure 3.4.22(a). The plate thickness at **A** is largely configured with $\pm \theta_1^\circ$ layers (Figure 3.4.22(b)); whereas, the θ_2° layer fills up the lower hole edge or **C** (Figure 3.4.22(c)). The laminate families at these locations are approximately (10/70/20) and (50/30/20), respectively. By examining the curvilinear fiber format in Figure 3.4.23, fibers are directed following the cutout geometry to effectively transfer the shear stress and reduce stress concentration around the vicinity of the plate cutout. This is clearly illustrated in the θ_2° layer at **C** (Figure 3.4.23(c)), which are the primary DVs in Steering I configuration. Initially composed of 0° orientation, θ_2° layer-angle vectors are shifted down the hole curvature to align with the primary load path (shear to axial loads). At **A**, θ_2° layer is not dominant because of the $\pm 45^\circ$ threshold (CGANG). As a result, the $+\theta_1^\circ$ layer (initially $+45^\circ$) becomes significant in Figures 3.4.23(a) and 3.4.23(b). Noticeably at **A**, the fiber vectors are steered to closely follow the primary load path. As for $-\theta_1^\circ$ layer, fiber directions gradually spread themselves out from **E** to **B**. Essentially with Steering I configuration, the $-\theta_1^\circ$ layer behaves as a -45° layer w.r.t. θ_2° layer at **B-C** curve and 90° layer w.r.t. $+\theta_1^\circ$ layer at **A-B** curve. Note that a portion of the plate thickness around **A** is contributed by θ_3° layer in Figure 3.4.22(d), where the laminate family is about (20/30/50). Referring to Figure 3.4.23(d), fiber vectors of θ_3° layer are steered to take transverse tensile loads at this location. By combining these layer-angle mappings in one plot, fiber orientations resemble a curvilinear laminate family that is balanced w.r.t. the local material coordinate. Away from the hole (**D** to **G**), the laminate family becomes a conventional quasi-isotropic laminate, or (25/50/25) family, again as expected.



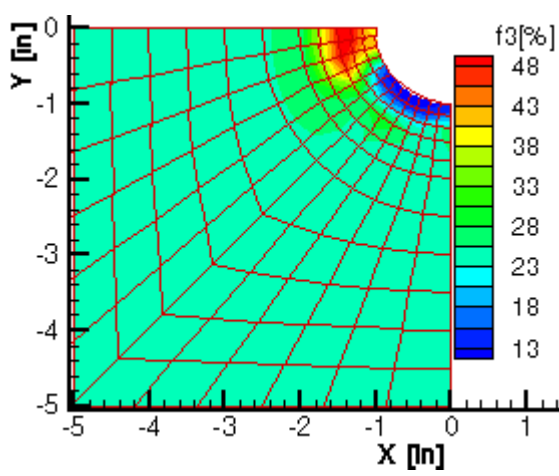
(a)



(b)



(c)



(d)

Figure 3.4.21: Layer-thickness contours for pl16L013.

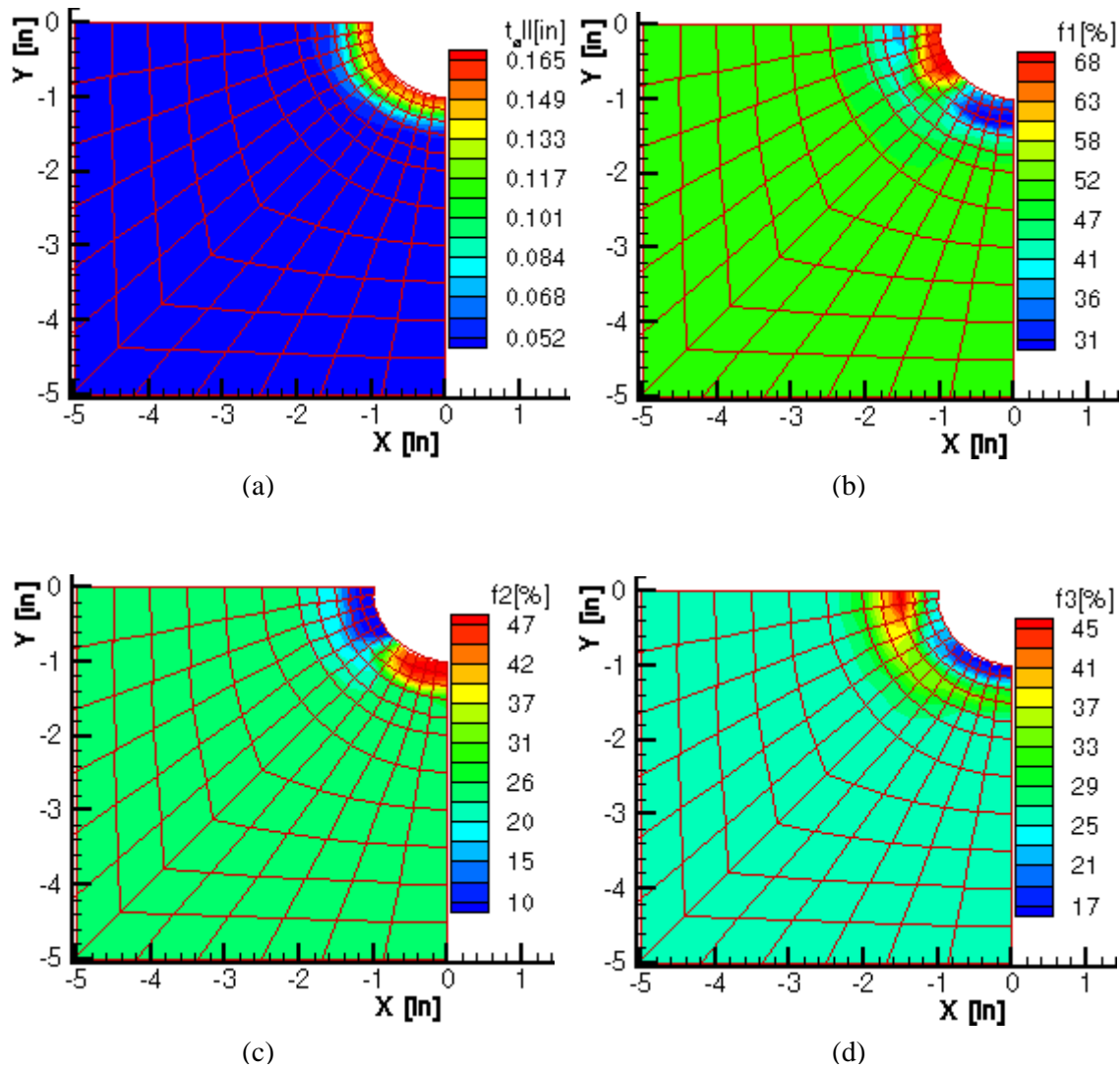
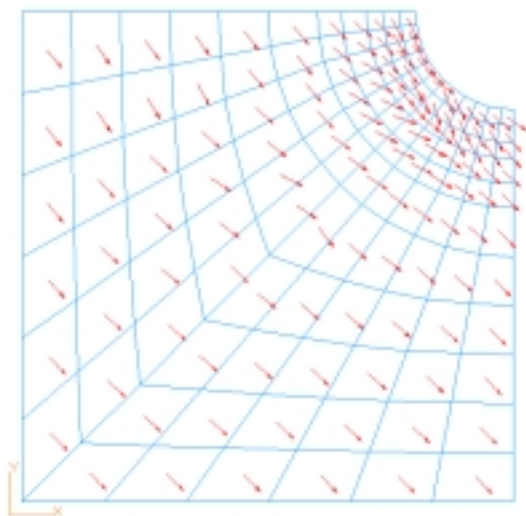
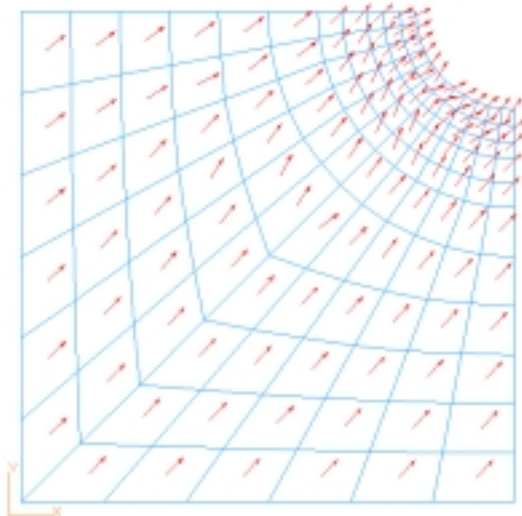


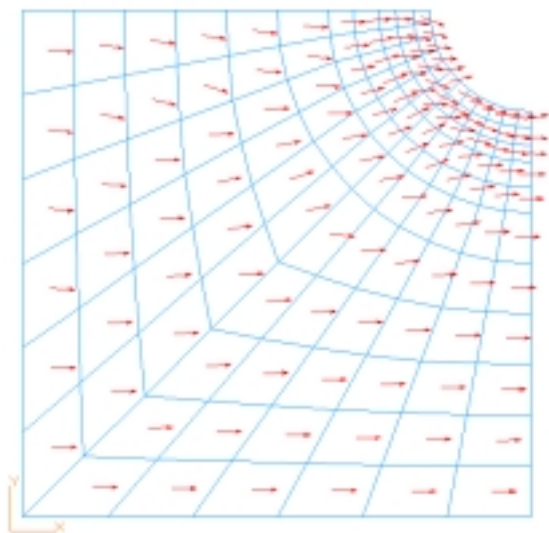
Figure 3.4.22: Layer-thickness contours for p116L113.



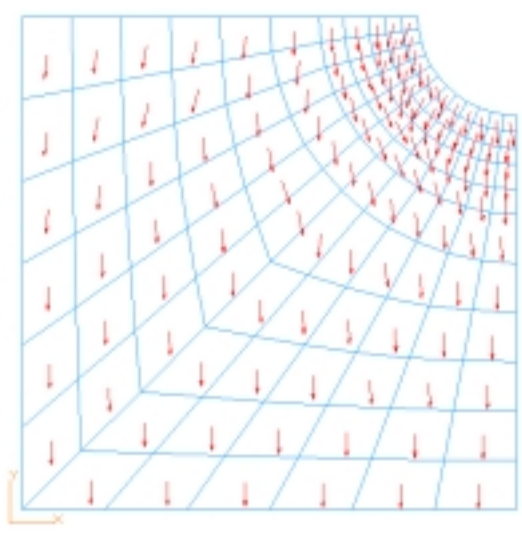
(a)



(b)



(c)



(d)

Figure 3.4.23: Layer-angle mappings for pl16L113.

Figures 3.4.24 and 3.4.25 show optimal laminates of the plate model based on Steering II configuration (pl16L213), where there are three layer-thickness and layer-angle DVs per finite element, respectively. The plate is thicker at the lower hole edge or **C**, as depicted in Figure 3.4.24(a) with (50/25/25) family. It is largely contributed by θ_2° layer, where the fibers are steered to follow the hole curvature and the axial tensile load path (see Figure 3.4.25(c)). At **A**, $\pm\theta_1^\circ$ and θ_3° layers play a major role, depicted with (20/40/40) family. In Figure 3.4.25(d), layer-angle mappings of θ_3° layer are directed to follow the transverse tensile load path. On the other hand, the $\pm\theta_1^\circ$ layers take up the shear loads from **A** to **C**. The $+\theta_1^\circ$ layer-angle forms a radial curvilinear fiber format to track the shear loads and hole geometry (Figure 3.4.25(a)); whereas, the $-\theta_1^\circ$ layer directions gradually spread out at **B** (Figure 3.4.25(b)). Away from the hole (**D** to **G**), the laminate family becomes a quasi-isotropic laminate. In fact at these locations, the laminate becomes a conventional $[\pm 45, 0, 90]_s$ design.

Figure 3.4.26 consists of the optimal layer-thickness and layer-angle mappings for pl16L313 with Steering III configuration. In Figure C6(a), the layer-thickness is concentrated at **B** with (15/65/20) family, which is largely contributed by $\pm\theta_1^\circ$ layers. $\pm\theta_1^\circ$ layer orientations are steered to overcome the shear load. At **C**, θ_2° layer is dominant due to the axial tensile load (Figure 3.4.26(c)). Here, the laminate family is approximately (55/25/20). Due to the transverse tensile load, $\pm\theta_1^\circ$ and a portion of θ_3° layer thicknesses are prominent at **A**. Referring to Figures 3.4.26(e) and 3.4.26(f), the $\pm\theta_1^\circ$ layer orientations are steered to become θ_3° along the hole vicinity at **A**. Similar to Steering I and II, the plate becomes a conventional quasi-isotropic laminate away from the hole (**D** to **G**).

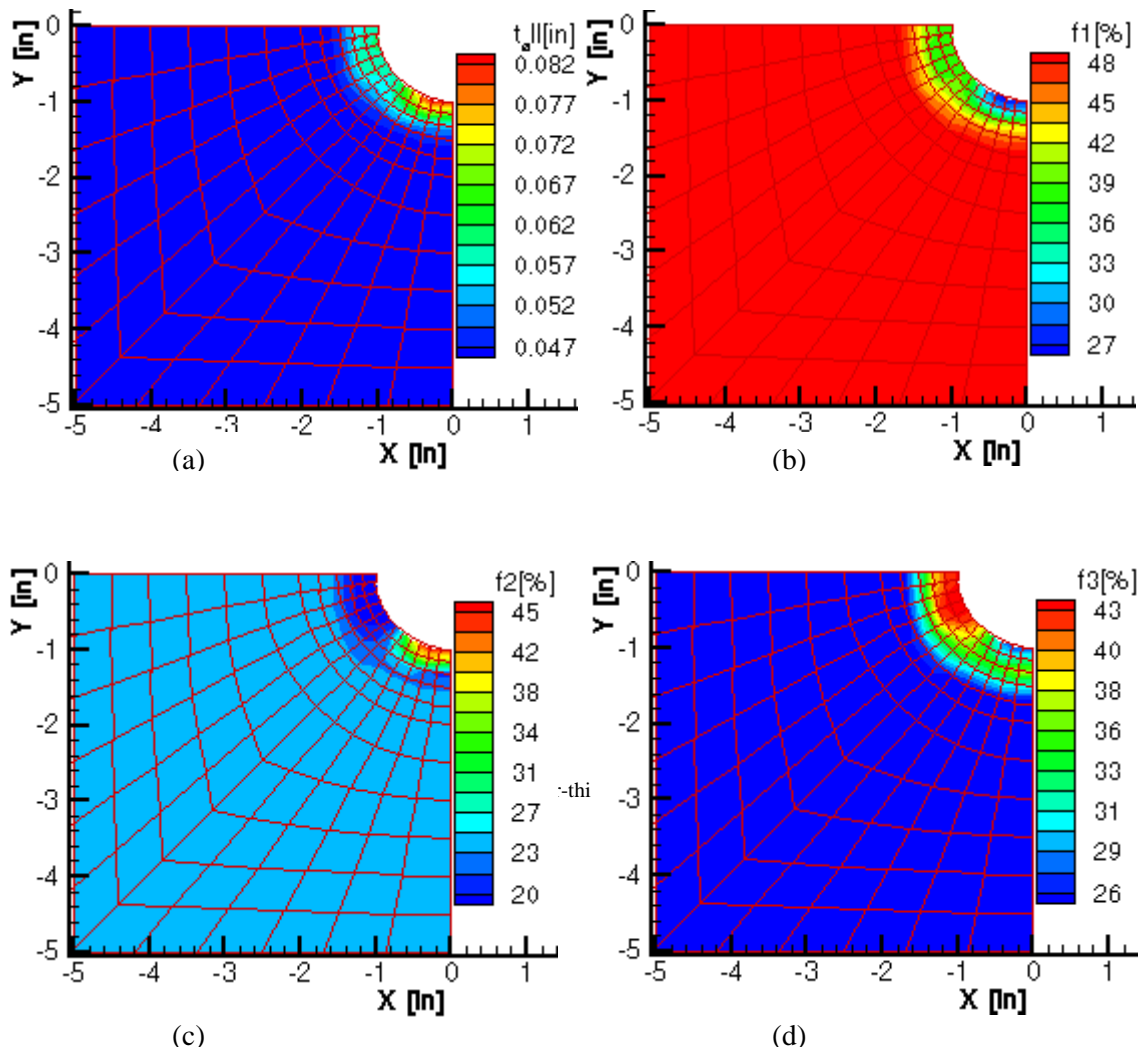


Figure 3.4.24 Layer Thickness Contours for p116L213.

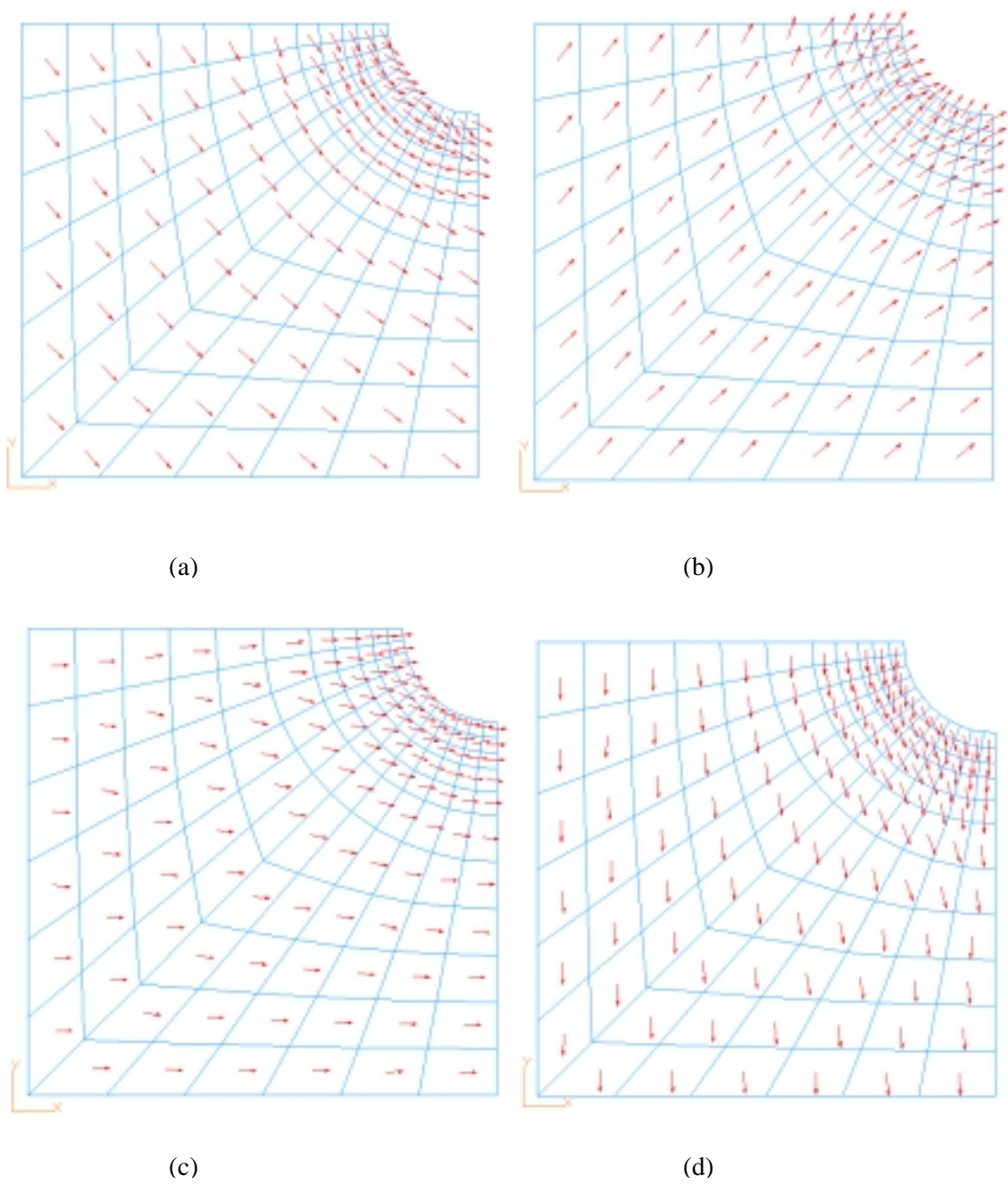


Figure 3.4.25: Layer-angle mappings for pl16L213.

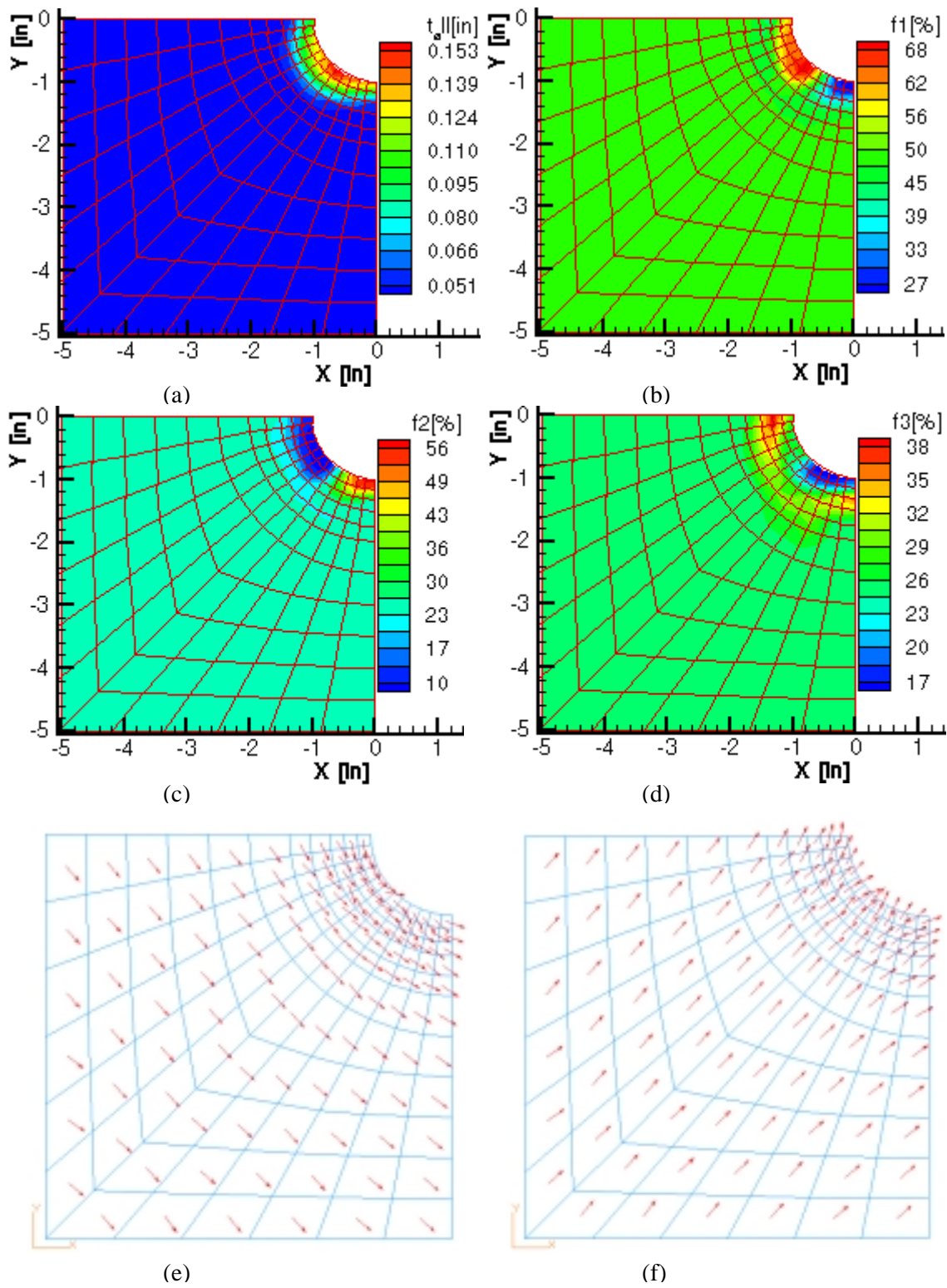


Figure 3.4.26: Layer-thickness contours and layer-angle mappings for pl16L313.

3.4.3.3 Square Plate with a Hole, $W/D = 5.0$, under Uniaxial Tensile Loads.

Weight savings of this model w.r.t. DV configurations are listed in Table 3.4.4. A greater weight reduction is seen with Steering II, followed by Steering III and Steering I. The baseline configuration (pl16L023) is presented in Figure 3.4.27. Based on Figure 3.4.27(a), the plate has more material at the lower hole edge or **C**. Due to the axial tensile loads, the 0° layer is significant at this location with (80/10/10) family. From **B** to **A**, the 0° layer thickness gradually decreases with increasing $\pm 45^\circ$ and 90° layers due to Poisson's effect. The laminate family at **A** is about (20/40/40). Around **A** vicinity, $\pm 45^\circ$ layers become dominant as the plate sees in-plane shear loads. The plate at this location behaves like a (30/45/25) laminate family. Away from the central cutout or **D**, the plate is a (60/28/12) laminate family. This is largely attributed to the uniaxial tensile loads.

Figures 3.4.28 and 3.4.29 show the optimal results based on Steering I configuration (pl16L123). Similar to the baseline, the plate is thicker at the lower hole edge or **C**. Due to the uniaxial tensile loads, the θ_2° layer (Figure 3.4.28(c)) is noticeable at this location with (80/10/10) family. Note in Figure 3.4.29(c), layer orientations are directed to follow the primary load path (shear to axial loads) from **B** to **C**. From **B** to **A**, more material are made up of $\pm \theta_1^\circ$ and a portion of θ_3° with (25/45/30) family. At **A**, θ_2° layer is not dominant because of the $\pm 45^\circ$ threshold (CGANG). As illustrated in Figures 3.4.29(a) and 3.4.29(d), both $+\theta_1^\circ$ and θ_3° layer orientations are steered down the hole curvature due to Poisson's effect. As for $-\theta_1^\circ$ layer (Figure 3.4.29(b)), fiber directions gradually spread themselves out from **E** to **B**. Interestingly at **G**, the plate is composed of (30/45/25) family. This is probably due to Poisson's effect. As a whole, the plate behaves as a (60/30/10) laminate family at plate boundaries (**E**, **F**) and **D** because of the uniaxial tensile loads.

Figures 3.4.30 and 3.4.31 are the optimal results based on Steering II configuration (pl16L223). Noticeably in Figure 3.4.30(a), the plate has a similar total layer-thickness contour as baseline (Figure 3.4.27(a)) and Steering I (Figure 3.4.28(a)) configurations, where more reinforcement are located at **C**. However, the curvilinear fiber formats are very different. When allowing every layer to vary angles from element to element, the fiber vectors tend to be aligned parallel to the axial load path beyond the hole vicinity. This is seen in Figures 3.4.31(a), 3.4.31(b), and 3.4.31(c) for $+\theta_1^\circ$, $-\theta_1^\circ$, and θ_2° layers, respectively. Whereas, the θ_2° layer (initially 90°) becomes almost orthogonal to these layers as illustrated in Figure 3.4.31(d), due to CGANG $\pm 45^\circ$ threshold. From **D** to **G**, the plate behaves generally as a (50/35/15) family. In terms of conventional laminate notation, the laminate at these locations is composed of (85/0/15). At **A**, $\pm \theta_1^\circ$ and θ_3° layers are dominant due to Poisson's effect, where layer angles are steered w.r.t. the hole curvature. From **B** to **C**, the laminate is made up of (60/30/10) family. Layer orientations of $\pm \theta_1^\circ$ and θ_2° layers are gradually becoming longitudinal reinforcement. This is necessary because the primary load trajectories at **B-C** curve vary from shear to axial tensile loads.

Finally, the optimal results based on Steering III configuration (pl16L323) are shown in Figure 3.4.32. A similar trend of fiber reinforcement is predicted, where more longitudinal-reinforcement material are gathered at the lower hole edge or **C** with (60/30/10) family in Figure

3.4.32(a). Indeed, $\pm\theta_l^\circ$ layer angles are tailored from initially $\pm45^\circ$ to almost 0° direction (Figures 3.4.32(e) and 3.4.32(f)) due to the uniaxial tensile load. From **A** to **B**, $\pm\theta_l^\circ$ layer angles follow the primary load trajectories (shear load) around the hole vicinity due to Poisson's effect. At **A**, the plate behaves as a (20/40/40) family. At plate boundaries and **D**, the plate is composed of 0° and 90° layers. Based on the conventional laminate family notation, the plate at these locations consists of (85/0/15), which is similar to Steering II configuration.

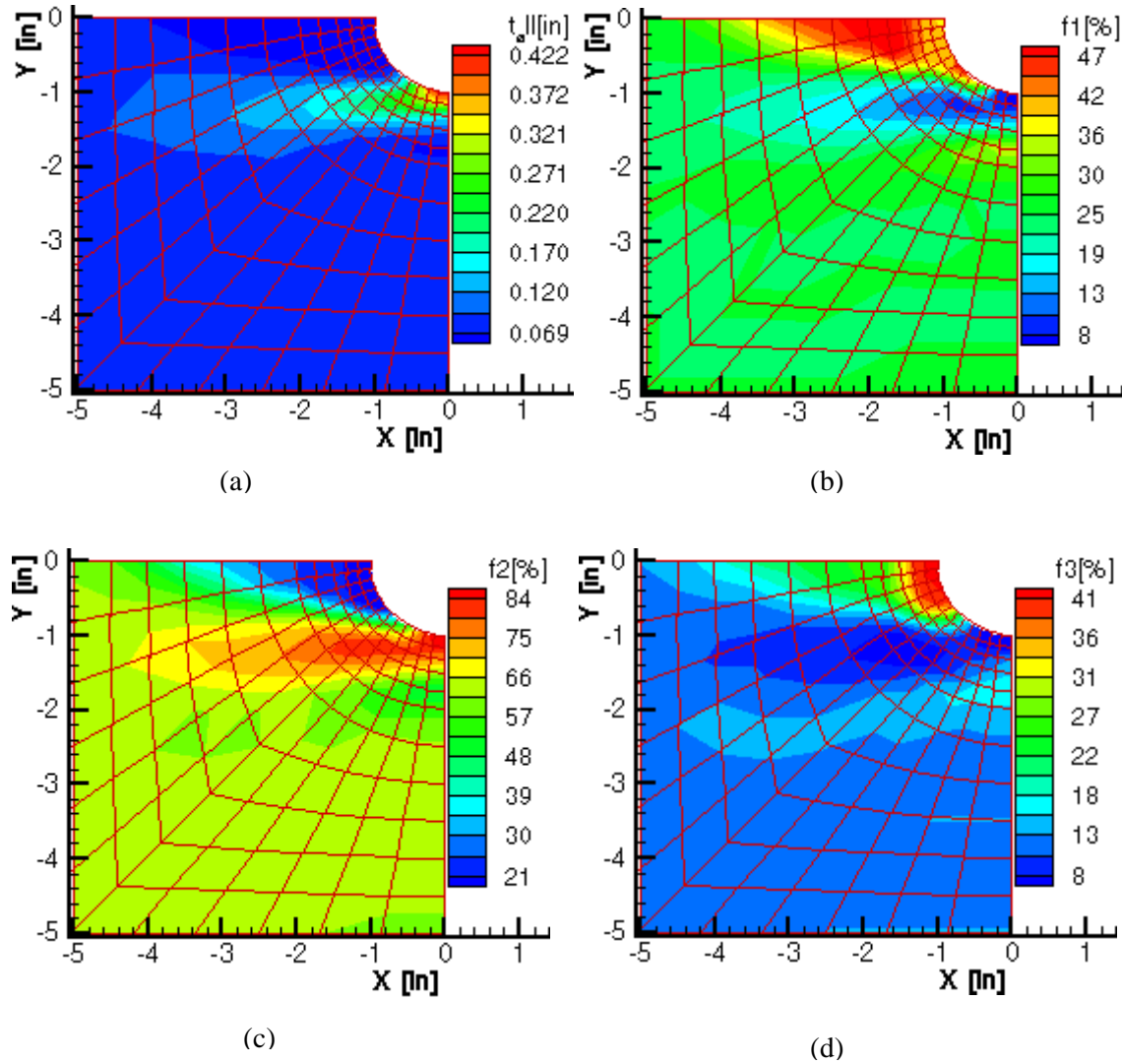


Figure 3.4.27: Layer-thickness contours for pl16L023.

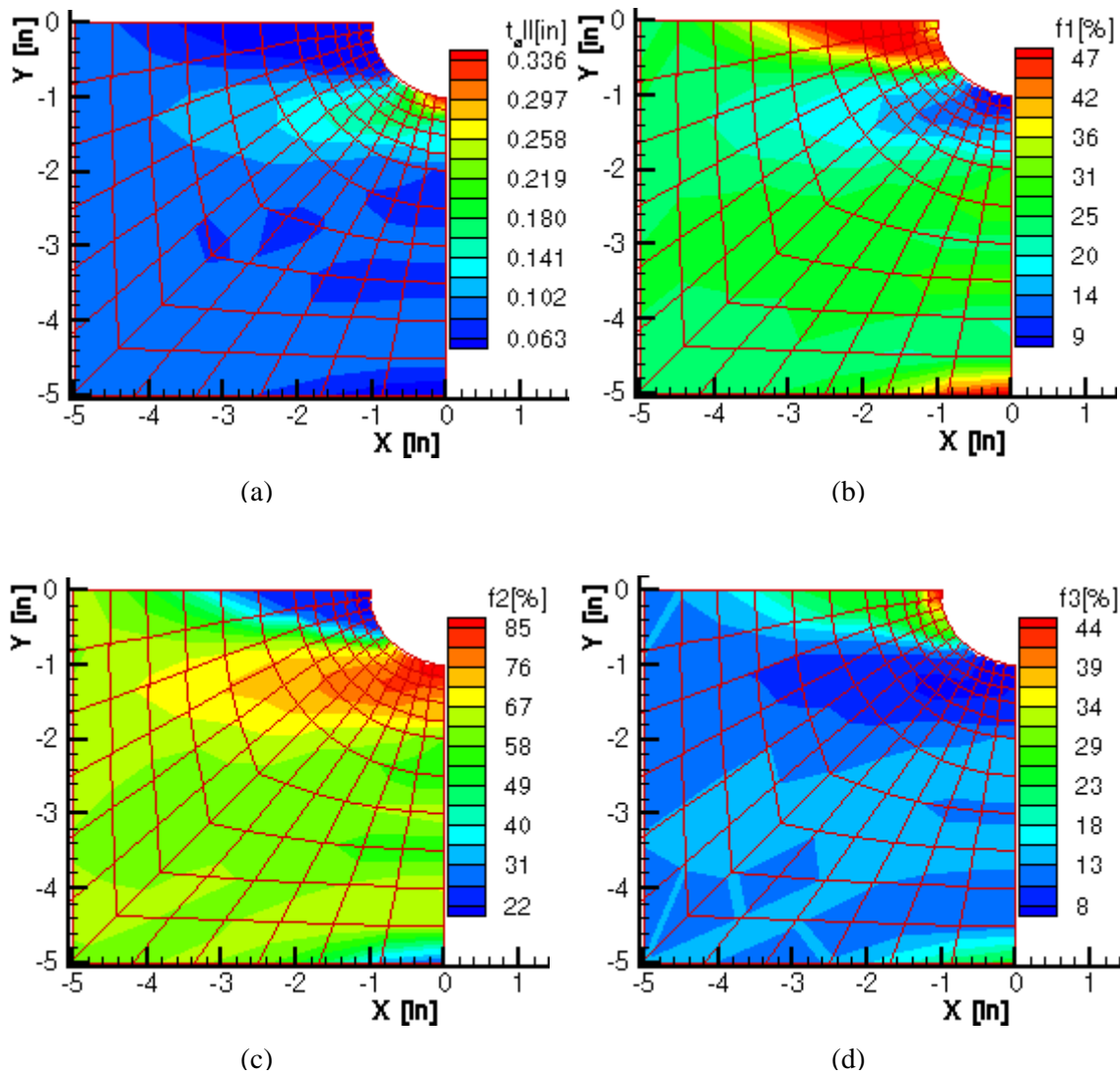
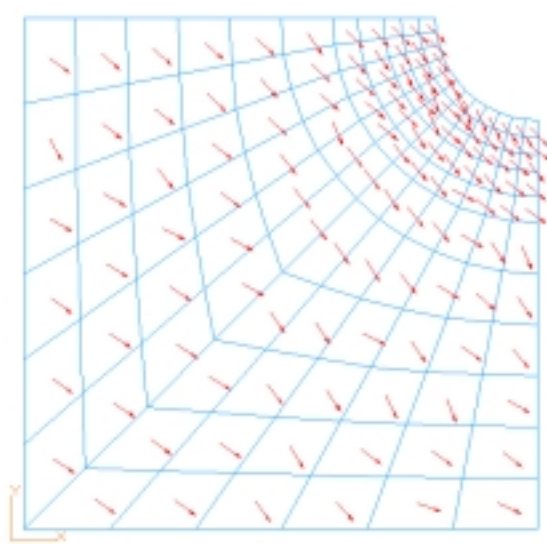
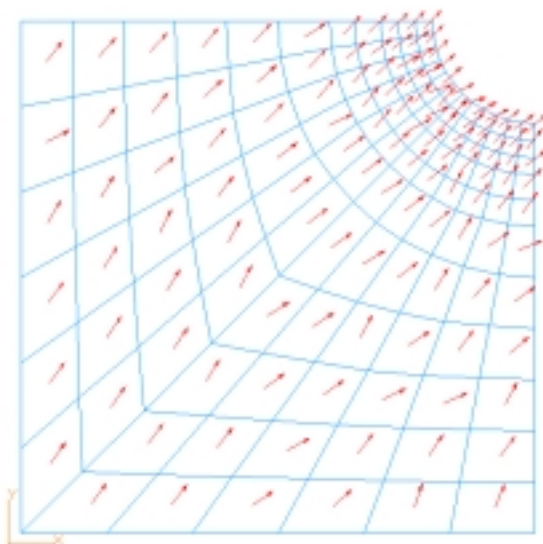


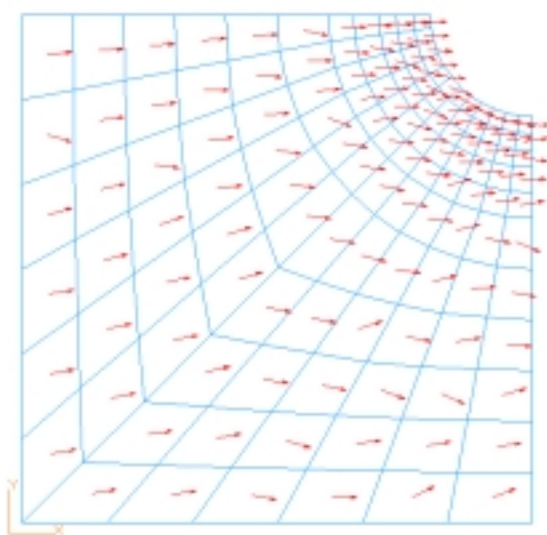
Figure 3.4.28: Layer-thickness contours for pl16L123.



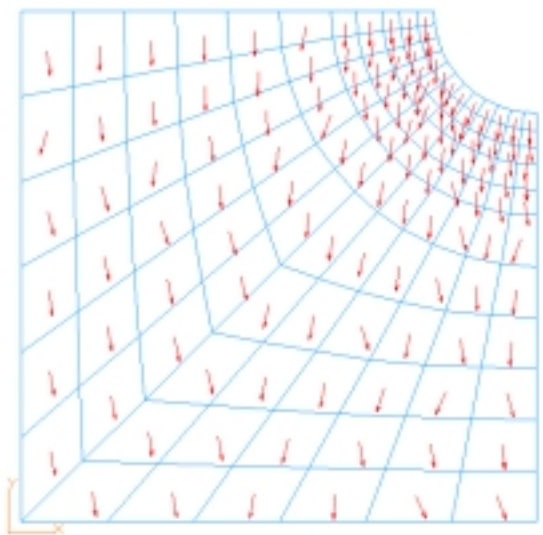
(a)



(b)



(c)



(d)

Figure 3.4.29: Layer-angle mappings for pl16L123.

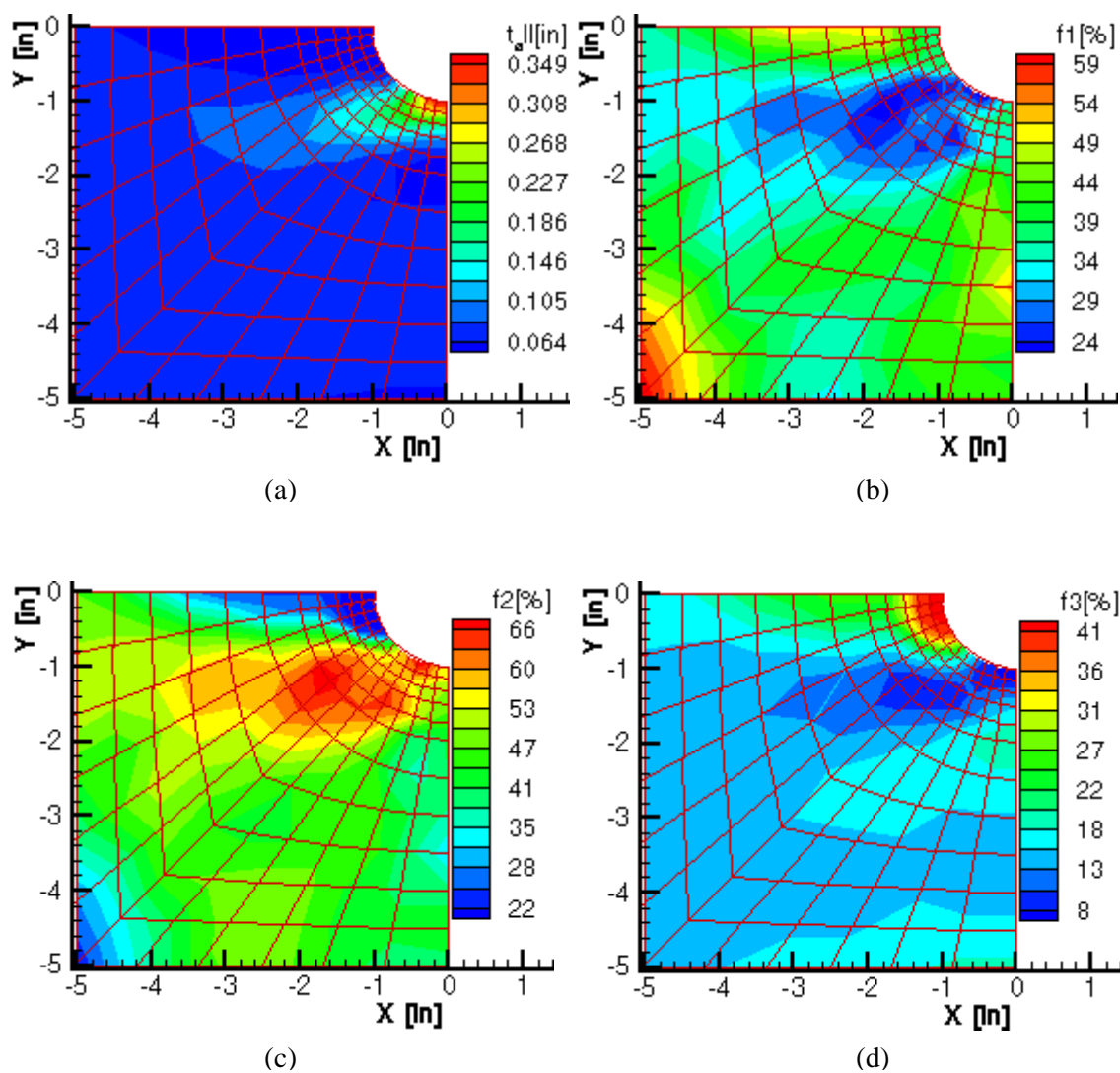
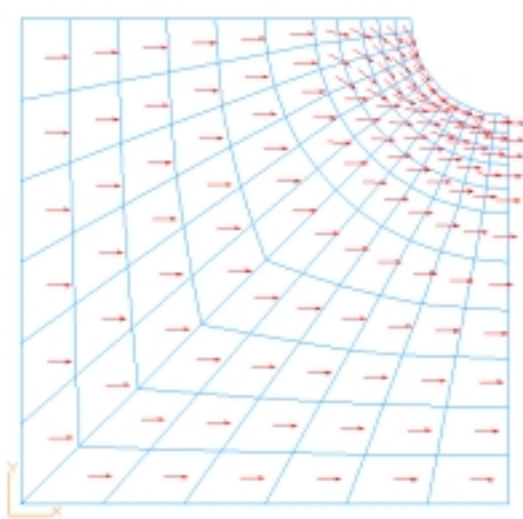
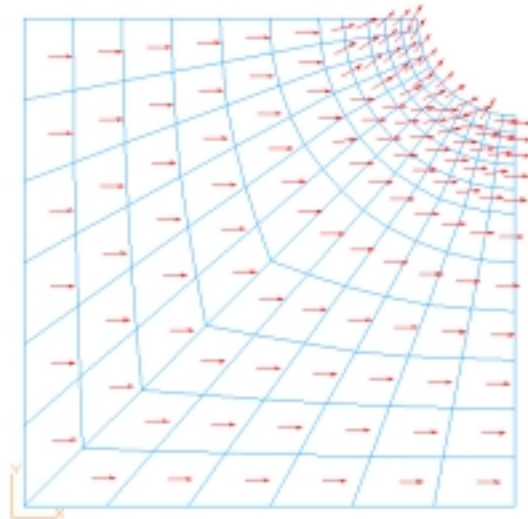


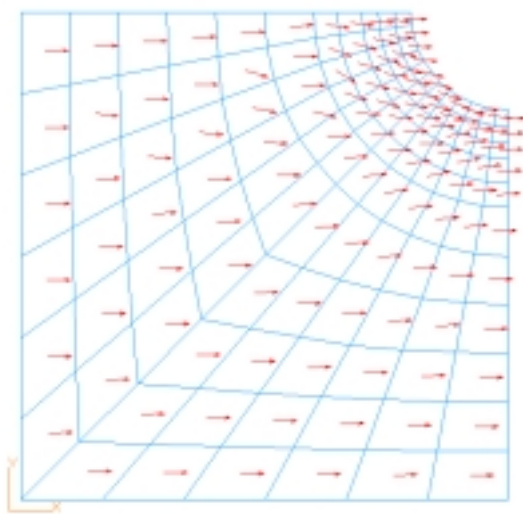
Figure 3.4.30: Layer-thickness contours for pl16L223.



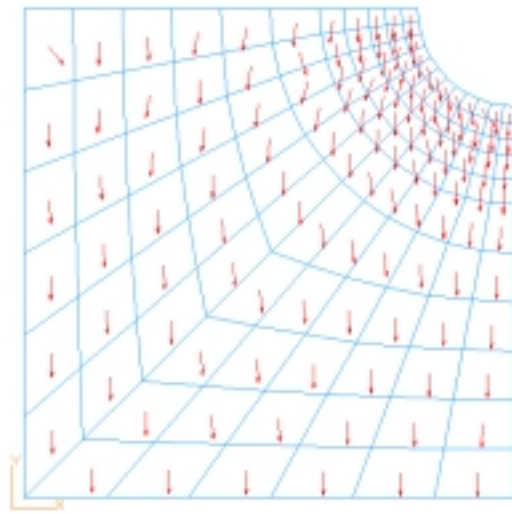
(a)



(b)



(c)



(d)

Figure 3.4.31: Layer-angle mappings for pl16L223.

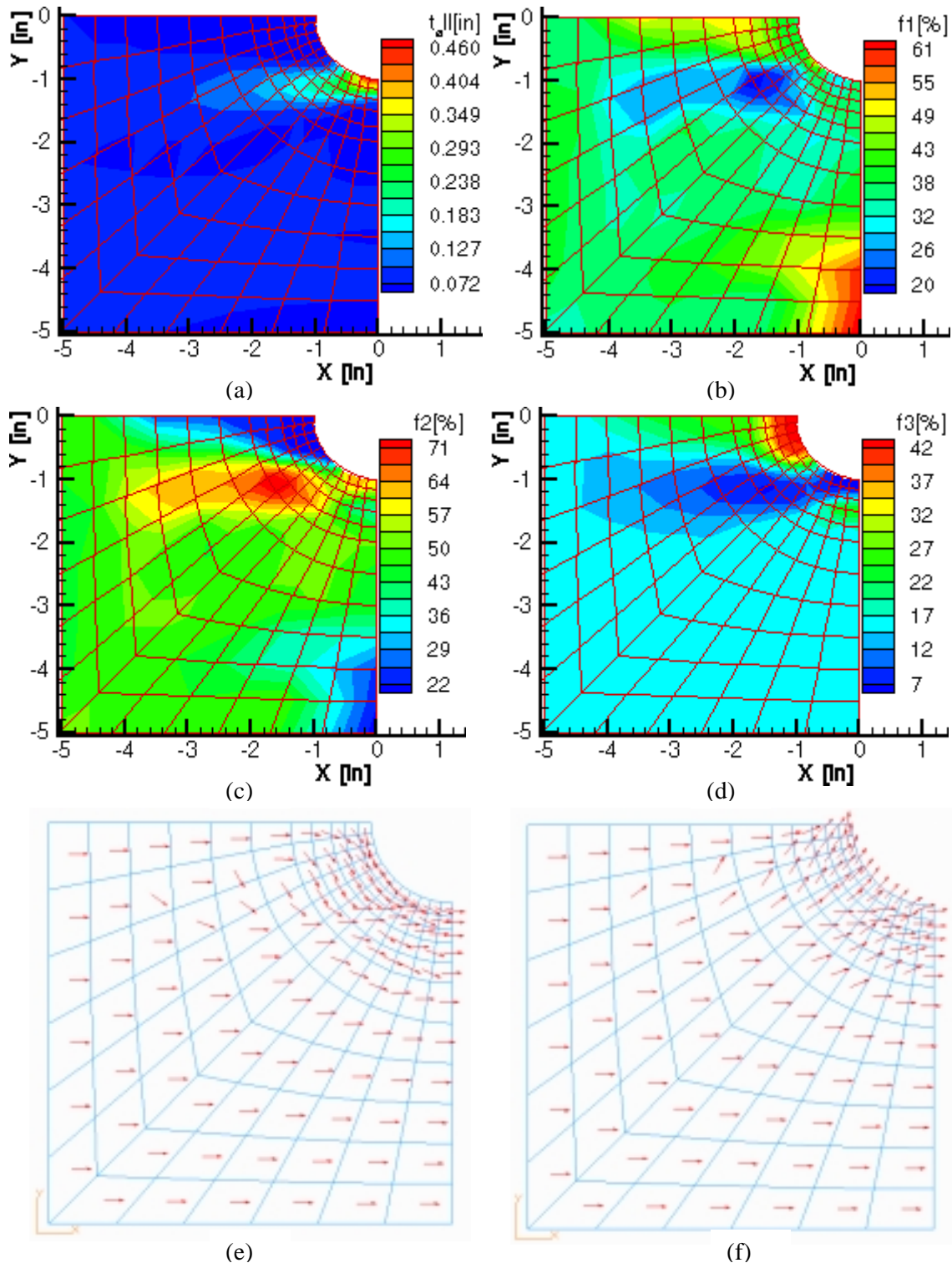


Figure 3.4.32: Layer-thickness contours and layer-angle mappings for pl16L323.

3.4.3.4 Square Plate with a Hole, $W/D = 5.0$, under In-plane Shear Loads.

Table 3.4.4 lists weight savings of this model w.r.t. DV configurations. A greater weight reduction is seen with Steering II, followed by Steering III and Steering I. The straight-line design (pl16L033) is depicted in Figure 3.4.33(a), where predicted fiber-reinforcement are shown primarily at plate boundaries due to in-plane shear loads. At **E**, the plate is composed of (10/80/10) family, where off-axis layers become dominant (Figure 3.4.33(b)). At **F**, 90° layer fills up the area with (10/15/75) family due to Poisson contraction in transverse direction. On the other hand, 0° layer significantly builds up at **G** due to Poisson contraction in the longitudinal direction. The laminate family is (75/15/10). Away from the boundary, the plate thickness gradually decreases to form a quasi-isotropic laminate or (25/50/25) family. Moving closely to the hole vicinity, the change in layer thickness contour is not apparent.

Figures 3.4.34 and 3.4.35 represent the optimal results of FS conceptual design based on Steering I configuration (pl16L133). The total layer-thickness contours (Figure 3.4.34(a)) seem identical with the baseline configuration (Figure 3.4.33(a)). At **E**, the plate is configured with (40/40/20) family, where $\pm\theta_1^\circ$ and θ_2° layers are dominant. Referring to Figures 3.4.35(a) and 3.4.35(b) for $\pm\theta_1^\circ$ layers, layer vectors are varied across the plate diagonal due to Poisson's effect. At the upper plate diagonal, $\pm\theta_1^\circ$ layers are steered to follow shear loads in transverse direction. On the other hand, the $\pm\theta_1^\circ$ layers are tailored w.r.t. shear loads in longitudinal direction at lower portion of the plate diagonal. This is also true for θ_2° and θ_3° layers, which are shown in Figures 3.4.35(c) and 3.4.35(d). Variations in these layer angles are noticeable across the diagonal and at the boundaries, largely attributed to in-plane shear loads.

Figures 3.4.36 and 3.4.37 are the optimal results of this model based on Steering II configuration (pl16L233). Essentially, more material are gathered at **F** and **G** with (15/50/35) and (65/20/15) families, respectively. In Figure 3.4.37(a), $+\theta_1^\circ$ layer orientations are steered to follow the shear load trajectories. As for $-\theta_1^\circ$ layer (Figure 3.4.37(b)), fiber directions gradually spread themselves out from **E** to **B**. In Figures 3.4.37(c) and 3.4.37(d), discontinuity in the variation of layer angles are seen at the plate boundaries. This effect is minimal at the hole vicinity. Note that a portion of θ_3° layer thickness fills up the area between **F** and **E** with (15/35/50) due to transverse Poisson contraction.

In Figures 3.4.38, the plate based on Steering III configuration (pl16L333) is thicker at the boundaries as predicted. A majority of layer reinforcement comes from θ_2° layer (Figure 3.4.38(c)) at **G** due to the longitudinal Poisson contraction. Here, the laminate family is about (75/15/10). At **E**, the plate thickness is largely contributed by $\pm\theta_1^\circ$ layers due to in-plane shear loads. As seen in Figures 3.4.38(e) and 3.4.38(f), layer angles are steered from **F** (transverse direction) to **E** (off-axis direction), and from **E** (off-axis direction) to **G** (longitudinal direction). Back to **F**, $\pm\theta_1^\circ$ and a portion of θ_3° layers are dominant with (10/70/20) and (15/40/45) families respectively due to shear loads in the transverse direction. At the hole vicinity, variations in layer angles are not significant because of minimal stress concentrations.

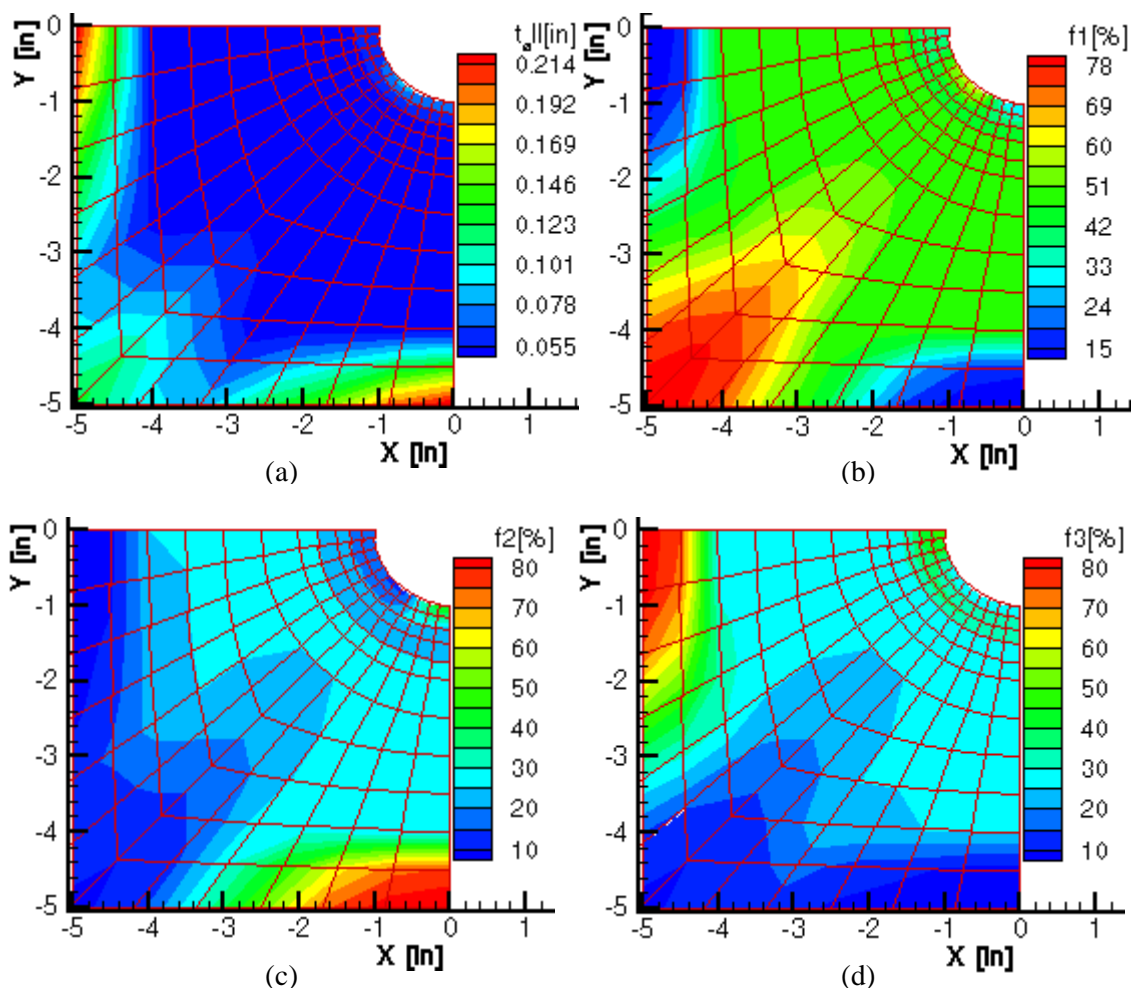


Figure 3.4.33: Layer-thickness contours for pl16L033.

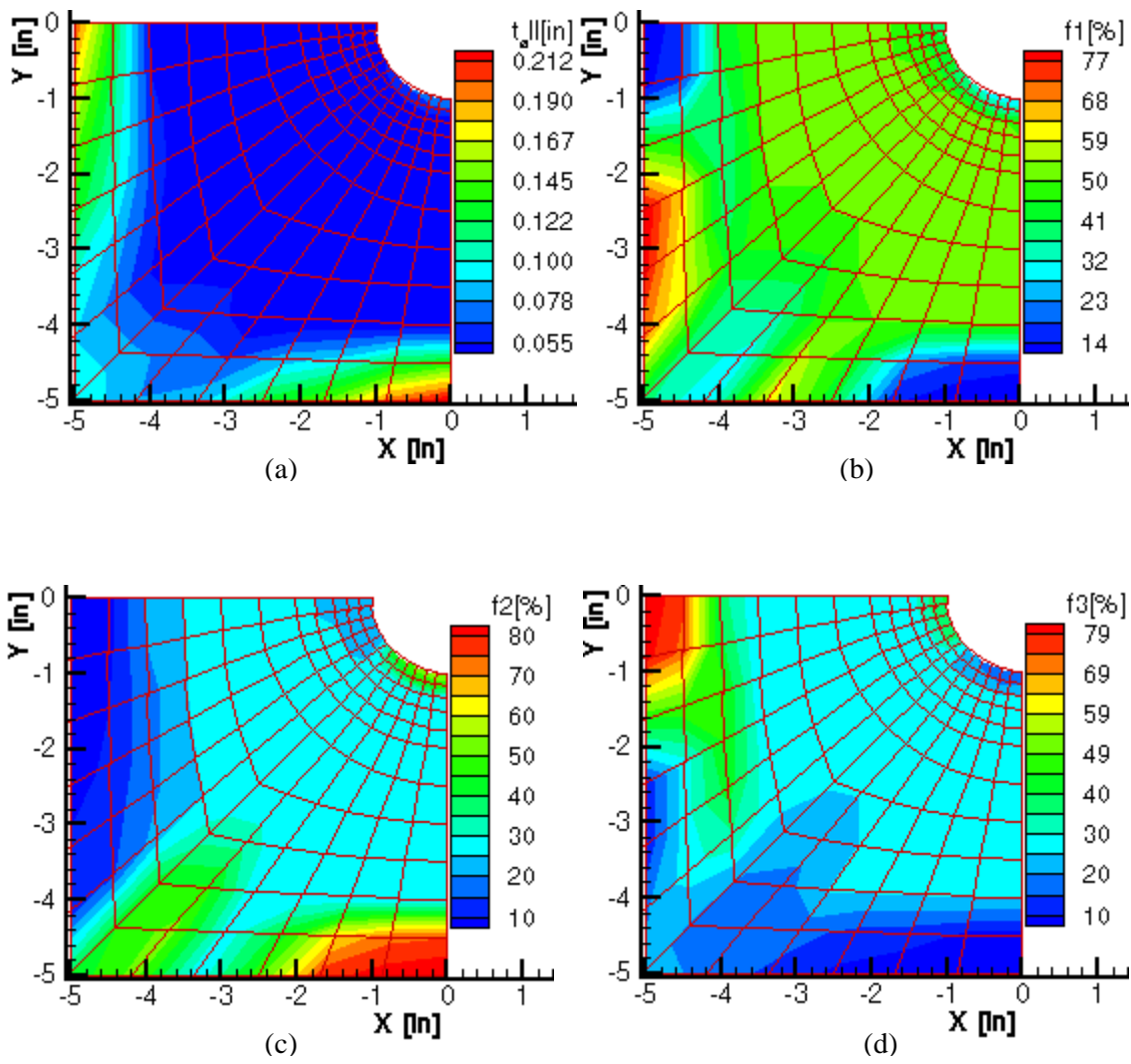
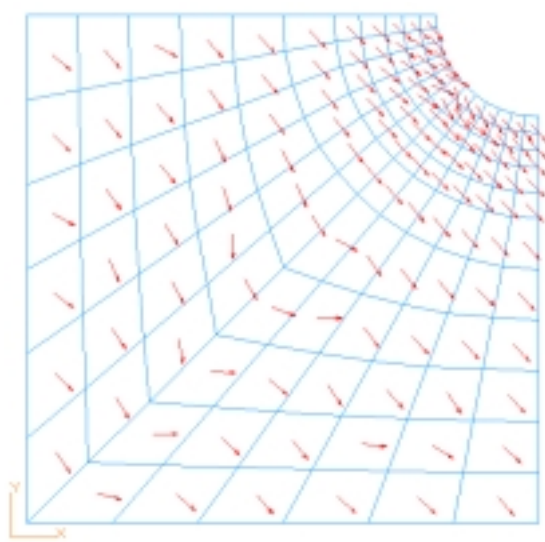
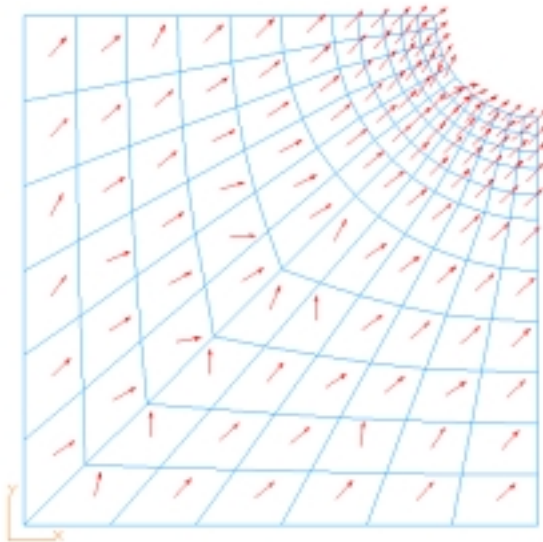


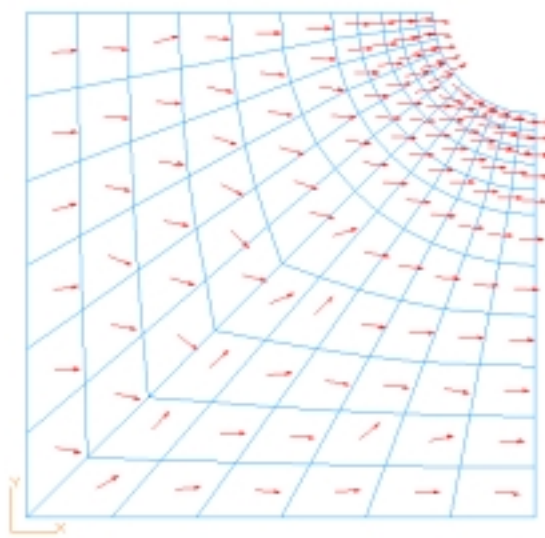
Figure 3.4.34: Layer-thickness contours for pl16L133.



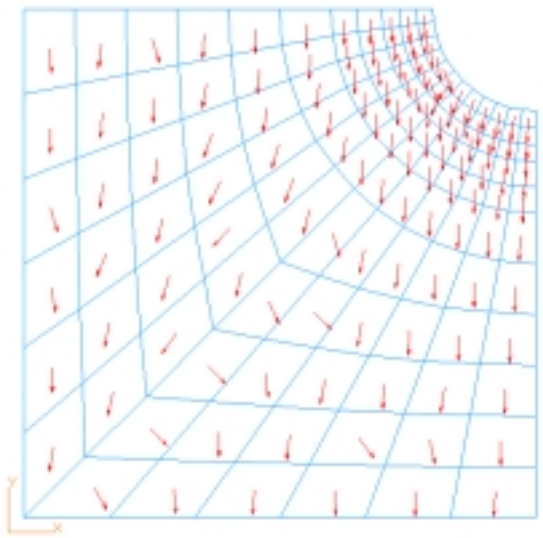
(a)



(b)



(c)



(d)

Figure 3.4.35: Layer-angle mappings for pl16L133.

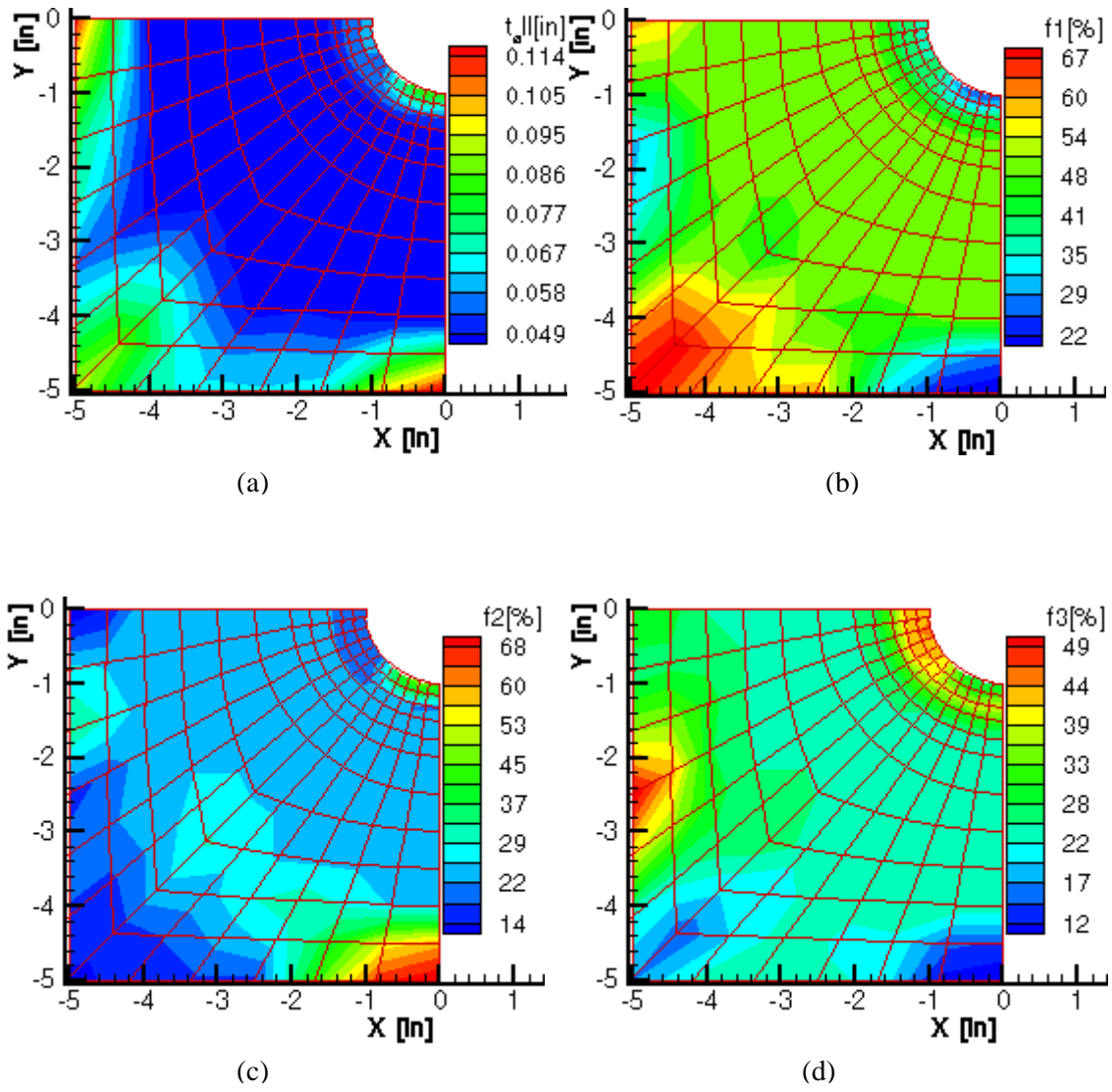
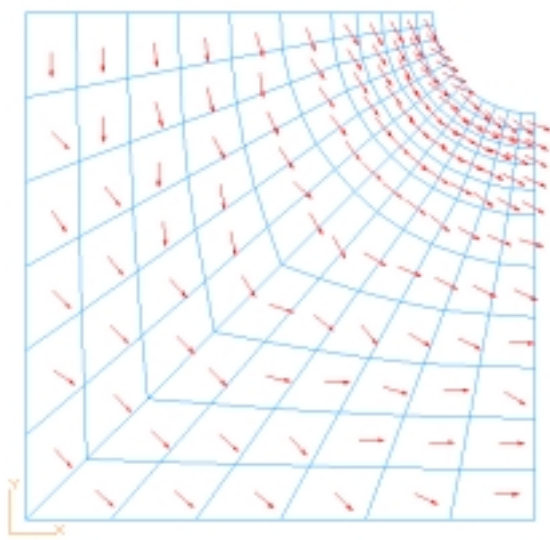
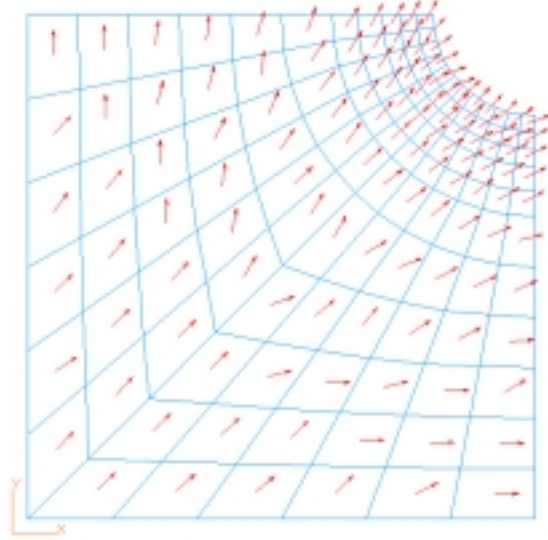


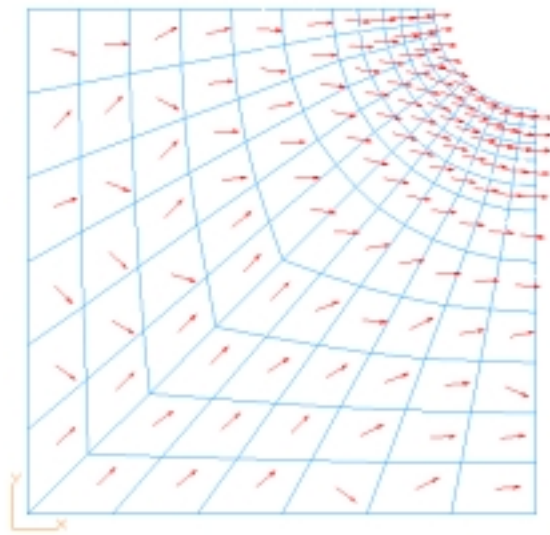
Figure 3.4.36: Layer-thickness contours for pl16L233.



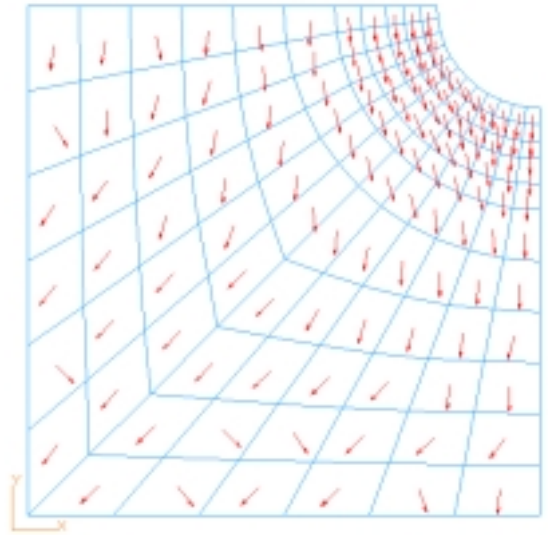
(a)



(b)



(c)



(d)

Figure 3.4.37: Layer-angle mappings for pl16L233.

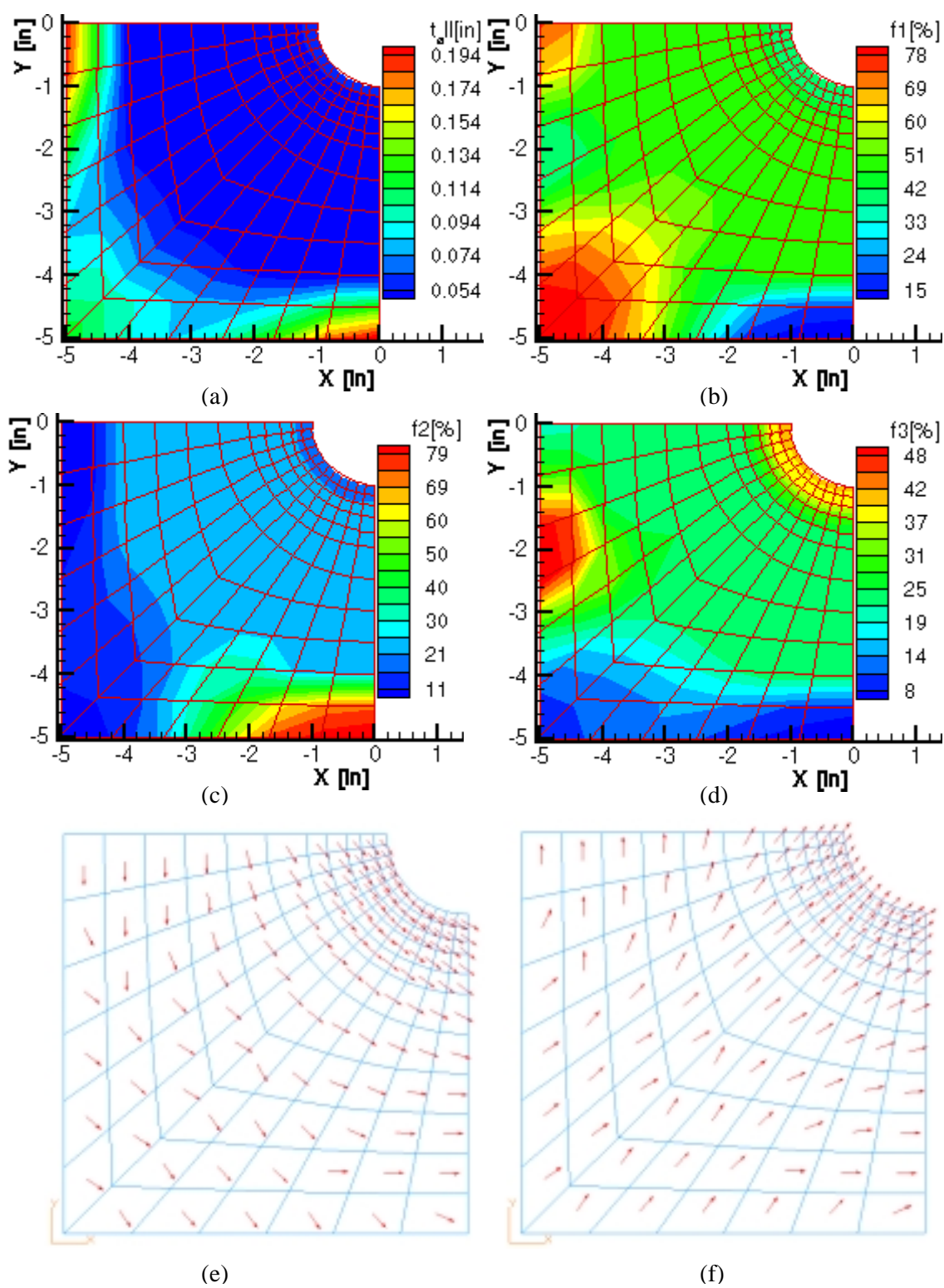


Figure 3.4.38: Layer-thickness contours and layer-angle mappings for pl16L333.

In summary, the effects of load paths on FS conceptual design have been clearly demonstrated from Sections 3.4.3.2 to 3.4.3.4 for $W/D = 5.0$ plate-with-a-hole models. The optimal layer-thickness contours and layer-angle mappings are very load-path sensitive, where both layer thickness and orientations are tailored significantly w.r.t. the primary load paths under different load-cases (bi-axial tensile, uniaxial tensile, and in-plane shear loads).

3.4.3.5 Effects of W/D parameter to FS Conceptual Design of Plate-with-a-Hole models, $W/D = 3.33$ and 2.5 , under Biaxial Tensile Loads.

The optimal results of FS conceptual design for these models are documented in Appendices C.1 and C.2. Weight savings w.r.t. DV configurations for these models are listed in Table 3.4.4, where Steering II is predicted to offer a greater payoff. Again, resultant laminates based on Steering II configuration may not be realistic due to the unbalanced issue. For a bigger hole cutout, Steering I seems to yield a lighter laminate compared to Steering III, although both are configured to have the same number of layer-angle DV. Note that Steering III yields balanced results w.r.t. the primary material coordinate; whereas, the resultant laminates based on Steering I are balanced w.r.t. the local material coordinate.

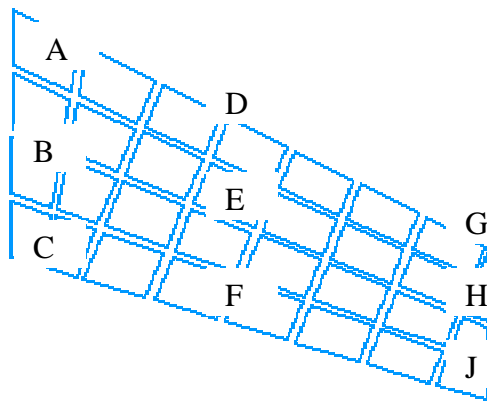
Comparing results of FS conceptual design for $W/D = 3.33$ and 2.4 (Appendices C.1 and C.2) with $W/D = 5.0$ plate, the variations of steering patterns do not show significant dependency on W/D parameter under identical load conditions. Although a larger W/D model seems to have a greater propagation or variation in layer thickness near the hole vicinity due to stress concentrations, the steering patterns of these models are very similar. An exception is seen for Steering I configuration, where for a larger W/D , the layer orientation mappings are discontinuous along the boundary. This is because when the central cutout increases in size, the influence of stress concentrations onto the boundary condition becomes significant.

3.4.3.6 Intermediate Complexity Wing (ICW) subjected to Aerodynamic Loads.

The ICW model has been set up to study potential advantages associating with FS conceptual design. Table 3.4.4 lists weight savings based on Steering II and III only. The Steering I configuration or VLAMINAT is not performed because of MBB-LAGRANGE's limitation in buckling formulations. From the results, Steering II has a greater payoff for both linear static and buckling analyses. Further verifications should be made for this configuration as the resultant laminates are unbalanced.

To help explain layer-thickness contours and layer-orientation mappings, several specific locations of the ICW model are labeled, which is shown in Figure 3.4.39. Figure 3.4.40 depicts layer-thickness contours of the baseline ICW model or ICW2L013. From Figure 3.4.40(a), more reinforcement are gathered around the trailing edge (T.E.) of the upper and lower skins. Here, 0° becomes significant due to axial compressive loads (buckling) and tensile loads, respectively. In fact, the upper skin has more material than the lower skin. The laminate family is approximately

(85/10/5) for both skins, as illustrated in Figure 3.4.40(c). On the other hand, the off-axis layers (Figure 3.4.40(b)) provide key reinforcement to the leading edge (L.E.) of the upper and lower skins due to shear loads and wing tip-deflection constraints. From **D** to **G**, the upper and lower skins are covered with (10/85/5) and (30/55/15) families, respectively. 90° layer reinforcement (Figure 3.4.40(d)) is not significant for both skins because the resultant lift force, in which the upper and lower skins sees axial compression and tension, are greater than the drag force in the transverse direction.



A: root leading edge (L.E.)

B: root mid-spar location

C: root trailing edge (T.E.)

D: $x/b \approx 0.5$, L.E.

E: $x/b \approx 0.5$, mid-spar

F: $x/b \approx 0.5$, T.E.

G: tip L.E.

H: tip mid-spar

J: tip T.E.

Figure 3.4.39: Specific location labeling for the ICW model.

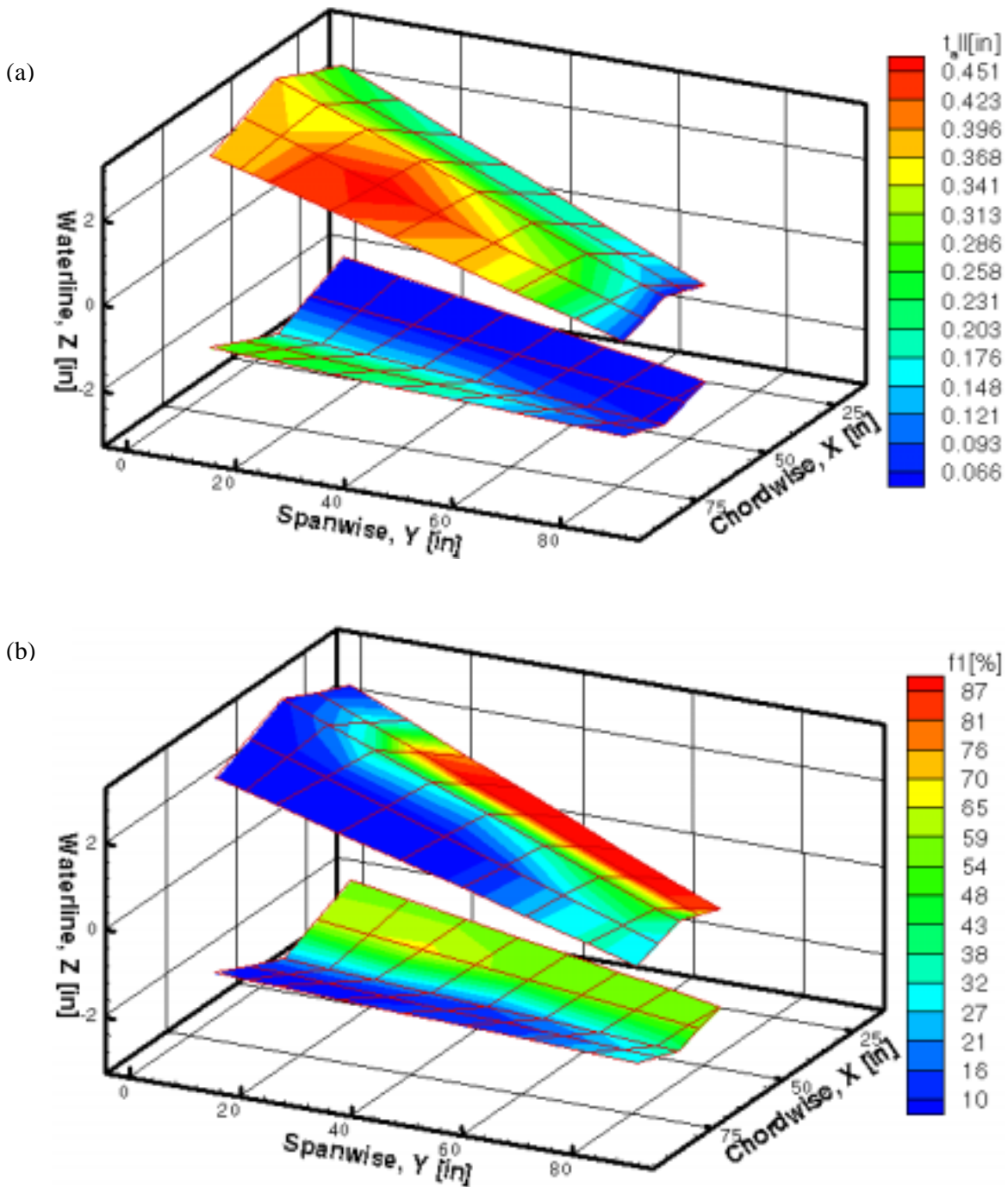
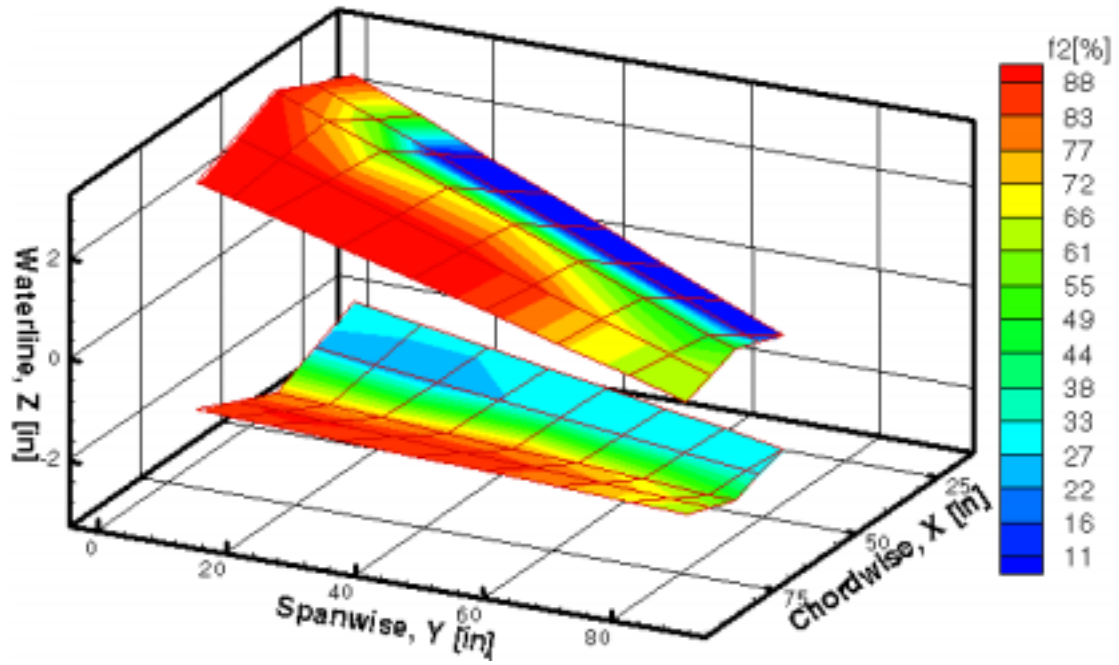


Figure 3.4.40: Layer-thickness contours for ICW2L013, total (top contour) and 1st (bottom contour) layers.

(c)



(d)

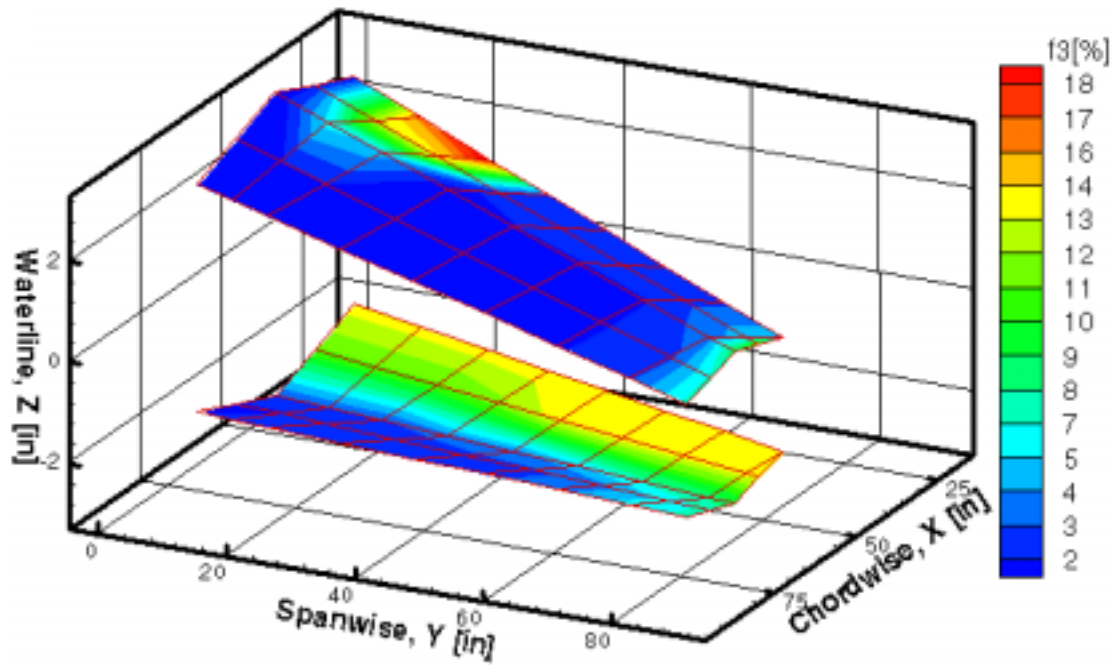


Figure 3.4.40 (contd.): Layer-thickness contours for ICW2L013, 2nd (top contour) and 3rd (bottom contour) layers.

Figures 3.4.41 to 3.4.43 show layer-thickness contours and layer-angle mappings for ICW2L213 based on Steering II configuration. In Figure 3.4.41(a), the total layer-thickness plot for this configuration shares similar contours with the baseline. More reinforcement are seen at T.E., especially from **C** to **F** for both skins. At these locations, θ_2° layer is dominant, where laminates are composed of (85/10/5) family. Notice in Figures 3.4.42(c) and 3.4.43(c), θ_2° layer orientations are aligned with the axial loads (i.e. compressive and tensile loads on upper and lower skins). Due to buckling loads, the upper skin is thicker than the lower skin. At wing tip, layer angles are steered to overcome wing-tip-deflection constraints. Similar steering patterns are observed for $\pm\theta_l^\circ$ layers in Figures 3.4.42(a), 3.4.42(b), 3.4.43(a), and 3.4.43(b). Referring to those thickness maps in Figure 3.4.41(b), $\pm\theta_l^\circ$ layers contribute partially to the longitudinal reinforcement of the lower skin's L.E. with about (30/55/15) and upper skin's **D** location with about (10/55/35). Interestingly, ICW shear loads are reinforced with θ_3° , noticeably in Figure 3.4.41(d). In fact, fiber orientations of this layer are shifted to align in $\pm 45^\circ$ direction w.r.t. the primary material coordinate (see Figure 3.4.16). At **A** and **G**, the laminate family associated with θ_3° is (10/10/80).

Finally, Figures 3.4.44 to 3.4.46 represent layer-thickness contours and layer-angle mappings for ICW2L313 based on Steering III configuration. In Figure 3.4.44(a), more material are assembled at T.E., especially from **C** to **F** for the upper skin. Here, 0° layer is dominant, where laminates are composed of (85/10/5) family at **C** and gradually become (50/45/5) family at **F**. Towards the outboard section of the upper skin, $\pm\theta_l^\circ$ layers play a key role in reinforcement. Notice in Figures 3.4.45(a) and 3.4.45(b), $\pm\theta_l^\circ$ layer orientations are steered to overcome wing-tip-deflection constraints. At these locations, the laminate family is (10/80/10). Similar steering patterns are observed for $\pm\theta_l^\circ$ layers in the lower skin. In Figure 3.4.44(b), $\pm\theta_l^\circ$ layers contribute to the longitudinal reinforcement of the lower skin's root L.E. with about (10/80/10) and outboard section with about (25/65/10) for shear reinforcement. 90° layer reinforcement (Figure 3.4.44(d)) is not significant for both skins, as predicted.

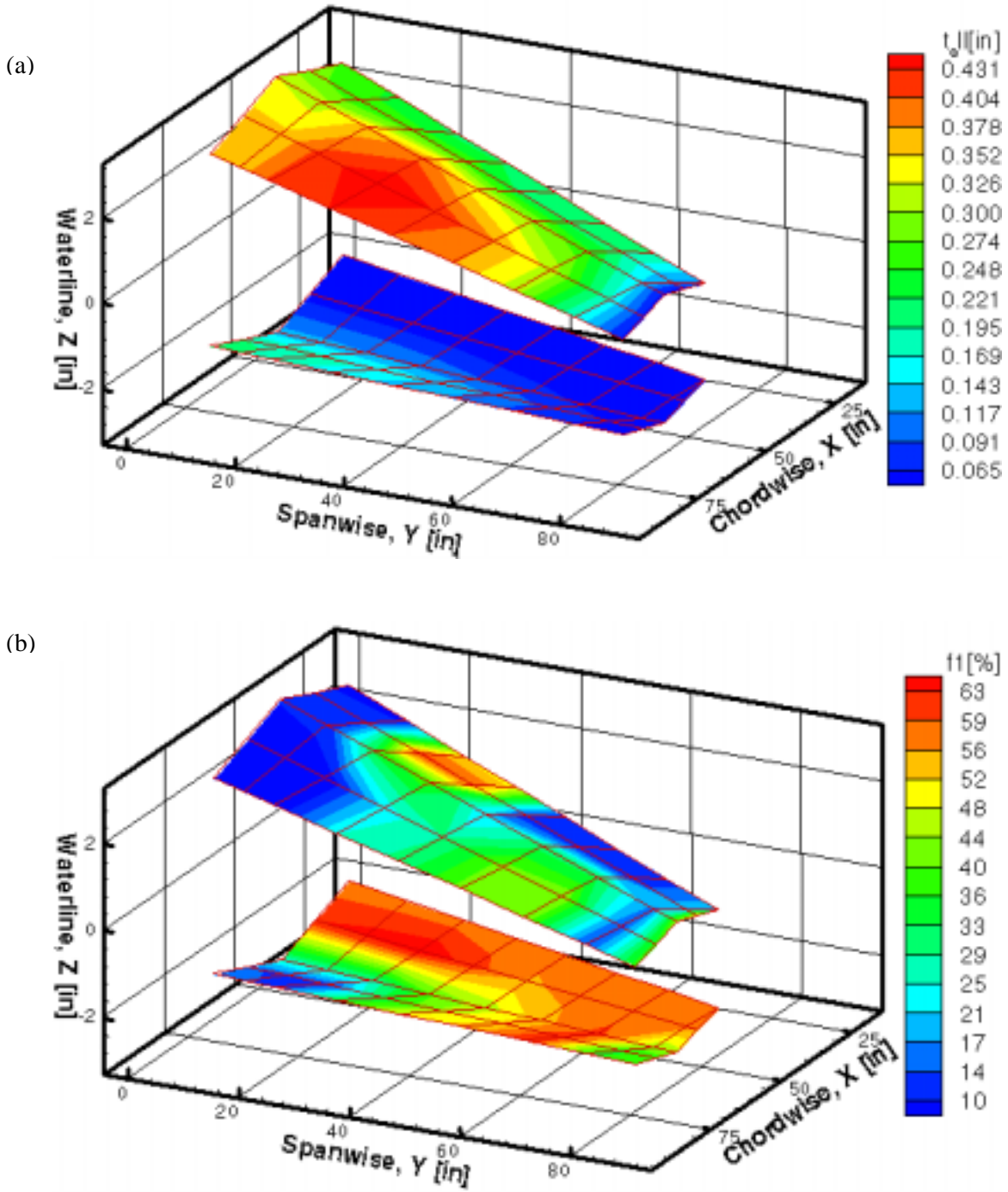
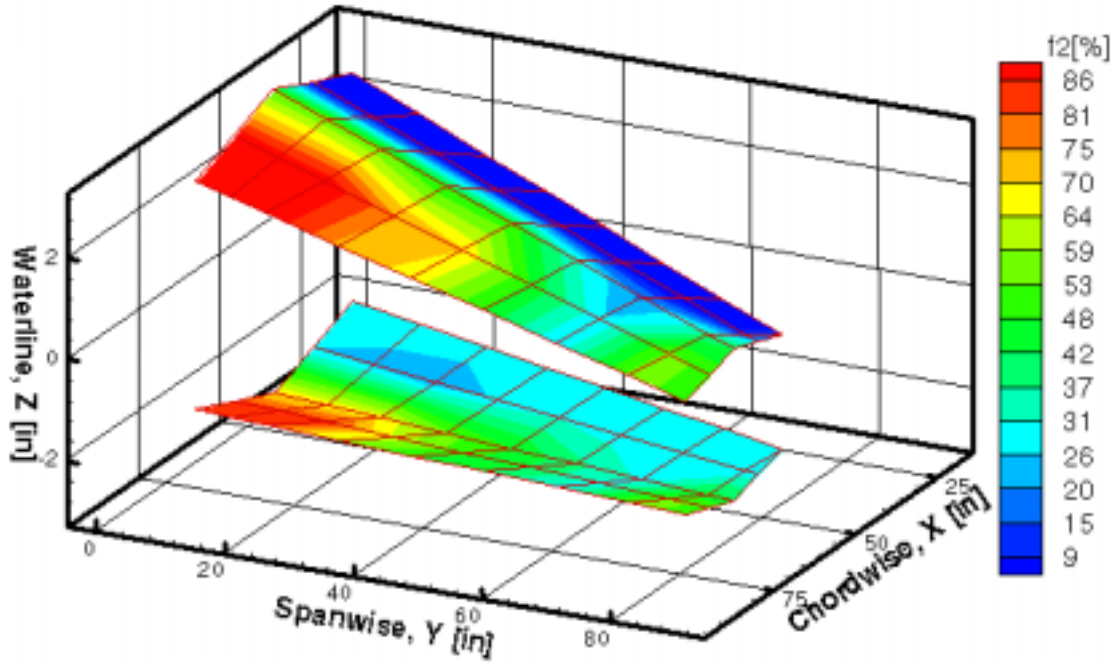


Figure 3.4.41: Layer-thickness contours for ICW2L213, total (top contour) and 1st (bottom contour) layers.

(c)



(d)

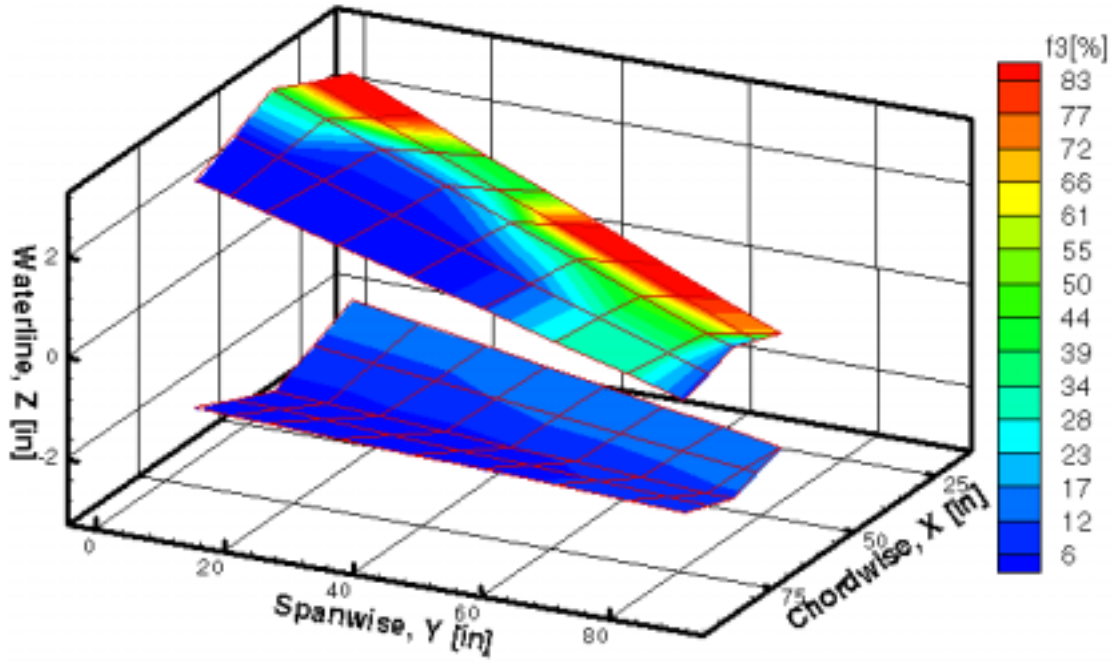


Figure 3.4.41 (contd.): Layer-thickness contours for ICW2L213, 2nd (top contour) and 3rd (bottom contour) layers.

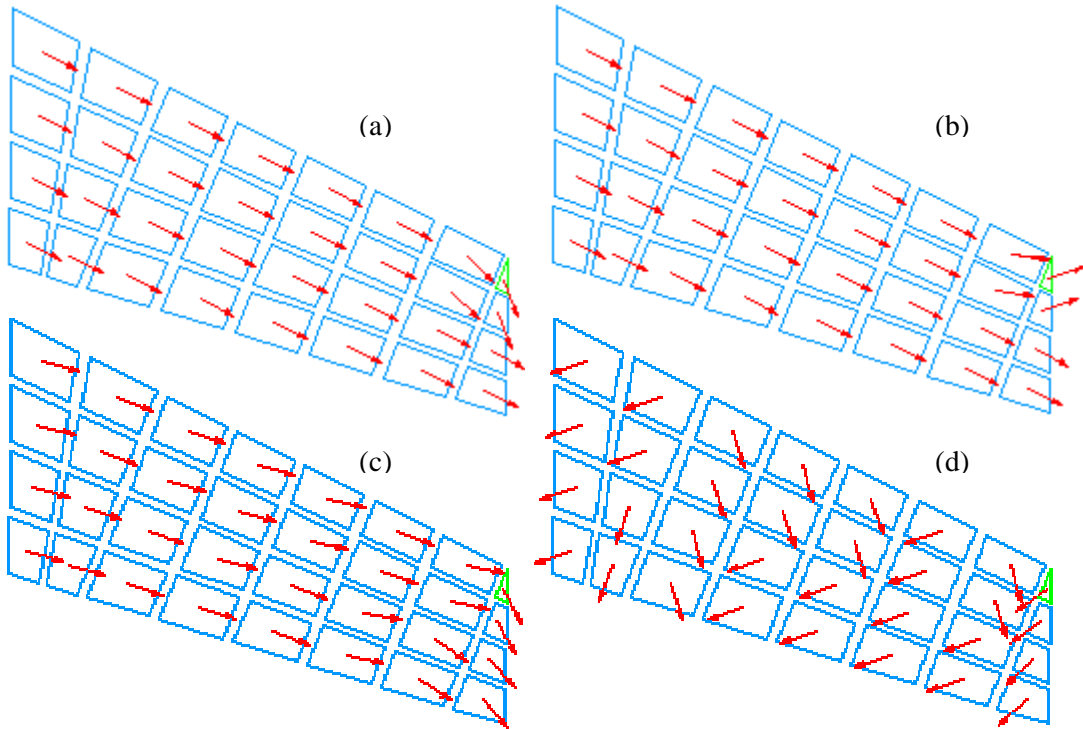


Figure 3.4.42: Layer-angle mappings for ICW2L213 upper skin.

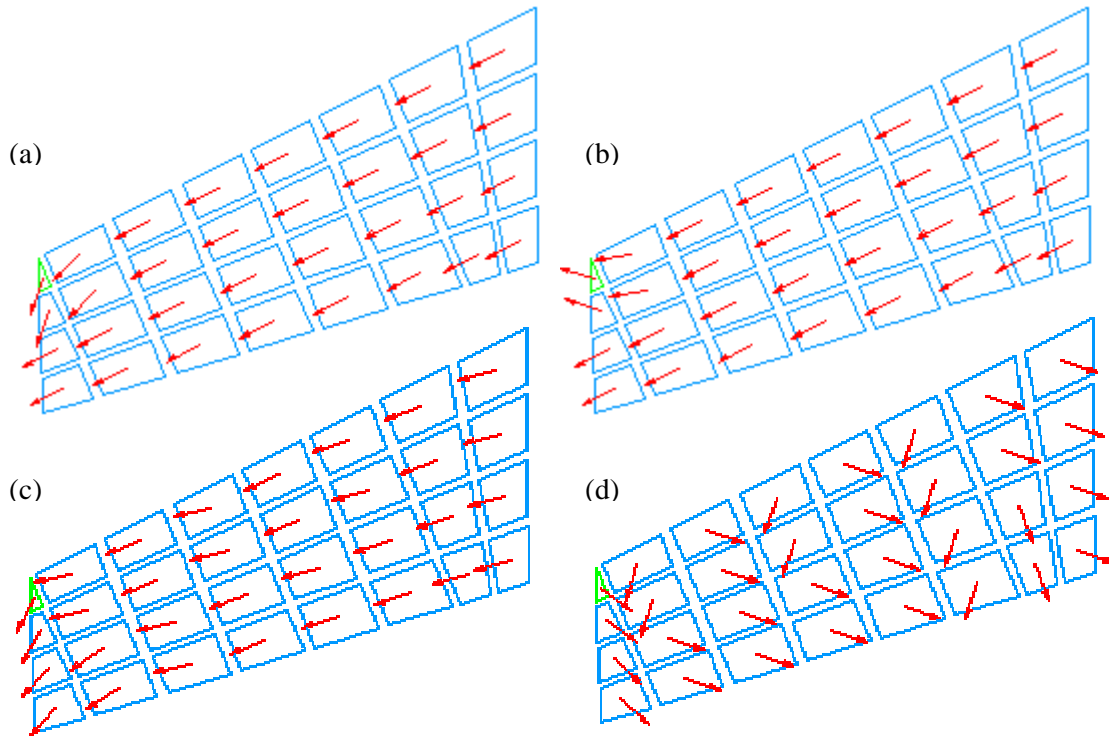


Figure 3.4.43: Layer-angle mappings for ICW2L213 lower skin.

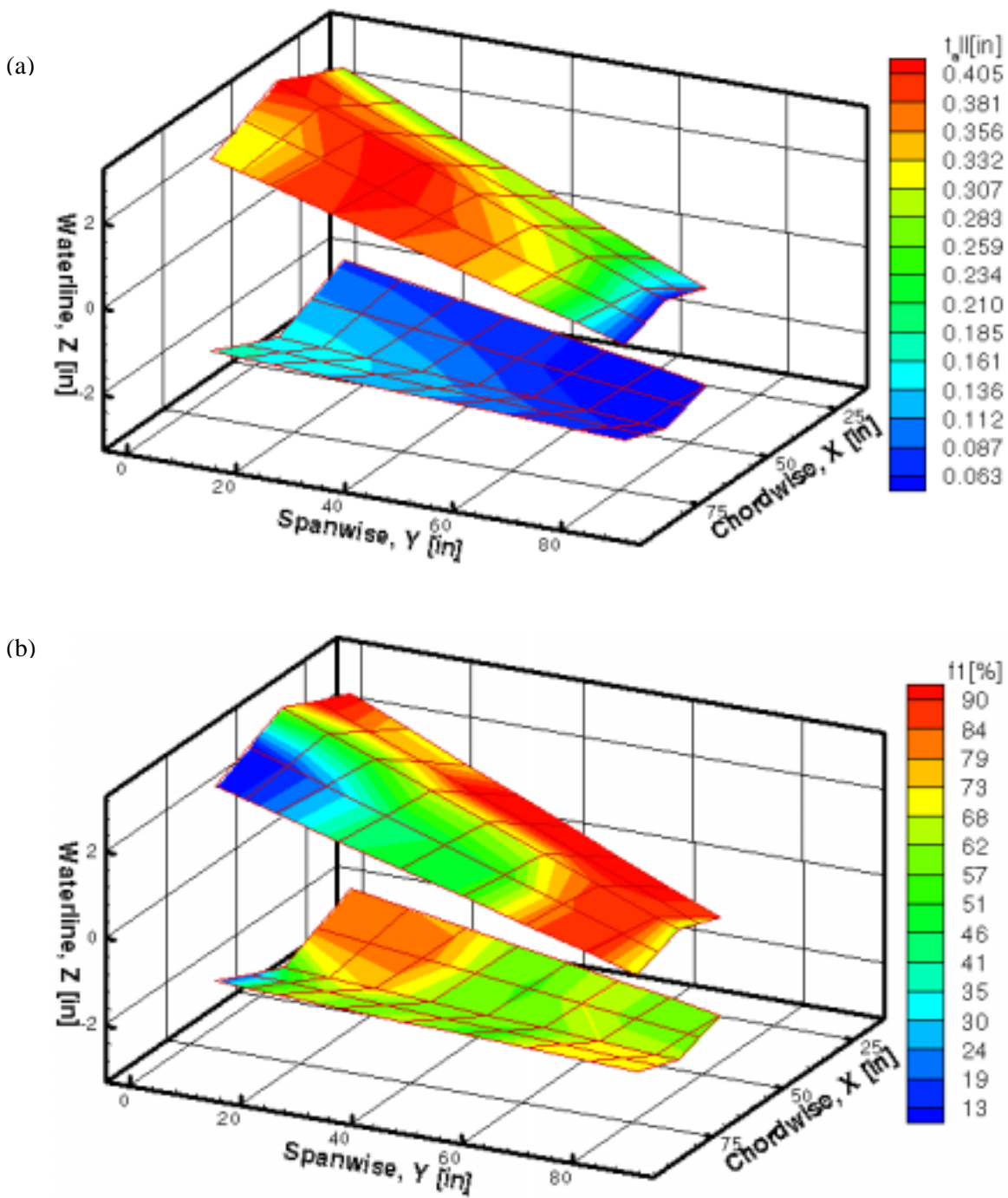


Figure 3.4.44: Layer-thickness contours for ICW2L313, total (top contour) and 1st (bottom contour) layers.

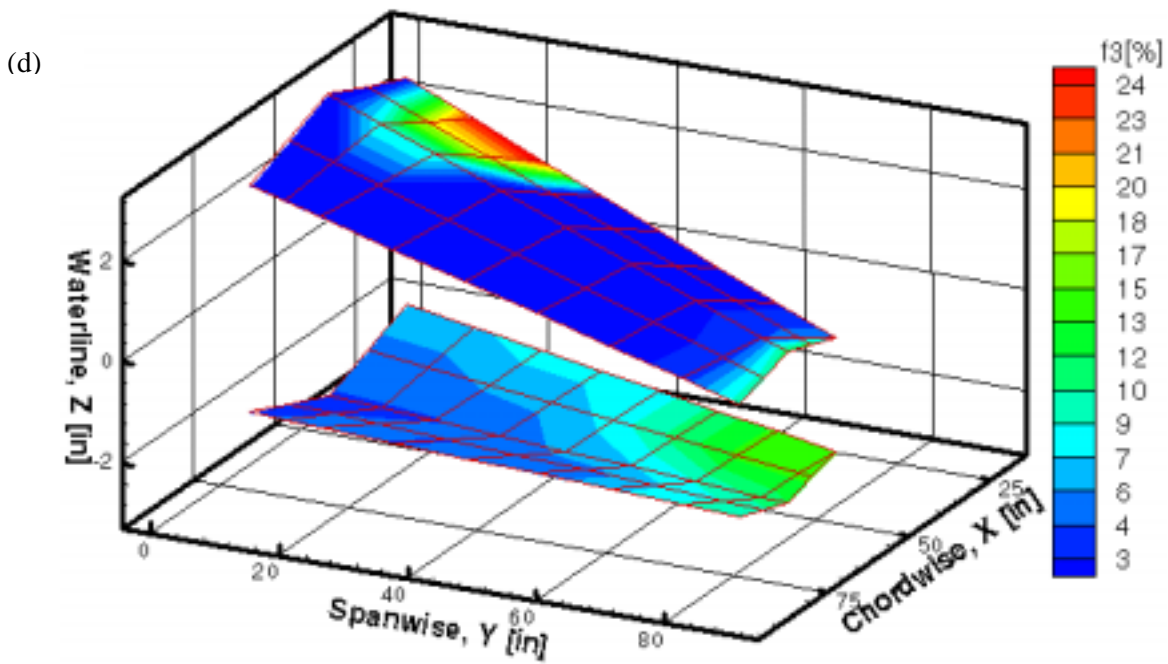
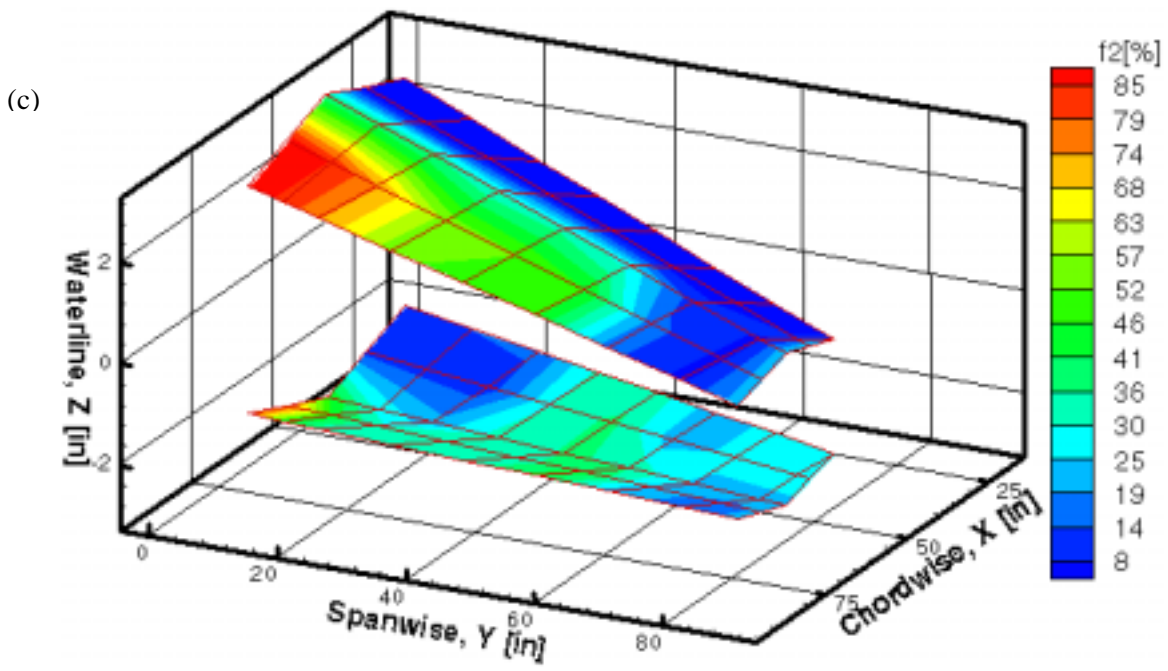


Figure 3.4.44 (contd.): Layer-thickness contours for ICW2L313, 2nd (top contour) and 3rd (bottom contour) layers.

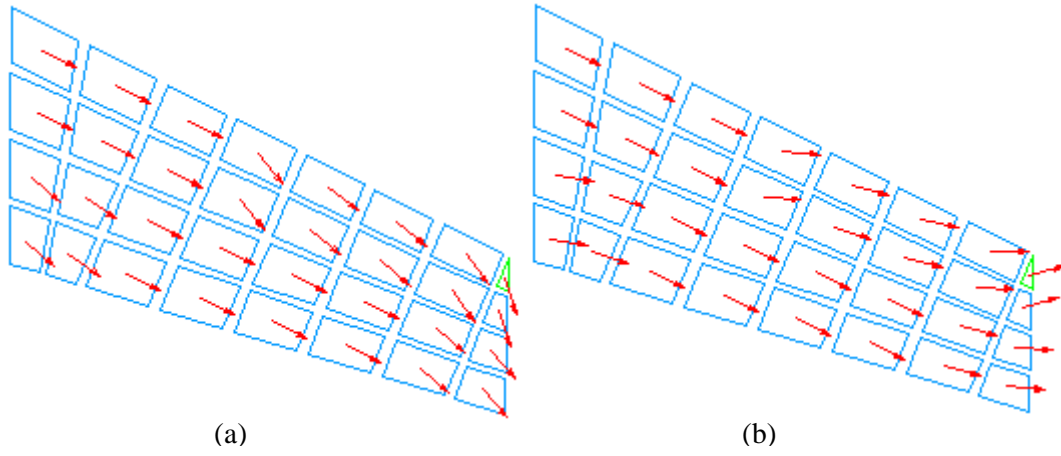


Figure 3.4.45: 1st and 2nd layer-angle mappings for ICW2L313 upper skin.

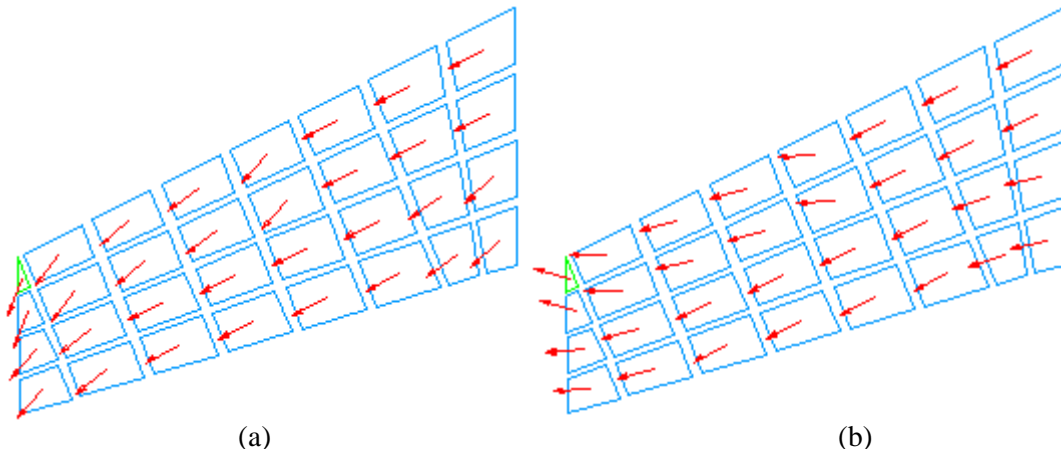


Figure 3.4.46: 1st and 2nd layer-angle mappings for ICW2L313 lower skin.

3.4.3.7 Cantilever Rectangular Panel under Transverse Loads.

The optimal results of FS conceptual design for this model are documented in Appendix C.3. Table 3.4.4 lists weight savings corresponding to this model based on DV configurations. Tremendous weight reduction (17%) is associated with Steering II, followed by Steering I (10%) and Steering III (3%). Again, resultant laminates based on Steering II configuration may not be realistic due to the unbalanced issue. The Steering III yields balanced results w.r.t. the primary material coordinate; whereas, the resultant laminates based on Steering I are balanced w.r.t. the local material coordinate.

3.4.3.8 Cantilever Cylindrical Tube under Combined Loads.

The optimal results of FS conceptual design for this model are documented in Appendix C.4. Weight savings of this model w.r.t. DV configurations are listed in Table 3.4.4, where Steering II is predicted to offer a greater payoff of about 26%. Steering III seems to yield a lighter laminate (25%) compared to Steering I (20%), although both are configured to have the same number of layer-angle DV.

3.4.4 Brief Conclusion for Preliminary Studies

Four preliminary studies have been performed to demonstrate potential benefits associated with FS conceptual design using MBB-LAGRANGE. The objective function of the optimization is minimum weight, subjected to various constraints such as MSTN or CMAT, CGAGE, CGANG, CDIS, and BUCK. Four DV configurations are proposed and defined in Table 3.4.1. The results of weight savings are listed in Table 3.4.4, where FS-related configurations are compared with the baseline design. From the studies, it is concluded that:

- ➔ **Weight savings of up to 27% for linear static analysis** is attainable, which is primarily based on Steering II configuration. However, further verifications and sound decisions must be made because of the unbalanced nature of this configuration.
- ➔ **Weight savings of up to 26% for linear static analysis** is achievable, which is associated with **Steering III configuration**. This configuration yields balanced results w.r.t. the primary material coordinate, which is more realistic and acceptable in composite laminate design.
- ➔ **Weight savings of up to 20% for linear static analysis** is reasonable, which corresponds to **Steering I configuration**. This resultant laminates are balanced w.r.t. the local material coordinate, but unbalanced w.r.t. the principal material coordinate. Further investigations are required to verify the macroscopic behavior and response of the laminates.
- ➔ **Weight savings of up to 6% for linear buckling analysis** is observable, which is primarily based on Steering II configuration. Again, the optimal results may not be

realistic due to unbalanced issue. In addition, MBB-LAGRANGE buckling formulations must be revisited for FS-related optimizations.

- ➔ **“Smooth” or continuous layer-thickness contours and layer-orientation mappings** following primary load paths are demonstrated in most of the preliminary studies
- ➔ **Optimal layer-angle mappings and layer-thickness contours are very load-path-sensitive.** As illustrated in the plate-with-a-hole models for $W/D = 5.0$, where layer orientations are tailored significantly w.r.t. the primary load paths under different load cases (bi-axial tension, uniaxial tension, and in-plane shear). However, the variations of steering patterns do not depend strongly on W/D parameter under identical load conditions. A larger W/D model may seem to have a greater propagation or variation in layer thickness due to stress concentrations near the hole vicinity. Also, with a greater W/D , layer orientations for Steering I configuration are discontinuous along the boundary due to the influence of stress concentrations. Nevertheless, the variation of steering patterns w.r.t. W/D parameter is generally insensitive.
- ➔ **MBB-LAGRANGE is a robust and efficient tool for fiber steering conceptual design.**

Based on these appealing results, further investigations and ultimately applications of FS conceptual design on existing aircraft structural components should be pursued and demonstrated. Improvements in MBB-LAGRANGE buckling formulations are required to incorporate better layouts of steered-fiber architecture onto airframe structures.

3.5.0. **Representative Aircraft Primary and Secondary Structures using Fiber Steering Conceptual Design**

This chapter discusses the application of fiber steering (FS) conceptual design on three representative aircraft primary and secondary structural components. Recently, there has been an increase in the use of composite materials on aircraft primary and secondary structures using fiber placement (FP) fabrication methods⁷. FS conceptual design can be applied on aircraft structural components, such as wings, horizontal stabilizers, canards, and fuselage. Significant weight savings are anticipated with the use of steered fiber architecture in both general aviation and military aircraft.

Existing air vehicles for commercial and military usage with possible demonstration of FS conceptual design have been identified. They are:

- ➔ **Wing:** a representative of a regional jet's primary structural component, denoted as BGE.
- ➔ **Aft pressure bulkhead:** a representative of a general aviation aircraft's secondary structural component, denoted as pb2.
- ➔ **Horizontal Stabilator:** a representative of a tactical fighter's primary structural component, denoted as F22.

These models are set up with MSC/PATRAN. The primary composite material in this investigation is IM7/8551-7A, while the metallic substructures are made of aluminum alloys (e.g. 2024-T3 aluminum sheets and extrusions). For composite structures, the initial laminate with $[\pm 45, 0, 90]_s$ is analyzed with MSC/NASTRAN based on static analysis and maximum strain failure criterion, STRN, to determine the initial layer thickness for each angle. Each layer consists of several plies of similar layer orientation, where each ply has a minimum gage of 0.0055 inch. The optimum laminates based on FS conceptual design can be obtained via MBB-LAGRANGE. For the sizing of metallic substructures, MSC/NASTRAN is employed based on aircraft structural design. A safety factor of 1.5 is imposed for all structural analyses.

Due to MBB-LAGRANGE limitation, Steering I or VLAMINAT[†] defines every single element as a layer-angle design variable (DV). This results in tremendous computational works because rangewise DV linking is not possible. Therefore, only baseline, Steering II and III configurations, are defined for each structural component, which are stated in Table 3.4.1. Rangewise DV linking are carefully defined based on the laminate's strain contours based on the initial laminate analysis via MSC/NASTRAN. These configurations are composed of symmetric laminates with $[\pm \theta_1, \theta_2, \theta_3]_s$. The baseline is a pure layer-thickness optimization with $[\pm 45, 0, 90]_s$. Layer thicknesses for the first two layers are linked as one DV in order to maintain balanced with respect to (w.r.t.) the principal material coordinate. The Steering II configuration has three angle DV per range of elements. $\pm \theta_1^\circ$ layers, are linked as one DV each for layer

[†] VLAMINAT: Whole laminate orientation is ONE angle DV; i.e., for $[\pm \theta_1, \theta_2, \theta_3]$ the θ_2° layer is the primary angle DV, with $\pm \theta_1^\circ$ and θ_3° layers linked to the local θ_2° DV at orientations of ± 45 deg and 90 deg respectively.

thickness and orientation, respectively. Note that Steering II laminate is unbalanced w.r.t. either the local or principal material coordinate. Steering III configuration, on the other hand, takes only one DV by linking $\pm\theta_l^0$ layers in $[\pm\theta_l, 0, 90]$. As a result, Steering III is balanced w.r.t. the principal material coordinate.

The objective function of the optimization is the structural weight. These structures are subjected to design constraints, such as maximum strain failure criterion (MSTN or CMAT), upper and lower layer thickness (CGAGE) and angle bounds (CGANG):

- CMAT: Longitudinal tensile strain, $\varepsilon_1^{tu} = 8533 \mu\text{in} / \text{in}$
 Longitudinal compression strain, $\varepsilon_1^{cu} = 7400 \mu\text{in} / \text{in}$
- CGAGE: For 1st, 2nd, and 3rd layers
 Lower layer thickness, $t_l = 0.011 \text{ inch}$ (2 plies)
 Upper layer thickness, $t_u = 0.500 \text{ inch}$ (~91 plies)
For 4th layer
 Lower layer thickness, $t_l = 0.0055 \text{ inch}$ (1 ply)
 Upper layer thickness, $t_u = 0.500 \text{ inch}$ (~91 plies)
- CGANG: **Angle threshold of $\pm 45^\circ$ are imposed onto all angle DVs.**

Note that the fourth layer in CGAGE is a minimum gage. This is intended to enable an oblique-symmetric laminate, $[\pm\theta_l, \theta_2, \theta_3]_{os}$. For the wing model (bge12), an additional constraint of maximum wing-tip vertical deflection (CDIS) is imposed. The buckling constraint (BUCK) is not applied on any of these models because of the limitations associated with MBB-LAGRANGE buckling formulations (see Section 3.3).

As stated in Section 3.3, Recursive Quadratic Programming by Powell (RQP2) is selected as the primary optimization algorithm. The termination parameters applied on these models are:

- Relative change in the objective function, $\varepsilon_f = 1.0 \times 10^{-3}$
- Relative change in DV, $\varepsilon_x = 1.0 \times 10^{-3}$
- Termination for Kuhn Tucker Conditions, $\varepsilon_{KTO} = 1.0 \times 10^{-4}$ for bge11 and bge12 (very large numbers of DV), and $\varepsilon_{KTO} = 1.0 \times 10^{-6}$ for pb2 and F22 (moderate numbers of DV).
- Maximum constraint violation, $\varepsilon_{res} = 1.0 \times 10^{-3}$

Also, the parameter for numerical gradient calculations, ε_G is set to 1.0×10^{-4} .

To study the potential weight savings, comparisons of weight savings are performed for all models between:

- Baseline and Steering II
- Baseline and Steering III

3.5.1 A Representative Wing of a Regional Jet.

The Bombardier Global Express (BGE) wing is selected as the representative regional jet primary structure suitable for performing the FS capability. The wing is a highly swept cranked wing. It is modeled as a three-bay wing without the winglet, each bay denoted as inboard (IB), midboard (MB), and outboard (OB). Table 3.5.1 summarizes the basic wing dimensions. For simplicity, NACA airfoils are used in this model instead of the actual airfoil, a third generation supercritical airfoil. The airfoil-shape variation across each bay is computed based on linear interpolation method.

The BGE wing is subjected to aerodynamic load as well as internal fuel loads. Three flight conditions, namely take-off, climb, and landing, are examined to determine the individual pressure coefficient profile in the spanwise and chordwise coordinates, as shown in Figure 3.5.1. Only take-off flight condition has been imposed on the optimization model to constitute the critical load case. The critical load factor of the airplane is determined to be 2.65 at 1022 ft² of wing area, 93,500 lbs of W_{TO} and 1.7 of $CL_{max \text{ clean}}$. Resultant forces are computed and mapped approximately to the finite element model based on each loading profile, which is generated via VORSTAB⁵¹. Table 3.5.2 lists parameters required for computations of pressure-coefficients distribution over the upper and lower skins.

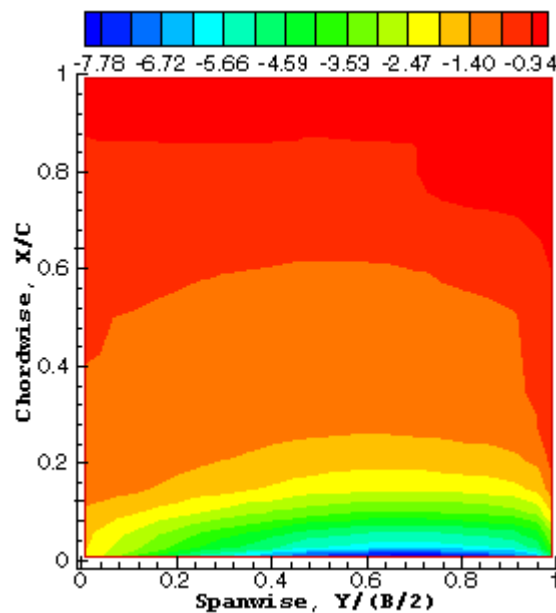
Table 3.5.1: Basic wing geometry of a representative regional jet wing or BGE wing.

Wing Geometry	Dimensions
Wing Aspect Ratio [~]	8.6
Wing Area [ft ²]	1,022
Wing Span [ft]	93.5
Dihedral [deg]	2.5
Wing Sweep at Quarter Chord [deg]	35.0
Wing Sweep at Leading Edge [deg]	39.0

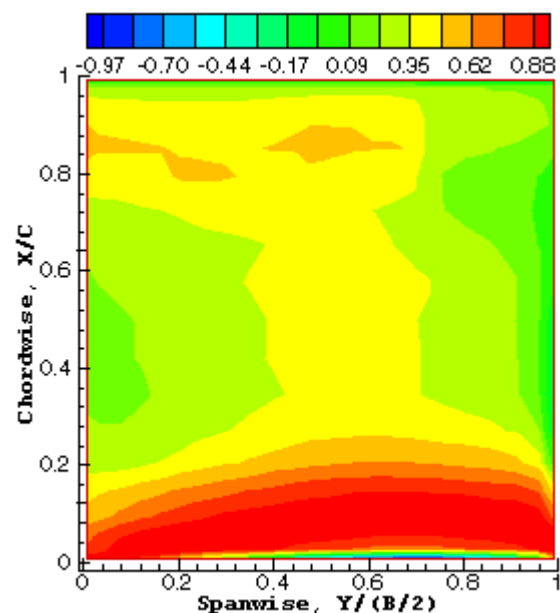
Table 3.5.2: Parameters required for VORSTAB computations of pressure coefficient distributions.

Parameters	Takeoff	Climb	Landing
Altitude, h [ft]	30.0	8000.0	0.0
Reynolds number, Re [$\times 10^6 \text{ ft}^{-1}$]	1.608	2.646	1.288
Mach number, M	0.227	0.467	0.181
Angle of attack, α [deg]	10.0	5.0	8.0
Flap deflection, δ_f [deg]	15.0	0.0	30.0
Aileron deflection, δ_a [deg]	0.0	0.0	0.0
Dynamic pressure, \bar{q} [psf]	76.11	239.5	48.75

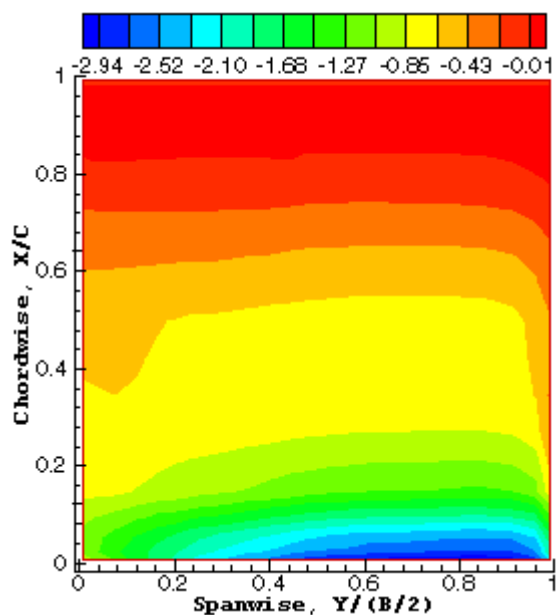
The wing is attached securely to the fuselage attachment points with wing root joints or center wing. Figure 3.5.2 shows the finite element discretization of the wing with aluminum substructure. The number and location of ribs and spars are modeled approximately according to the actual aircraft. Table 3.5.3 lists the attributes for these structures. A safety factor of 1.5 is imposed to the sizing of these components based on aircraft structural analyses.



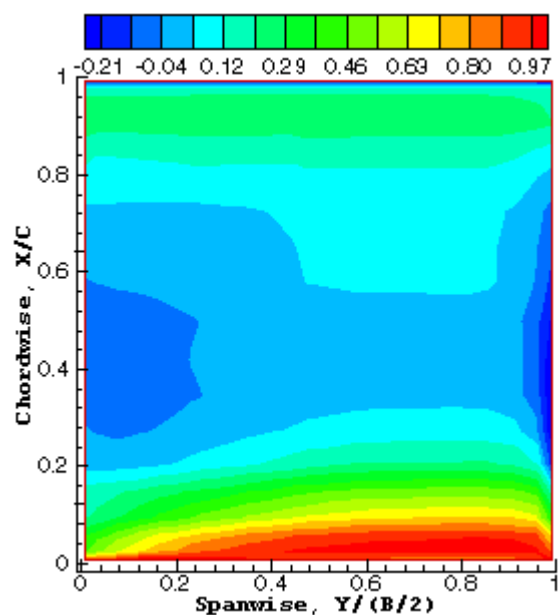
Upper skin, take-off flight condition



Lower skin, take-off flight condition



Upper skin, climb flight condition



Lower skin, climb flight condition

Figure 3.5.1: Coefficients of pressure distribution over BGE wing models at various flight conditions.

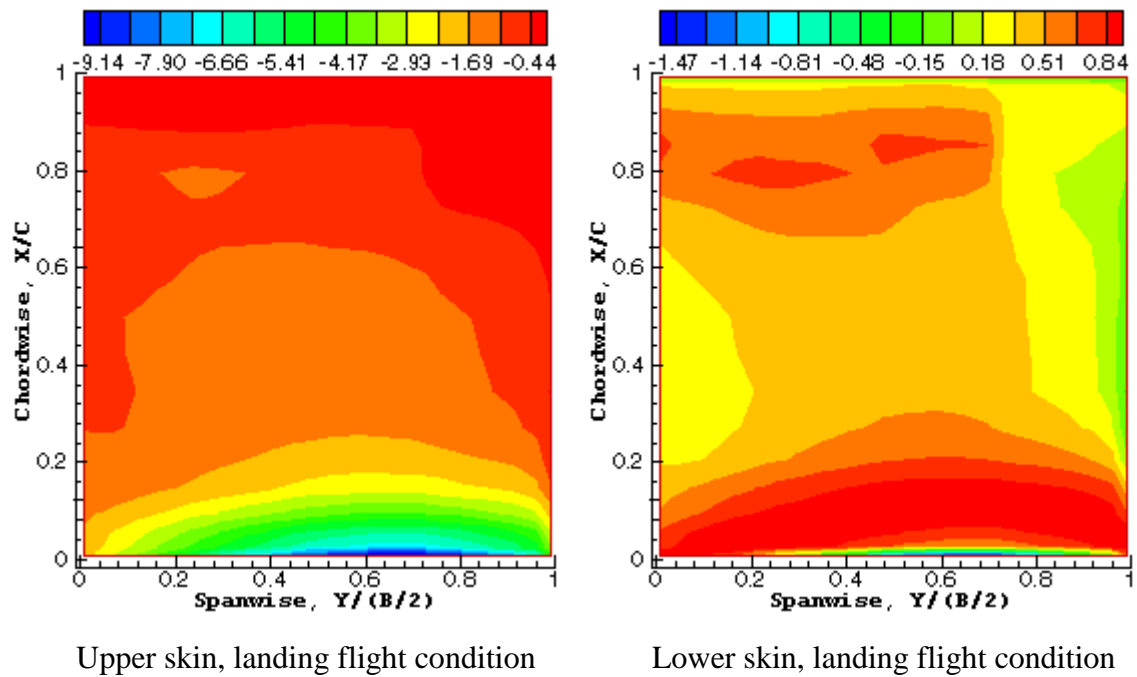


Figure 3.5.1(contd.): Coefficients of pressure distribution over BGE wing models at various flight conditions.

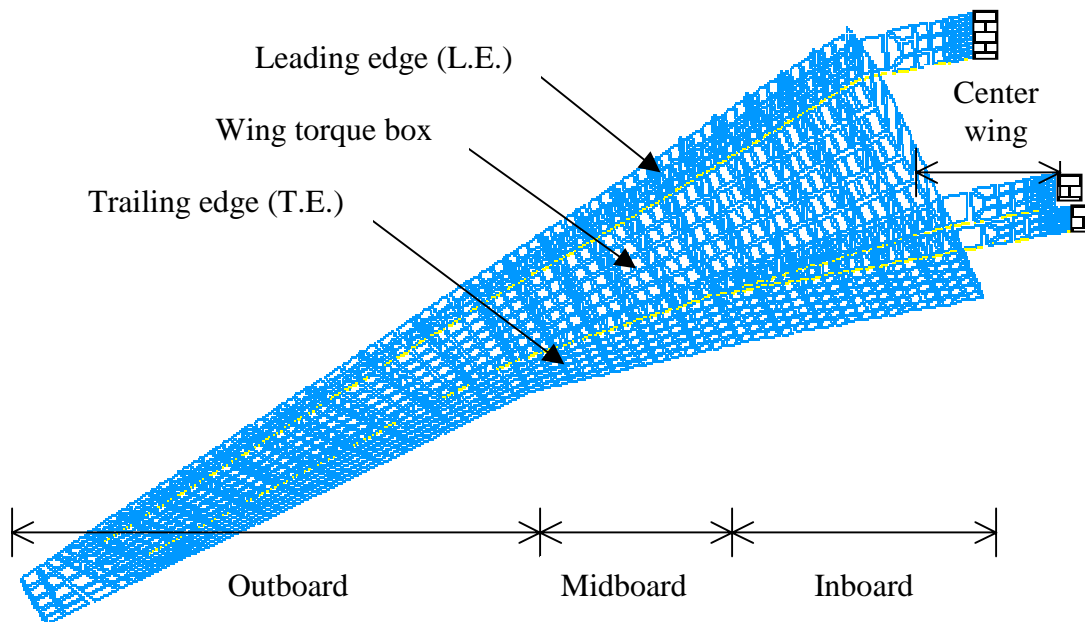


Figure 3.5.2: Finite element discretization of a representative general aviation wing subjected to aerodynamic and internal fuel loads.

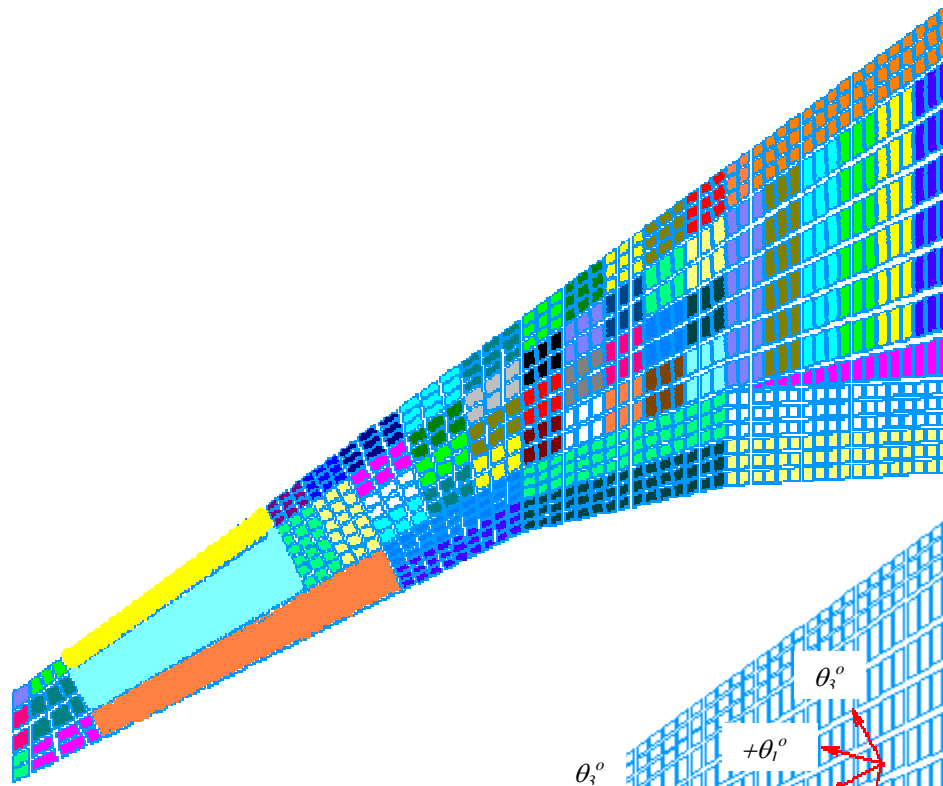
Table 3.5.3: Attributes of BGE wing substructures.

Substructure	Finite Element	Material	Failure Mode
Ribweb	CQUAD4 [†] & CTRIA3 ^{††}	2024T3 sheet	Shear buckling
Sparweb	CQUAD4	2024T3 sheet	Compression & shear buckling
Upper Spar Caps	CBEAM ^{†††}	2024T3 extrusion	Compression buckling
Lower Spar Caps	CBEAM	2024T3 extrusion	Tension sizing
Center Wing Sparweb	CQUAD4	7075T6 sheet	Compression & shear buckling
Center Wing Upper Spar Caps	CBEAM	2024T3 extrusion	Compression buckling
Center Wing Lower Spar Caps	CBEAM	2024T3 extrusion	Tension sizing

To implement the FS conceptual design, BGE wing skins are designed as monolithic composite skins. Figure 3.5.3(a) illustrates the rangewise DV definitions over upper and lower wing skins, which are carefully defined based on strain contours. The laminate family rosettes are also shown in Figure 3.5.3(b) from IB to OB sections. Similar design objective and constraints are imposed on BGE wing as described in the previous paragraphs. An additional constraint to this model is the peak wing tip deflection (CDIS) of 70.0 in. Figure 3.5.4 shows the nomenclature of BGE wing. The finite element and design optimization attributes for this model are listed in Tables 3.5.4 and 3.5.5. The resultant laminates based on baseline, Steering II and Steering III configurations are presented as layer-thickness contour and layer-angle mapping plots in Section 3.5.4.2.

[†] CQUAD4 is an isoparametric membrane-bending or plane strain quadrilateral plate element
^{††} CTRIA3 defines an isoparametric membrane-bending or plane strain triangular plate element
^{†††} CBEAM defines a beam element.

(a)



(b)

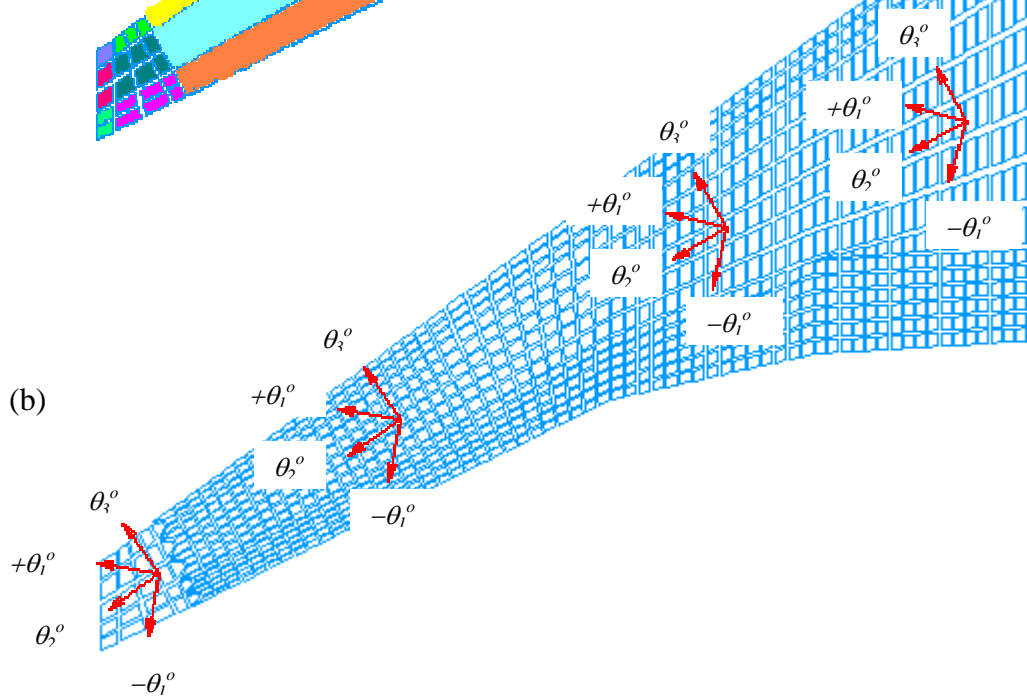


Figure 3.5.3: Schematics of (a) rangewise DV definitions (same-color ranges of elements carry identical material properties) and (b) laminate family rosettes of BGE wing.

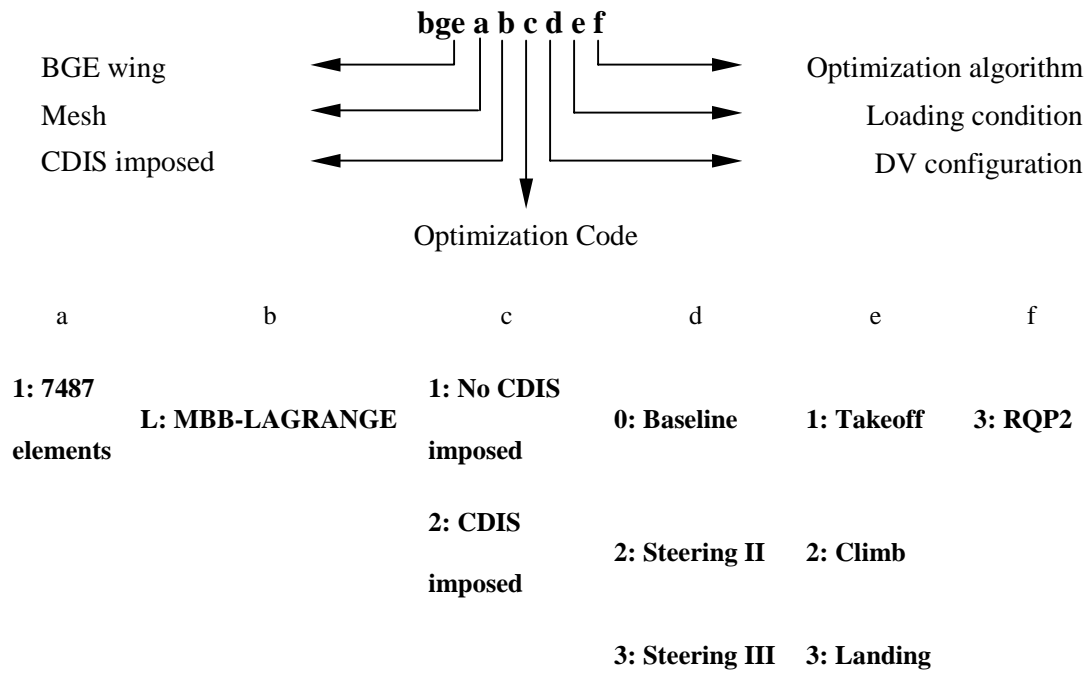


Figure 3.5.4: Nomenclature of a representative regional jet wing.

Table 3.5.4: Finite element and design optimization attributes for representative aircraft structural components.

Attributes	pb2	bge11	bge12	F22
Number of Elements	1604	7487	7487	4444
Number of Nodes	563	2212	2212	1032
Number of DOFs	2675	13005	13005	6132
Number of Sizing or Layer-thickness Design Variables	672	354	354	210
Number of Constraints	3167	13505	13515	3184

Table 3.5.5: Lists of number of layer-angle design variables for representative aircraft structural components in Steering II, and III configurations.

Model	Steering II	Steering III
pb2	494	224
bge11	354	118
bge12	N/A	118
F22	210	70

3.5.2 A Representative Aft Pressure Bulkhead of a General Aviation Aircraft.

A representative aft pressure bulkhead of a general-aviation passenger cabin (Cessna, Raytheon, Learjet, Dassault, Gulfstream, etc.) has been identified to demonstrate the application of FS conceptual design. Typical pressure bulkheads, which are made of isotropic material such as aluminum, are reinforced with longerons and other stiffeners⁵⁴. For composite pressure bulkheads, they are usually configured as monocoque structures with several plies of prepreg cloth. Traditionally, these prepreg cloth are hand-laid up on a male mandrel and cured in the autoclave environment. An example of this aft pressure bulkhead is that of the Raytheon Premier I⁵⁵. Raytheon employs FiberSIM^{9,10} to simulate how the fibers conform to the complex contour and generate appropriate flat patterns for hand lay-up. As depicted in Figure 3.5.5, darts and splices are made to reduce fiber distortion and eliminate fiber wrinkling and tears. The resultant structure weights only 11 lbs, which consists of three plies of 0.0085 inch thick prepreg. It has been tested to withstand an ultimate static pressure of 16.8 psi. However, major expenditure for this structure is the costly hand lay-up fabrication method. Therefore, it is desired to implement FS conceptual design to this structure so that the fabrication process can be automated with the fiber placement. This will substantially reduce the cost of manufacturing with minimal labor fees. Also, it is possible to eliminate the design and analysis via FiberSIM, while controlling the problems associated with the geometrical-induced fiber distortion, wrinkling and tears. In this case, darts and splices may not be necessary. A path generator, such as ACRAPLACE or SCADS, may be required to simulate the placement of each individual tow onto the mandrels.

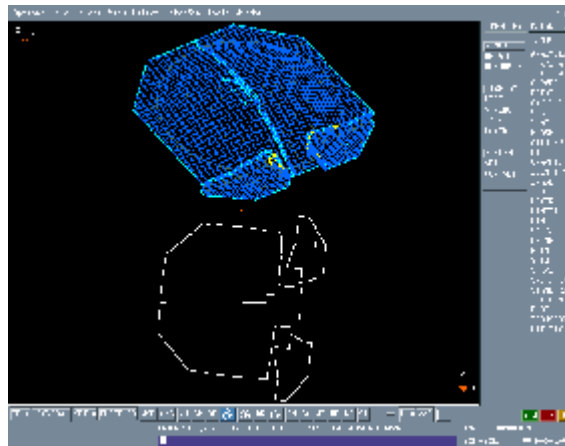


Figure 3.5.5: FIBERSIM screen dump showing darts and splices added to the virtual plies of an aft pressure bulkhead of Raytheon Premier I (copied from Ref. 55).

The representative geometry, loads, and finite element discretization have been established with MSC/PATRAN and MSC/NASTRAN. The geometry is assumed to be a spherical cap of 67.25-in diameter and 8.3-inch maximum depth (part of a 72.6-in radius sphere). The dome bulkhead is uniformly attached to the fuselage shell with a flange, which adhesively bonded and riveted to the shell and the bulkhead. The operating pressure of this model is assumed to be 8.4 psi. The pressure bulkhead is designed to meet an ultimate pressure of 16.8 psi. CONVERT, a simple FORTRAN 77 code based on MSC/NASTRAN input format, is written to convert surface pressure into nodal pressure loads. This is to account for the inability of MBB/LAGRANGE to transform surface pressure into nodal forces because it only supports membrane elements.

Figure 3.5.6 represents the finite element discretization (CQUAD4 membrane) of a quarter spherical pressure bulkhead subjected to a cabin pressure of 16.8 psi. Due to symmetry, only a quarter of the pressure bulkhead is modeled. The layer-angle mappings for the initial laminate, which constitute the laminate family rosettes, are illustrated in Figure 3.5.7. The longitudinal axes of the principal material coordinate (red vectors) are shown in Figure 3.5.6. Attributes of this model can be found in Tables 3.5.4 and 3.5.5, while the nomenclature is described in Figure 3.5.8.

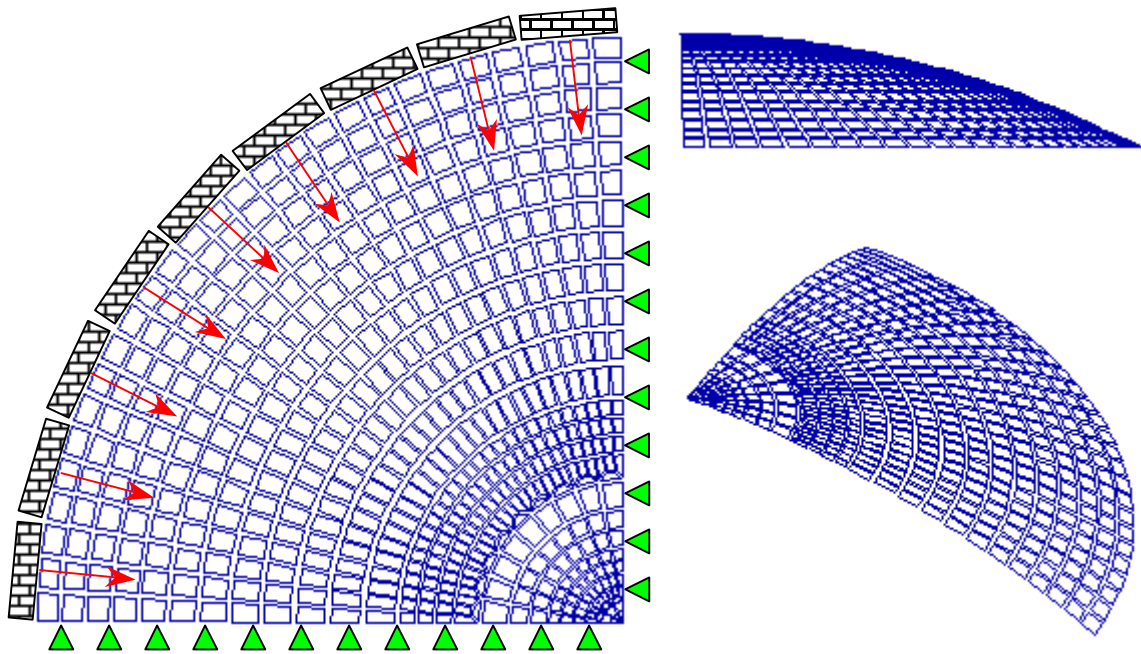


Figure 3.5.6 Finite element discretization of a representative pressure bulkhead under cabin pressure in (a) planar, (b) side, and (c) isometric views.

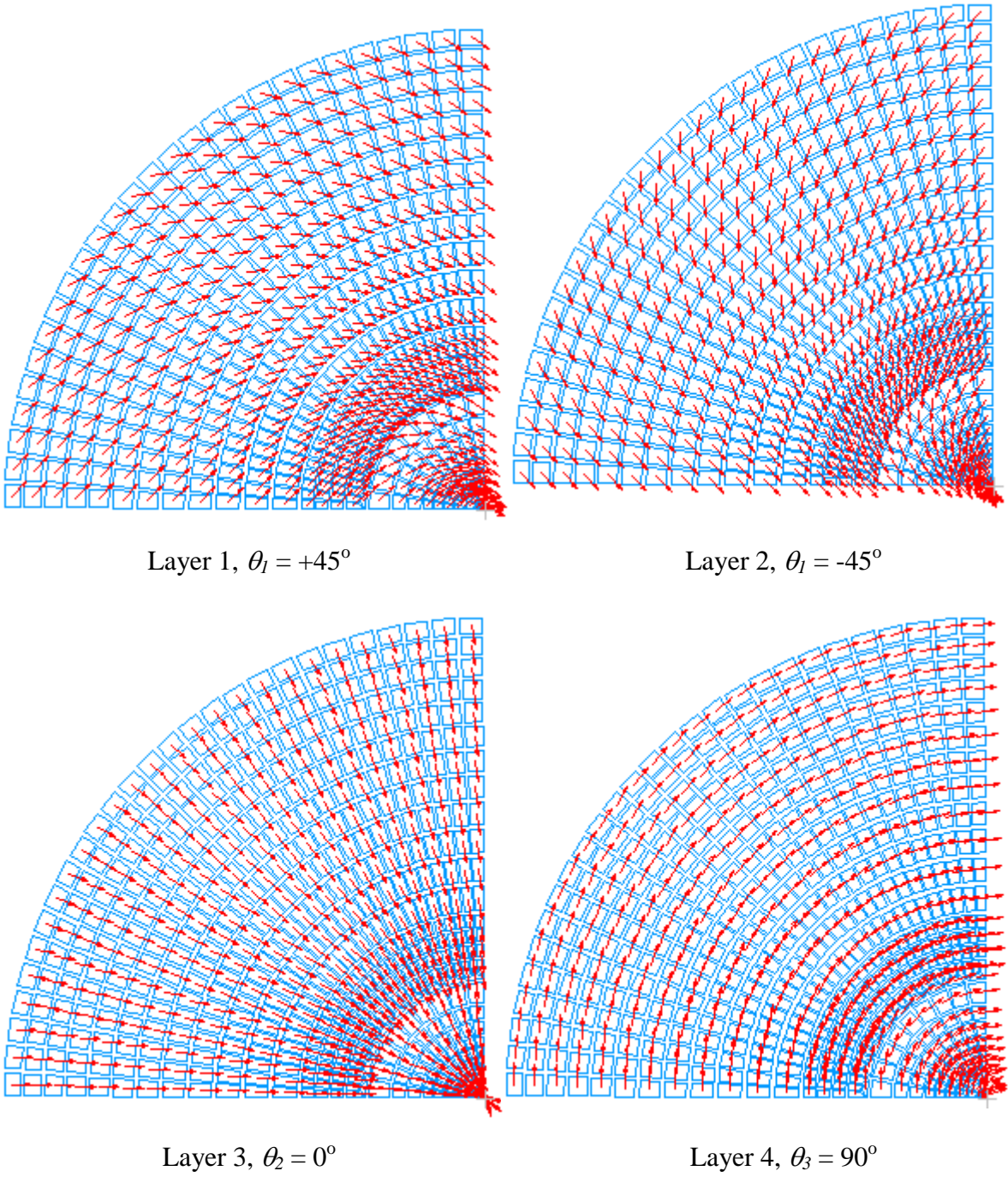


Figure 3.5.7: Layer-angle mappings for baseline design of pb2 model.

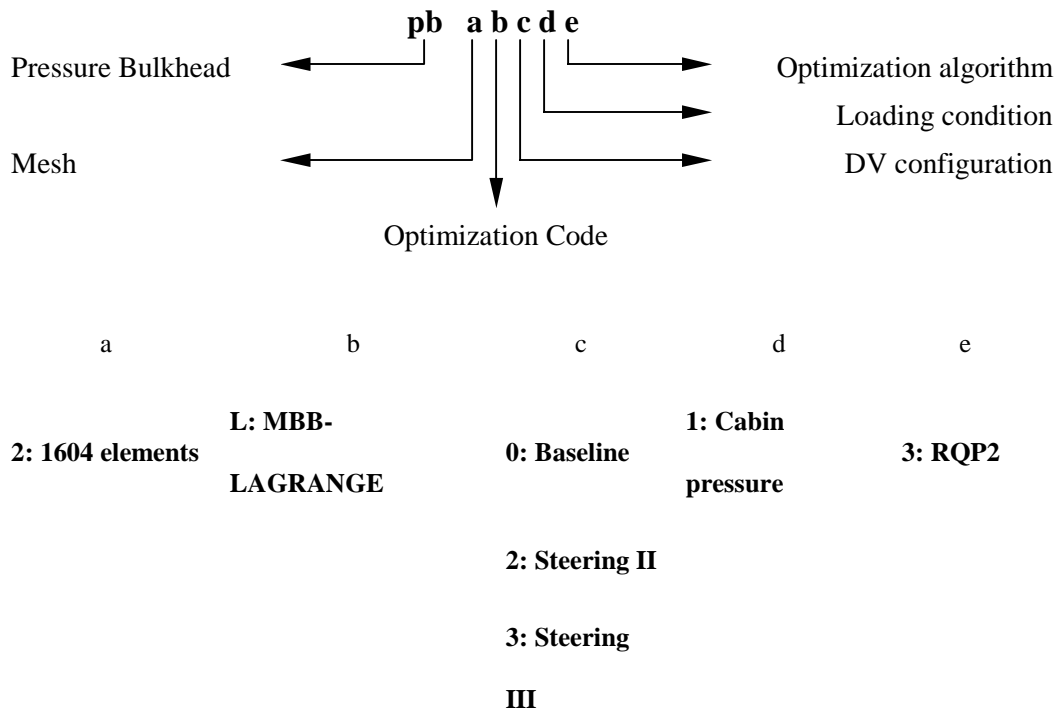


Figure 3.5.8: Nomenclature of a representative aft pressure bulkhead.

The resultant laminates based on FS conceptual design are presented as layer-thickness contour and layer-angle mapping plots in Appendix E.1.

3.5.3 A Representative Horizontal Stabilator of a Tactical Fighter.

A representative horizontal stabilator of a tactical fighter (F15, F18, F22, etc) has been selected for investigating the use of FS conceptual design in military aircraft. The representative geometry and aerodynamic loads at high speed and altitude have been established based on F22 horizontal stabilator. Figure 3.5.9 shows the finite element discretization of the horizontal tail. It is a all-movable five-edged horizontal tail with aspect ratio of 0.7, tail area of 136 ft², tail span of 29 ft, tail sweep of 42 degrees at leading edge (L.E.) and 17 degrees forward at trailing edge (T.E.), and no dihedral or twist. Tail surfaces are modeled as aluminum honeycomb cores with bonded composite skins. The airfoil shape is based on NACA 0008 biconvex airfoil. The pivot shaft of the tail, an IM7/977-3 (graphite/epoxy) towpreg part, is a 10-in diameter cylinder at the tail root and an approximately 4-in wide rectangular spar at the tail tip. It has been fabricated by Alliant Techsystems using state-of-the-art FP manufacturing⁵⁶. The pivot shaft serves as the structural spar of the horizontal stabilator and is attached to the fuselage's bell crank housing. Table 3.5.6 summarizes the attributes of F22 horizontal stabilator substructures.

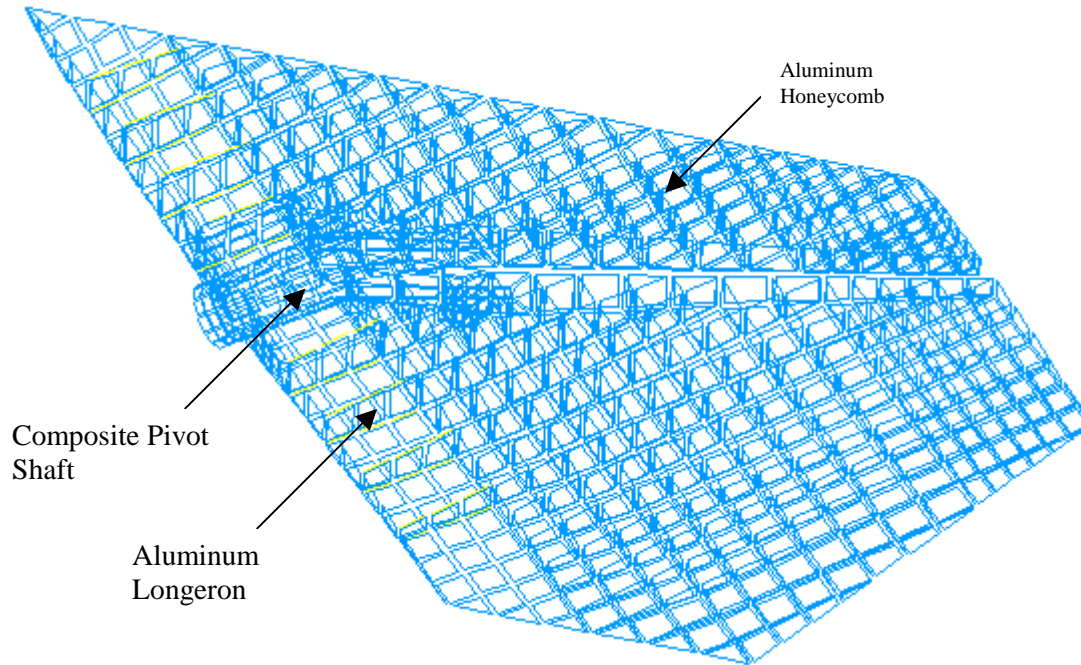


Figure 3.5.9 Finite element discretization of a representative military horizontal stabilator subjected to aerodynamic loads at high speed and altitude.

Table 3.5.6: Attributes of F22 horizontal stabilator substructures.

Substructure	Finite Element	Material	Failure Mode
Ribweb	CSHEAR [†] & CTRIA3	7075T6 sheet	Shear buckling
Spar	CQUAD4	IM7/977-3 towpreg	STRN ^{††}
Longeronweb	CQUAD4	7075T6 sheet	Compression & shear buckling
Honeycomb core	CSHEAR	5052 sheet	Shear buckling

[†] CSHEAR defines a shear panel element
^{††} STRN is maximum strain failure criterion.

Two flight conditions, namely high and low angle of attack (AOA) maneuvers, have been chosen and documented in Figure 3.5.10 via VORSTAB. The high AOA flight condition is selected and demonstrated based on FS conceptual design. Critical load factor of 9.0 and safety factor of 1.5 are imposed respectively on the model. The laminate family rosettes are shown in Figure 3.5.11 for different layers. Rangewise DV definitions over the upper and lower composite skins are shown in Figure 3.5.12, which are described based on strain contours. Similar design objectives and constraints are performed on this model, where the model's nomenclature is depicted in Figure 3.5.13. The resultant laminates based on baseline, Steering II and Steering III configurations are presented as layer-thickness contour and layer-angle mapping plots in Appendix E.2.

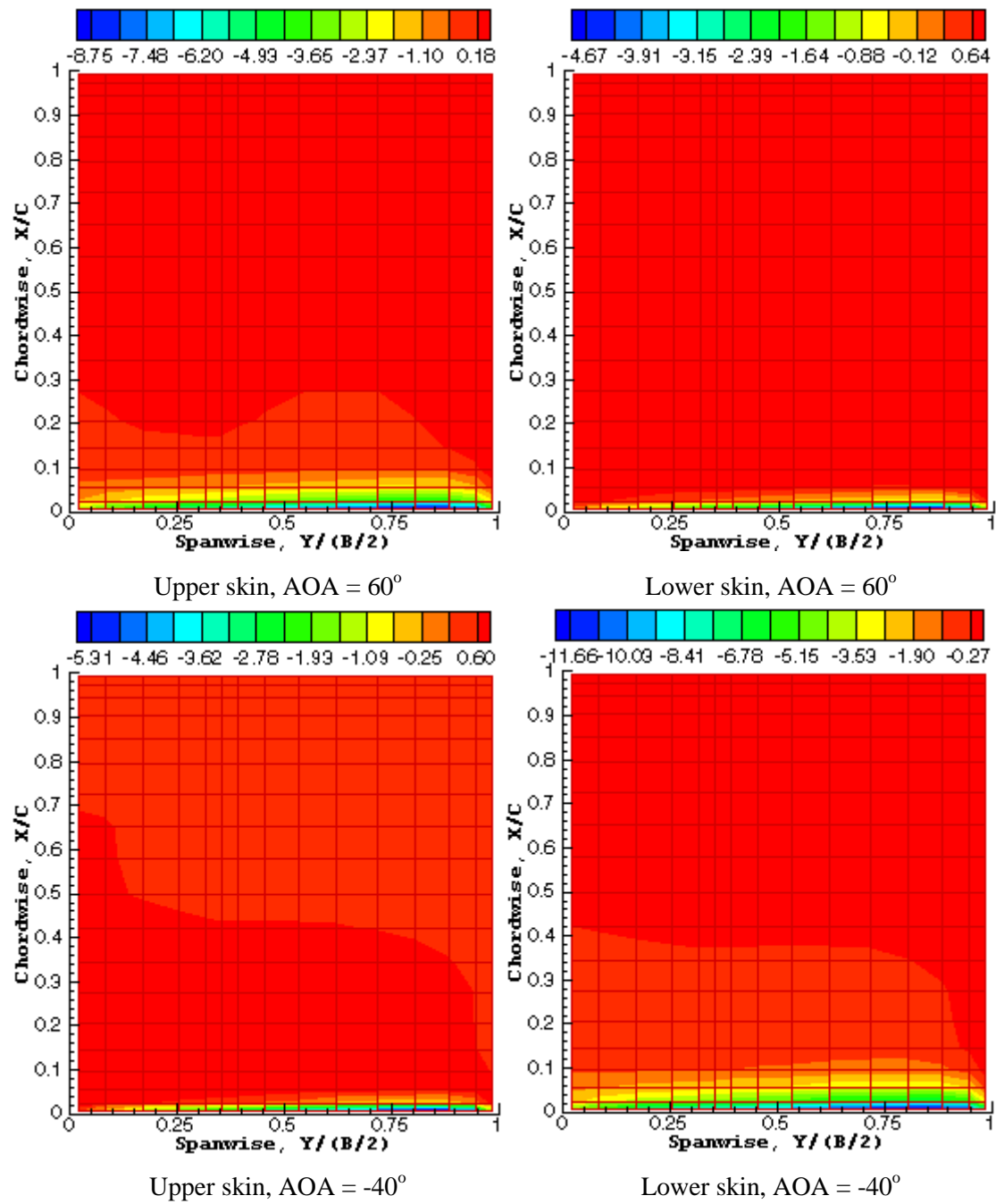


Figure 3.5.10: Coefficients of pressure distribution over F22 horizontal stabilator at various flight conditions.

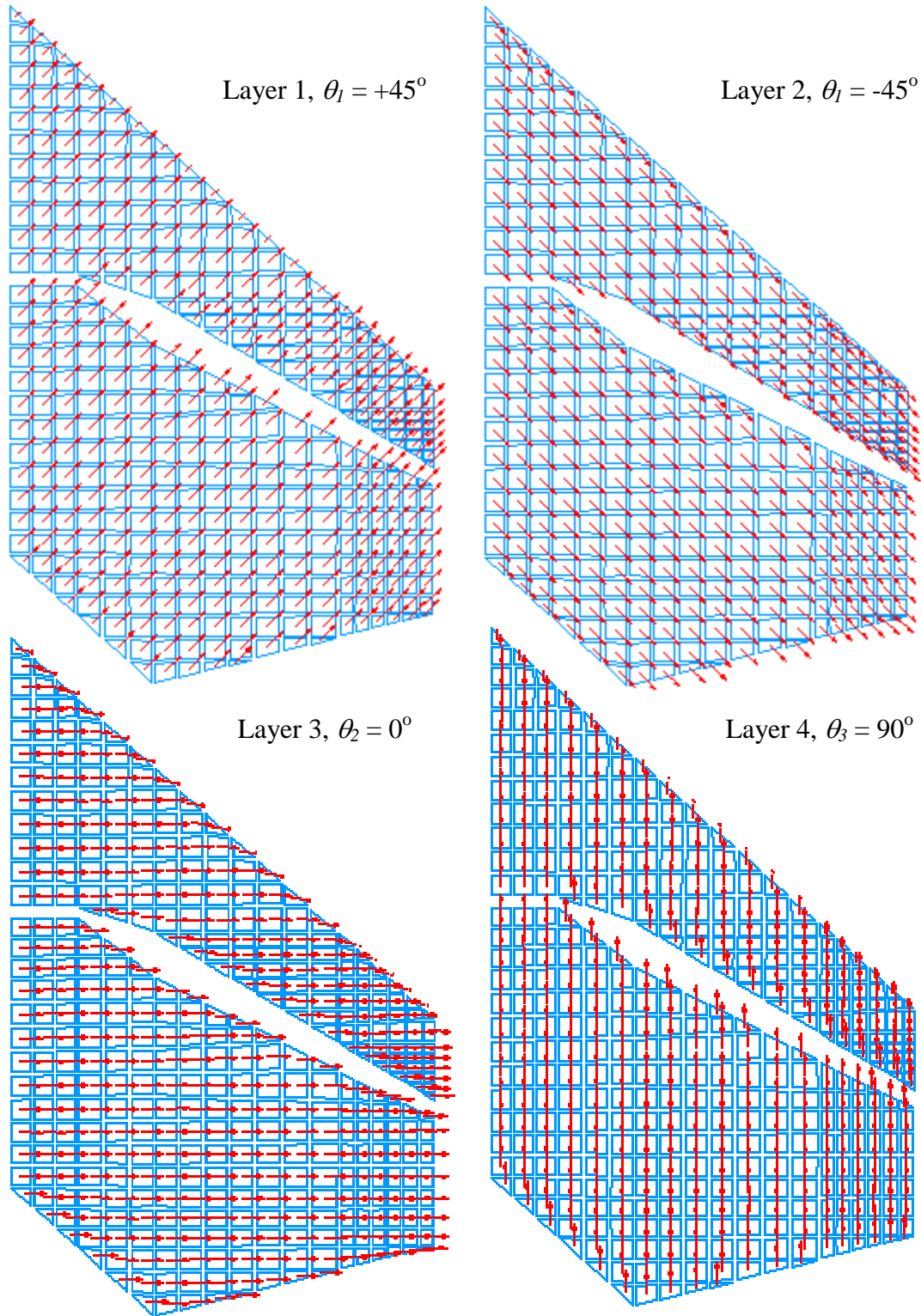


Figure 3.5.11: Layer-angle mappings for baseline design of F22 model.

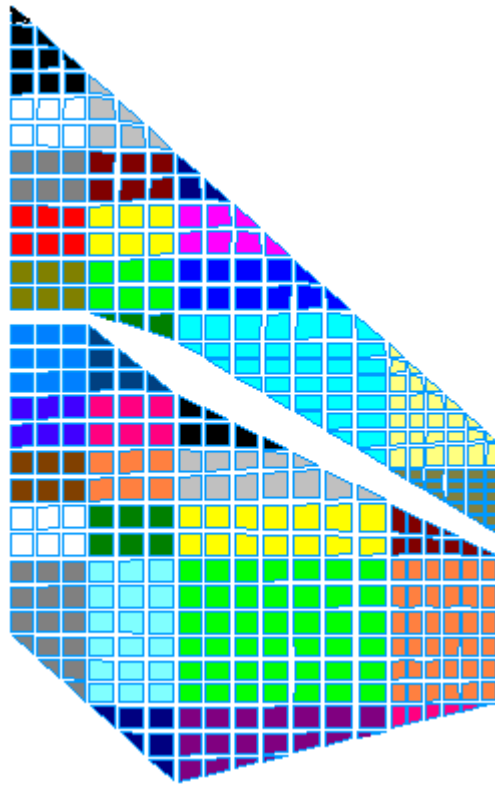


Figure 3.5.12: Schematics of rangewise DV definitions for F22 model (same-color ranges of elements carry identical material properties).

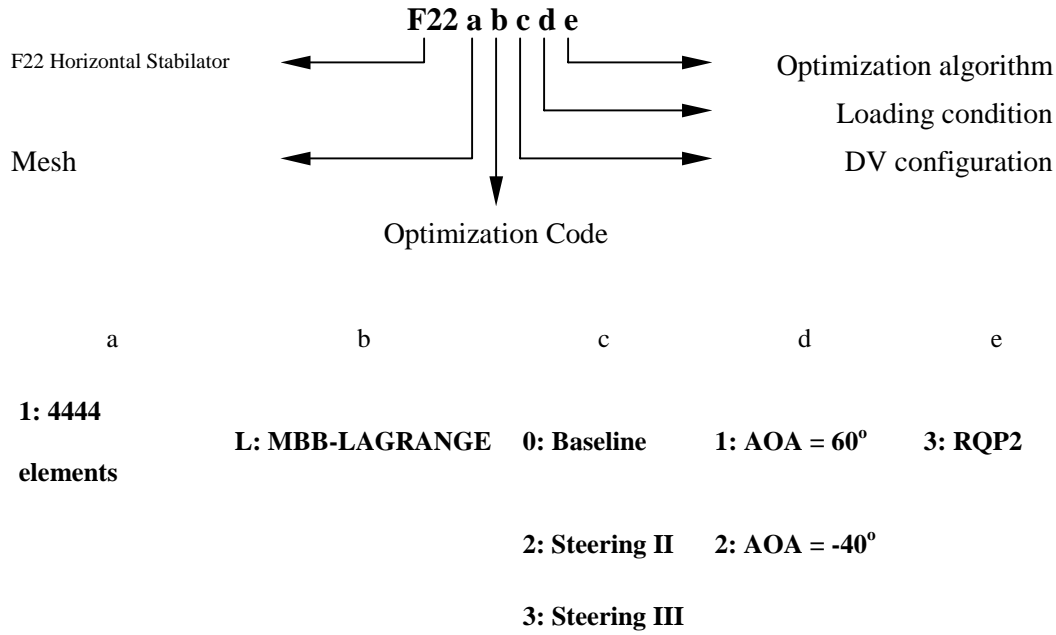


Figure 3.5.13: Nomenclature of a representative horizontal stabilator.

3.5.4 Results and Discussion

Three representative aircraft primary and secondary structural components have been studied to demonstrate potential payoffs of using FS conceptual design. The models are established with MSC/PATRAN, analyzed with MSC/NASTRAN, and finally optimized with MBB-LAGRANGE. The optimal designs of BGE wing are presented in the following paragraph, while pb2 and F22 models are shown in Appendix E as layer-thickness contours and layer-angle mappings. In layer-thickness contours, there are four plots:

- ➔ Total layer thickness in inches, t_{all} , at page top left, denoted as (a)
- ➔ 1st and 2nd layer thickness in percentage, $2t_1$, at page top right, denoted as (b)
- ➔ 3rd-layer thickness in percentage, t_2 , at page bottom left, denoted as (c)
- ➔ 4th-layer thickness in percentage, t_3 , at page bottom right, denoted as (d)

On the other hand, four layer-angle mappings are presented respectively as:

- ➔ Curvilinear fiber format of $+\theta_l^\circ$ layer at page top left, denoted as (a)
- ➔ Curvilinear fiber format of $-\theta_l^\circ$ layer at page top right, denoted as (b)

- Curvilinear fiber format of θ_2° layer at page bottom left, denoted as (c)
- Curvilinear fiber format of θ_3° layer at page bottom right, denoted as (d)

3.5.4.1 Weight savings of Structures Exhibiting Steered-Fiber Architecture.

Table 3.5.7 summarizes the weight savings for representative aircraft structural components using FS conceptual design. As predicted in BGE wing, the greatest weight reduction is seen with Steering II configuration for up to 17% followed by Steering III configuration for up to 11% in the static case. However, further verifications and sound decisions must be made because of the unbalanced nature of Steering II configuration. In addition, Steering III yields balanced results w.r.t. the primary material coordinate. Weight savings associated with the pressure bulkhead (pb2) and the horizontal stabilator (F22 model) are not representative because it is composed of minimum-gage laminates and the layer-orientation mappings are not smooth.

With the presence of CDIS constraints, both baseline and Steering III configurations of the bge12 model are about 45% heavier than the bge11 model. For bge12 model, the Steering II configuration is not converged due to tremendous computations in the DV-to-constraint sensitivity analyses. This problem can be resolved if the number of DV is reduced while increasing the percentage of constraint restriction, POR, to allow only violated constraints in sensitivity analyses.

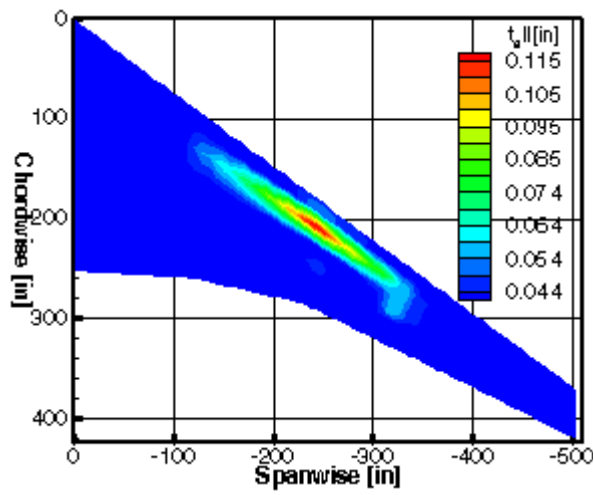
Table 3.5.7: Summary of structural weight savings for representative aircraft structural components using FS conceptual design.

Model	Weight saving [%] with FS conceptual design	
	Steering II	Steering III
Representative Pressure Bulkhead, pb2	4.0	2.3
Representative Wing, bge11	16.8	10.5
Representative Horizontal Stabilator, F22	29.6	6.5
Maximum weight savings [%], static	29.6	10.5

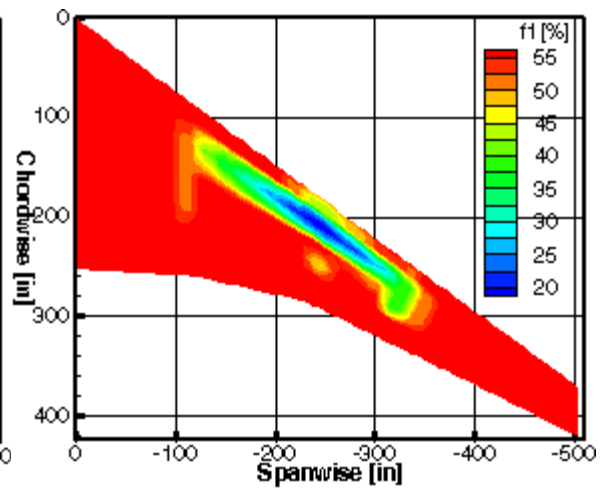
3.5.4.2 Representative Wing Structure of General-Aviation Aircraft.

The BGE model has been set up to study potential advantages associating with FS conceptual design. Table 3.5.7 lists weight savings based on Steering II and III only. From the results, Steering II has a greater payoff as predicted. Note that the resultant laminates corresponding to Steering II may not be realistic because of the unbalanced issue. The bge12 model is about 45% heavier than the bge11 model due to CDIS constraints.

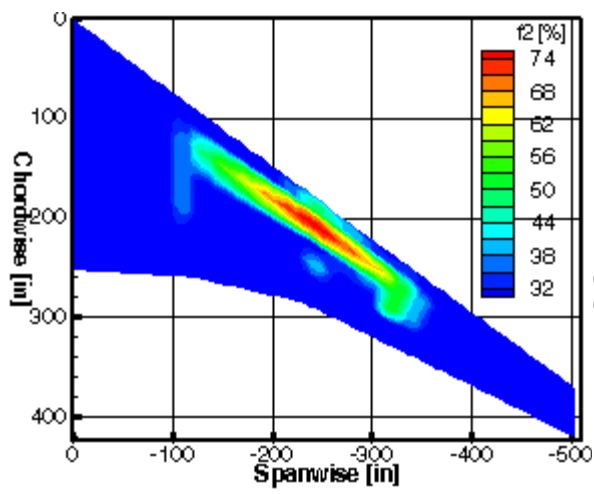
Figures 3.5.14 and 3.5.15 represent layer-thickness contours of the baseline bge11 model or bge11L013. From Figures 3.5.14(a) and 3.5.15(a), more reinforcements are gathered around the wing torque box in the midboard and outboard of the lower and upper skins. Here, the 0° layer becomes significant due to axial tensile (lower skin) and compressive (upper skin) loads, respectively. Comparing Figures 3.5.14(c) and 3.5.15(c), the upper skin has more materials than the lower skin. Layer-thickness contours are more widespread in the upper skin than in the lower skin. At the peak layer-thickness contour, the laminate family is approximately (75/20/5) for both skins. On the other hand, the off-axis layers (Figures 3.5.14(b) and 3.5.15(b)) provide key reinforcements to the leading edge (L.E.) and trailing edge (T.E.) of the lower and upper skins due to shear loads. Note that the 90° layer (Figures 3.5.14(d) and 3.5.15(d)) also contributes to shear reinforcements at L.E. and T.E. In fact, both $\pm 45^\circ$ and 90° layers exhibit almost identical contour trends. However, 90° family is relatively lower than $\pm 45^\circ$ and 0° families. This is illustrated at L.E. and T.E, where the peak laminate family is (30/55/15).



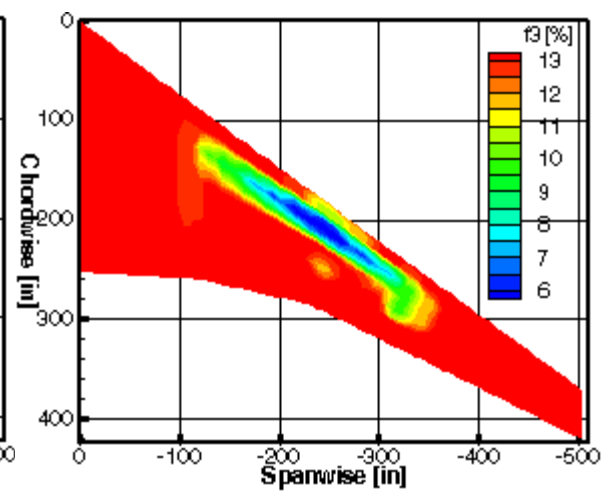
(a)



(b)



(c)



(d)

Figure 3.5.14: Layer-thickness contours for bge11L013 lower skin.

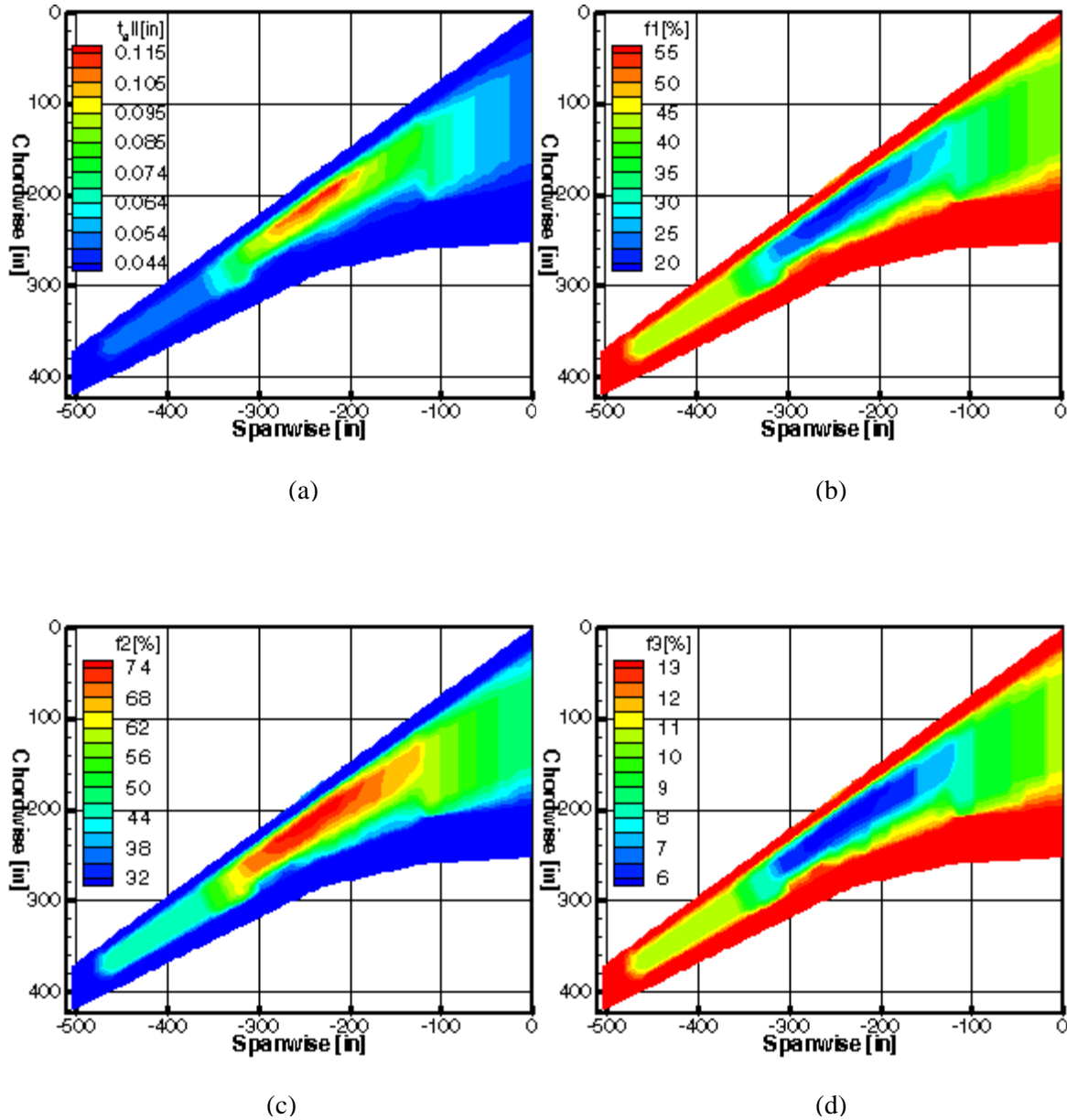


Figure 3.5.15: Layer-thickness contours for bge11L013 upper skin.

Figures 3.5.16 to 3.5.17 show layer-thickness contours for bge12L013 based on the baseline configuration. Basically, the total layer-thickness plot for bge12L013 shares similar contours with bge11L013. With the additional inclusion of CDIS constraints, the reinforcements of both upper and lower skins are quite alike, especially at the wing torque box. Similarly, the 0° layer is dominant at these locations due to wing bending stresses, where the peak laminate family is (85/10/5) in Figures 3.5.16(c) and 3.5.17(c). $\pm 45^\circ$ layers actively contribute to the wing's shear

reinforcements and tip deflection, especially at L.E. and T.E. The 90° layer is insignificant to the overall reinforcement. However, the layer-thickness contours for both $\pm 45^\circ$ and 90° layers are almost identical.

Figures 3.5.18 to 3.5.21 show layer-thickness contours and layer-angle mappings for bge11L213 based on Steering II configuration. In Figures 3.5.18(a) and 3.5.20(a), the total layer-thickness contours for this configuration demonstrate more reinforcements in the wing torque box, especially at the midboard-outboard section of the upper skin. Compared with the baseline, the contours corresponding to Steering II configuration are more concentrated and narrow. This is because of the absence of CDIS constraints. For the most part, axial-reinforcements play a major role in wing stiffening, which are attributed to θ_2° and a portion of $\pm\theta_1^\circ$ layers. Noticeably in Figures 3.5.18(c) and 3.5.20(c), the laminate family at peak contours behaves like a (35/55/10) in the lower skin and (60/30/10) in the upper skin, respectively. Apparently in Figures 3.5.19(a) and 3.5.19(b), $\pm\theta_1^\circ$ layer orientations in the lower wing's torque box are aligned to follow the axial axes of the local material coordinates depicted in Figure 3.5.7. Consequently, they provide axial reinforcements due to wing bending. Initially configured as the 0° layer, the θ_2° layer orientations are also steered in the axial direction from inboard to outboard w.r.t. the local material coordinates (see Figure 3.5.19(c)). At the tip of wing, both upper and lower skins are primarily stiffened with $\pm\theta_1^\circ$ layers due to tip shear and deflection. Here, the laminate family is (30/55/15) for both skins. The layer orientations are tailored to become off-axis direction at the tip, which is observed in Figures 3.5.19(a) and 3.5.19(b) for lower skin, and Figures 3.5.21(a) and 3.5.21(b) for upper skin. At the inboard's L.E., $\pm\theta_1^\circ$ layers are dominant. In Figures 3.5.19(a), 3.5.19(b), 3.5.21(a) and 3.5.21(b), the fiber angles are steered due to shear loads. On the other hand, reinforcements associated with θ_3° layer are not significant. In Figures 3.5.19(d) and 3.5.21(d), θ_3° layer angles seem to settle in off-axis and transverse directions w.r.t. θ_2° layer, providing transverse reinforcements to the wing.

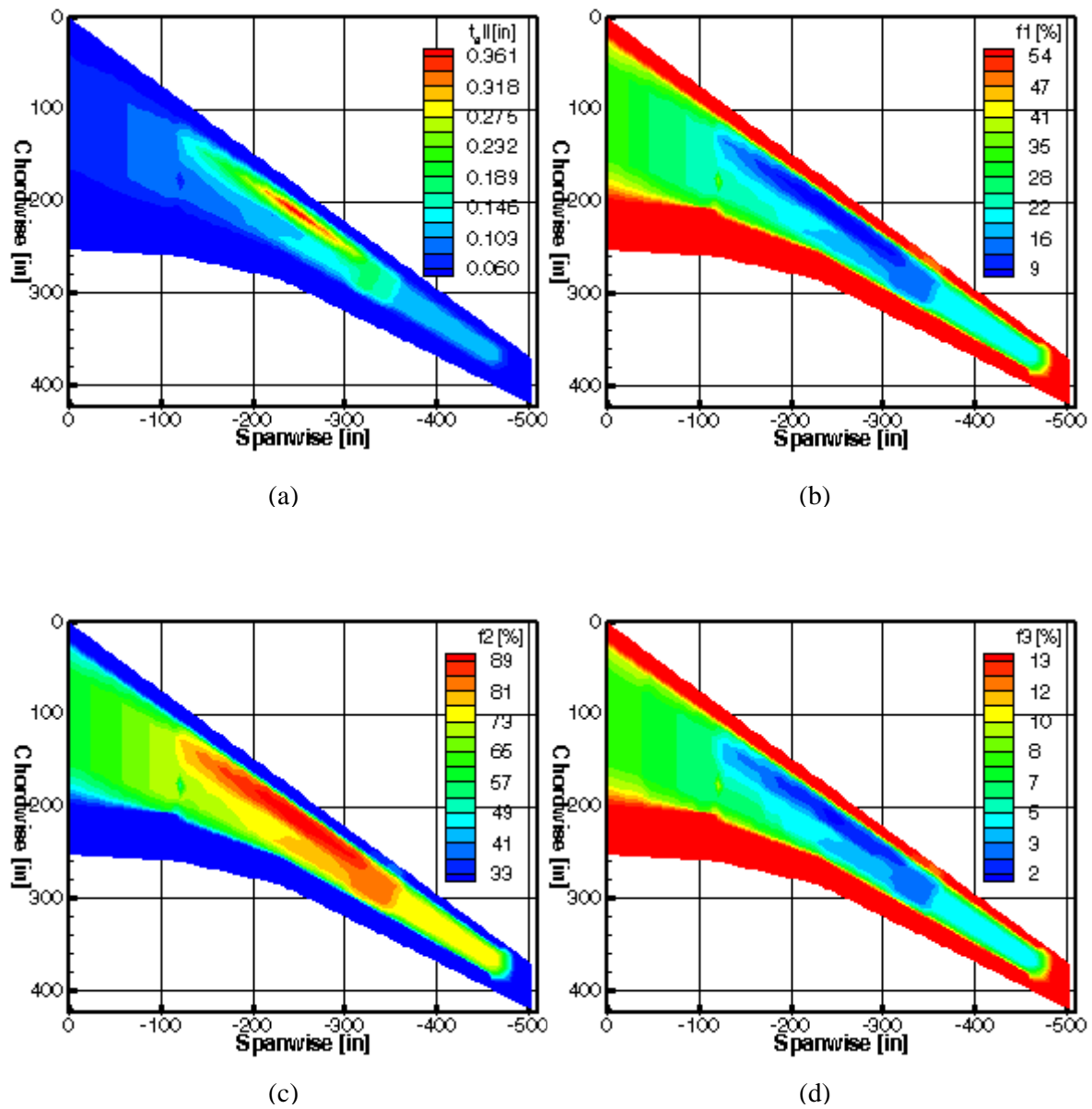


Figure 3.5.16: Layer-thickness contours for bge12L013 lower skin.

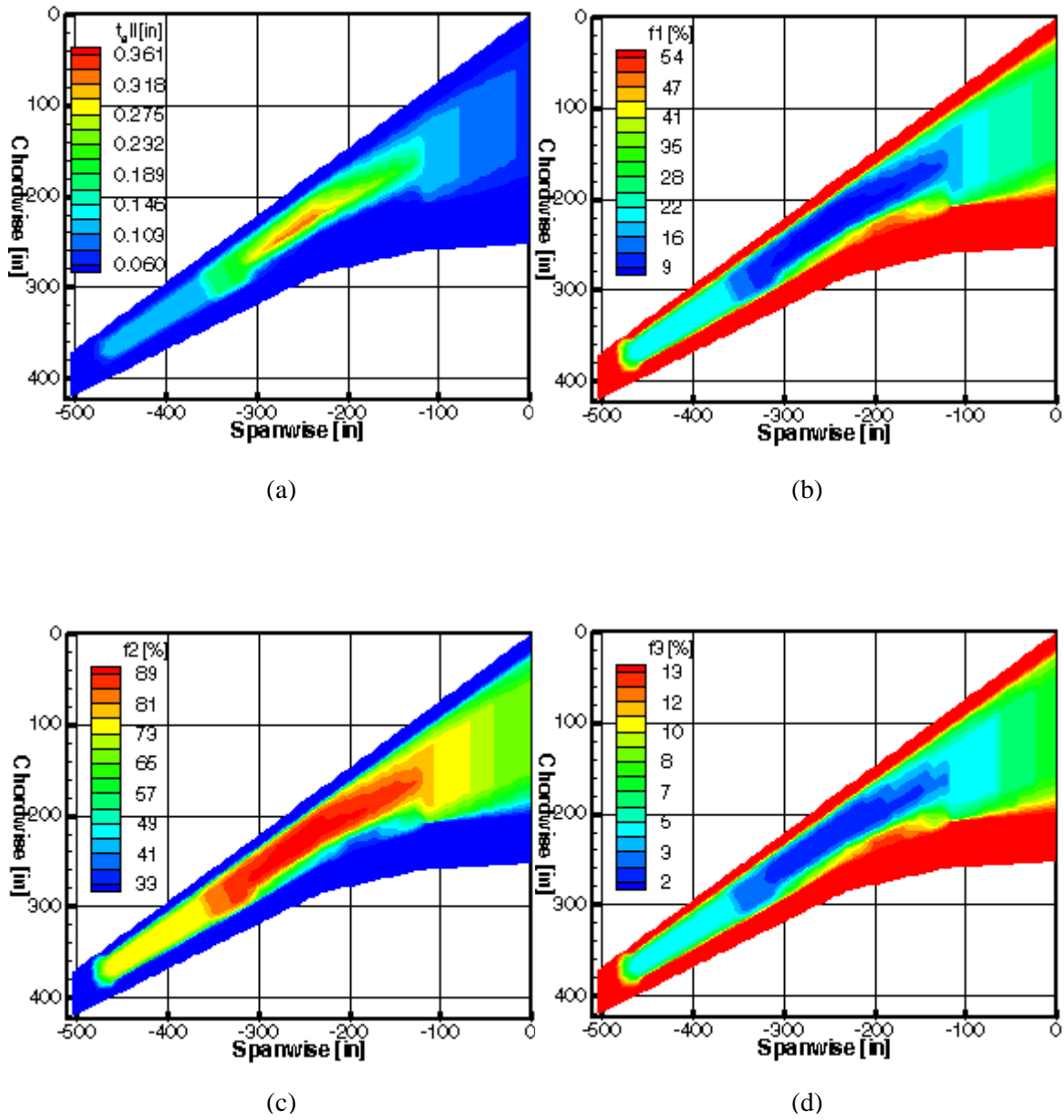
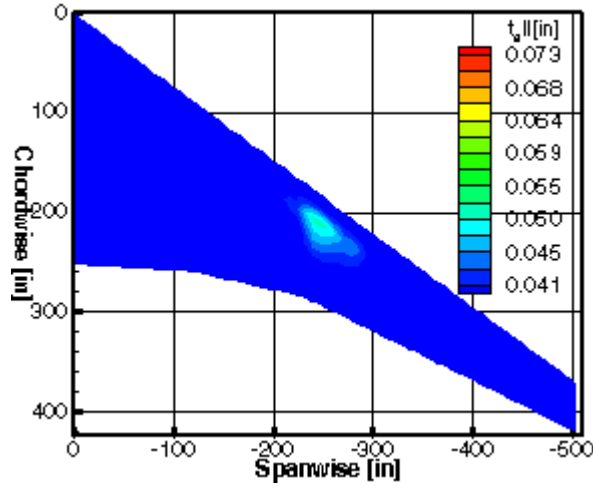
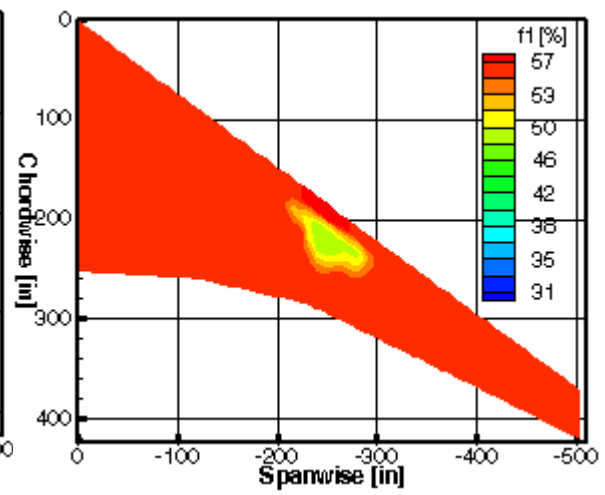


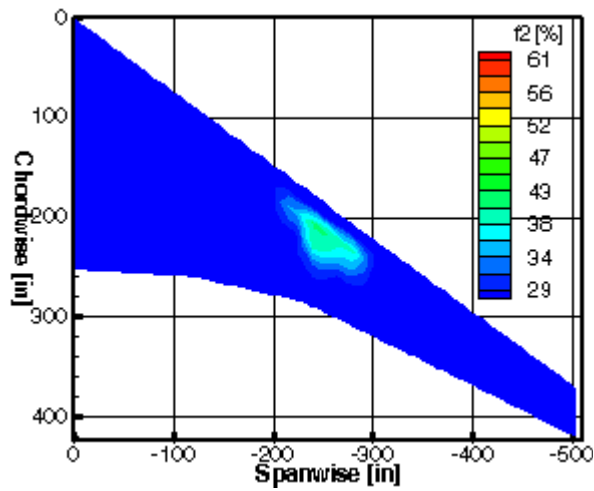
Figure 3.5.17: Layer-thickness contours for bge12L013 upper skin.



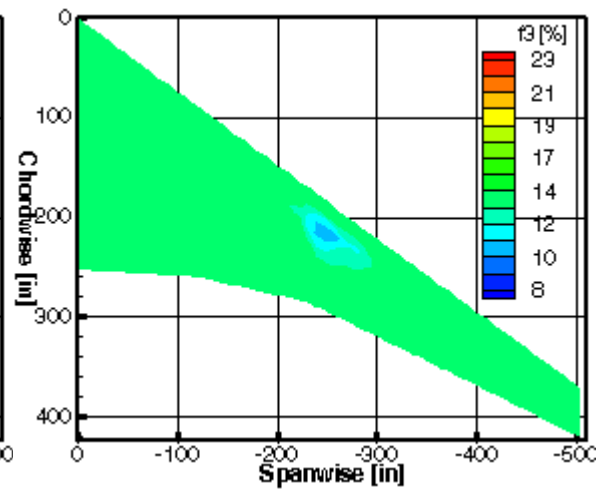
(a)



(b)



(c)



(d)

Figure 3.5.18: Layer-thickness contours for bge11L213 lower skin.

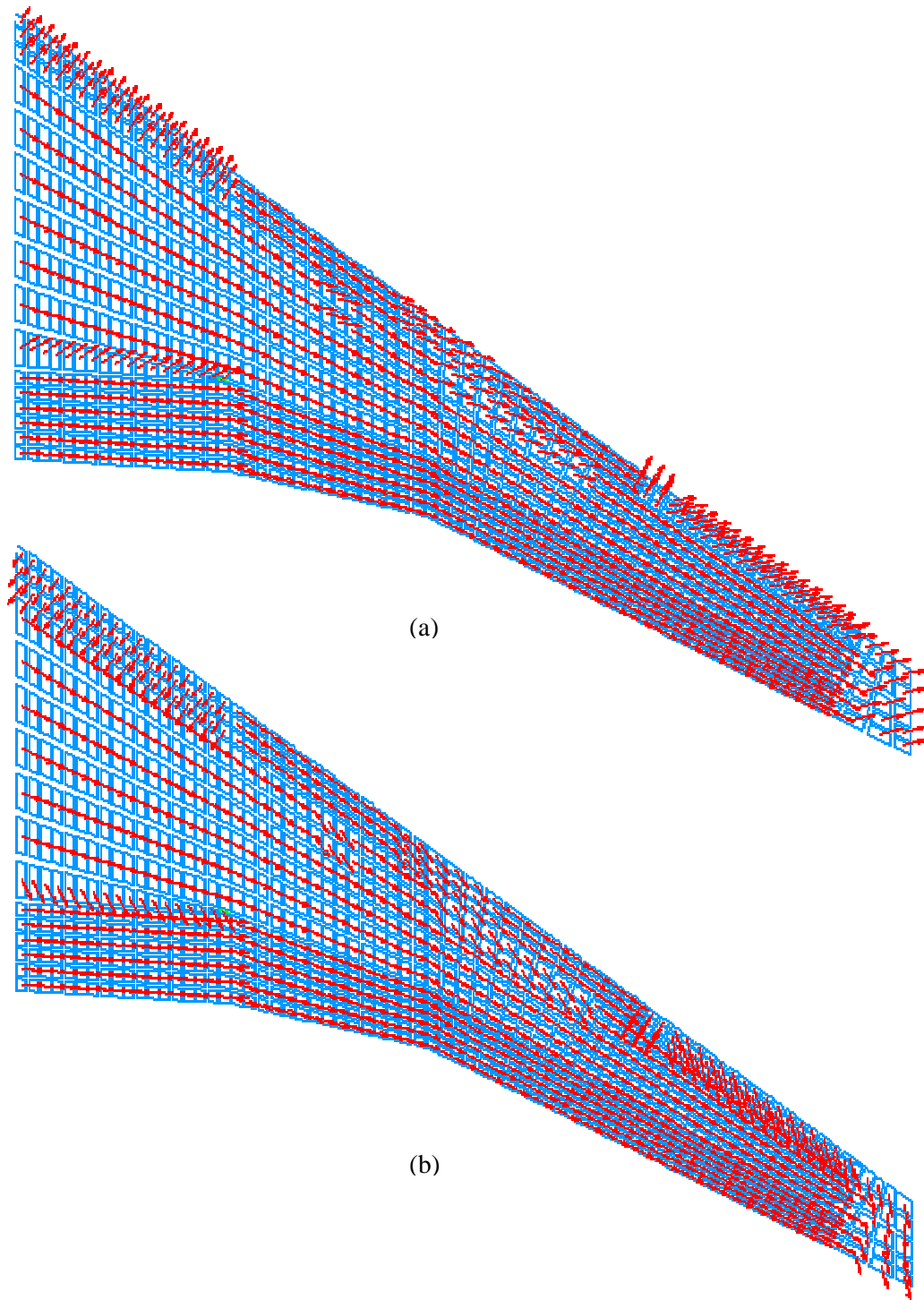


Figure 3.5.19: 1st and 2nd layer-angle mappings for bge11L213 lower skin.

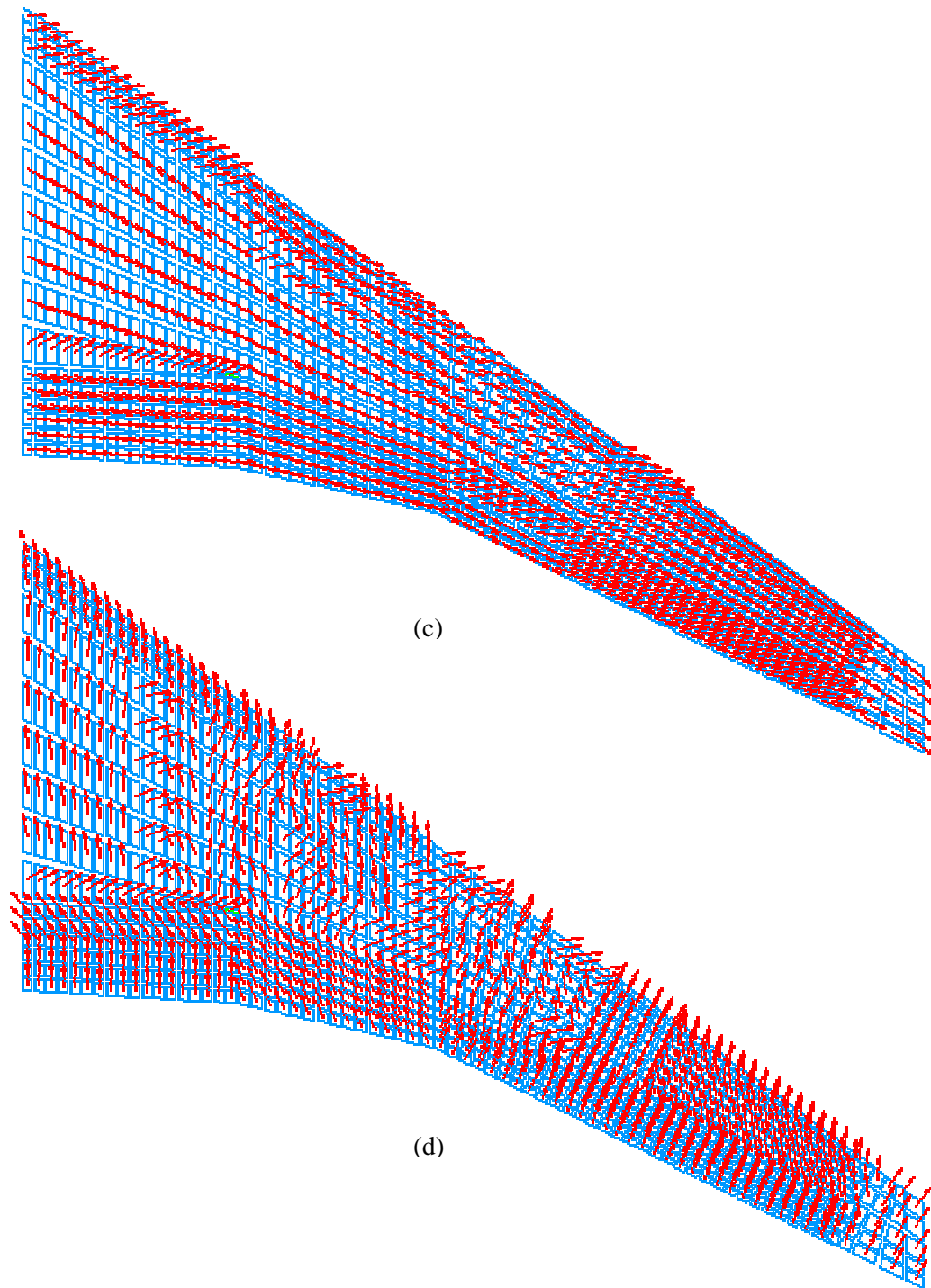


Figure 3.5.19(contd.): 3rd and 4th layer-angle mappings for bge11L213 lower skin.

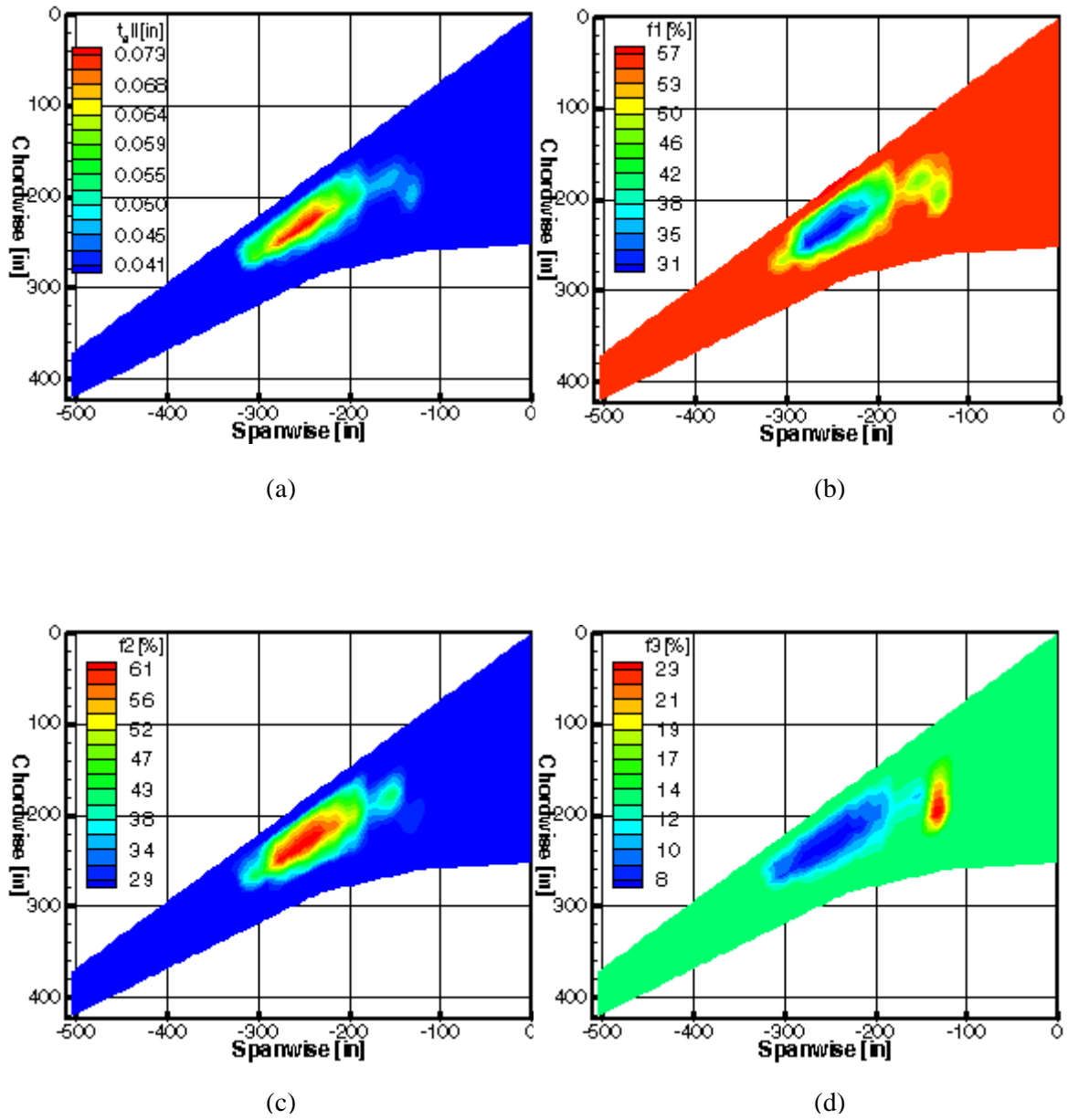


Figure 3.5.20: Layer-thickness contours for bge11L213 upper skin.

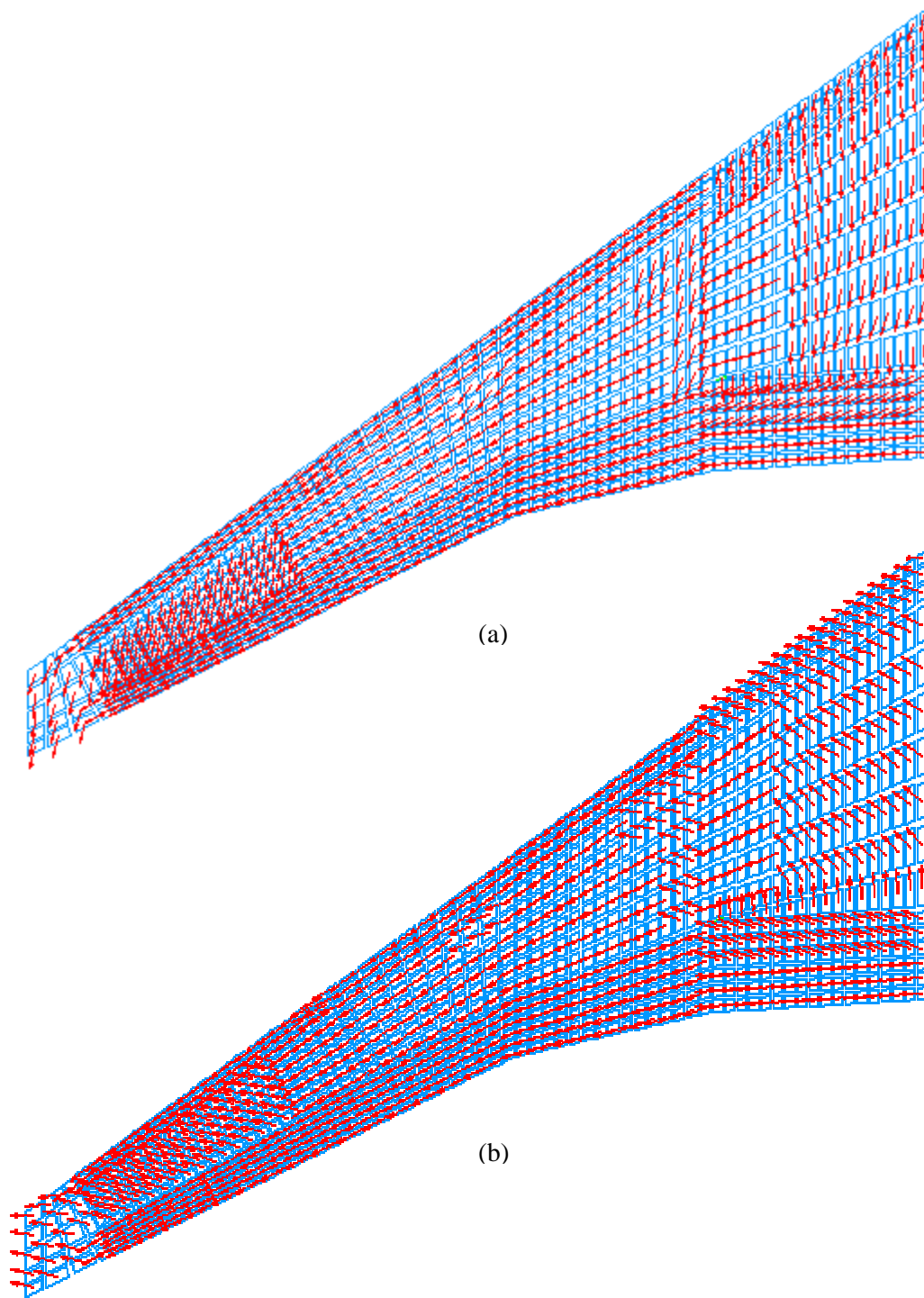
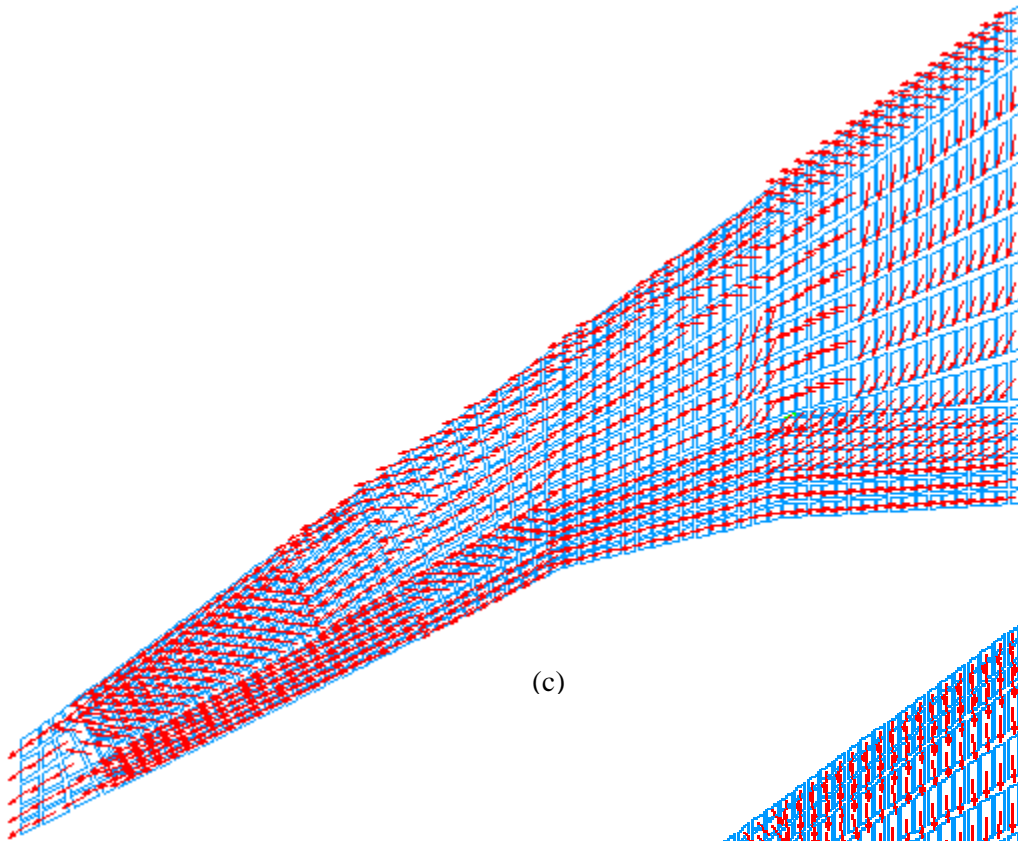
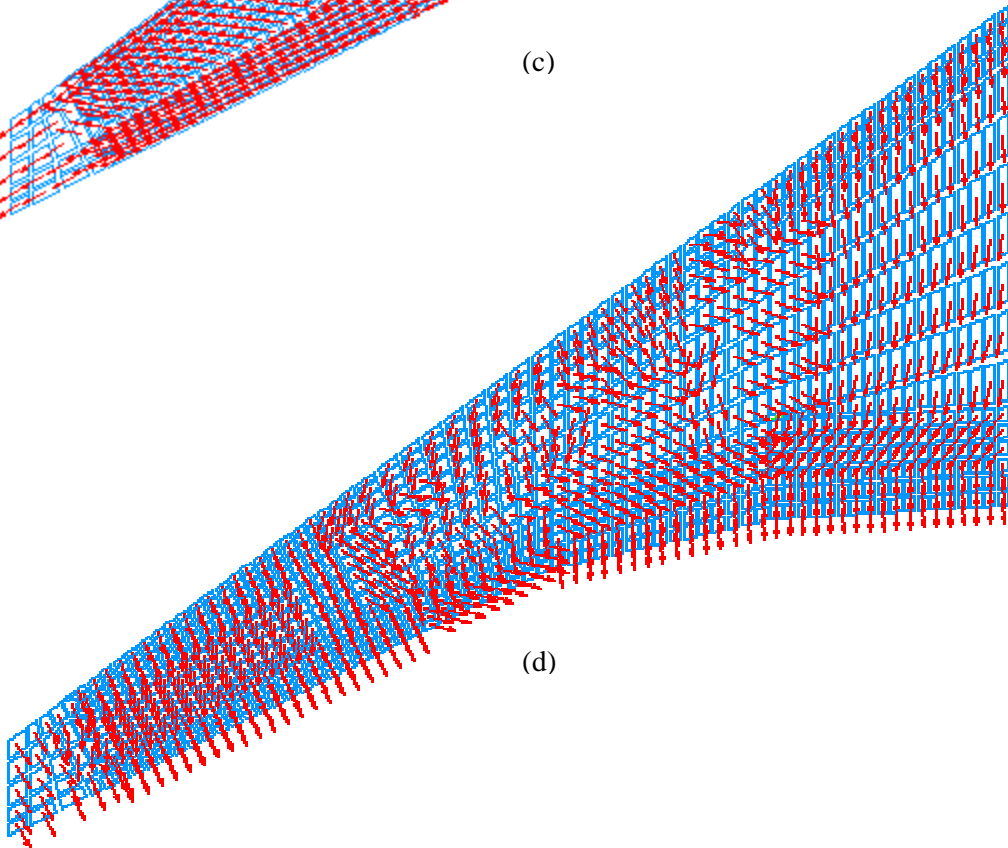


Figure 3.5.21: 1st and 2nd layer-angle mappings for bge11L213 upper skin.



(c)

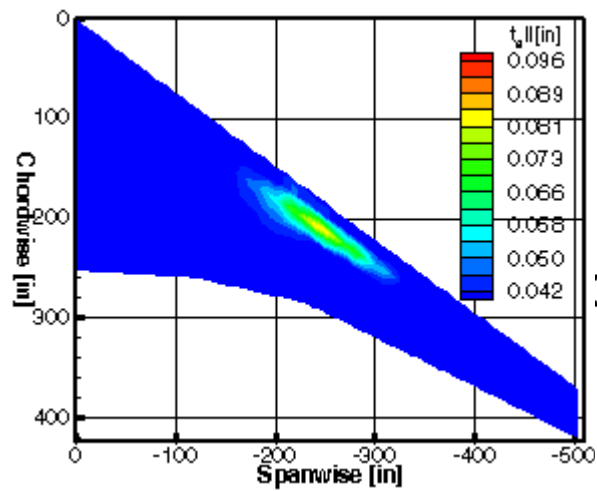


(d)

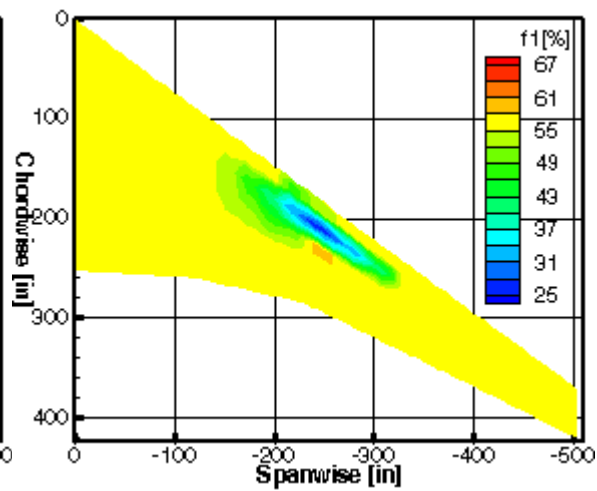
Figure 3.5.21(contd.): 3rd and 4th layer-angle mappings for bge11L213 upper skin.

Figures 3.5.22 to 3.5.25 represent layer-thickness contours and layer-angle mappings for bge11L313 based on Steering III configuration. In Figures 3.5.22(a) and 3.5.24(a), more materials are assembled at the wing torque box in the midboard-outboard sections. Here, the 0° layer is again dominant due to wing bending stresses, where laminates are composed of (70/25/5) family for both skins in Figures 3.5.22(c) and 3.5.24(d). The upper skin is thicker and has a more widespread contour due to longitudinal compressive loads as compared with the lower skin. At the L.E. and T.E. sections, $\pm\theta_l^\circ$ layers play a key role in reinforcement. Notice in Figures 3.5.23(a), 3.5.23(b), 3.5.25(a), and 3.5.25(b), $\pm\theta_l^\circ$ layer orientations are steered from axial to off-axis directions at the wing tip for shear reinforcements. A majority of the wing skin is composed of (30/60/10) at these locations. The 90° layer reinforcement (Figures 3.5.22(d) and 3.5.24(d)) is not significant for both skins, as predicted.

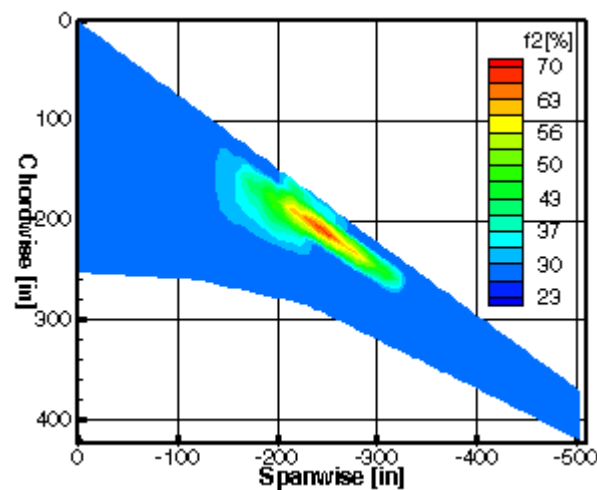
Finally, Figures 3.5.26 to 3.5.29 represent layer-thickness contours and layer-angle mappings for bge12L313 with the additional implementation of CDIS constraints at the wing tip. The total layer-thickness contours of this model show similar trends when compared with the bge12L013 baseline model, as illustrated in Figures 3.5.26(a) and 3.5.28(a). More materials are accumulated at both upper and lower wing torque box in the midboard, where reinforcements are attributed to the 0° layer. Here, the wing skins behave as a (70/25/5) laminate family in Figures 3.5.26(c) and 3.5.28(c). At the wing tip, the torque box is strengthened with $\pm\theta_l^\circ$ layers due to wing-tip deflection constraints. The laminate family is approximately (20/70/10) for both skins, as depicted in Figures 3.5.26(b) and 3.5.28(b). In fact, towards the outboard section of wing skins, $\pm\theta_l^\circ$ layer orientations are steered to overcome CDIS constraints, which are illustrated in Figures 3.5.27(a), 3.5.27(b), 3.5.28(a), and 3.5.28(b). At the L.E. and T.E. of both skins, $\pm\theta_l^\circ$ layers also play a key role in reinforcement. In the inboard section, $\pm\theta_l^\circ$ layers contribute to the longitudinal reinforcement of these locations. Until reaching the outboard, $\pm\theta_l^\circ$ layers become sensitive to wing bending stresses and shear loads. The layer angles are tailored to follow off-axis directions. Generally, the laminate family is (35/55/10) at these locations. As predicted, 90° layer reinforcement (Figures 3.5.26(d) and 3.5.28(d)) is not significant for both skins, although layer-thickness varies from bay to bay. The 90° layer constitutes the minimum gage solution.



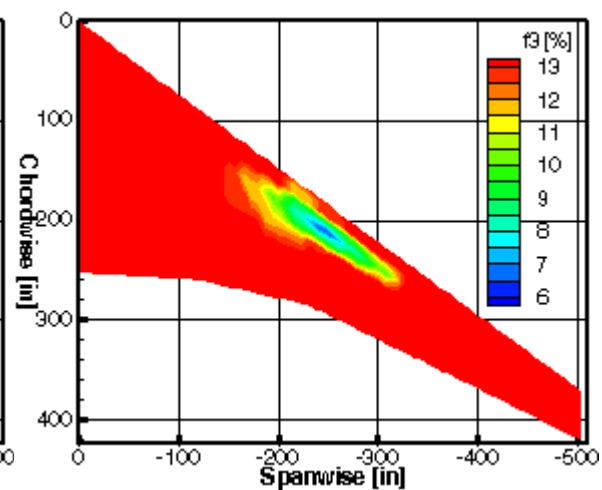
(a)



(b)



(c)



(d)

Figure 3.5.22: Layer-thickness contours for bge11L313 lower skin.

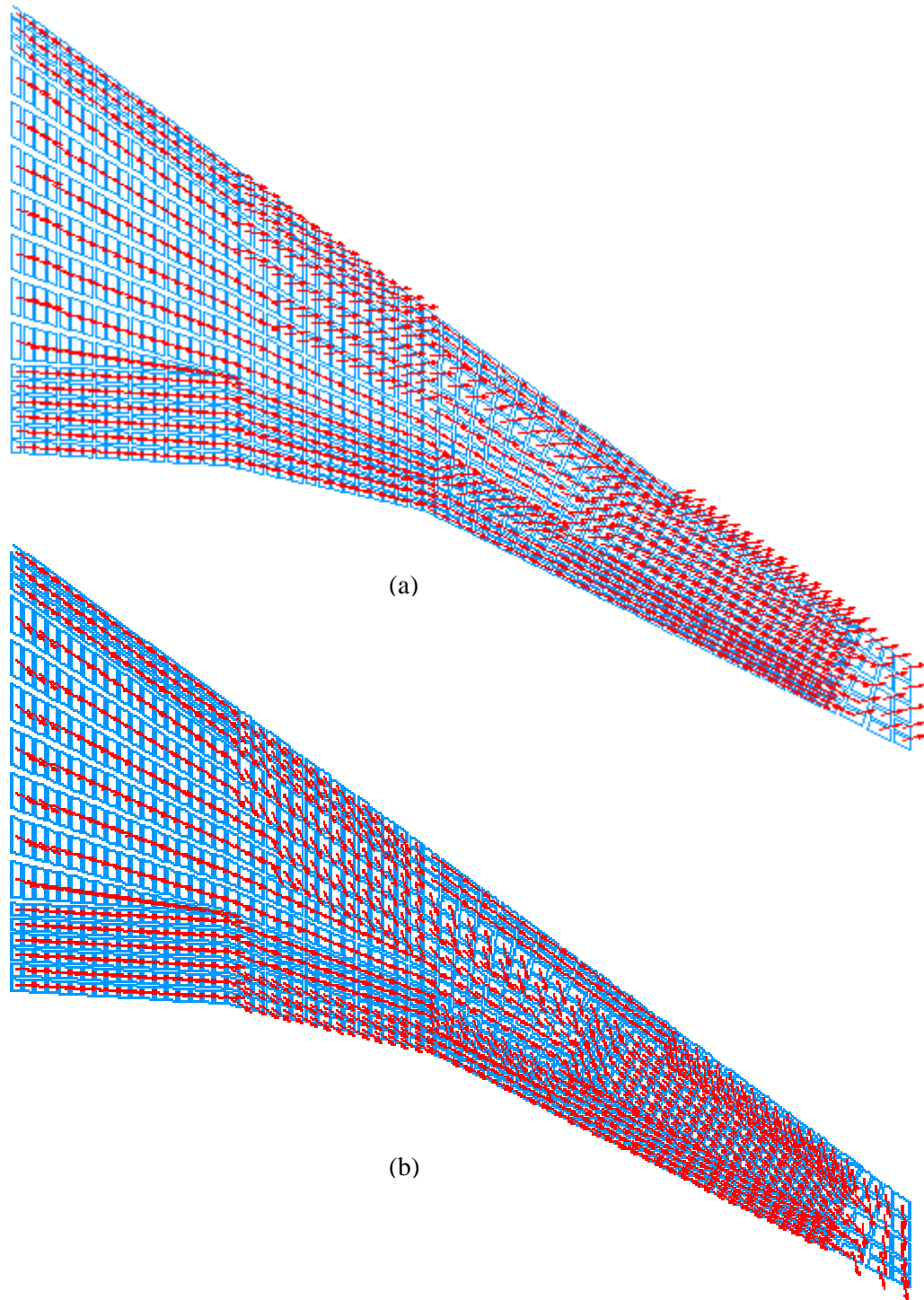
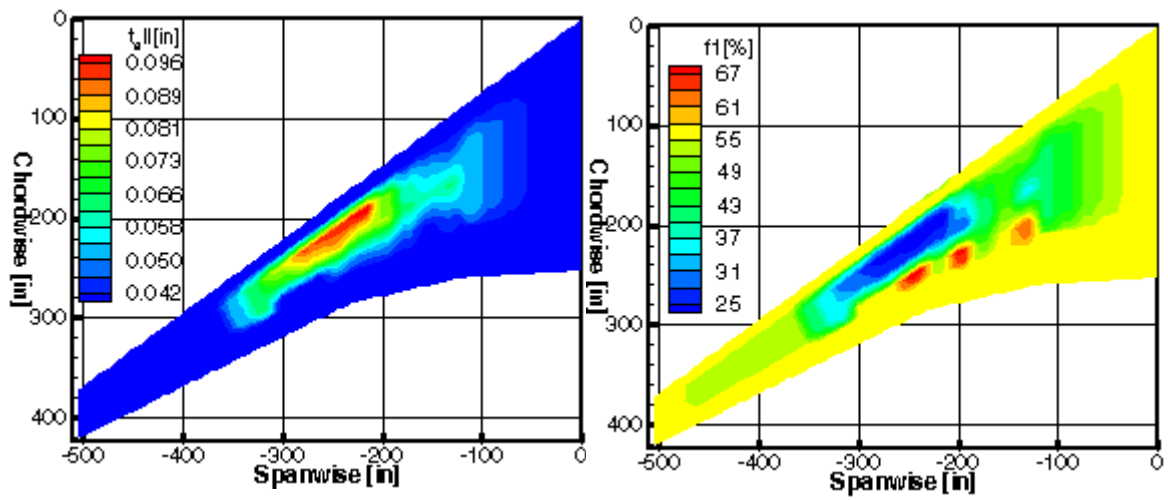
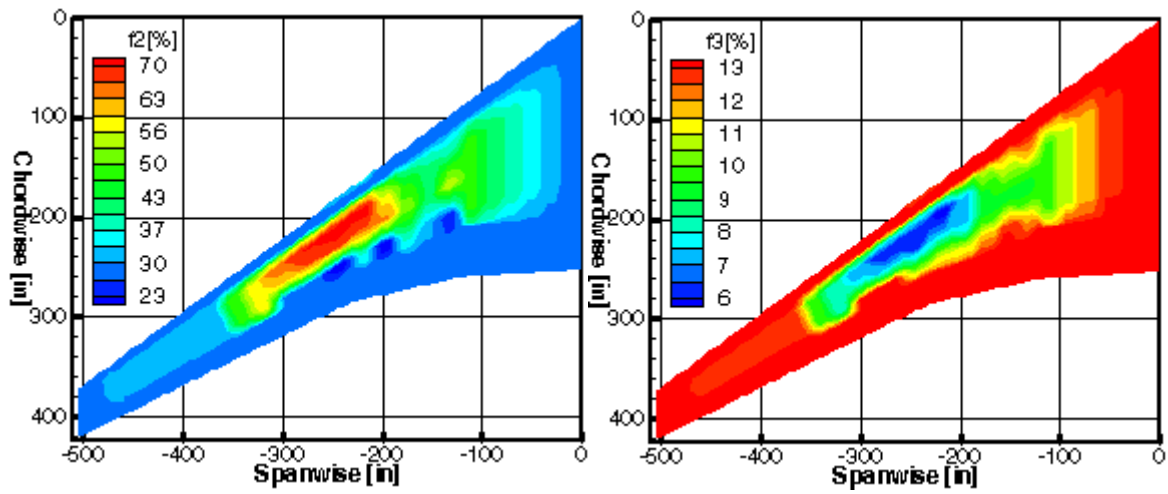


Figure 3.5.23: 1st and 2nd layer-angle mappings for bge11L313 lower skin.



(a)

(b)



(c)

(d)

Figure 3.5.24: Layer-thickness contours for bge11L313 upper skin.

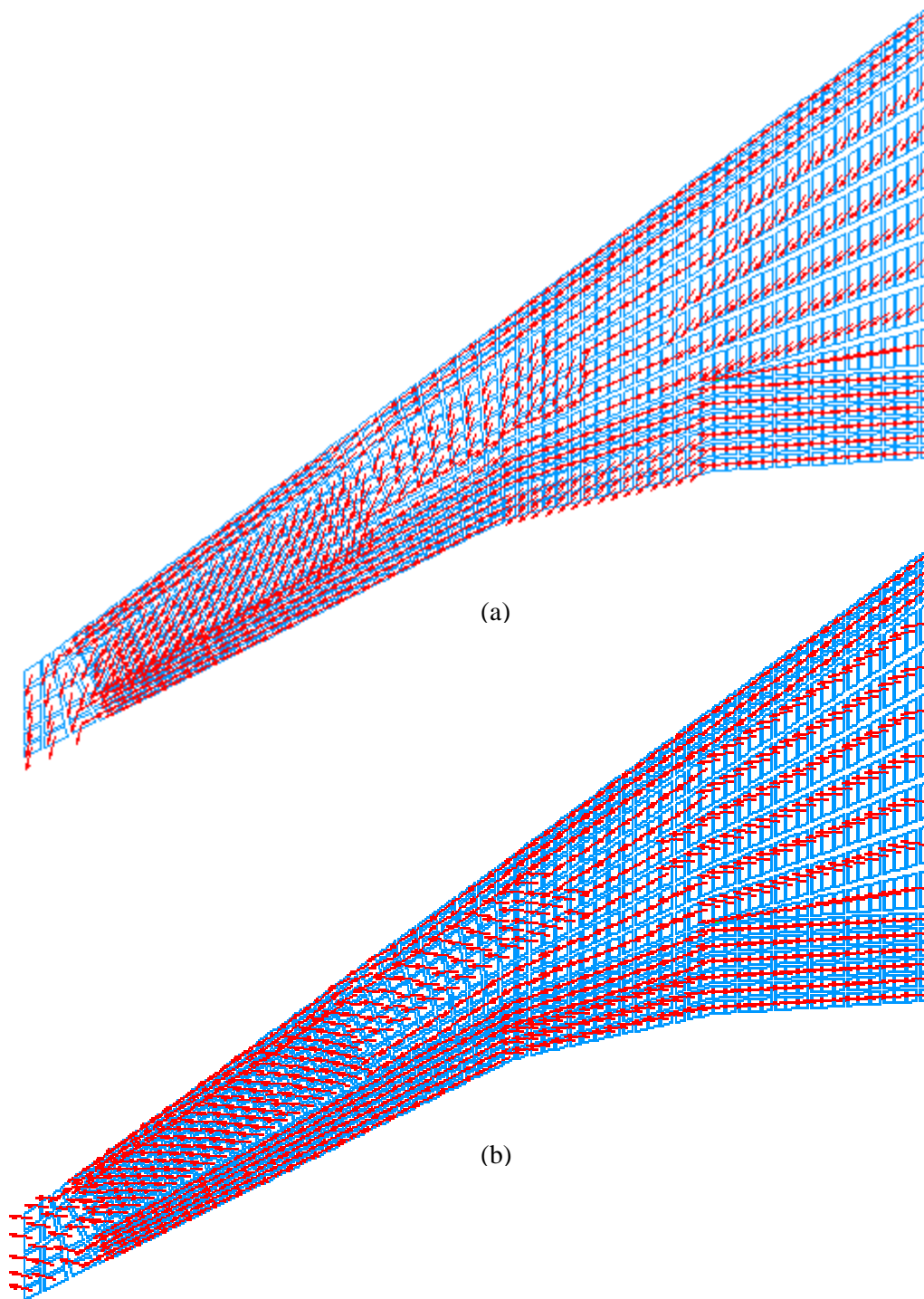


Figure 3.5.25: 1st and 2nd layer-angle mappings for bge11L313 upper skin.

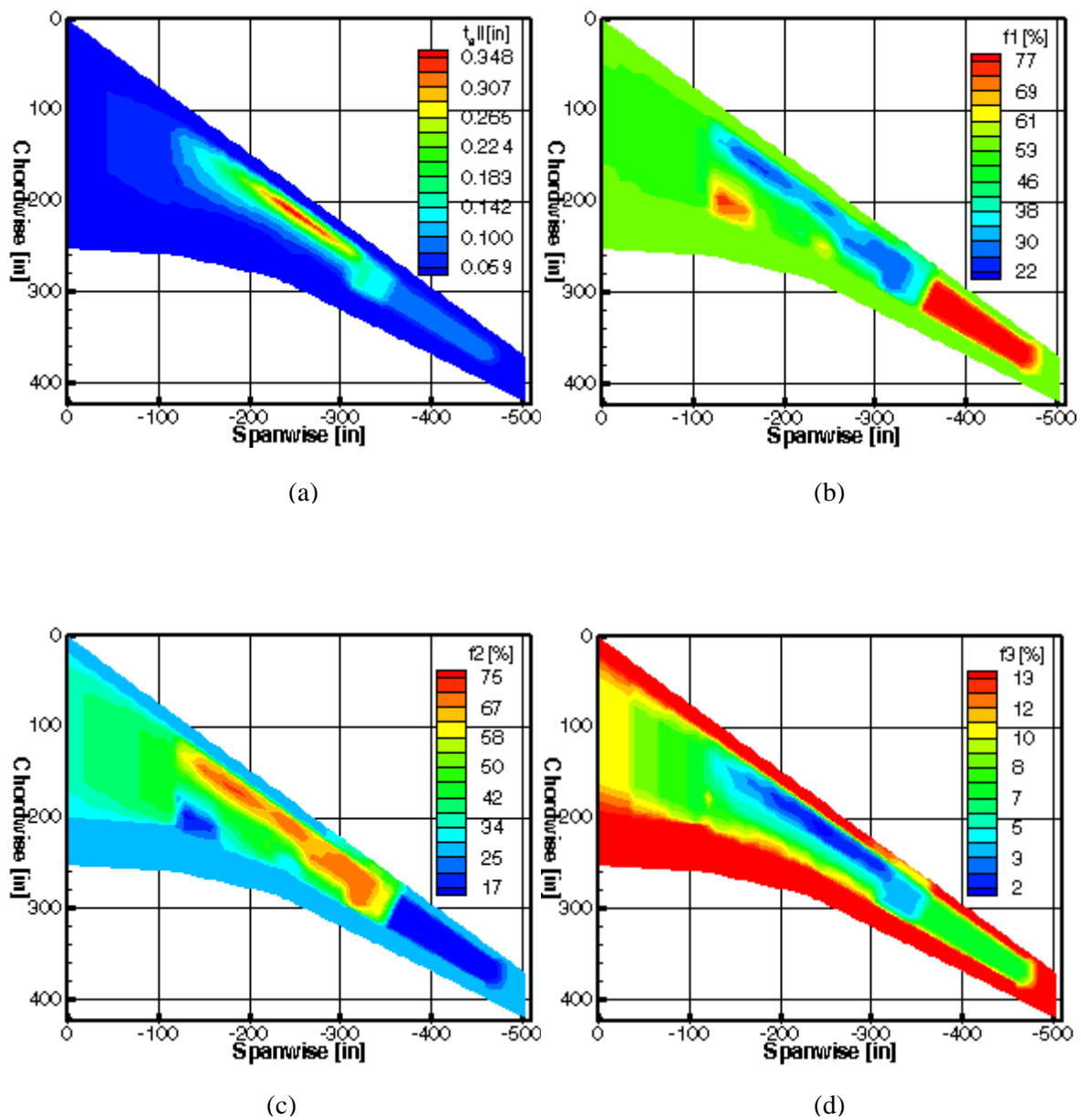


Figure 3.5.26: Layer-thickness contours for bge12L313 lower skin.

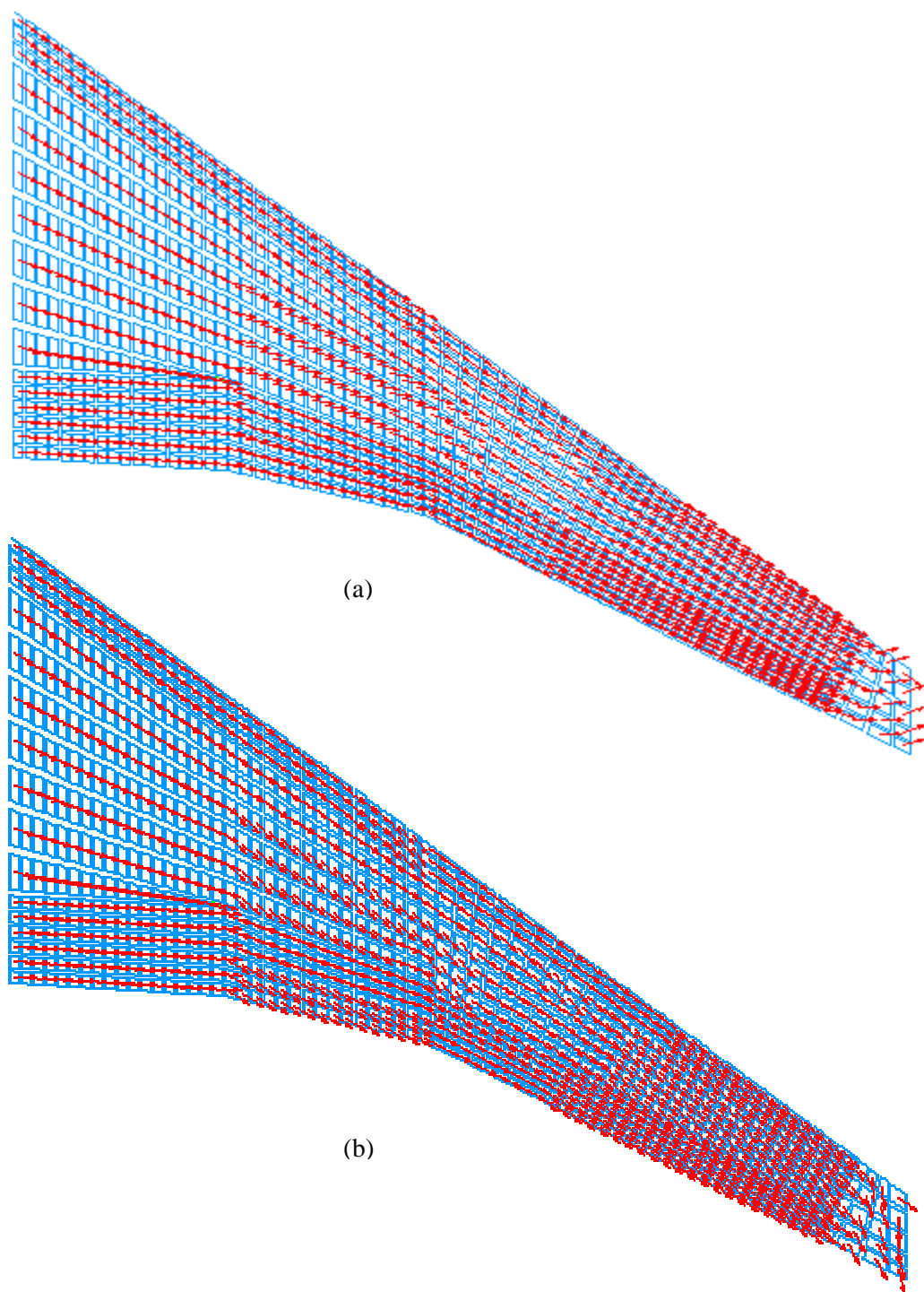
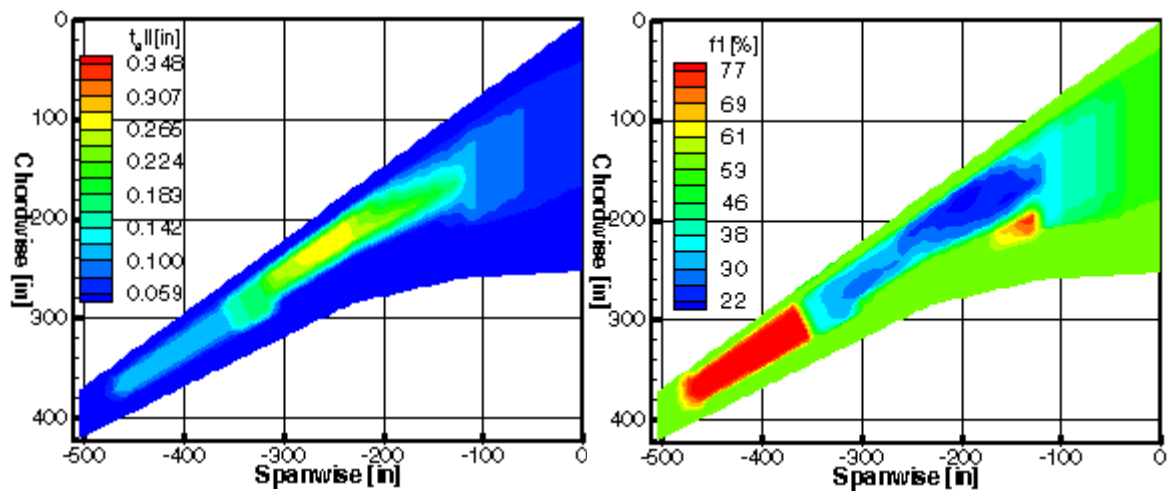
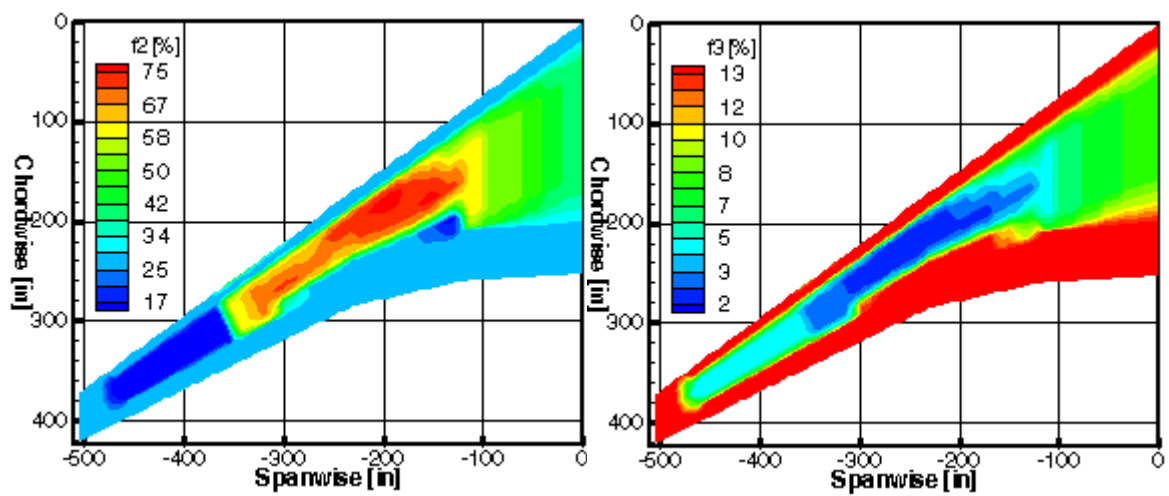


Figure 3.5.27: 1st and 2nd layer-angle mappings for bge12L313 lower skin.



(a)

(b)



(c)

(d)

Figure 3.5.28: Layer-thickness contours for bge12L313 upper skin.

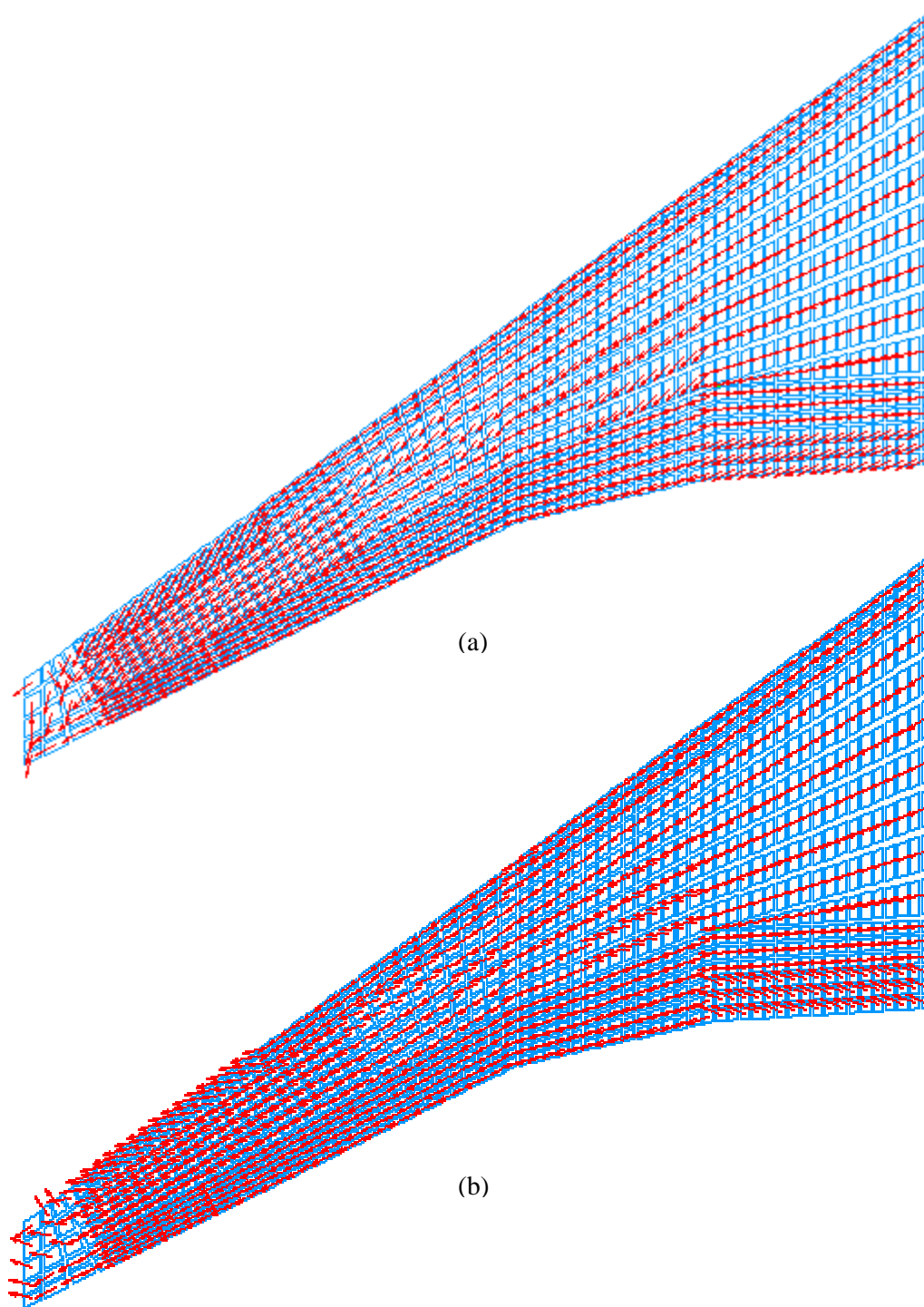


Figure 3.5.29: 1st and 2nd layer-angle mappings for bge12L313 upper skin.

3.5.4.3 Representative Pressure Bulkhead of General-Aviation Aircraft.

Results of FS conceptual design for the pressure bulkhead, which are shown in Appendix E.1, are not representative. Since the structure is composed of minimum-gage laminates, the gradient-based optimizations could probably reach local minima. The FS effects become insignificant as the optimizations terminate with fulfilling minimum-gage requirements (CGAGE). As a result, layer-thickness contours and layer-orientation mappings are not smooth.

3.5.4.4 Representative Horizontal Stabilator of Military Aircraft

The F22 model has been set up to demonstrate FS conceptual design using MBB-LAGRANGE, where weight savings based on Steering II and III are listed in Table 3.5.7. From the results, Steering II has a greater payoff as predicted. However, the FS-related results are not realistic and manufacturable because the layer-thickness contours and layer-orientation mappings are not “smooth”, which are documented in Appendix E.2. This is probably due to a gross rangewise definition, as shown in Figure 3.5.12. FS results of F22 model can be improved with a fine rangewise definition.

3.5.5 Brief Conclusion

Three representative primary and secondary aircraft structures have been analyzed to demonstrate potential benefits associated with FS conceptual design using MBB-LAGRANGE. The objective function of the optimization is minimum weight, subjected to various constraints such as MSTN or CMAT, CGAGE, CGANG, and CDIS. Two FS-related configurations, namely Steering II and III, have been analyzed. The weight savings based on FS conceptual design are compared with the baseline configuration, which are listed in Table 3.5.7. From the studies, it is concluded that:

- ➔ **Weight savings of up to 17% for linear static analysis** is attainable, which is primarily based on Steering II configuration of BGE wing. Due to the unbalanced nature of this configuration, further verifications and sound decisions must be made.
- ➔ **For Steering III configuration, weight savings of up to 11% for linear static analysis** is observable. This configuration yields balanced results w.r.t. the primary material coordinate, which is more realistic and acceptable in composite laminate design.
- ➔ **“Smooth” rangewise continuity** are seen in **layer-thickness contours and layer-orientation mappings**, especially demonstrated in BGE wing.
- ➔ **Careful selections of rangewise DV-linking based on strain contours** yield satisfactory FS-related results, especially represented by BGE wing.
- ➔ **Due to minimum-gage solutions, pb2 model is not representative.** It is recommended to impose a greater load factor so that FS conceptual design can be demonstrated.

- ➔ Again, **MBB-LAGRANGE** is a **robust and efficient tool for fiber steering conceptual design**, even with large amounts of design variables.

In summary, composite structures exhibiting steered fiber architecture offer potential payoffs based on constant-rangewise finite-element discretization and gradient-based structural optimization. Optimal design of primary and secondary composite structures can be obtained by allowing layer thickness and layer orientations to vary across the structures. Significant weight reduction and enhanced load-carrying performance for fiber-steering solutions can be achieved. At no additional cost, FS-related designs can be fabricated with the use of state-of-the-art fiber placement (FP) machines. This novel design concept provides impetus in culminating FP technology as well as related CAD and CAE technologies.

3.6.0. Conclusions and Recommendations

3.6.1 Conclusion of Fiber Steering Conceptual Design

This paper investigates the potential payoffs of composite structures using fiber steering (FS) conceptual design. It calls for the tailorability of curvilinear-family laminates to specific internal load paths, which involves simultaneous optimizations of both rangewise layer thickness and orientations. A curvilinear-family laminate consists of four layers or $[\pm\theta_1, \theta_2, \theta_3]_s$. Each layer is composed of a collective of several 0.0055-inch plies. Structures exhibiting steered-fiber architecture have been shown to improve load capability and ultimately weight reductions. The design concept has been successfully demonstrated on four preliminary and three representative aircraft models under various load cases:

Preliminary Studies

- ➔ **Plate with a hole:** three square plate-with-a-hole models with different width-to-diameter (W/D) parameters subjected to various loads (bi-axial tension, uniaxial tension, and in-plane shear). W/D are 5.0, 3.33, and 2.5.
- ➔ **Wing Torque Box:** An intermediate complexity wing (ICW) subjected to aerodynamic loads.
- ➔ **Cantilever panel:** a cantilever rectangular panel subjected to transverse loads
- ➔ **Cantilever tube:** A cantilever cylindrical tube subjected to combined loads (bending, compression and torsion)

Representative Primary and Secondary Aircraft Structural Components

- ➔ **Wing:** a representative of a regional jet's primary structural component or BGE wing
- ➔ **Aft pressure bulkhead:** a representative of a general aviation aircraft's secondary structural component or pb2 model
- ➔ **Horizontal Stabilator:** a representative of a tactical fighter's primary structural component or F22 model.

Using MBB-LAGRANGE as the main computational tool throughout the research, this gradient-based and finite-element structural optimization routine enables robust and efficient demonstrations of FS conceptual design. It is configured solely on [A] matrix or composite-membrane computations with several mathematical programming algorithms available for structural optimization. Recursive Quadratic Programming by Powell (RQP2) is the primary optimization algorithm for FS-related problems.

Four design variable (DV) configurations, namely baseline, Steering I, II and III, have been proposed and defined for four preliminary models. All four configurations are composed of symmetric laminates, but each has different balance properties. The baseline configuration is a pure layer-thickness optimization design with $[\pm 45, 0, 90]_s$ and is balanced with respect to (w.r.t.) the principal material coordinate. The Steering I configuration has one angle DV per element with $[\pm \theta_1, \theta_2, \theta_3]_s$, where the θ_2° layer is the primary DV. $\pm \theta_1^\circ$ and θ_3° layers are linked to θ_2° DV with $\pm 45^\circ$ and 90° respectively. In this case, the laminate is balanced w.r.t. the local material coordinate. The Steering II configuration has three layer-angle DV per element or range of elements with $[\pm \theta_1, \theta_2, \theta_3]_s$. $\pm \theta_1^\circ$ layers, are linked as one DV each for layer thickness and orientation, respectively. However, Steering II laminate is unbalanced w.r.t. either the local or principal material coordinate. Finally, Steering III configuration takes only one DV by linking $\pm \theta_1^\circ$ layers in $[\pm \theta_1, 0, 90]$. As a result, Steering III is balanced w.r.t. the principal material coordinate.

The objective function for these models is minimum structural weight, while maximum strain failure criterion with only fiber-related failure modes (longitudinal tension and compression), upper and lower layer thickness, and $\pm 45^\circ$ angle thresholds are design constraints under different loading cases. Displacement or maximum wing-tip deflection and critical-buckling constraints are also included onto some of the models. Nevertheless, improvements in MBB-LAGRANGE buckling formulations are required to incorporate better layouts of steered-fiber architecture onto airframe structures. This is further explained in the Section 3.6.3.

Optimal results corresponding to FS conceptual design are presented in Section 3.4.3 and Appendix C for preliminary models, and Section 3.5.3 and Appendix E for preliminary and aircraft models respectively as layer-thickness contours and layer-angle mappings following the curvilinear laminate family (Section 3.1.2) definitions. Results of weight savings for each model are listed in Tables 3.4.4 and 3.5.7, where FS-related configurations (Steering I, II and III) are compared with the baseline design. From the studies, it is concluded that:

- ➔ **Weight savings of up to 27% for linear static analysis** is attainable, which is primarily based on **Steering II configuration**. However, further verifications and sound decisions must be made because the resultant laminate is unbalanced w.r.t. either the local or principal material coordinate. Computational efforts for Steering II configuration are greater than Steering I and II because of the additional layer-angle DV per element or range of element.
- ➔ **Weight savings of up to 26% for linear static analysis** is achievable, which is associated with **Steering III configuration**. This configuration yields balanced results w.r.t. the primary material coordinate, which is more realistic and acceptable in composite laminate design.
- ➔ **Weight savings of up to 20% for linear static analysis** is reasonable, which corresponds to **Steering I configuration**. This resultant laminates are balanced w.r.t. the local material coordinate, but unbalanced w.r.t. the principal material coordinate. Steering I configuration is the best candidate of FS conceptual design because the primary or axial

load trajectories are governed only by the primary layer angle, θ_2 . The off-axis and transverse load paths are contributed by $\pm\theta_1$ and θ_3 , respectively. Nevertheless, further investigations are required to verify the macroscopic behavior and response of the laminates.

- ➔ **Weight savings of up to 6% for linear buckling analysis** is observable, which is primarily based on Steering II configuration for ICW model. Again, the optimal results may not be realistic due to issues of unbalanced laminates. In addition, MBB-LAGRANGE buckling formulations must be revisited for FS-related optimizations.
- ➔ **“Smooth” or rangewise continuous layer-angle mappings and layer-thickness contours** are demonstrated in most of the studies.
- ➔ **Optimal layer-angle mappings and layer-thickness contours are very load-path-sensitive.** This is illustrated in the plate-with-a-hole models in Section 3.4.3, where layer orientations are tailored significantly w.r.t. the primary load paths under different load cases (bi-axial tension, uniaxial tension, and in-plane shear). However, the variations of steering patterns do not depend strongly on W/D parameter under identical load conditions. A larger W/D model may seem to have a greater propagation or variation in layer thickness near the hole vicinity due to stress concentrations. Also, with a greater W/D, layer orientations for Steering I configuration are discontinuous along the boundary due to the influence of stress concentrations. Nevertheless, the variation of steering patterns w.r.t. W/D parameter is generally insensitive.
- ➔ Careful **selections of rangewise DV-linking based on strain contours** yield satisfactory FS-related results, especially represented by BGE wing model in section 3.5.4.2.
- ➔ **Structures with minimum-gage solutions do not exhibit continuous layer-angle mappings and layer-thickness contours.** This is particularly true for pb2 and F22 models in Sections 3.5.4.3 and 3.5.4.4. It is recommended to impose a greater load factor so that FS conceptual design can be demonstrated.
- ➔ All in all, **MBB-LAGRANGE is a robust and efficient tool** for fiber steering conceptual design.

3.6.2. Recommendations for Future Works

The present work sets a milestone for FS conceptual design of composite structures based on the finite-element level. The optimal results are derived from gradient-based optimizations, where layer sizing and orientations are essentially constant-rangewise. The next step is to incorporate this novel design concept into existing CAD/CAM/CAE for FP technology. According to Section 3.1.3, the optimal results of layer-thickness contours are rounded for discrete solutions and best stacking sequences using a stacking sequence realizer (e.g. PACKS¹⁵). The layer-orientation mappings can be simulated as topological-continuous towpreg

paths using geometry analysis and intelligent front-end tools (e.g. SCADS^{16,57}). With the aid of the knowledge-based composite design package (e.g. PACKS), the manufacturability and design practices are also taken into consideration. A final detailed finite element analysis (FEA) is carried to ensure design feasibility under prescribed preliminary requirements. Finally, the computer numerical controlled (CNC) code is generated and is fed into the FP machine to fabricate the parts.

In Table 3.3.1, MBB-LAGRANGE has another optimization module that supports topological design variables, called constructive design variable. The constructive design models, which is introduced in Ref. 27, has the capabilities to parametrically define:

- ➔ Topological ply distribution using bicubic Bezier-patches, as shown in Figure 3.6.1(a)
- ➔ Topological prepreg courses using discrete-point spline interpolation technique, as presented in Figure 3.6.1(b).

For a simple structure, the layer thickness and orientation design variables can be represented by a single curve or starting course. The application surface and layer periphery are then parametrically described using several “filling” methods, such as shifted-fiber²⁸, parallel-fiber²⁸, band-offset⁵⁷, fixed-angle⁵⁷, and laminate-family⁵⁷ methods. This can be performed using SCADS. The advantages of the constructive design concept can be summarized as:

- ➔ Constructive design models directly yield producible laminates
- ➔ Manufacturing constraints, such as minimum and maximum steering radii, can be considered.

However, the computational efforts involving constructive design models can be overwhelming.

Finally, two additional analysis areas should be explored to investigate potential payoffs associated with FS conceptual design:

- ➔ Buckling (in-plane) response of monocoque panels exhibiting steered-fiber architecture, as illustrated in Figure 3.6.2
- ➔ Vibration characteristics of composite sandwich panels exhibiting steered-fiber architecture, as depicted in Figure 3.6.3.

The proposed research would provide a novel conceptual design for composite panels subjected to stability and dynamic environments. Composite panels having steered fiber architecture offer improved buckling³² and damping characteristics^{33,34} by tailoring local fiber orientations to specific internal load paths of the structures.

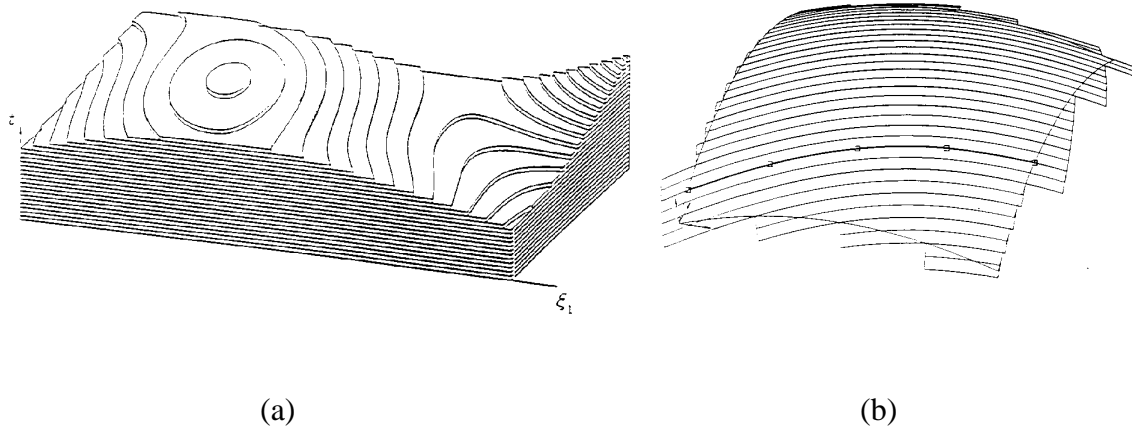


Figure 3.6.1: Schematics of constructive design models for (a) topological ply distribution and (b) topological prepreg courses (taken from Ref. 27)

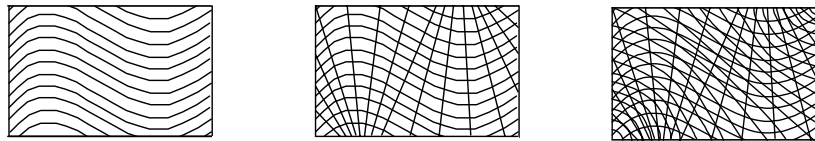


Figure 3.6.2: Schematics of fiber steering configurations for buckling panels.

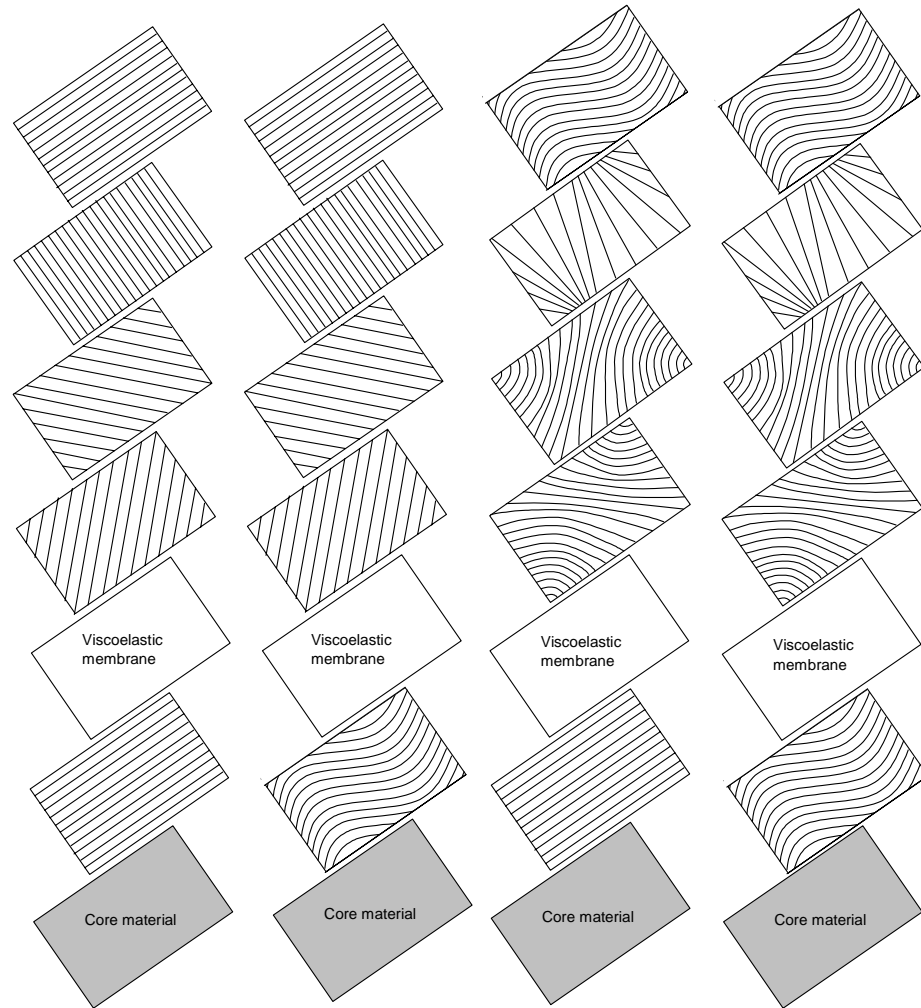


Figure 3.6.3: Schematics of baseline and steering configurations for vibration panels in exploded view.

3.6.3. Recommendations for MBB-LAGRANGE Improvements

Recommendations for MBB-LAGRANGE improvements are itemized as follows:

- ➔ Provide more functionality and improve user friendliness of MBB-LAGRANGE. A supplemental graphic user interface (GUI) would be very useful in defining the input data, such as layer thickness and angle design variables.
- ➔ Incorporate composite plate elements so that arbitrary rod elements added around every quadrilateral and triangular membrane element can be eliminated. This would significantly reduce the time required to create the input file.
- ➔ Support sensitivity analysis and optimization for non-fiber failure criteria, i.e., transverse tensile and compressive strain allowables, and in-plane shear allowable.
- ➔ Include a methodology to utilize layer-angle design variables with buckling constraints for different boundary conditions (simply-supported, clamped, and free) would be very beneficial. Current version of MBB-LAGRANGE only allows pure layer-thickness optimizations. Also, only simply supported on all four edges is permitted.
- ➔ Enable user interactions in describing different objective functions and constraints.
- ➔ Alter VLAMINAT, a predefined DV-linking function in MBB-LAGRANGE, so that constant-rangewise design variables are permitted. Current version of MBB-LAGRANGE defines every single element as a layer-angle design variable (DV). This results in tremendous computational works because rangewise DV linking is not possible.

3.7 Appendix A: Material Properties

Table A1: Material properties for IM7/8551-7A or Graphite/Epoxy tape.

Conditions and parameters:

- Temperature: room temperature
- Humidity/moisture: dry
- Nominal thickness, $t = 0.0055$ inch/ply
- Density, $\rho = 0.057$ lb/in³
- Poisson's ratio, $\nu_{12} = 0.3$

Engineering Constants		B-basis allowable strains	
Longitudinal tensile modulus, E_1^T [x10 ³ ksi]	22.8	Ultimate longitudinal tensile strain, ε_1^{TU} [μin/in]	12800
Longitudinal compressive modulus, E_1^C [x10 ³ ksi]	22.3	Ultimate longitudinal compressive strain, ε_1^{CU} [μin/in]	11100
Transverse tensile modulus, E_2^T [x10 ³ ksi]	1.29	Ultimate transverse tensile strain, ε_2^{TU} [μin/in]	7020
Transverse compressive modulus, E_2^C [x10 ³ ksi]	1.29	Ultimate transverse compressive strain, ε_2^{CU} [μin/in]	13200
In-plane shear modulus, G_{12} [x10 ³ ksi]	0.79	Ultimate in-plane shear, γ_{12}^U [μin/in]	29200

Table A2: Material properties for IM7/5260 or Graphite/BMI tape.

Conditions and parameters:

- Temperature: room temperature
- Humidity/moisture: dry
- Nominal thickness, $t = 0.0055$ inch/ply
- Density, $\rho = 0.057$ lb/in³
- Poisson's ratio, $\nu_{12} = 0.3$

Engineering Constants		B-basis allowable strains	
Longitudinal tensile modulus, E_1^T [x10 ³ ksi]	23.9	Ultimate longitudinal tensile strain, ε_1^{TU} [μin/in]	16400
Longitudinal compressive modulus, E_1^C [x10 ³ ksi]	21.6	Ultimate longitudinal compressive strain, ε_1^{CU} [μin/in]	8657
Transverse tensile modulus, E_2^T [x10 ³ ksi]	1.40	Ultimate transverse tensile strain, ε_2^{TU} [μin/in]	7500
Transverse compressive modulus, E_2^C [x10 ³ ksi]	1.40	Ultimate transverse compressive strain, ε_2^{CU} [μin/in]	4640
In-plane shear modulus, G_{12} [x10 ³ ksi]	1.00	Ultimate in-plane shear, γ_{12}^U [μin/in]	13500

Table A3: Material properties for 2024T3 aluminum alloy sheet.

Conditions and parameters:

- Temperature: room temperature
- Density, $\rho = 0.101 \text{ lb/in}^3$
- Humidity/moisture: dry
- Poisson's ratio, $\nu = 0.33$

Engineering Constants		A-basis allowable stresses	
Longitudinal tensile modulus, E [$\times 10^3$ ksi]	10.5	Ultimate longitudinal tensile stress, F^{TU} [ksi]	63.0
Longitudinal compressive modulus, E^C [$\times 10^3$ ksi]	10.7	Yield longitudinal tensile stress, F^{TY} [ksi]	47.0
In-plane shear modulus, G [$\times 10^3$ ksi]	4.0	Yield longitudinal compressive stress, F^{CY} [ksi]	39.0
		Ultimate in-plane shear, F^{SU} [ksi]	39.0

Table A4: Material properties for 2024T3 aluminum alloy extrusion.

Conditions and parameters:

- Temperature: room temperature
- Density, $\rho = 0.101 \text{ lb/in}^3$
- Humidity/moisture: dry
- Poisson's ratio, $\nu = 0.33$

Engineering Constants		A-basis allowable stresses	
Longitudinal tensile modulus, E [$\times 10^3$ ksi]	10.8	Ultimate longitudinal tensile stress, F^{TU} [ksi]	60.0
Longitudinal compressive modulus, E^C [$\times 10^3$ ksi]	11.0	Yield longitudinal tensile stress, F^{TY} [ksi]	44.0
In-plane shear modulus, G [$\times 10^3$ ksi]	4.1	Yield longitudinal compressive stress, F^{CY} [ksi]	37.0
		Ultimate in-plane shear, F^{SU} [ksi]	31.0

Table A5: Material properties for 7075T6 aluminum alloy sheet.

Conditions and parameters:

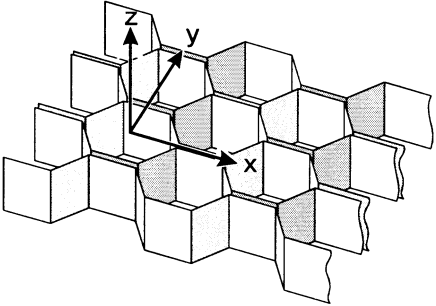
- Temperature: room temperature
- Density, $\rho = 0.101 \text{ lb/in}^3$
- Humidity/moisture: dry
- Poisson's ratio, $\nu = 0.33$

Engineering Constants		A-basis allowable stresses	
Longitudinal tensile modulus, E [$\times 10^3$ ksi]	10.3	Ultimate longitudinal tensile stress, F^{TU} [ksi]	76.0
Longitudinal compressive modulus, E^C [$\times 10^3$ ksi]	10.5	Yield longitudinal tensile stress, F^{TY} [ksi]	69.0
In-plane shear modulus, G [$\times 10^3$ ksi]	3.9	Yield longitudinal compressive stress, F^{CY} [ksi]	68.0
		Ultimate in-plane shear, F^{SU} [ksi]	46.0

Table A6: Material properties for 5056 aluminum alloy hexagonal honeycomb.

Conditions and parameters:

- Temperature: room temperature
- Density, $\rho = 0.101 \text{ lb/in}^3$
- Humidity/moisture: dry
- Poisson's ratio, $\nu = 0.33$

Engineering Constants		B-basis allowable shear stresses	
Longitudinal/Ribbon modulus, $E_{11} \approx E_{33}$ or E_x [ksi]	45.0	Ultimate flatwise shear, τ_{13}^U [ksi]	1.94
Transverse modulus, $E_{22} \approx E_{33}$ or E_y [ksi]	45.0	Ultimate transverse shear, τ_{23}^U [ksi]	1.43
Flatwise modulus, E_{33} or E_z [ksi]	900.0		
Flatwise shear modulus, $G_{12} \approx G_{13}$ or G_{xy} [ksi]	78.0		
Transverse shear modulus, $G_{23} \approx G_{13}$ or G_{yz} [ksi]	78.0		
Ribbon shear modulus, G_{13} or G_{xz} [ksi]	210.0		

3.8 Appendix B: Sample MBB-LAGRANGE Input File

MBB-LAGRANGE input file is structured based on three sections or decks:

- ➔ Design Control Deck
- ➔ Case Control and Bulk Control Deck
- ➔ Optimization Data Deck

```
***** DESIGN CONTROL DECK *****
PROJECT = PL15L111
$ TASK = OPTIMIZATION
$ TASK = ANALYSIS
$ TASK = INPUT
$ TASK = SENSITIVITY
TASK = OPTIMIZATION
$ ANALYSIS = STATIC (Static Analysis)
$ ANALYSIS = BUCKLING (Buckling Analysis)
$ ANALYSIS = EIGEN (Eigenvalue calculations)
$ ANALYSIS = AEROELASTIC (Aeroelastic Analysis)
$ ANALYSIS = FLUTTER (Flutter points Analysis)
$ ANALYSIS = TRESPONSE (Dynamic Transient Response)
$ ANALYSIS = FRESPONSE (Frequency Response)
$ ANALYSIS = MODCOORD (Transformation in Modal Coordinate)
$ ANALYSIS = LANCOORD (Transformation in LANCZOS-Coordinate)
$ ANALYSIS = LANGCOORD (LANCZOS-Transformation for gradients,
$                      corresponding to pure LANCOORD analysis)
$ ANALYSIS = GENAER (Only Generalization of the Aerodynamic Forces)
ANALYSIS = STATIC
$ STRATEGY = IBF (Inverse Barrier Function)
$ STRATEGY = MOM (Method of Multipliers)
$ STRATEGY = SLP (Sequential Linear Programming)
$ STRATEGY = SRM (Stress Ratio Method)
$ STRATEGY = RQP1 (Recursive Quadratic Programming by Schittkowski)
$ STRATEGY = RQP2 (Recursive Quadratic Programming by Powell)
$ STRATEGY = GRG (Generalized Reduced Gradients)
$ STRATEGY = CONLIN (Convex Linearization)
$ STRATEGY = QPRLT (Quadratic Programming with Reduced LineSearch Technique)
$ STRATEGY = SCP (SCP/MMA: Sequential Convex Programming)
STRATEGY = RQP2
$ SENSITIVITY = AUTO (automatic selection based on chosen opt. algorithm)
$ SENSITIVITY = NUMERIC (Numerical gradient calculation via Finite
$                      Difference Method)
$ SENSITIVITY = DESIGNSPACE (Design Space Method, for SLP, RQP1, RQP2,
$                      GRG, and CONLIN)
$ SENSITIVITY = STATESPACE (State Space Method, for SLP, RQP1, RQP2,
$                      GRG, and CONLIN)
$ SENSITIVITY = EXTENDED (Extended State Space Method for IBF & MOM)
SENSITIVITY = AUTO
$1111111222222233333334444444555555566666667777777888888899999999
$ TRSENSITIV = DIRECT (Direct Procedures)
$ TRSENSITIV = ADJOINT (Adjoint procedures for State Space Method)
$1111111222222233333334444444555555566666667777777888888899999999
$ DERIEVEC = NELSON (procedure by Nelson)
$ DERIEVEC = WANG (procedure by Wang)
$ DERIEVEC = FOX (procedure by FOX)
$1111111222222233333334444444555555566666667777777888888899999999
$ SEARCHDIR = QNDFP (after Davidon-Fletcher-Powell)
$ SEARCHDIR = QNBFGS (after Broyden)
$ SEARCHDIR = QNORSP (after Oren-Spedicato)
$1111111222222233333334444444555555566666667777777888888899999999
$ LINESEARCH = GOLDENSECTION (Golden Section Search)
$ LINESEARCH = POLYNOMIAL (Polynomial Approximation, e.g quadratic/cubic)
$ LINESEARCH = LUND (after Lund, not for MOM)
$ LINESEARCH = HERPOL (Hermite-Polynomial-Approximation)
$1111111222222233333334444444555555566666667777777888888899999999
```

```

$ PARAMETER = NOFIX
$ PARAMETER = TESTOPT
$ PARAMETER = OUTGRD
PARAMETER = OUTGRD
$ OUTPUT = NOINAN (no output for start analysis)
$ OUTPUT = NOENDAN (no output for final analysis)
$ OUTPUT = NONE (output neither for start nor for final analysis)
$ OUTPUT = ALL
OUTPUT = NOINAN
$ DATAL = PRE (In the input part, a universal file (*.UNV0) for IDEAS-
$               Supertab containing initial structure and preprocessing
$               data will be created)
$ DATAL = POST (In the design part, a universal file (*.UNV1) containing
$               postprocessing data will be created)
$ DATAL = ALL (2 universal files of final design will be created for supertab)
$111111122222223333333344444444555555556666666777777778888888899999999
$ RESTART : Optimization starts w/ the design variables saved in *.RST
$ WARMST : Optimization resumed w/ all in *.WST
$111111122222223333333344444444555555556666666777777778888888899999999
$ FIXALL : All structural variables which are not explicitly defined as
$           design variables in Optimization Data Deck are considered
$           fixed or constant.
$ VARALL : All structural variable which are not explicitly defined as
$           fixed variables are considered design variables.
$ NOFIX : No strength constraint check in fixed elements, i.e. strength
$           constraints will ONLY be checked in variable elements.
$ VLAMINAT : Whole laminate orientation is ONE ANGLE design variables
$ VANGLE : Each layer has a different angle design variables
FIXALL
$ BANDMIN : Bandwidth minimization of the stiffness matrix.
$ NASDECK : Create NASTRAN bulk data deck output of final design
$ PATNEU : PATRAN Neutral files are created
$ NASTIN : NASTRAN Bulk data deck and case control deck are created
$ ENDCONTROL : ends the control design deck
BANDMIN
NASDECK
ENDCONTROL
***** CASE CONTROL & BULK DATA DECK *****
SUBCASE 1
$ Subcase name : Default
  SPC = 1
  LOAD = 1
BEGIN BULK
$PSHELL | --PID-- | --MID1-- | ---T--- | --MID2- | 12I/T3- | --MID3- | --TS/T- | --NSM-- | ----- |
$----- | ---Z1--- | ---Z2--- | --MID4- |
PSHELL   5         3         .1         3
$----- | --PID-- | --ZO--- | --NSM-- | --SB-- | --FT-- | --TREF-- | --GE--- | --LAM-- | ----- |
$----- | --MID1-- | --T1--- | THETA1- | --SOUT1- | --MID2- | --T2--- | THETA2- | --SOUT2- | ----- |
PCOMP    1         1.3+6 STRN
+PP1     2         0.011 45.0 YES 2         0.011 -45.0 YES +PP1
+PP2     2         0.011 0.0 YES 2         0.011 90.0 YES
$-PBAR- | --PID-- | --MID-- | ---A--- | ---I1-- | ---I2-- | ---J--- | --NSM-- | ----- | ----- |
PBAR     2         1         .001 1.0E-3 1.0E-3 1.0E-3
$-CBAR- | --ELD-- | --PID-- | ---GA-- | ---GB-- | ---X1-- | ---X2-- | ---X3-- | ----- | ----- |
CBAR     522        2         22        21        0.        0.        1.
$-MAT1- | --MID-- | ---E--- | ---G--- | ---NU-- | --RHO-- | --ALPHA- | --TREF-- | ---GE-- | ----- |
$----- | --ST-- | ---SC-- | ---SS-- | -MCSID- |
MAT1     1         1.07+7 .33 .101
+MAT1    20.E+7 15.E+7 12.E+7
$----- | --MID-- | ---E1-- | ---E2-- | --NU12- | --G12-- | --G1Z-- | --G2Z-- | --RHO-- | ----- |
$----- | --A1-- | ---A2-- | --TREF- | --XT-- | --XC-- | --YT-- | --YC-- | --S-- | ----- |
$----- | --GE-- | --F12-- | --STRN- |
MAT8     2         22.80+6 1.29+6 0.300 0.79+6 0.057 +MM3
+MM3     0.        0.        0.        0.0128 0.0111 0.00702 0.0132 0.0292 +MM4
+MM4     1.0
$-GRID- | ---ID-- | ---CP-- | ---X1-- | ---X2-- | ---X3-- | ---CD-- | ---PS-- | ----- | ----- |
GRID     1         0-0.70711-0.70711 0.00000 0
$CQUAD4 | --EID-- | --PID-- | ---G1-- | ---G2-- | ---G3-- | ---G4-- | --THETA- | -ZOFFS- |
CQUAD4   1         1         1         2         4         3 135.000
$CTRIA3 | --EID-- | --PID-- | ---G1-- | ---G2-- | ---G3-- | --THETA- | -ZOFFS- |
CTRIA3   101        50         1         3         11        100

```

```

$-SPC1-|---C---|---G1---|---G2---|---G3---|---G4---|---etc---|-----|-----|-----|
SPC1      1          3456      9      THRU      24
$-LOAD-|---SID---|---S---|---S1---|---L1---|---S2---|---L2---|---S3---|---L3---|-----|
LOAD      10         1.        5.        5        2.        3        5.        7
$-FORCE-|---SID---|---G---|---CID---|---F---|---N1---|---N2---|---N3---|-----|
FORCE      1          45        0-1000.003.648787
$CORD2R-|---CID---|---RID---|---A1---|---A2---|---A3---|---B1---|---B2---|---B3---|-----|
$-----|---C1---|---C2---|---C3---|-----|-----|-----|-----|-----|
CORD2R      1          27.83      56.2200 1.20545-34.9127 56.2176 1.20545+      AV
+          AV 27.8323-6.52271 1.16698
ENDDATA

```

***** OPTIMIZATION DATA DECK *****

```

>OPTIMIZATION
$--POR---|---HYP/REL-|---RKF---|---FDD/GAM-|ALPHA1/T1|---CUT/T2--|-----|---RATMG--|
$ POR : % of Restricted Constraints
$       (0.0 = all constraints are considered)
$       (1.0 = only the violated constraints are considered)
$ HYP : Hypercube reduction factor for SLP, L=HYP*(Max.Gage-Min.Gage)
$       (Default: Automatic calculation of HYP)
$ RELSCA: Relaxations factor for CONLIN, min {f+RELSCA*f(x0)(d^2-1)}
$       (Default = 1.0)
$ RKF : Penalty term for IBF / Response factor for MOM (Default for IBF = 0.2)
$       (Default for MOM = 1.0)
$ FDD : Drawdown factor for IBF (Default = .5)
$ GAMMA : Control of asymptotes for SCP, 0.01=< GAMMA =<1 (Default = .5)
$ ALPHA1: Vector length of line search for GRG (Default = .5)
$ T1 : Control of asymptotes for SCP, 0.1=< T1 =<0.99 (Default = .7)
$ CUT : Control of active constraints of the approximated model for CONLIN
$       (Default = 2.0)
$ T2 : Control of asymptotes for SCP, 1.=< T2 =<10.(Default = 1.15)
$ RATMG: Ratio of max. active constraints, only for SLP, RQP1, RQP2, SCP
$       (Default = 1.0)
$
$ 0.0
$-----|-----|-----|-----|-----|-----|-----|-----|-----|-----|
$--EPSF--|---EPSX---|---EPSKTO---|---EPSL---|---EPSG---|---EPSRES---|
$--EPSF--|---EPSX---|---TOL---|---EPSL---|---EPSG---|---EPSRES---|
$ EPSF : Relative change of objective, only for IBF, MOM, SLP, GRG, CONLIN
$       (Default = 1.E-2, for GRG 1.E-4)
$ EPSX : Relative change of variables, only for IBF, MOM, SLP, CONLIN
$       (Default = 1.E-2)
$ EPSKTO: KUHN TUCKER EPSILON, for RQP1, RQP2, GRG, SCP (Default = 1.E-6)
$ TOL : Internal termination for the accuracy of approximated constraints
$       Only for CONLIN (Default = 1.E-3)
$ EPSL : Optimization epsilon, line search for IBF, MOM (Default = 1.E-2)
$ EPSG : GRADIENT EPSILON, accuracy for finite differencing (Default = 1.E-4)
$ EPSRES: Max. violation of constraints for IBF, MOM, SLP, GRG, CONLIN
$       (Default = 1.E-2, for GRG 1.E-3)
$
$ 1.E-3      1.E-3      1.E-7      1.E-4      1.E-3
$IOP|-NIT|-NDD|-NCC|-CUT|-MGL|-NWD|NWTM|-JT|-RES|-NFR|
$IOP|-NIT|-NDD|-NCC|-CUT|IALG|-IAS|NWTM|-JT|-RES|-NFR|
$ IOP : Output request
$ NIT : Max. number of iterations
$ NDD : Draw-down number for IBF, MOM
$ NCC : Max. number of constraints for CBAR (current version = 1)
$ ICUT : Number of old iterations for SLP
$ MGL : Flag for square interpolation for SLP (0=None, 1=Interpolation)
$ IALG : Flag for square interpolation for SCP (1=SCP, 2=MMA)
$ NWD : Number of watch dog iterations for RQP2
$ IAS : Control of asymptotes for SCP
$ NWTM : Max. # of Newton iterations in Line search > 3 for GRG (default = 10)
$ JT : Type of approximation of the cost function for CONLIN (default = 0)
$ RES : Selection of constraint types with penalty functions for QPRLT and GRG
$       (1 w/o constraints, 2 equality constraints, 3 all constraints)
$ NFR : Number of reduced gradients for QPRLT
$       Number of Fletcher Reeves Steps for GRG
$ 901      20          1          10          3          20

>CGAGE
$-ABS--|---PID1---|---PID2---|---NLA1---|---NLA2---|---GCL---|---GCU---|
$-PERC-|---PID1---|---PID2---|---NLA1---|---NLA2---|---GCL---|---GCU---|
$ ABS : Absolute input of gage constraints
$ PERC : Percentage input of gage constraints

```

```

$ PID1 : Starting property ID
$ PID2 : Ending property ID.
$ NLA1 : Starting layer number
$ NLA2 : Ending layer number.
$ If ABS is used:
$     GCL: Absolute value of lower gage constraints.
$     GCU: Absolute value of upper gage constraints.
$ If PERC is used:
$     GCL: % reduction of the lower gage constraints, e.g. 0.1
$     GCU: % addition of the upper gage constraints.
ABS      1      1      1      4      .0005      .5

>CGANGLE
$--ABS--|--PID1--|--PID2--|--NLA1--|--NLA2--|--GCL--|--GCU--|
$--DEL--|--PID1--|--PID2--|--NLA1--|--NLA2--|--GCL--|--GCU--|
$ ABS : Absolute input of gage constraints
$ DEL : Percentage input of gage constraints
$ PID1 : Starting property ID
$ PID2 : End property ID.
$ NLA1 : Starting layer number
$ NLA2 : End layer number.
$ If ABS is used:
$     GCL: Absolute value of lower gage constraints.
$     GCU: Absolute value of upper gage constraints.
$ If DEL is used:
$     GCL: Reduction of initial ply angle (in degs)
$     GCU: Addition of initial ply angle (in degs)
DEL      1      1      1      4      45.      45.

>CMAT
$---MID---|--EPSXT---|--EPSXC---|--EPSYT---|--EPSYC---|---EPSS---|-----|
$-----|---B1---|---B2---|---CMREF---|
          2  1.280E-02 1.110E-02 0.702E-02 1.320E-02 0.292E-01
          0.000E+00 0.000E+00 0.000E+00

>CDIS
$CDIS1--|---ID---|-----|---NID1---|---NINC---|---NIDN---|---LC1---|---LINC---|---LCN---|+
$+-----|---xl---|---xu---|---yl---|---yu---|---zl---|---zu---|
$ CDIS1 : Displacement constraints, case #1
$ ID : card number
$ NID1 : Starting node ID
$ NINC : Node increment
$ NIDN : Ending node ID
$ LC1 : Starting load case
$ LINC : Load case increment
$ LCN : Ending load case
$ xl/u : Lower/Upper displacement constraint in local x-direction
$ yl/u : Lower/Upper displacement constraint in local y-direction
$ zl/u : Lower/Upper displacement constraint in local z-direction
CDIS1  1000      1      THRU      4      1      +
+      -2.0

>BUCK
$===== SUBBLOCK 1: General Input =====
$-IBID--|--IBTYP--|--ISTYP--|--ICTYP--|--IMAT--|--NLA--|--FMOS--|--RABFA--|--RABFB--|
$--G1---|--G2---|--G3---|--G4---|-----|-----|-----|-----|
$ IBID : Buckling field ID
$ IBTYP : Buckling formula ID
$      1 -> membrane
$ ISTYP : Buckling field from ID
$      1 -> Normal plane rectangular buckling field
$      2 -> Plane rect. buckling field, size corrected by ALPA & ALPB
$ ICTYP : Boundary condition ID
$      1 -> Simply supported
$ IMAT : Material ID for the buckling field
$ NLA : Number of layers which must be constant within the buckling field
$ G1..G4: Grid point ID of the buckling field's corner nodes.
          2      1      1      1      95      4
          20     51     50     21
$===== SUBBLOCK 2: List of elements =====

```

```

$ Single Element Buckling Field
$-NORM-|-----|-----|-----|-----|-----|-----|-----|-----|
$-IEL1-|-IEL2--|-IEL3--|-IEL4--|-IEL5--|-IEL6--|-IEL7--|-IEL8--|-IEL9--|
$ IEL1..IEL9 : Element IDs
$ Range of Elements Buckling Field
$-THRU-|-----|-----|-----|-----|-----|-----|-----|
$-ISTA-|--IEND-|--IINC-|-----|-----|-----|-----|-----|
$ ISTA : Starting Element ID
$ IEND : Ending element ID
$ IINC : Element increment (default = 1)
NORM
    1457    1458    1556    1557    1560    1561
THRU
    1574    1577        1
FEND

>DES VARIABLES
$ SINGLE: Single Element input
$-----NDV-----|
$-(COMP)-|-SINGLE--|--NEL1---|--NEL2---|--NEL3---|--NEL4---|--NEL5---|--NEL6---|
$ NDV : New Design Variables
$ COMP : Composite Material. Blank field for isotropic material
$ NEL1...NEL6 Up to six element IDs may be linked as one design variable
$             Composite materials are defined as a combination of the element
$             number (up to 7 digits) and the layer number (2 digits) separated
$             by a period. For instance, 8000.02
$
$ RANGE      : Range element input
$-----NDV-----|
$-(COMP)-|--RANGE--|---N1S---|---N1E---|---N2S---|---N2E---|---N3S---|---N3E---|
$ N1S : Initial Range (Element ID)
$ N1E : Final Range (Element ID)
$ N1S...N3E Up to three ID range may be linked as one design variable
NEW DESIGN VARIABLES
    COMP SINGLE          1.01    17.01    33.01

>DANGLE
$-----NLA-----|
$-----|-LNUM1-|-LNUM2-|-LINC--|--NLA1-|-NLA2--|-NINC--|-MFAC--|
$ NLA : New Layer Angles
$ LNUM1 : Initial Element Number
$ LNUM2 : Final Element Number
$ LINC : Element Number Increment
$ NLA1 : Initial Layer Number
$ NLA2 : Final Layer Number
$ NINC : Layer Number Increment
$ MFAC : Multiplication Factor for DANGLE LINKING
NEW Layer Angles
    1      33      16      3      3
    1      33      16      4      4      -1

ENDE

```

3.9 Appendix C: Fiber Steering Conceptual Design of Preliminary Studies

3.9.1 Plate with a hole, $W/D = 3.33$, under bi-axial tensile loads.

Layer-thickness contours of the conventional design (pl25L013) are shown in Figures C1. The plate is thicker at **B**, where a majority of reinforcement comes from $\pm 45^\circ$ layers (Figure C1(b)) to overcome in-plane shear loads. The laminate family is approximately (10/80/10). Both 0° and 90° layers are dominant at **C** and **A** respectively due to biaxial tensile loads. At **C**, Figure C1(c) shows that the plate is a (80/10/10) family under axial tensile loads; whereas the plate becomes (10/15/75) at **A** in Figure C1(d) under transverse tensile loads. Away from the hole (**D** to **G**), the laminate family generally behaves as a quasi-isotropic laminate.

Figures C2 and C3 represent an optimal laminate based on Steering I configuration or pl25L113. Interestingly, more reinforcement are found at the lower hole edge or **C** in Figure C2(a). Here, the plate is a (75/15/10) family, where θ_2° layer becomes significant due to axial tensile loads. Note in Figure C3(c), θ_2° layer are shifted down the hole curvature (from **B** to **C**) to effectively align with the primary load path (shear to axial loads). From **A** to **B**, $\pm\theta_1^\circ$ and a portion θ_2° layers play a main role in fiber reinforcement. The $+\theta_1^\circ$ and θ_2° layer vectors are steered from transverse tensile to in-plane shear loads around the hole vicinity, as depicted in Figures C3(a) and C3(d) respectively. The laminate families associated with $+\theta_1^\circ$ and θ_2° layers are approximately (10/60/30) and (10/35/55). As for $-\theta_1^\circ$ layer, fiber trajectories gradually open out from **E** to **B** in Figure C3(b) to overcome shear loads. Away from the hole (**D** to **G**), the laminate family becomes a (30/40/30) laminate.

Figures C4 and C5 show an optimal laminate of the plate model based on Steering II configuration (pl25L213). The plate is thicker at the lower hole edge or **C**, as depicted in Figure C4(a) with (70/20/10) family. It is largely attributed to θ_2° layer, where the fibers are steered to follow shear load at **B** and axial tensile load paths at **C** (see Figures C4(c) and C5(c)). From **A** to **B**, $+\theta_1^\circ$ layer becomes comparatively governing, as it forms a radial curvilinear fiber format to track the shear loads in Figure C5(a) with (10/60/30) family. Note in Figure C5(b), $-\theta_1^\circ$ layer directions gradually broaden out from **E** to **B** to enhance shear reinforcement. In Figure C5(d), layer-angle mappings of θ_3° layer are directed to follow the transverse tensile load path at **A**. Away from the cutout, the laminate becomes a conventional $[\pm 45, 0, 90]_s$ design with (25/40/35) family.

Figure C6 consists of the optimal layer-thickness and layer-angle mappings for pl25L313 based on Steering III configuration. In Figure C6(a), the layer thickness is concentrated at **B** with (10/80/10) family. It is largely contributed by $\pm\theta_1^\circ$ layers, where layer orientations are steered to overcome the shear load (Figures C6(e) and C6(f)). At **C**, θ_2° layer is dominant due to the axial tensile load (Figure C6(c)). Here, the laminate family is approximately (65/25/10). Due to the transverse tensile and shear loads, $\pm\theta_1^\circ$ layer is prominent from **A** to **B**. Referring to Figures C6(e) and C6(f), $\pm\theta_1^\circ$ layer orientations are aligned in transverse direction at **A** and gradually steered in shear direction. Away from the hole (**D** to **G**), the plate behaves as a (25/45/30) laminate.

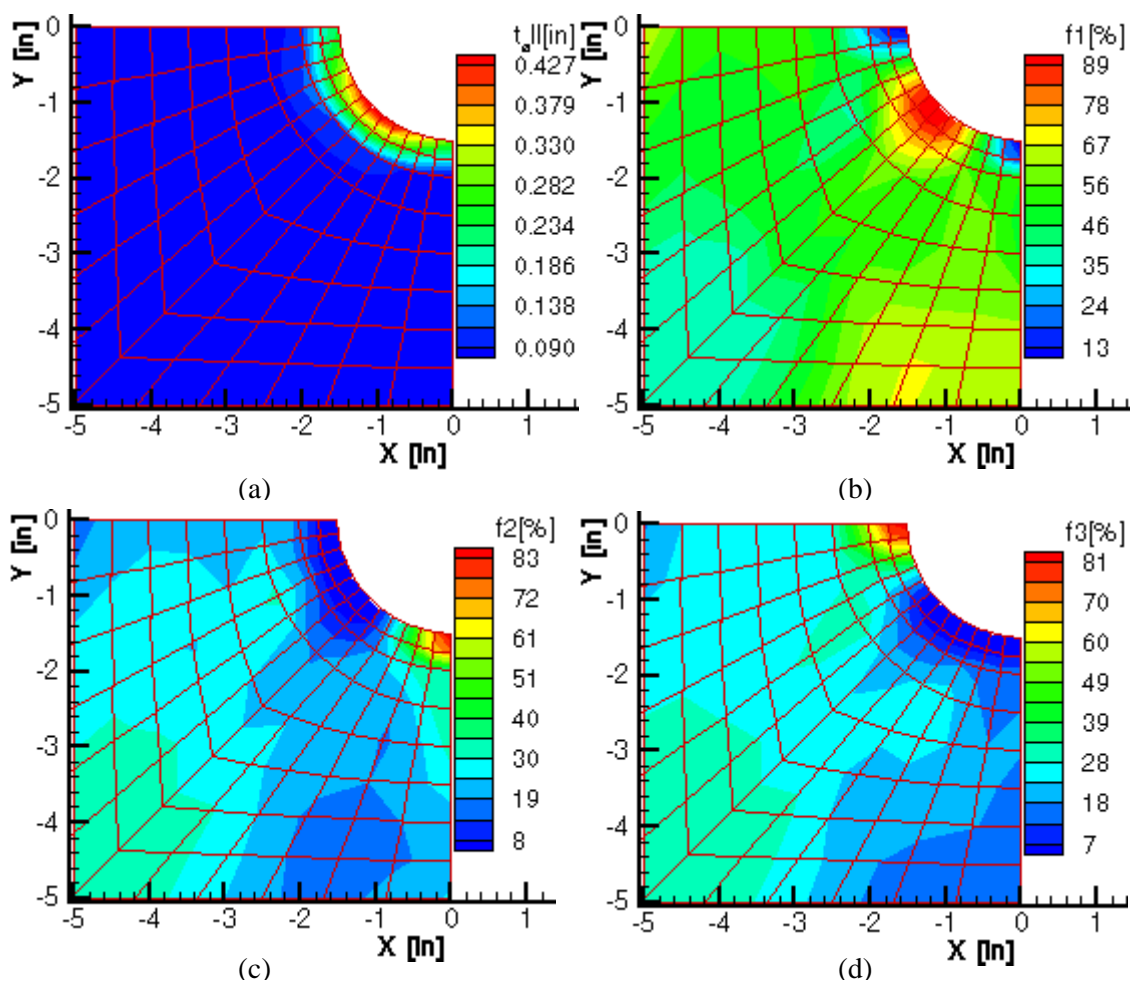


Figure C1: Layer-thickness contours for pl25L013.

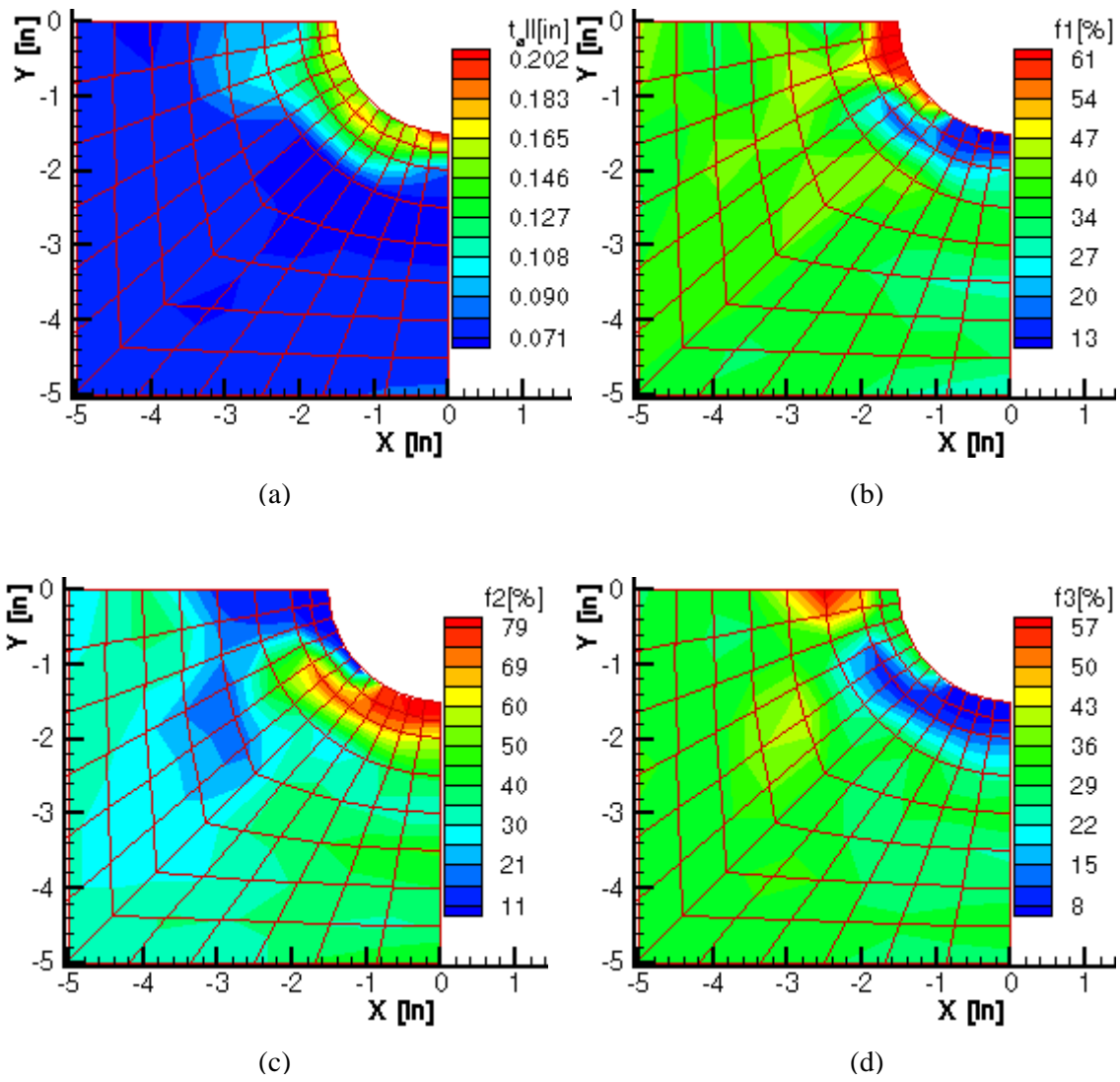


Figure C2: Layer-thickness contours for pl25L113.

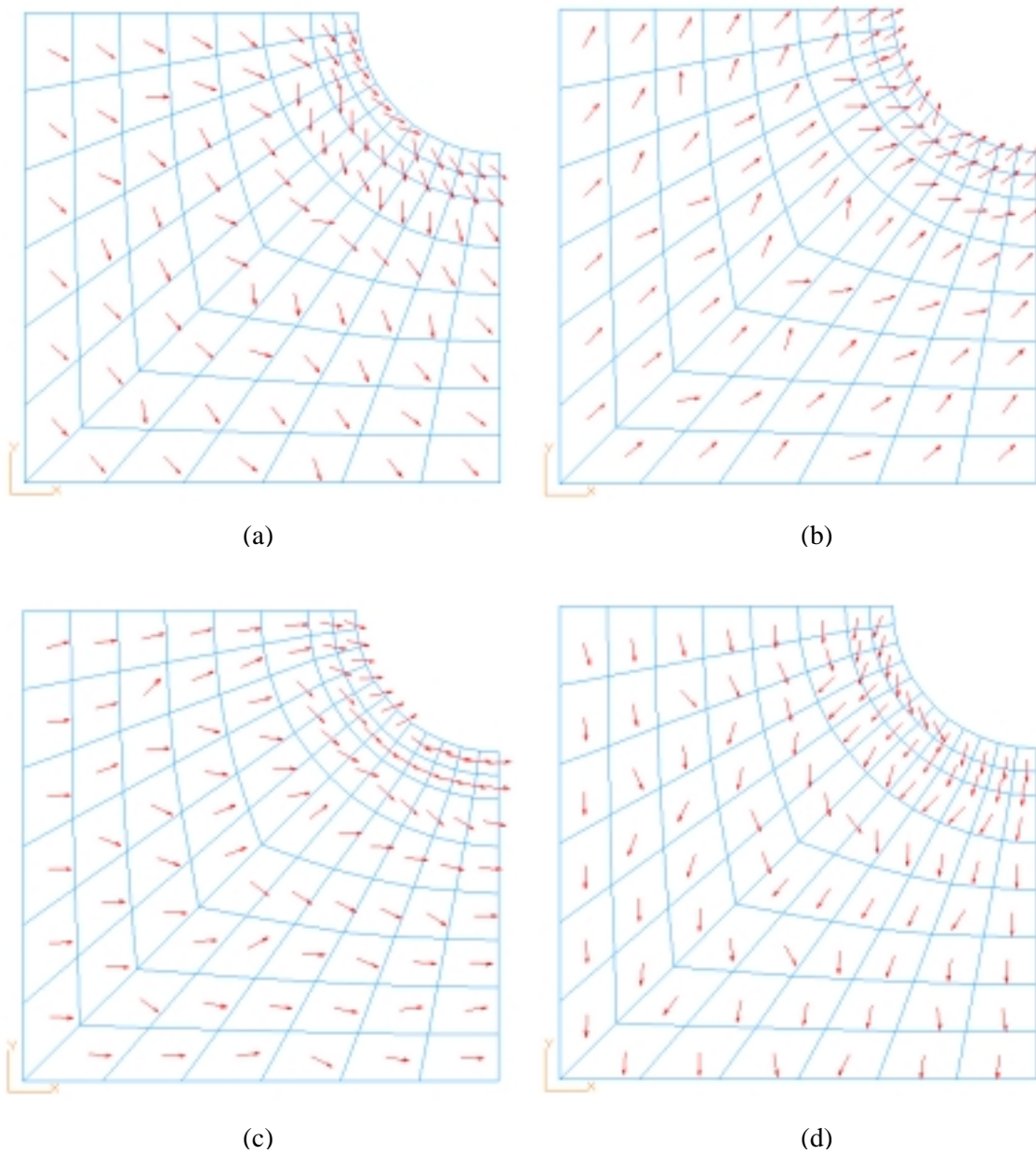


Figure C3: Layer-angle mappings for pl25L113.

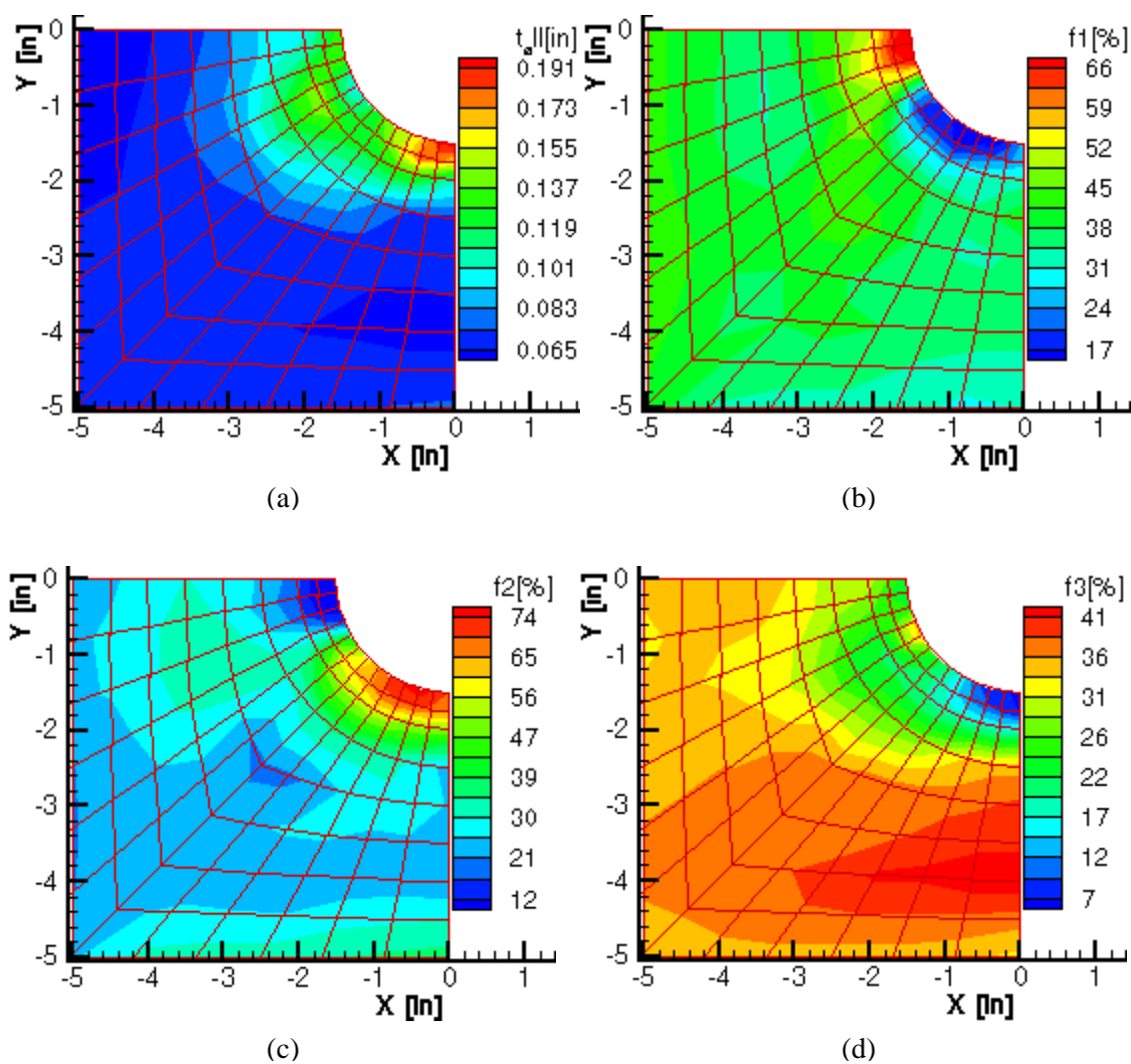


Figure C4: Layer-thickness contours for pl25L213.

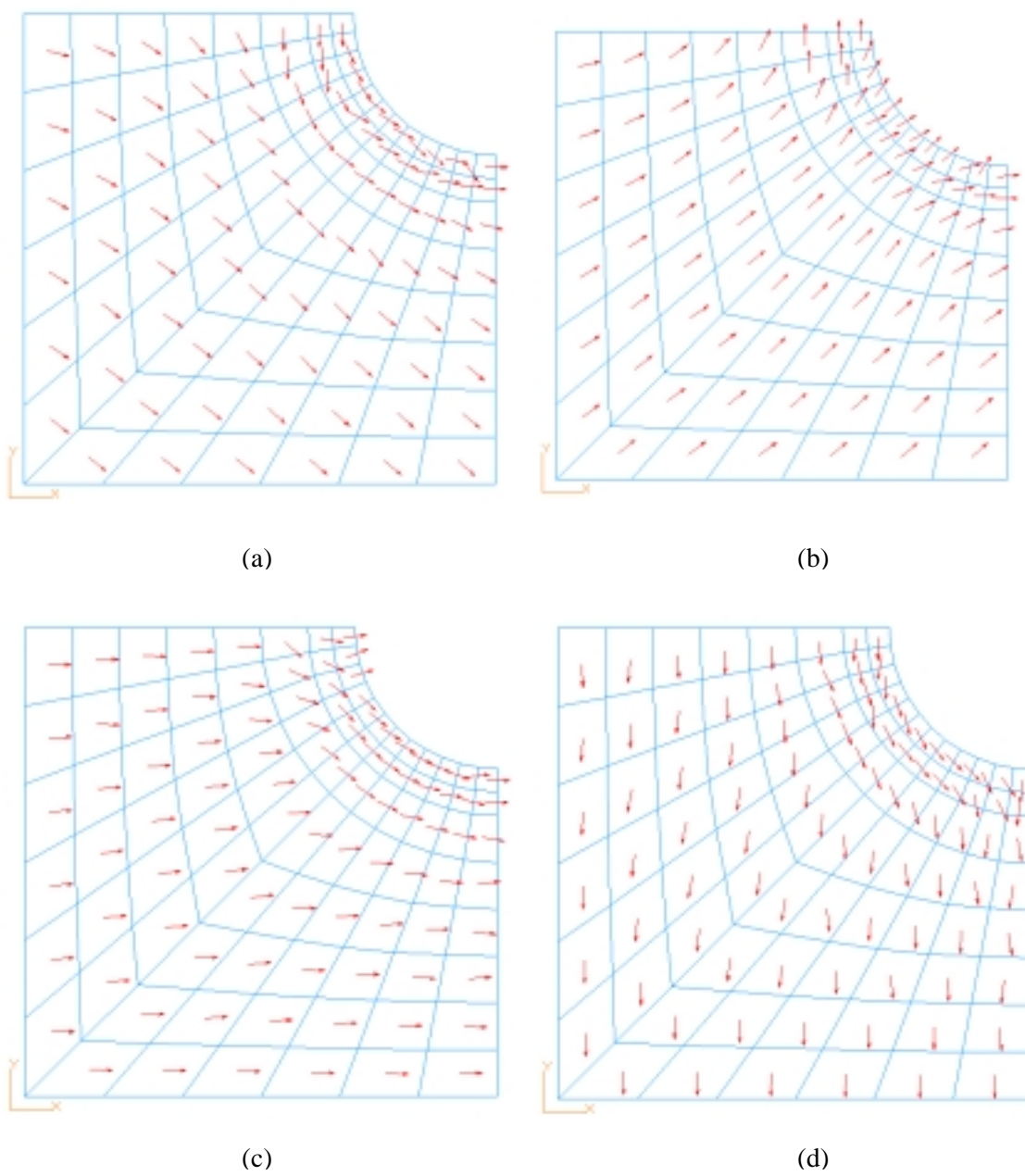


Figure C5: Layer-angle mappings for pl25L213.

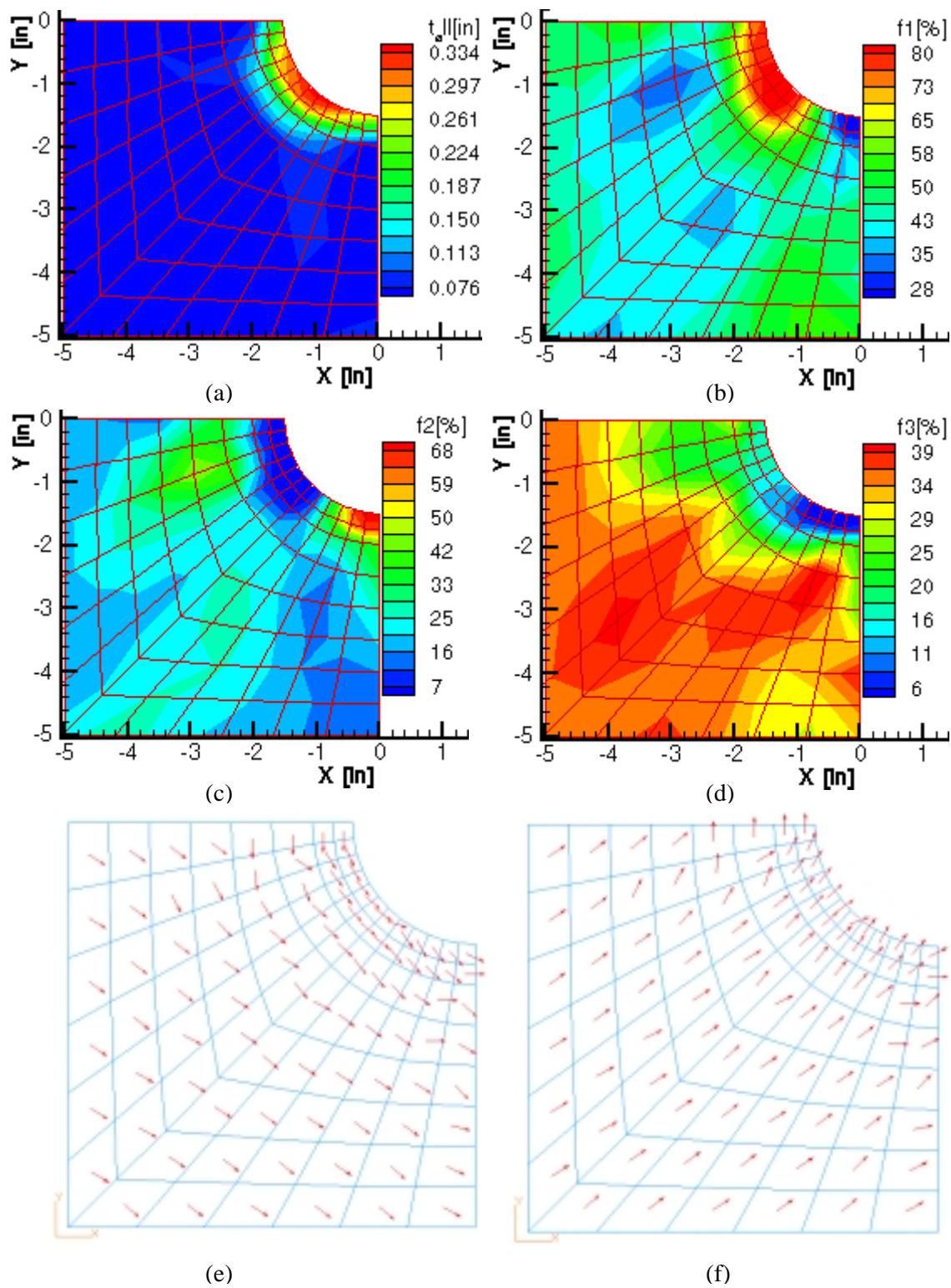


Figure C6: Layer-thickness contours and layer-angle mappings for pl25L313.

3.9.2 Plate with a hole, $W/D = 3.0$, under bi-axial tensile loads.

Figure C7 shows the straight-line design (pl34L013) of this model. More material are gathered at **B** as predicted, where the laminate family is approximately (7/86/7). A majority of reinforcement comes from $\pm 45^\circ$ layers (Figure C7(b)) due to in-plane shear loads. At **C**, Figure C7(c) shows that the plate is a (80/13/7) family under axial tensile loads; whereas the plate becomes (7/13/80) at **A** in Figure C7(d) under transverse tensile loads. Away from the hole (**D** to **G**), the laminate family generally behaves as a quasi-isotropic laminate.

Figures C8 and C9 represent an optimal laminate based on Steering I configuration or pl34L113. More reinforcement are established around the hole vicinity in Figure C8(a). Due to axial tensile loads, θ_2° layer is configured with (75/15/10) family at **C**. As illustrated in Figure C9(c), fiber trajectories of θ_2° layer are steered from **B** to **C** to effectively align with the primary load path (shear to axial loads). From **A** to **B**, $\pm\theta_1^\circ$ and θ_2° layers play a main role in fiber reinforcement. The $+\theta_1^\circ$ and θ_2° layer vectors are steered from transverse tensile to in-plane shear loads around the hole vicinity, as depicted in Figures C9(a) with (10/40/50) and C9(d) with (10/30/60) respectively. As for $-\theta_1^\circ$ layer, layer orientations gradually spread out from **E** to **B** in Figure C9(b) to withstand shear loads. Away from the hole, discontinuity in the variation of layer vectors is observed. The results probably reach the local minima in gradient-based optimizations.

Figures C10 and C11 show optimal results of the plate model based on Steering II configuration (pl34L213). The plate has more reinforcement around the hole vicinity in Figure C10(a). The band of layer thickness contour (measured radially from cutout to plate boundaries) is noticeably wider compared with other plate models. At **C**, the plate is composed of (70/20/10) family, as depicted in Figure C10(a). It is largely attributed to θ_2° layer, where the fibers are steered to follow shear load at **B** and axial tensile load paths at **C** (see Figures C11(c)). The $+\theta_1^\circ$ and a portion of θ_3° layers also resemble similar fiber trajectories with θ_2° layer at these locations. From **A** to **B**, $+\theta_1^\circ$ layer becomes comparatively dominant, as it forms a radial fiber format to track shear loads in Figure C11(a) with (10/60/30) family. The contribution of θ_3° layer in the plate reinforcement is not significant from **A** to **B**. However, θ_3° layer angles are tailored to align with transverse load path at **A** and shear load path at **B**. In Figure C11(b), $-\theta_1^\circ$ layer directions gradually broaden out from **E** to **B** to enhance shear reinforcement. Away from the cutout, the laminate becomes a conventional $[\pm 45, 0, 90]_s$ design with approximately (25/40/35) family.

Finally, Figure C12 consists of the optimal layer-thickness and layer-angle mappings for pl34L313 based on Steering III configuration. In Figure C24(a), the layer thickness is concentrated at **B** with (10/80/10) family. It is largely influenced by $\pm\theta_1^\circ$ layers, where layer orientations are steered to overcome the shear load (Figures C12(e) and C12(f)). At **C**, θ_2° layer is dominant due to the axial tensile load (Figure C12(c)). Here, the laminate family is approximately (70/20/10). Due to transverse tensile and shear loads from **A** to **B**, substantial reinforcement come from $\pm\theta_1^\circ$ layer, where layer orientations are aligned in transverse direction at **A** and gradually steered in shear direction. Away from the hole (**D** to **G**), the plate behaves as a (25/40/35) laminate.

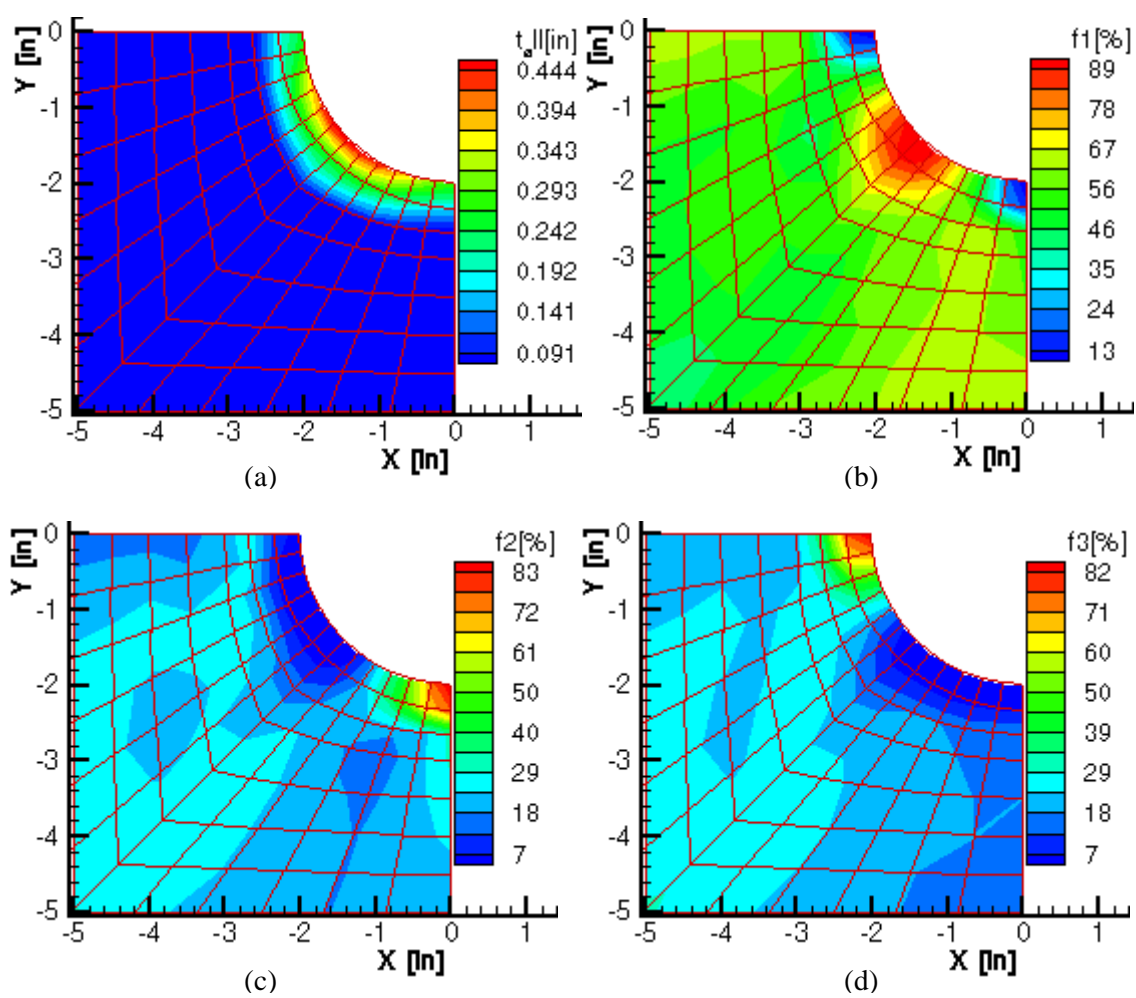


Figure C7: Layer-thickness contours for pl34L013.

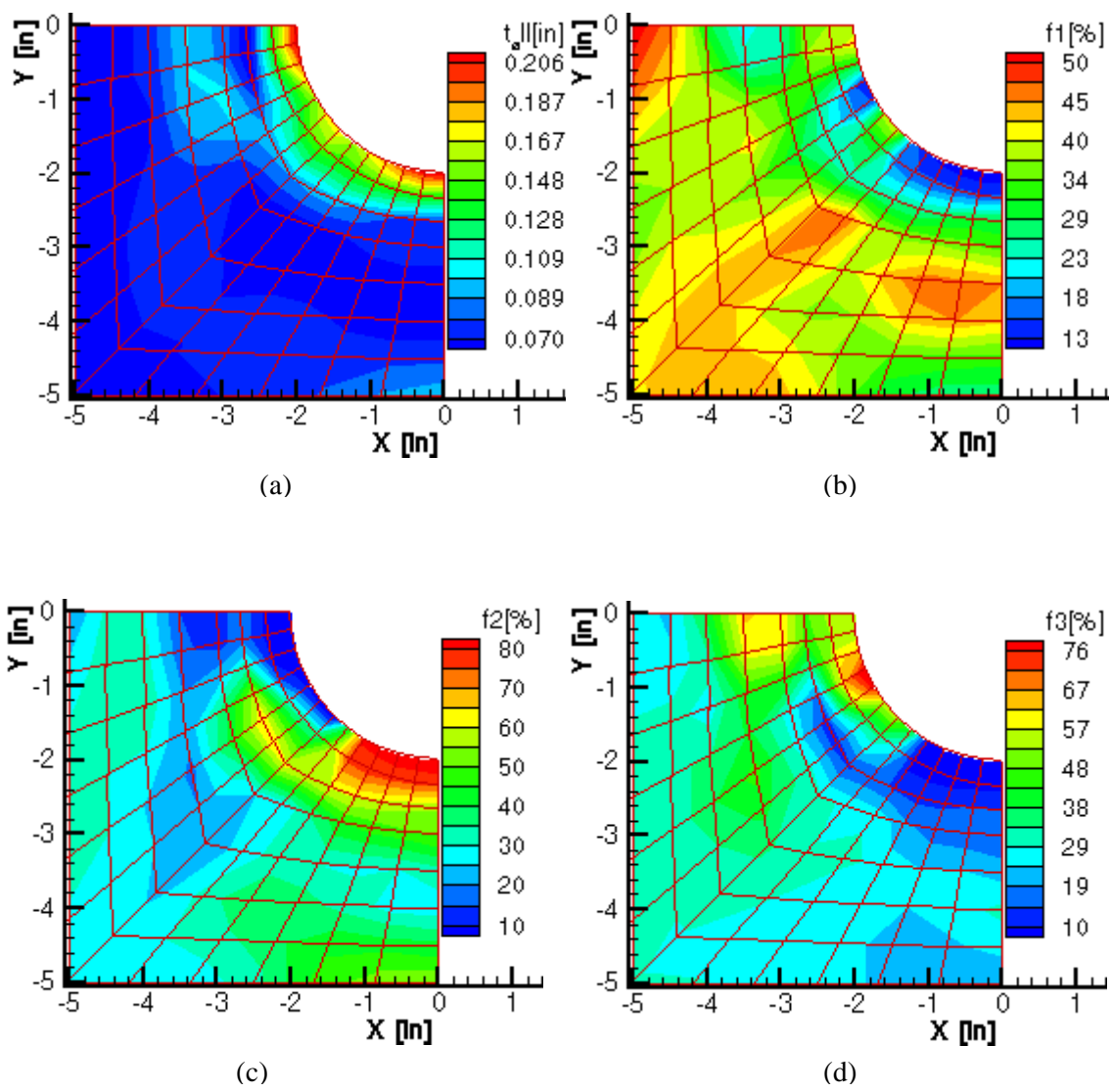
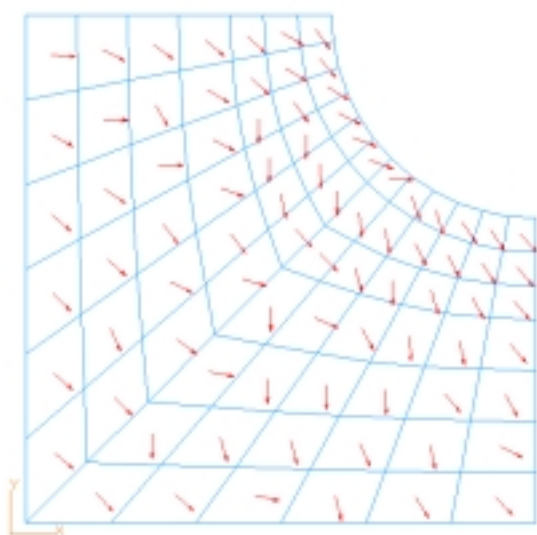
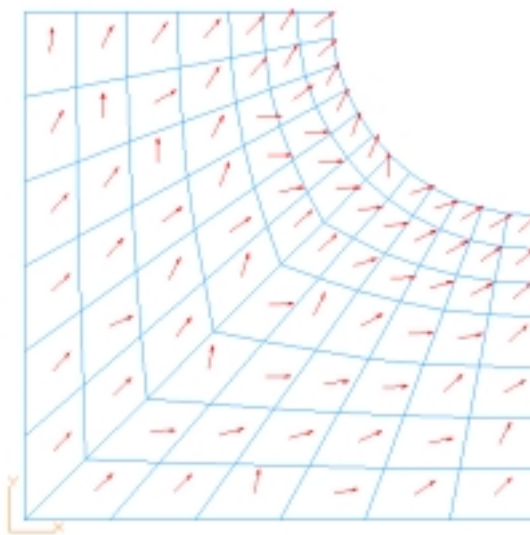


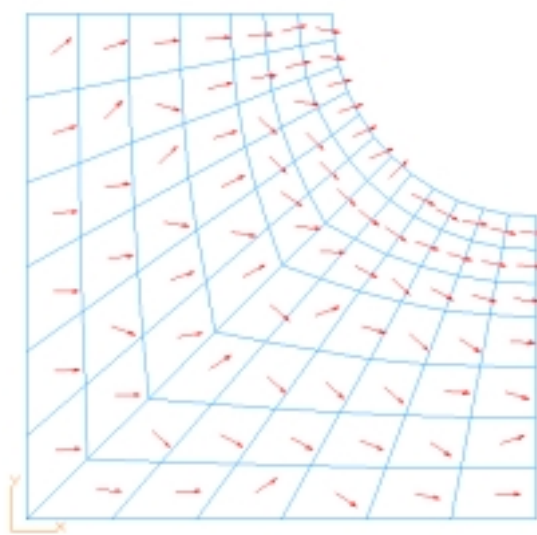
Figure C8: Layer-thickness contours for pl34L113.



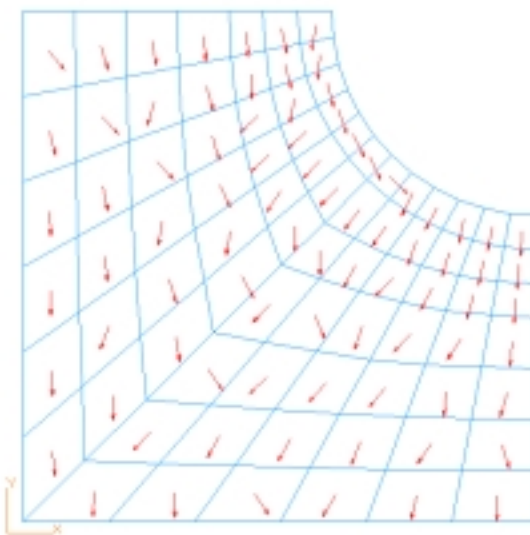
(a)



(b)



(c)



(d)

Figure C9: Layer-angle mappings for pl34L113.

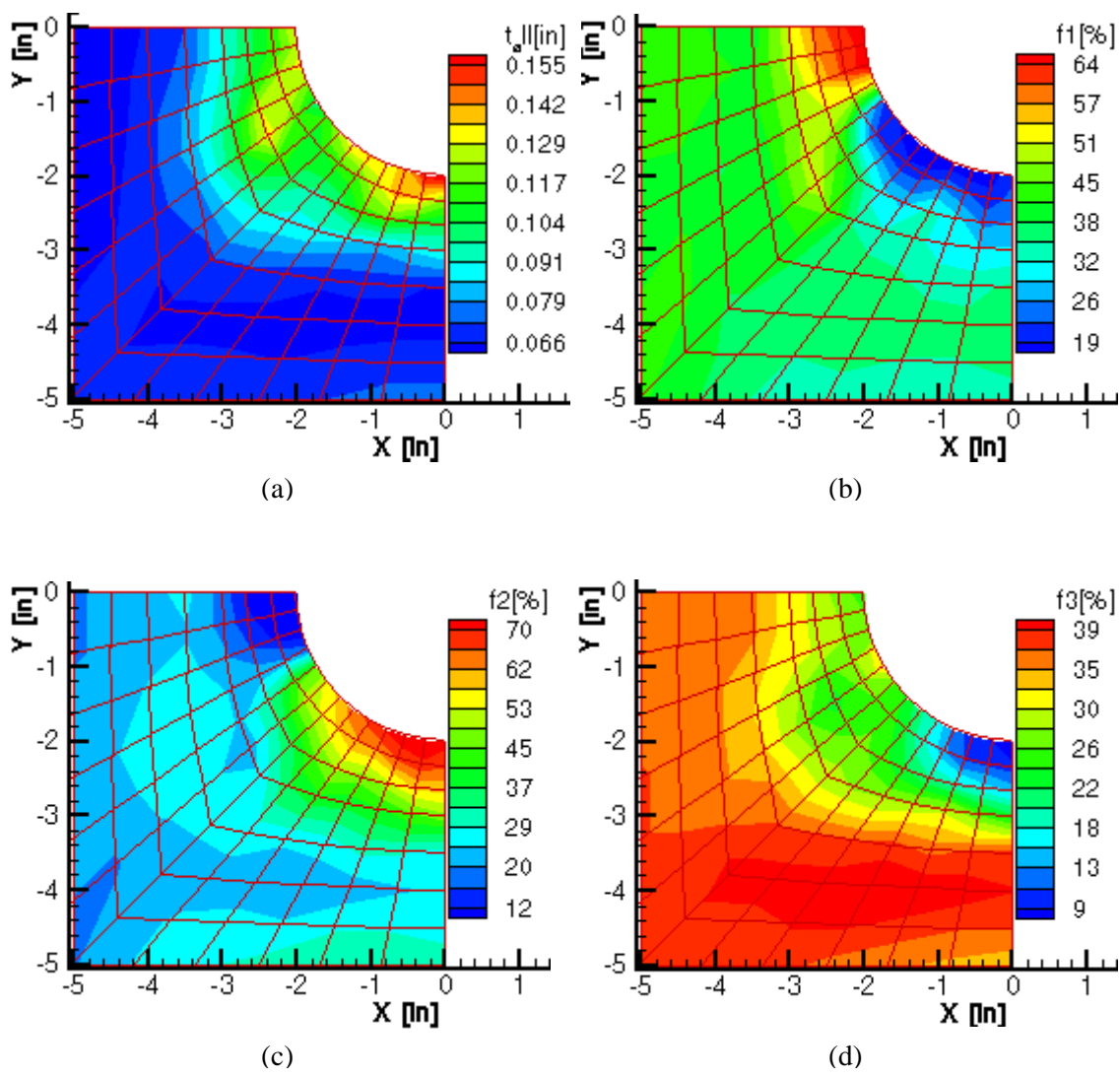


Figure C10: Layer-thickness contours for pl34L213.

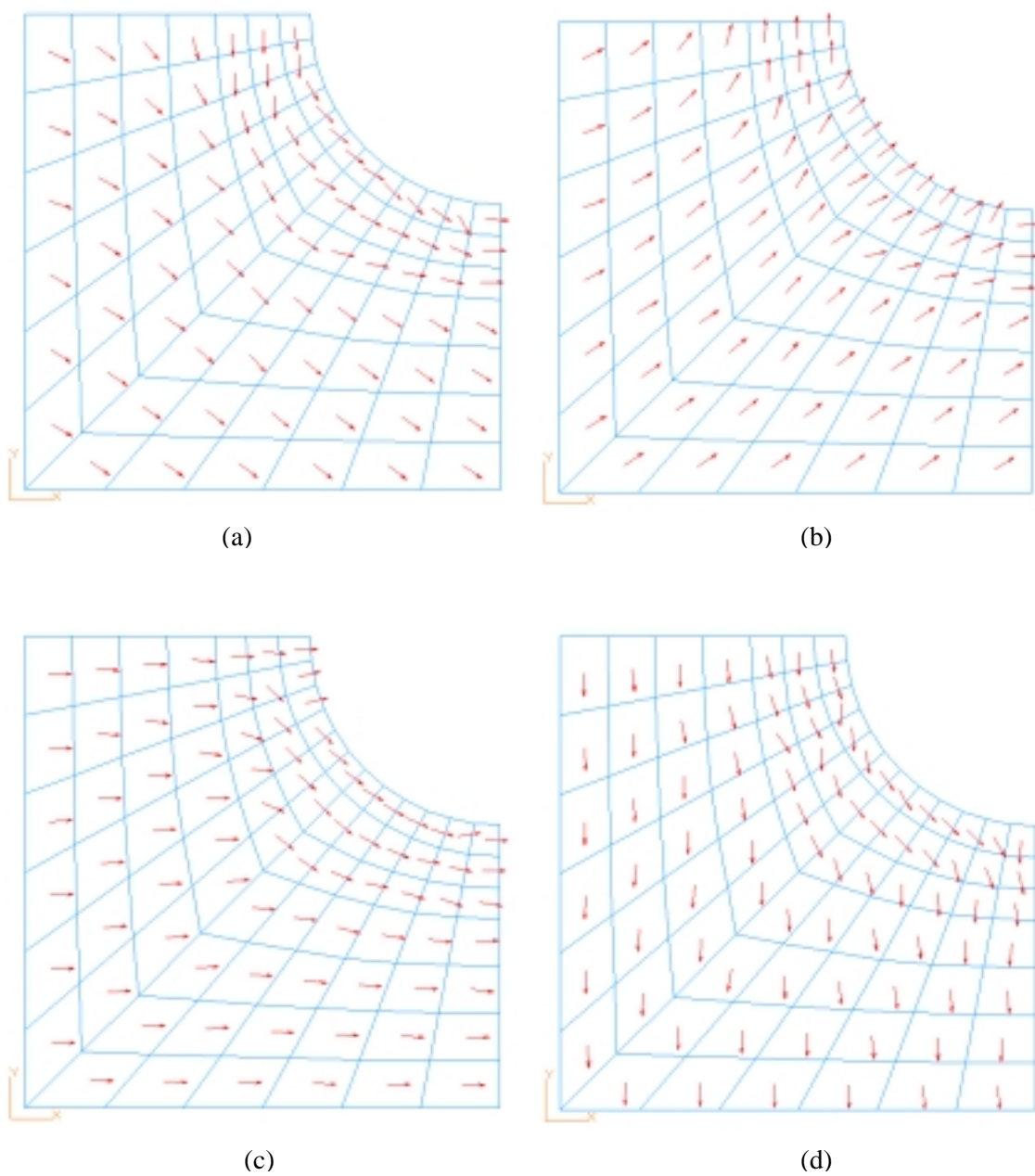


Figure C11: Layer-angle mappings for pl34L213.

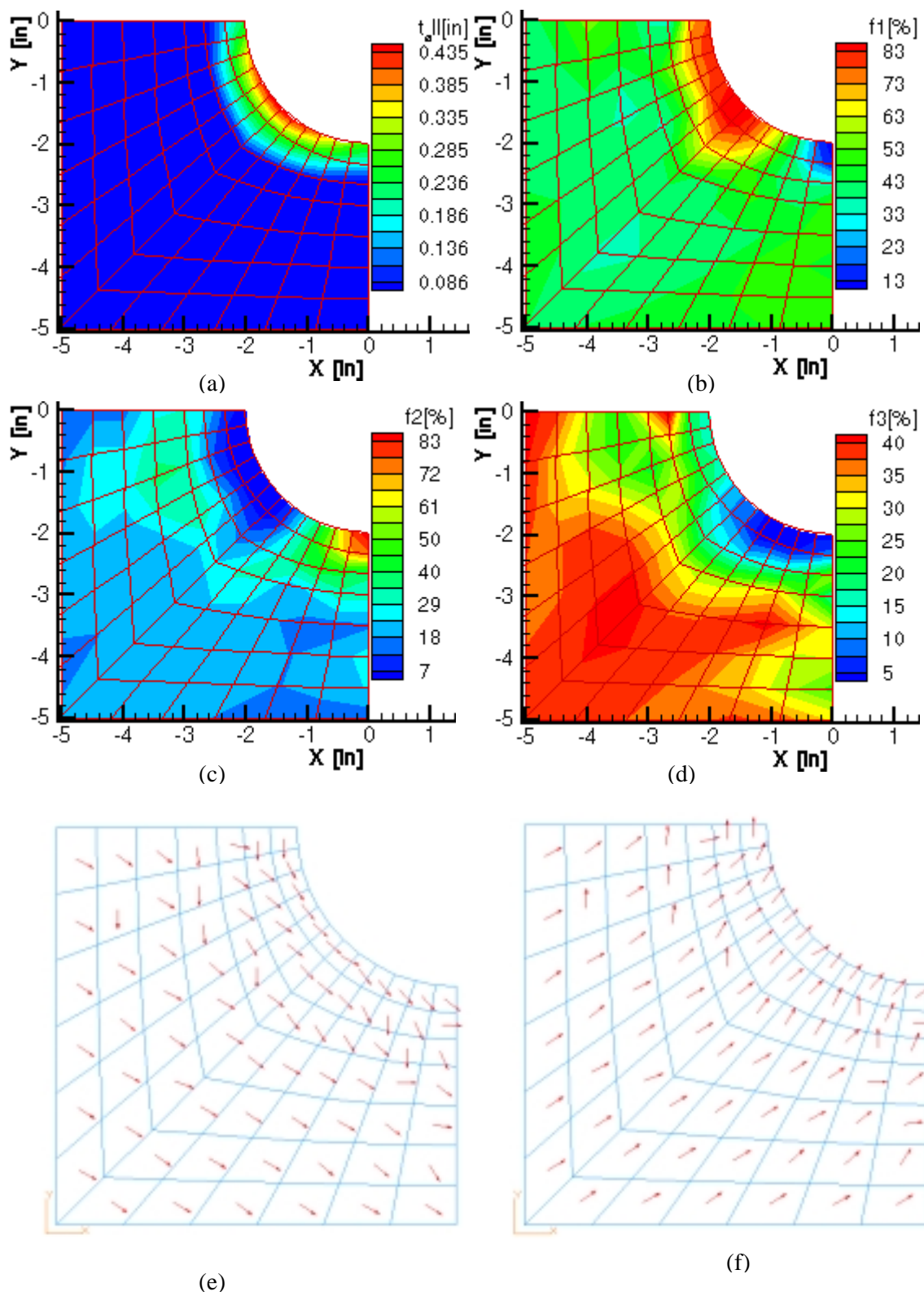


Figure C12: Layer-thickness contours and layer-angle mappings for pl34L313.

3.9.3 Cantilever rectangular panel under transverse loads.

Specific locations of this model are labeled accordingly in Figure C13 to help explaining the results of FS conceptual design. Figure C14 illustrates the baseline design (cb1L013) for a cantilever rectangular panel under transverse loads. More reinforcement are gathered at A and C, as predicted in Figure C14(a). It is largely attributed to the 0° layer. In Figure C14(b), $\pm 45^\circ$ layers play a key role in shear reinforcement in the panel's middle and free end regions, where laminate families are about (20/60/20) at B, (15/70/15) at F, (20/60/20) at G, (15/70/15) at H, and (20/60/20) at J, respectively. Note that a portion of 90° layer reinforcement is comparable at G and J due to transverse loads (see Figure C14(d)). At D and E, 0° becomes significant with (75/15/10) family in Figure C14(c) due to Poisson's effect.

With Steering I configuration (cb1L113) in Figures C15 and C16, the panel has more material at A and C as predicted. At these locations, fiber reinforcement come from θ_2° layer, where the laminate family is (80/12/8) in Figures C15(c) and C16(c). Note that fibers in the top (A-D) and bottom (C-E) regions are aligned in the longitudinal direction so that tensile and compressive loads are effectively transferred. In the middle regions or F, substantial reinforcement are contributed by θ_2° and $\pm\theta_1^\circ$ layers due to shear loads. The laminate family is about (40/45/15). In Figures C15(b) and C16(b), $\pm\theta_1^\circ$ layers become significant to withstand shear loads at H and also transverse loads at B, G, and J, where the laminate families are (25/55/20) at H, and (25/50/25) at B, G, and J, respectively.

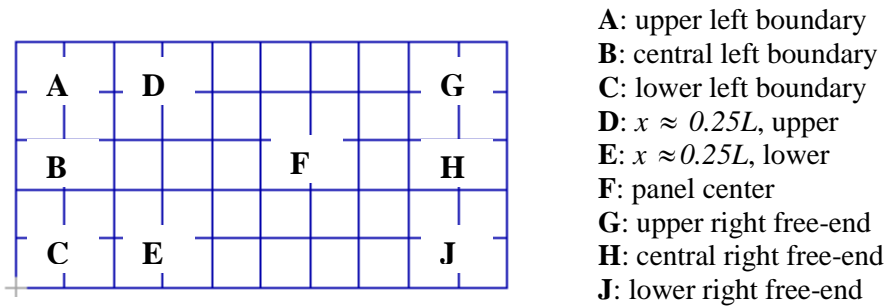


Figure C13: Specific location labeling for the cantilever panel.

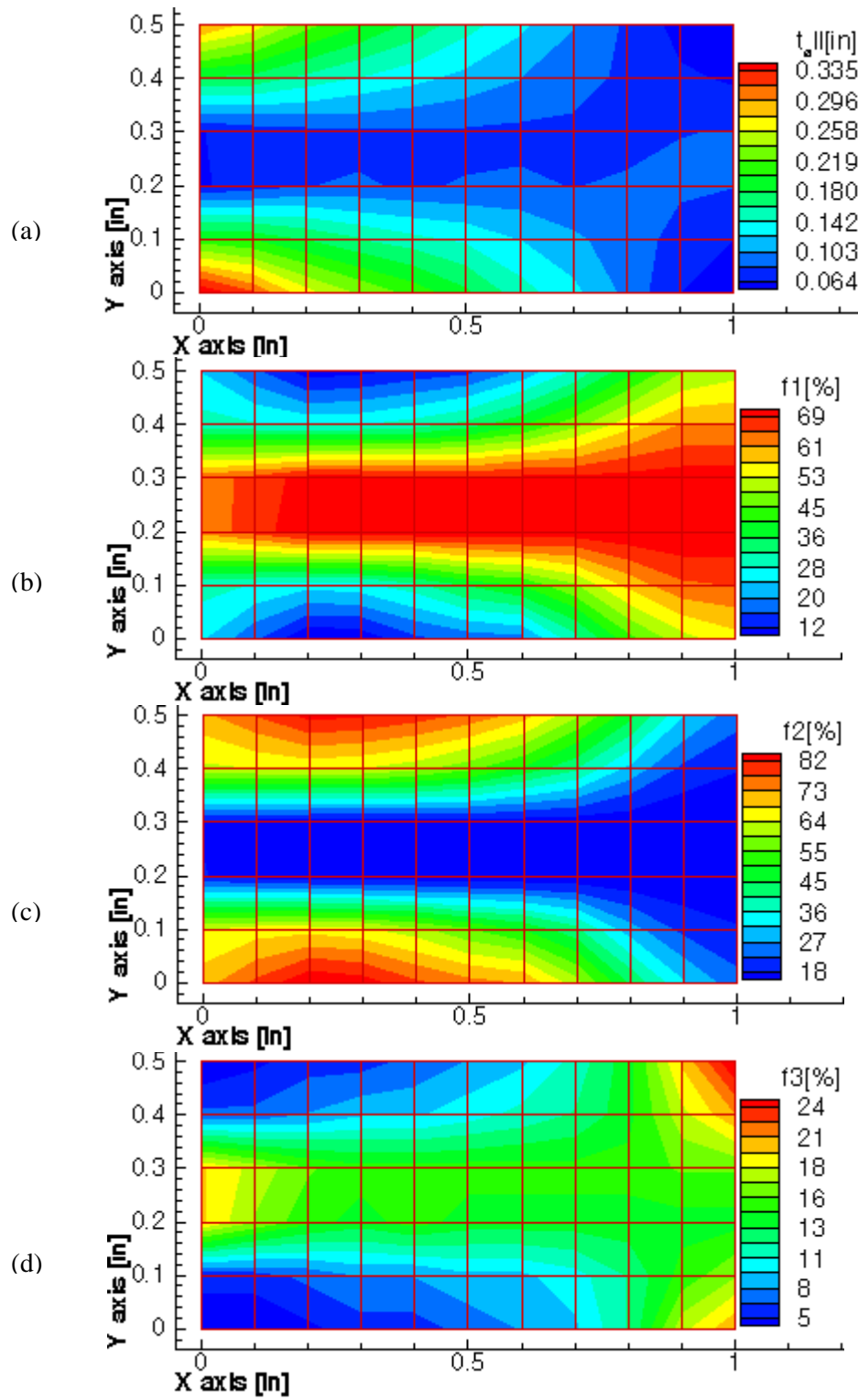


Figure C14: Layer-thickness contours for cb1L013.

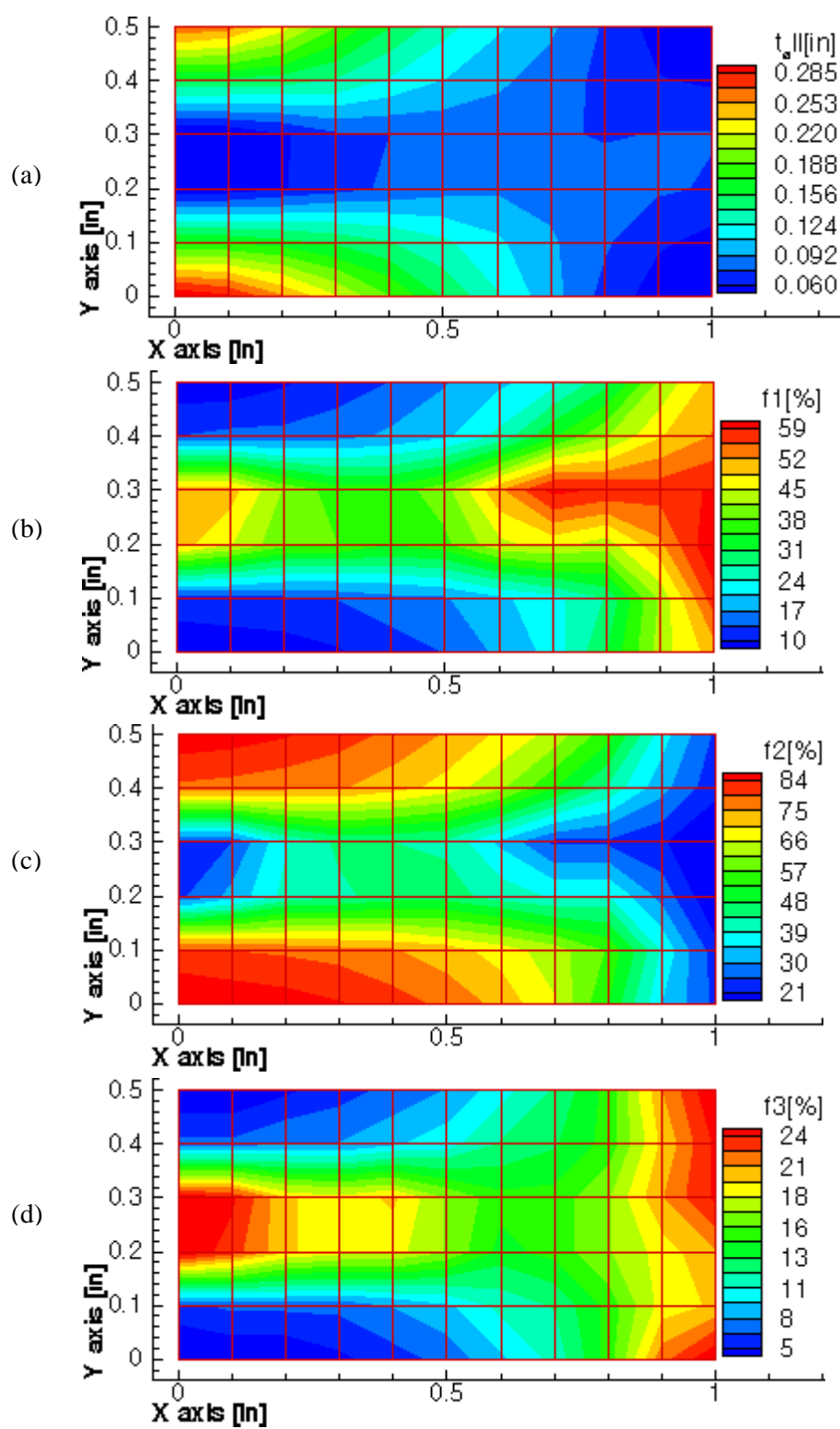


Figure C15: Layer-thickness contours for cb1L113.

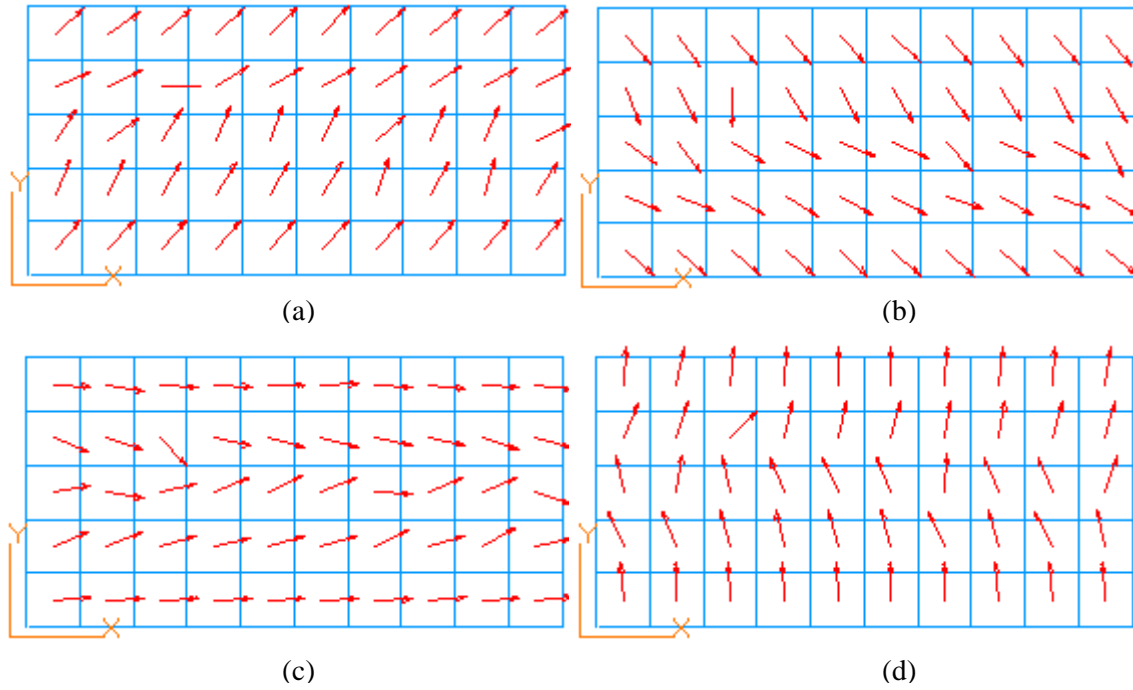


Figure C16: Layer-angle mappings for cb1L113.

Comparing with Figure C15(a), similar total layer-thickness contours are found in Figure C17(a) based on Steering II configuration (cb1L213). At A-D and C-E regions, the panel is configured with θ_2° layer and a portion of $\pm\theta_1^\circ$ layers, where the laminate family is approximately (60/30/10) in Figures C17(c) and C17(b). In fact, layer angles corresponding to these layers are steered to follow the axial load paths (see Figures C18(a) to C18(c)). At G and J (free end), $\pm\theta_1^\circ$ layer angles are tailored to overcome the shear loads. Note that θ_2° fibers are shifted in off-axis directions to follow shear-load trajectories in the middle regions or F, together with reinforcement from $\pm\theta_1^\circ$ layers. The panel at F is composed of (40/40/20) family. In Figures C17(d) and C18(d), θ_3° layer are noticeably gathered at B, G, and J with (25/50/25) due to transverse loads.

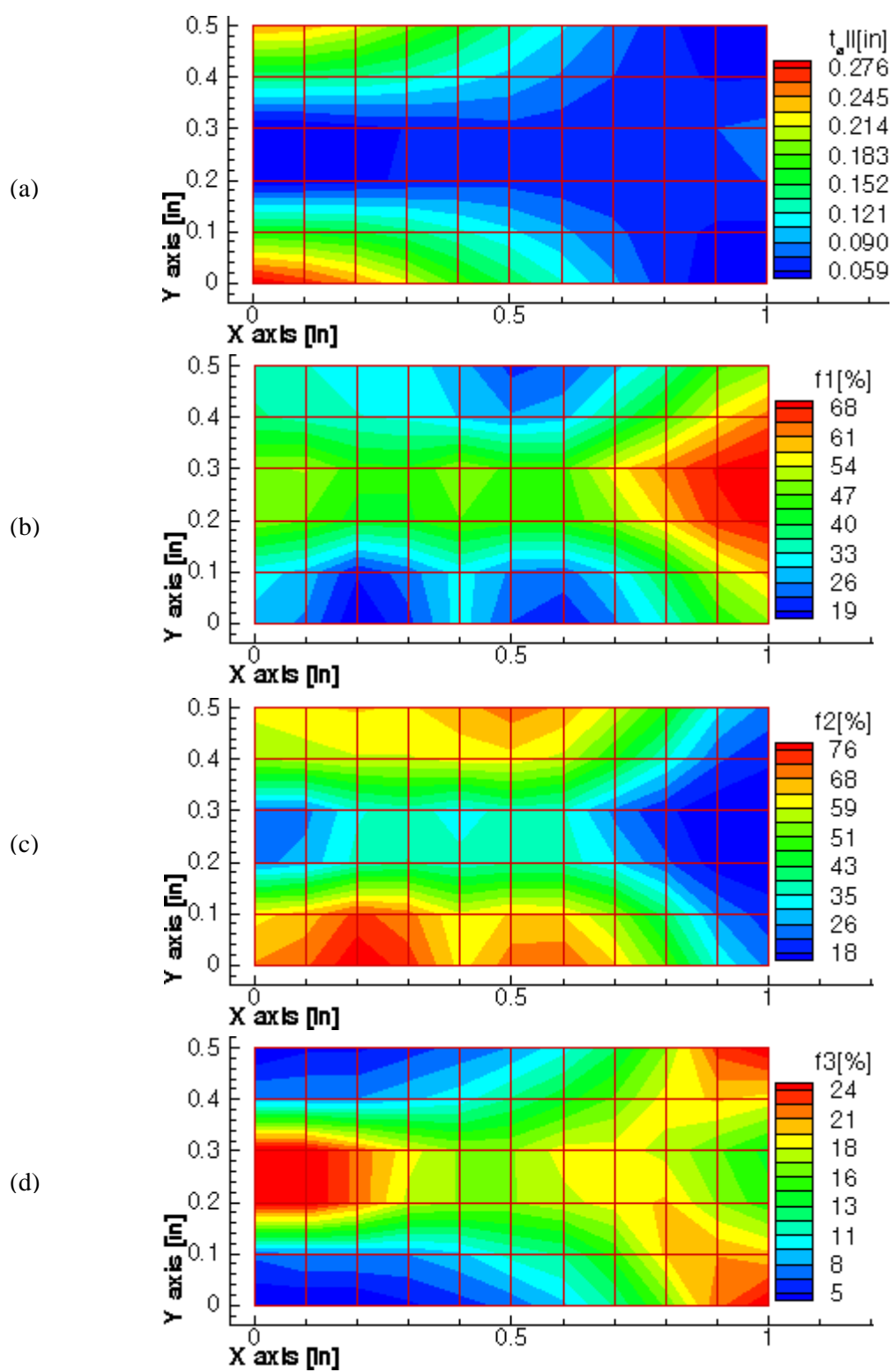


Figure C17: Layer-thickness contours for cb1L213.

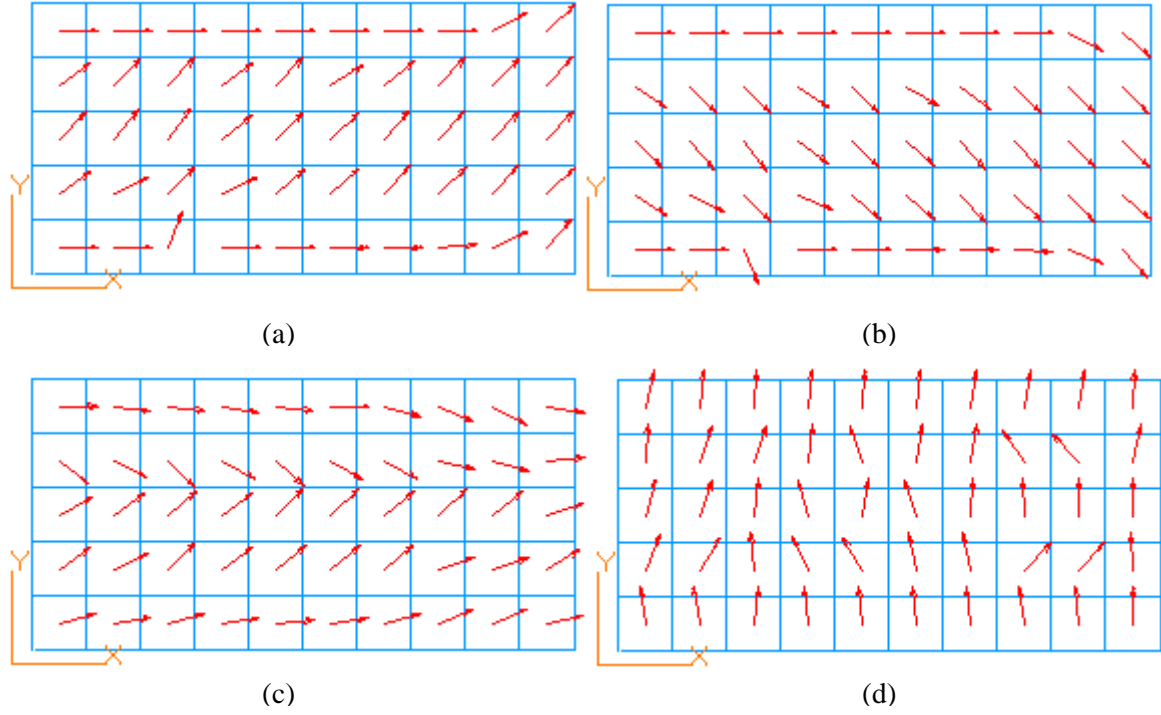


Figure C18: Layer-angle mappings for cb1L213.

Finally, the resultant layer-thickness contours for Steering III configuration (cb1L313) are quite similar with the baseline design. Substantial reinforcement are found at A and C as predicted. It is largely attributed to the 0° layer as shown in Figure C19(c). In Figure C19(b), off-axis layers play a major role in shear reinforcement at B, F, G, H, and J respectively. The laminate family at these locations is about (20/65/15). The steering effect of $\pm\theta_l^\circ$ layers is not significant, as illustrated in Figures C20(a) and C20(b). Only a portion of layer vectors is shifted to align in axial tensile and compressive direction at A and C. In Figure C19(d), a portion of 90° layer reinforcement gathers at G and J due to transverse loads.

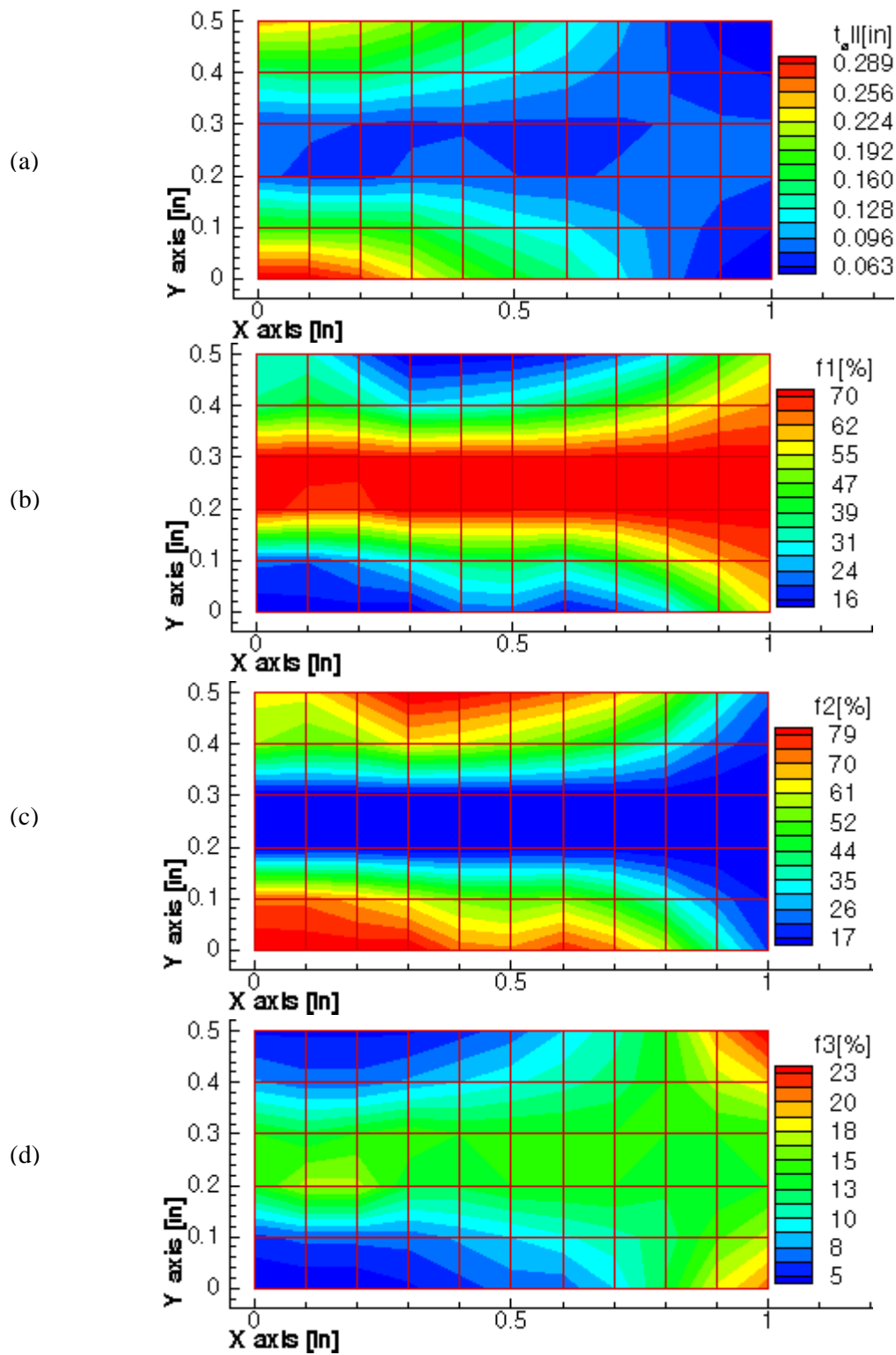


Figure C19: Layer-thickness contours for cb1L313.

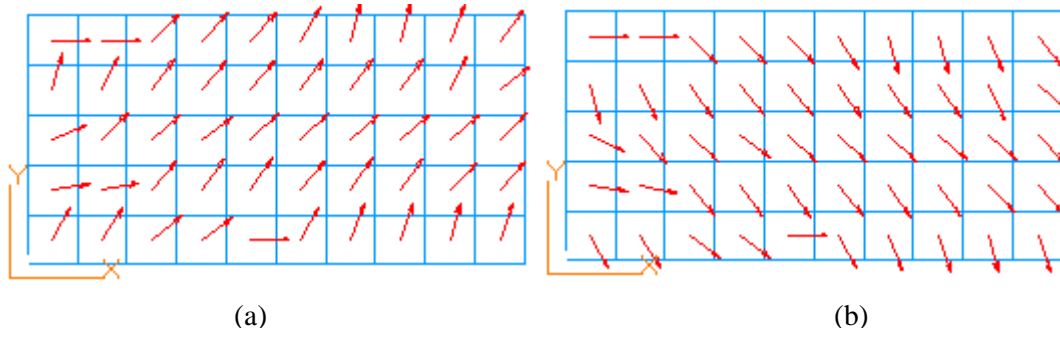


Figure C20: Layer-angle mappings for cb1L313.

3.9.4 Cantilever cylindrical tube under combined loads.

Figure C21 shows the layer-thickness contours for tb1L073 or baseline design, where the tube front (top contour of Figure C21(a)) has more reinforcement than aft. Generally, the reinforcement drops from tube-front middle regions with (60/35/5) family to tube-aft middle regions with (30/63/7) in hoop direction. In both cases, 90° -layer contribution is insignificant. At the fixed boundary, the tube is thicker due to Poisson's effect, which is primarily reinforced with the 0° layer.

Figures C22 and C23 represent the optimal result for this model based on Steering I configuration (tb1L173). Compared with the baseline, similar trends in the layer thickness contour are seen. The tube front (top contour of Figure C22(a)) has more reinforcement than aft. And, the reinforcement drops from tube-front middle regions with (85/10/5) family to tube-aft middle regions with (70/20/10) in hoop direction. In both cases, θ_2° layer contributes to the tube's primary reinforcement; whereas, θ_3° -layer contribution is insignificant. Note in Figure C23(c), a slight change in the θ_2° layer orientations from axial direction can be seen due to combined loads. Other layers ($\pm\theta_1^\circ$ and θ_3°) are tailored w.r.t. the θ_2° layer, as illustrated in Figures C23(a), C23(b), and C23(d), respectively.

The layer-thickness contours and layer-orientation mappings for tb1L273 and tb1L373 are shown and discussed in this section because similar trends of these plots are obtained.

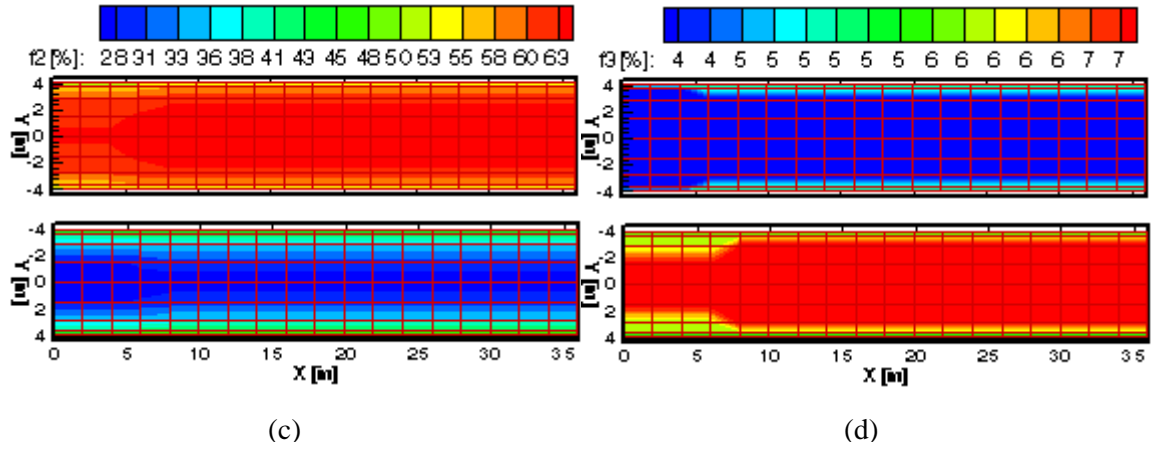
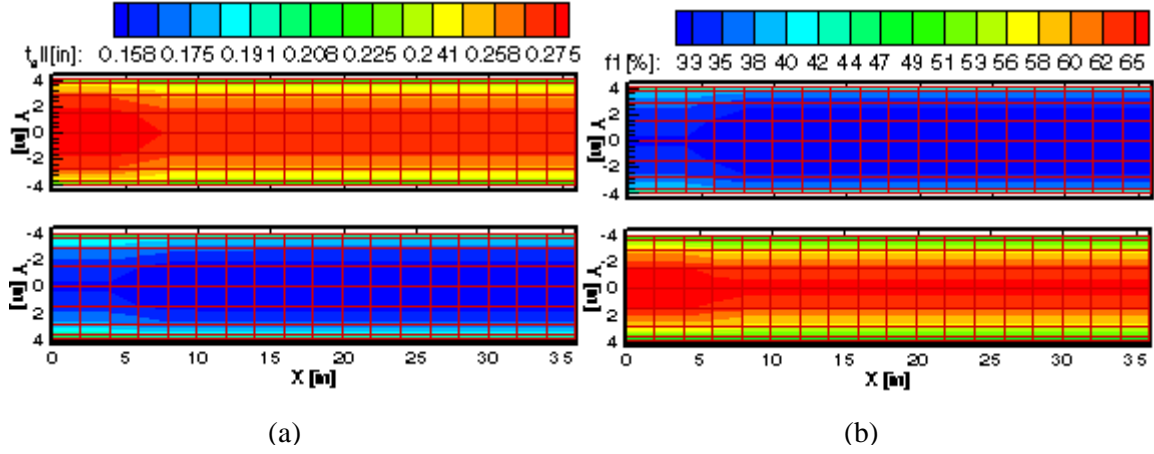


Figure C21: Layer-thickness contours for tb1L073 (front and aft views).

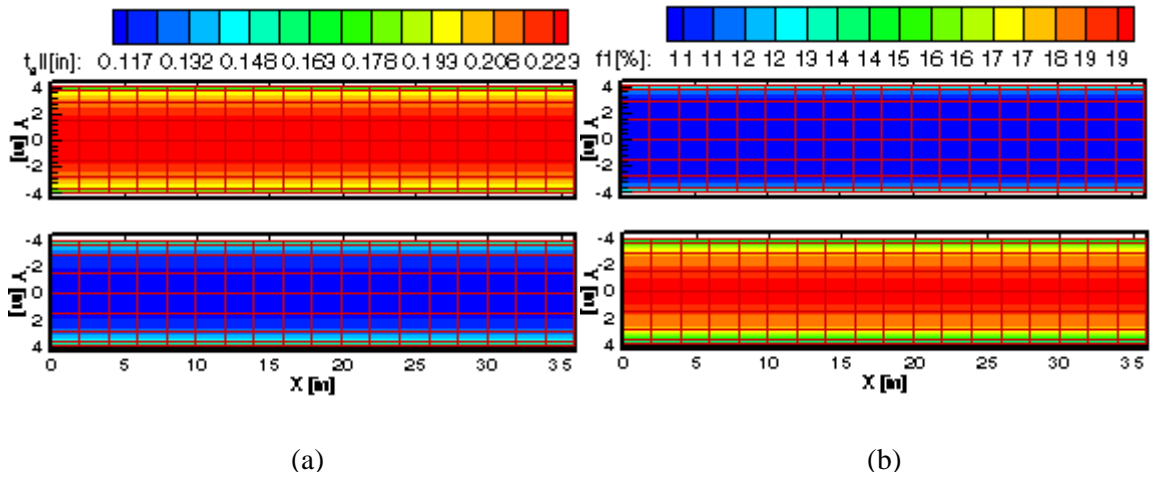


Figure C22: Layer-thickness contours for tb1L173 (front and aft views).

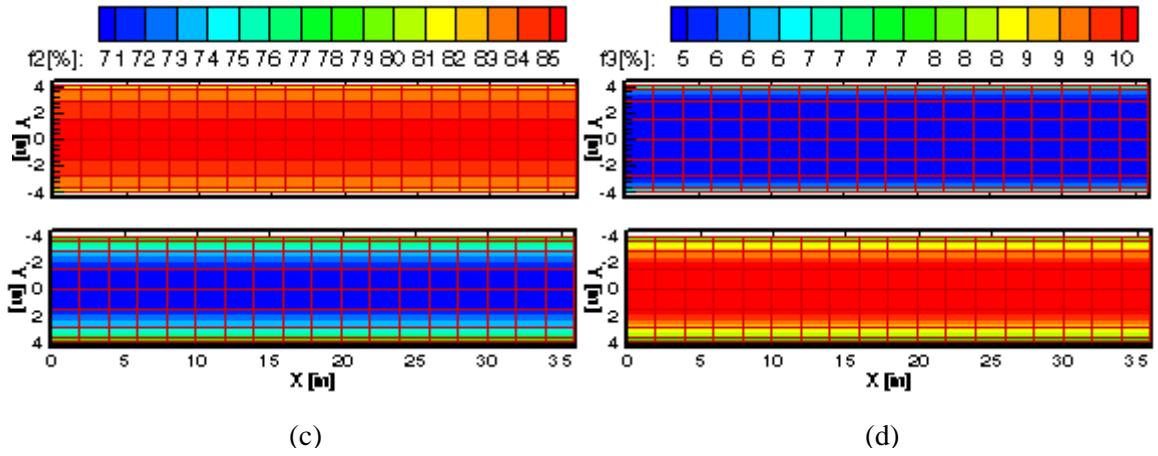


Figure C22(contd.): Layer-thickness contours for tb1L173 (front and aft views).

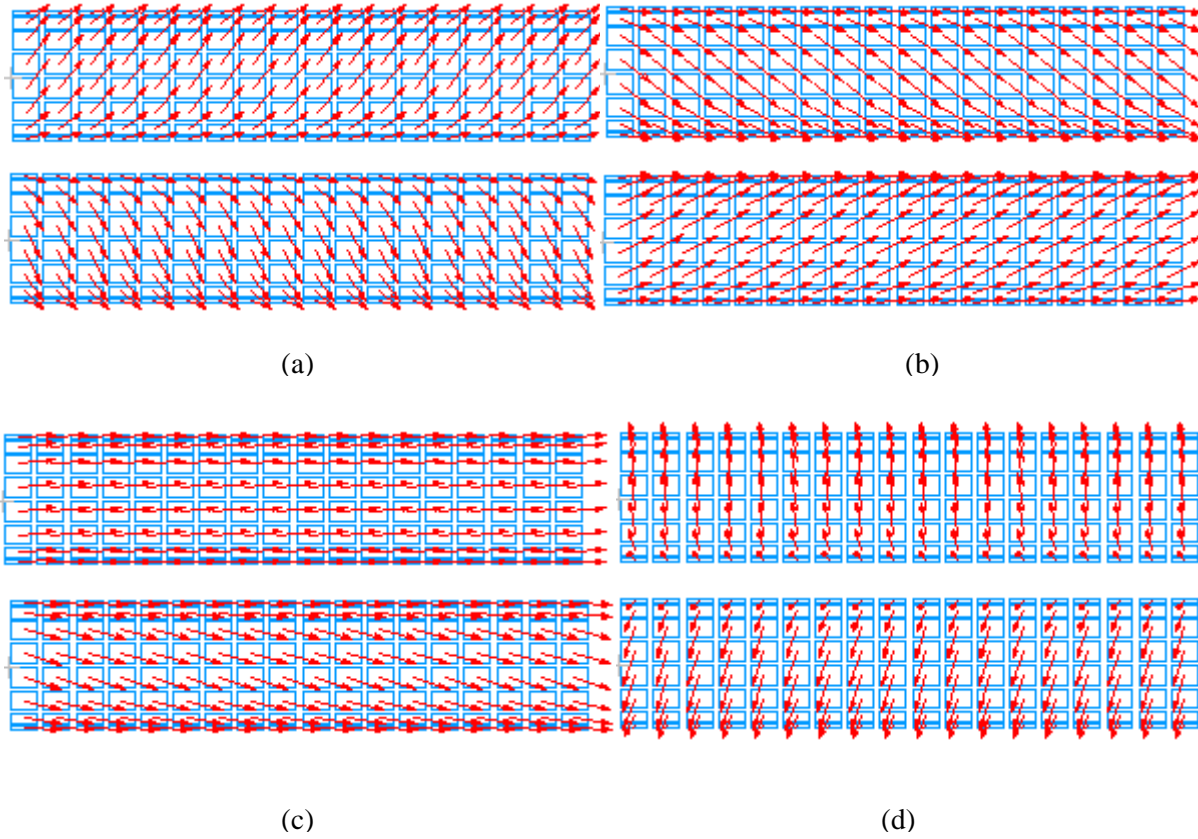


Figure C23: Layer-angle mappings for tb1L173 (front and aft views).

3.10 Appendix D: Fiber Steering Conceptual Design of Preliminary Studies Using MSC/NASTRAN SOL 200

Two test models, namely the cantilever panel under transverse loads and the plate-with-a-hole ($W/D = 5.0$) under bi-axial tensile loads, have been set up for trial runs based on fiber steering (FS) conceptual design via MSC/NASTRAN SOL 200 optimization. The purpose of this section is to document MSC/NASTRAN capability in performing structural optimization according to FS conceptual design. Only the baseline and Steering I configuration have been analyzed (see Table 3.4.1 and Figure 3.4.7). The models are composed of CQUAD4 membrane elements with IM7/8551-7A as the carbon/epoxy composite material. Similar composite layouts are defined, where the initial laminate is $[\pm 45, 0, 90]_s$ with four layers. Each layer consists of a collective of several plies, where each ply has a minimum gage of 0.0055 inch. The objective function for these models is the structural weight, while first-ply fiber-related failure based on maximum strain failure criterion (STRN), upper and lower layer thickness (CGAGE), and angle bounds (CGANG) are design constraints, as follows:

→ STRN: Longitudinal tensile strain, $\varepsilon_1^{tu} = 12800 \mu\text{in} / \text{in}$

Longitudinal compression strain, $\varepsilon_1^{cu} = 11100 \mu\text{in} / \text{in}$

→ CGAGE: Lower bound layer thickness, $t_l = 0.011 \text{ inch}$ (2 plies)

Upper bound layer thickness, $t_u = 0.500 \text{ inch}$ (~91 plies)

→ CGANG: Angle threshold of $\pm 45^\circ$ are imposed onto all angle design variables (DVs).

The optimization algorithm for this task is the method of feasible direction (MFD). Another algorithm, called sequential quadratic programming (SQP), seems to yield similar optimal results.

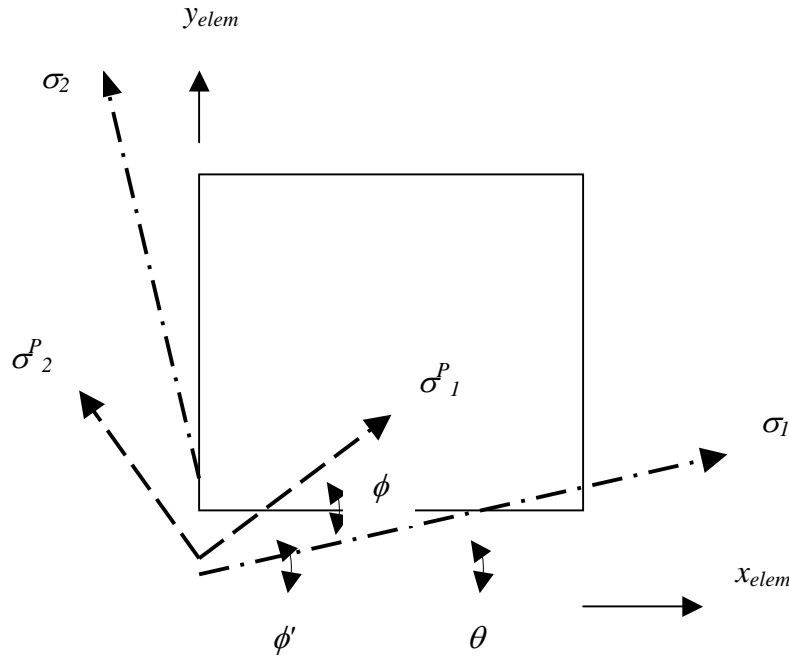
After the first trial with the baseline and Steering I configurations for the cantilever panel, it seems that MSC/NASTRAN SOL 200 does not configure to change both layer thickness and angle simultaneously. Essentially, MSC/NASTRAN only allows variations in the layer thickness DVs to fulfill STRN and other constraint requirements at the first place, while letting the layer angle DVs to remain unchanged. Therefore, a design response or constraint based on Hyer's work²⁰ is imposed:

$$0.0001 \leq \frac{\phi - \theta}{\phi} \leq 0.01 \quad (\text{D.1})$$

where ϕ is the principal stress direction

θ is the fiber orientation.

Figure D.1 shows the coordinate systems, fiber orientation, and principal stress direction.



x_{elem}, y_{elem}	Shell element coordinate system
σ_1, σ_2	Fiber material coordinate system
σ_1^P, σ_2^P	Principal coordinate system
ϕ'	$\phi' = \phi + \theta$

Figure D1: Schematics of coordinate systems, fiber and principal stress orientations.

The results of FS conceptual design for the test models are listed in the following paragraphs. The baseline configuration (pure layer-thickness optimization) yields optimal laminates, as compared with MBB-LAGRANGE results in Chapter 4.3 for the plate-with-a-hole model and Appendix C for the cantilever panel, respectively. However, the results associated with Steering I configuration were not optimal. The optimization job for the plate-with-a-hole model, Steering I configuration, was terminated abruptly. MSC/NASTRAN reached “a best compromise infeasible design” for these models because it has an apparent limitation in performing optimization with layer-thickness and layer-orientation DVs simultaneously. The maximum constraint violation could not be met because the design response with respect to Equation D.1 was huge. Equation D.1 may be revisited to correctly impose FS capability via MSC/NASTRAN.

3.10.1 Cantilever panel under transverse loads

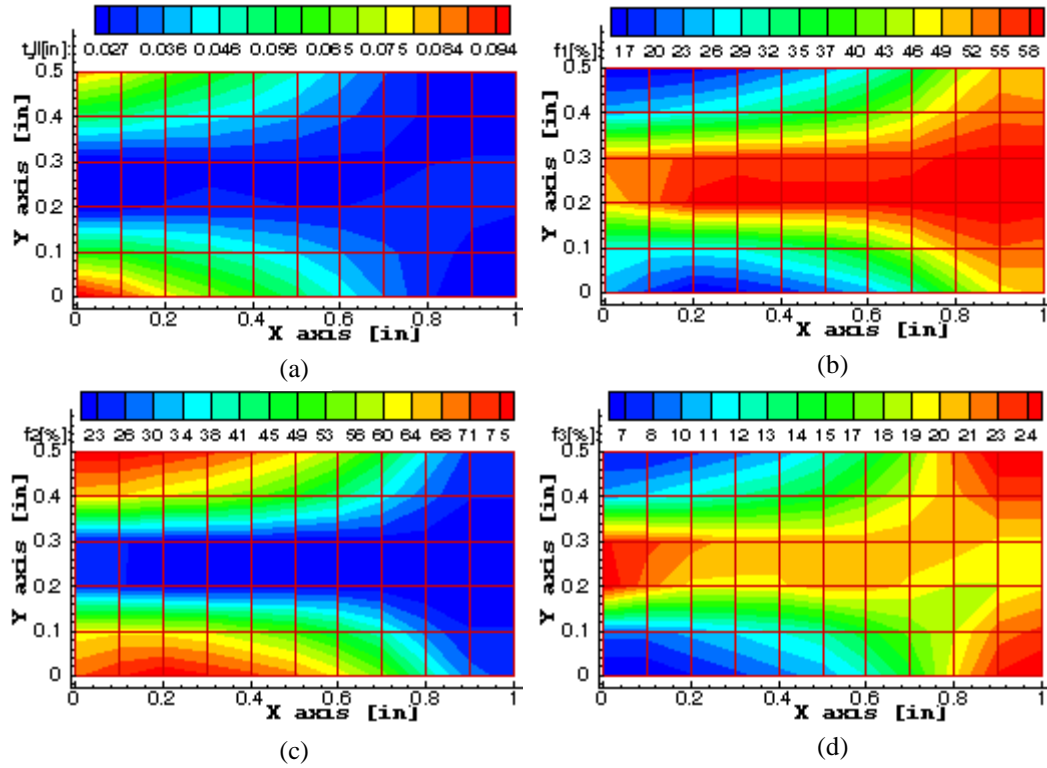


Figure D2: Layer-thickness contours for cb1N011, baseline configuration.

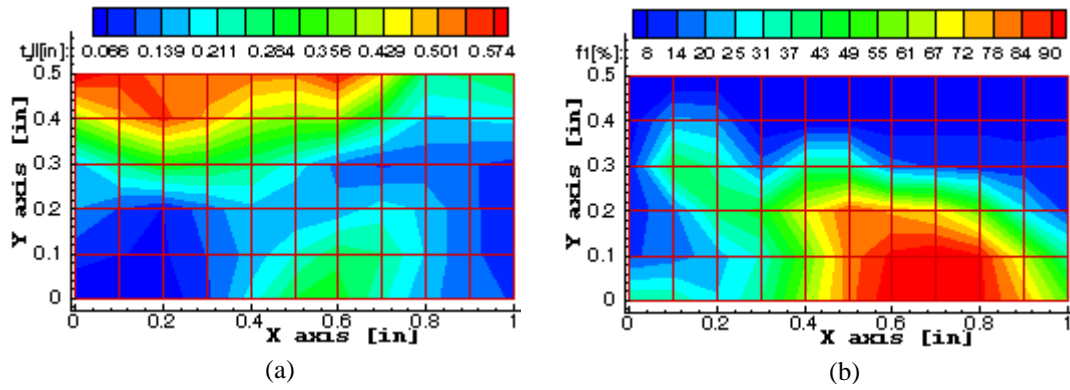
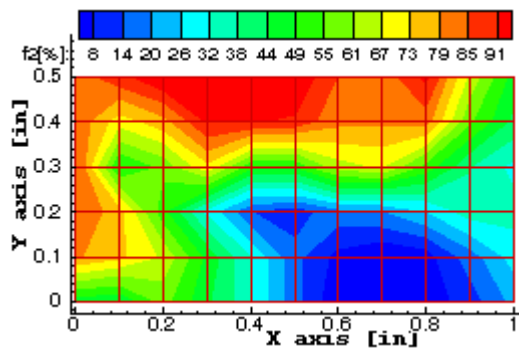
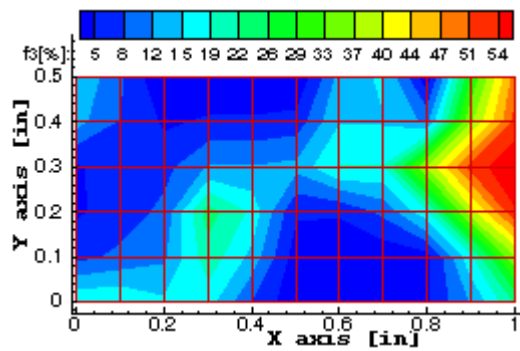


Figure D3: Layer-thickness contours for cb1N111, Steering I configuration.

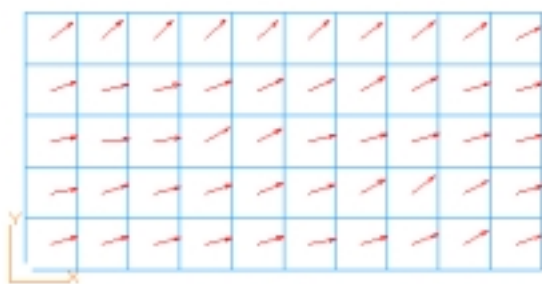


(c)

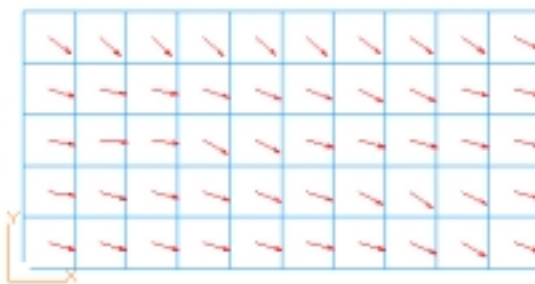


(d)

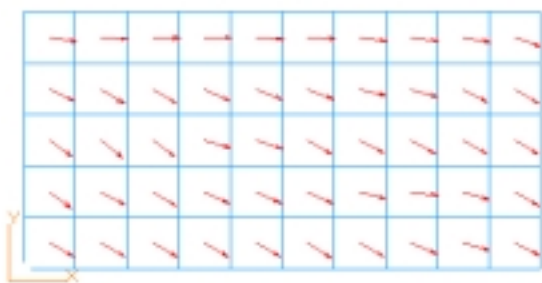
Figure D3 (contd.): Layer-thickness contours for cb1N111, Steering I configuration.



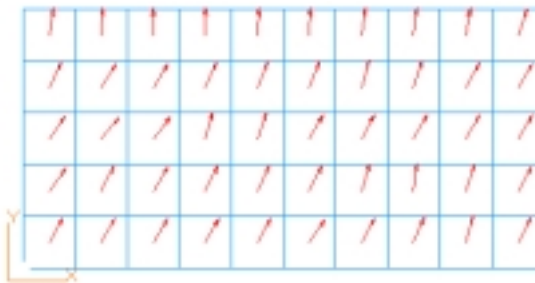
(a)



(b)



(c)



(d)

Figure D4: Layer-angle mappings for cb1N111, Steering I configuration.

3.10.2 Plate-with-a-hole model, $W/D = 5.0$, under bi-axial tensile loads.

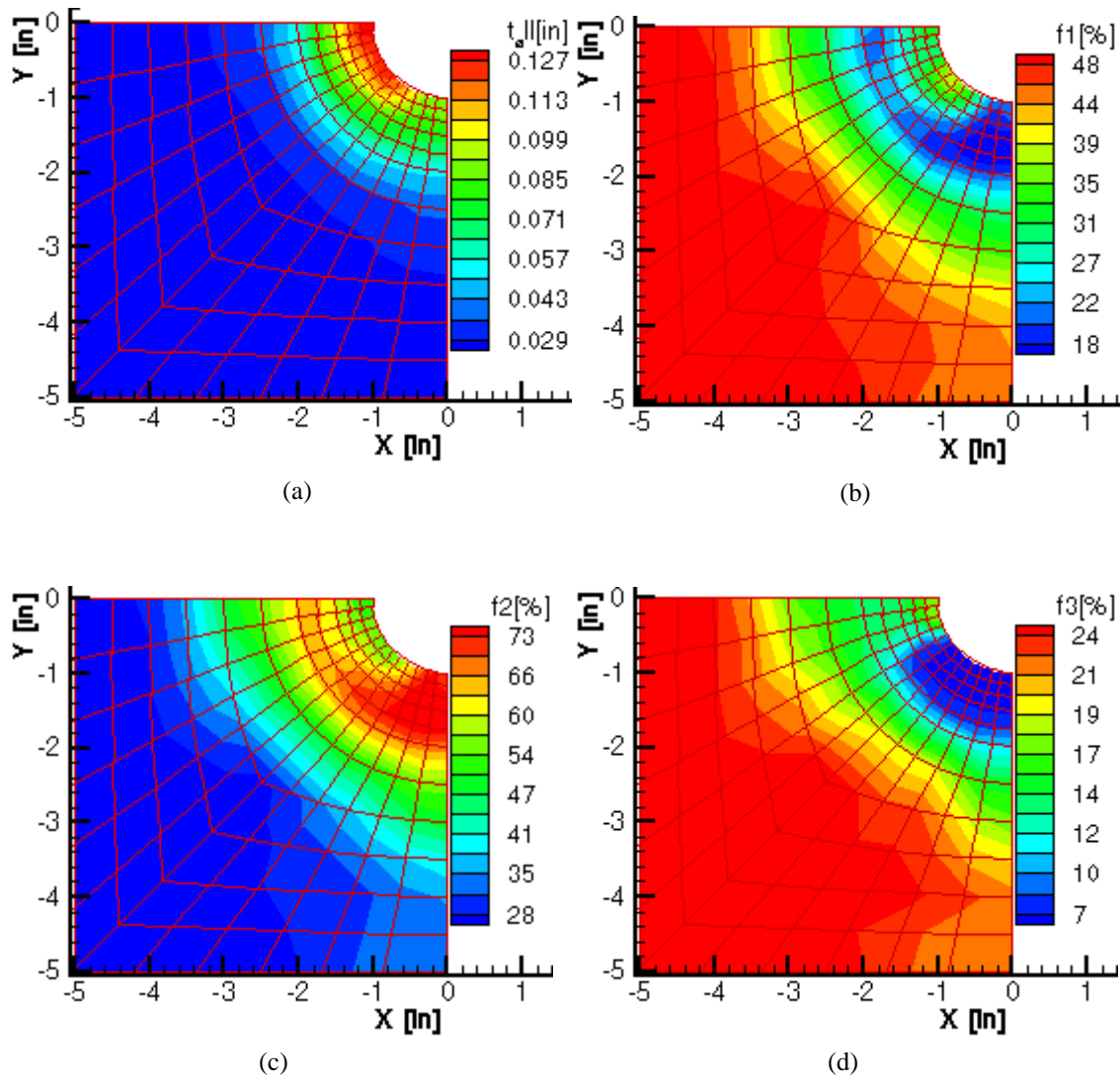


Figure D5: Layer-thickness contours for pl16N011, baseline configuration.

3.11 Appendix E: Fiber Steering Conceptual Design for Representative Aircraft Structural Components

3.11.1 Fiber steering conceptual designs for a representative general-aviation's pressure bulkhead, subjected to cabin pressures.

The baseline configuration (pb2L013) is presented in Figure E1. Based on Figure E1(a), the hemisphere pressure bulkhead has almost uniform thickness (from 0.04 to 0.07 inches) throughout the structure. Due to hoop stresses, $\pm 45^\circ$ layers become dominant in shear reinforcement, especially in the center of the quarter hemisphere. The laminate family at this location is approximately (20/60/20). At the pressure-bulkhead-to-fuselage attachment, 0° and $\pm 45^\circ$ layers are significant with (40/45/15) family. Apparently at the fixed boundary, fiber reinforcements are largely attributed to hoop stresses in the radial direction and Poisson's effect. At the symmetrical boundaries, a portion of the 90° layer becomes significant following hoop stresses and Poisson's effect in the circumferential direction.

Figures E2 and E3 show the optimal results based on Steering II configuration (pb2L113). Similar to the baseline, the entire pressure bulkhead has almost uniform thickness. Comparatively, more materials are gathered at the center of the quarter hemisphere, as seen in Figure E2(a). Due to hoop stresses, a majority of $\pm \theta_1^\circ$ layer orientations (Figures E3(a) and E3(b)) tend to align in the shear direction w.r.t. the local material coordinates. At the fixed boundary, $\pm \theta_1^\circ$ layer angles are tailored in the radial direction due to hoop stresses and corresponding Poisson's effect. A portion of reinforcement at this location is contributed by θ_2° layer in the radial direction and θ_3° layer in the shear direction, respectively. The laminate behaves as a (30/55/15) family. Initially aligned in the radial direction, the θ_2° layer angles generally remain unchanged, as shown in Figure E3(c). This is also true for θ_3° layer angles, which remain in the circumferential direction to provide transverse-related reinforcements (see Figure E3(d)).

Finally, the optimal results based on Steering III configuration (pb2L313) are shown in Figures E4 and E5. A similar trend of fiber reinforcement is predicted, where more materials are gathered at the center of the quarter hemisphere in Figure E4(a). In Figure E4(b), the pressure bulkhead is largely reinforced with $\pm \theta_1^\circ$ layer at the lower symmetrical boundary, where the laminate family is about (20/70/10). Note in Figures E5(a) and E5(b), $\pm \theta_1^\circ$ layer angles are gradually shifted to align in the circumferential direction at the center of the quarter hemisphere. Here, some reinforcements in the radial direction are supported by the 0° layer. The laminate family becomes (45/45/10) in Figure E4(c). At the fixed boundary, $\pm \theta_1^\circ$ and 0° layers become dominant, where fiber reinforcements are largely attributed to hoop stresses in the radial direction and Poisson's effect. As seen in Figures E5(a) and E5(b), $\pm \theta_1^\circ$ layer angles are tailored in shear directions.

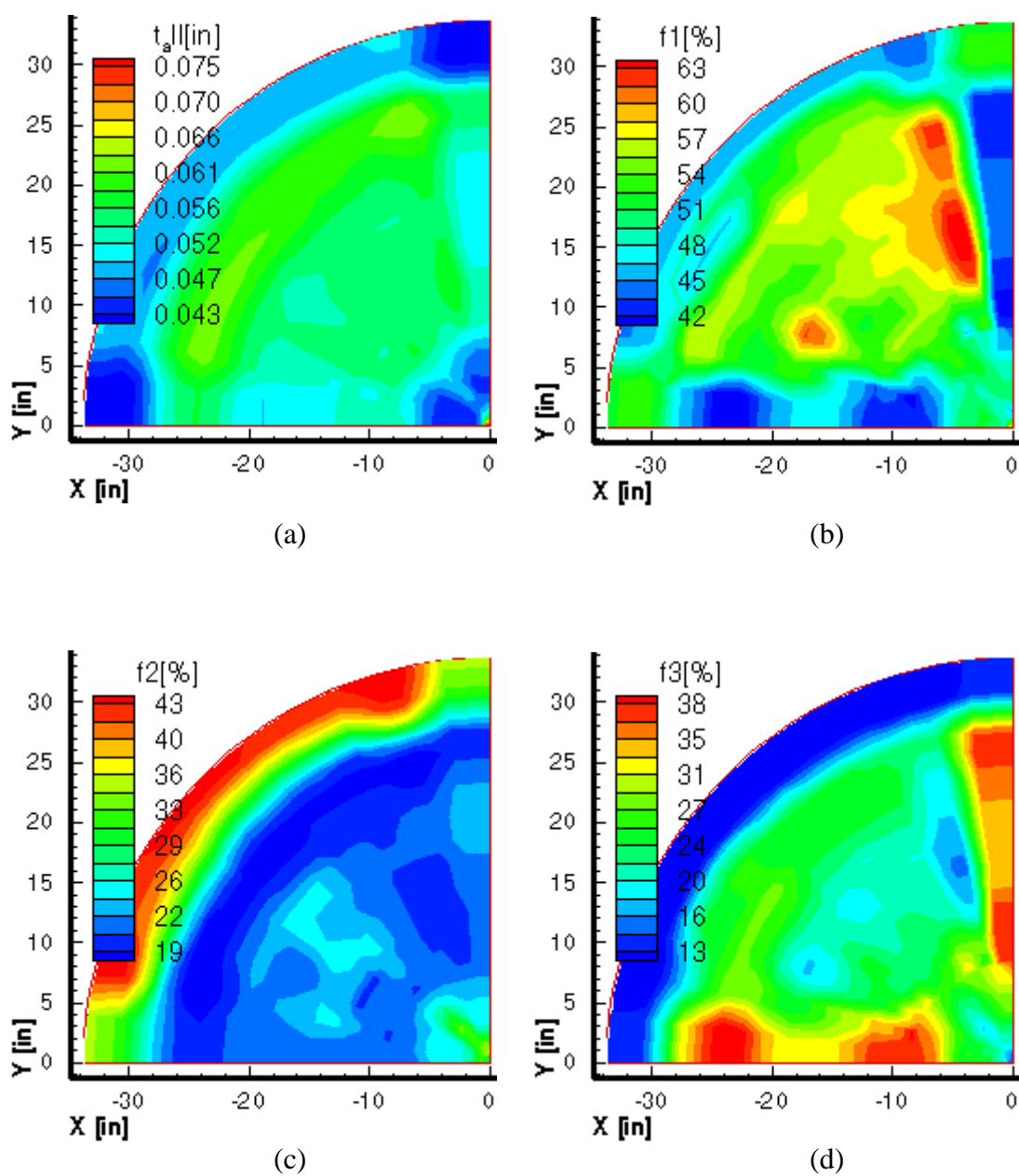


Figure E1: Layer-thickness contours for pb2L013.

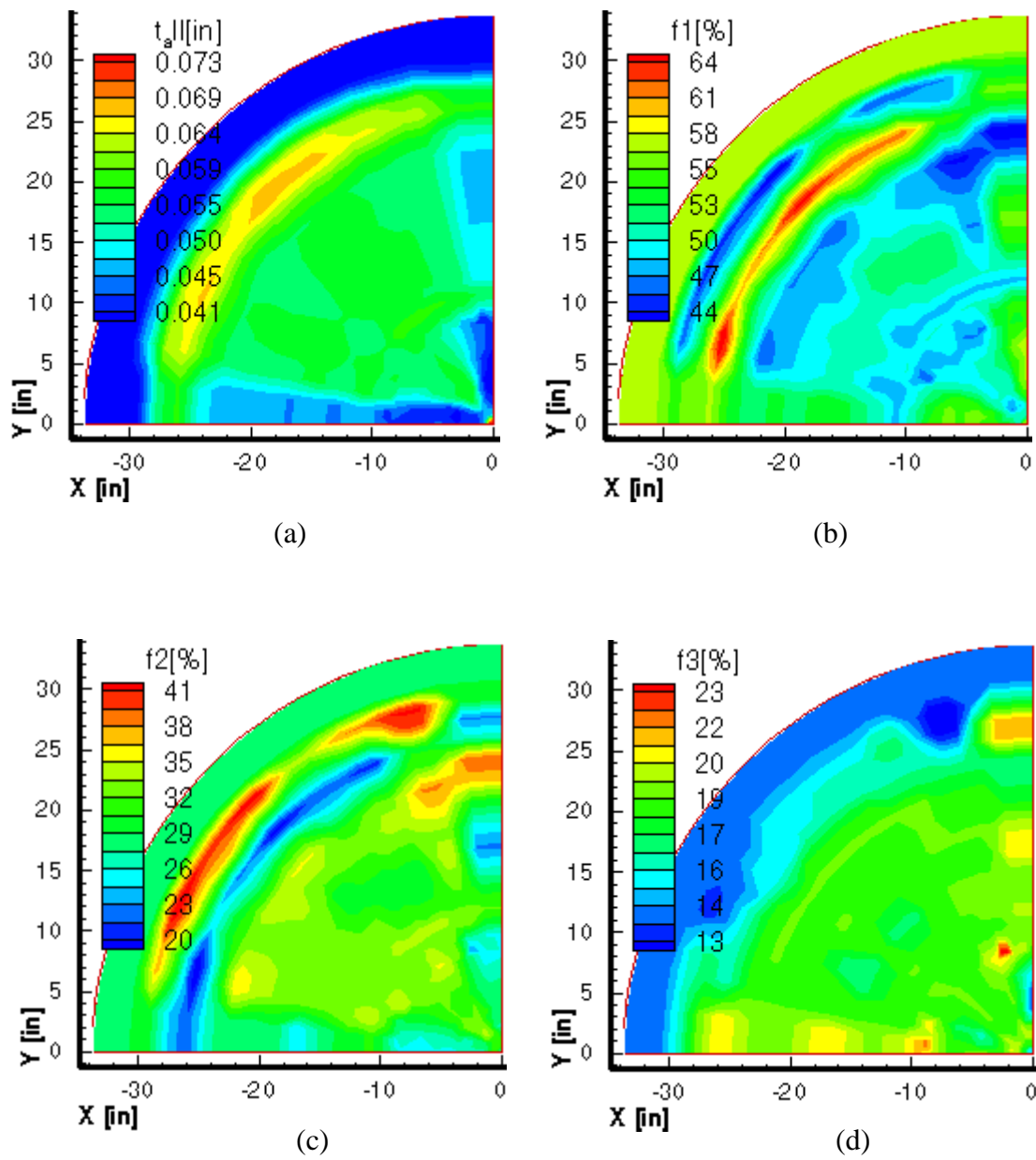


Figure E2: Layer-thickness contours for pb2L213.

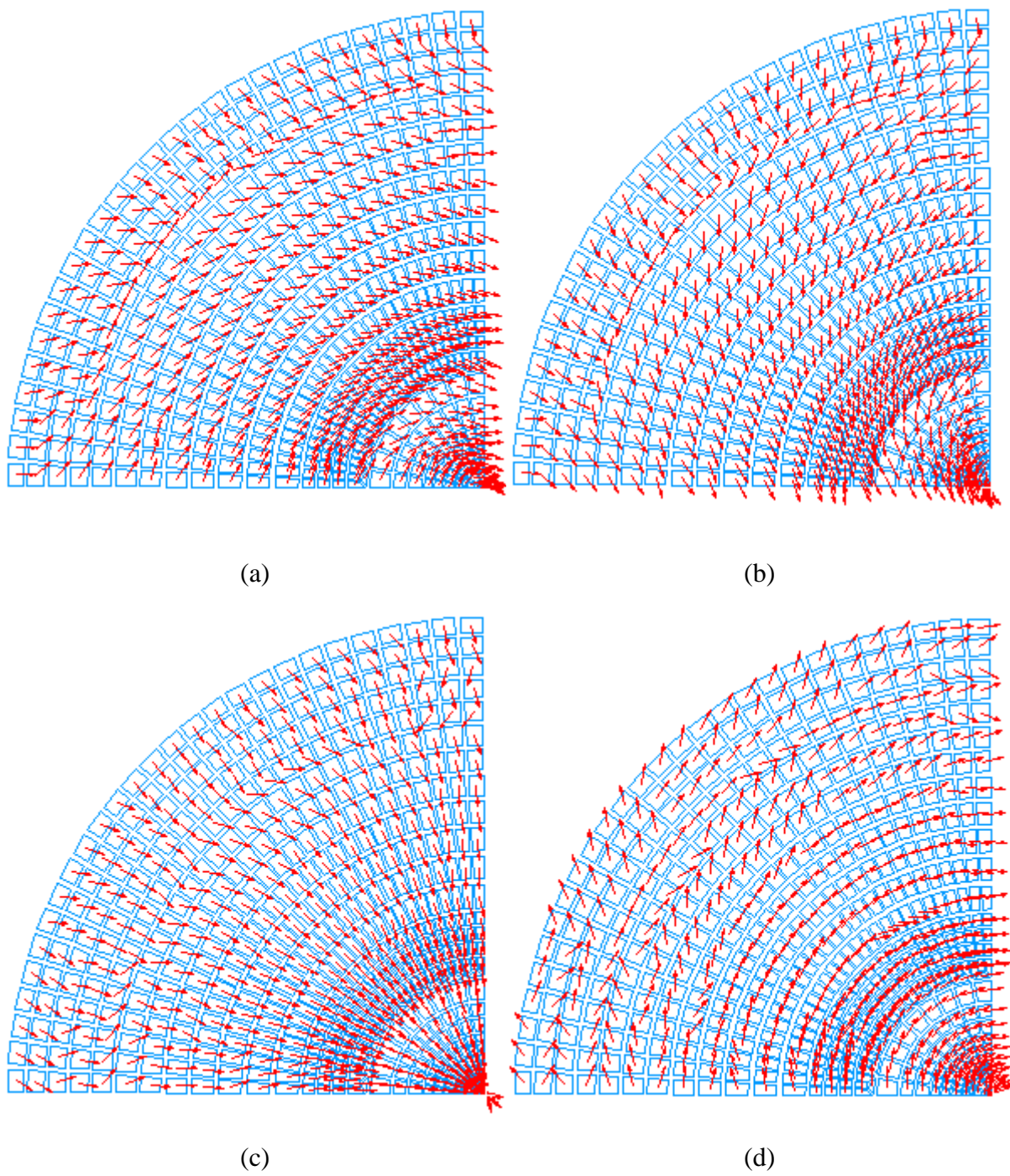
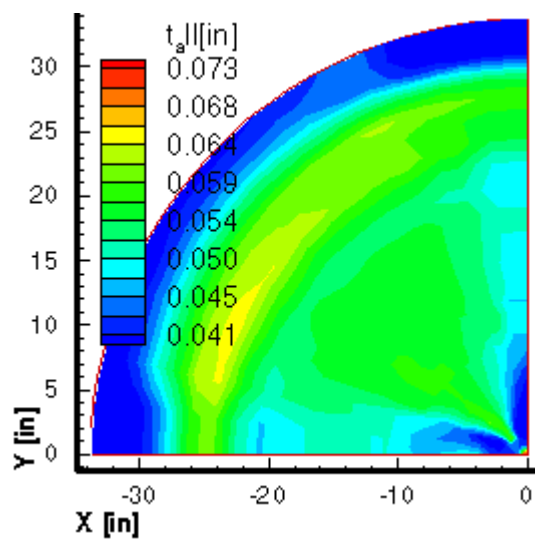
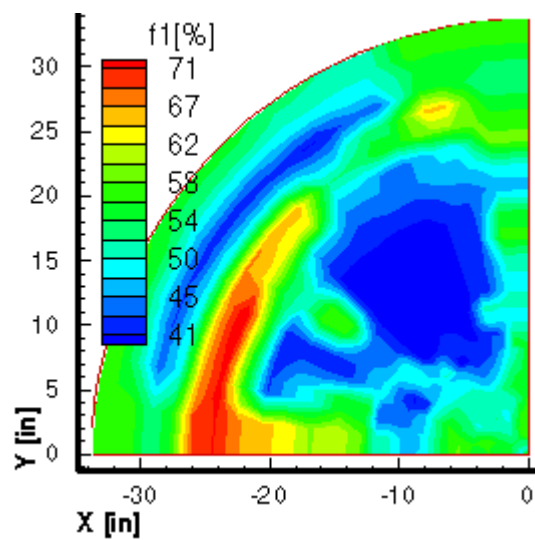


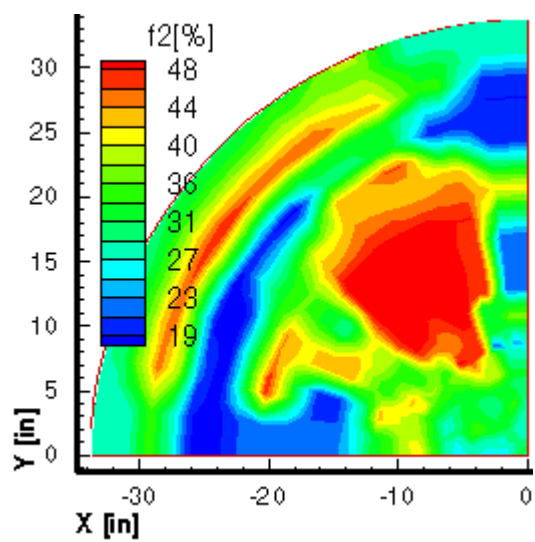
Figure E3: Layer-angle mappings for pb2L213.



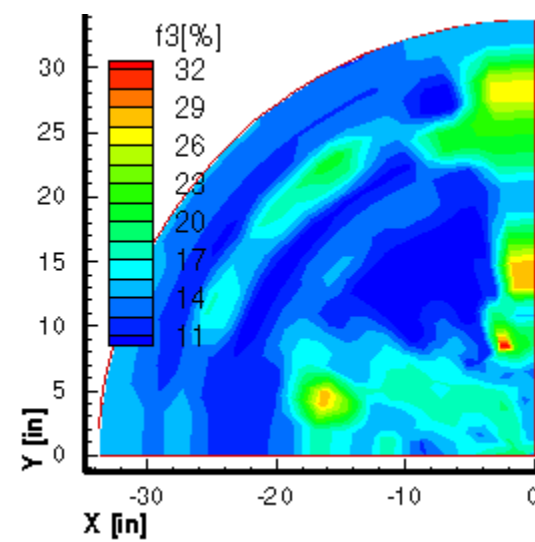
(a)



(b)

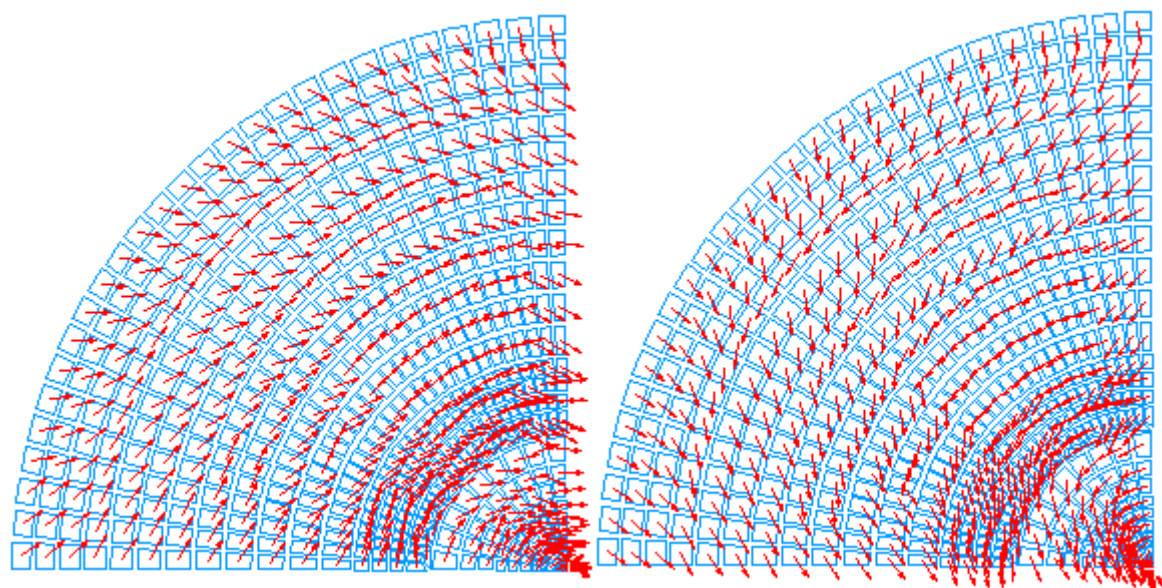


(c)



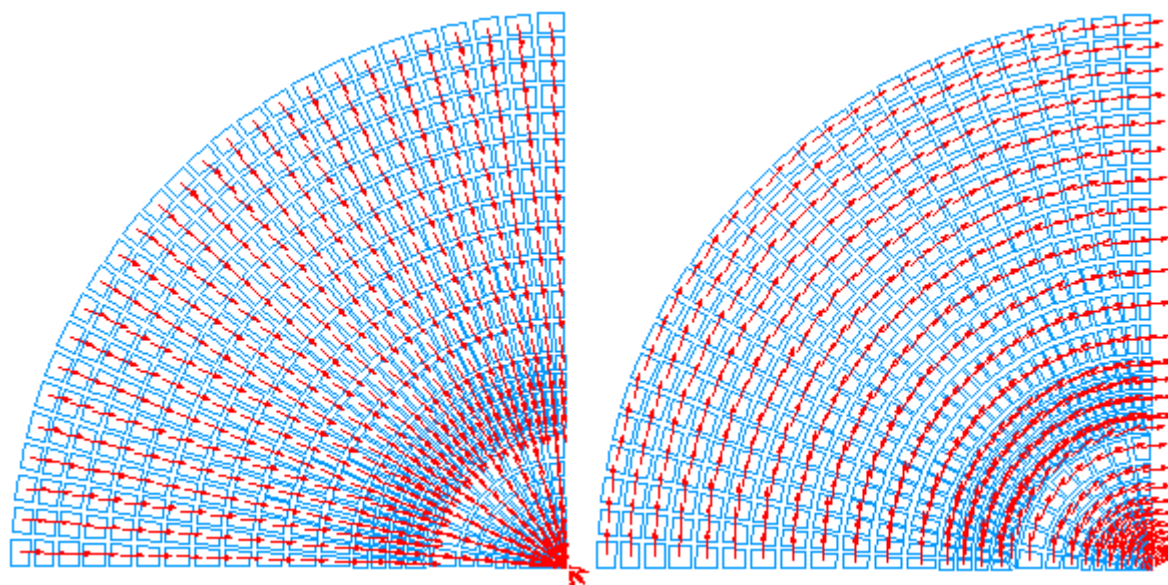
(d)

Figure E4: Layer-thickness contours for pb2L313.



(a)

(b)



(c)

(d)

Figure E5: Layer-angle mappings for pb2L313.

3.11.2 Fiber steering conceptual designs for a representative military horizontal stabilator, subjected to aerodynamic loads.

Figures E6 and E7 show layer-thickness contours of the baseline F22 model or F22L013. In Figure E6(a), the layer-thickness variation is not obvious. Basically, the entire tail lower skin is configured with (30/55/15) laminate family. As it is designed to be an all-movable component, the pivot shaft experiences torsion under high AOA aerodynamic loads. As a result, both tail skins are subjected to shear and transverse loadings. Obviously, the 45° layer becomes dominant due to shear stresses. This is shown in Figures E6(b) and E7(b). Around the midspar in Figures E6(d), the lower skin reinforcements are largely contributed by the 90° layer due to transverse loads, where the laminate family becomes (15/20/65). In the upper skin, more reinforcements are accumulated around the midspar. Here, the off-axis layers provide key reinforcements to overcome shear stresses. The laminate family is about (10/70/20), as shown in Figure E7(a). The layer-thickness contours vary greatly from the tail root down the tail tip. As a whole, the upper skin behaves closely like a (25/55/20) laminate with almost 16 plies. While most reinforcements come from 45° layers, a portion of 0° and 90° layers are gathered around the pivot shaft and at the L.E. This suggests that the tail experiences uneven load distribution on the upper skin.

Figures E8 to E11 show layer-thickness contours and layer-angle mappings for F22L213 based on Steering II configuration. In Figure E8(a), the entire lower skin is generally composed of only 7-ply laminates or minimum-gage solutions. The lower skin laminate family is about (30/55/15). Although Steering II demonstrates a weight saving of about 30% from the baseline configuration, the steering results are not representative because layer orientations are not optimized. As illustrated in Figures E9 and E11, the layer directions become rangewise discontinuous while fulfilling CGAGE requirements. Consequently, the layer-thickness contours are not continuous or smooth especially in Figure E10 for upper skin. Because the optimization jobs are terminated at various layer directions, each layer seems to have thicker zones at different locations. However, the thickest zones carry only 12 plies. The problem associated with minimum gage can be resolved if a greater load intensity or load factor is asserted.

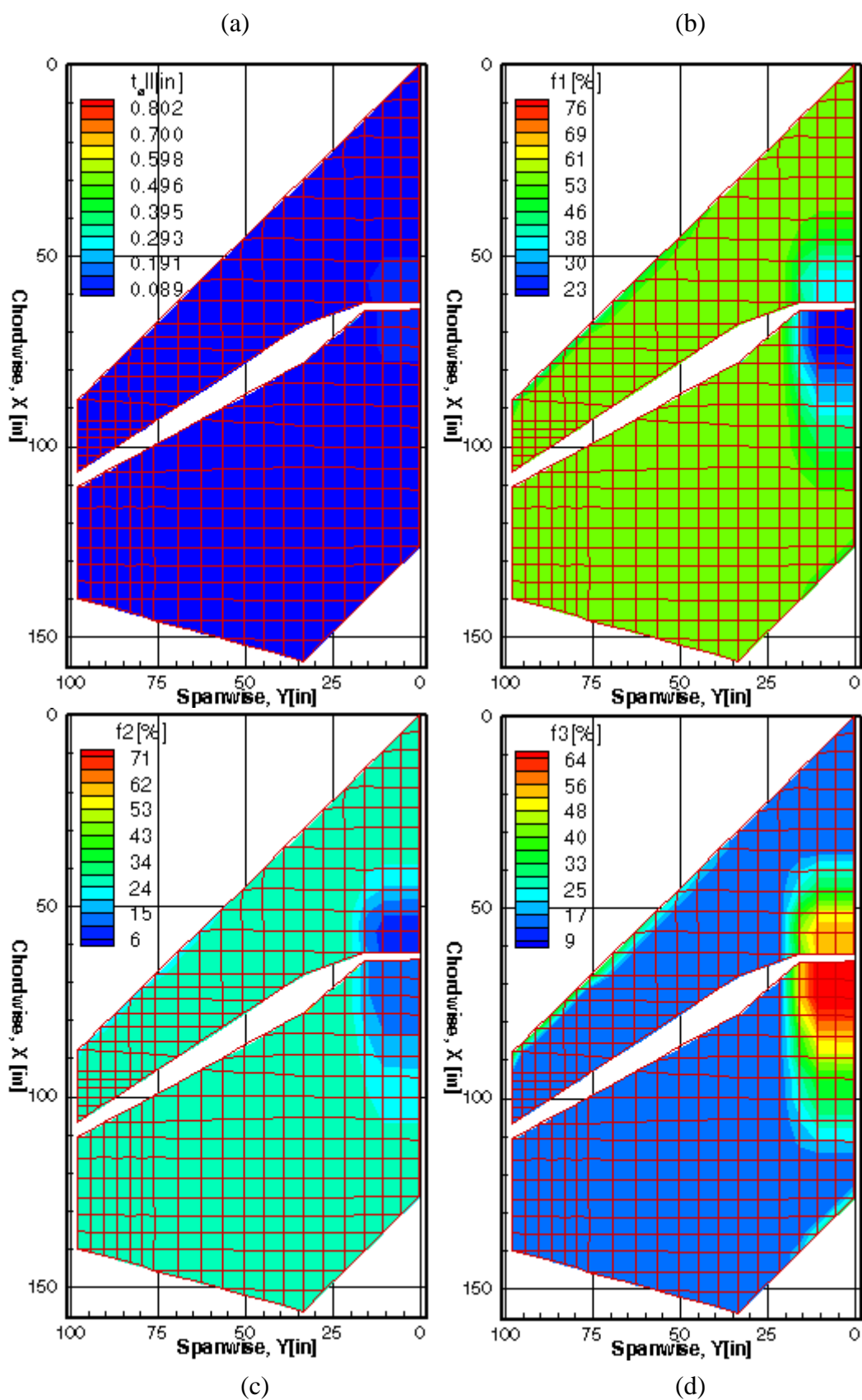


Figure E6: Layer-thickness contours for F22L013 lower skin.

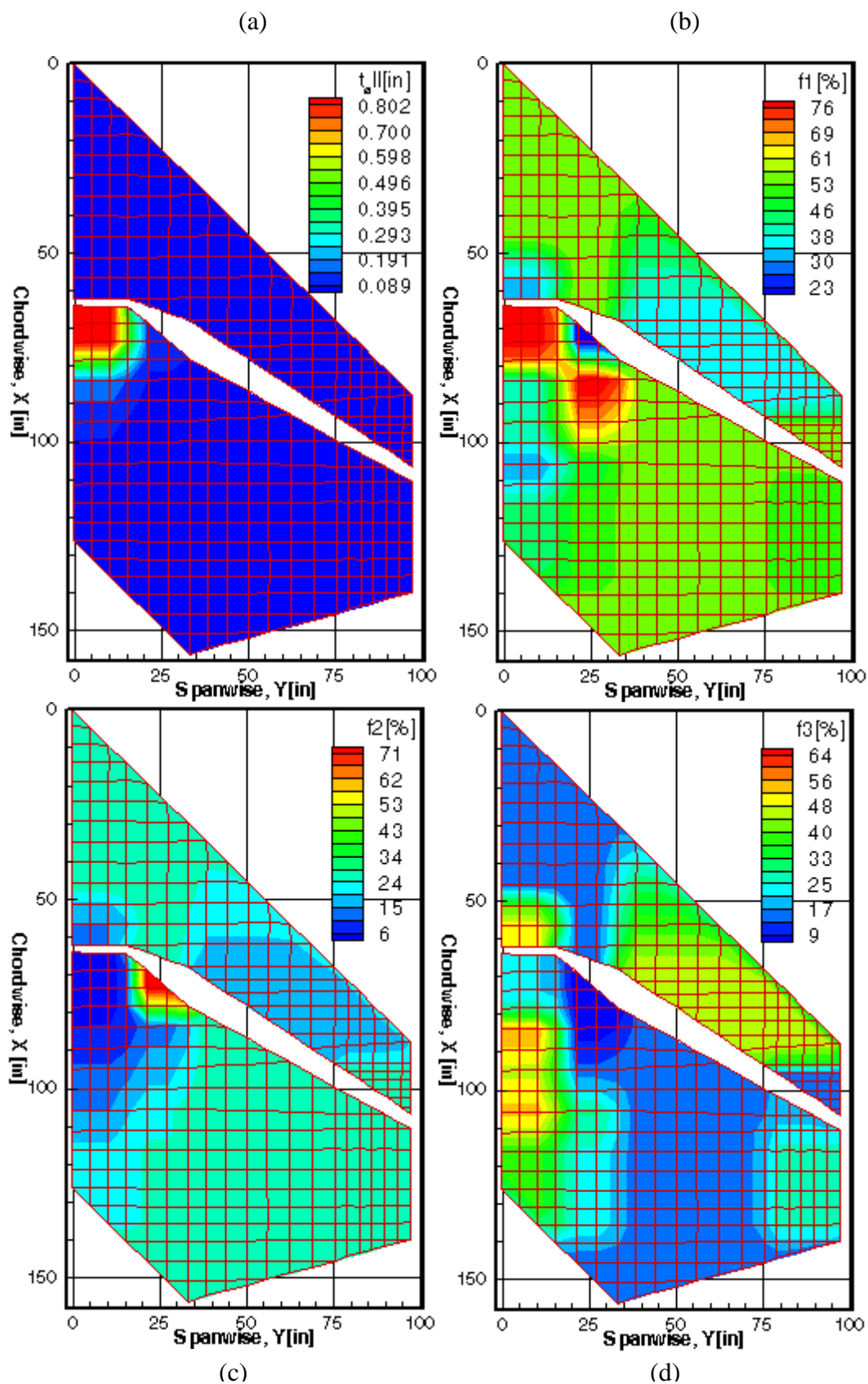


Figure E7: Layer-thickness contours for F22L013 upper skin.

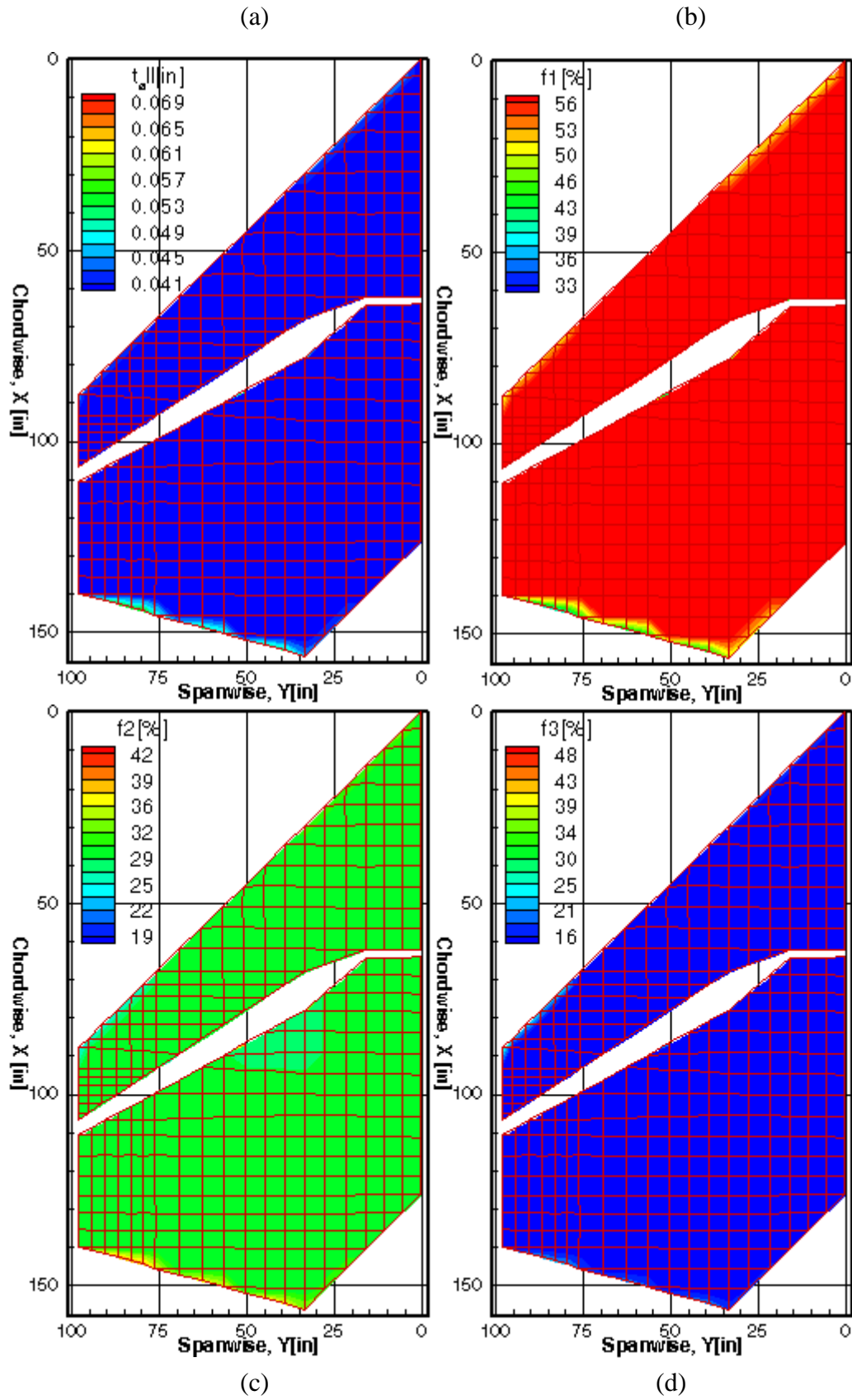


Figure E8: Layer-thickness contours for F22L213 lower skin.

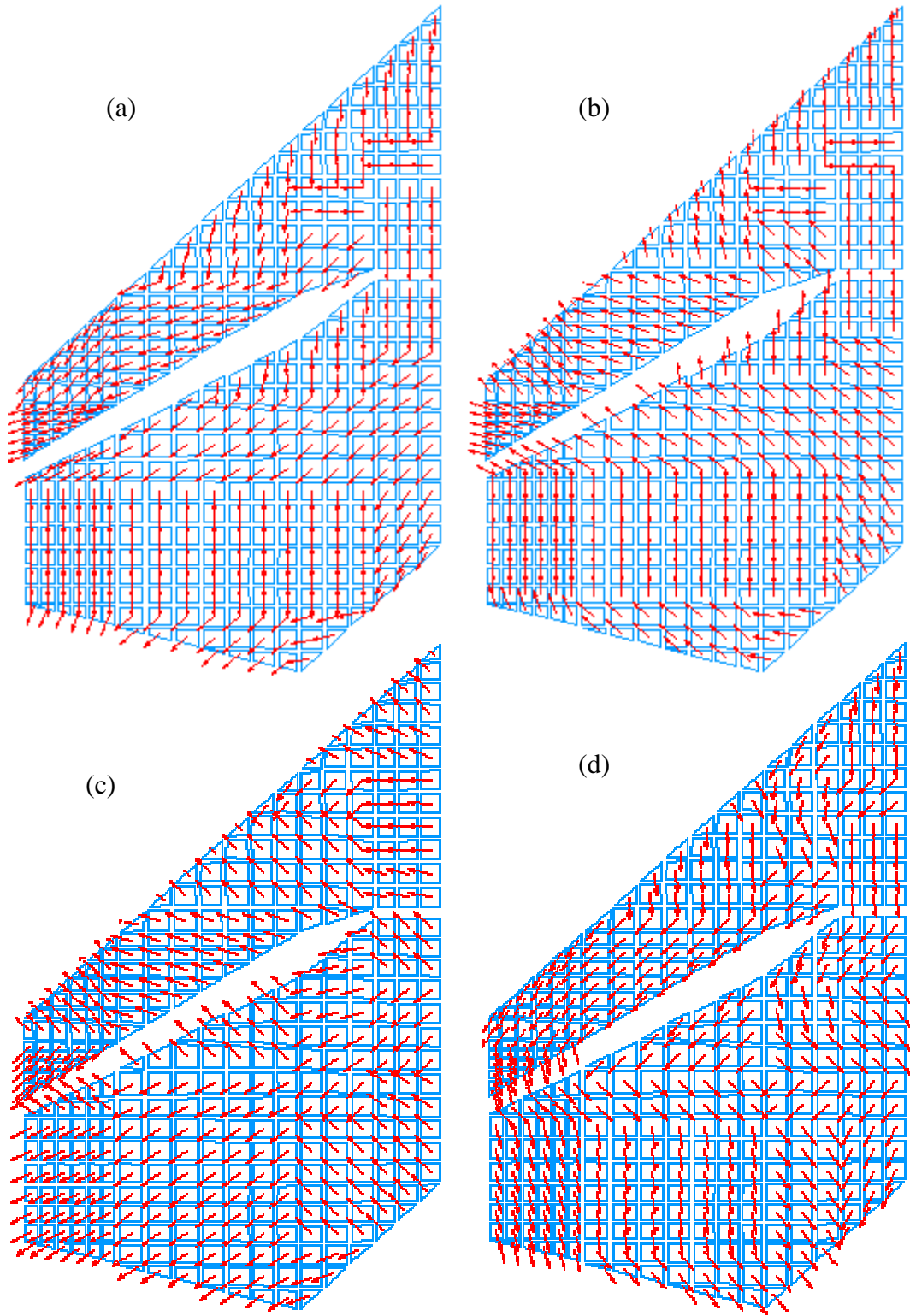


Figure E9: Layer-angle mappings for F22L213 lower skin.

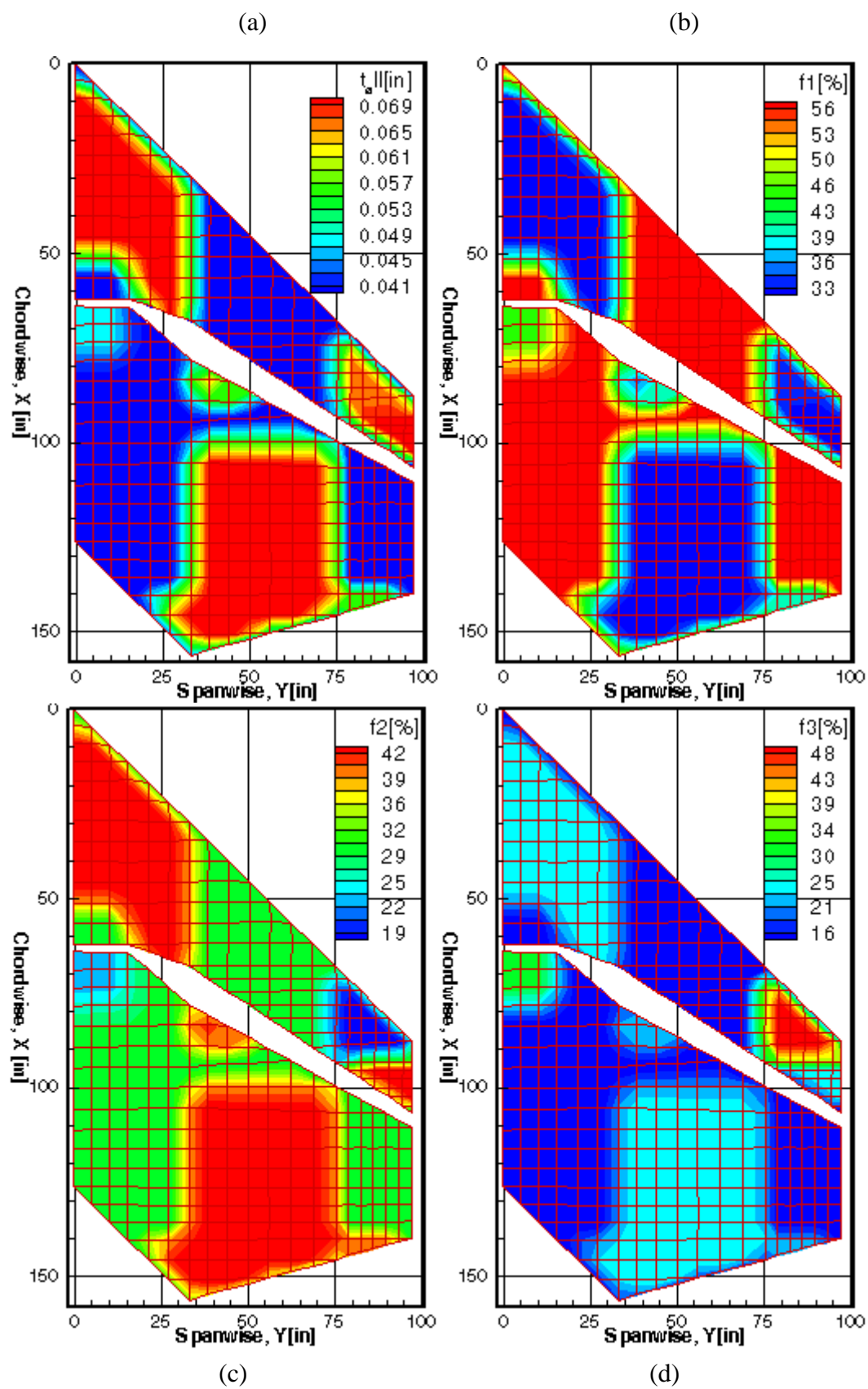


Figure E10: Layer-thickness contours for F22L213 upper skin.

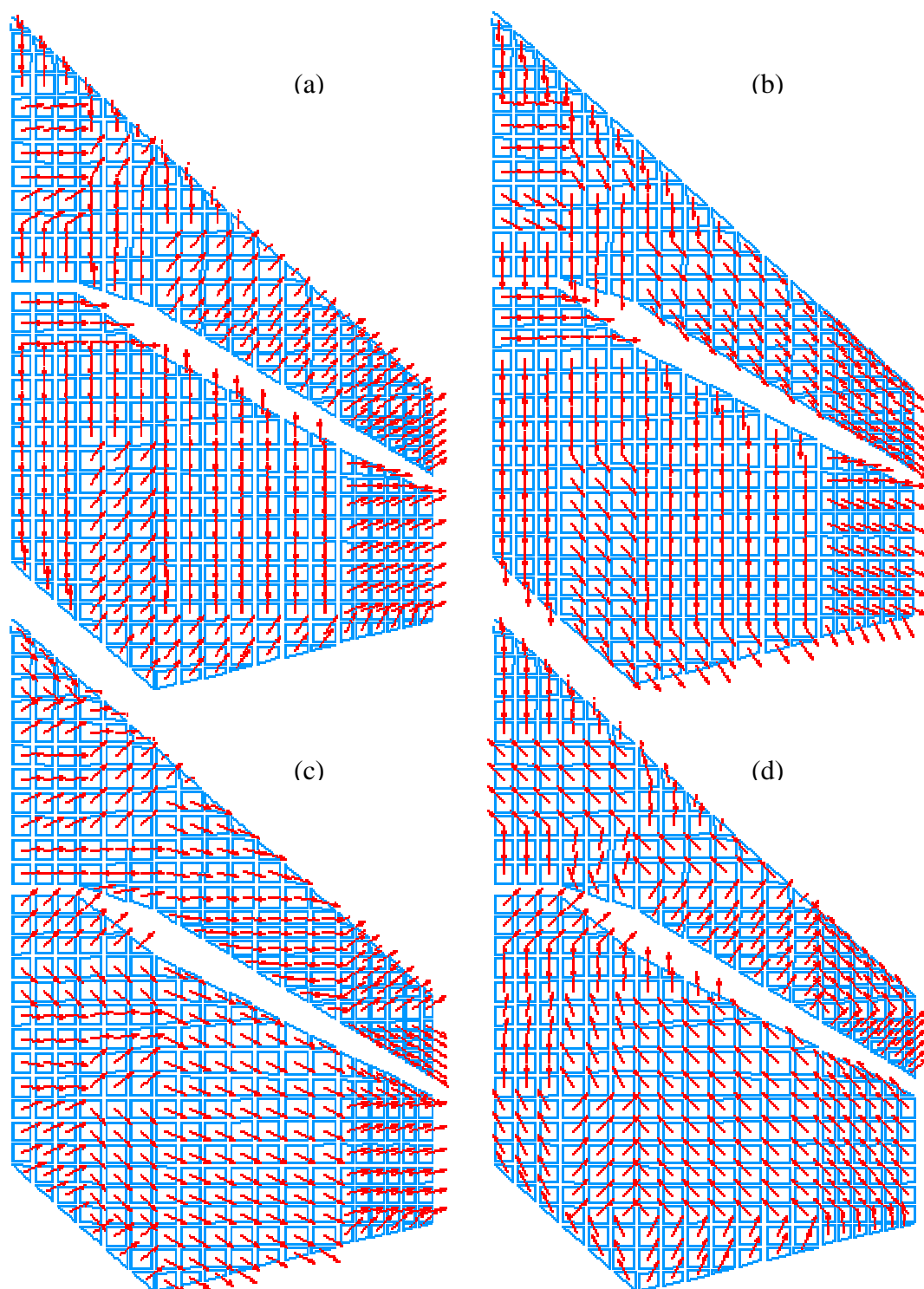


Figure E11: Layer-angle mappings for F22L213 upper skin.

Finally, the results corresponding to Steering III configuration of this model are presented in Figures E12 to E14. For the most part, both tail skins are configured with minimum gage solutions or 7-ply laminates as depicted in Figures E12(a) and 30(a). The resultant FS designs may not be representative as the layer angles are not optimized. Noticeably in Figures E12(a), an anomaly occurs also in the vicinity of the lower midspar. Concentrations of layer thickness at this location are probably due to local minima in the optimizations. The same scenario is depicted in Figure E14(d), where a dimple of 90° layer thickness is gathered at the L.E. Similar to F22L213 case, a greater load factor is required to demonstrate FS conceptual design.

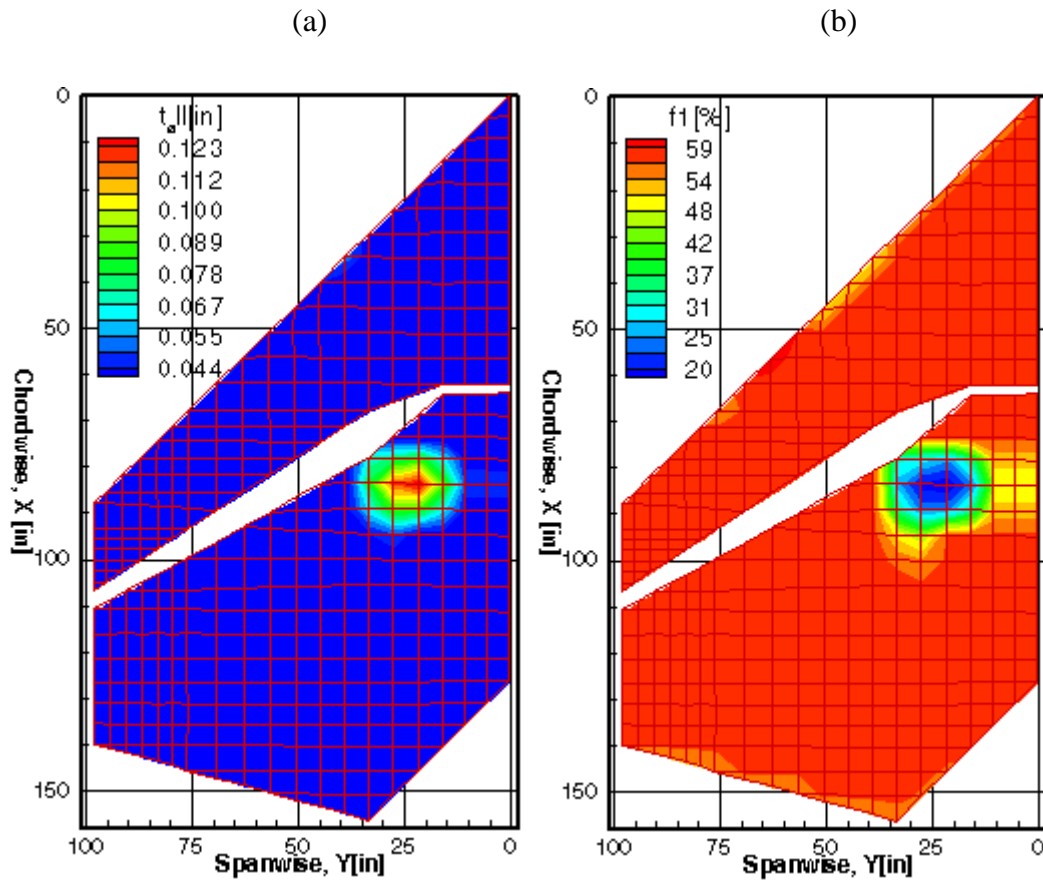


Figure E12: Layer-thickness contours for F22L313 lower skin.

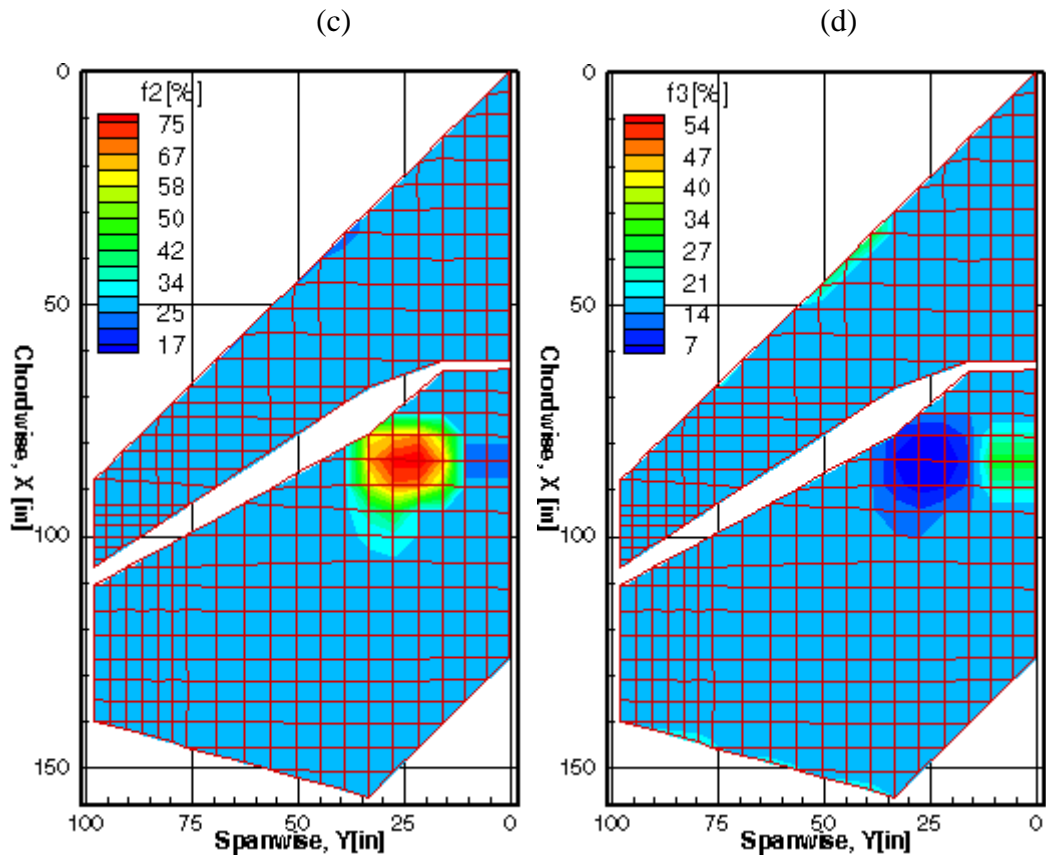


Figure E12(contd.): Layer-thickness contours for F22L313 lower skin.

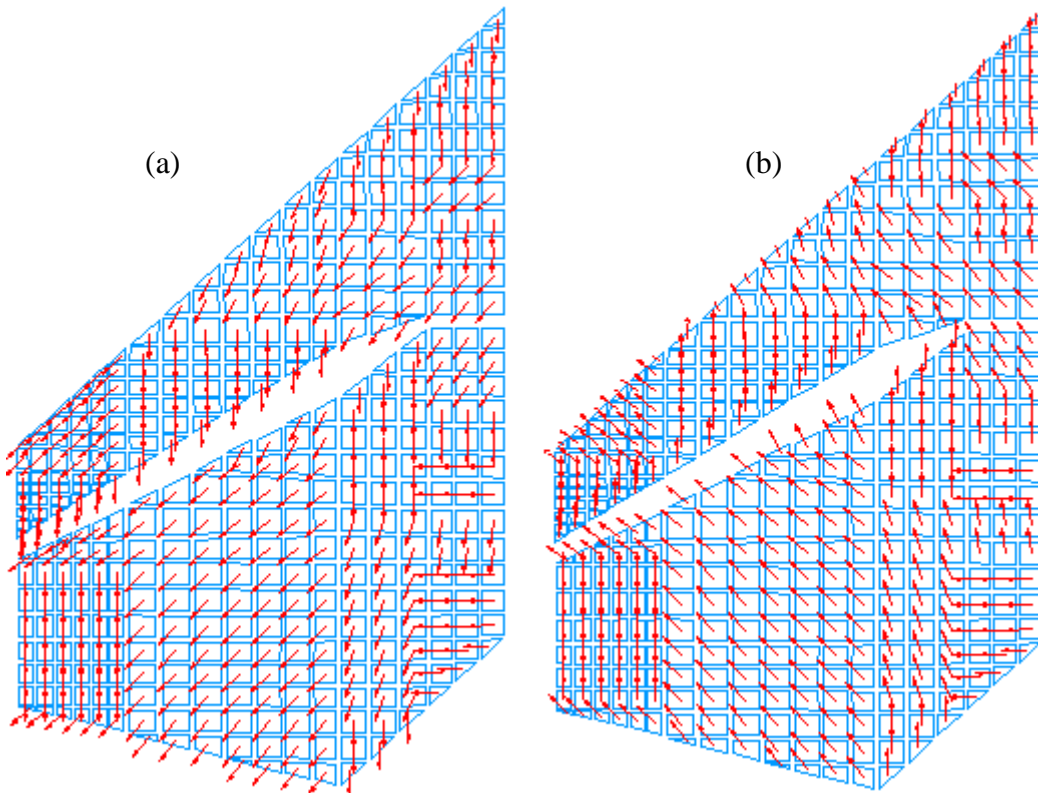


Figure E13: Layer-angle mappings for F22L313 lower and upper skins.

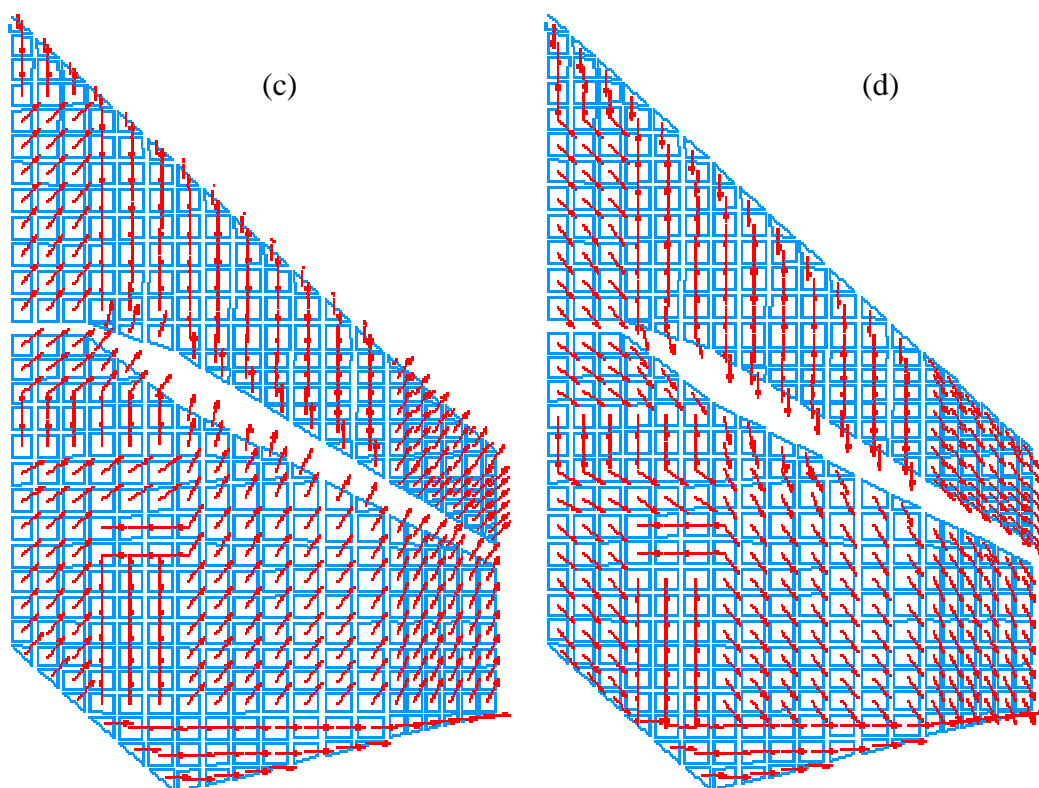


Figure E13(contd.): Layer-angle mappings for F22L313 lower and upper skins.

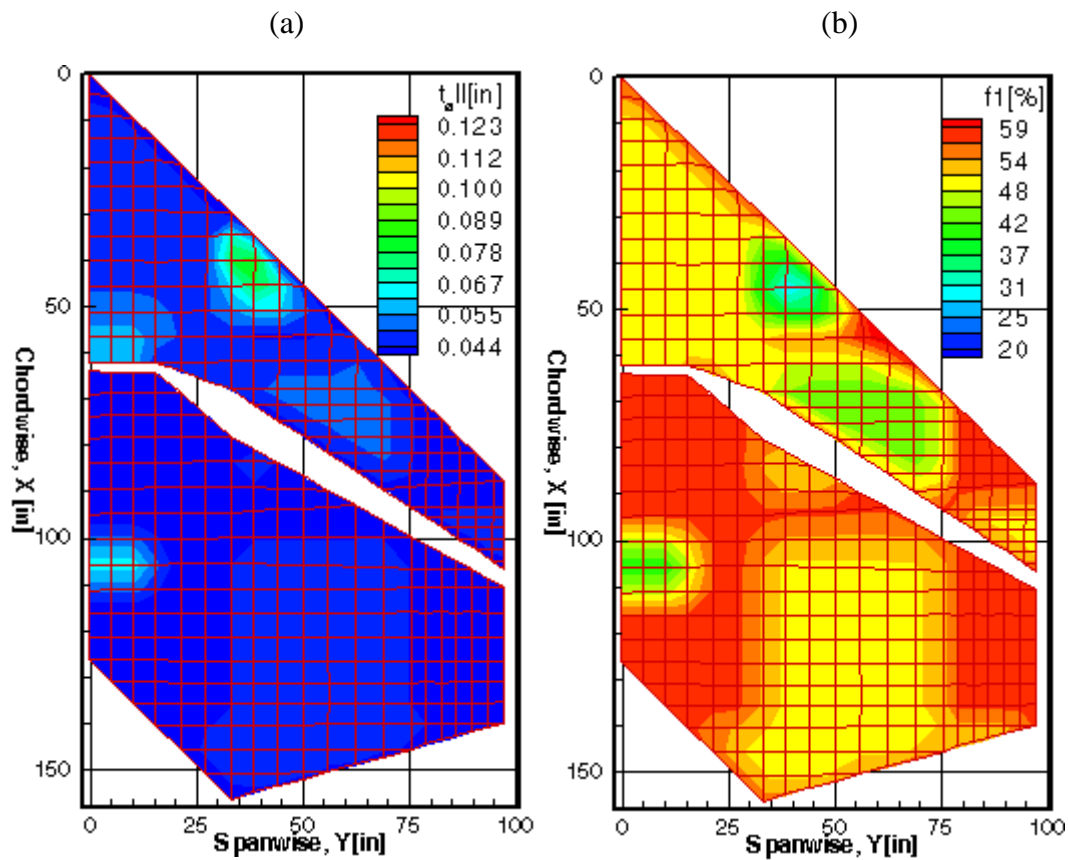


Figure E14: Layer-thickness contours for F22L313 upper skin.

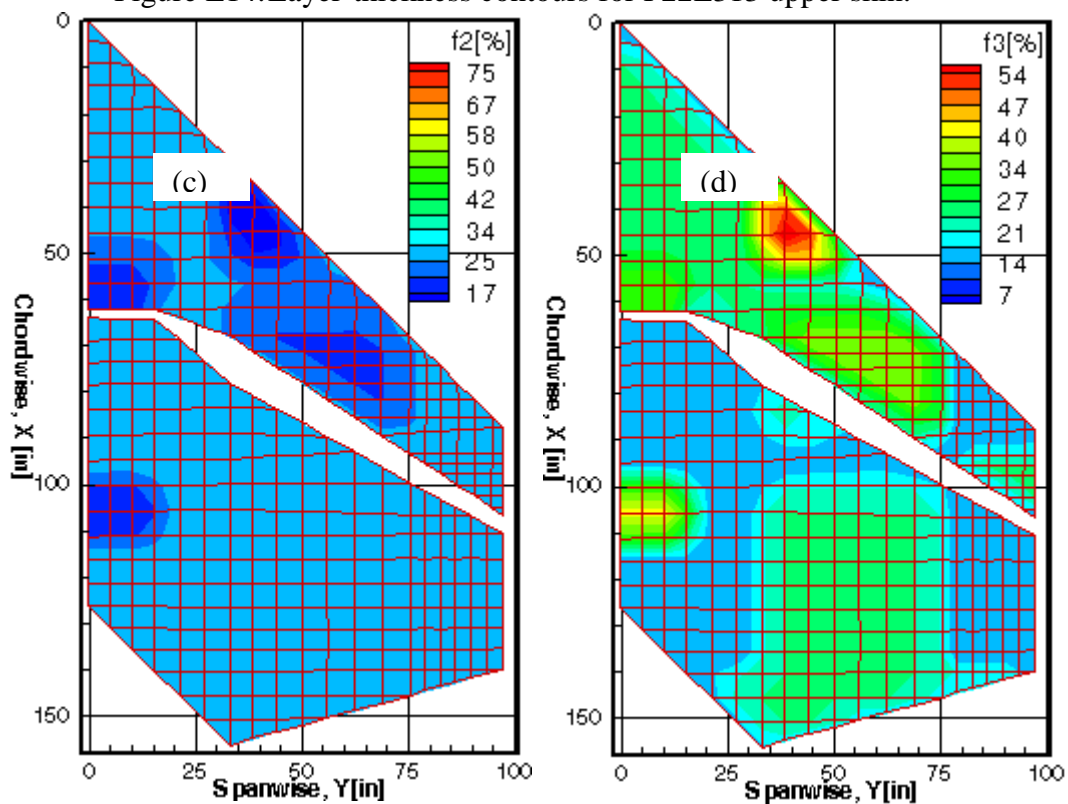


Figure E14(contd.): Layer-thickness contours for F22L313 upper skin.

4.0 NONDESTRUCTIVE EVALUATION AND MECHANICAL TESTING OF STEERED FIBER COMPOSITES

NOMENCLATURE

ACP	Affordable Composite for Propulsion
ACT	Advanced Composites Technology
ASTM	American Standard Test Material
ATCAS	Boeing 7 ft x 10 ft Crown Panel Program
ATP	Automated Tow/Tape Placement
CS	Cross Section (Photomicrograph)
DV	Design Variable
FCS	Flaw Cross Section (Photomicrograph)
FHC	Filled Hole Compression
ICAPS	Douglas 4 ft x 5 ft Skin Panel Program
IITRI	Illinois Institute of Technology Research Institute
ILS	Interlaminar Shear
KUME	University of Kansas Mechanical Engineering Department
LCM	Longitudinal Compression Modulus
LCS	Longitudinal Compression Strength
LT	Longitudinal Tension (00)
NC	Numerical Control
NDE	Nondestructive Evaluation
RC	Resin Content
RFI	Resin Film Infusion
RQP	Recursive Quadratic Programming
SAMPE	Society for the Advancement of Material and Process Engineering
SCADS	Steered Composite Analysis and Design System
STDEVA	Standard Deviation
SVTP	Simultaneous Velocity Thickness and Profile
TBR	Tow Buckling Rate
TCM	Transverse Compression Modulus
TCS	Transverse Compression Strength
TT	Transverse Tension (900)
UNC	Unnotched Compression
UNDET	Ultrasonic Nondestructive Evaluation Technique
UNT	Unnotched Tension
USNA	United States Naval Academy
VARTM	Vacuum Assisted Resin Transfer Molding
θ	Fiber angle (degree)
α_{dc_nf}	Coefficient of Attenuation for direct contact, near field, (dB/mm)
H_n	Echo amplitude H
α_{dl_nf}	Coefficient of Attenuation for delay line, near field, (dB/mm)
S_E	Ratio of two successive echo amplitude H (dB).

S_R	Ratio of incomplete reflection acoustic impedance, Z ($\text{g/cm}^2 \mu\text{s}$)
Z_n	Acoustic impedance
ρ_n	Density (g/cm^3)
V_n	Velocity ($\text{cm}/\mu\text{s}$)
E_c	Longitudinal modulus of elasticity, MPa
F_{cu}	Ultimate compressive strength, MPa
G_{xz}	Through-thickness shear modulus, MPa
h	Coupon thickness, mm
l_g	Length of gage section, MPa
M	Bending Moment, kg-mm
C	Centroidal Distance, mm
I	Moment of inertia, mm^4

4.1.0. Introduction

Fiber placement technology is a modern, automated method of manufacturing composite structure. This manufacturing method has received significant attention recently due to well-documented success in producing complex composite structures in a cost-effective manner. What is not well documented is that the capabilities of existing fiber placement hardware far exceed the capabilities of current design engineering tools, particularly with respect to the ability to fabricate structures exhibiting steered or curvilinear fiber paths.

Curvilinear fiber path geometry modeling (fiber steering) techniques using fiber placement have been developed in recent years to optimize a composite structure. Fiber steering offers significant improvements in manufacturing risk and manufacturing cost compared with conventional tools like a discrete model optimization. The fiber placement process is capable of producing complex geometry and fiber paths, improved repeatability and highly reduced scrap rate (2-15% vs. 50-100%). The benefits of this technology are significant weight and cost saving, part tailoring for performance, and the ability to steer fibers in the primary load path direction and around access regions to optimize part performance and fabrication efficiency.

This section addresses techniques associated with problems in material property evaluation of steered fiber structures. Nondestructive Evaluation (NDE) techniques and mechanical testing of steered fiber composite material are discussed as well.

4.2.0. Review Of Literature

Technologies of fiber reinforced composite material have long been developed for design, analysis, and manufacturing processes. Along with the development of these technologies, automated fiber composite manufacturing techniques such as fiber placement receive a spot light in modern composite industries in order to achieve cost-effective manufacturing capabilities. Even though fiber placement has achieved great improvement in cost-effective manufacturing, many technical matters still remain in early development stages. In particular, fiber steering technology is one of the most modern research areas. Previous works addressing these matters will be discussed in this section as follows:

- Fiber Placement
- Steering Effect, Steering Radius Investigation
- Tow Waviness
- Fiber Misalignment Effect
- Nondestructive Evaluation
- Specimen Size Effect

4.2.1 Fiber Placement

Over last 20 years, automated fiber placement processes have been developed by many researchers [1-7]. Grant and Benson [1] showed a brief history of the fiber placement process through Hercules ACT program, Douglas ICAPS Program, and Boeing ATCAS Program. In SAMPE Symposium, 1991, Enders and Hopkins [2] presented a production seven-axis fiber placement machine that manipulates individual prepreg tow materials into a 24-tow collimated unidirectional band. Grant [3] summarized the current and future utilization of automated fiber placement processes as well. NASA Langley, collaborating with several research organizations, has conducted research to develop the automated fiber placement process for fabrication of high performance complex composite structures [4-7]. Several different fabrication methods and materials are examined for cost-effective fabrication. Vacuum Assisted Resin Transfer Molding (VARTM), Resin Film Infusion (RFI), and Automated Tow/Tape Placement (ATP) were considered as the methods [4], and polymer-matrix-impregnated carbon fiber tows [5], AS4/PEEK towpreg and IM7/Radel 8320 slit tape [6] and thermoplastic ribbon (PIXA/IM7) [7] were used as candidate materials.

4.2.2. Steering Effect, Steering Radius Investigation

A manufacturing procedure for laminates containing steered fibers has been studied by Kelly et al.[8]. Dr. Kelly used a Cartesian robot system to fabricate a specimen that had trajectories parallel to the principal stress vectors. The steered specimen achieved 10% peak load improvement over the baseline group. Fiber steering and steering radius effect have been investigated by Robert Flory and Edward Bernardon in Charles Stark Draper Laboratory [9]. Draper set up a simple test to perform in-plane steering tests with a variety of different tow

widths to investigate the relationship between fiber steering, material width, and fiber micro-buckling. The tests showed that the minimum radius the fiber bandwidth could steer through with acceptable fiber micro buckling was linearly related to the bandwidth of the material being steered. In this test, three courses of ½" wide tow at different radii of curvature were laid up with an opinion from a major composite design and manufacturing company to determine "acceptable" fiber micro-buckling. These acceptability limits of steering have to be validated in other sources. Based on the results of the test, ½" wide tape wrinkle test showed 48" of minimum steering radii would be "OK". In addition, the results showed the relationship between the minimum steering radius and tow width variation. The 1/8" wide tow material was determined to be "OK" with less than 20" of the minimum steering radius, but this will be investigated with mechanical testing to prove the stability of mechanical properties. The Draper report discussed several design issues that needed to be quantified to allow design engineers to make machine design trade-offs. The other design issues were roller/shoe conformability to complex geometric shapes, non-productive time, lay-up head speed, and gross part shape complexity.

4.2.3. Tow Waviness

Fiber waviness is a type of manufacturing defect commonly observed both in-plane and out-of-plane within a laminate. The layer waviness occurs in thick crossply or multidirectional laminates as a consequence of lamination residual stresses built up during curing[10]. Due to the difficulties involved in measuring natural fiber waviness, many researchers have resorted to creating artificial fiber waviness models to investigate the effect of waviness on composite strength [10-20]. In 1967, Tarnopol'skii, Portnov, and Zhigun completed the analytical approach addressed to the prediction of the Young's modulus of wavy composite with uniform waviness [11]. Chou and Takahashi developed a similar model for investigating the longitudinal and transverse tensile behavior of flexible composites for iso-phase and random-phase cases[12]. With similar analytical models, many investigators focused on the relationship between fiber waviness and compressive strength. Mrse and Piggott [13] found different levels of process-induced in-plane fiber waviness in thermoplastic composites fabricated from different prepreg materials. Componeschi, E. T. [14] observed that compressive strength varies linearly with fiber out-of-plane waviness for initial misalignment angles on the order of one degree.

Hasio and Daniel [15,16] investigated the effect of fiber waviness on stiffness and strength reduction of unidirectional composites under compressive loading. Two out-of-plane geometric models were assumed to be planar sinusoidal for uniform waviness and to decay linearly from a maximum at the midsurface to zero on the outer surfaces for graded waviness. Based on these models, major Young's modulus and compressive strength in unidirectional composites degrade significantly as the fiber waviness increases. The results of unidirectional specimens demonstrated a 30% reduction in strength and 6% reduction in stiffness respectively compared with a normal aligned specimen [15]. Also they observed a 42% drop in axial stiffness for cross-ply specimens with uniform, controlled levels of out-of-plane waviness [16]. The paper concluded that experimental results were in good agreement with predictions based on analytical models. The paper was mainly focused on the analysis of out-of-plane fiber waviness. P. J. Joyce and T. J. Moon [17] presented data from a series of compression tests examining the effects of varying levels of in-plane fiber waviness. The results of compression tests showed 30% to 50% linear reduction in compressive strength for moderate off-axis angles (~ 5 degree)

and nearly 70% strength reduction for more severe waviness (10-15 degree). Also they observed approximately 75% of test specimens were failed by in-plane kink banding and 50% of the specimens exhibited complementary kink bands with mixed in-plane and out-of-plane character. Rai et al.[18] found that the reduced stiffness of their testing components could be affected by a combination of both fiber waviness (out-of-plane) and fiber misalignment (in-plane). Many researchers observed decreased compressive strength with increasing fiber waviness through their researches [19,20].

In this report, the effects of in-plane fiber waviness via compressive strength for an advanced fiber composite will be investigated. Due to the highly complicated scheme of fiber orientation (steering; continuous varying fiber orientation), the development of analytical models will be continued in further research, but the effect of fiber waviness will be discussed with the results of compressive tests. Main causes of fiber waviness in steered fiber composites will be discussed in Section 4.5.2. As one of the effects of local fiber waviness, the microscopic method for steering radius investigation (will be discussed in Section 4.5.2.2.1) becomes inconclusive.

4.2.4. Fiber Misalignment Effect

As discussed in the fiber waviness effect, in-plane and out-of-plane localized fiber waviness significantly affect fiber composite properties such as longitudinal tensile modulus or compressive strength, delaminating fracture toughness, and laminate consolidation [21-23]. For example, the longitudinal compression strength drops a 50% in strength on fiber angular misalignment, from 1° to 2° [21]. Claus [24] researched the effect of random filament misalignment on the strength of a unidirectional reinforced composite. He discussed that filament misalignment, at least to the degree that may reasonably arise during composite fabrication, is much less detrimental to composite tensile strength than a distribution of filament breaking strains. Yurgartis [25] presented a technique for measuring the distribution of fiber misalignments in 2-D and 3-D cases in the range of $\pm 10^\circ$. A carbon fiber composite, APC-2 was examined for the investigation and this particular composite is found to lie with $\pm 3^\circ$ of the mean fiber direction. The method can provide a full bivariate distribution, which includes both in-plane and out-of-plane misalignments, but it is impractical for very small misalignment and it is difficult to determine the slope of the misalignment.

4.2.5. Nondestructive Evaluation

Haffner et al. [26] developed a contact-free laser-ultrasonics system to investigate the feasibility and development of a scanning apparatus for c-scan images and material nondestructive evaluation. C-scan images were compared to a conventional piezo-electric nondestructive evaluation system for verification. Wooh [27] studied quantitative ultrasonic methods to detect several types of defects such as embedded film patch, impact damage, matrix cracking, fatigue damage, thermally induced cracks, fabrication defects, interlaminar grease spots, fiber fracture, and porosity. Also, he developed computer-aided digital data acquisition and processing for acoustic imaging. Williams and Doll [28] found generally 5% to 10% increases in attenuation for specimens fatigued at 80% of static strength. They measured the narrow band ultrasonic longitudinal wave velocity and attenuation as a function of the transfiber compression-compression fatigue of unidirectional graphite/epoxy composites. Hsu et al. [29] presented techniques to detect and characterize defects in composite materials, steered and non-

steered composites. Simultaneous Velocity Thickness and Profile (SVTP) Imaging technique was utilized to create surface contours and cross-sectional profiles using ultrasonic scans, and interface imaging technique was used for characterizing fiber orientation in composite panels. They also investigated the interlaminar shear strength (with ASTM D 2344-84 method) and its correlation to anomalies revealed by scans. They concluded that the short beam tests for steered and non-steered panels behaved similarly.

4.2.6. Specimen Size Effect

In general, the larger material volume increases the probability of flaws. Large brittle bodies tend to fail at lower stress levels than smaller ones under the same kind of uniform stress fields. This phenomenon is known as “Size Effect”. Zweben [30] summarized several evidences of the size effect based on his previous works [31,32] as follows:

- Composite tensile failure associated with statistical fiber break accumulation
- Tensile coupons 18-51% weaker than impregnated strands
- Tensile ring 23% weaker than coupons
- Flexural strength can exceed
 - Tensile strength by 44%
 - Compression strength by 56%
- Four-point bend strength:
 - 100-ply coupon 15% weaker than 25-ply
- Laminate strength decreases with increasing hole diameter
- Pressure Vessel burst strength decreases with increasing size
- For compression coupons with three holes in series vs. one hole:
 - Static strength 11% lower
 - Fatigue life 69% lower

He predicted the compression of coupons and structure strengths based on Weibull theory, and concluded possible 25-40% strength reduction with an assumption of Weibull Modulus of 25. Also, he found the coupon data might be very nonconservative for large structures. Camponeschi [33] examined several different composite materials for compression strength. For example, S2 Glass/Epoxy showed 20% drops in compression strength, and carbon/epoxy showed the same pattern. In-plane, longitudinal compression modulus was found

to be insensitive to specimen thickness. Wisnom [34] used four-point bending and pinned-end buckling test to investigate the effect of specimen size with scaled specimens of 25, 50 and 100 plies. Both tests gave similar results and showed a significant decrease in strength with increasing specimen size. The tensile strain decreased by 8% for each doubling of specimen size. He found a reduction in compressive strength with specimen size larger than the reduction in tensile strength.

All of these previous works focused on the size effect with the variation of thickness in order to increasing the material volume, but this paper conducted the investigation of size effect through the variation of specimen width because the known flaws (i.e. gap, tow drop and add, and overlap) in steered fiber structure were dominant in-plane.

4.3. Previous Data and Methods Review

4.3.1 Review Data

Test data from Boeing and the United States Naval Academy (USNA) has been reviewed in the year 2000 summary annual report [44]. The most interesting data from these previous tests was the axial compression response of steered fiber coupons. The data shows the strength is steadily decreasing from the baseline to the 58cm, 84 cm, and 109cm samples as shown in Figure 4.3.1. Since the larger radii samples exhibit less steering, the strength should be higher, and thus the trend is counter-intuitive. Most of the tests for this project were focused on additional axial compression tests in order to further investigate reasons for the unusual data.

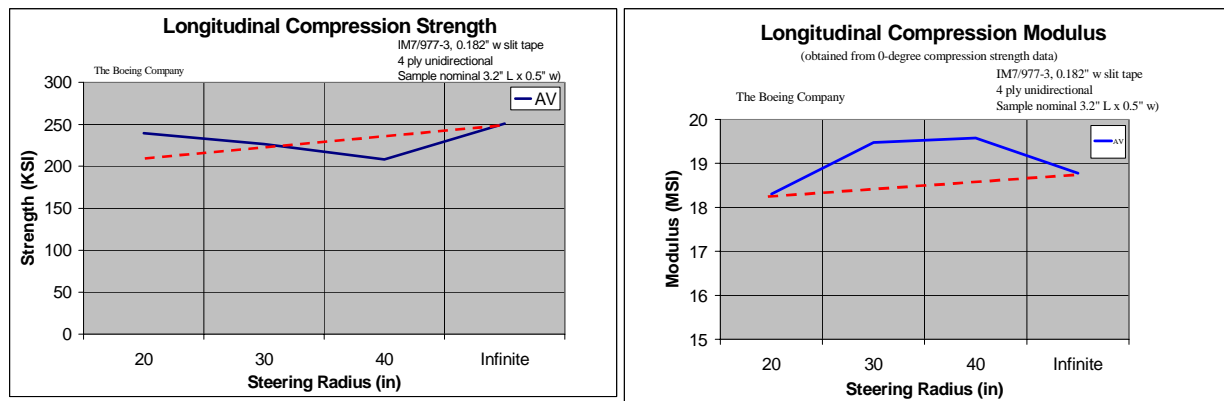


Figure 4.3.1 Longitudinal Compression Strength and Modulus Data from Boeing Company

4.3.2. Review Previous Methods

All previous compression tests utilized the ASTM D-695 test method. This method is widely used in modern industry because of its cost effectiveness and ease of use. ASTM D-695 and similar tests may not be appropriate for steered fiber composites because a conventional

compression load path is not solely in the fiber direction (Figure 4.3.2). The purpose of steered fiber composites is to steer the fiber along the load path to increase the strength of a part, yet standard test methods do not allow loading a sample the way it would be loaded if it were in an actual part, making them of dubious value. Strength results are likely to be sensitive to edge effects.

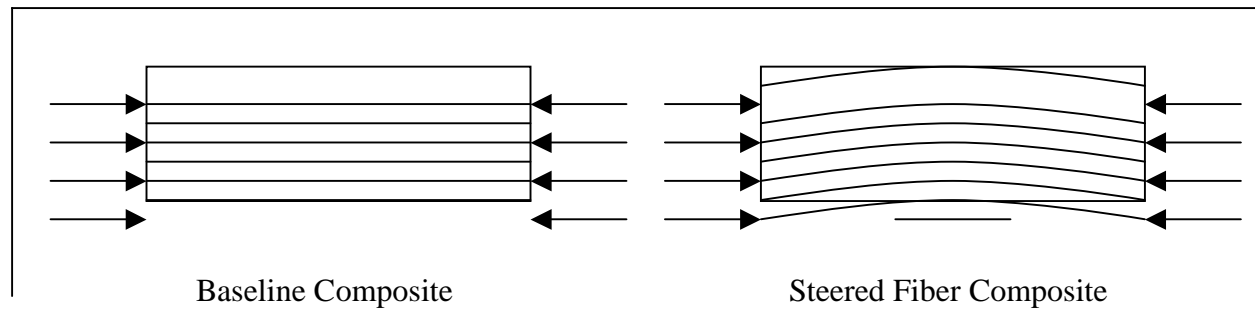


Figure 4.3.2 Compression Load Path for Baseline and Steered Fiber Composite

A steered fiber composite sample may exhibit much less apparent 0° compression strength than a conventional or baseline composite sample because of the difference in load paths discussed above. The failure stress depends on the radius of the steered fiber; the smaller the radius the more difference there is between the load path and the fiber path and, theoretically, the weaker the sample. This effect can be investigated by testing unsteered coupons and steered coupons of three different radii: 58 cm, 84 cm, and 109 cm in further research.

4.4 Research Facilities

In this section, the applied research facilities in the University of Kansas will be presented.

4.4.1. NDE (Dolphin) Machine

The Aerospace Engineering department at the University of Kansas has a SONIX CSF 1000-3X digital 3-axis automated immersion ultrasonic system with capabilities for A-scan, B-scan and C-scan testing in through-transmission or pulse-echo mode. Figure 4.4.1 shows the details of this system.

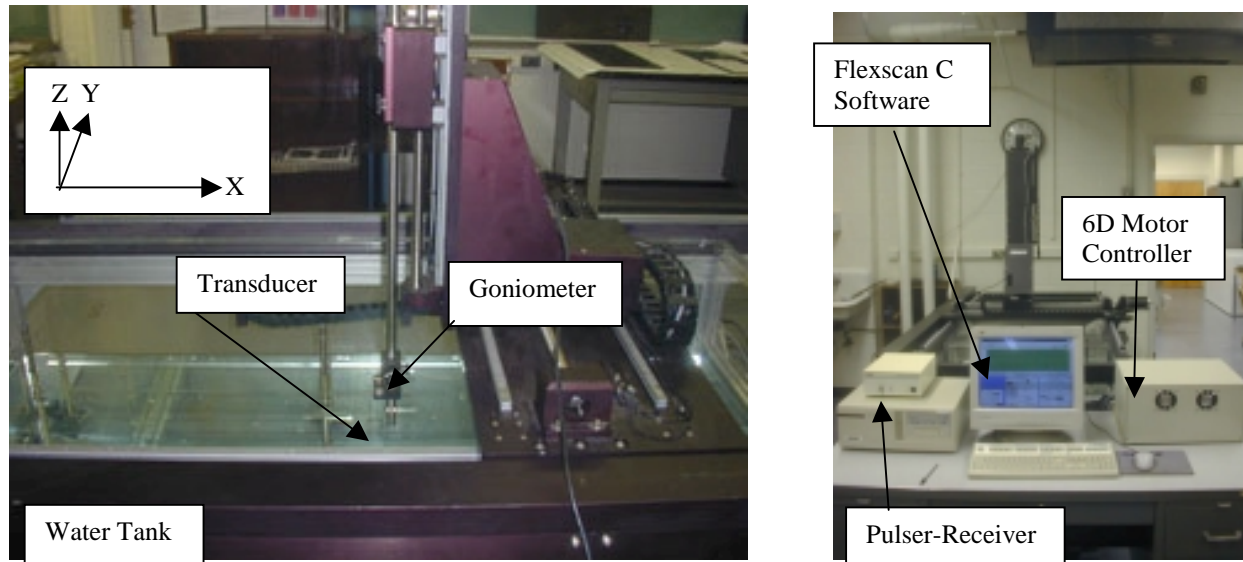


Figure 4.4.1 KU_NDE (Dolphin), SONIX 6D CSF 1000-3X

The system was designed for up to six axes of motion, but is currently configured for 3-axes of motion. This system capability is adequate for the current research because all testing panels are flat plates. After investigating with various types of transducers, a 5 MHz focused probe in pulse-echo mode was selected. The advantages of this probe include reduced noise and increased sensitivity to small flaws than other available probes. The pulse-echo mode was selected because flaw location and flaw size can be accurately determined and because the scanning object is too large to use in through transmission mode with a single scan.

4.4.1.1 Dolphin Test Fixture

To achieve consistent quality ultrasonic scans requires maintaining parallelism between the scanning object and the scanning axis. This is not always trivial due to factors such as deflection in the bottom plate of the water tank, a curved scanning object, or a test fixture that is not level. In addition a side-edge free test fixture tends to move due to vibrations of the axis control motors. The project team developed a test fixture to solve these problems. The test fixture is level adjustable, can accommodate different size objects, and is anti-slip. Figure 4.4.2 shows the text fixture layout. In addition, a front-surface follower gate is employed when scanning to trigger the data capture gates at a specified time delay from the front surface echo. The fixture material is 2.54 cm thick epoxy-glass and scannable envelope is 123 cm x 63cm.

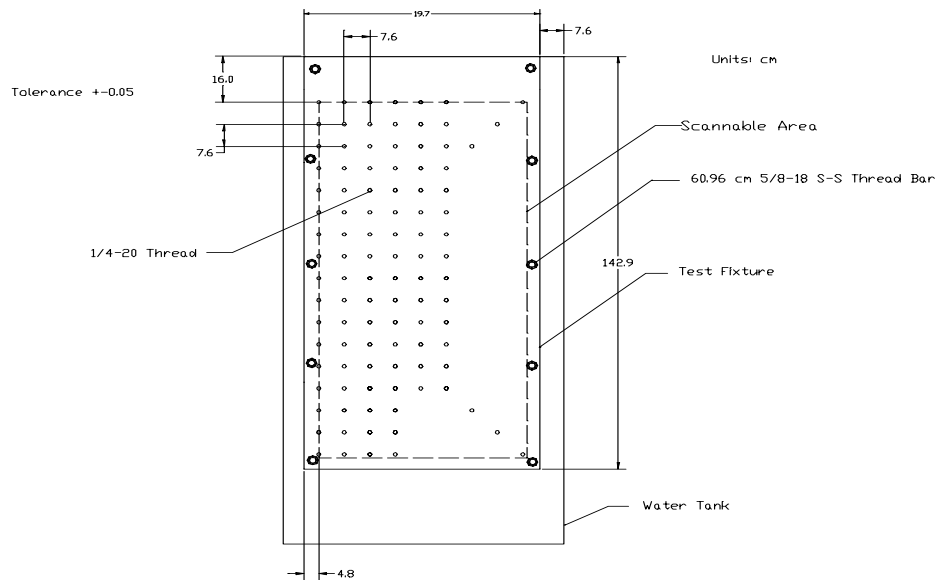


Figure 4.4.2 NDE Test Fixture

4.4.2. Diamond Cutter

The available panels from the Boeing Company and Northrop-Grumman need to be cut for the mechanical test coupons. Typically a water-jet cutter is being used in the industries, but the team utilizes two different types of diamond cutters, a Diamond section saw, Figure 4.4.3, and an ISOMET 1000 Precision Saw, Figure 4.4.4. The Diamond section saw has installed with 20.32cm dia. x 0.14cm thk x 1.59cm arbor size Buehler diamond cutter blade and is running at a fixed speed of 1725 rpm. The project team made a fixture (91.44cm x 91.44cm) to hold panels for a precision cutting capability. The ISOMET 1000 precision saw has a 17.8cm dia. x 0.05cm thk x 1.27cm arbor size diamond blade with a adjustable speed capability.

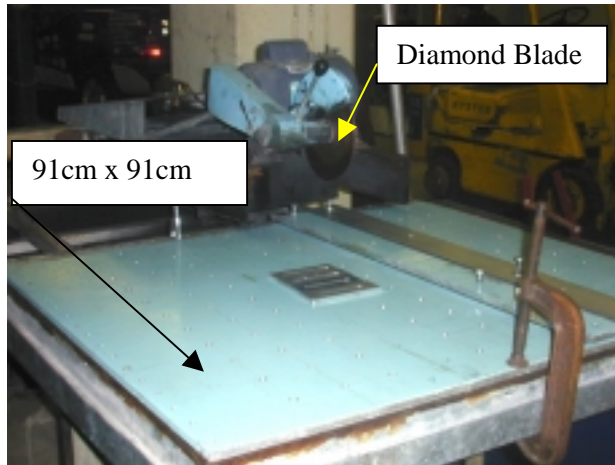


Figure 4.4.3 The Diamond Section Saw



Figure 4.4.4 ISOMET 1000

4.4.3. Specimen Grinder and Polisher

The compression test coupons require a higher level of accuracy in its dimensions. The rectangularness and parallelness of the specimens must be within 0.001” tolerances. These requirements can not be satisfied by using a cutter only without trimming process. The trimming process was done by a 3-axis wheel grinder (Figure 4.4.5). For the photomicroscopy test preparation, Ecomet V polisher (Figure 4.4.6) was utilized. The grit sizes of 120, 240, 400, and 600 polishing papers were used.



Figure 4.4.5 Specimen Grinder



Figure 4.4.6 Ecomet V Polisher

4.4.4. Photomicroscopy and Camera System

The composite lab in Aerospace Engineering Department at KU has a photomicroscopy system to investigate the fiber layout and the visual conformation of defects on the laminate and has a camera system to capture the images of laminate. The microscopic system has the zoom capability of x200, x400, x800, and x1200. The following Figures 4.4.7 and 4.4.8 show the systems. The camera system enables x3 to x10 inspections.



Figure 4.4.7 Photomicroscopy System

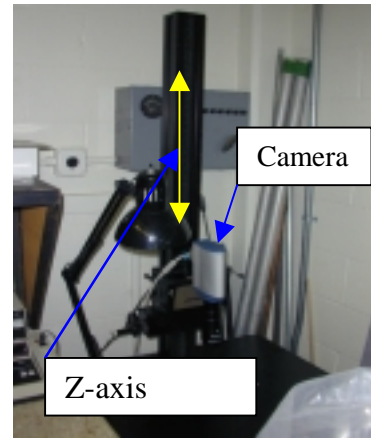


Figure 4.4.8 Camera System

4.4.5. Mechanical Test Machine (Instron)

An MTS-Upgraded Instron mechanical testing machine (Figure 4.4.9) is available for this project. The maximum capacity of the machine is 10,206 kg (100 KN Load Cell). The machine can be installed with various fixtures for tests such as compression, tension, bending and in-plane shear. Also it has a capability of load cycling fatigue testing. The control system is retrofitted by MTS Company. The control system is based on a user-friendly window base software, Testworks.

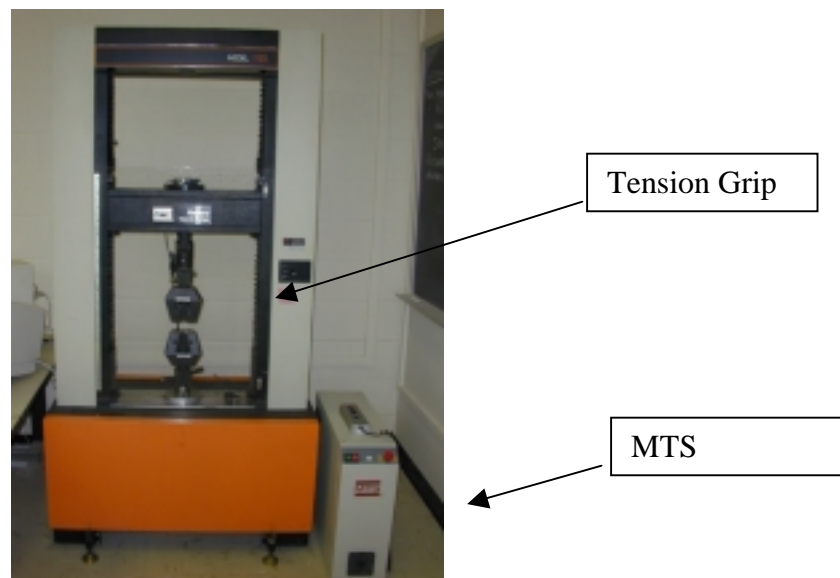


Figure 4.4.9 MTS-Upgraded Instron Mechanical Testing Machine

4.4.6 Compression Test Fixtures

Two different compression test fixtures were selected to complete the test of steered composite test for this project.

4.4.6.1 Fixture 1: ASTM D 695

The ASTM D 695 fixture is used to test composite materials in uniaxial compression. The straight-sided test specimen is 8.08cm long and 1.27cm wide, the thickness depending on the testing material, typically the order of 0.102cm. Because of the short gage length (0.478cm), it is impossible to attach a strain gage to measure the strain value of tested material. Thus, two tests are specified. A specimen without tabs is loaded to a minimum strain of 0.3 percent, using double-sided strain gage system to measure strain. This can obtain the compressive modulus. A second specimen with tab is then tested to failure, to determine the compressive strength. This test fixture is commonly used in industries because of less cost, easy to handle, and reasonable success. This test method is used for the Boeing test coupons in this project because of the characteristic of steered composites discussed previously. In addition, the output of this test method can be directly compared with the previous data.

Figure 4.4.10 shows the ASTM D 695 compression test fixture manufactured by Wyoming Test Fixtures Inc.[45]

4.4.6.2 Fixture 2: ASTM D 3410

Due to the width limitation of ASTM D 695 test method, another type of compression test fixture, ASTM D 3410 Method B Test Fixture (Figure 4.4.11), was selected. The test fixture is called IITRI compression test fixture, introduced by the Illinois Institute of Technology Research Institute (IITRI) in 1977. The test fixture is designed to accommodate tabbed specimens 13.97cm long, and any width up to 3.81cm, as specified by the ASTM standard. The fixture consists of four parts, a flat wedge grip, mating block, lower block, and head holder. Alignment rods guide the upper and lower blocks. The fixture can be used to test gage length specimens from zero to 5.08cm. The load that is applied to the fixture is transferred from the wedge grips to the specimen tabs through shear, and from the tabs to the test specimen through shear. Since the data resulting from this method is sensitive to the flatness of the coupons, a special care of specimen preparation is necessary. This test method is not commonly used because of weight and cost consideration. But this test method provides an advantage to test the widest specimens.

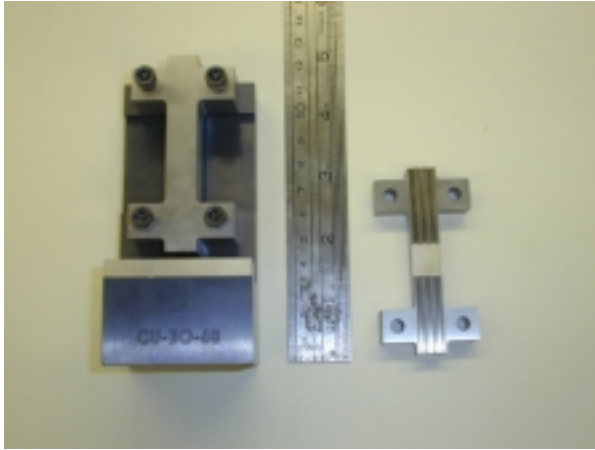


Figure 4.4.10 : ASTM D 695 Fixture



Figure 4.4.11: ASTM D 3410 Fixture

4.5 Panel and Specimen Identification

Each test specimen must be clearly marked to ensure that each coupon is associated with the correct information. Table 4.5.1 lists the names of the test panels from Boeing and Northrop-Grumman based on the composite panel description rule defined in Table 4.5.2. The description rule identifies the specimens and provides critical information about the specimen, such as the radius of the location it was taken from and the type of testing it will undergo.

Table 4.5.1 Identification of Available Boeing and Northrop-Grumman Panels

	Boeing	Northrop-Grumman
Baseline	A3C4_B A3D4_B	N3C4_B N3D4_B
Steered	A3C3 A3D1 A3D3	N3E4_1 N3E4_2 N3E5_1 N3E5_2 N3E6_1 N3E6_2

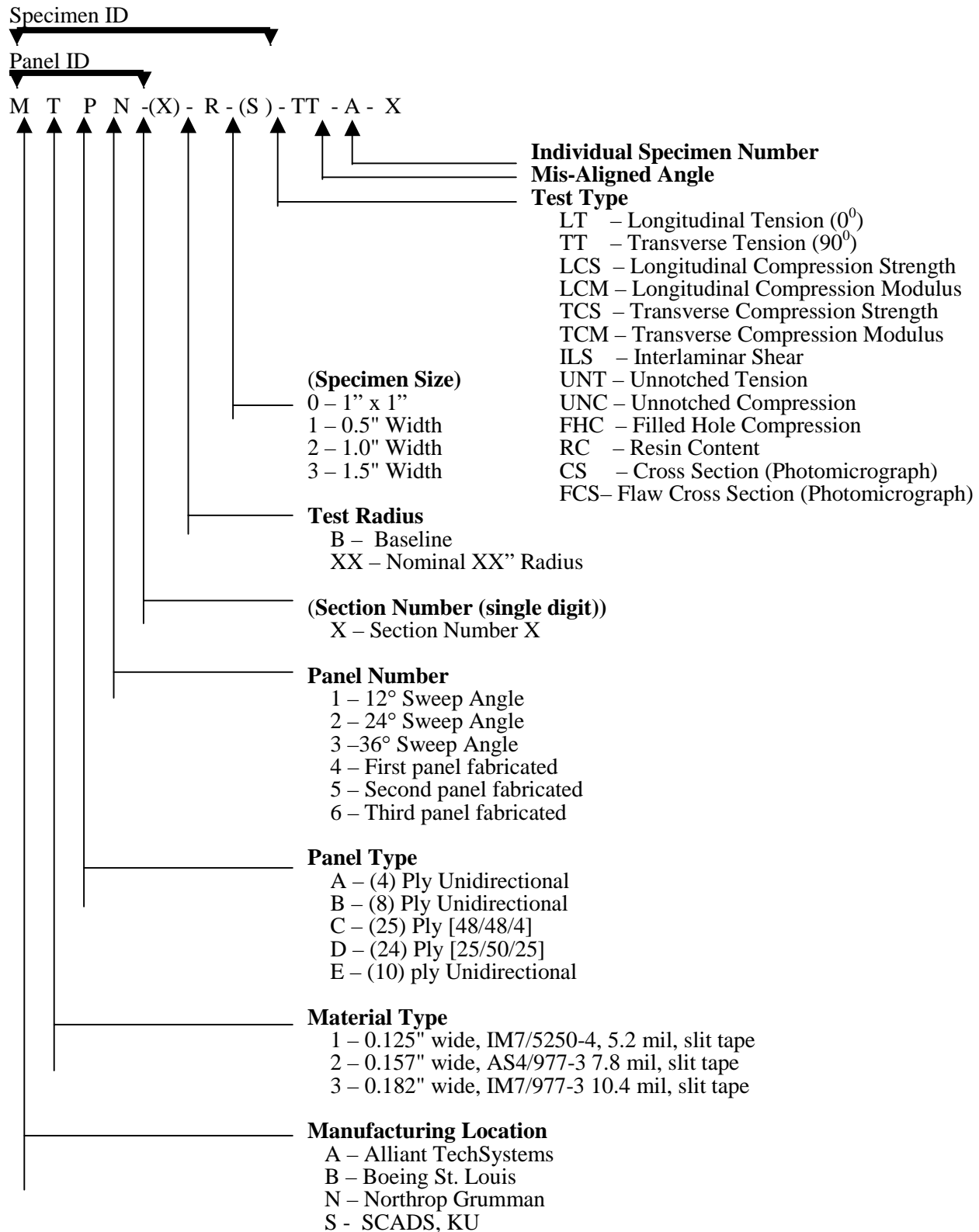
4.5.1 Panel Fiber Orientation

The panels from Northrop-Grumman are unidirectional steered fiber panels with ten layers. The Boeing panels are either twenty-four or twenty-five layers thick. The nominal fiber orientation of individual layers for the Boeing panels can be summarized as follows:

25-layer panel: $[3(-45/45/0_2)/90]_{0S}$

24-layer panel: $[-45/45/90/0_2/-45/45/90_2/45/-45/0]_S$

Table 4.5.2 Composite Panel and Mechanical Test Specimen Description



4.5.2 Centerline and Radius Identification

Reference geometry is one of the most important parameters in testing a steered fiber composite material because every location has a different fiber orientation unless the coupons are positioned symmetrically about the centerline of a panel at the same radius. One issue identified with the previous testing was that the location of previous test coupons was not clearly defined with respect to the baseline panel [46]. There was no indication of an origin point or a reference point. The determination of the radius and centerline of the steered fiber composite panels will be discussed in this section.

4.5.2.1 Centerline Identification.

The centerline (plane of circumferential symmetry) of the steered fiber composite panels from Boeing was identified using a photographic method. Two small coupons were selected from inboard and outboard locations of the panel, including the centerline defined by Boeing, polished to a 20μ finish at a 0° layer, and photographed with a high resolution (1200 x 1600 pixel) digital camera. The normal vectors of two tangent lines to the tow boundary were identified at inboard and outboard locations. By matching these vectors, the centerline of the panel was defined as shown in Figure 4.5.1.

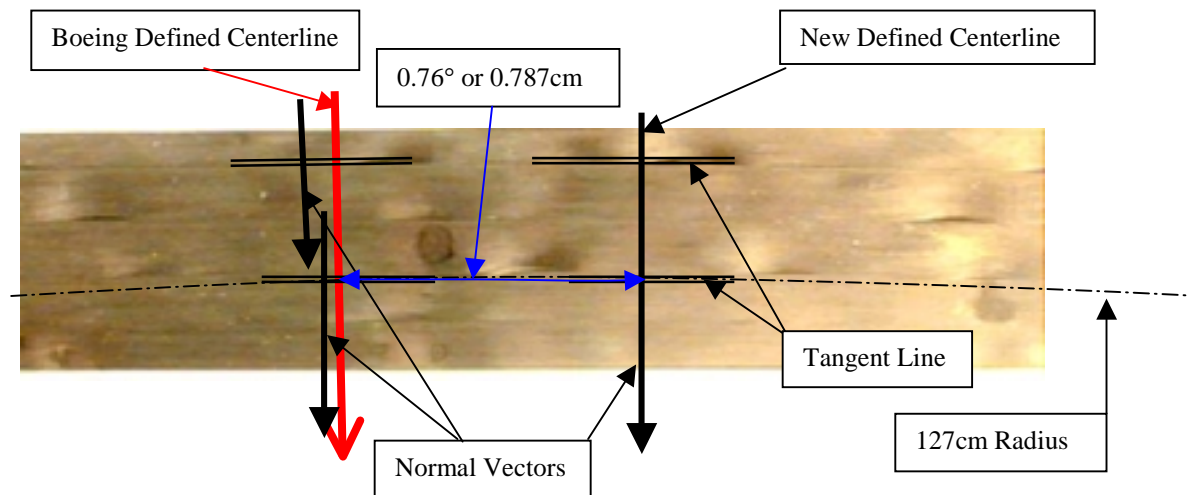


Figure 4.5.1 Centerline Identification of Samples for Existing Fiber Steering Tests Are Incorrectly Located.

With this simple method, one potential source of error in the existing test data was identified. The panel centerline appears to have been mislocated and misoriented, implying that all previous coupons were asymmetric with respect to fiber angle and curvature. Analytical predictions for expected mechanical response of asymmetric test coupons are underway, but such geometric effects will clearly introduce undesirable bending within the test coupon.

4.5.2.2 Radius Identification

There are three different methods to define the radius of a panel, the microscopic method, the photographic method, and the digitizer method

4.5.2.2.1 The Microscopic Method.

Photomicroscopy made it possible to measure the fiber angle of a 0° layer at any location on the panel. The panel was sectioned at a desired location, polished to a 5μ finish, and photographed at high magnification (800X). Figure 4.5.2 is a sample photomicrograph of the cross sectional surface of a tow from one such coupon [44].

The radius of a given location on a panel can be calculated with two equations. Figure 4.5.3 shows that the fiber angle, θ can be determined from the relationship between the length (a) and width (b) of the observed fiber cross section [25]. The steered radius of a single fiber, R or r, can then be calculated using a known distances, S from the panel centerline to the fiber.

$$\theta = \text{SIN}^{-1} (b / a) \quad \text{Eq. (4.5.1)}$$

$$R = S / \text{TAN}(\theta) \text{ or } r = S / \text{SIN}(\theta) \quad \text{Eq. (4.5.2)}$$

Table 4.5.3 shows the summary of predicted steering radii of two sample panels using the microscopic method. .

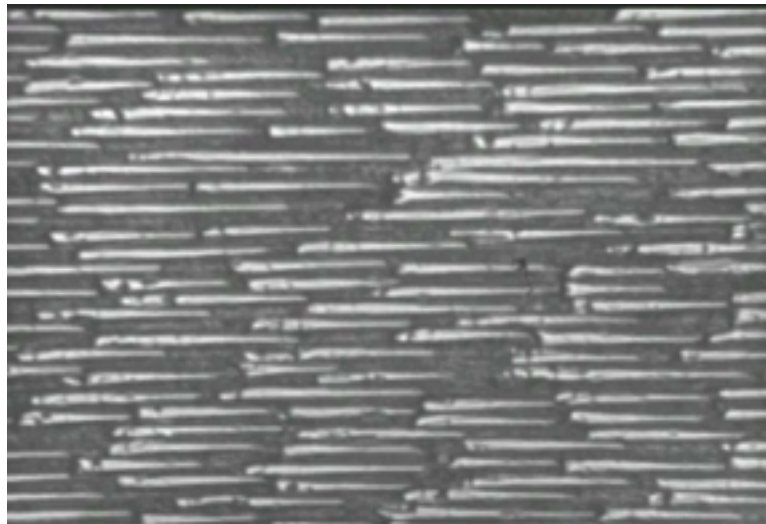


Figure 4.5.2 Cross Sectional Surface of Tow Illustrates Angular Orientation of Individual Fibers

4.5.2.2.2 The Photographic Method.

A macro-photographic method was used to determine the radius of a steered panel for a discrete 0° layer. Figure 4.5.4 shows three points (A, B, and C) on the tow boundary of a 0° ply. The radius of the panel at that location can be calculated by making an arc with the three points and finding the radius of that arc. Local fiber waviness, which obfuscated results in the microscopic methods, is readily apparent in Figure 4.5.4.

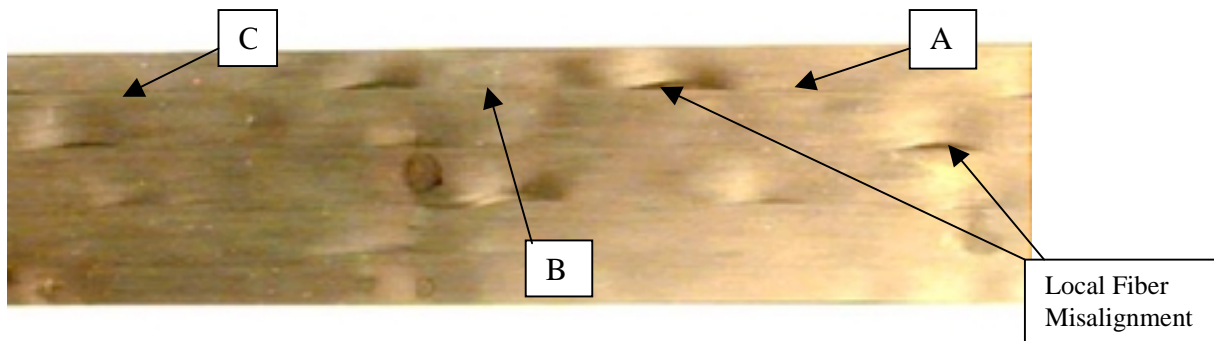


Figure 4.5.4 Layer 5 (0°) of a Representative Steered Fiber Panel (A3D3) Illustrates Local Tow Waviness Common in Fiber Steering and Fiber Placement.

The radii at the bottom side of two representative test panels (A3D1 and A3D3) were found to be 49.81 cm and 51.79 cm, respectively. These results were almost identical to the 50.8 cm nominal radius calculated by Boeing. Therefore, the radius of the panel at the bottom side is assumed to be 50.8 cm for both of the panels as initially documented. This radius is used to identify the nominal location of future test coupons.

4.5.2.2.3 The Digitizer Method

Both of the aforementioned methods of radius identification were inadequate. The effects of compaction and curing distorted local fiber orientation enough to invalidate the first two methods and the third method was developed because of its reduced sensitivity to these distortions. The digitizer method made use of a digitizing tablet to follow a single tow boundary across its entire length, mapping it with a series of points. These points were then imported to AutoCAD and an arc was curve-fit to find the radius. This method is much less sensitive to the effects of small local fiber distortions because of the greater number of points generated with the digitizer. Results from this method correlated closely with the approximate radius identified by the manufacturer. One problem of this method is that at smaller radius locations fewer points were found and the error is correspondingly greater. The following Figure 4.5.5 shows an example of radius determination using the method.

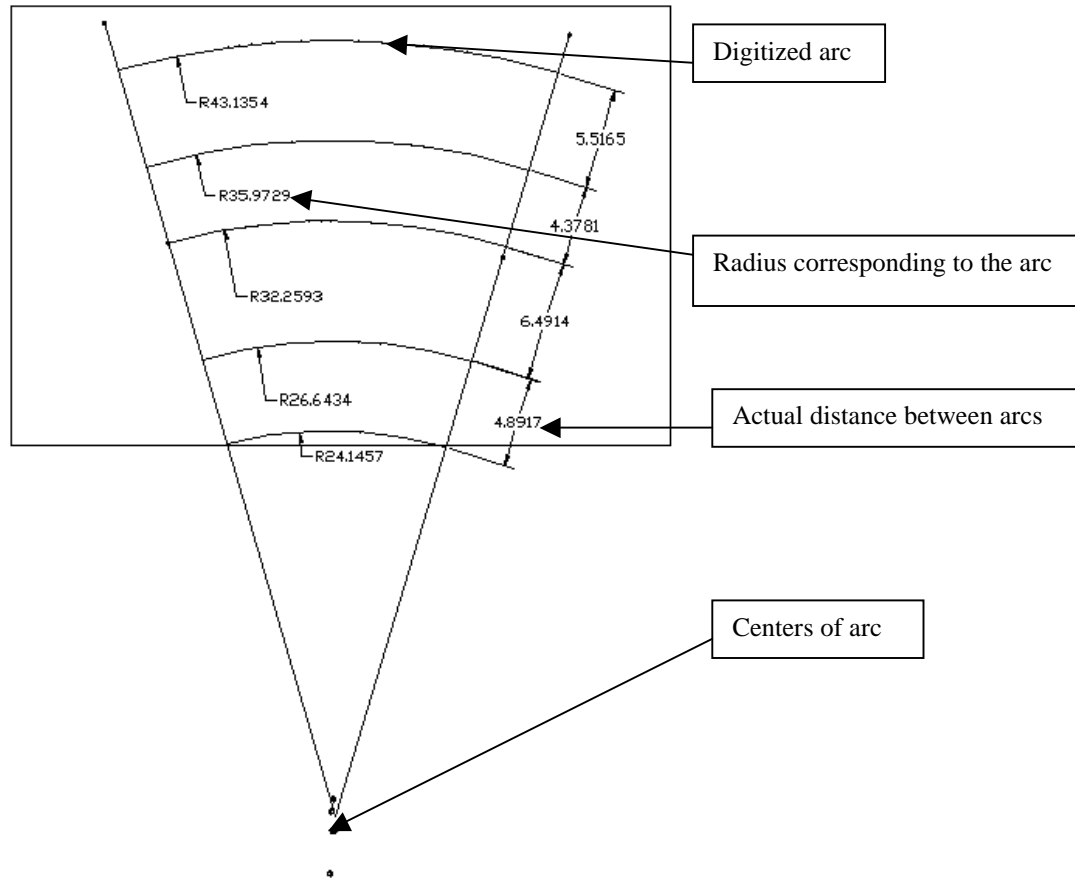


Figure 4.5.5 Steering Radius and Center Identification for N3E6_2 Panel

4.5.3 Minimum Steering Radius Investigation

As discussed before, the steering capability is not limited by machine capabilities but by how much the tow material can lay up without buckling. The 45.72cm of steering radius has been defined as an acceptable minimum radius for steered composites by the industries. This limitation was not determined based on a proven technology but with a simple engineering judgement. The smallest radius of the panel was identified as 61 cm that even it supposed to be about 46 cm based on the information from manufacture. This phenomenon was found in most panels. This effect may come from the curing process of panels. Further investigation is needed to identify the cause and effect of this problem.

4.5.4 Tow Layout Identification

A tow path on any of the steered fiber panels in this project should theoretically make a perfect arc at a given radius. An examination of the test panels, however, revealed that this did not occur.

4.5.4.1 Tow Geometry Effect Investigation

Tow geometry was investigated in both the vertical (through-the-thickness) and lateral (in-plane) directions. A photomicrograph of tow geometry in the vertical direction is shown in Figure 4.5.6. A photograph of tow geometry in the lateral direction can be seen in Figure 4.5.7. Figure 4.5.6 shows the cross sectional view of the panel at a location where the tow boundary of a layer experiences curvature in the vertical direction. This layer waviness is important because it has been shown to significantly affect the mechanical properties of composite materials [47]. The tow boundary shows a clear example of tow drops and overlaps. Layer waviness generally coincided with inhomogeneities under the layer. The layers above and below the waviness either expanded or were compressed during compaction and curing in order to make the net panel thickness uniform. Figure 4.5.6 shows that layer 12 does not match the theoretical baseline due to local tow drops and overlaps. The curvature function of this layer will be extracted for use in later analyses.

In many cases, the observed tow alignment did not match the nominal tow alignment (Figure 4.5.7). Each tow side boundary should be on an arc of a certain radius, but many tow boundaries were mis-aligned. Possible causes include:

- Tow buckling due to fiber steering
- Fiber wash due to compaction and curing
- Inhomogeneities under the layer
- Vibration of fiber placement tow head during placement.

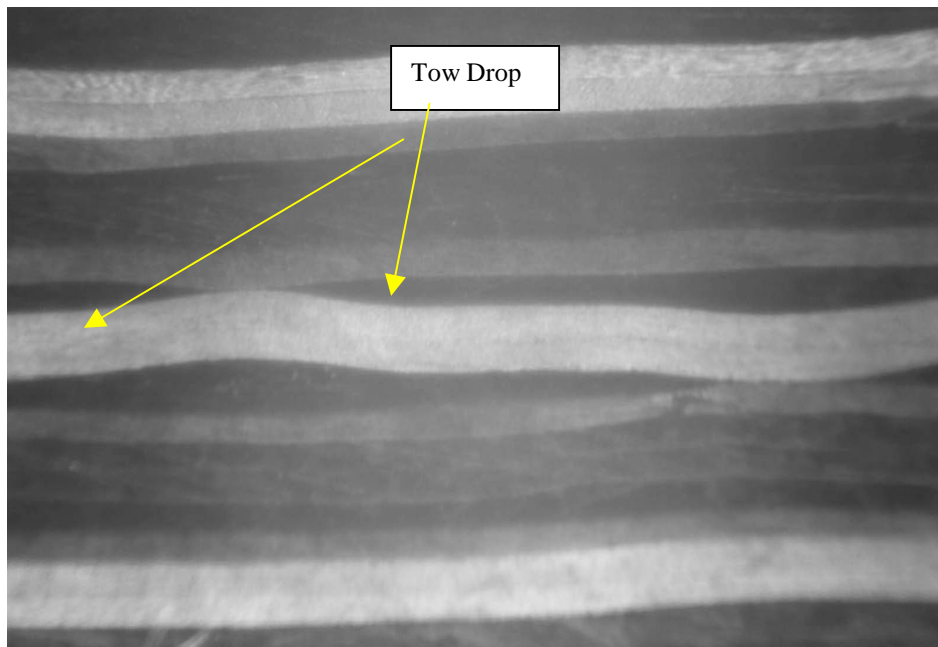


Figure 4.5.6 Cross sectional view of a sample panel (A3D3, inboard, upper side, left section)

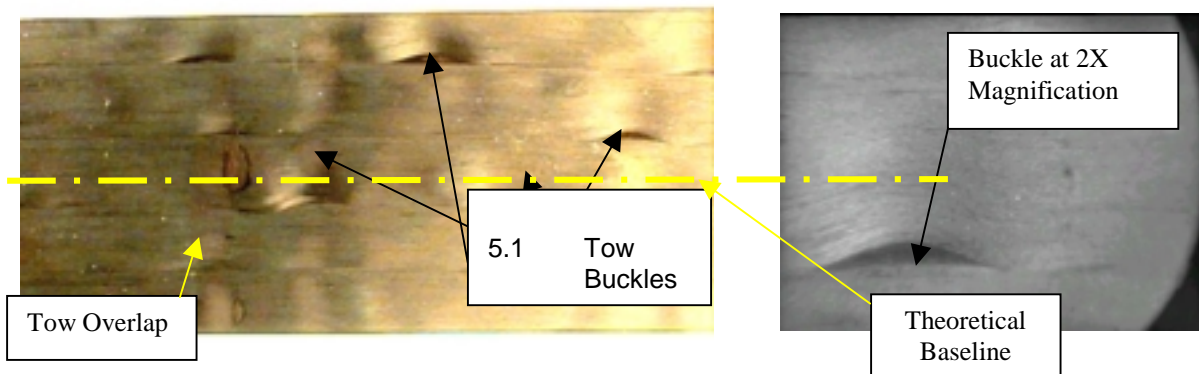


Figure 4.5.7 Tow Buckling in a Sample Panel Fiber Steered Panel (A3D3, inboard, upper side, center section)

Tow buckling is a common effect in steered fiber composites. Tensions force on the outer radii of a tow and a compression force on the inner radii of a tow during placement cause the tow to buckle. Compaction forces will flatten these in the through-the-thickness direction to achieve uniform panel thickness, but that worsens the buckling in the lateral direction. Tow buckling can be quantified using the following formula:

- Tow Buckling Rate (TBR) = No. of buckles / Unit area (35.48 cm^2)

The average values of TBR for this project were found to be 1.12, 0.74 and 0.77 as a function of steering radii of 58 cm, 84 cm and 109 cm, respectively. The corresponding standard deviations were found to be 0.413, 0.318 and 0.348 respectively. Tow buckling results show more buckles on a tow occurring at smaller panel steering radii. In particular, areas where the radius is shorter than 76.2cm shows rapid increments of TBR.

4.5.4.2 Mis-Centered Effect Investigation

The centerline alignment of test coupons is one of the most important features in a steered fiber composite test. The Boeing Company, as with most commercial composite manufacturers, currently uses a tolerance of 2° in centerline alignment. This misalignment allowable was developed as an accepted variation in conventional linear composites. Steered fiber composites can be more sensitive to misalignment, and this tolerance could cause significant variations in mechanical testing for larger radius specimen by making the fiber path of each sample different. The project team has identified an actual misalignment of 0.76° in the centerline of one test panel, as previously addressed. This may have caused the unidirectional compression data that Boeing collected to not follow an identifiable trend [48]. In order to further investigation of this effect, mechanical testing of compression coupons with 0°, 5° and 10° misalignment is currently being performed.

4.6.0. Non-Destructive Evaluation And Mechanical Testing

In this section, the detail technical challenges such as NDE and mechanical compression test will be discussed. Figure 4.6.1 shows the summary of research plan in a flow chart format.

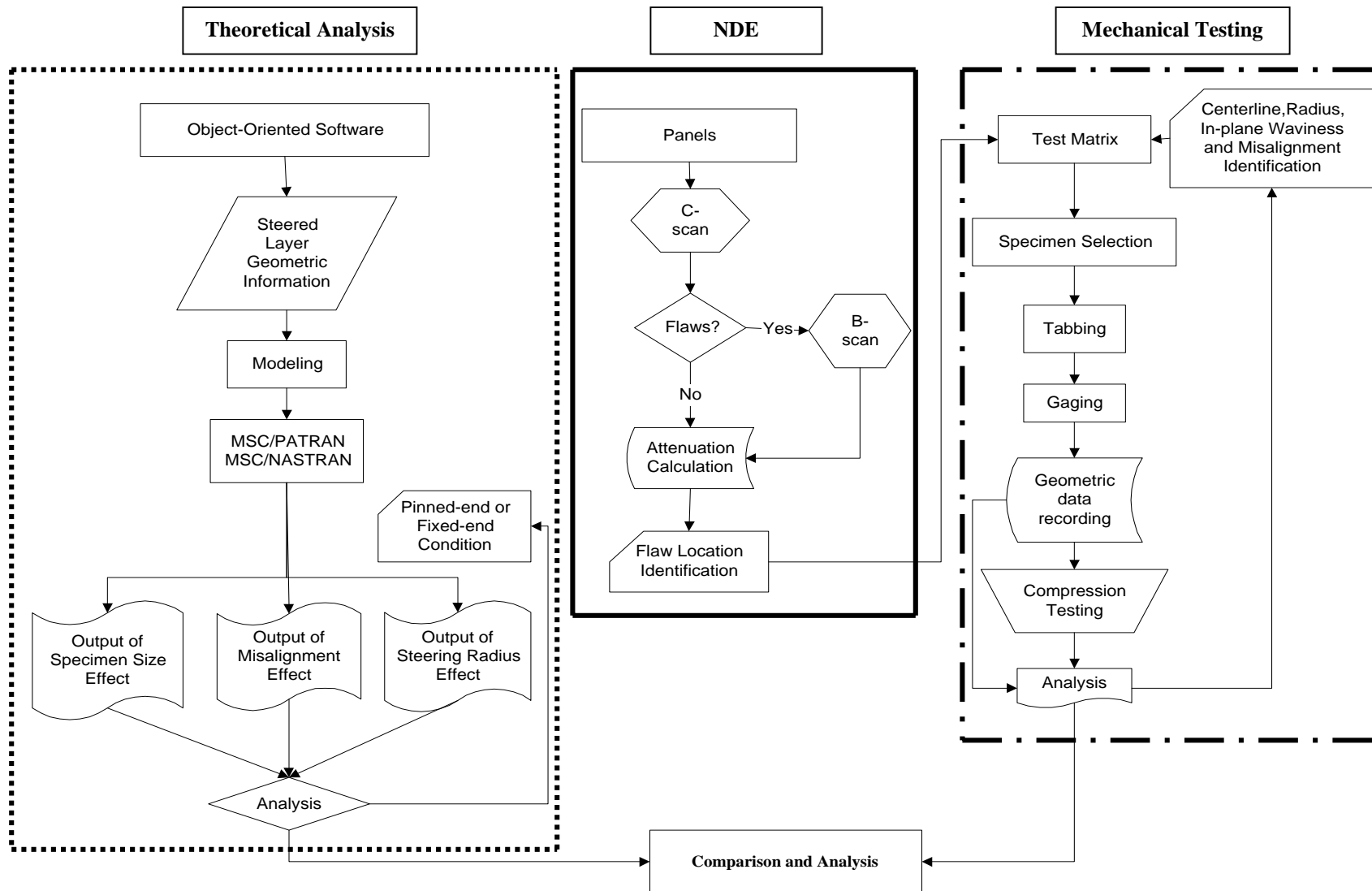
4.6.1. Non-Destructive Evaluation (NDE)

There are many different techniques to investigate a material without inducing damage. Applicable techniques include X-ray, Eddy Current, Acoustic Emission, and others. The project team decided to use the Ultrasonic Nondestructive Evaluation Technique (UNDET) based on its cost effectiveness and minimal environmental effect. Ultrasonic NDE provides relatively high accuracy in flaw detection, location, classification, thickness measurement, evaluation of bond quality, and determination of elastic moduli (material stiffness).

4.6.1.1 NDE for Flaw Identification

Every material has a certain percentage of internal flaws, but steered fiber material can have a higher percentage due to manufacturing problems such as overlaps, gaps, resin rich or resin lean areas, or debonding of layers due to tow drops and adds. The Boeing panels were scanned in pulse-echo mode using back surface focus, without setting individual gates for intermediate layers. This setting generally provides an interlayer flaw detection capability, but has proven to be ineffective for identifying every flaw, especially when another type of flaw is located at the same position. For example, an overlap flaw causes an amplified signal or diversified signal that makes it difficult to evaluate the characteristics of the flaw. This phenomenon is more likely because of the use of pulse-echo mode.

Figure 4.6.1 Summary of Research Plan



In this project, detailed ultrasonic scanning was performed with intermediate data capture gates set on every three layers after a pre-selection process for test coupon location was completed. Figure 4.6.2 shows example scanning results for a 24 layer panel (A3D1) utilizing eight discrete gates. The longitudinal wave velocity in the test material was found to be 0.302 cm/ μ s. Each gate was 0.52 μ s wide. Gate 1 is set on the layer 23 and back surface. Gate 2 through Gate 8 are set on layer 2 through layer 22.

As shown in Figure 4.6.2, an obvious flaw was detected between layer three and layer four located at 43.2 mm X, 7.6 mm Y and 2.0 mm from the top surface. The calculated attenuation at the location of the flaw (to the depth of the flaw) was found to be 3 dB/mm, where 1dB/mm of attenuation was the standard value at flaw-free locations. The attenuation of the flaw differed slightly from the standard attenuation, indicating the existence of a flaw. The attenuation of the back surface response for the flaw location was the same as at the standard location, 1dB/mm, indicating the flaw might be small enough to ignore.

There are several methods of calculating the attenuation of a panel on the basis of multi-echo sequences. These methods include selecting a scanning arrangement like direct contact or delay line, and near or far field. The following two methods [49] were utilized in the calculations.

Calculation Method 1: The Coefficient of Attenuation for direct contact, near field, α_{dc_nf} (dB/mm)

$$\alpha_{dc_nf} = 20 \log (H_n/H_{n+1})/2d \quad \text{Eq. (4.6.1)}$$

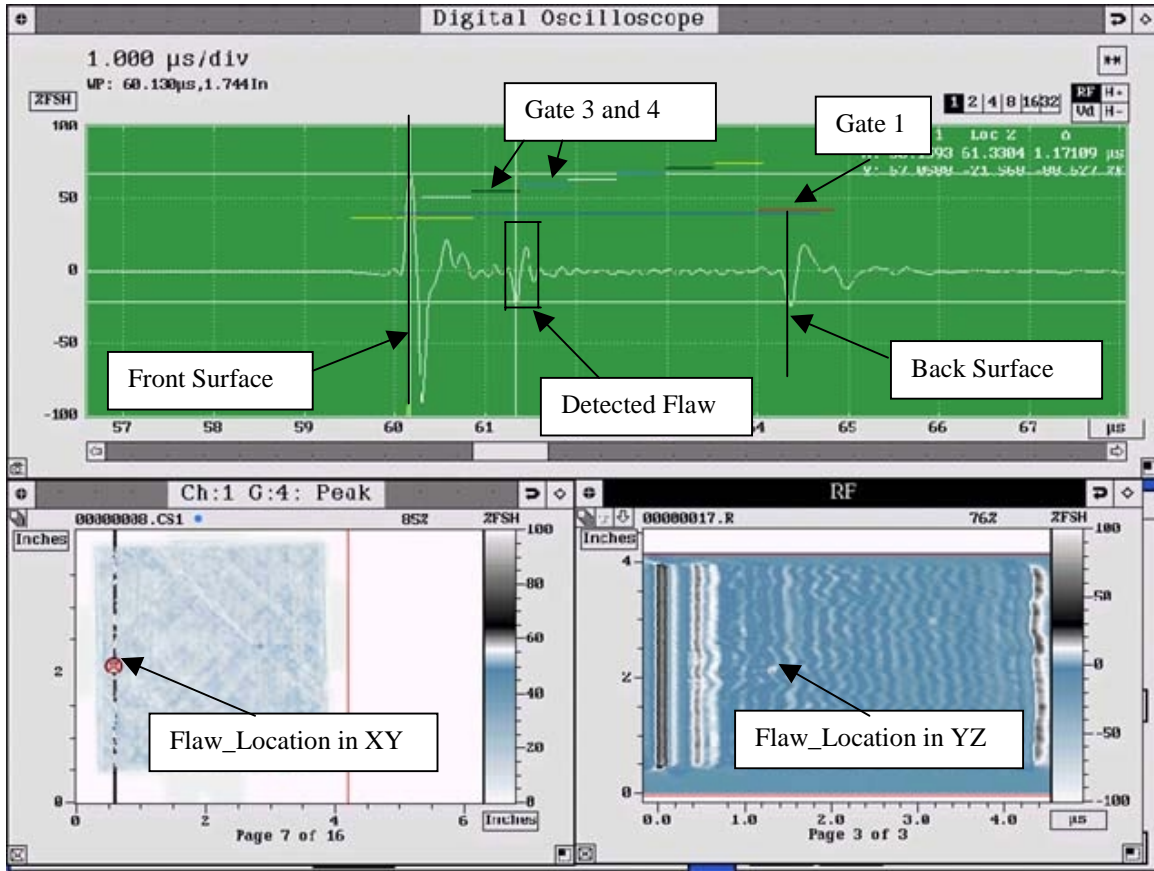


Figure 4.6.2 Flaw Detection with Ultrasonic C-Scan.

Calculation Method 2: The Coefficient of Attenuation for delay line, near field, α_{dc_nf} (dB/mm)

$$\alpha_{dl_nf} = (S_E - S_R) / 2d \quad \text{Eq. (4.6.2)}$$

S_E is the ratio of two successive echo amplitude H (dB).

$$S_E = 20 \log (H_n / H_{n+1}) \quad \text{Eq. (4.6.2.1)}$$

S_R is the ratio of incomplete reflection acoustic impedance, Z (g/cm² μs)

$$S_R = 20 \log \{ (Z_2 + Z_1) / (Z_2 - Z_1) \} \quad \text{Eq. (4.6.2.2)}$$

Z_n is the acoustic impedance, $Z_n = \rho_n V_n$

and ρ_n = density (g/cm³), V_n = velocity (cm/μs)

Both methods are only valid for a non-focused probe. A focused probe has more complicated transmitting and reflecting patterns and induces additional energy losses due to beam spreading. All scanning in this project was performed with a focused transducer to provide improved resolution of the scanned objects. The calculated attenuation, however, was still based on Eq. (4.6.1). This value is not the true attenuation of the material, but it is still a valuable indicator of the relative quality of the panel because it shows the differences between the material at a flaw section and at a standard section.

Following Figure 4.6.3 shows an example panel manufactured by Northrop Grumman. The panel size is found to be 66cm width x 66cm height with a fan shape.

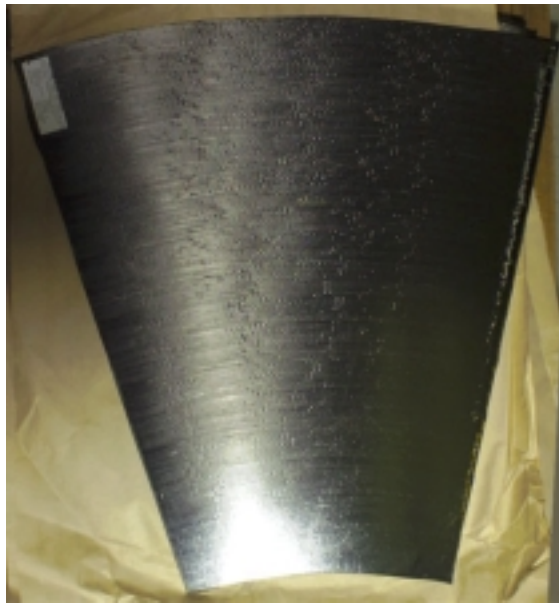


Figure 4.6.3 Example of 10-Layer Unidirectional Panel (N3E5_1)

The panel was impossible to scan at once because of the limitation of scan capability, 60.98cm x 121.92cm scan envelopes. Two separate scans were necessary. One is for the upper part and the other is for the lower part. The dividing section was indicated with two small stickers attached at the middle of the panel. Figure 4.6.4 shows example scanning results with a 5 MHz focused probe in pulse-echo mode for a 10-layer unidirectional panel (N3E5_1) utilizing five discrete gates. The longitudinal wave velocity in the test material was found to be 0.299 cm/ μ s. Each gate was 0.262 μ s wide. Gate 1 is set on the layer 9 and back surface. Gate 2 through Gate 5 are set on layer 1 through layer 8.

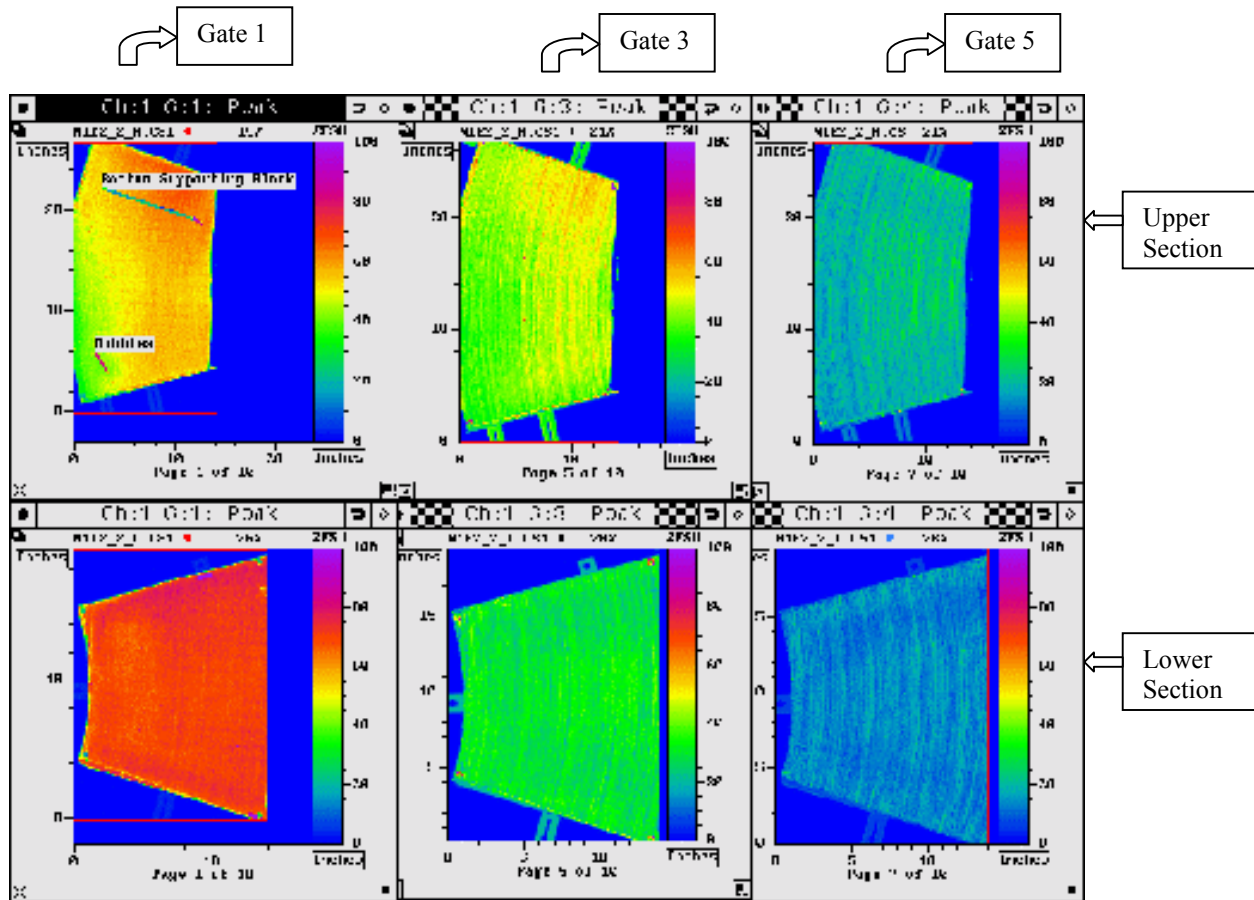


Figure 4.6.4 Example Scanning Results for a 10-Layer Unidirectional Panel (N3E5_1)

All areas of each available test panel were scanned using pulse-echo and through transmission ultrasonic inspection techniques to verify their quality and to document internal anomalies. This quality information was used to aid coupon location within the panels for the mechanical testing phase of this project. Results of this ultrasonic inspection, location of expected flaws, and location of mechanical test coupons were used to aid test coupon selection for future mechanical testing.

4.6.1.2 Panel Fiber Orientation Identification

Another benefit of C-scans in ultrasonic NDE is the ability to identify fiber orientation within the laminate. The fiber orientation of several panels was investigated using microscopic tests and NDE. This investigation was necessary to define the fiber orientation on each layer for a numerical analysis. The microscopic test method is a definite way of determining the local fiber orientation, but it requires sectioning the panel (a destructive method). The interface C-scan images, a nondestructive test result, reveal fiber orientation of plies due to the presence of inhomogeneities (e.g resin rich regions, tow overlaps or tow gaps). Figure 4.6.5 (page following) illustrates discrete data capture gates set at the expected layer interface locations based on sample thickness, velocity and total number of plies.

Figure 4.6.6 shows a clear image of the fiber orientation between the sixth and seventh layers. In both interface C-scans, a probe with a center frequency of 20MHz, an element diameter of 0.64 cm and a focal length of 5.1cm was used. The image shows boundaries of the 5.1cm wide courses and other inhomogeneities. Tests were performed in collaboration with D.K. Hsu and the Center for Nondestructive Evaluation at Iowa State University [50]. The fiber orientation most dominant in the C-scan is that of the layer most recently passed. Internal data capture gates may be placed at specific time intervals to capture features of specific layers in the laminate.

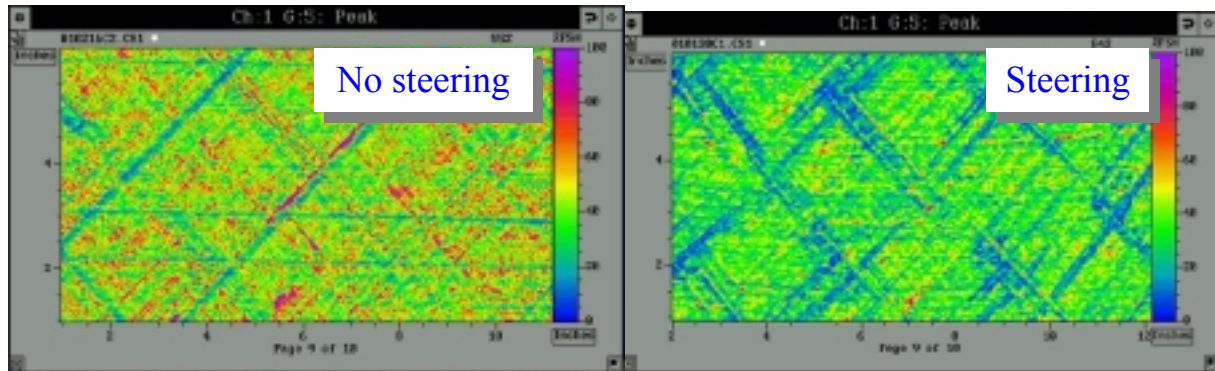


Figure 4.6.6 C-scan Images for Baseline (A3C4_B) and Steered (A3C3) Panels Illustrate Local Orientation of Tows and Courses Through features such as Overlaps and Gaps.

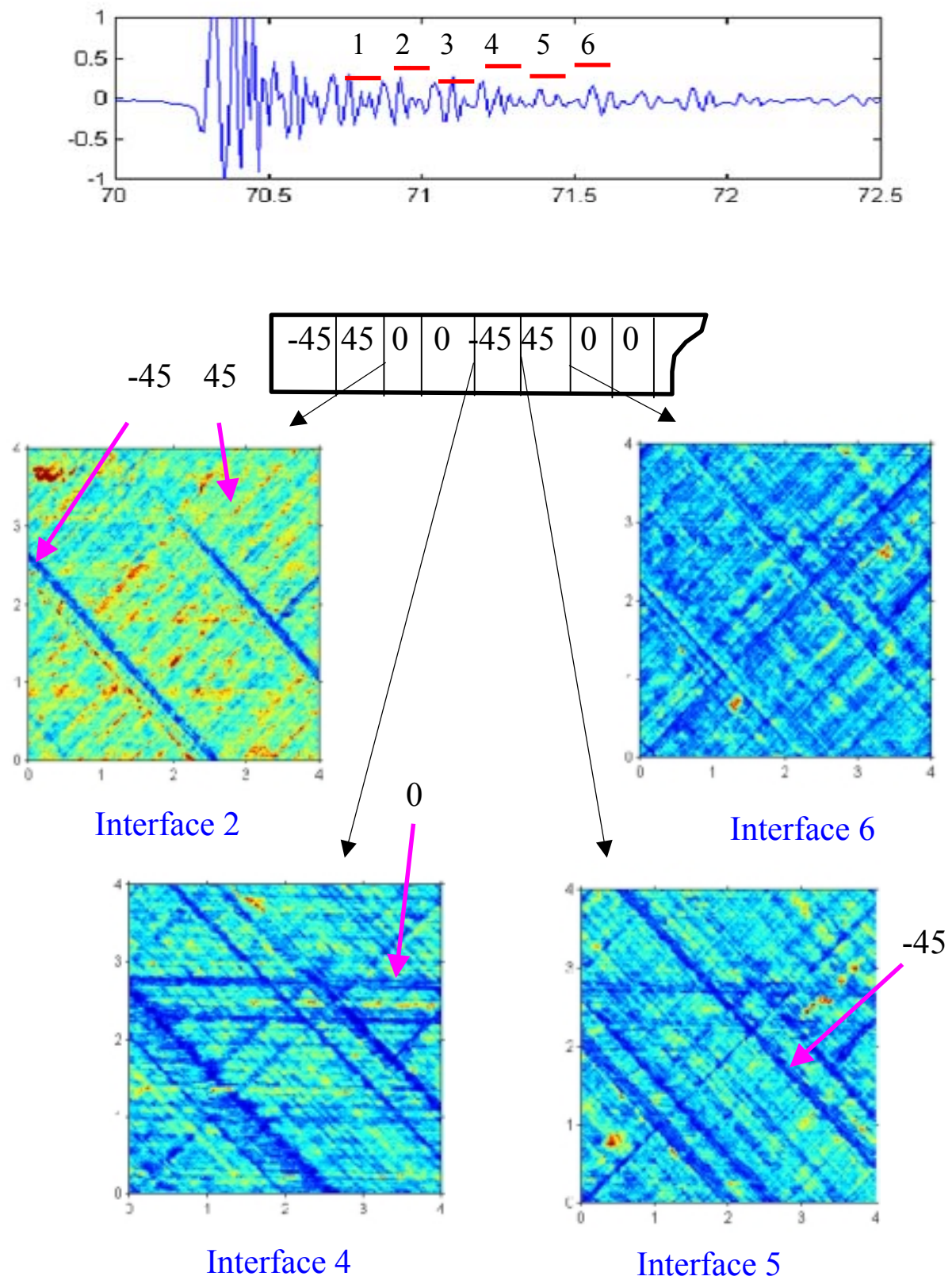


Figure 4.6.5 Fiber Orientation Identification with Interface Ultrasonic C-Scan

4.6.2 Preparation for Mechanical Testing

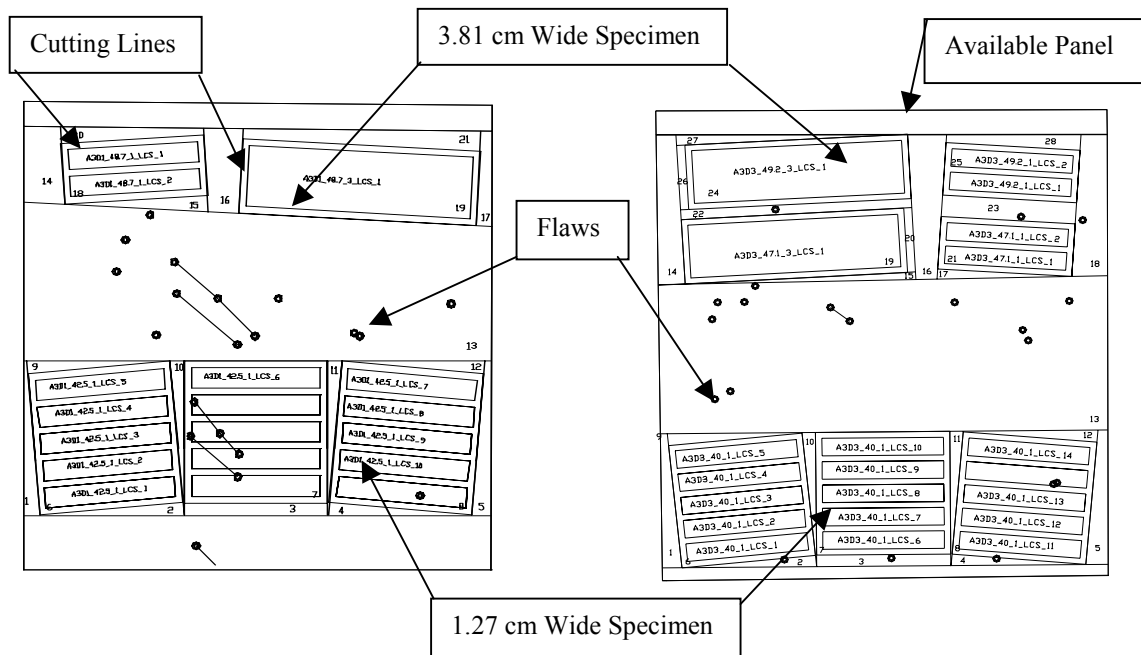
Mechanical testing of family samples is currently underway and thus complete results will not be addressed in this paper. Data from “unidirectional” but steered samples are addressed herein.

4.6.2.1 Test Method Selection

Three different sizes of test specimens are investigated, from 1.27 cm and 3.81 cm in width and 8.08 cm and 13.97 cm in length for the Boeing panels to 1.27 cm, 2.54 cm and 3.81 cm in width and 13.97 cm in length for the Northrop-Grumman panels. The ASTM D 695 test method is utilized for the 1.27 x 8.08 cm specimen and the IITRI ASTM D 3410 test method is utilized for remaining specimens. ASTM D 3410 should yield more realistic results due to the increased coupon width, but the ASTM D 695 coupons will be directly comparable to previous test data. Different width and different radius samples are tested, as it is believed that the strength of a specimen will be dependent on both the radius of the fibers in the sample and the size of the sample. The strength dependency on the radius was briefly mentioned previously, and the related research of the effect of size variation was discussed as in the literature review. Testing samples of different sizes will reveal whether or not these effects exist, and if more testing is necessary to quantify them.

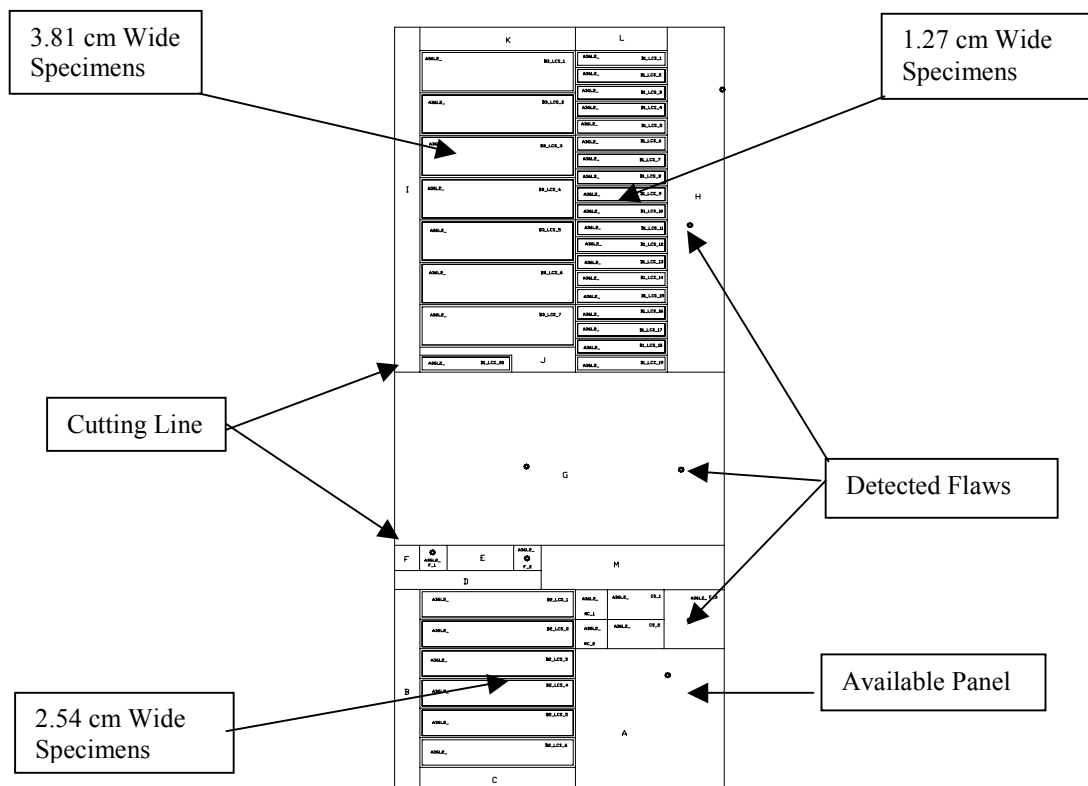
4.6.2.2 Specimen Selection and Layout

The specimen layout was selected to avoid panel flaw locations detected with NDE. The locations were determined to maximize the number of usable specimens. Mechanical properties are assumed to be the same along the centerline within a tolerance of 6.35 cm for the steered panels. The specimens for ASTM D 695 test have been selected at roughly 96.5 cm radius because the experimental mechanical test data from Boeing was obtained at 96.5 cm radius. This selection will allow a direct comparison of the two data sets. The test specimens in panel A3D1 were selected at a radius of 106.68 cm due to the need to avoid flaws. For the Northrop-Grumman panels, all specimens were obtained from 58 cm, 84 cm and 109 cm due to the lack of space of 50.8 cm radius specimens. The ASTM D 3410 method B compression test allows the various widths of test coupons, 1.27cm to up to 3.81cm. Three different width size coupons, 1.27cm, 2.54cm, and 3.81cm, were selected to investigate the effect of different width. At least five coupons were needed for each test to satisfy the requirement of ASTM standard but the matrix for the Boeing steered panels could not satisfy the minimum specimen requirement due to the limitation of material availability. Figure 4.6.7 and Figure 4.6.8 show the layout of the selected specimens on each panel with the indication of the detected flaws.



(a) Panel A3D3 Specimen Layout

(b) Panel A3D1 Specimen Layout



(C) Panel A3D4_B

Figure 4.6.7 Specimen Layout for Boeing Panels

4.6.3 Test Matrix Identification

As discussed before, many interested observations have been found to identify the effects of mechanical properties. The observations are:

- Radius Variation
- Specimen Width Variation
- Mis-Centered Effect (Misalignment Effect)
- Minimum Steering Radius Effect
- Curing Effect
- Tow Geometric Effect
- Tow Buckling Effect
- The Effects of Known Defects- Gap, Overlap, Drop, Twist, Missing, Loose, Splice, etc.

The first four topics among the observations are selected to be investigated in this report through the mechanical testing with the available panels. On the other hand, the investigation of the other effects remains for future research because of the lacking of manufacturing capability at current time. The remaining tests require a wide variation of specimens and detailed information of as-placed layers. While accounting for the availability and feasibility of testing material, the test specimens are obtained and can be seen in Table 4.6.1. The Boeing panels are prepared mainly for comparison with the previous data. The unidirectional steered Northrop Grumman panels are used for the investigation of the effects.

Table 4.6.1 Available Test Specimens for Three Boeing Panels and Six NG Panels

Manufacturer	Panel Identification	Specimen Size (cm)	Specimen Identification
Boeing (Alliant)	A3D4	1.27 x 8.08	A3D4_0_B_1_LCS_0_1 ~ 20
	A3D4	3.81 x 13.97	A3D4_0_B_3_LCS_0_1 ~ 7
	A3D4	-	A3D4_0_B_0_RC_1 ~ 2
	A3D4	-	A3D4_0_B_0_CS_1 ~ 2
	A3D4	-	A3D4_0_B_0_FCS_1 ~ 3
	A3D1	1.27 x 8.08	A3D1_0_42.5_1_LCS_1 ~ 10
	A3D1	1.27 x 8.08	A3D1_0_48.7_1_LCS_1 ~ 2
	A3D1	3.81 x 13.97	A3D1_0_48.7_3_LCS_1
	A3D3	1.27 x 8.08	A3D3_0_40.0_1_LCS_1 ~ 10
	A3D3	1.27 x 8.08	A3D3_0_47.1_1_LCS_1 ~ 2
	A3D3	3.81 x 13.97	A3D3_0_47.1_3_LCS_1
	A3D3	1.27 x 8.08	A3D3_0_49.2_1_LCS_1 ~ 2
	A3D3	3.81 x 13.97	A3D3_0_49.2_3_LCS_1
Northrop- Grumman (NG)	N3E4_1	2.54 x 13.97	N3E4_1_23_2_LCS_0_1 ~ 5
	N3E4_1	2.54 x 13.97	N3E4_1_33_2_LCS_0_1 ~ 5
	N3E4_1	2.54 x 13.97	N3E4_1_43_2_LCS_0_1 ~ 5
	N3E4_2	2.54 x 13.97	N3E4_2_23_2_LCS_10_1 ~ 5
	N3E5_1	3.81 x 13.97	N3E5_1_43_3_LCS_0_1 ~ 5
	N3E5_1	3.81 x 13.97	N3E5_1_33_3_LCS_0_1 ~ 5
	N3E5_1	3.81 x 13.97	N3E5_1_23_3_LCS_0_1 ~ 5
	N3E5_2	2.54 x 13.97	N3E5_2_43_2_LCS_0_1 ~ 5
	N3E5_2	1.27 x 13.97	N3E5_2_43_1_LCS_0_1 ~ 5
	N3E5_2	2.54 x 13.97	N3E5_2_33_2_LCS_0_1 ~ 5
	N3E5_2	1.27 x 13.97	N3E5_2_33_1_LCS_0_1 ~ 5
	N3E5_2	2.54 x 13.97	N3E5_2_23_2_LCS_0_1 ~ 5
	N3E5_2	1.27 x 13.97	N3E5_2_23_1_LCS_0_1 ~ 5
	N3E6_1	2.54 x 13.97	N3E6_1_43_2_LCS_5_1 ~ 5
	N3E6_1	2.54 x 13.97	N3E6_1_43_2_LCS_10_1 ~ 5
	N3E6_1	2.54 x 13.97	N3E6_1_33_2_LCS_5_1 ~ 5
	N3E6_1	2.54 x 13.97	N3E6_1_33_2_LCS_10_1 ~ 5
	N3E6_1	2.54 x 13.97	N3E6_1_23_2_LCS_5_1 ~ 5
	N3E6_2	2.54 x 13.97	N3E6_2_43_2_LCS_5_1 ~ 5
	N3E6_2	2.54 x 13.97	N3E6_2_33_2_LCS_5_1 ~ 5
	N3E6_2	2.54 x 13.97	N3E6_2_23_2_LCS_5_1 ~ 5

Most of specimens will be utilized for multi-effect investigation. For example, the test results of N3E6_2_43_2_LCS_5_XX can be used for the investigation of 109cm radius variation, 2.54 cm coupon width, and 5 degree of misalignment effect. A total of 134 specimens are prepared and the usage of the specimens can be seen in Table 4.6.2.

Table 4.6.2 Test Matrix for Mechanical Test

Specimen ID	Radius Variation (cm)	Width Variation (cm)	Mis-alignment (degree)	No. of Specimen
A3D4_0_B_1_LCS_0_11~15	---	1.27	0	5
A3D4_0_B_3_LCS_0_1~5	---	3.81	0	5
A3D1_0_42.5_1_LCS_0_6~10	108	3.81	0	5
A3D1_0_48.7_1_LCS_0_1~2	124	1.27	0	2
A3D1_0_48.7_3_LCS_0_1	124	3.81	0	1
A3D3_0_40.0_1_LCS_0_6~10	102	1.27	0	5
A3D3_0_47.1_1_LCS_0_1~2	120	1.27	0	2
A3D3_0_47.1_3_LCS_0_1	120	3.81	0	1
A3D3_0_49.2_1_LCS_0_1~2	125	1.27	0	2
A3D3_0_49.2_3_LCS_0_1	125	3.81	0	1
N3E4_1_23_2_LCS_0_1~5	58	2.54	0	5
N3E4_1_33_2_LCS_0_1~5	84	2.54	0	5
N3E4_1_43_2_LCS_0_1~5	109	2.54	0	5
N3E4_2_23_2_LCS_10_1~5	58	2.54	10	5
N3E5_1_43_3_LCS_0_1~5	109	3.81	0	5
N3E5_1_33_3_LCS_0_1~5	84	3.81	0	5
N3E5_1_23_3_LCS_0_1~5	58	3.81	0	5
N3E5_2_43_2_LCS_0_1~5	109	2.54	0	5
N3E5_2_43_1_LCS_0_1~5	109	1.27	0	5
N3E5_2_33_2_LCS_0_1~5	84	2.54	0	5
N3E5_2_33_1_LCS_0_1~5	84	1.27	0	5
N3E5_2_23_2_LCS_0_1~5	58	2.54	0	5
N3E5_2_23_1_LCS_0_1~5	58	1.27	0	5
N3E6_1_43_2_LCS_5_1~5	109	2.54	5	5
N3E6_1_43_2_LCS_10_1~5	109	2.54	10	5
N3E6_1_33_2_LCS_5_1~5	84	2.54	5	5
N3E6_1_33_2_LCS_10_1~5	84	2.54	10	5
N3E6_1_23_2_LCS_5_1~5	58	2.54	5	5
N3E6_2_43_2_LCS_5_1~5	109	2.54	5	5
N3E6_2_33_2_LCS_5_1~5	84	2.54	5	5
N3E6_2_23_2_LCS_5_1~5	58	2.54	5	5
Total				134

4.6.4 Specimen Preparation

All specimens are prepared based on ASTM D-695 [51] and ASTM D-3410 standard test methods [52]. All unidirectional composite coupons for ASTM D-3410 procedure B compression test method are prepared as tabbed with back-to-back strain gages. The back-to-back strain gages provide a correction for any bending of the specimen and detection of Euler buckling. An appropriate gage length for ASTM D-3410 compression test method was determined to be 1.32 ~ 1.42 cm by using Eq. 4.6.3 to compensate for beam-column effects produced by bending moments induced by specimen and fixture tolerances where a conservative assumption of pinned-end conditions for column buckling was made.

$$l_g \leq 0.9069h \sqrt{\left(\frac{E_c}{F_{cu}}\right) \left(1 - \frac{1.2F_{cu}}{G_{xy}}\right)} \quad \text{Eq. 4.6.3}$$

where:

E_c = longitudinal modulus of elasticity, MPa

F_{cu} = ultimate compressive strength, MPa

G_{xz} = through-thickness shear modulus, MPa

h = coupon thickness, mm

l_g = length of gage section, MPa

ASTM D-695 test methods were selected to test the Boeing panels. Each coupon size is 8.08 cm x 1.27 cm. Complete testing requires two specimens, one with tabs and a gage length of 0.51 cm for strength properties and another untabbed with back-to-back strain gages system for modulus measurement. In strain gage selection, the difference of test coupon width is considered. Two different strain gages are utilized in the test, M-M CEA-06-250UW-120 Strain Gage, 120.0±0.5% in Resistance w/ 2.065±0.5% gage factor for 1.27cm and 2.54cm coupon width specimens and M-M CEA-06-250UV-120 Strain Gage, 120.0±0.3% in Resistance w/ 2.110±0.5% gage factor for 3.81cm coupon width specimens. Figure 4.6.9 shows the specimens with back-to-back strain gages, with tab and without tab.

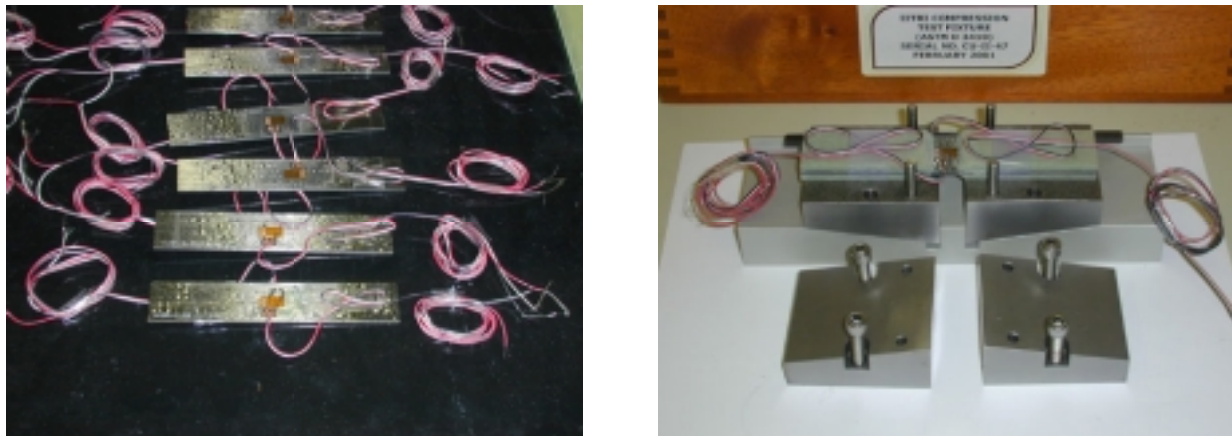


Figure 4.6.9 Coupons with Strain Gage and Tab

4.6.4.1 Tabbing Material Manufacturing

The tabbing material is composed of a 50/50 mix (by volume) of woven fiberglass and an epoxy resin. The epoxy resin is composed of resin and hardener in 1:1 mixture by weight and volume. DPL 962 Epoxy Resin and V40 Curing Agent are used as the resin and the hardener. The gel time of the mixture is approximately 2 hours. To determine the amount of resin needed the length, width and thickness of the woven fiberglass was measured to find the volume of resin. The density of the resin and the mixing ratio were then used to calculate the mass of resin and hardener required. The two parts were then thoroughly mixed and an equal amount of each was applied between each layer of fiberglass. This method of calculating the amount of resin was used in all three tabbing samples. The only difference was that for the second and especially the third tabbing sample, additional resin was added to account for resin sticking to the container in which it was mixed.

After the tabbing samples were constructed, photographs were taken through a microscope and they were analyzed for the area ratio of the flaws that the sample contained. The area ratio, or percentage of area that is part of a flaw, results are shown in Table 4.6.3.

Table 4.6.3 Area Ratio for Tabbing Material Samples

	Area Ratio_Tab 1 (%)	Area Ratio_Tab 2 (%)	Area Ratio_Tab 3 (%)
Point 1	10.9	5.77	2.80
Point 2	7.59	2.64	1.26
Point 3	16.15	1.51	1.29
Point 4	11.11	1.23	1.28
Av._AR (%)	11.44	2.79	1.66

Some variation in tabbing material is acceptable, due to the fact that the tab stiffness is an order of magnitude less than that in the coupons. As such, the manufacturing standard for tabbing material was assumed to be 5 %.

Tab 1: 8 Layers, 13.64 kg/cm² pressure, 1 hour curing w/ 120° F

Tab 2: 16 Layers, 17.05 kg/cm² pressure, 1 hour curing w/ 120° F +15 min. temperature ramping time and apply compaction roller on each layer, use a flange (12.7cm x 12.7cm)

Tab 3: 16 Layers, 13.64 kg/cm² pressure, 2 hour curing w/ 120° F +15 min. temperature ramping time and apply compaction roller on each layer, use a flange (12.7cm x 12.7cm), and minimize fiber steering.

As a result, the third tabbing method provides the most reasonable area ratio in tab laminate and has been utilized to manufacture all tabs for the mechanical testing.

4.6.5 Test Procedures

In this section, the detail compression test procedures will be discussed such as machine and strain gage calibration, specimen geometric data, data acquisition system, and step-by-step procedures.

4.6.5.1 Test machine and gage calibration

Calibration of the testing machine is very important in order to obtain accurate test data. The MTS-Upgraded Instron mechanical testing machine utilized in this project has a capability of automatic electrical load cell calibration as well as a strain gage channel. The problem with this machine was that only one channel of strain gage was available, so that the back-to-back strain gage system could not be applicable for simultaneous data recording. As discussed, the back-to-back strain gages was a key detection system to identify bending and Euler buckling. Using an external data acquisition system, which can have multi-channel gage monitoring, solved this problem. A remaining problem was how to calibrate the sensors. Manual calibrations for the load cell and strain gages were selected by using well-known alloys of aluminum, brass, and stainless steel.

4.6.5.2 Load cell calibration

Load cell calibration was done by two different methods, manual Calibration with known weights and with known materials like Brass and Stainless Steel. Calibration with known weights provided an initial slope, but it was not sensitive enough to construct a completed plot. Calibration with known materials provided another points of the calibration curve such as yield strength. Calibration factor was found to be 0.9868 after comparing with the theoretical yield strength of the materials and the actual test results.

4.6.5.3 Strain gage channel calibration

Aluminum 6061-T6 was used to identify a calibration factor for the strain gages. As shown in Figure 4.6.10, the average modulus was found to be 15.46 and 17.20 for channel 1 and channel 2. These values were compared with the theoretical value and obtained the correctional factors, 0.8789 and 0.8778 for channel 1 and channel 2 respectively.

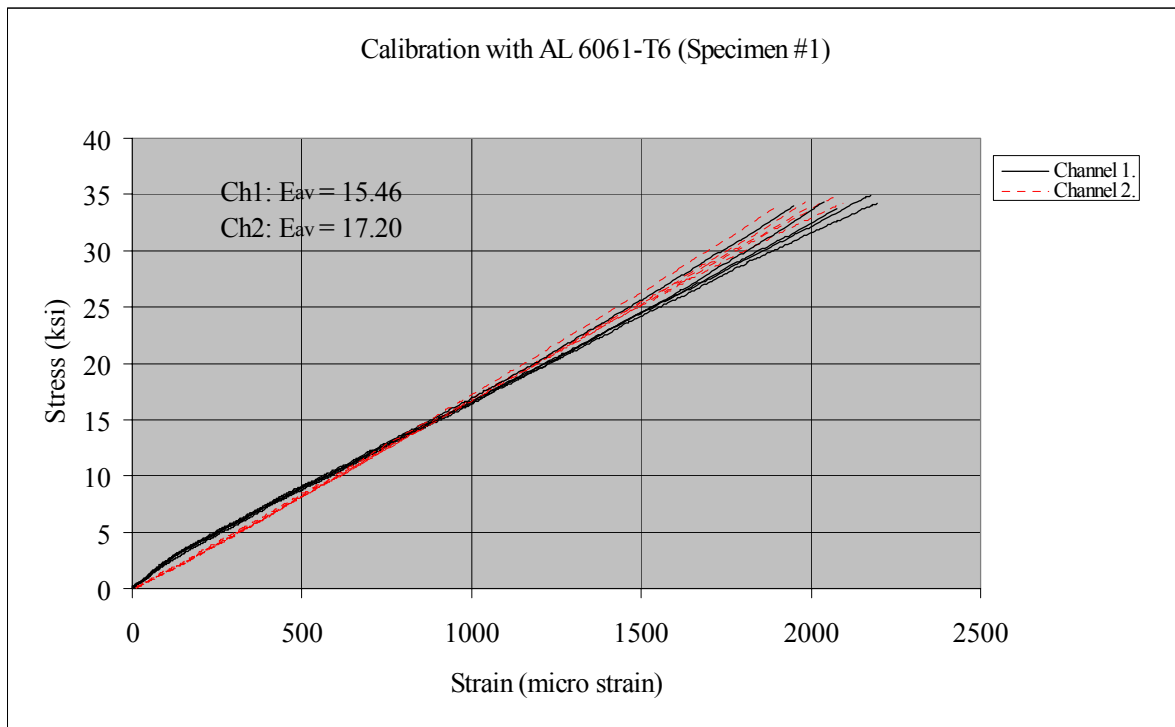


Figure 4.6.10 Mechanical Test for Calibration using AL 6061-T6

4.6.5.4 Specimen geometric data inspection

The geometric information of each specimen was recorded as references for the future analysis of compression test. The information includes the geometric data such as gage length, thickness on tab sections and gage sections, overall length, and specimen width.

4.6.5.5 Data acquisition system

Due to lacking of multi-data recording capability of the MTS-Upgraded Instron Mechanical Testing Machine, a data acquisition system was considered for capturing two strain gages and load cell data simultaneously. The DASyLab data acquisition system with WBK-16 module (especially designed for strain gages) was selected. The system was able to extend by adding more modules. Each module was able to handle up to 8 different channels. One channel for the load cell and two channels for the back-to-back strain gages were synchronized in time. Sampling rate of data acquisition was selected to be 10 Mhz. Excitation voltage was 5.0 VCD and input range was -50mV to $+50\text{mV}$. The data was filtered with low pass operation at 100 Hz. Block average operation used average function of 10 blocks. Wheatstone Full-bridge configuration for the load cell and three-wire Quarter-bridge circuit for strain gages were used. Figure 4.6.11 shows a schematic of data acquisition system with MTS-upgraded Instron compression test equipment set-up.

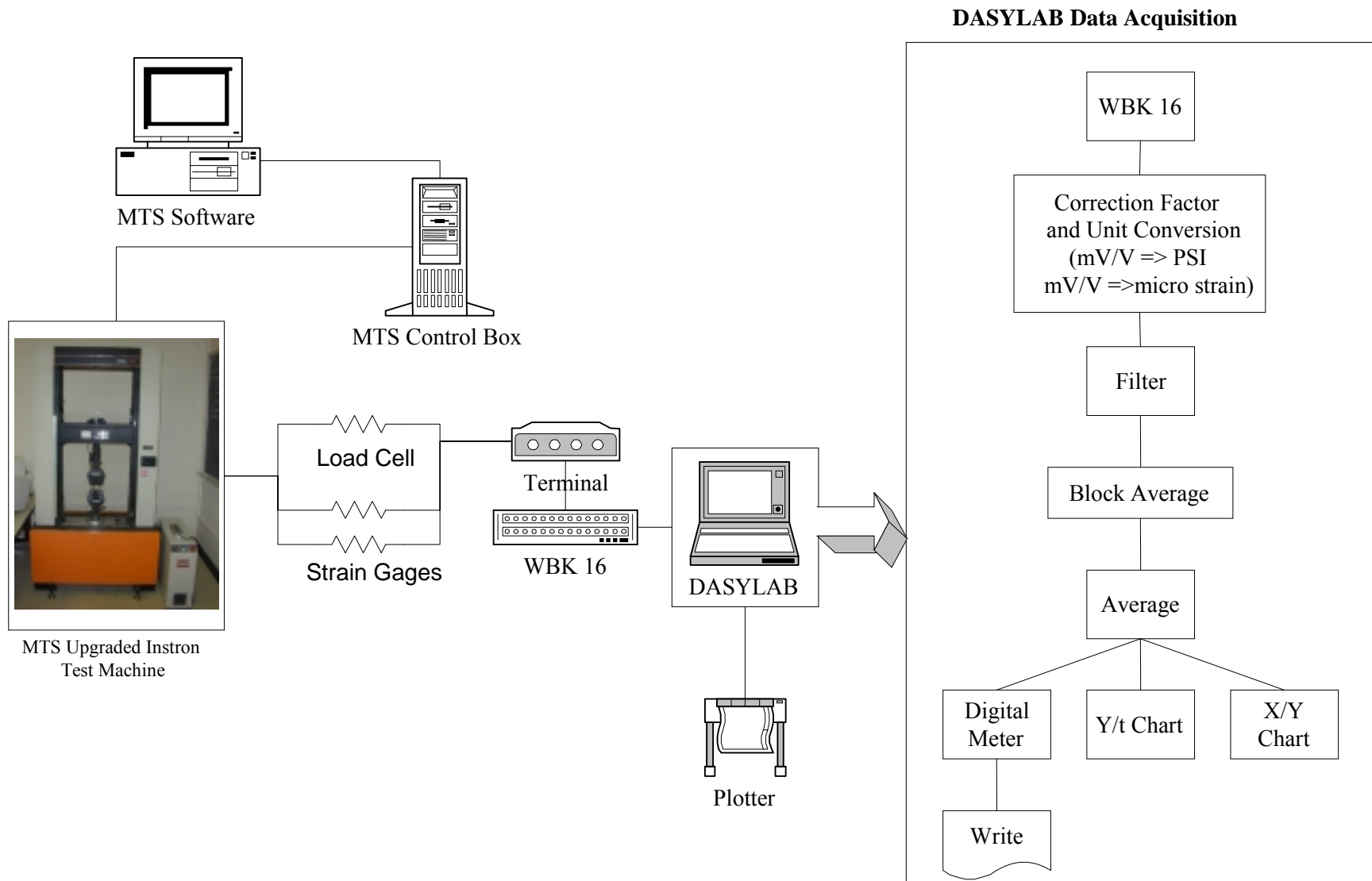


Figure 4.6.11 Schematic of Data Acquisition System

4.6.6 Results and Analysis

Mechanical compression tests were performed to quantify the mechanical properties of steered fiber composites. As documented before, the original mechanical test plan has setup with two different steered panels, family panels from Boeing and unidirectional panels from Northrop Grumman. Test specimens from both panels were prepared for the compression test with the MTS upgraded test machine at KU. Based on the specification of the MTS machine, the loading capacity supposed to be 9,091kg, but in reality the machine was able to handle up to 6,818kg only. Due to the limitation of the machine loading capacity, it was limited to test the specimens from the Boeing company. The untested coupons remain for further investigation with a higher capacity loading machine. The mechanical compression test in this report will be focused on the unidirectional steered fiber composites. The detailed mechanical tests will be proceeded in the following feature effect examinations:

- Radius variation effect test
- Width variation effect test
- Misalignment effect test
- Minimum steering radius test

4.6.6.1 Data Post Processing

All mechanical compression test data were obtained based on the proposed test matrix with the back-to-back strain gage system. The majority of recorded data shows bending and buckling effects due to the imperfect specimen geometry and panel thickness variation. These effects can be seen clearly in Fig.A of Figure 4.6.12. The right hand side curve indicates tensional bending effect and the left-hand side curve shows the effect of compression bending. Since the compression bending under compression loading is dominant in specimen failure, failure stress has been corrected based on the following relations(Eq. 4.6.4);

$$E\epsilon_1 \text{)Compression Bending} = \sigma_0 \text{)Measured Stress} - \left| \frac{Mc}{I} \right| \text{ Bending Stress} \quad \text{Eq. 4.6.4}$$

$$a\sigma = E\varepsilon_1$$

$$E = 2\sigma_0/(\varepsilon_1 + \varepsilon_2)$$

Eq. 4.6.4.b

Eq. 4.6.4.

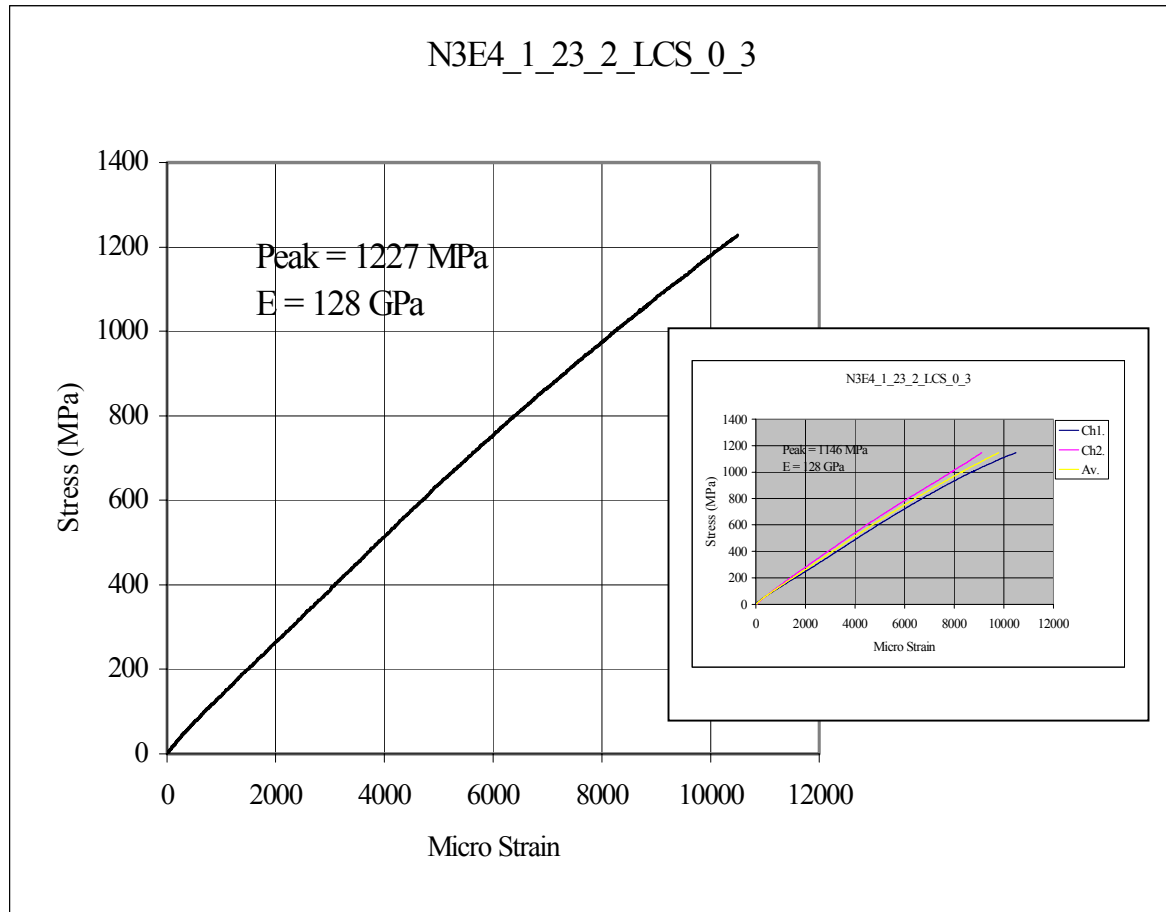


Figure 4.6.12. Corrected Stress-Strain Curve of N3E4_1_23_2_LCS_0_3 [5]

After all test data have been corrected, it is possible to construct a database for mechanical properties of unidirectional steered composites. In order to obtain a meaningful database, the data were filtered with the following criteria:

- Ignore data from specimens with de-bonding strain gage in early loading stage
- Ignore data from specimen with de-bonding tab
- Ignore data from specimen with unusual breaking pattern and location (i.e. fracture occurs under tab)
- Check data with Tow Buckling Rate of the specimen and decide the acceptance of the data
- Ignore data that makes standard deviation 10% higher than average of failure stress

4.6.6.2 Results and Analysis of Experimental Test Data

As mentioned before, these experiments focus on the four feature effects. In this report, two feature effects will be considered simultaneously like specimen width and steering radius variation and misalignment and steering radius variation. Misalignment and specimen width variation will not be addressed in this paper due to insufficient experimental data. The effect of minimum steering radius will be discussed by comparing overall data. Figure 4.6.13 and 4.6.14 show the failure stress and Young's modulus of ten ply unidirectional steered composite under uniaxial compression load. Vertical bars on each data points indicate data scatter band of \pm one standard deviation. Overall results are consistent with prediction and are discussed below.

4.6.6.2.1 Specimen width and steering radius variation

Graphs a) and c) in Figure 4.6.13 show the failure stress response according to the variation of steering radius and specimen width. As a result, it is observed that there is no significant effect due to the radius variation. A minor positive slope shown in graph c) tells that the larger steering radius has the better failure characteristic, as expected, but the effect is almost negligible. On the other hand, there is a quite interesting effect in specimen width variation. Specimen width from 1.27cm to 2.54cm do not show any variation in failure stress. The 3.81cm of width specimens have about 25% drop in failure stress. Further research is needed to identify this phenomenon due to insufficient experimental data. More than half of the required specimens were not broken due to the limit of loading capability of the test machine. This implies that the accepted data points might be the lower boundary of a scatter band and are not reliable as a completed data set. The failure stresses for 1.27cm and 2.54cm width specimens were found to be 1.31 to 1.52 Gpa, respectively. Graphs b) and d) in Figure 4.6.13 show the Young's modulus of steered composites. There is not much variations, however a slight increment of Young's modulus was observed due to the increment of specimen width. Young's modulus for the 84cm radius and 1.27cm width coupons show about 3% lower Young's modulus than that of the other specimens. Overall data for the steered fiber composites shows about 13% Young's modulus drop compared to the Young's modulus of non-steered unidirectional carbon fiber materials, 155GPa. This is expected and illustrates the nature of unidirectional test methods on curvilinear coupons. This does not indicate an inherent reduction in material stiffness.

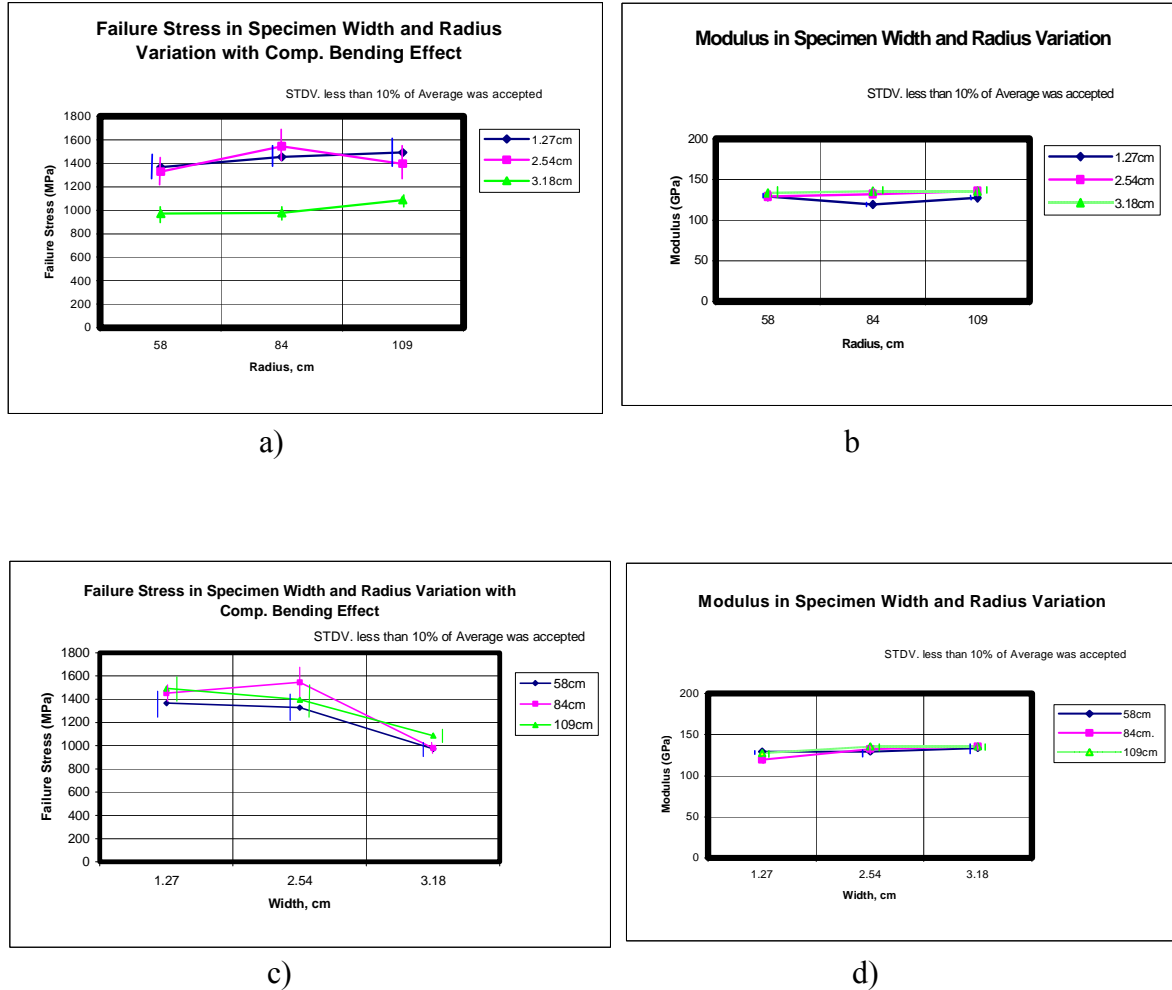


Figure 4.6.13. Experimental Data of Failure Stress and Modulus in Width and Radius Variation

4.6.6.2.2 Misalignment And Steering Radius Variation

Figure 4.6.14 shows the effect of fiber misalignment and specimen width variation in failure stress and Young's modulus of the steered fiber composites. It is obvious that the coupon on fiber misalignment is the most significant effect in compression mechanical properties of steered composites. Graphs a) and c) indicate that initial fiber misalignment produce a large drop in failure stress regardless of the different steering radius. The fiber misalignment of 5° and 10° produces about 45% and 55% of reduction compared with the failure stress of 0° misalignment. The steering radius effects are negligible in the failure stress as shown in the width and radius variation investigation. The modulus variation is clear with the variation of misalignment, with 35%-40% of Young's modulus reduction observed at these misalignment angles. Graphs b) and d) show this effect in graphical format.

Test data from Boeing and the United States Naval Academy (USNA) has been reviewed in the year 2000 summary annual report [4]. The most interesting data from these previous tests was the axial compression response of steered fiber coupons. The data shows the strength is steadily decreasing from the baseline to the 58cm, 84 cm, and 109cm samples. Since the larger radii samples exhibit less steering, the strength should be higher, and thus the trend is counter-intuitive. As documented in the previous report, the Boeing Company likely allows two degrees of tolerance in fiber angle orientation in production part, and likely one degree of tolerance in these steering coupons. Experimental data for coupon misalignment demonstrate that their coupon variation was likely due to misalignment. Most importantly, off-axis or misaligned coupons still demonstrate no significant variation in compression mechanical response with fiber steering radius.

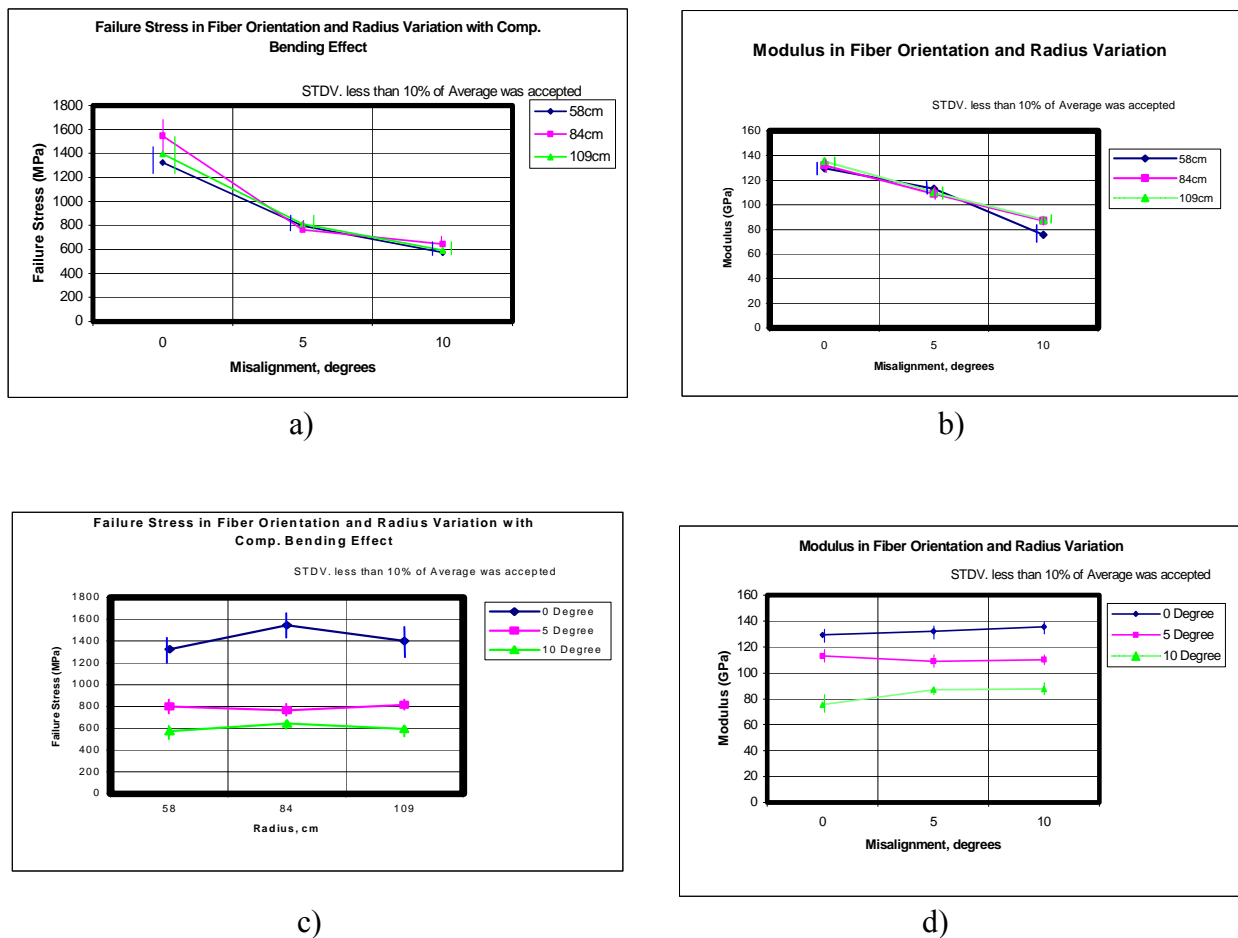


Figure 4.6.14. Experimental Data of Failure Stress and Modulus in Fiber Misalignment and Radius Variation

4.6.6.2.3 Minimum steering radius investigation

As discussed in the previous report [1], current industries are accepting 46cm radii as a minimum steering radius without mechanical test. In this report, the mechanical test for minimum steering radius investigation was done up to 52cm because of available test samples. Experiments were performed in the range of 58cm, 84cm and 109cm respectively. Figure 4.6.13 and 4.6.14 show the failure stresses with variation of radius. The data indicate that there are no significant stress changes between the different radii. This matter indicates 58cm steering radius is acceptable to be a minimum steering radius, even though previously documented tow buckling rates indicate clear trends along the radius changes [48]. The investigation must be continued to find the global minimum steering radius with mechanical testing.

4.6.7 Theoretical Model and Analysis

It is very important in a technical project that the output of theoretical models and analyses agree with practical results. If the results are in conflict with one other, it has to be explainable. The fiber axis in steered materials is not linear, and thus the applied compression load is not aligned with the axis of test specimen. One of the most important assumptions in conventional compression tests is that the applied compression load is aligned with the fiber axis in test materials. This fiber misalignment directly violates that assumption and will bring significantly different results in compression test. These problems in modeling can be solved by using object-oriented design and analysis tools; SCADS[53] developed in this project as one of the main tasks. The design and analysis tools provide the capability of self-positioning tow representations, simulating the manufactured part, using specified fiber angle control methods. The innovative modeling includes detailed information of fiber architecture such as exact location of known defects and specific local geometric fiber curvatures. The model will be analyzed by using a pre-existing finite element tool, MSC/PATRAN and MSC/NASTRAN, and provides optimal design solutions.

In this project, the detail modeling of steered fiber panels was done based on information obtained from the Northrop panels. The information includes tow width, number of tows in a course, and steering radius. For improved modeling, specimens for the theoretical model were selected at the same location on the panels where the mechanical test specimens were obtained.

The coupons were created with the SCADS software system as follows. The main panel surface and boundary geometry was created with AeroCADD, exported as an IGES file and read into SCADS. Individual plies were defined with the same properties as the Northrop panels. The tow width was defined as 0.318 cm, and the layer thickness was defined as 0.0264cm, making a total panel thickness of 0.185 cm with seven plies.

The coupon locations were defined in the original AeroCADD file. The coupons are 2.54cm by 13.97 cm and were centered on the corresponding radius point (i.e 58cm, 84cm and 109cm). The misaligned coupons were created by taking the 13.97cm length line and rotating it about one end by the specified angle. The 2.54cm width line was also rotated, then the pieces

were put together and the coupon re-centered at the radius point. The four corner points for each coupon were recorded and input into SCADS so that a MSC/NASTRAN bulk data (.bdf) file could be extracted. The elements were defined as square shells with an edge distance of 0.25 cm. The bulk data file was then imported into MSC/PATRAN and boundary conditions and loads were applied with certain assumptions as follows:

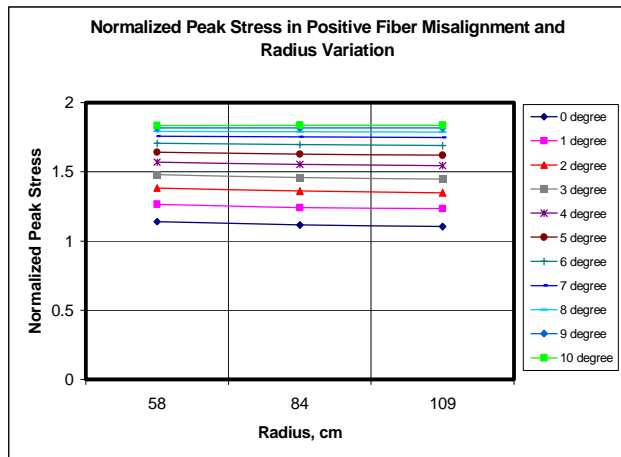
- Fixed-end conditions at the grips
- No slip problems on specimen grip
- No manufacturing defects other than the known defects.
- No misalignment on fiber architecture from theoretical alignment.

The test section length in this analysis was 1.27cm, the gage length used in destructive mechanical testing. The elements were with an edge distance of 0.127cm square. A constant displacement of 0.0064cm (corresponding to 5000 microstrain) was placed on one end of the test section.

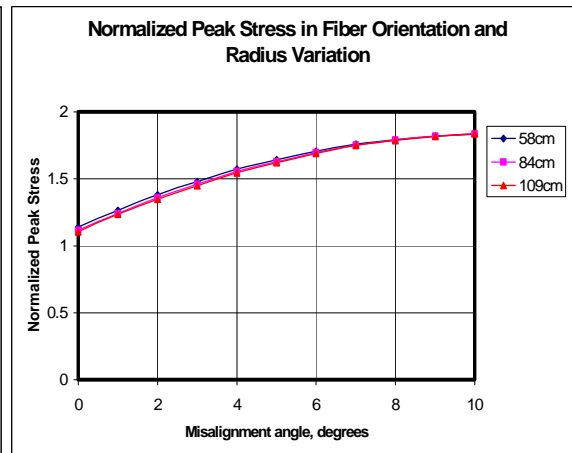
Graphs a) and b) in Figure 4.6.15 show the normalized peak stresses with steering radius and fiber misalignment variation. Nominal stress (non-steered) was found to be 776 Mpa and used in normalizing the peak stresses. Since the absolute magnitude of the stress is of less interest than the stress concentration caused by the effect of fiber steering, peak theoretical stress is normalized to this nominal applied stress. The graphs show the dominant feature effect is fiber misalignment. The misalignment of 5° and 10° bring about reduction of 47% and 67% compared with the effect of 0° misalignment. The radius variation effect is observed very minor (2%) in steered fiber composites. The result of this effect has been proved with the experimental result (3% variation).

In addition, negative misalignment effect is also investigated in the theoretical analysis and shown in c) in Figure 4.6.15. The fixed end boundary condition produces slightly different results in positive and negative misalignment. The test section method was used for negative misalignment with the only difference that the coupons were rotated right-end down instead of right-end up as in the previous two analyses.

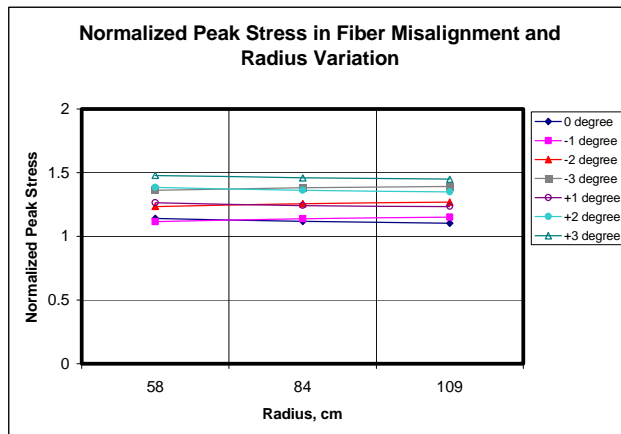
In the width variation study, the width of the test section was changed from 1.27cm to 3.18cm in increments of 0.64cm. The same element sizes, boundary conditions, and forced displacements were used for this as for the test section analysis. Graph d) in Figure 4.6.15 shows the effect in the 58cm radius case only. Since there was no predicted variation due to specimen width, the other radius case was omitted in this paper.



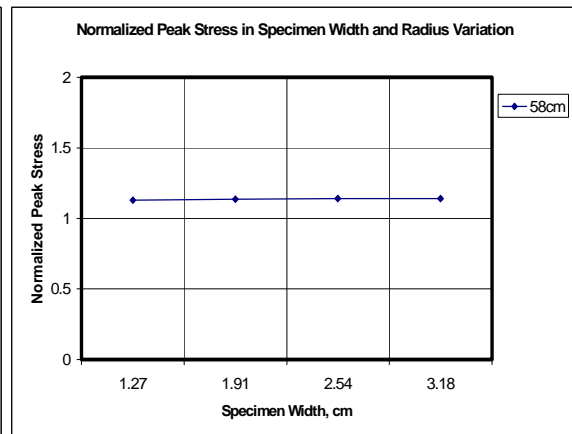
a)



b)



c)



d)

Figure 4.6.15 Theoretical Test Data of Normalized Peak Stress in Misalignment and Radius Variation

4.7.0. Conclusions And Recommendations

As a conclusion, analyzed results of the theoretical models are compared with the output of experimental compression tests. Both theoretical data and experimental data show the same trends as follows:

- The dominant feature effect in steered fiber composites is the sample misalignment, and initial misalignment brings significant changes in mechanical properties.
- The steering radius variation has little affect on compression properties (about 2-3 %).
- The specimen width variation is also found to be a minor effect.
- The minimum steering radius is proved 52cm or less of steering radius in this project.

Research activities outlined offer significant advances in approaches for quality control and mechanical properties for steered fiber composites. These observations have the potential to develop guidelines in steered fiber composite manufacturing to define part quality.

Mechanical testing addressed in this paper is performed with conventional methods that assume the fiber axis is coincident with the longitudinal axis of the coupon, but steered fiber architectural structure will also have transverse and in-plane shear components as well as significant free-edge effects. A new mechanical test standard should be established to account for these effects.

A limiting factor in this project was the availability of steered fiber panels. The expense of constructing steered fiber panels with existing fiber placement hardware limits the amount of testing that can be performed and the breadth of trade study parameters. A new low-cost fabrication method would enable more extensive testing to be performed.

Due to the limitation of test machine capacity, the ready-to-test Boeing coupons were in hold for further investigation. A new test machine is in place, and tests will commence in Fall 2004.

5.0 Effect of Common Tow Features on Compressive Properties of Unidirectional Composite

The technology of automated fiber placement has the potential to create cheaper, stronger, and lighter composite structures. One issue faced with fiber placement is the existence of gaps, overlaps, and twists within the composite laminate. Such flaws could have the possible effect of reducing the local stiffness and strength of the laminate. The impact of the flaws is dependent on the size, number, and location. Finite element analyses of a slight single flaw show a slight difference in the strength properties of laminates with the gap and overlap flaws, with the effect governed by the severity and extent of the flaw. Compressive mechanical testing on isolated flaw specimens representing unflawed, 100% gap, 50% gap, 50% overlap, and twist agrees with the Nastran analysis and shows that there is a negligible effect of the flaws in stiffness and the point of nonlinearity.

5.1 Introduction

Fiber placement is a process that combines the differential material payout capabilities of filament winding and the compaction and precision of automatic tape laying. In this process, thin strips of pre-impregnated fibers, called tows, are drawn under tension through a computer controlled dispensing head onto a tool geometry. Most industrial fiber placement machines have the capability to dispense multiple tows at varying rates to accommodate the tool geometry. By controlling individual tow dispensing rates the fiber orientation can be controlled with great precision. For example, when placing tow in a curved trajectory the tows at the inner radius are dispensed more slowly than the tows at the outer radius to allow for even payout of fibers around the curve [5.1,5.7].

Fiber placed composites are known to have several common flaws inherent to the lay-up process. This includes gaps, overlaps, and tow twists, as well as kinks and fiber buckles [5.1,5.7]. A gap or overlap can occur when the fiber placement machine mis-feeds or the wrong placement information is given by the user. Twists occur due to material flaws or improper installation of the materials. The effect of such local flaws on mechanical performance is not yet fully understood. To better understand the effects, these flaws are being investigated to see what their affect is on the initial stiffness, point of nonlinearity, and axial strength under uniaxial compression loading.

5.1.1 Feature types

There are common tow features that occur within fiber placement technology. These features, called flaws, are inherent to the process. The flaw includes gaps, overlaps, and tow twists, as well as kinks and fiber buckles [5.1,5.7]. A gap or overlap can occur when the fiber placement machine miss feeds or the wrong placement information is given by the user. Gaps and overlaps typically range from very small, less than 0.254mm (0.01 in), to a full tow width. Twists occur due to material flaws or improper installation of the materials. Twists occur because tows become twisted when feed through the fiber placement head. The effect of flaws

on mechanical performance is not yet fully understood [5.15]. To better understand such effects, these flaws are being investigated to determine their influence on the initial stiffness, point of nonlinearity, and axial strength.

The features addressed in this study are 100% tow width gaps, 50% tow width gaps and overlaps, and twists. Figure 5.1 through Figure 5.3 show examples of these features created with the fiber placement process.

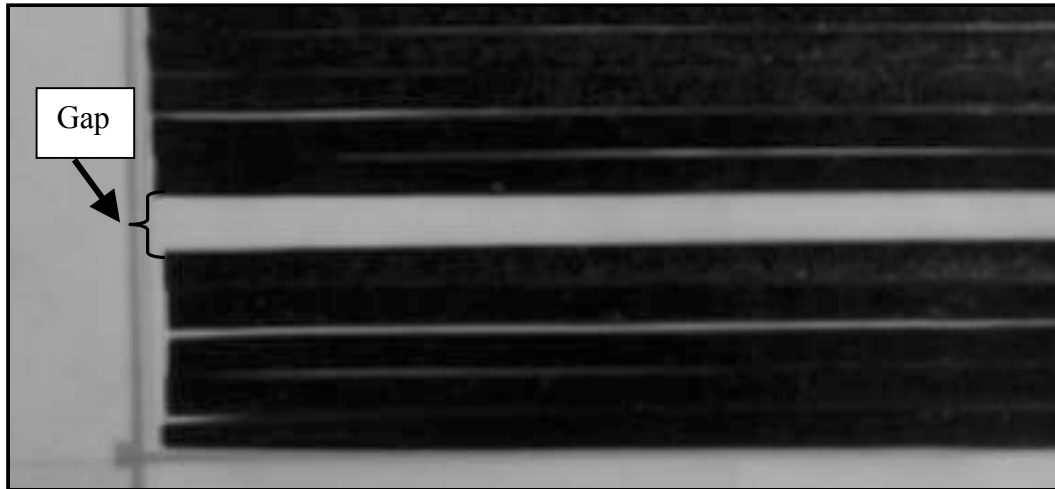


Figure 5.1 Gap Flaw Created by Fiber Placement

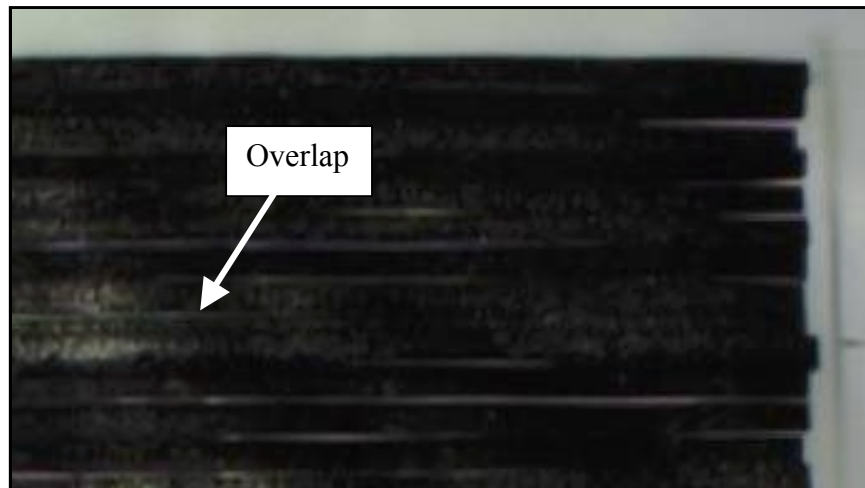


Figure 5.2 Overlap Flaw Created by Fiber Placement

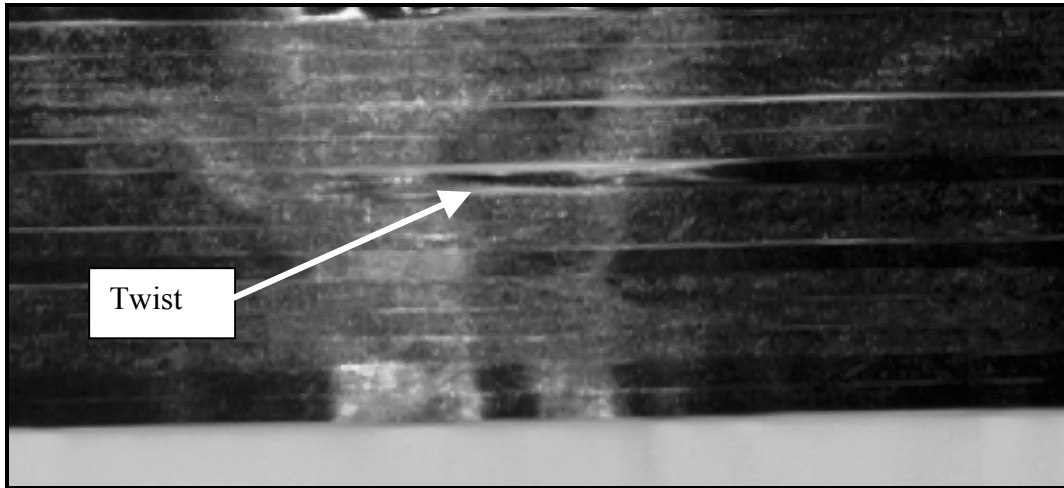


Figure 5.3 Twisted Tow Flaw Created by Fiber Placement

5.1.2 Literature Review

Fiber placement technology is a relatively new automated manufacturing process for composites. It combines the differential payout of filament winding with the compaction and cut/restart capabilities of automated tape laying. The main reasoning behind this technology was to create more control over the orientation of the fibers within a ply and to reduce the cost of manufacturing by reducing scrap. Fiber placement has the unique ability to steer tows, thin strips of fibers, to orient the fiber with the load path. This is accomplished by laying down multiple tows, up to thirty, side by side using a single placement head. The tows are fed from a creel into the placement head where they are compacted on the surface of the tool [5.7]. Each tow can be laid at a different rate depending on the radius of curvature of the path that the tow is following. This allows for tight cornering of the fibers and small turning radii, on the order of twenty inches [5.1,5.7]. This has a large advantage over tape laying machines that can only lay small turn radii of about twenty feet without buckling or kinking the tape at the inner radius. Other advantages include cost savings. Fiber placement typically produces anywhere from 2% – 15% scrap. Compared to conventional hand lay-up, that produces 50% - 100% scrap, the advantages become more clear [5.1].

Composite materials have been known for having specific architectural flaws, or features, that could affect mechanical properties. Tow gaps and overlaps and buckled tow features have been characterized since the start of composite structures. It is practically a given in hand-lay-up due to human error and complex part geometries. With automated lay-up processes, such as tape laying and fiber placement machines these flaws still exist, but are less noticeable. Automated lay-up has reduced the number of these flaws, especially when compared to hand lay-up, but they have not been eliminated. [5.7,5.15] Fiber placement has been shown to produce tow gaps and overlaps, twisted tows, and buckled tows. The gaps and overlaps are generally, but not exclusively, from the process of adding and dropping tows [5.6,5.7]. Tow twists and tow buckles can occur during the lay-up process. The twist typically occurs when a tow is fed upside down into the placement head and is transferred onto the part. Buckles typically occur when a tow is placed at a turning radius that is too sharp for the width of tow to handle.

Since there is a change in fiber volume at the flaw location it is reasonable to assume that there will be a reduction in strength. Sawicki and Minguet found strength reductions of 5% to 27% with a 0.003 inch wide gap or overlap. Their tests included multiple directional laminate specimens with and without holes. They determined that the cause of the failures was due to out-of-plane waviness. Their finite element analysis shows that failure was driven by interactions of in-plane compression and interlaminar shear stresses in the wavy zero degree plies [5.15].

Gaps and overlaps create out-of-plane waviness in the plies above and below the flaw. Therefore it is important to understand the effects that wavy layers have on the performance of composite structures. There are really two ways to approach the wavy layer problem. The first is to use 2-D woven fabrics that produce waviness because of the undulation from the weave itself. The second approach is to use prepreg tapes and induce waviness by some intentional means.

Fabrics have inherent layer waviness that results from the weave pattern. This is illustrated in Figure 5.4. Because of the undulation from the weave and the stacking of weaves, there exists the possibility that two or more undulations can be stacked on top of each other. This is called nesting of waves. If it is believed that one wavy layer can reduce the properties of the composite then it stands to reason that multiple waviness and nested waviness would be even worse. Breiling and Verhulst performed compression testing on three different nesting scenarios: stacked, split span, and diagonal nesting. The different scenarios were compared to a randomized nesting of the waviness. Breiling found that there was a reduction in strength of 7.7% to 8.0%, 9.1% to 10.9%, and 11.6% for the stacked, split span, and diagonal nesting specimens, respectively [5.16]. Verhulst's research differed from Breiling's because he used two different weave patterns where Breiling used the same weave pattern but two different test methods. Verhulst found that there was a reduction in strength of 26.3% and 26.6%, 12.8% and 30.1%, and 11.6% and 39.9 for stacked, split span, and diagonal nesting specimens and 6K and 3K weave patterns, respectively [5.17].

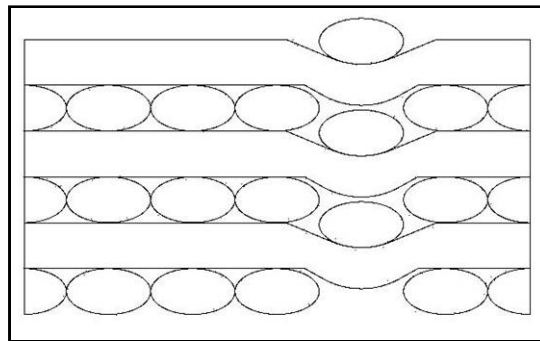


Figure 5.4 Layer Waviness Example of 2-D Woven Laminates

Composite structures made from tape and tow materials are susceptible to two kinds of fiber waviness: in-plane and out-of-plane. In-plane fiber waviness is generally found at the surface of the composite and typically does not exceed a few layers thick [5.9]. Out-of-plane

waviness on the other hand is found within the composite and can span many layers. Out-of-plane waviness is generally caused by flaws such as gaps and overlaps.

In-plane waviness is generally characterized as a sinusoidal wave function with a wavelength, amplitude and frequency. Since the strength of the fiber is in the longitudinal direction it should be clear that there will be a reduction in the strength of the composite due to the wavy fibers. Highsmith proposes that under compression significant in-plane shear strain occurs resulting in local failure of the matrix. Once the matrix has failed the fibers have no transverse support and they buckle. Highsmith developed a simple way to predict the strain to failure for composites with in-plane fiber waviness [5.18]. Moon discusses the effect of part length on the process induced fiber waviness in composite laminates. Moon also simplified the waviness of the fibers as a sine wave. Moon found that for unidirectional composites part length had little effect on the length of the wavy regions of the composite. She also, noted that the wavy region is localized on the surface and in the center of the composite. The largest impact that the part length had was on the number and distribution of the wavy regions [5.9]. Moon also performed compression testing on specimens with in-plane wavy fibers to see the effect. She noted that the presence of even a small amount of waviness was comparable to the stress concentrations associated at the tab termination [5.19]. Hale found that in-plane waviness that is out-of-phase results in large interlaminar normal and shear strains. He concluded that the largest effect was due to amplitude, but local interactions among waves could have a significant contribution [5.20]. Hale also used Moiré interferometry to show that misalignments in fiber based composites create large free-edge interlaminar shear strains [5.21].

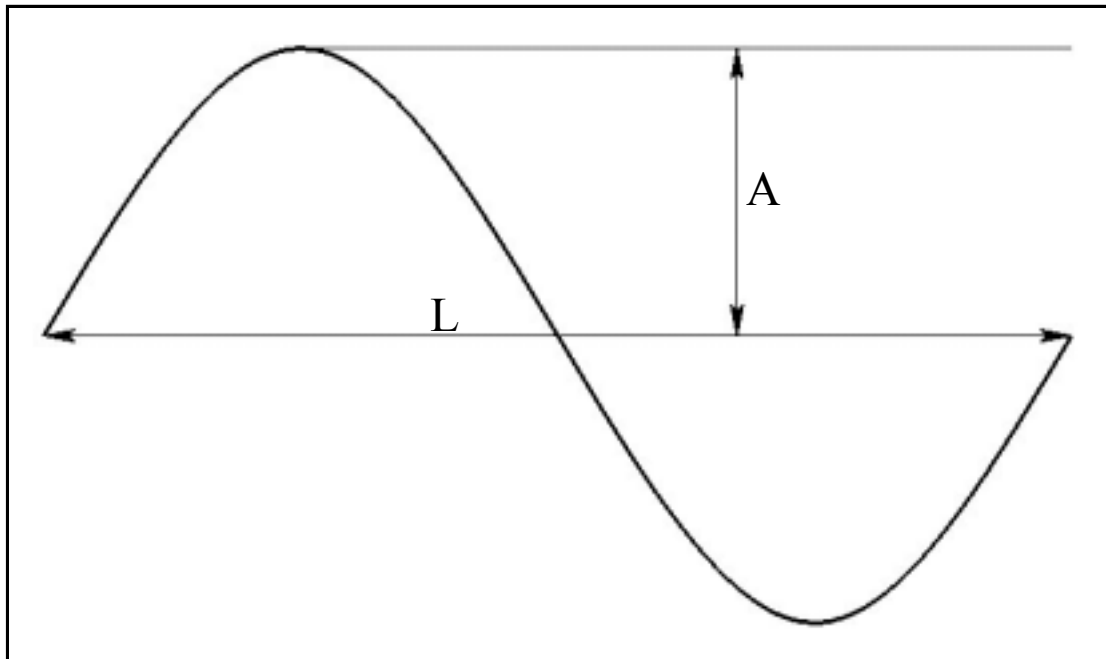


Figure 5.5 Idealized Representation of a Wavy Fiber

Like with 2-D weaves, composites made with tape and tow can have out-of-plane waviness. Both theoretical and experimental research has been performed on out-of-plane

waviness in composites. Raouf came up with an analytical approach to study the effects of layer waviness on interlaminar stresses. His work focused on composite plates that are simply supported and in cylindrical bending with layer waviness near one of the supports. He concluded that the presence of waviness may introduce significant increases in both interlaminar normal and shear stresses. He also noted that the maximum interlaminar stresses occur at a waviness ratio, A/L , of about ± 0.5 [5.11].

Experimental research performed by Hsiao looked at the effects of waviness on the compressive behavior of unidirectional and crossply composites. Uniform and graded waviness was fabricated into both unidirectional and crossply laminates, with the crossply laminates having wavy interior 0° plies. The unidirectional specimens with uniform waviness and a waviness ratio of 0.043 showed a significant reduction in modulus of 42% that closely agreed with predictions. The unidirectional specimens with graded waviness and a waviness ratio of 0.02 showed only a slight reduction in modulus of 6% but a significant reduction in compressive strength around 30%. This also agreed closely with predictions. The crossply specimens with a waviness ratio of 0.018 showed only a slight reduction in modulus, but a significant reduction in compressive strength of 15% to 20% [5.13].

Bradley researched the effects of two wave formations, single layer waviness and three nested layer waviness. For both single and nested wavy layers the compressive strength was reduced by 12.1% and 35.8%, respectively. However, the finite element predictions did not match the experimental strength results. This lead him to conclude that the finite element model was not a good estimator of compressive strength when predicting for wavy layers [5.5].

Adams performed research on static compression testing on wavy layered specimens. His specimens were a single central wavy layer. His testing shows a reduction in static strength of 1% to 36% even though the wavy layer only made up 20% of the total thickness. He also concluded that with increasing waviness ratio the compression strength reduction also increased [5.14]. Additional work by Adams suggests that there is a limit to the effect that wavy layer has on the compressive strength of laminates. He tested specimens with nested wavy layers and determined the reduction in compressive strength. He found that a steady 35% reduction in compressive strength occurs when 33% or more of the 0° plies contain wavy layers. Also, he concluded that when the percentage of wavy layers is greater than 33% the of the total 0° plies the compressive strength reduction is approximately equal to the percentage of wavy layers [5.12].

5.2 Experimental Approach

A total of ten panels were constructed, tabbed, sectioned, and compressively tested. This section describes the fabrication and testing process for two materials: fiber and matrix tape and fiber and matrix tow. This chapter will be a detailed explanation of the testing, as well as manufacturing procedures and inspection methods. Table 5.2.1 lists the material properties of the two types of prepreg tow and tape that are used. The thicknesses of the materials are 0.0052 in. and 0.0104 in. for tow and tape, respectively. The tow material has a width of 0.125 in. It should be noted that the material properties listed in Table 5.2.1 represent a close approximation of the materials used based on laboratory characterization and engineering judgment. Although fully characterized design properties may differ slightly, this observation is of little importance since the study compares the results of flawed and unflawed samples of the same material.

Table 5.2.1 Material Properties for Tape and Tow Prepreg

	IM7/3501-6 [Tape]	G30-S20/977-2 [Tow]
$E_{1,T}$ (psi)	22.5E6	22.8E6
$E_{1,C}$ (psi)	22E6	22.3E6
E_2 (psi)	1.8E6	1.3E6
G_{12} (psi)	0.85E6	0.79E6
ν_{12} (~)	0.3	0.3
ϵ_1 ($\mu\text{in/in}$)	11,000	12,800
ϵ_2 ($\mu\text{in/in}$)	-11,000	-11,100
γ_{12} ($\mu\text{in/in}$)	23,000	29,200
$F_{1,TU}$ (ksi)	300	323
$F_{1,CU}$ (ksi)	-240	-220
$F_{2,TU}$ (ksi)	9.0	9.05
$F_{2,CU}$ (ksi)	-30	-17
ρ (lb/in ³)	0.059	0.059
α_1 (in/in/°F)	0.4E-6	-0.3E-6
α_2 (in/in/°F)	0.2E-4	0.16E-4
Thickness (in.)	0.0104	0.0052
Tow Width (in.)	0.125	- -

5.2.1 Fabrication

Five different panels have been fabricated for each type of material used in this research. Each panel is fabricated in a 9 inch by 9 inch well and plunger in a heated platen press. Ten sample coupons are subsequently sectioned from each panel, as shown in Figure 5.2.1. The coupon width was determined from the nominal width of five tows of material G30-S20/977-2. The panels produced at the University of Kansas are cut and laid up by hand.

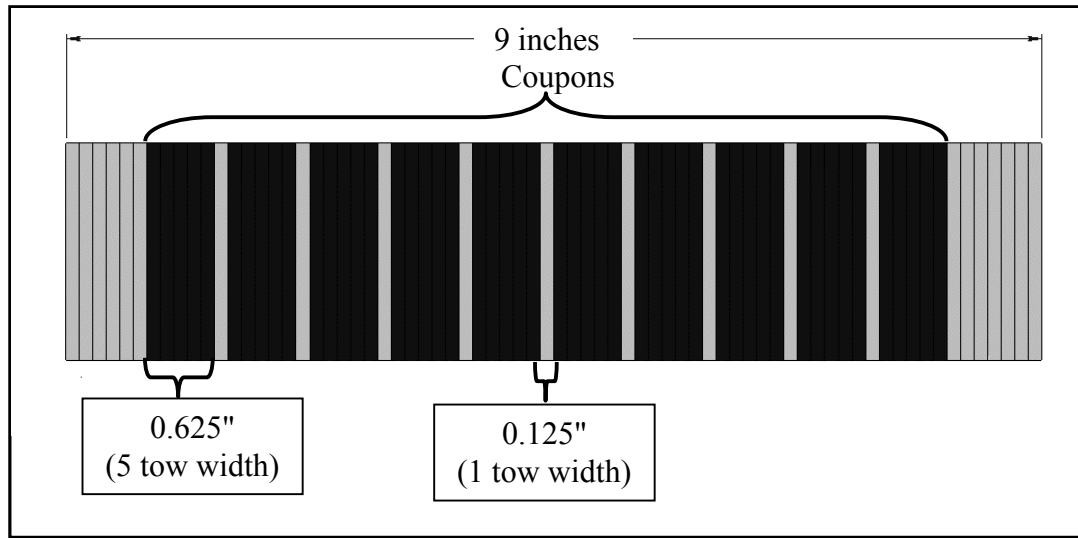


Figure 5.2.1 Coupon Lay-Out for Square 9 inch Panel

5.2.1.1 Buckling Calculations

Theoretical analyses of the proposed test specimens have been performed to verify the flaws will have an effect on the mechanical properties of the overall laminate. Before fabricating panels a buckling analysis was first performed. The dimensions of the specimen are taken from the ASTM D 3410 method B testing procedure. The buckling calculations are performed on test sections with dimensions of 0.75 in. gage length, 0.625 in. width and a ply thickness of 0.0052 in. and 0.0104 in. for tow and tape, respectively. The 0.625 in. width comes about from Five tow width of 0.125 in. By using five tows the flaws can be placed in the center of the specimen.

The buckling calculation is an iterative process. First a number of laminate plies must be chosen. Next, the D matrix must be calculated.

$$D_{ij} = \frac{1}{3} \sum_{k=1}^N (Q_{ij})_k (z_k^3 - z_{k-1}^3) \quad \text{Equation 5.1 [5.2]}$$

The next step is to calculate the buckling load that is associated with the laminate. This is done by using terms from the D matrix.

$$N_x = -\pi^2 \left[D_{11} \left(\frac{m}{a} \right)^2 + 2(D_{12} + 2D_{66}) \frac{1}{b^2} + D_{22} \left(\frac{a}{m} \right)^2 \frac{1}{b^4} \right] \quad \text{Equation 5.2 [5.3]}$$

Where:

N_x is the axial running load

D_{11} , D_{12} , D_{22} and D_{66} are terms from the D matrix.

m is the buckling mode taken to be one.

a and b are the length and width, respectively.

The axial running load is multiplied by the width of the test section to give the critical buckling load.

These calculations are repeated until a critical buckling load is determined to be sufficiently larger (in our case assumed 50% to be larger) than the critical compressive failure load. For the two types of material, tow and tape, the number of layers needed to produce the required thickness to resist buckling is 19 and 11, respectively.

Another equation for calculating the thickness for the specimens is given in the ASTM D 3410 testing standards. Equation 5.3 is not used for this research because the equation is too conservative with the thickness, predicting 0.15 in. and 0.17 in. plies for tow and tape, respectively. It is believed that the effect of a single flaw within the specimen would be washed out by a laminate that is too thick.

$$h \geq \frac{l_s}{0.9069 \sqrt{\left(1 - \frac{1.2F^{cu}}{G_{xz}}\right) \left(\frac{E^c}{F^{cu}}\right)}} \quad \text{Equation 5.3 [5.4]}$$

Where:

- E^c = Longitudinal Modulus of Elasticity, MPa [psi]
- F^{cu} = Ultimate Compressive Strength, MPa [psi]
- G_{xz} = Through-thickness Shear Modulus, MPa [psi]
- h = coupon Thickness, mm [in]
- l_g = length of Gage Section, mm [in]

5.2.1.2 Tape Fabrication Method

Tape prepreg is the simplest to use in this fabrication method. The first task is to cut 9 inch by 9 inch plies. A large spool of tape prepreg is taken out of storage and allowed to acclimate. Next the spool is rolled out and 9 inch by 9 inch squares are measured with each square lined up so that the fibers run parallel to two parallel sides. This ensures that the fibers all align with the principle fiber direction.

Next the well and plunger is readied for lay-up, shown in Figure 5.2.2. The first step is to coat the aluminum well and plunger with Release All Safelease 30, a release agent. After the release agent is applied a release film and a porous release cloth are cut to the size of the top and bottom plates of the well and plunger. The release films are next taped to the bottom well plate. The tape used is Flash Breaker I, made by Airtech Advanced Materials Group, which can withstand the temperatures of the curing process. When the porous release cloth is taped down the tape is placed in a pattern so that the panel's bottom surface and top edge are discernable, as shown in Figure 5.2.3.

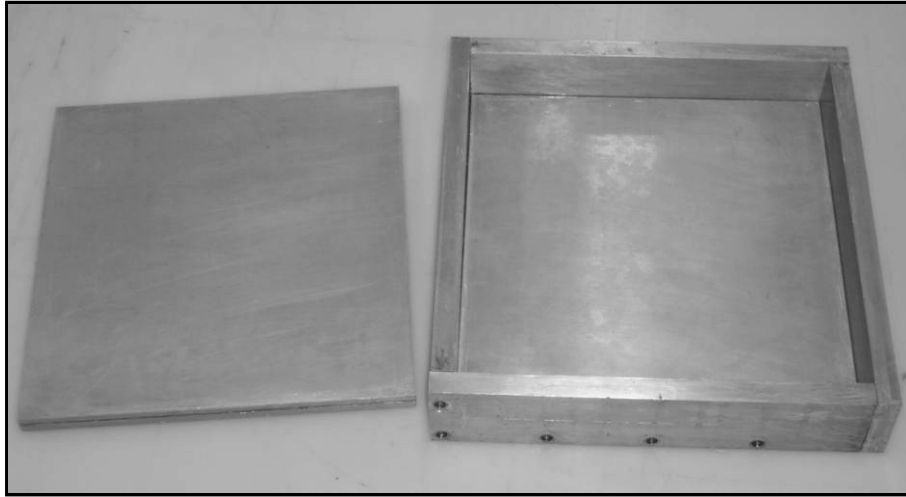


Figure 5.2.2 Drawing of Well and Plunger

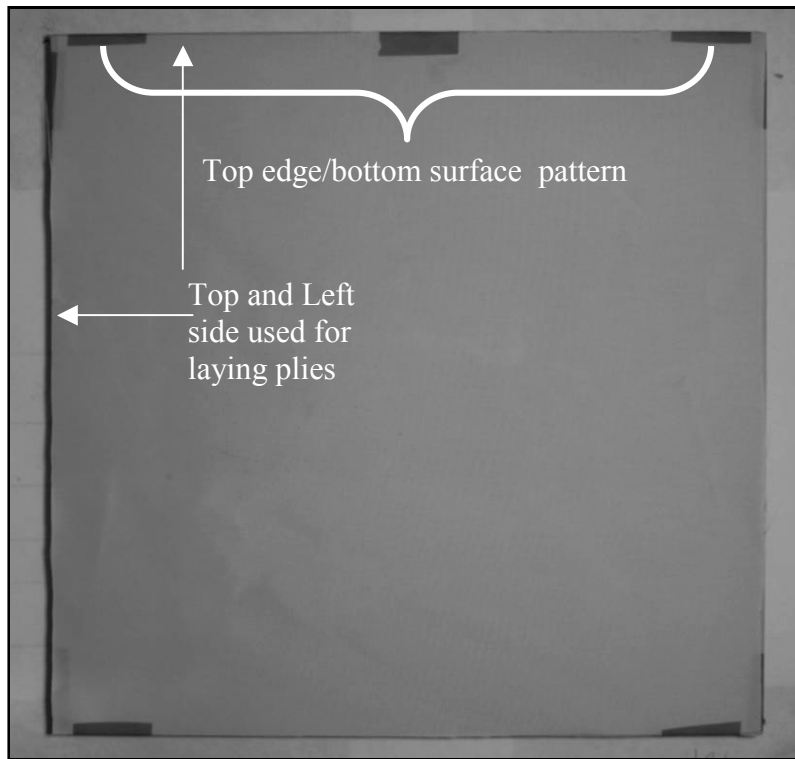


Figure 5.2.3 Bottom Plate of Well and Plunger Showing Tape Pattern

The well and plunger is now ready for fabrication. The first ply is aligned with the top and left sides of the plate as shown in Figure 5.2.3. Each additional ply is stacked one on top of another until the central flaw ply is reached. The flaw ply is made up of many smaller strips that are 9 in. in length, spaced to ensure that subsequently sectioned coupons will each contain one flaw. The flaw ply is laid out by laying the first ply furthest to the left on the plate. The subsequent strips are then laid with the use of spacer strips as shown in Figure 5.2.4 and Figure 5.2.5. The spacer strips allow for a even distribution of the flaws across the ply. The next strip

will be laid along the right edge of the spacer, with the next spacer placed at the left edge of the previous strip. The following ply strip is then placed to the right of the spacer. The spacer strips are cut of differing width depending on the flaw that needed. For the gap flaws the spacer has a width that extends past the previous strip. This extensions includes the flaw width and the next strip is placed along side the spacer. For the 50% overlap flaw a spacer that is less than the width of the previous strip used. The shorter width allows the next strip to be placed overlapping the previous by half a tows width. This is continued until the strips have covered the plate. The final full plies are laid up in the same manner as mentioned previously. The twist flaws do not need a spacer because the strips are laid directly next to the previous with the twist strip being twisted before applying.

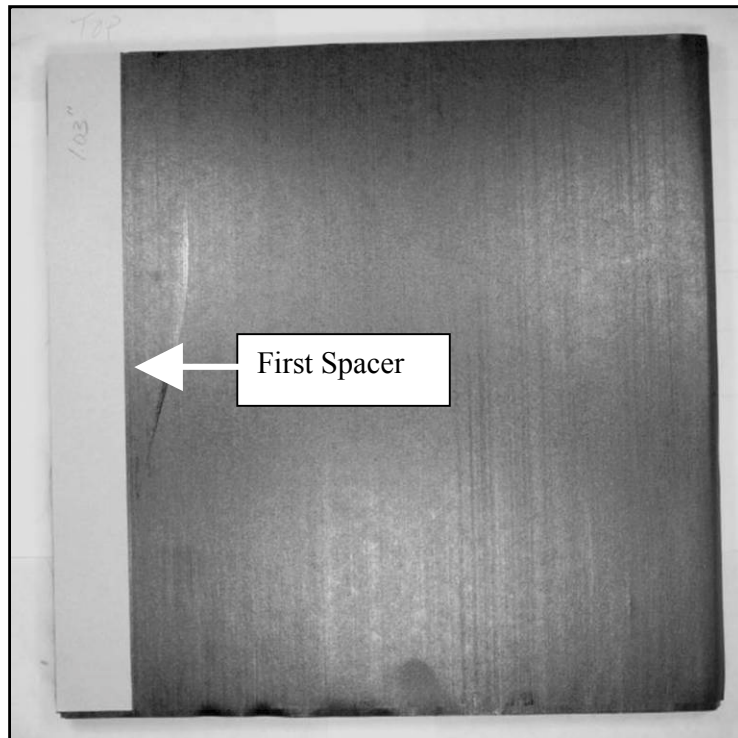


Figure 5.2.4 First Spacer Location

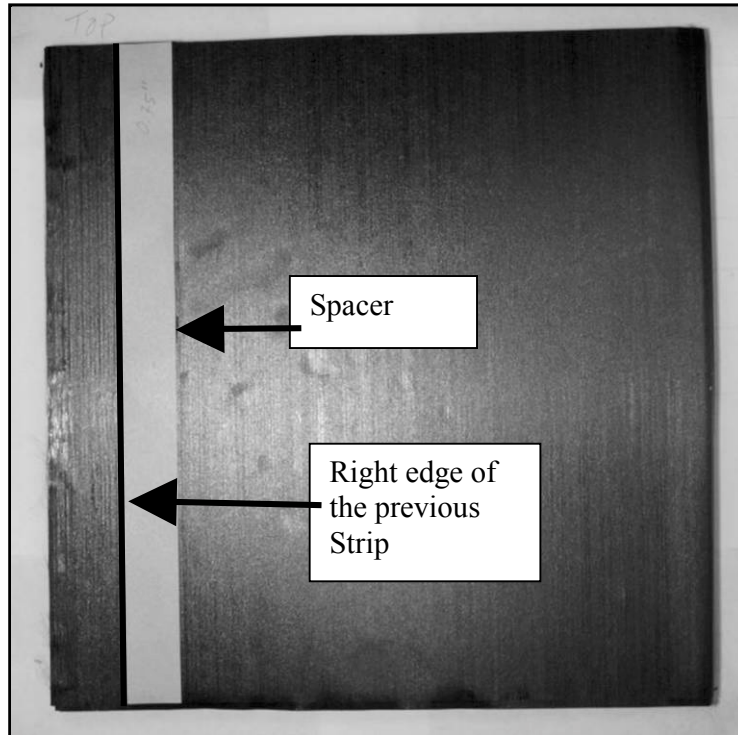


Figure 5.2.5 Location of Subsequent Spacers

The panel is now ready for curing, but first the top porous release cloth and nonporous release film are placed on top of the panel. Then the top plate, also known as the plunger, is placed into the well cavity. The well and plunger are placed in a heated press and cured. The curing cycle is:

- 1) Ramp up to 250 °F and hold for one hour
- 2) Ramp up to 350 °F and hold for two hours

The pressure that the panel is subjected to during the cure cycle is 25 psi.

5.2.1.3 Tow Fabrication Method

Tow prepreg is more difficult to fabricate by hand than is tape. This is because the number of tows range in the thousands for one panel, because individual tows have to be cut and laid up by hand. The first step is to take a spool of tow prepreg out of storage and allow it to acclimate. Next the tows are unrolled and cut to the required length of just over nine inches. Once the required number of tows have been cut, the task of laying up the plies is undertaken. This is accomplished by taking sheets of release film and marking them with lines to align the tows. Then the first tow is placed along the aligning lines. The subsequent tows are placed after the first until there are enough tow to measure 9in. across is created, as shown by Figure 5.2.6 and Figure 5.2.7.

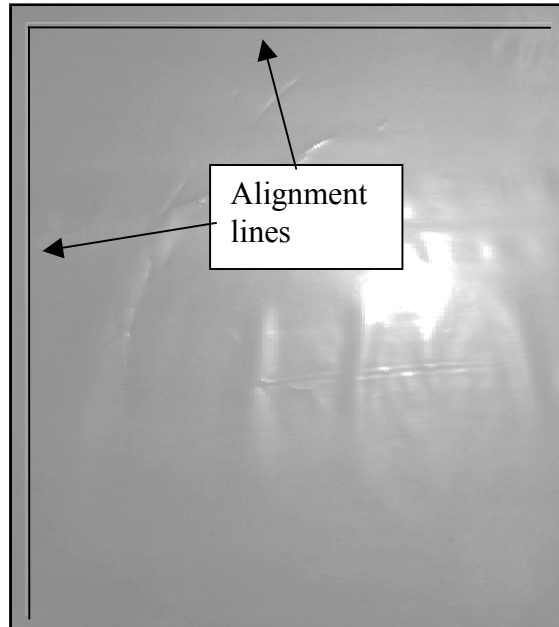


Figure 5.2.6 Release Film with Alignment Lines for Laying Up Tow Plies

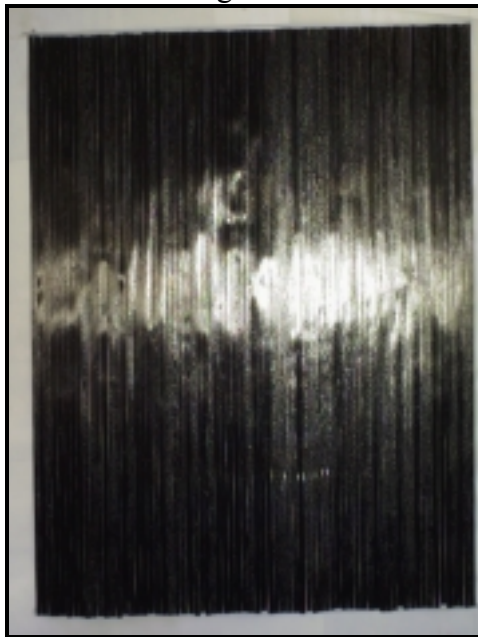


Figure 5.2.7 Single Ply of Tow Prepreg

When the required number of plies are finished the well and plunger is prepared for use, as described in section 5.2.1.2. The flaw plies that are created for the tow panels are created in much the same way as mentioned above. Tows are laid side by side until the location of a flaw is reached. At the flaw locations a variety of different methods are used to accurately space the flaws. For the case of a full tow gap the space is determined by a tow. The tow is laid down and then removed after the next tow is laid. The twist space is also determined by a tow, but in this case the tow is twisted at the center and left in place. The half gap flaw has to use a spacer to guarantee the proper flaw size. The half overlap is made by laying half the next tow over the top

of the previous one at the flaw location. Examples of the flaw plies are shown in Figure 5.2.8 and Figure 5.2.9. The panel is now laid up and cured in the same manner as mentioned in Section 5.2.1.2.

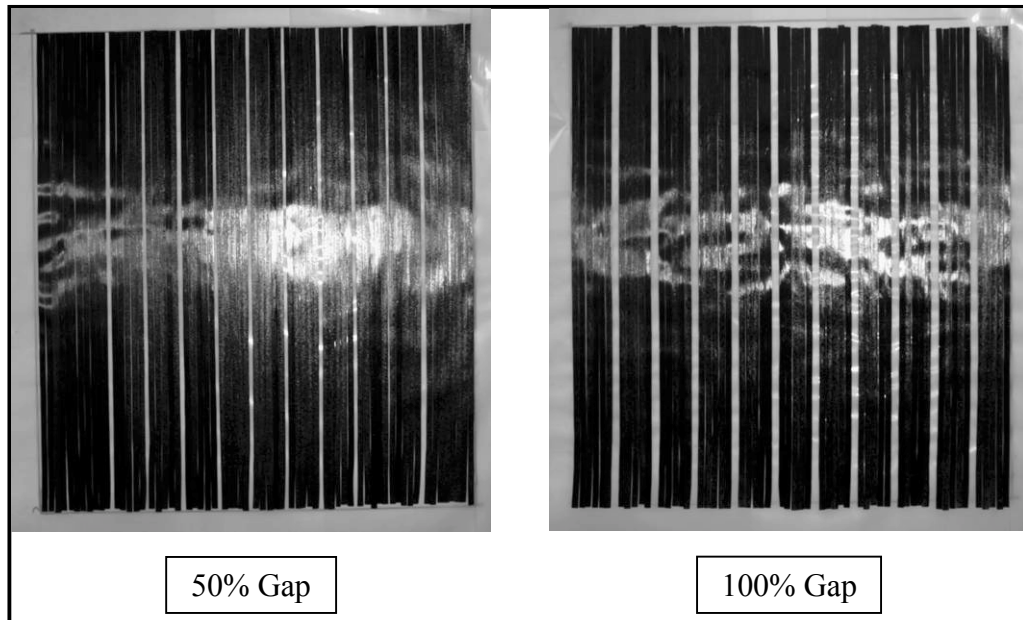


Figure 5.2.8 50% and 100% Gap Tow Flaws for a Single Ply

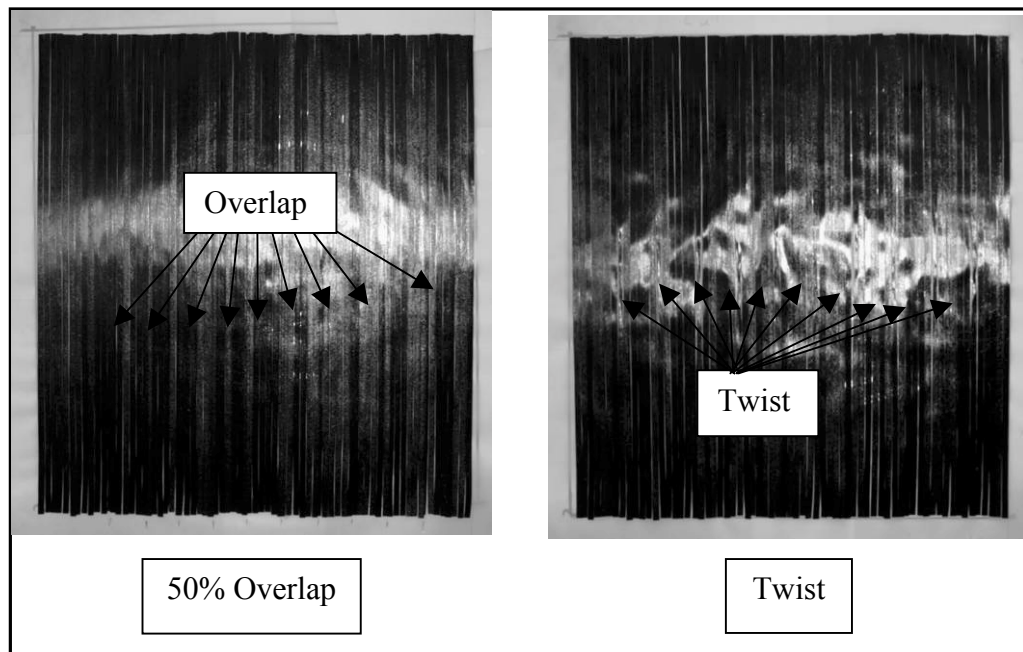


Figure 5.2.9 50% Overlap and Twist Tow Flaws for a Single Ply

5.2.2 Non-Destructive Evaluation

Non-Destructive Evaluation (NDE) testing of unidirectional composites is performed for two reasons. First, NDE is used to detect major flaws in the composite such as voids, inclusions and delaminations. Second, NDE is used to find the gap, overlap and twist flaws in the panels. Figure 5.2.10 is the NDE machine used to perform tests. The Aerospace Engineering department at the University of Kansas has a SONIX CSF 1000-3X digital 3-axis automated immersion ultrasonic system with capabilities for A-scan, B-scan and C-scan testing in through-transmission or pulse-echo mode. The scans made for this study were a pulse-echo, immersion scanning, with a common half inch, 5 Mhz focused probe, with a three inch focal length. The results from the scans will be discussed in Section 5.3.2.



Figure 5.2.10 Ultra Sonic NDE Machine and Controller

5.2.3 Tabbing

After the panels are cured a tabbing material is bonded in place. The tabbing material is a 36 in. X 48 in., 0.125 in. thick, fiberglass/epoxy composite sheet manufactured by Acculam™ Accurate Plastics Inc. The tabbing panels are sectioned into 4.125 in. X 9 in. rectangular pieces. This will allow for a 0.75 in. gage section. To minimize the stress concentration at the gage section one of the 9 in. edges is ground to a 45 degree bevel, as shown in Figure 5.2.11.

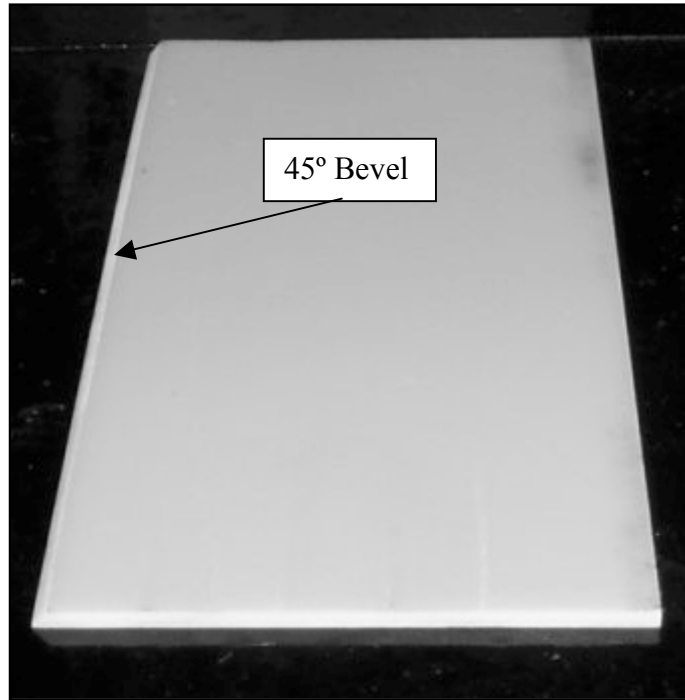


Figure 5.2.11 Glass/Epoxy Tabbing with 45 Degree Bevel

The gage section is marked on the panels along the center, perpendicular to the fiber direction. Marks are made by lightly scratching the surfaces of the panels with a scalpel at the correct locations. The tabs on each side are spaced 0.75 in. apart, with bevels facing each other. The gap between the two tabs are centered on the panel, as shown in Figure 5.2.12. The tabs are then bonded onto the panels using a two part epoxy paste, Hysol Epoxi-Patch-Structural Adhesive®.

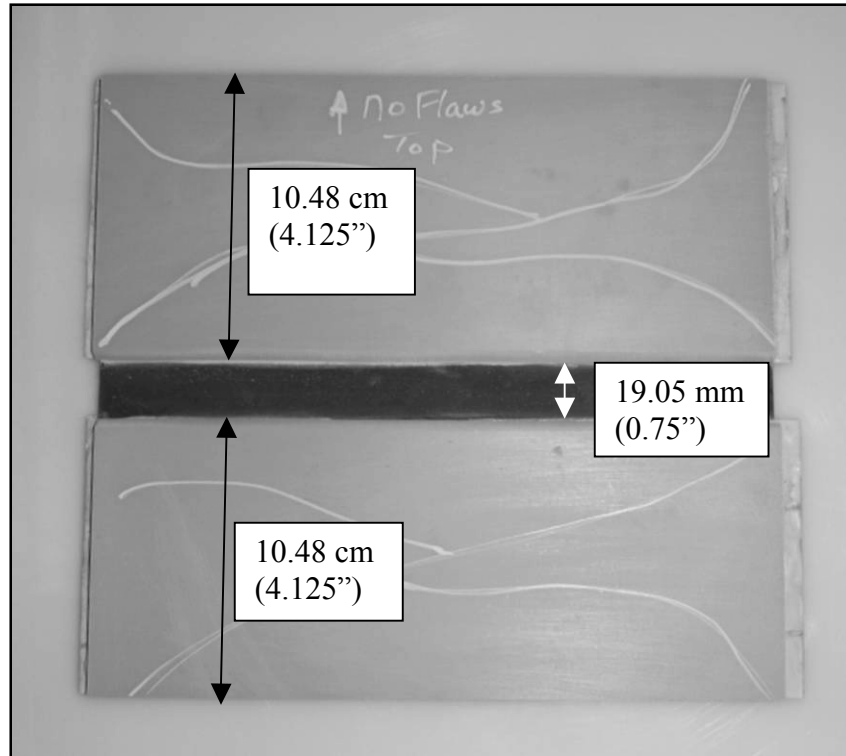


Figure 5.2.12 Tabbed Panel Showing Positions of Tabbing

5.2.4 Microscopy Study

A microscopy study allows for the exact location of the flaws and fiber lay out for fiber volume determination. The composite lab in the Aerospace Engineering Department at KU has a photomicroscopy system to investigate the fiber layout and the visual conformation of defects in the laminate. The microscopic system has the zoom capability of x200, x400, x800, and x1200. To find the flaws the panels are trimmed and sectioned into easily polishable sections. Typically a water-jet cutter is used in the industry, but the team utilizes a diamond cutter, shown in Figure 5.2.13.



Figure 5.2.13 Diamond Cutter

The sectioned ends then have the cut edge polished until individual fibers are visible under magnification. The sections are polished using fine grit wet/dry sandpaper and a series of polishing cloths and compounds at the strip grinder and rotary polishing stations shown in Figure 5.2.14.



Figure 5.2.14 Grinding/Polishing Stations

Under magnification the fibers are easily visible and flaw locations can be found. The locations were marked where the flaws should be, before sectioning, and then checking the locations under a microscope. A clearly defined boundary of the plies and the flaw location is expected to be found, as shown in Figure 5.2.15. The location of the flaw is marked on the panel for future reference. After finding the flaw a picture is taken using a digital camera connected to

the microscope. With this picture a threshold can be taken using Scion Image® turning the picture into black and white. The black represents the resin/epoxy and the white is fiber. The number of pixels can be counted from this picture and the ratio of white to black can be calculated to approximate the fiber volume.

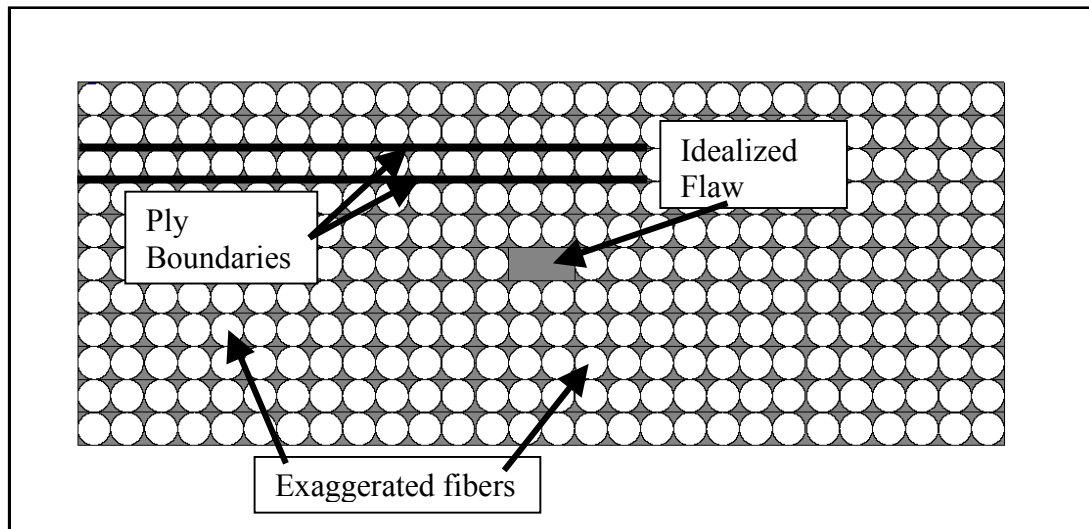


Figure 5.2.15 Idealized Gap Flaw Location Viewed On Axis

5.2.5 Sectioning and Gauging

5.2.5.1 Sectioning

The tabbed panels must be sectioned into test coupons. The first step in sectioning the panels is to mark the locations of the coupons. First a paper layout of the panel is made in a 1:1 ratio based on the microscopy results. The paper layout is then taped to the panel with double sided tape, making sure that the panel and layout are aligned properly. Next a scalpel is used to cut through the paper and lightly score the top of the tabs. The marks are too light to see easily so they must be darkened. To darken the scored line a fine tipped permanent marker is used.

With the panels marked it is necessary to label the individual coupons. The coupons are labeled as shown in Figure 5.2.16 and Figure 5.2.17. The positioning and direction of the labels is important. As the coupon is read the top of the coupon is to the right and the bottom is to the left. This is crucial for later measurements.

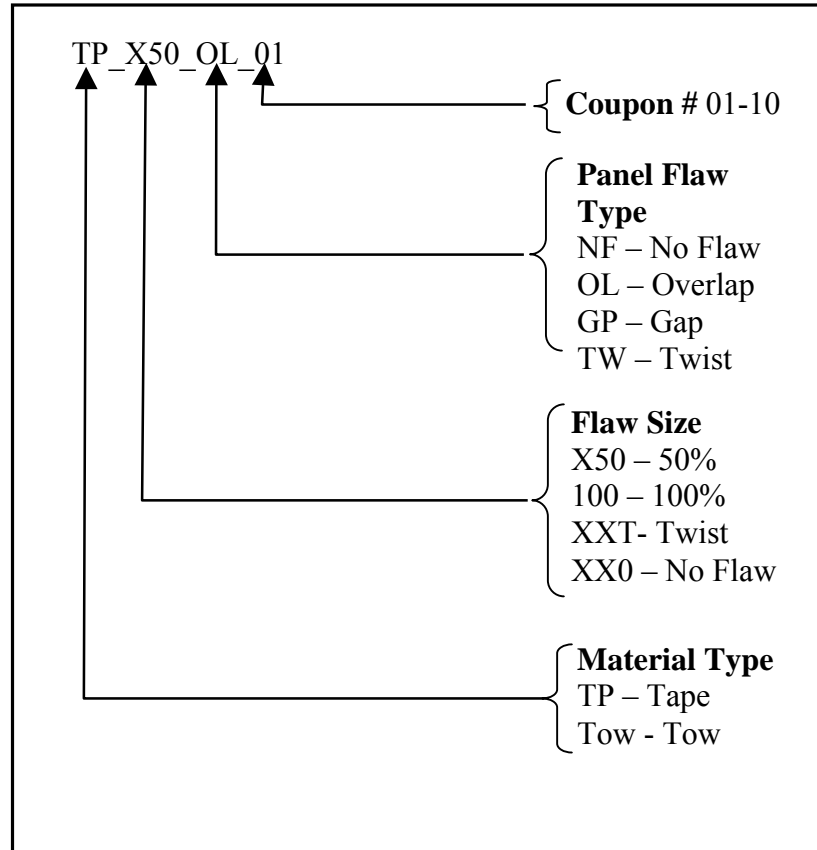


Figure 5.2.16 Coupon Label Nomenclature

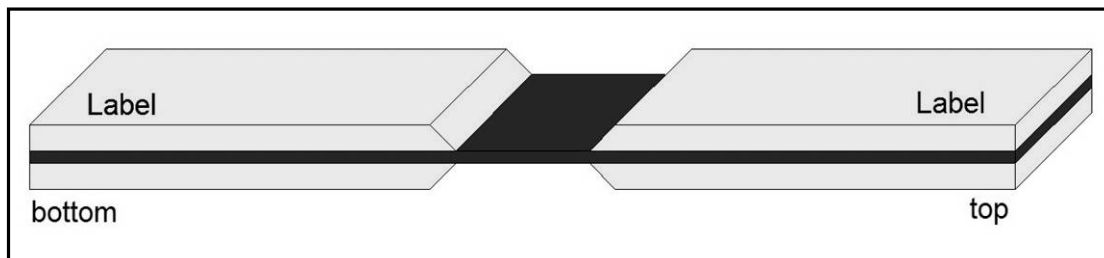


Figure 5.2.17 Label Location on Coupons

Now the coupons are marked and ready for sectioning. Again a water-jet cutter is typically used in industry, but we use a radial diamond cutter. The diamond cutter is installed with 8 in. dia. x 0.06 in. thick x 0.626 in. arbor size Buehler diamond cutter blade and is running at a fixed speed of 1725 rpm. A 36 in. x 36 in. fixture is available to hold panels for a precision cutting capability.

Now that the coupons are sectioned out of the panels they need to be ground within a tolerance, using the grinder shown in Figure 5.2.14. The tolerance expected with the available equipment is ± 0.003 in. This grinding is performed by hand, which creates two problems. When grinding by hand the top and bottom corners are ground more than the middle. This causes the coupons to be wider at the center than at the ends. The other problem that arises is

unparallel side edges. The coupon is difficult to maintain perfectly normal to the grinding surface and therefore the sides become sloped, as shown in Figure 5.2.18.

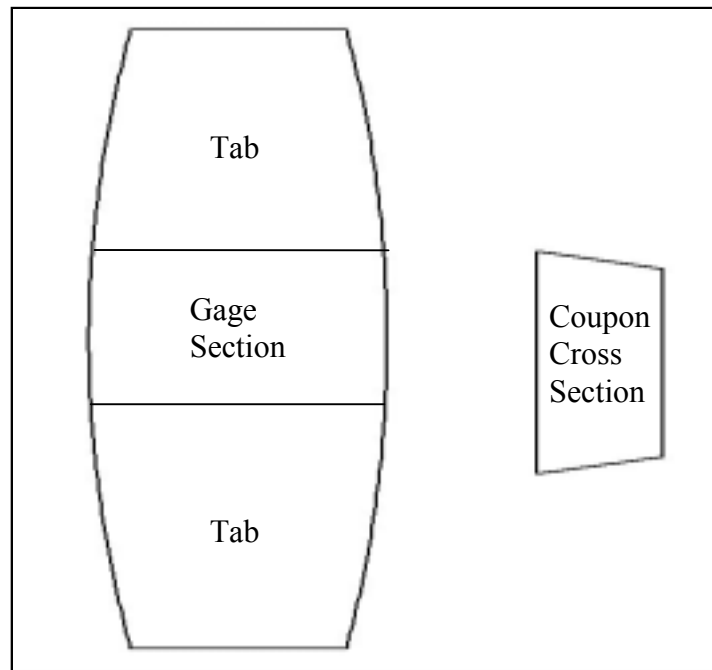


Figure 5.2.18 Exaggerated Examples of Problems Due to Grinding

5.2.5.2 Gauging

The gages used for mechanical test are a CEA-series student gages. The gages are a general purpose family of constantan alloy strain gage widely used in experimental stress analysis. The gages feature polyimide-encapsulated grids and exposed copper-coated integral solder tabs. Each gages has a 120 ohm resistance and a gage factor of 2.08 nom. The usable temperature range of the gages is -100 °F to 350 °F. The sectioned coupons are marked for gage placement on both sides of the coupon. This is done by marking the center line in both longitudinal and transverse directions, as shown in Figure 5.2.19. The mark is made by lightly scratching the surface of the gage section. The scratch is just heavy enough to be visible but light enough that it does not damage the coupon.

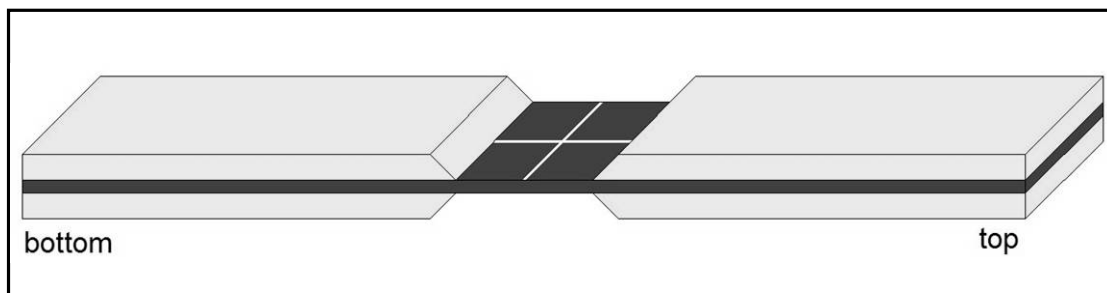


Figure 5.2.19 Centerline Marks for Gage Placement

The gages are adhered to the coupons using M-bond 200, a general purpose adhesive with a simple application process. Last, leads are soldered to the gage tabs making sure not to heat the tabs over 300 F, as this will destroy the tabs. Gages are applied to both sides of the coupon to detect bending and Euler buckling during mechanical testing.

5.2.6 Data Acquisition System

There are two systems used to collect data. Both systems consist of a Computer and up to eight channels of input data. The data acquisition software is Labview®, which has the capability to accept up to 16 simultaneous input signals. The data input device is a combination, SCXI-1000/1520/1314 strain box. The SCXI-1000 chassis houses the SCXI-1520 8-Channel Universal Strain Gage Input Module. The SCXI-1314 is the front-mounting terminal block is connected to the SCXI-1520 so that wire hook-ups can be made easily. A VI (VI) is used to interface between the user and the computer. The VI is a Labview® program that gives a real time display of the data being acquired. Also, the VI has input parameters for gage factors, calibration factors, gage resistance and specimen geometry. Output by the VI is in the form of two strain indicators for divergence and a data file with all stress and strain data collected. Labview is equipped with an input channel explorer, or measurements and automation explorer (MAX). Within MAX are the three input channels used for data acquisition. The first two are for the strain gages and are configured as one-quarter Wheatstone bridges. The third is for the load cell and it is configured to identify the voltage difference from the loads cell's full Wheatstone bridge. The connections and data flow paths are illustrated in Figure 5.2.20 and Figure 5.2.21.

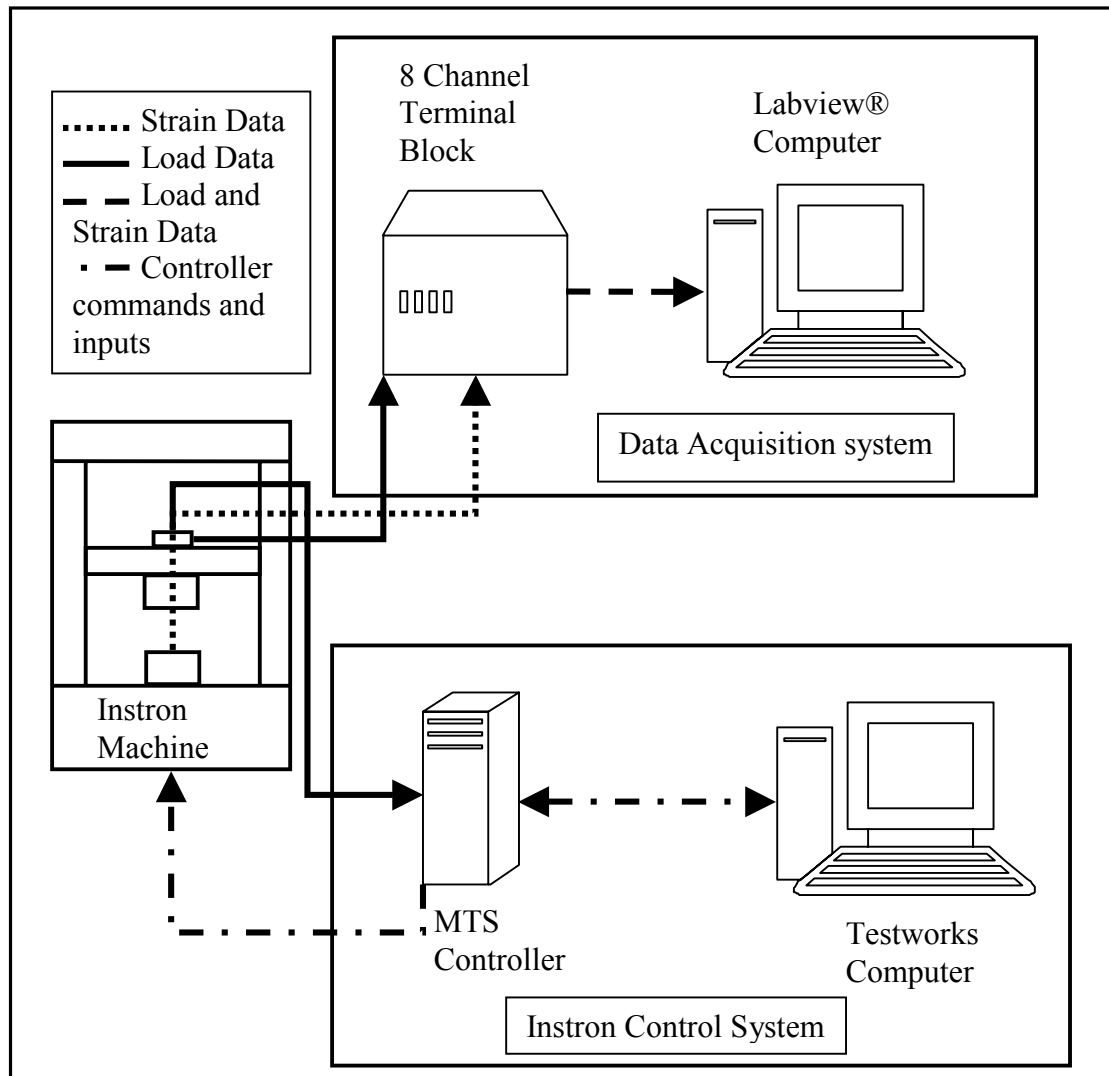


Figure 5.2.20 Schematic of MTS Data Acquisition and Control Systems

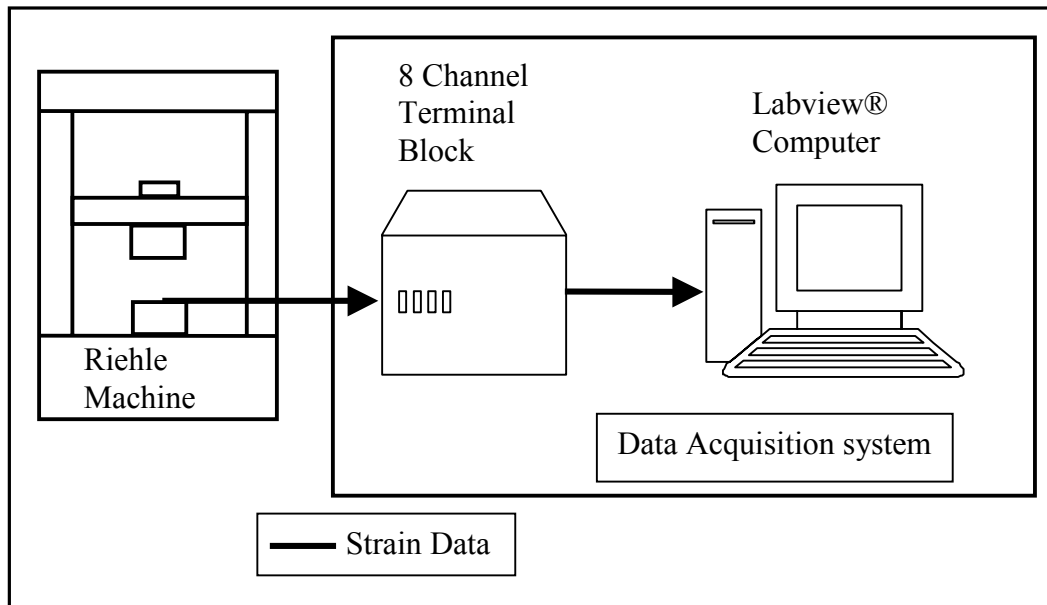


Figure 5.2.21 Schematic of Riehle Data Acquisition and Control Systems



Figure 5.2.22 Data Acquisition Computer and 8 Channel Terminal Block

There are two VIs that are used to collect data. Each is used with a different testing machine. The LabView VI that are used to collect data are similar, but differ on key functions. Both VI collect strain data from strain gages, but one VI does not collect load cell data. Instead this VI is setup to incrementally increase the load after a data point has been collected. This means that the data is collect in a manual fashion by clicking on a bottom within the VI. Both VI also create a file that is specified by the used for the later analysis.

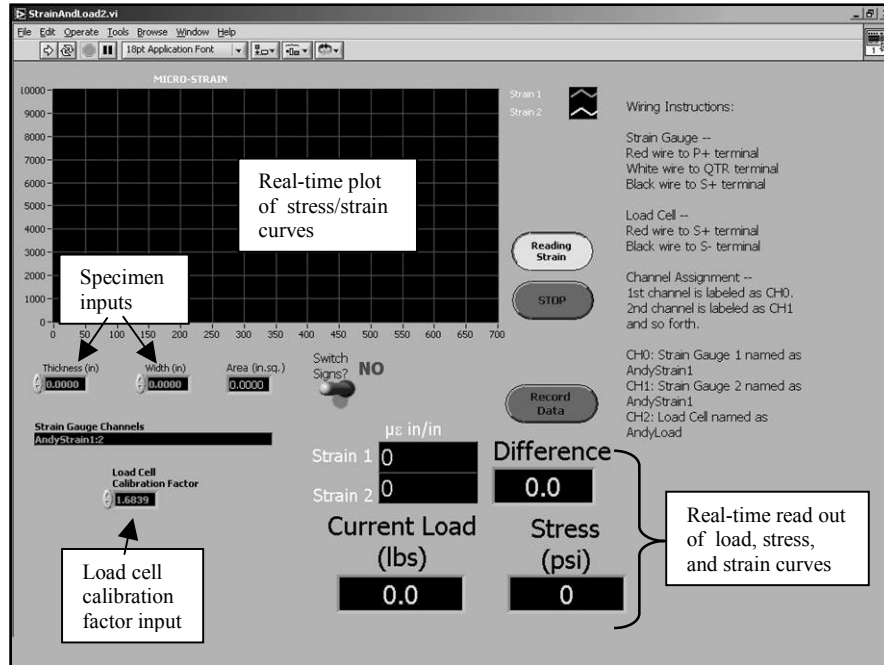


Figure 5.2.23 Front Panel of Data Acquisition Program For MTS Setup

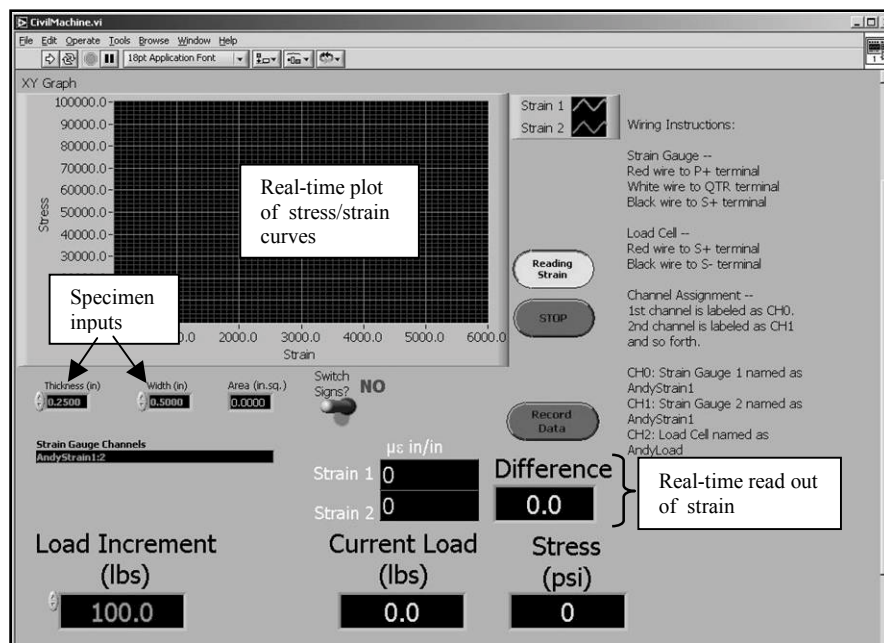


Figure 5.2.24 Front Panel of Data Acquisition Program for Riehle Setup

5.2.7 Fixtures and Machinery

5.2.7.1 Test Machinery

Two different machines are available for mechanical testing, an MTS-Upgraded Instron and a Riehle tension/compression machine. The maximum capacities of the machines are 22.5

kips or 100 kN Load Cell and 60 kips. The MTS-Upgraded Instron machine can be installed with various fixtures for tests such as compression, tension, bending and in-plane shear. Also it has a capability of load cycling fatigue testing. The control system is retrofitted by the MTS Company that is based on a user-friendly Windows® base software, Testworks.

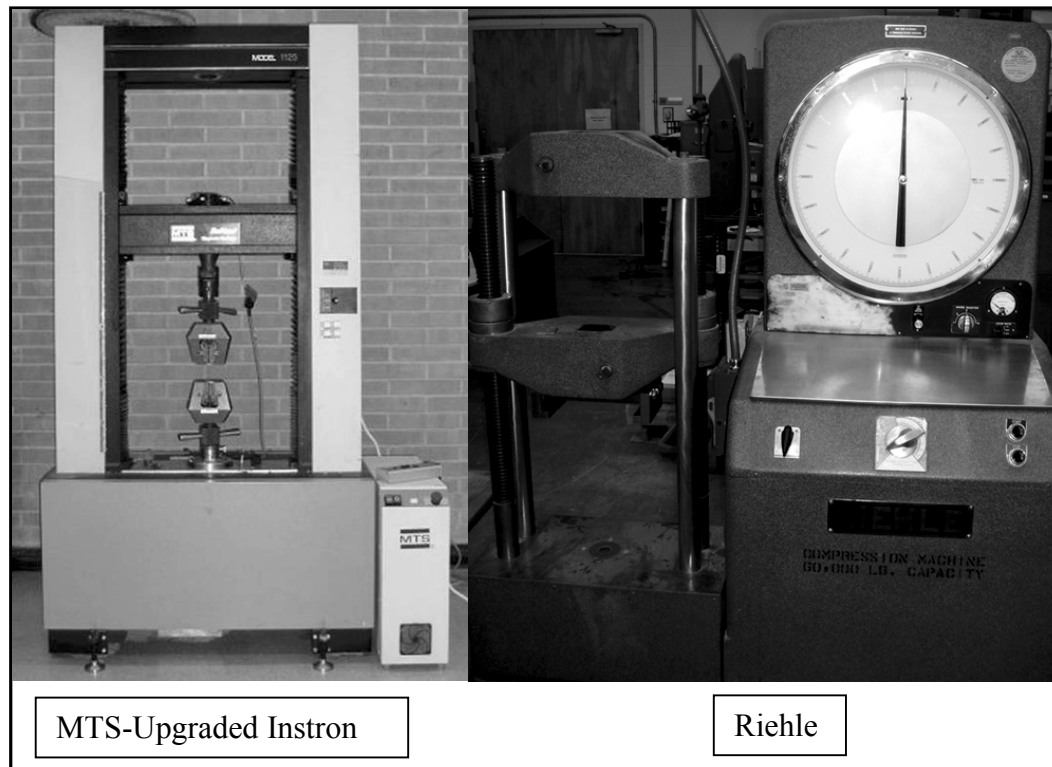


Figure 5.2.25 Mechanical Testing Machinery

The Riehle machine has a built in tension fixture and can be equipped with an IITRI compression test fixture. The control system consists of a start and stop button and a load rate dial. Load is displayed on the large dial indicator on the front of the machine.

5.2.7.2 Test Fixture

Due to the need for the test specimens to be more than a single tow width the ASTM D 3410 Method B Test Fixture, was selected. The test fixture called IITRI compression test fixture was introduced by the Illinois Institute of Technology Research Institute (IITRI) in 1977. The test fixture is designed to accommodate tabbed specimens 5.5 in. long, and any width up to 1.5 in., as specified by the ASTM standard. The fixture consists of four parts, a flat wedge grip, mating block, lower block, and head holder. Alignment rods guide the upper and lower blocks. The fixture can be used to test gage length specimens from zero to 2 in. The load that is applied to the fixture is transferred from the wedge grips to the specimen through shear. Since the data resulting from this method is sensitive to the flatness of the coupons, a special care of specimen preparation is necessary. This test method is not commonly used because of weight and cost consideration. But this test method provides an advantage to test the widest specimens [5.4].



Figure 5.2.26 ASTM D 3410 Compression Fixture

The testing standard, ASTM D 3410 Method B recommends sizes for the testing specimens. The recommendations are listed in Table 5.2.2. The specimen size used for the testing is listed in Table 5.2.3. The specimens have strain gages on two sides to ensure that there is no bending in the specimen due to the compressive load. Data is taken from the strain gages as well as from a load cell on the compression machine. The data is used to determine the compression modulus of elasticity. The ultimate load of each specimen with a flaw will be compared to the ultimate load of the specimen with no flaw. This comparison should give a reduction in the mechanical properties of the specimens.

Table 5.2.2 ASTM D 3410 Method B Recommendations [5.4]

Dimension		Tolerance	
Width mm, [in]	10 [0.5]	Width	$\pm 1\%$ of width
Gage Length mm, [in]	10-25 [0.5-1.0]	thickness	$\pm 1\%$ of thickness
Tab length mm, [in]	65 [2.5]	Tab thickness	$\pm 1\%$ of width
Overall Length mm, [in]	140-155 [5.5-6.0]		
Tab Thickness mm, [in]	1.5 [0.06]		

Table 5.2.3 Recommended Specimen Dimensions [5.4]

Dimension		Dimension	
Width mm, [in]	16 [0.625]	Tab length mm, [in]	60 [2.375]
Gage Length mm, [in]	19 [0.75]	Tab Thickness mm, [in]	3 [0.125]
Overall Length mm, [in]	140 [5.5]		

5.2.8 Experimental Procedure

In this section, the detailed compression test procedures will be discussed such as machine and strain gage calibration, specimen geometric data, and step-by-step procedures. The experiments conducted for this research are destructive compression tests of composite specimens with various flaws located within. Five types of specimens are tested: unflawed, 100% and 50% tow gap, 50% tow overlap and tow twist. The procedure for testing is as defined in ASTM D3410 [5.4].

5.2.8.1 Test machine calibration

Calibration of the testing machine is very important in order to obtain accurate test data. The MTS-Upgraded Instron mechanical testing machine utilized in this project has a capability of automatic electrical load cell calibration as well as a single strain gage channel. The problem with this machine was that only one channel of strain gage data was available, so that the back-to-back strain gage system could not be applicable for simultaneous data recording. As discussed in Section 5.2.5.2, the back-to-back strain gages are a key detection system to identify bending and Euler buckling. Using the external data acquisition system, discussed in section 5.2.6, solves this problem.

5.2.8.1.1 MTS/Instron Load Cell Calibration

Calibration with known materials provided a means to verify calibration of the load cell in our external data acquisition system. The calibration is done by placing a material of known modulus of elasticity into the tension testing fixture and loading it until ultimate failure. The load is then compared to the actual ultimate value taken from the "Military Handbook 5".

Calibration of the load cell for use with Labview® consisted of connecting both the MTS/Testworks system and the Labview® system to the load cell. Both systems read a different load, but the Testworks® computer is known to be correct. Next a material is placed into the tension grips and loaded while the reading from both systems are recorded. A plot of the load collected is made and a linear relationship is found between the two. One aluminum sample was tested and a synchronization factor was found to be 1.6839.

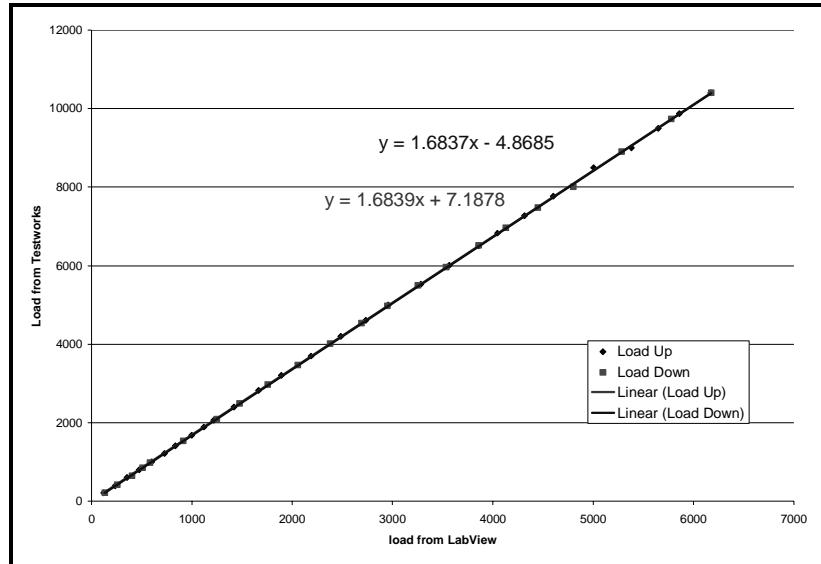


Figure 5.2.27 Load Cell Synchronization Curve

5.2.8.1.2 Riehle Verification

The Riehle test machine is calibrated every year, and thus does not need to be recalibrated. The machine, however, utilizes a dial gage for load and we need verification that the data acquisition system will function with the machine. For this verification process, a material with known material properties is loaded and the data is recorded. In this case the material is 6061-T6 aluminum. The verification allows for a comparison of the stiffness determined from test to the stiffness from the material fact sheet. The stiffness of 6061-T6 aluminum is 10.1×10^3 ksi for compression. Five samples were tested and the mean stiffness for the aluminum is 9.72×10^3 ksi with a 2.8% standard deviation in compression. The mean has 3.7% variation in stiffness from the Military Handbook 5 value and is less than a five percent variation. The variation can easily be contributed to experimental errors including coupon misalignments and gage misalignments.

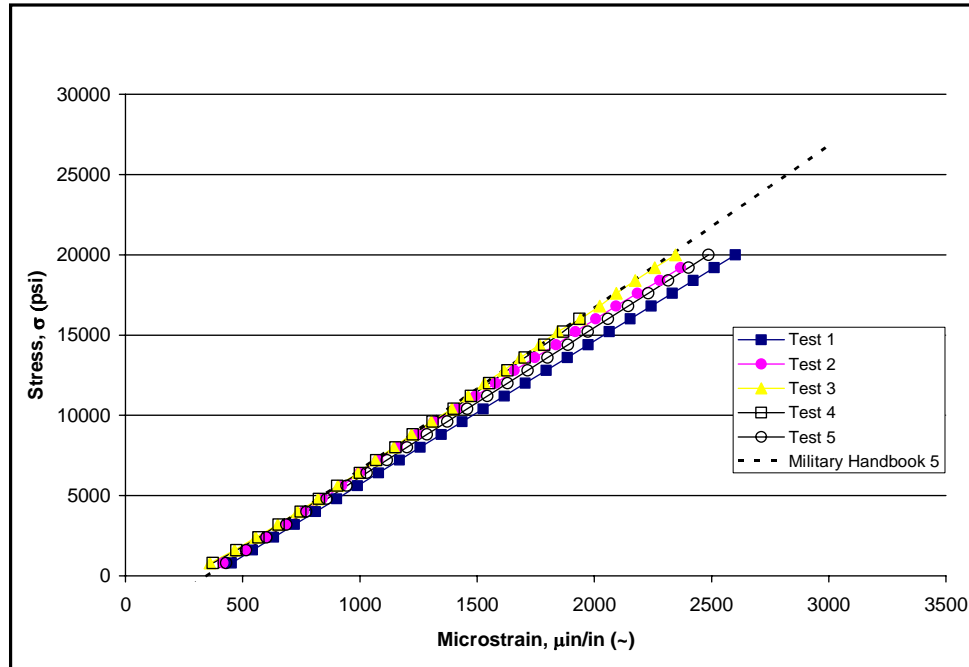


Figure 5.2.28 Riehle Calibration Curves

5.2.8.2 Testing Procedures

In this section the compression testing procedure will be discussed in step-by-step detail. Two procedures will be discussed, one for the MTS/Instron machine and one for the Riehle machine.

5.2.8.2.1 MTS Procedure

- 1) Turn on MTS machine and load Testworks®

Powering up the MTS controller and loading Testworks® requires that the power button be pressed on the controller and double clicking on the Testworks® icon and then logging on. Then select the test button. This brings up a screen that allow the user to select a test method. The test method used is called "AE_COMP_AY". This method is set up to run the test machine in compression. The displacement rate is set at 0.02 inch/min. This is slower than what is specified in reference 5.4 in order to be more conservative.

- 2) Turn on Labview® computer

Turning on the Labview® computer consists of first turning on the SCXI 1000/1520/1314 box and booting then the computer. Once the computer is booted, Labview® is loaded and "strainandload2VI" is opened.

- 3) Measure width and thickness of the gage section of the specimen and enter in Labview® vi
- 4) Place specimen in the fixture grips

Placing the specimen in the grips jig can introduce a lot of error because the specimen are not of a standard size. First, one side of the grips is placed in the alignment jig, as shown in Figure 5.2.29. Next a spacer bar for a 0.75 inch wide specimen is placed up against the top pegs. Since the specimen is not 0.75 inches in width the specimen must be offset from the spacer bar.

This is performed by only a visual reference and can induce alignment errors, and subsequent sample bending.

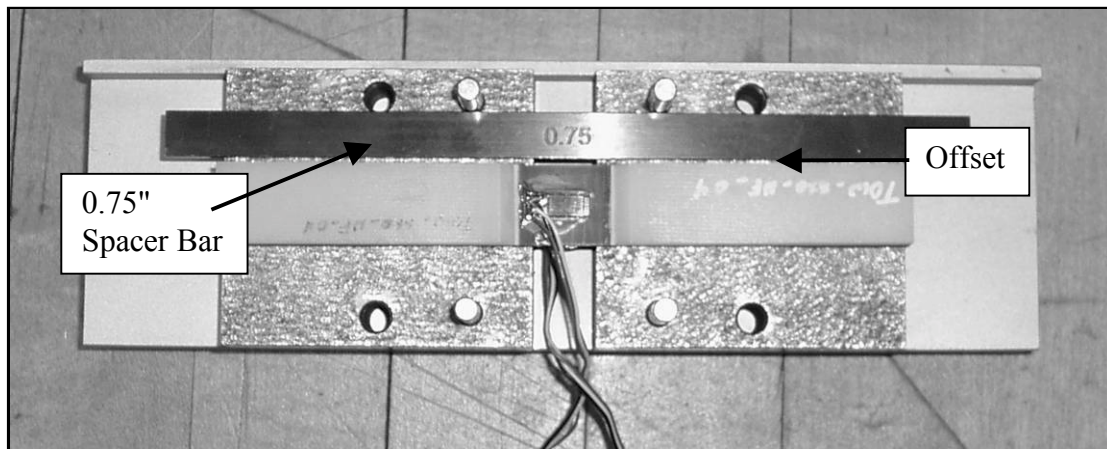


Figure 5.2.29 Alignment Jig Set Up

Now the specimen is positioned at the center of the grip and is ready for the other half of the grips. The other half of the grip slides over the pegs and is bolted to the bottom half. The bolts must be tightened in a crossing pattern so that there is no twisting of the specimen, as shown in Figure 5.2.30.

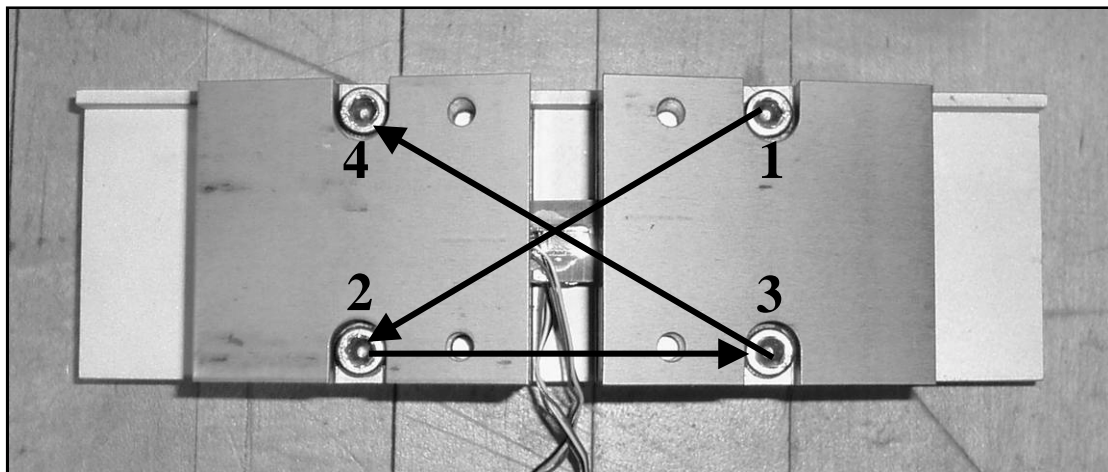


Figure 5.2.30 Specimen Gripped and Ready with Tighten Pattern

5) Place gripped specimen in fixture

The gripped specimen is placed in the test fixture and has the strain gage wires stretched towards the SCXI 1000/1520/1314 box, as shown in Figure 5.2.31. The top of the fixture is then moved down to meet the grips using the MTS controller remote control. The top of the fixture is positioned so that the grips are within the fixture but not loaded, as shown in Figure 5.2.31. Note that there is a gap between the top mount of the fixture and the top of the specimen. The top of the fixture will meet the top mount once the test has begun and the specimen will begin to load.

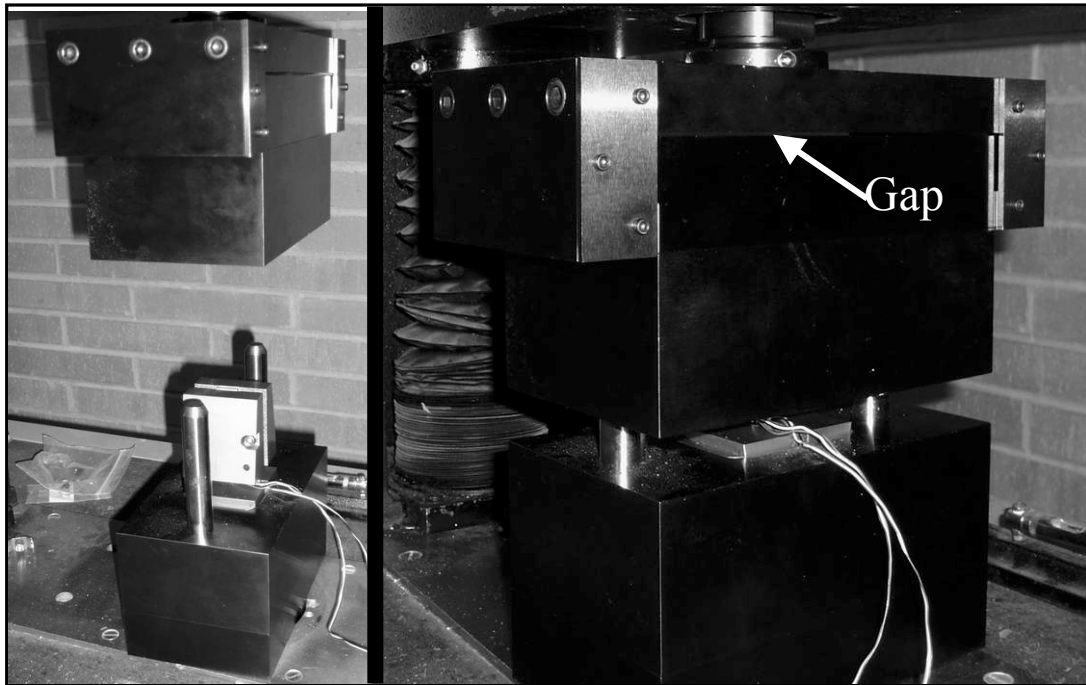


Figure 5.2.31 Test Fixture Preparations

Next the Gage wires are connected to the SCXI 1000/1520/1314 box. Red is connected to the P+ terminal. White is connected to the QRT terminal and black is connected to the S+ terminal. The load cell wires are connect to the S+ and S- terminals for red and black, respectively.

6) Strain gage setup

To setup the strain gages MAX must first be opened. With MAX open, "Data Neighborhood" is expanded in the explorer window. Under "Data Neighborhood" are two channels labeled "Andystrain1" and "Andystrain2". Each must be selected and the properties must be displayed. In the channel properties the gage factor and resistance is entered. After entering the gage factor and resistance the gages must be calibrated and zeroed. This is performed by selecting the calibration button and choosing "null correct and shunt calibration" and clicking start. To verify that the calibration is correct and working properly, there are two values on the right side of the window. The values are measured and simulated strain readings. If the two values do not match then there is something wrong, like the gage wires are not connected correctly or the gage and wires are damaged.

7) Start the test

Before running the test the chart in the Labview® vi must be cleared. This is so the data plot starts at zero. Next, click run on Testworks®. Then Click run on Labview®. When the dialog come up asking to save the data click "yes" and choose a location and file name. Last click on the "Collect Data" button in Labview® when the specimen begins to take load.

8) Load and unload specimen to alleviate misalignments in fixture

There may be bending due to misalignments in the fixture. This can be alleviated by loading up the specimen and unloading until the reading between the two strain gages agree..

9) Repeat steps (7) and (8) two – three times as needed to alleviate fixture misalignments.

10) When the specimen breaks stop collecting data by clicking the collect button and stop the vi

11) Repeat (3) –(10)

5.2.8.2.2 Riehle Procedure

1) Turn on Riehle machine

The machine has a switch on its back side.

2) Turn on Labview® computer

Turning on the Labview® computer consists of first turning on the SCXI 1000/1520/1314 box and booting the computer. Once the computer is booted, Labview is loaded and "civilmachine.vi" is opened.

Steps 3) through 6) are identical to the MTS procedure.

7) Start the Riehle test machine

To start the machine the load rate must be selected and the start button must be depressed. The controls are labeled and located on the front of the machine.

8) Load and unload specimen to alleviate misalignments in fixture

There may be bending due to misalignments in the fixture. This can be alleviated by loading and unloading the specimen.

9) Repeat steps (7) and (8) two – three times as needed

10) Set the load rate on the Riehle machine

The load rate is controlled by a knob on the front of the test machine, as pictured in Figure 5.2.32. The setting is for 0.02 in/min. Notice that there is no marking for 0.02 in/min. Therefore, the exact load rate is not known. A mark located on the dial is believed to be 0.02 in/min and is used.

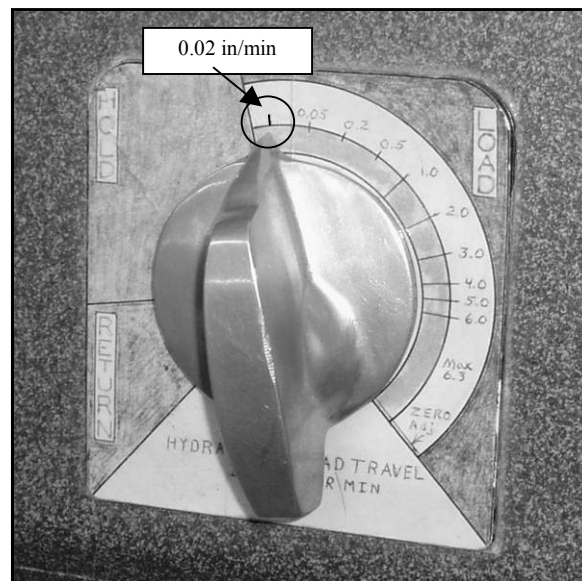


Figure 5.2.32 Load Rate Adjustment Knob for the Riehle Test Machine

11) Start the Riehle machine and the Labview VI.

12) Every one hundred pounds collect a data point

The collect data button in the LabVIEW VI is depressed at every 100 pounds. This collects and records two strains and records a load and stress.

13) When specimen breaks or if the difference in strain becomes greater than 2000 microstrain, stop the Riehle testing machine and stop VI.

Stopping the test machine is done by depressing the stop button and returning the load rate dial to the return position.

14) If the specimen breaks proceed to 15). Otherwise, start the test over again.

15) Repeat (3) –(13)

5.3 Analysis and Discussion

In this section the results from analyses and testing are presented and discussed. Analysis results discussed include a Nastran analysis, NDE analysis, photomicroscopy study, and mechanical testing analysis. Also discussed will be the methods by which the results were obtained.

5.3.1 Finite Element Analysis

Numerical analyses have been performed to determine how much effect gap and overlap flaws have on the uniaxial compressive mechanical performance of unidirectional composites. Three Nastran analyses were performed. The first analysis is axial, where the flaw runs in the same direction as the load being applied. The second analysis is off-axis, where the flaw runs perpendicular to the load directions. The third is a combination of the first two. The flaw runs the direction of the load but the rest of the laminate has a fiber direction perpendicular to the load. The specimens analyzed include flaws of no flaw, 100% and 50% tow gaps, and 50% overlap tow gaps. Figures 5.3.1 to 5.3.3 show where the flaw is located within the on-axis, off-axis and combination specimen sections. These samples are described in greater detail in sections 5.3.1.1 -5.3.1.3.

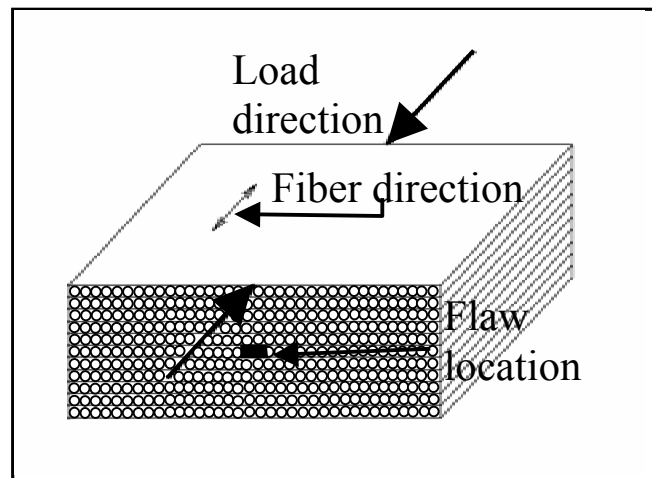


Figure 5.3.1 Specimen Illustration Showing Flaw Location for On-Axis Model

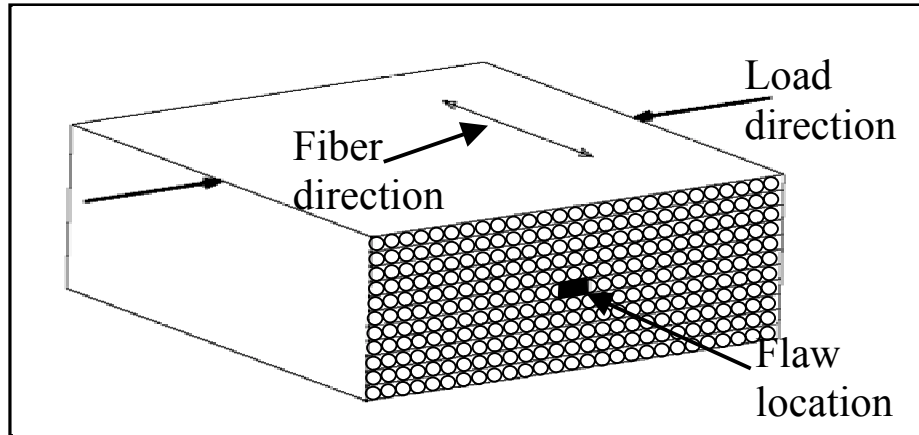


Figure 5.3.2 Specimen Illustration Showing Flaw Location for Off-Axis Model

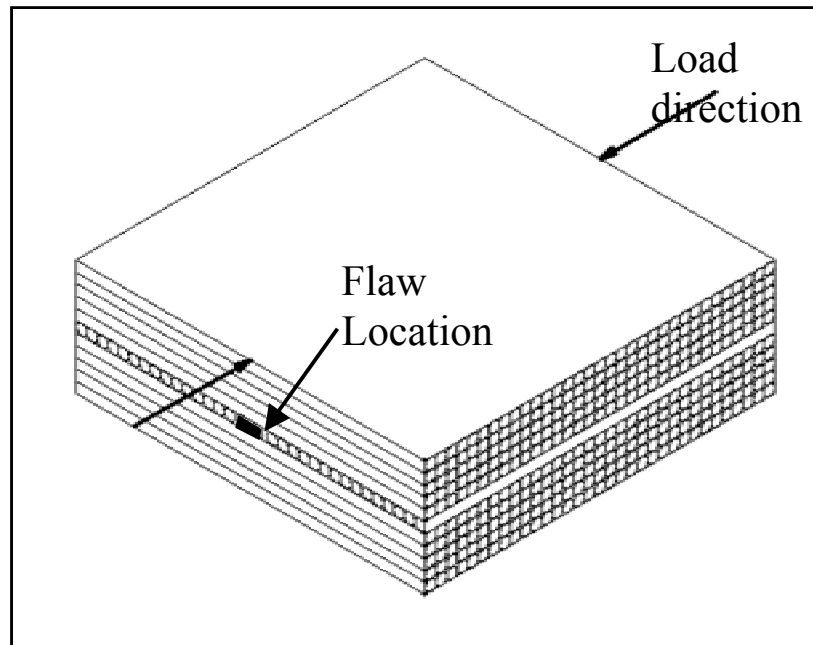


Figure 5.3.3 Specimen Illustration Showing Flaw Location for Combination Model

5.3.1.1 On-Axis Analysis

The on-axis analysis consists of a no flaw, 100% and 50% gap and 50% overlap analysis. Each flaw had its own unique stacking sequence:

- [5(0), 0, 5(0)] – Unflawed
- [5(0), resin rich zone, 5(0)] – Gap flaw
- [12(0)] – Overlap flaw

The gap flaws vary in width, but maintain the same stacking sequence.

The model is created as half of the gage section. This can be done because the flaws run the length of the specimen and there is an axis of symmetry across the center. Since the specimen is symmetrical the boundary condition constraints at that point are more lax than that

of an end. All that is required are constraints that oppose the load at the bottom of the specimen. Two more additional constraints are needed to retain rigid body motion. The first is a constraint at that keeps the specimen from rotating out-of-plane, and the second restricts movement in the transverse direction. Figure 5.3.4 shows the boundary conditions and where they are located. To create a compressive load on the specimen a distributed load equaling 1000 lbs, in the negative Y-direction, is placed along the top edge of the specimen, as shown in Figure 5.3.4.

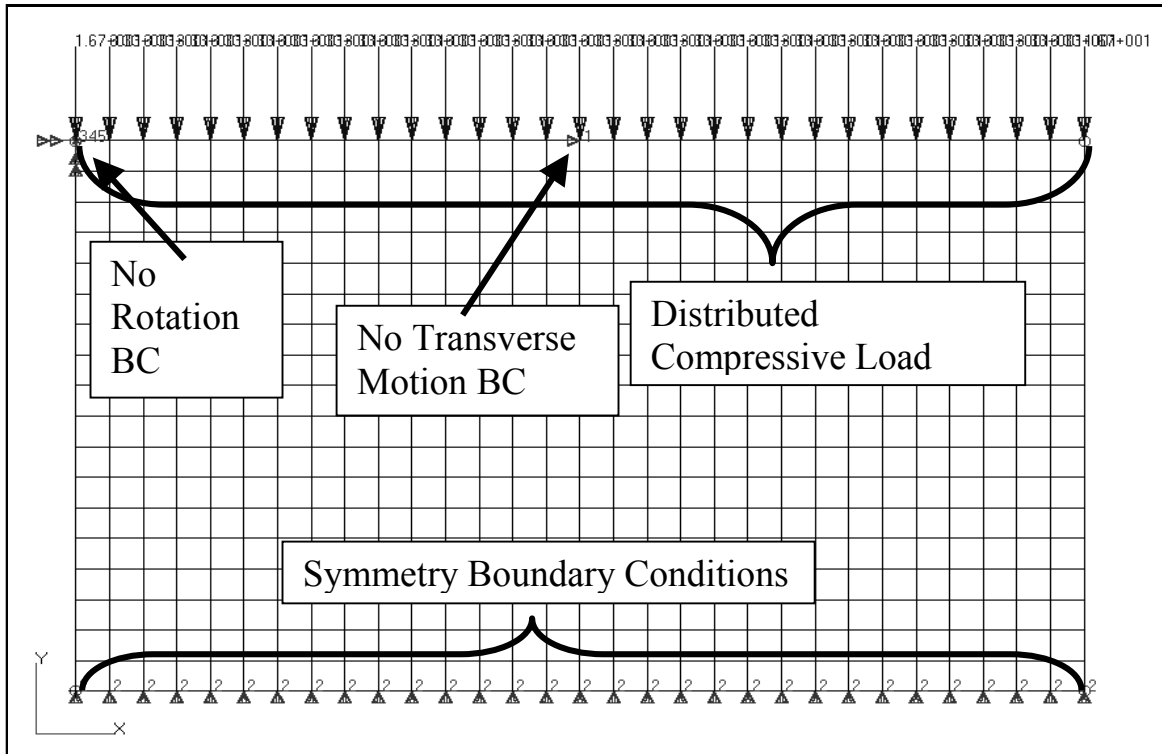


Figure 5.3.4 On-Axis Loads and Boundary Conditions

The sample is constructed of 540 square elements with 30 across the width and 18 in length. Each of the five tows is modeled with six elements. This allows for all the flaws analyzed to be modeled with either a six element width or a three element width. The gap flaws are considered to be a resin rich zone in the flaw location, and the overlap flaw is a thin strip where there is an extra layer of fibers. If the samples are examined from the end they would look like Figures 5.3.5-5.3.7 where the circles represent the elements and the dark areas are resin. Notice that the 50% overlap is one ply thicker than the rest of the specimen at the flaw location. The twist flaw is not modeled due to its difficult geometry, and due to the likelihood that the twist response is between the gap and overlap response.

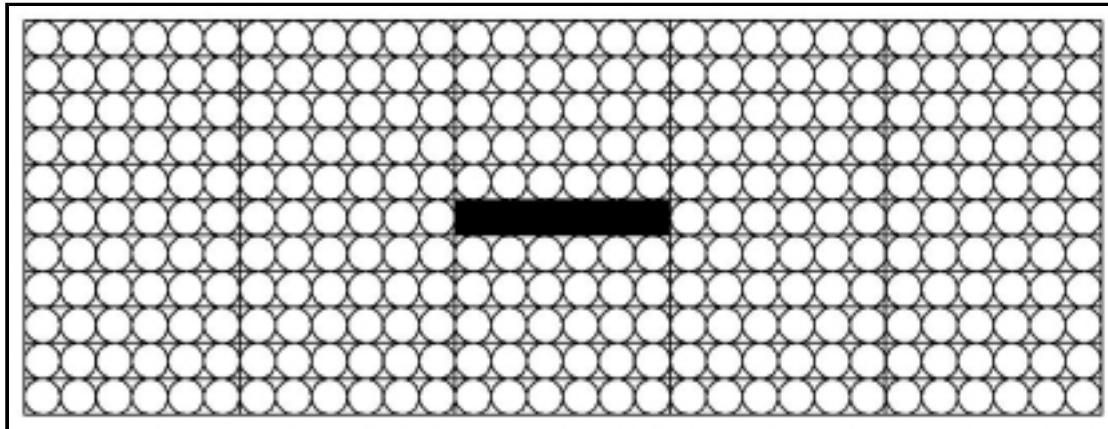


Figure 5.3.5 On-End Representation of 100% Gap Sample

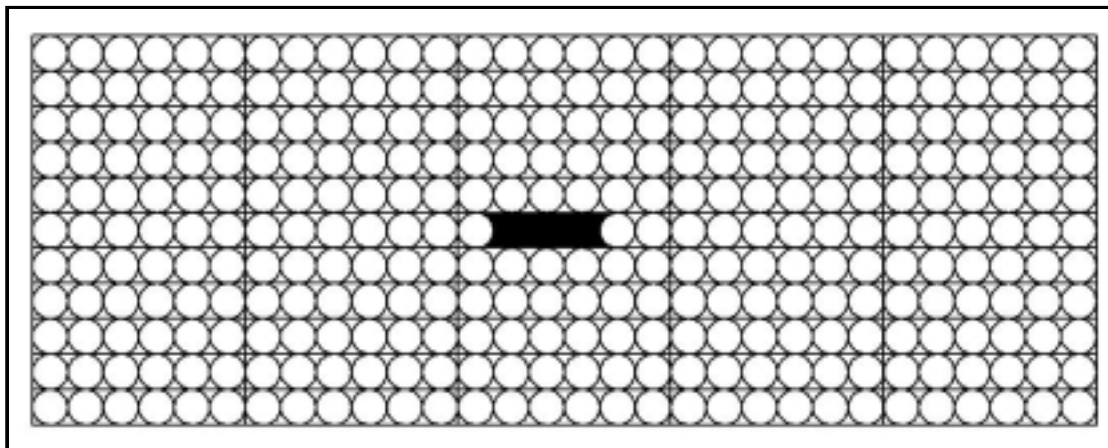


Figure 5.3.6 On-End Representation of 50% Gap Sample

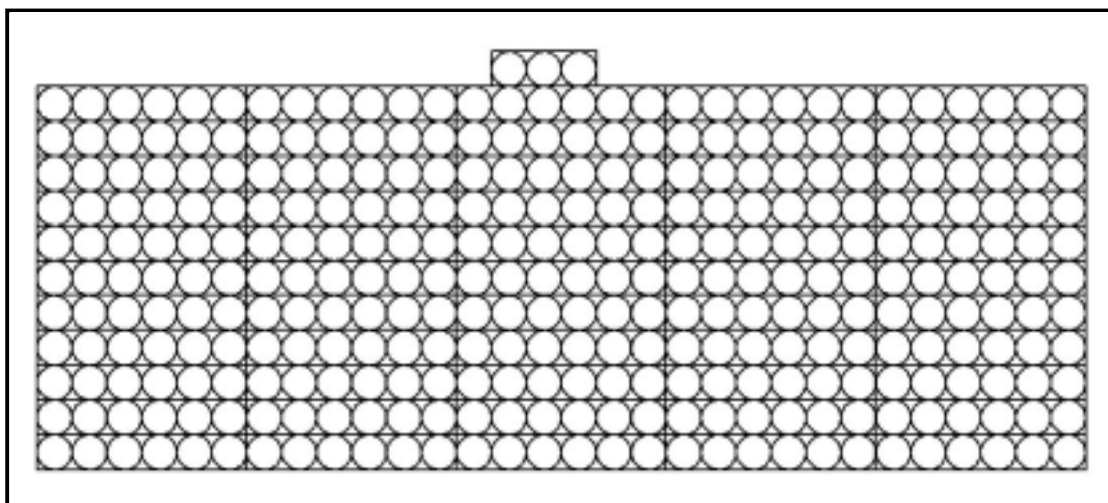


Figure 5.3.7 On-End Representation of 50% Overlap Sample

Strength, which is a function of the applied load, is negatively proportional to the critical stress. The critical load is the maximum stress within the sample at a given load. When the critical stress reaches the failure stress the sample fails. The critical stress is not the failure load. Thus the failure load is the applied load that results in a critical stress greater than or equal to the failure stress.

The results from the analyses are shown in Figure 5.3.8 and listed in Table 5.3.1. The base line stress is $-1.65\text{E}+3$ psi. Table 5.3.1 lists the critical stress for each flaw condition and the percent difference that each has compared to the specimen with unflawed sample. The largest percent difference is 3.0% given by the 100% flaw sample. This is small and would be difficult to see in mechanical testing because a scatter of 5% is expected. Even though, mechanical testing is needed because there could be secondary effects like layer waviness that was not modeled for this analysis. From Table 5.3.1 it is clearly seen that all the specimens with flaws have reductions in strength. The flaws make up less than 2% of the composite sample. Thus the slight effect of the flaws does not seem unreasonable.

Table 5.3.1 Critical Stress for Common Tow Flaw Compressive Analyses

Flaw Type	Critical Stress (psi)	Percent Difference (%)
No Flaw	-1.65E+3	- -
100% Tow Gap	-1.70E+3	3.0
50% Tow Gap	-1.69E+3	2.4
50% Tow Overlap	-1.66E+3	0.61

This data trend shows that the more severe the flaw the more likely the strength will be reduced. The severity of these flaws ranked highest to lowest is: 100% gap, 50% gap, 50% overlap. Clearly the 100% gap flaw has the largest effect on strength as it is the most severe flaw.

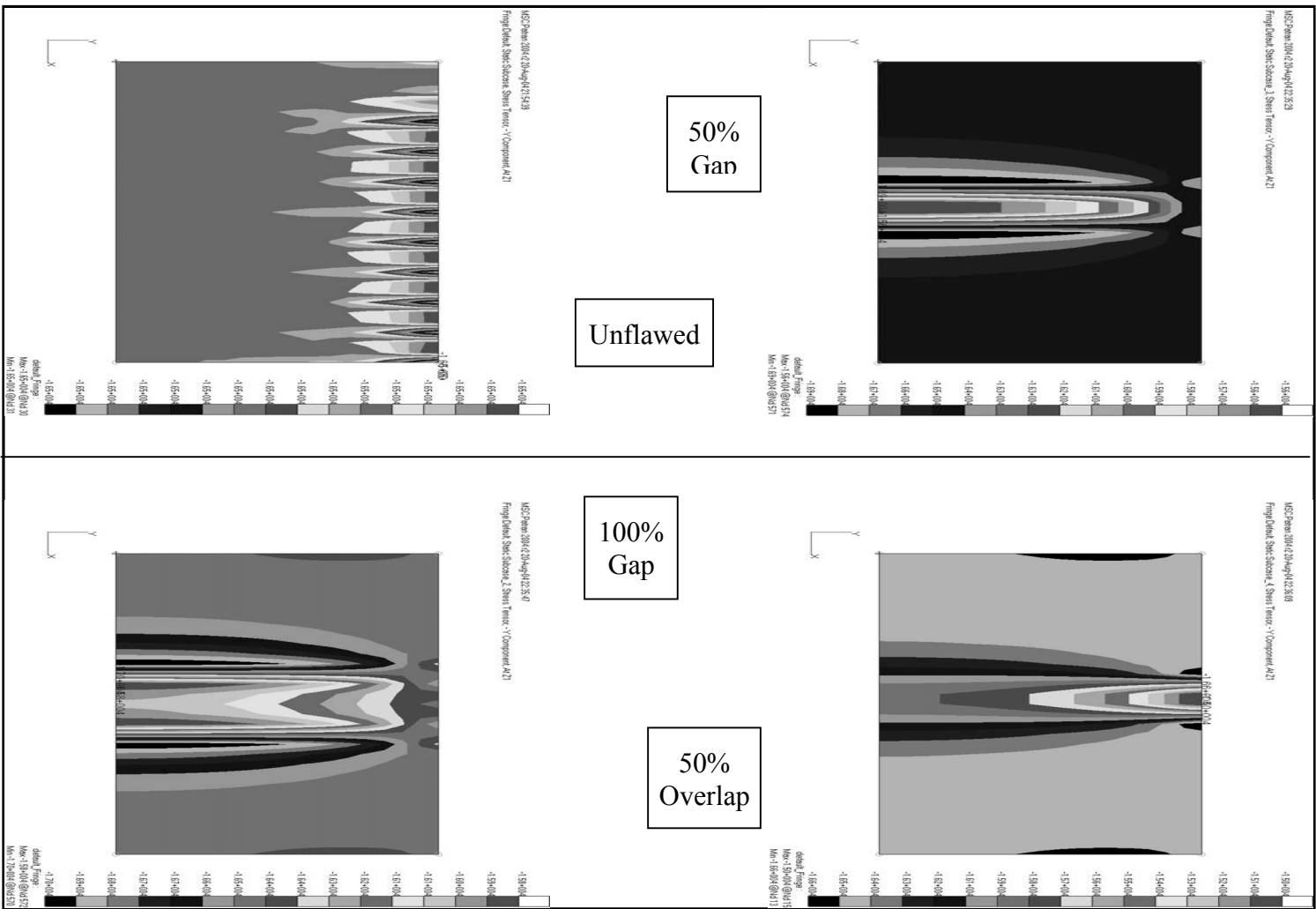


Figure 5.3.8 Nastran Analysis Results for On-Axis Flaws

5.3.1.2 Off-Axis Analysis

The off-axis analyses, like the on-axis, consist of a unflawed, 100% and 50% gap and 50% overlap analysis. Each flaw has its own unique stacking sequence as listed.

- [5(90), 90, 5(90)] - Unflawed
- [5(90), resin rich zone, 5(90)] – Gap Flaw
- [12(90)] – Overlap Flaw

The gap flaws vary in width, but maintain the same stacking sequence.

The model is created as a full gage section. This must be done because the flaws run the width of the specimen, at the center. Since the specimen is not symmetrical the boundary conditions that constrain the specimen are stricter than that of half a specimen. Now the required constraints have to be a fixed-fixed condition at the bottom of the specimen to simulate the grips of a compression test. One additional constraint is needed to ensure that the only movement that the specimen sees is in the axial direction. This constraint keeps the specimen from rotating out-of-plane and restricts movement in the transverse and out-of-plane directions. Figure 5.3.9 shows the boundary conditions and where they are located. To create a compressive load on the specimen a distributed load equaling 1000 lbs is also placed along the top of the specimen.

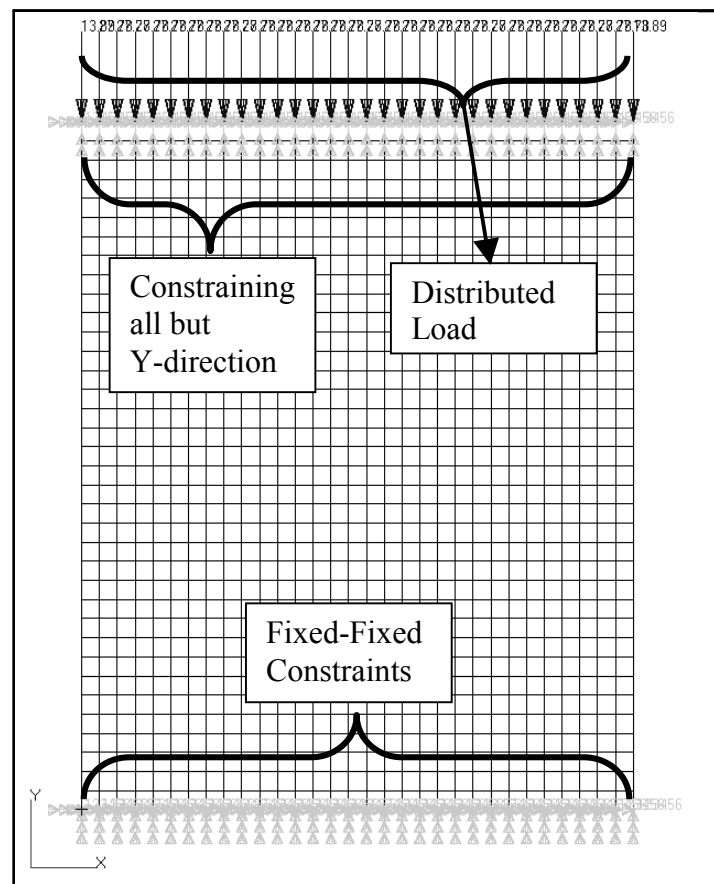


Figure 5.3.9 Off-Axis Loads and Boundary Conditions

The gap flaws are a resin rich zone in the center of the laminate as shown in Figure 5.3.2. The width of the gap varies depending on the gap type. The overlap flaw is modeled as a three element strip at the center where there is an extra layer of fibers. The laminate at the center strip location is one ply thicker than the rest of the specimen, as shown in Figure 5.3.7

The results from the analyses are shown in Figure 5.3.10 and listed in Table 5.3.2. The base line stress is $-2.14\text{E}4$ psi. Table 5.3.2 lists the critical stress for each flaw condition and the percent difference that the each has compared to the specimen with no flaw. The flaws in this case have little to no effect on the stress levels with the large effect being less than 1%. The flaw only makes up a small percentage of the specimen and therefore has little influence on the global response. Also the load direction is perpendicular to the fiber and flaw direction. The Poisson's effect will cause the sample to expand laterally, but there is no constraint in the lateral direction. Therefore stress is not present in the center of the gage section where the flaw is located and there is no effect from the flaw. In the axial direction the resin has the largest effect on the stiffness and strength of the laminate. Therefore the flaws will have little or no effect on the compressive strength of the laminate across the fibers. The data only gave a small difference in the stresses. The fabrication and mechanical testing of specimens is not warranted.

Table 5.3.2 Critical Stress for Common Tow Flaw Compressive Analyses

Flaw Type	Critical Stress (MPa, [psi])	Percent Difference (%)
No Flaw	$-2.14\text{E}4$	- -
100% Tow Gap	$-2.15\text{E}4$	0.47
50% Tow Gap	$-2.14\text{E}4$	0.00
50% Tow Overlap	$-2.14\text{E}4$	0.00

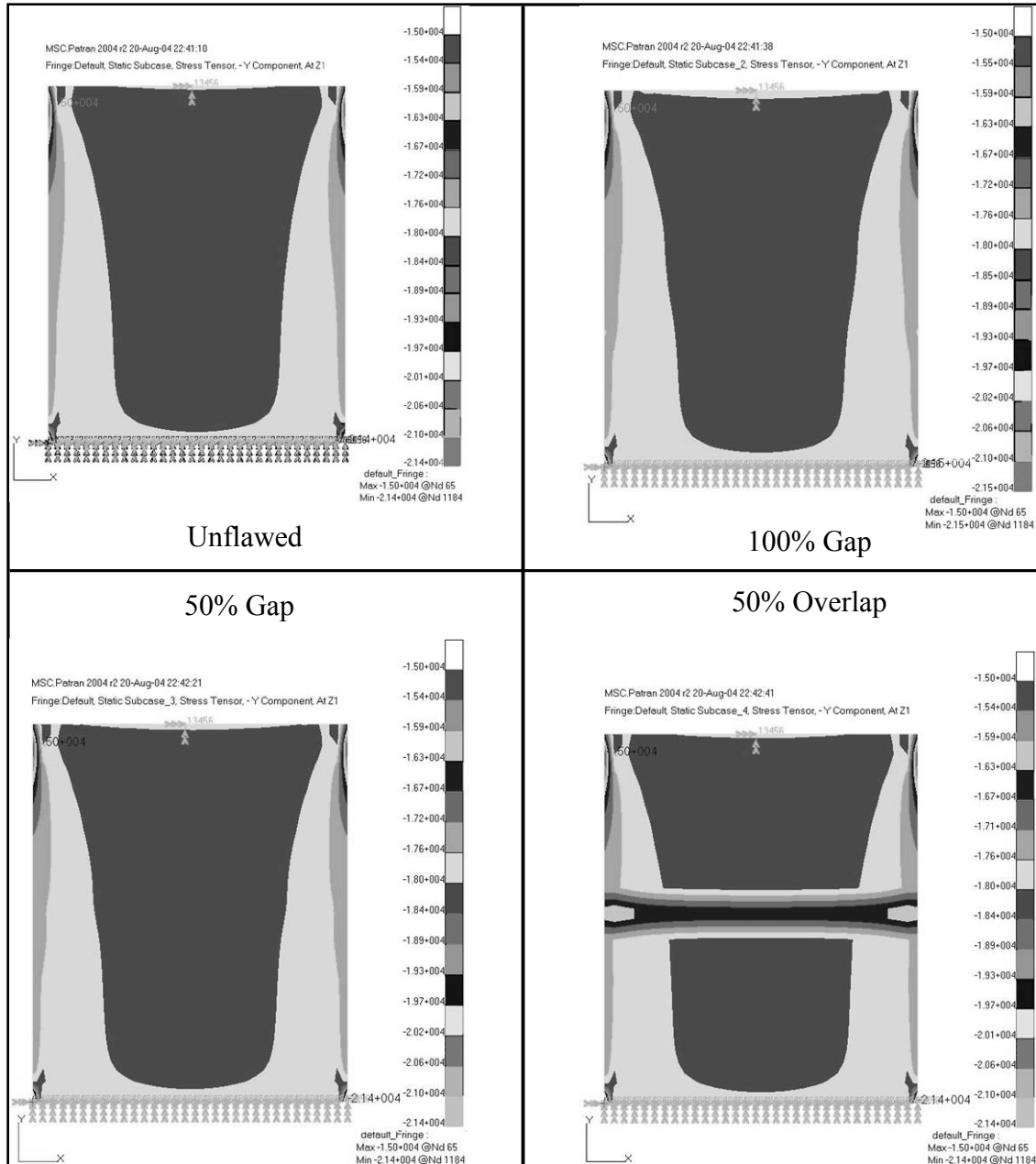


Figure 5.3.10 Nastran Analysis Results for Off-Axis Flaws

5.3.1.3 Modified Off-Axis Analysis

The modified off-axis analysis, like the on-axis and off-axis, consist of a unflawed, 100% and 50% gap and 50% overlap analysis. Each flaw has its own unique 11 ply stacking sequence as listed:

- [5(90), 0, 5(90)] - Unflawed
- [5(90), resin rich zone, 5(90)] – Gap Flaw
- [5(90), 2(0), 5(90)] – Overlap Flaw

The gap flaws vary in width, but maintain the same stacking sequence.

The model is created as half of the specimen. This can be done because the flaws run the length of the specimen and there is an axis of symmetry across the center. Since the specimen is symmetrical the boundary conditions that constrain the specimen are more lax than that of an entire specimen. All that is required is constraints that oppose the load at the bottom of the specimen. Two more additional constraints are needed to ensure that the only movement that the specimens see is in the axial direction. The first is a constraint at that keeps the specimen from rotating out-of-plane, and the second restricts movement in the transverse direction. The boundary conditions and where they are located are the same as with the on-axis analysis.

The sample is constructed of 540 square elements with 30 across the width and 18 in length. The width is taken from the five tows having six elements across. This allows for all the flaws analyzed to be modeled with either a six element width or a three element width. The gap flaws are considered to be a resin rich zone in the flaw location, and the overlap flaw is a thin strip where there is an extra layer of fibers. If the samples were examined so the ends were visible they would look like Figures 5.3.11-5.3.13, where the circles represent the elements and the dark areas are resin. Notice that the 50% overlap is one ply thicker than the rest of the specimen at the flaw location. The twist flaw is not modeled due to its difficult geometry.

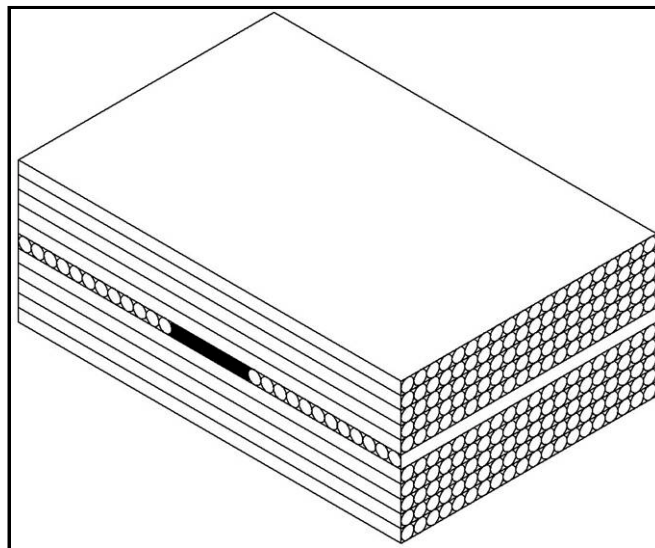


Figure 5.3.11 Representation of 100% Gap Sample

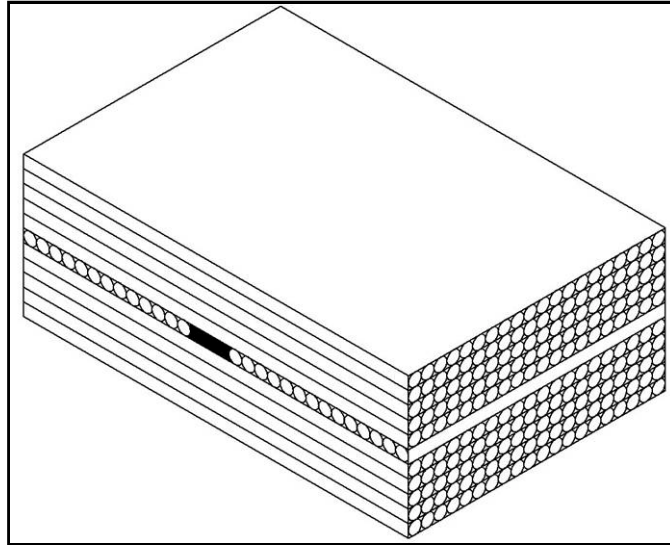


Figure 5.3.12 Representation of 50% Gap Sample

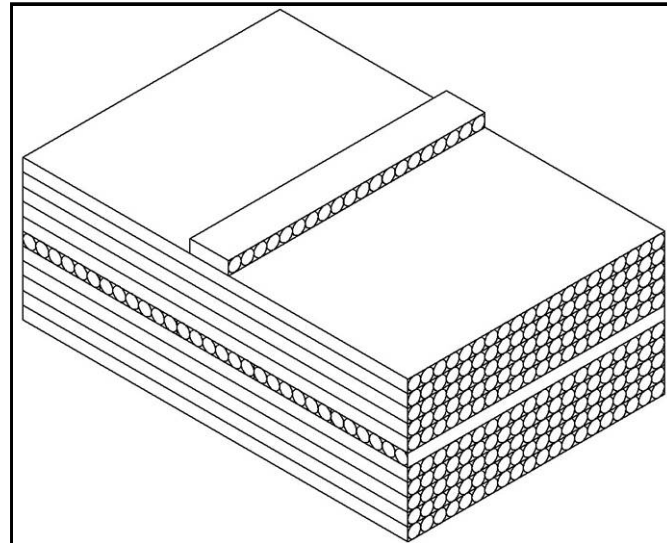


Figure 5.3.13 Representation of 50% Overlap Sample

Strength, which is a function of the applied load, is negatively proportional to the critical stress. The critical load is the maximum stress within the sample at a given load. When the critical stress reaches the failure stress the sample fails. The critical stress is not the failure load. Thus the failure load is the applied load that results in a critical stress greater than or equal to the failure stress.

The results from the analyses are shown in Figure 5.3.14 and Table 5.3.3. The base line stress is $-1.40\text{E}+4$ psi. The largest percent difference is 2.9% given by the 100% flaw sample. This is small and would be difficult to see in mechanical testing because a scatter of 5% is expected. From Table 5.3.3 it is clearly seen that all the specimens with flaws have reductions in strength. The next step for this study would be to build specimens with flaw and destructively test them to determine the actual reduction in strength. Unfortunately the theoretical difference is

much too small to indicate that there will be a noticeable difference in the mechanical testing. Therefore it is concluded that there is no need to fabricate and mechanically test specimens.

Table 5.3.3 Critical Stress for Common Tow Flaw Compressive Analyses

Flaw Type	Critical Stress (psi)	Percent Difference (%)
No Flaw	-1.40E+4	- -
100% Tow Gap	-1.44E+4	2.9
50% Tow Gap	-1.43E+4	2.1
50% Tow Overlap	-1.41E+4	0.71

Like with the on-axis analysis, this data trend shows that the more severe the flaw the more likely the strength will be reduced. The severity of these flaws ranked highest to lowest is: 100% gap, 50% gap, 50% overlap. Clearly the 100% gap flaw has the largest effect based on the results in Table 5.3.3.

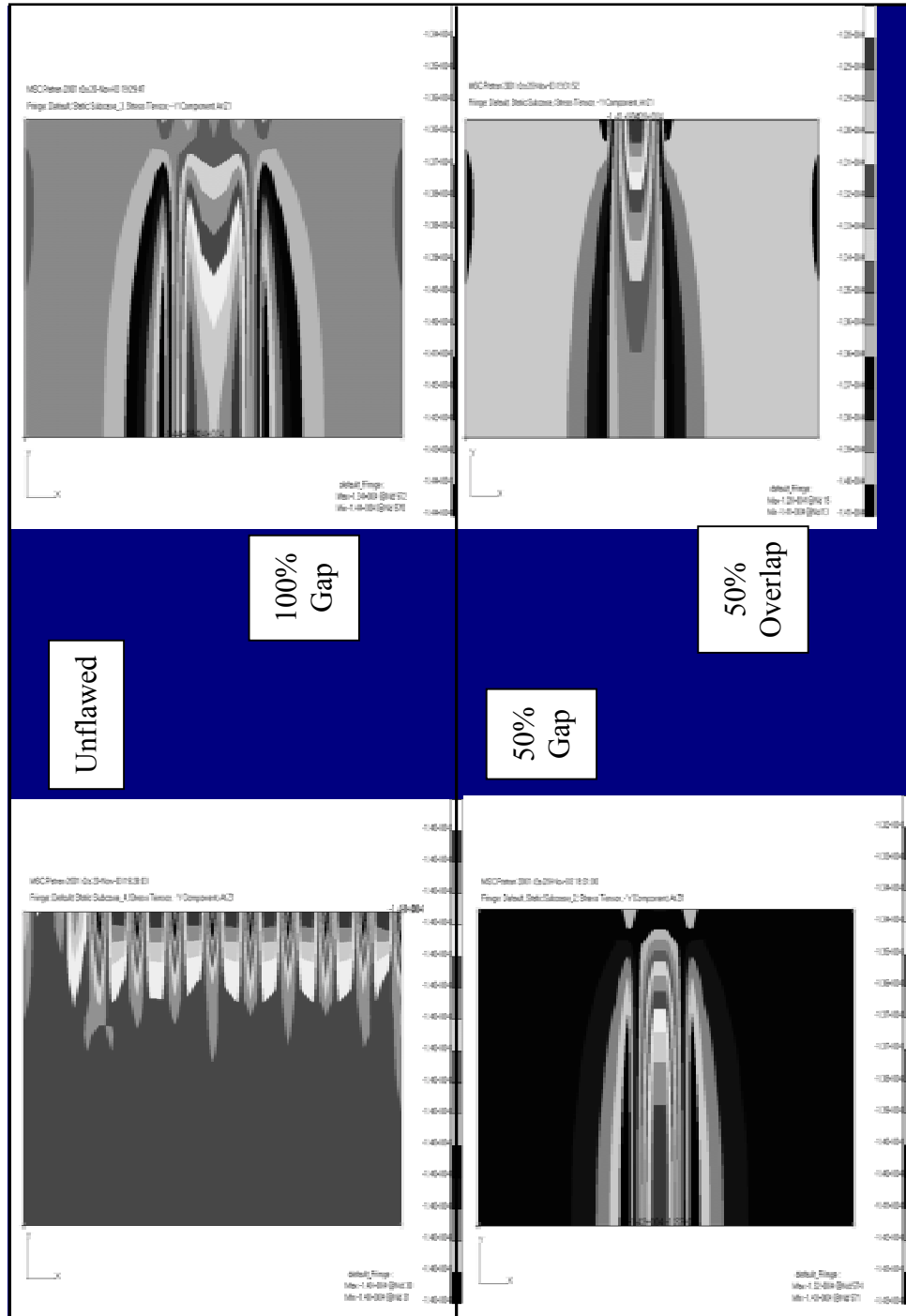


Figure 5.3.14 Nastran Analysis Results for Modified Off-Axis

5.3.2 Nondestructive Evaluation

Ultrasonic nondestructive evaluation was used to determine the quality of the panels fabricated. The panels were scanned with the C-scan capabilities of the SONIX CSF 1000-3X. The quality of the panels is assessed relative to each of the other panels. Inconsistencies in the

time of flight (TOF) and energy amplitude readings are looked for to determine the quality. These inconsistencies may represent flaws such as voids, delaminations, or inclusions. If there is an inconsistency in the C-scan this will exhibit as an area of different color that indicate a change in energy amplitude and TOF. The histogram of the energy reading for the panel is also examined. The histogram shows the distribution of the energy for the panel. The distribution is best if it is not spread out, but in a single peak. The latter is, of course, not practical as we are using a broadband ultrasonic transducer, with a center frequency of 5 Mhz. Nonetheless, the wider the distribution the worse the quality of the panel.

The scan images show the panels in the upright position. The top edge is at the top of the image and the top surface is facing up with the fibers running from top to bottom edge. Figure 5.3.15 illustrates this point. Figure 5.3.15 and Figure 5. through Figure 5. (Appendix A) are the C-scans for the panels fabricated for this research. The histograms for each panel clearly show that the panels are relatively consistent in mechanical properties. The C-scans also show that there are no apparent voids, delaminations, or inclusions in the panels scanned. This indicates that the panels are uniform in mechanical properties. Something that should be noted is the lack of flaws present in the C-scan images. The expected results from the C-scan are that the flaws will scatter the energy at the boundaries. This would have shown up in the energy scan image, but is clearly not present. The presence of lines indicating fiber direction is apparent though.

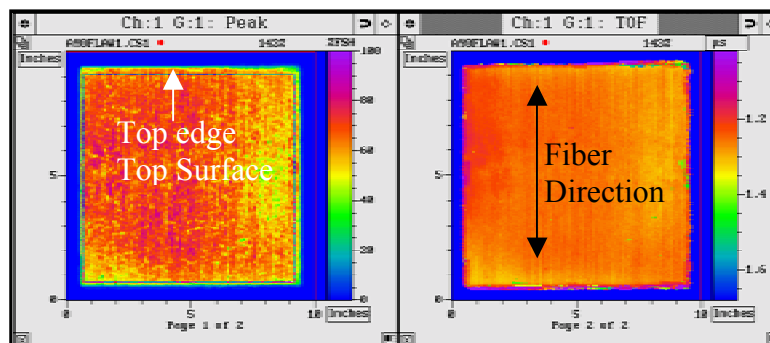


Figure 5.3.15 Peak Energy and TOF for Panel without Flaws (Tape Panel)

The time of flight (TOF) image, Figure 5.3.15, gives an indication of the thickness variation within a panel. If there is thickness gradient in the panel the TOF image will change color dramatically. In Figure 5.3.15 the color of the image does not vary much on the scale. Therefore it can be assumed that the panel thickness is reasonably constant.

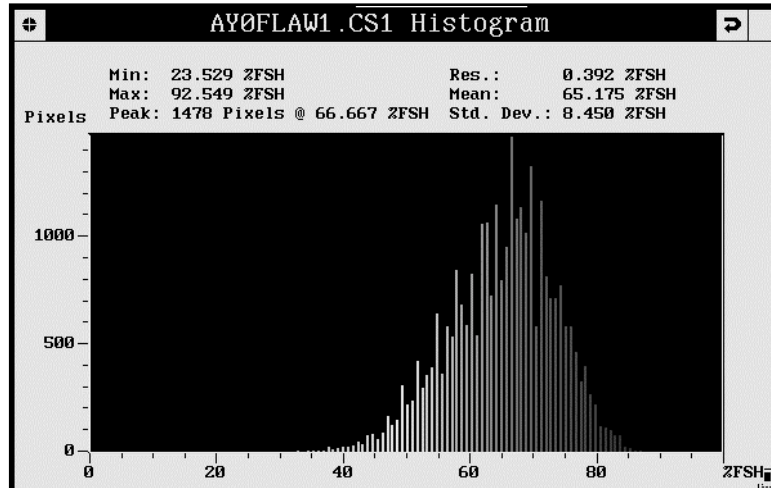


Figure 5.3.16 Histogram for Panel without Flaws (Tape Panel)

5.3.2.1 Attenuation Analysis

Attenuation is a measure of the quality of a material in nondestructive testing. If the attenuation was something that is of interest, then a attenuation measurement would be taken. For this research a relative comparison between panels is all that is needed to show the attenuation. All panels were scanned at the same energy setting so that a direct comparison can be made. The relative difference from panel to panel is determined using Equation 5.4.

$$\Delta \text{Atten} = 20 \log_{10} \left(\frac{\% \text{FSH}_r}{\% \text{FSH}} \right) \quad \text{Equation 5.4 [5.22]}$$

Where:

$\% \text{FSH}_r$ is the peak energy of the reference panel as a percentage threshold

$\% \text{FSH}$ is the peak energy as a percentage threshold

The panels with the highest peak energy are selected at the reference panel and the change in attenuation is calculated with respect to the reference panel. For both the tape and tow calculation the non-flawed panels have the largest peak energies. The calculated values for change in attenuation are tabulated in Table 5.3.4.

Table 5.3.4 Attenuation Data

	Peak Energy (%FSH)	Tape Attenuation Change (dB)	Peak Energy (%FSH)	Tow Attenuation Change (dB)
No Flaw*	66.667		83.922	
50% Gap	37.647	4.96	59.608	2.97
Twist	66.667	0.00	69.804	1.60
100% Gap	66.667	0.00	63.529	2.42
50% Overlap	66.667	0.00	59.608	2.97

A variation of 15 dB in a panel's response correlates to a 3% reduction in the axial modulus and a 5 dB variation is well within the industry accepted standards [5.23]. The largest change in attenuation is 4.96 and 2.97 dB for the tape and tow panels, respectively. There would appear to be no noticeable difference in each panel.

The variation in attenuation is in some part due to thickness differences and not variations in material properties. This attenuation difference should be characterized experimentally, but was not considered for this research and therefore not collected. To get an idea of how much change in attenuation is from thickness differences take a material with 100 dB/m, a fairly lossy material. Using the panel thicknesses from two panels, non-flawed ($t_1 = 0.0735$ ") and 50% gap ($t_2 = 0.0787$), the following calculation for the change in attenuation due to thickness is:

$$\Delta_{\text{atten}} = (t_2 (\text{in}) - t_1 (\text{in})) \times 100 \text{dB/m} \times 0.0254 \text{m/in} = 0.01 \text{dB}$$

This amount is very small and can be considered negligible when compared to the 5dB overall change in attenuation [5.23].

5.3.3 Photomicroscopy Studies

5.3.3.1 Flaw Locations

The initial rationale for polishing the edges of the panels was to make sure that the flaws are located in the place that they are suppose to be. But, the actual flaws within the panels are much more subtle than are shown in Figure 5.2.15. What was found is the fibers from around the gaps had filled in the gaps, as shown in Figure 5.3.17. Also, the ply boundaries are indiscernible from each other. This makes it increasingly more difficult to locate the flaws. To discern the flaw from the otherwise normal laminate, an area of less dense fiber volume must be found. There is a discernible pattern within the fibers that shows a path the fibers took to fill in the gaps, as shown in Figure 5.3.17.

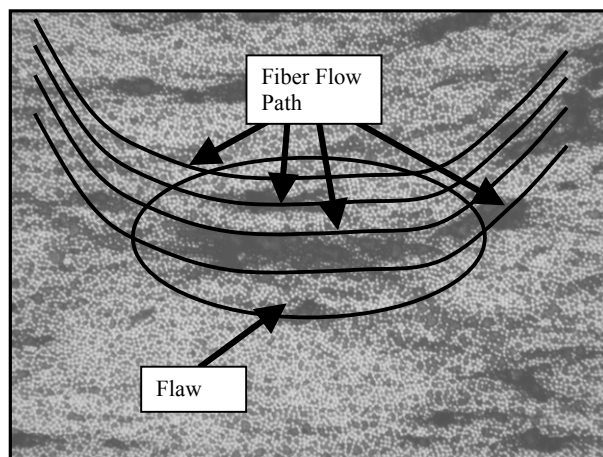


Figure 5.3.17 Gap Flaw from Photomicroscopy 10X

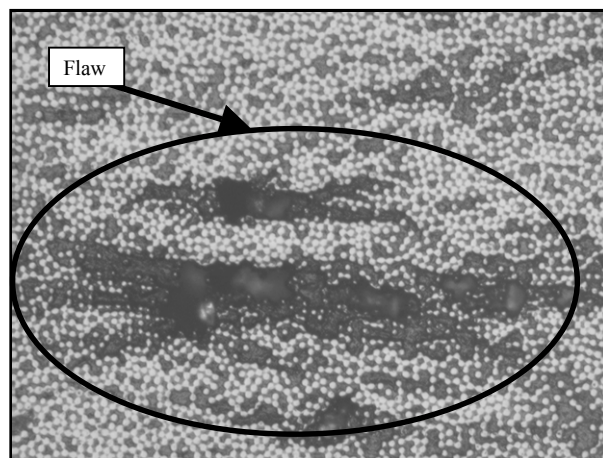


Figure 5.3.18 Gap Flaw from Photomicroscopy 20X

This discovery led to the realization that if there are fibers within the gap then the actual flaw does not match the theoretical analysis model. This leads us to consider the implications of the reduced mechanical properties prediction if the flaw does not match the theoretical model. The theoretical model assumed that there would be only a resin filled zone at the flaw location. Now there are fibers filling the gaps and therefore added strength within the flaw.

5.3.3.2 Damaged Fibers and Delaminations

During the testing there seemed to be a reduction in stiffness and premature buckling. In order for these to happen there must be a reduction in fiber volume or ply delaminations. To investigate this, several coupons were polished on the edge and under magnification individual fibers were examined for fractured fibers and delaminations.

A fiber fracture itself is a common occurrence in composites. There are many ways that fibers can be fractured without undermining the integrity of the laminate. Within an uncured composite there are broken fibers. Fibers can be damaged during fabrication. The process of cutting and polishing a composite can cause fiber to break. Also, if the fibers are not aligned properly the ends will look like fractures when in fact they are not. These types of fractures make it difficult to say with certainty that a significant fracture event has taken place. Evidence of a fracture event is found when there is a large area of fibers that have been fractured. An area of fractures with a delamination close by also signifies a fracture event. In Figure 5.3.19 the magnification is at least 20X. The fractures that are pointed out appear to be large but in fact are quite small when considering the magnification. Thus, there is no evidence that significant fractures have been taking place.

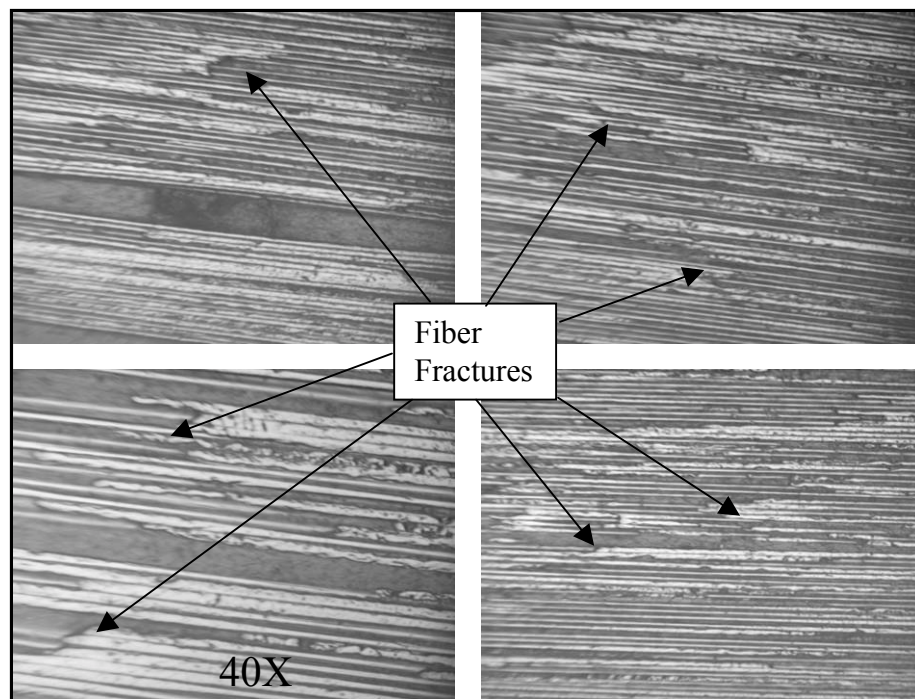


Figure 5.3.19 Fiber Fracture Examples 20X

5.3.4 Mechanical Testing

The mechanical testing produced data from two strain gages and one load cell. With this data and the known thickness and width of the specimens a stress-strain curve can be plotted for each set of strain and load. The plot in Figure 5.3.20 is a representative stress-strain curve for the specimens tested. This data is "raw" and for the most part not useful. In Figure 5.3.20 it is

seen that there is bending in the test, characterized by the separation in the plots of gage 1 and 2. Also notice the rapid divergence at the end of the curves which is believed to be buckling. A number of causes can be contributing to why this plot looks the way it does. The causes for bending include: bending due to misalignments in the specimen, bending due to thickness differences in the specimen, and bending from thickness differences in the tabbing bond line. The strain gages being misaligned could also contribute to the divergence of the curves, though the individual response would remain linear. Buckling, caused by the specimen being too thin, can also be induced prematurely by bending. In this section the data will be normalized to fiber volume and bending for comparison. Also, the results from the effects of the introduced flaws on initial stiffness, onset of nonlinearity, and strength will be discussed.

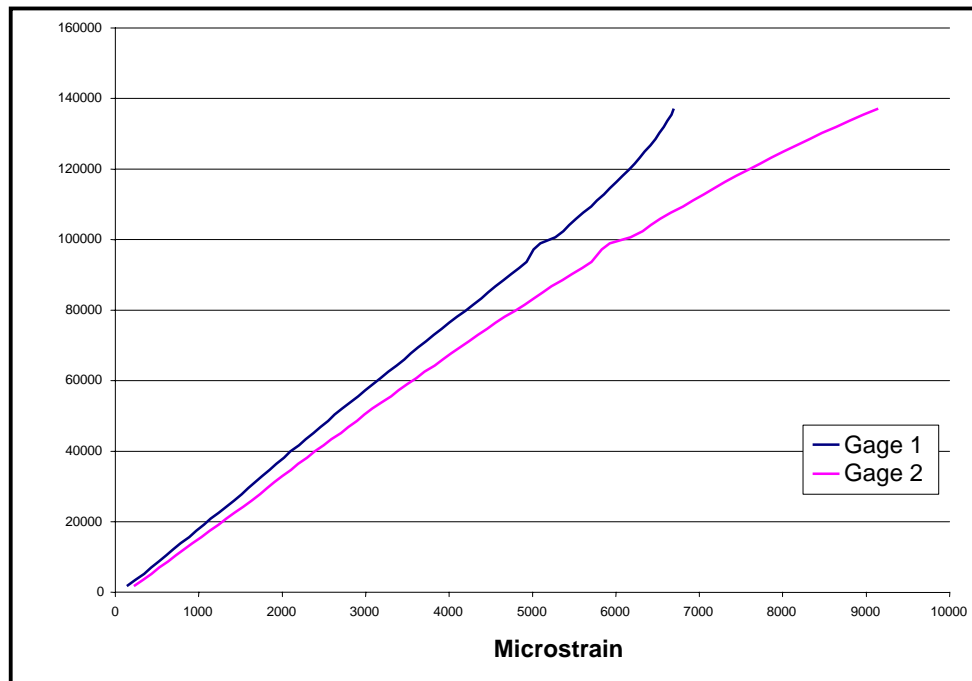


Figure 5.3.20 Raw Stress-Strain Curve Example

5.3.4.1 Normalization of Raw Data

The raw data collected during mechanical testing is typically skewed. This is because the specimens are not the same. The specimens have different dimensions that make the data difficult for comparison and differing fiber volumes. To make comparisons the specimens have to be normalized to some nominal value. In this case the specimens are normalized to fiber volume and bending.

To normalize to fiber volume a ratio of actual to nominal thickness is multiplied times the value of interest. In the case of stiffness some approximations are used. The equation for stiffness of a unidirectional laminate is given in Equation 5.5, wherein it is assumed that fiber volume is invariant in sample width. To normalize the measured stiffness a ratio of actual thickness to nominal is multiplied times the stiffness, as seen in Equation 5.6.

$$E_{\text{meas}} = E_f \left(\frac{t_f}{t_{\text{act}}} \right) + E_m \left(1 - \frac{t_f}{t_{\text{act}}} \right) \quad \text{Equation 5.5 [5.2]}$$

$$E_{\text{norm}} = E_{\text{meas}} \left(\frac{t_{\text{act}}}{t_{\text{nom}}} \right) \quad \text{Equation 5.6}$$

To normalize the raw data to bending, an understanding of the data is required. The data is collected as two simultaneous strains at one stress. Figure 5.3.21 shows how there are two strains associated with one stress. By normalizing the data to bending there are stresses calculated for each strain.

The stress from the test is calculated as P/A , but this stress is not the "true" stress resulting from the strain response, because bending is involved. The true stress should be the test data stress plus or minus the stress due to bending. This is indicated by the arrows in Figure 5.3.21.

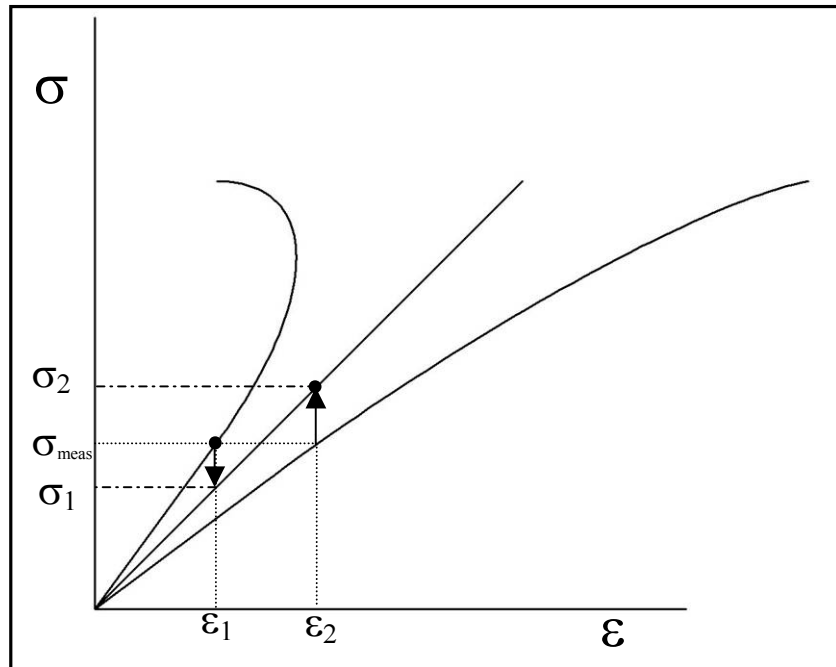


Figure 5.3.21 Illustration for Normalizing for Bending

In this situation it is known that the strains are "true" but the stress is not. Also known is the axial load, P , cross sectional area, A , distance from the neutral axis, c , and moment of inertia, I . Equation 5.7 is the three dimensional Hooke's law for a material. The strain in the transverse and through thickness direction are not known and are of no concern since test data is in the longitudinal direction. Therefore, the lower two equation in Equation 5.7 are ignored. Also, due to the specimen not being constrained in the test section, the stress in the transverse and through thickness direction is zero within the gage section and can thus be discarded.

$$\begin{aligned}
\varepsilon_1 &= \frac{\sigma_1}{E_1} - \frac{\sigma_2}{E_2} v_{21} - \frac{\sigma_3}{E_3} v_{31} \\
\varepsilon_2 &= -\frac{\sigma_1}{E_1} v_{12} + \frac{\sigma_2}{E_2} - \frac{\sigma_3}{E_3} v_{32} \\
\varepsilon_3 &= -\frac{\sigma_1}{E_1} v_{13} - \frac{\sigma_2}{E_2} v_{23} + \frac{\sigma_3}{E_3}
\end{aligned}$$

Equation 5.7 [5.24]

If equation 5.8 is added to the stress in equation 5.7 then equation 5.7 becomes equation 5.9. Now there are two equations with two unknowns, the local stiffness and moment, E and M, respectively. Solving for E and M Results in Equations 5.10 and 5.11.

$$\sigma_b = \pm \frac{Mc}{I}$$

Equation 5.8

$$\varepsilon = \frac{P/A \pm Mc/I}{E}$$

Equation 5.9

$$E = \frac{2P}{A(\varepsilon_1 + \varepsilon_2)}$$

Equation 5.10

$$M = \frac{-PI(\varepsilon_1 + \varepsilon_2)}{Ac(\varepsilon_1 + \varepsilon_2)}$$

Equation 5.11

Now using the stiffness calculated from equation 5.10 and the strains obtained from the test, new stresses are computed. The result is a single stress-strain curve that is normalized to bending, as shown in Figure 5.3.22.

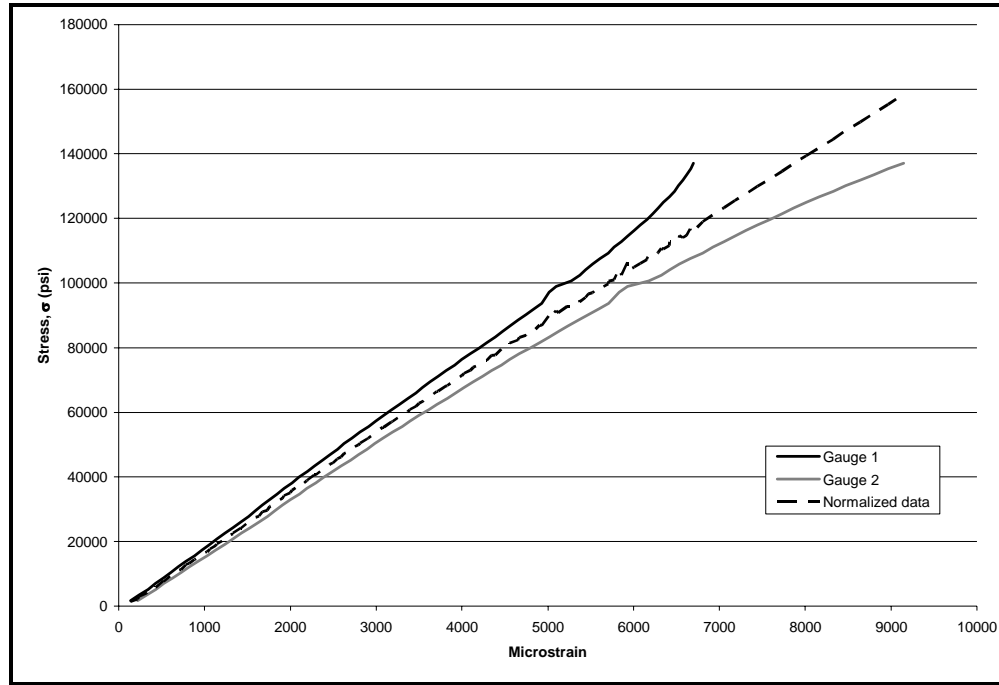


Figure 5.3.22 Representative Plot of Bending Normalized Data

5.3.4.2 Initial Stiffness

The introduction of flaws such as gaps, overlaps, and twists into a laminate could cause a change in stiffness. This would happen due to an increase or reduction in the fiber volume. Since gaps theoretically leave a resin rich area at the location of the gap, a reduction in the stiffness would be apparent in experimental data. Overlaps and twists would leave little or no gaps for a resin rich area and therefore would most likely not affect the stiffness of the laminate. To calculate the stiffness a function in Excel, called 'slope', is used to calculate the stiffness from each stress-strain curve and the bending normalized stress-strain curve. A range of data is selected that is believed to be in the linear elastic range of the material. This range is chosen to be between approximately 500 $\mu\epsilon$ and 2,000 $\mu\epsilon$.

Some of the specimens were loaded and unloaded multiple times without failure. In such cases the mean average is calculated. Next a mean average and standard deviation are calculated from the specimen averages for each family. Figure 5.3.23 and Figure 5.3.25 represent typical mean averages for the raw data and normalized to bending data, respectively. The raw and normalized data plots for all other families are located in Appendix B. Tables 5.3.6 to 5.3.8 list the data for each family.

Table 5.3.5 Initial Axial Compression Stiffness Raw Data for Tape Specimens

Specimen #	Non-Flawed	100% Gap	50% Gap	50% Overlap	Twist
	106 psi				
1	17.76	18.13	18.57		18.15
2		17.59	17.73	18.27	17.22
3	17.32	18.78	17.72	17.26	17.25
4		17.95	18.15	18.32	17.94
5	17.97	18.90	17.28	19.00	16.99
6		18.70	17.98	18.07	17.80
7	15.48	18.96		17.90	18.21
Mean	17.13	18.43	17.90	18.14	17.65
St Dev	1.14	0.53	0.44	0.57	0.49

Table 5.3.6 Initial Axial Compression Stiffness Normalized Data for Tow Specimens

Specimen #	Non-Flawed	100% Gap	50% Gap	50% Overlap	Twist
	106 psi				
1	19.07	19.13	19.50	20.07	19.36
2	19.06	19.43	19.86	20.16	19.65
3	19.65	19.83	20.36	19.95	19.84
4	20.09	19.24	20.13	20.76	19.72
5	19.94	19.31	20.85	20.06	20.92
6	19.63	19.34	20.17	20.73	20.29
7	19.26		19.82	20.68	20.11
Mean	19.53	19.38	20.10	20.34	19.99
% St Dev	2.1	1.2	2.1	1.8	2.6

Table 5.3.7 Initial Axial Compression Stiffness Normalized Data for Tape Specimens

Specimen #	Non-Flawed	100% Gap	50% Gap	50% Overlap	Twist
	106 psi				
1	17.73	17.88	18.48		17.98
2		17.06	17.65	18.29	17.18
3	17.31	18.62	17.72	17.28	17.29
4		17.90	18.16	18.30	18.05
5	17.92	18.60	17.23	19.01	16.90
6		18.74	17.94	18.03	17.19
7	14.98	18.64		17.90	18.23
Mean	16.98	18.21	17.86	18.13	17.55
% St Dev	8.0	3.4	2.4	3.1	3.0

The points labeled Gage 1, Gage 2, and Average are the stiffness calculated from gages 1 and 2 and the average between the two gages, in Figure 5.3.23. The data series in Figure 5.3.25 is the normalized mean data. The solid line is the mean average of the averages between the gages, for the family. The Dashed lines are the standard deviation band about the mean.

Figure 5.3.23 also illustrates anomalies that occur during testing. Specimens 1, 2, and 6 show a large difference in the stiffness taken from gages 1 and 2. This behavior can be attributed to bending during the test, gage misalignment, or a combination of both. From looking at the ultrasonic scans of this panel it can be seen that the bending is not from a thickness gradient in the specimen. The panel is reasonably consistent in thickness. Each specimen has a measured thickness difference in the tabbed sections. Figure 5.3.24 shows location where the tabs are measured. The tab section thickness difference is due to one or several of the following thickness variations:

- 1) $t_1 = t_2 > t_3 = t_4$ or $t_5 = t_6 > t_7 = t_8$
- 2) $t_1 = t_3 > t_2 = t_4$ or $t_5 = t_7 > t_6 = t_8$
- 3) $t_1 = t_2 = t_3 = t_4 \neq t_5 = t_6 = t_7 = t_8$
- 4) $t_1 \neq t_2 \neq t_3 \neq t_4 \neq t_5 \neq t_6 \neq t_7 \neq t_8$

Equation 5.12

These differences cause a moment to form during the test that produce bending.

The difference in the thickness at the tab section can be attributed to two causes. First is if the tabs are not of consistent thickness. This is unlikely because the tab material is purchased from a reputable dealer who certifies their material to Mil-I-24768/27 GEE-F standards. This leaves the second possibility, tab bond line thickness variation. The bonded tab thickness varies for each coupon. The measurements for the samples are located in Tables 5.8.1 – 5.8.10 in Appendix D.

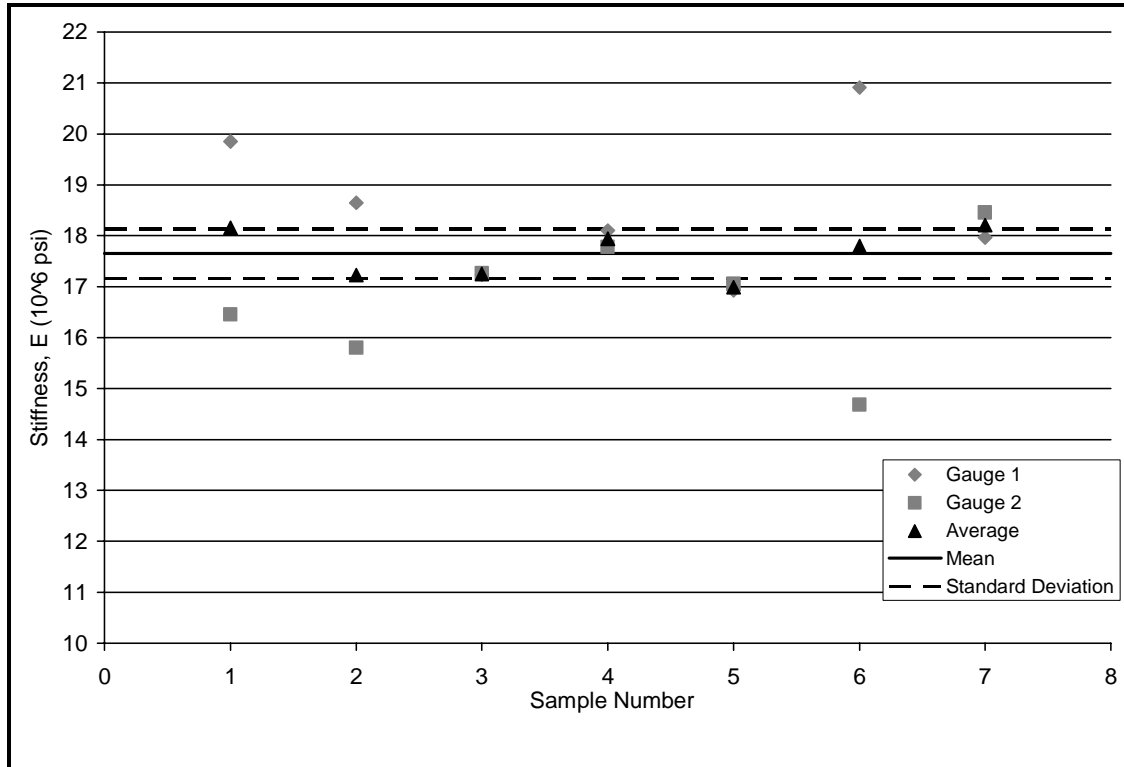


Figure 5.3.23 Initial Axial Compression Stiffness for Twist Tape Specimens

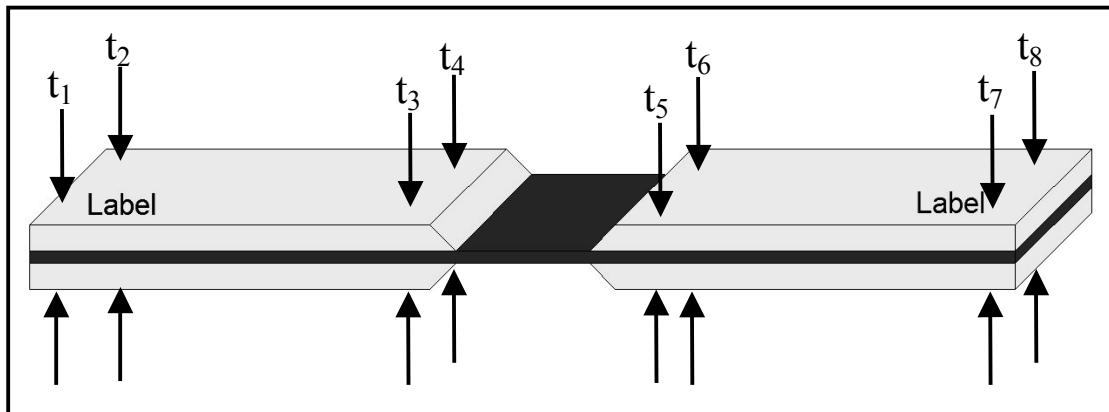


Figure 5.3.24 Thickness Measurements at the Tabs

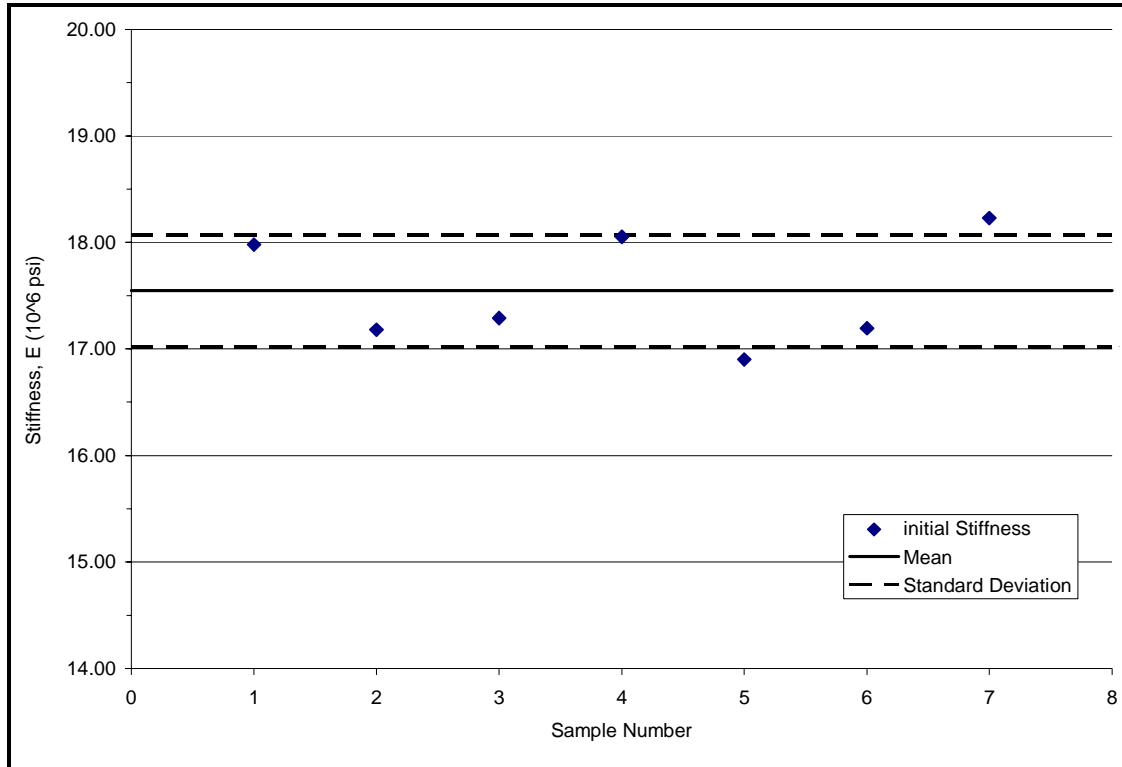


Figure 5.3.25 Initial Axial Compression Stiffness for Twist Tape Specimens Normalized to Bending

Two other possible reasons to explain the difference between gages 1 and 2 is gage misalignment and fixture misalignment. If a gage were misaligned the readings from that gage would not be entirely for the axial direction. A portion of the readings will be in the transverse direction, which was not of interest in this research. The fixture alignment had to be in alignment with the testing machine being used. If the testing machines load axis was different from that of the neutral axis of the specimen then a moment will be present and bending would occur. In specimens 3, 4, 5, and 7 the bending appears to be minimized. In each of these specimens the thickness in the tab sections was reasonably consistent. The variation that is present is most likely due to gage misalignments and misalignment in the fixture. How much each contributes cannot be known with any certainty.

A comparison of the initial stiffness of each family is made in Figure 5.3.27 and Figure 5.3.26. The data points represent the mean average and the vertical lines are the standard deviations for each family. The shaded region represents the baseline range of the non-flawed family.

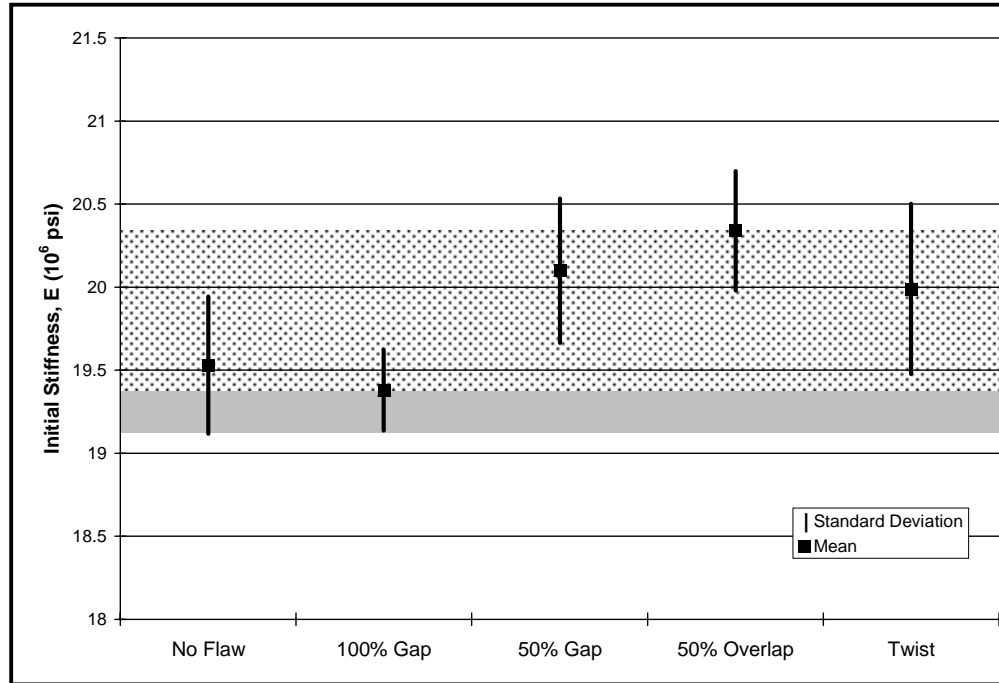


Figure 5.3.26 Axial Compression Stiffness Comparison Between the Tow Families

Like with the tape families the unflawed tow family has a stiffness that is lower than the flawed families. The attenuation can not be attributed to the reduction in this property because the Δ dB is within a 5% margin for each panel which is considered good in industry. There is a 1.4% difference between the largest and smallest standard deviation for the tow families. This indicates that the bending involved in testing was experience evenly by all families and is not the reason for the low unflawed family stiffness. As with the tape families testing was performed on two separate machines, but in this case only the first three samples of the unflawed family were tested on the MTS/Instron machine. But upon examining the data for these samples it was discovered standard deviation for this family was only 2.1% and the data from the MTS/Instron machine was scattered between the data from the Riehle machine. Thus, the use of two testing machines seems to have no effect on the data collected.

The specimens fabricated from prepreg tow show that all families have a similar standard deviation, with 1.4% difference between largest and smallest. The standard deviation can be attributed to any of the causes of bending, discussed previously, which can cause a large variability. Again the fabrication methods cannot have an affect on the amount of scatter created. The panels all have comparable properties, as discussed in Section 5.3.2.

The non-flawed family is considered the baseline for the comparison. Again the non-flawed family has a lower stiffness than the other families with one exception, the 100% gap family. The 100% and 50% gap and twist families seems to have a different stiffness than the non-flaw family, but it still overlaps the standard deviation of the non-flawed family. The dotted area in Figure 5.3.26, spanning from the lowest mean to the highest. contains at least a portion of each families data. The percent difference between the largest mean, 50% overlap family, and

the lowest mean, 100% gap, 4.7%. Because of this, it would be difficult to claim that these families have different stiffness due to their induced flaws.

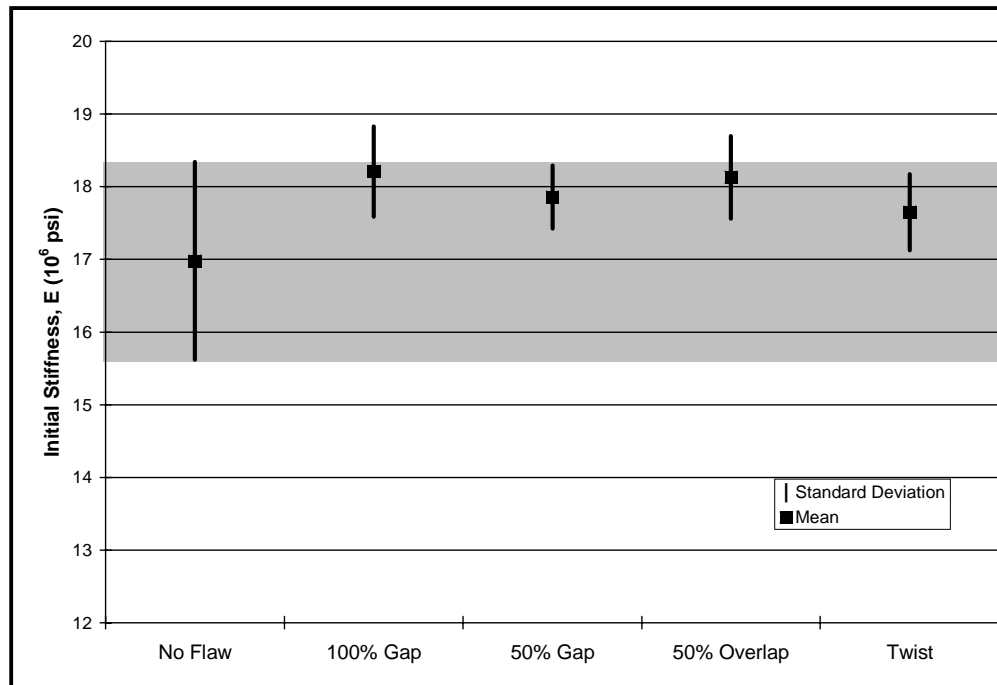


Figure 5.3.27 Axial Compression Stiffness Comparison Between the Tape Families

In Figure 5.3.27 the mean stiffness of the unflawed panel is lower than the other families. This should not be case. Instead the flaws should cause the stiffness to be lower in the flawed families. In Section 5.3.2.1 the attenuation was looked at to see if the properties are different for the panels. The properties are within a 5% margin that which is considered good in industry. Also examined was the bending in all the families. The bending in the unflawed family does not seems to be different from any other family in the tape group judging from the measurement in Appendix D. Thus the bending effect seems to not have an impact on the stiffness. The only other possibility is from the use of two different testing machines. The unflawed family was completely tested on the MTS/Instron machine and the other families were tested on the Riehle machine. The comparison shown in Figure 5.3.27 shows that all the flawed families have a larger stiffness. But as discussed with the tow group the use of two machines does not seem to have an effect on the data.

The specimens fabricated from prepreg tape show that the non-flawed family has a large standard deviation. The large standard deviation can be attributed to any of the causes of bending mentioned previously. The mean value of the unflawed family is less than that of the other families. This is not as expected. It is expected that the non-flawed family would have a greater stiffness than that of the 100% and 50% gap families and approximately the same stiffness as the 50% overlap and twist families. The properties of the families is not a factor in this because the panels are of comparable properties. Bending in the specimens, as described previously, and the use of two different machines during testing most likely are the cause of the large amount of scatter in the non-flawed family.

The non-flawed family is considered the baseline for comparison. Since the standard deviation is large, the other families at least partially fall within the bounds of the non-flaw standard deviation. There would appear to be no effect due to investigated flaws on stiffness in these tape specimens.

5.3.4.3 Onset of Nonlinearity

When a material is subjected to bending there is a point at which the stiffness becomes nonlinear. As discussed in Section 5.0 the testing had bending, the test specimens were experiencing nonlinear behavior after certain points in the tests. In other words, bending and later buckling became evident during the tests. This was the main reason for normalizing for bending. If bending is the only factor causing the nonlinearity in the raw data then normalizing to bending should create a straight line with constant slope. Instead the bending normalization created a stress-strain curve that was linear to a point and then became nonlinear.

To find the point at which the data became nonlinear a curve fit is applied to the normalized stress-strain curve. The stiffness at any point along the curve is needed to find the nonlinear point, so the derivative of the curve fit equation is taken. A change in stiffness of three percent was chosen to determine the stress at which a specimen is exhibiting nonlinear behavior. The strain is input in the curve fit derivative and the resulting stiffness is compared to the initial stiffness, calculated earlier. When the stiffness change reaches 3% then the stress value is recorded.

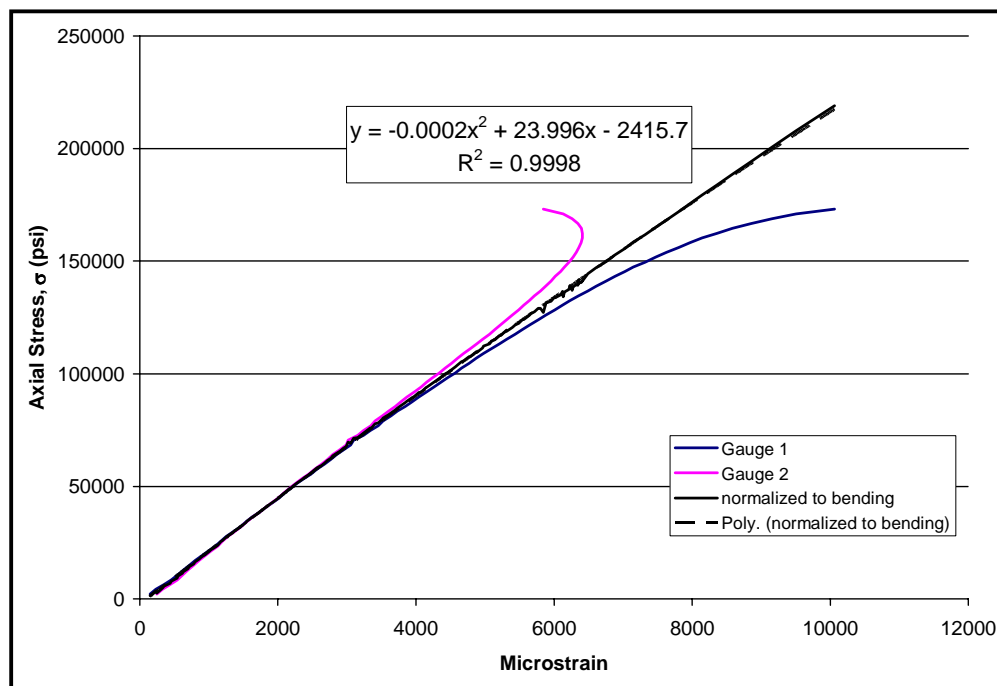


Figure 5.3.28 Curve Fit Example

Mean average values for each specimen and the family are calculated. The values for each specimen are listed in Table 5.3.8 And Table 5.3.9. Figure 5.3.29 and Figure 5. through Figure 5., in Appendix C, show the spread and standard deviation for each family.

Table 5.3.8 Mean Tow Axial Compression Stress for Onset of Nonlinearity

Specimen #	Non-Flawed	100% Gap	50% Gap	50% Overlap	Twist
	psi				
1	44258	57822	55808	62846	66870
2	47481	41419	57302	51508	58929
3	44310	39767	46961	55070	70005
4	58875	55623	49121	63120	70882
5	64841	55158	46799	62476	41669
6	--	47639	44325	53557	41805
7	68272	--	53174	40839	44530
Mean	54673	49571	50498	55631	56384
St Dev	10710	7775	4964	8118	13427
% St Dev	19.6	15.7	9.8	14.6	23.8

Table 5.3.9 Mean Tape Axial Compression Stress for Onset of Nonlinearity

Specimen #	Non-Flawed	100% Gap	50% Gap	50% Overlap	Twist
	psi				
1	41914	52631	54287	--	53447
2	--	77468	43374	34010	58610
3	38346	56969	46189	60964	79858
4	--	32915	53067	43989	49310
5	36359	36555	58929	33934	124251
6	--	32961	45235	70835	112630
7	36479	33730	--	44690	47043
Mean	38275	46176	50180	48070	75021
St Dev	2591	17006	6139	14900	31728
% St Dev	6.8	36.8	12.2	31.0	42.3

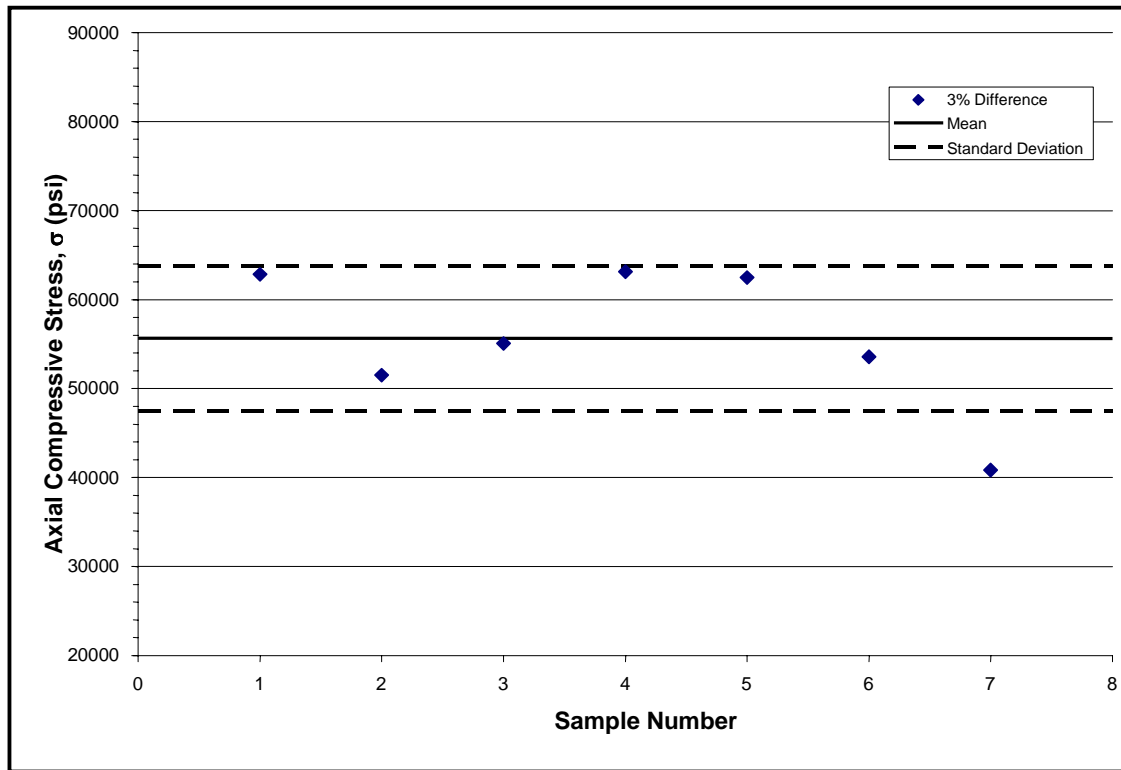


Figure 5.3.29 Onset of Nonlinearity for 50% Overlap Tow Specimens

From looking at Table 5.3.8, Table 5.3.9, and Figure 5.3.29 it can be seen that there is large variation in the families. As discussed in Section 5.3.2.1 the material properties of the specimens do not vary widely. This leaves only a few possible explanations: fiber failures and specimen bending. In Section 0 it was shown that there are fibers failing in the transverse direction. These failures are mostly induced from bending of the specimen. The causes of bending have been discussed in Section 0.

All data has been normalized to fiber volume and attenuation calculations have been performed. As discussed in Section 5.3.2.1 the attenuation between panels is less than 5 dB which is a quality composite in industry. Thus the material properties of the data is directly comparable within tape or tow groups. Nonetheless, the onset of nonlinearity for the unflawed tape family is lower than the other families. In Section 0 the use of two testing machines was discussed to try and explain the apparent reduction in stiffness of the unflawed family. It was determined that the use of two testing machines was not a factor in the lowered stiffnesses and thus is not be a factor for the onset of nonlinearity.

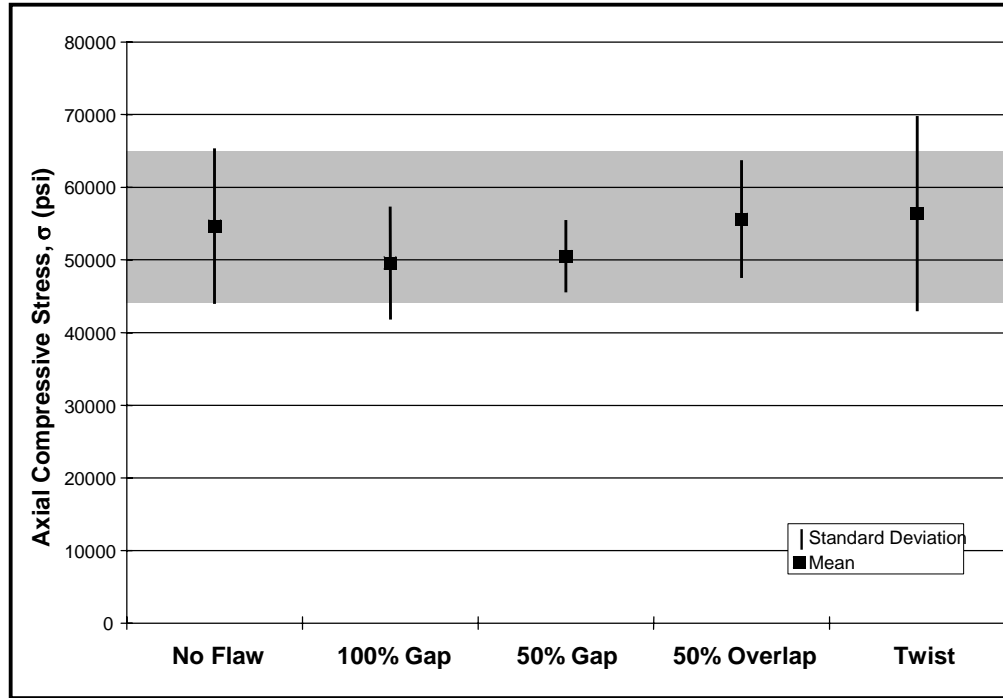


Figure 5.3.30 Nonlinearity Onset Comparison Between the Tow Families

The tow family's mean values show a trend that indicates that the flaws have an effect on the onset of nonlinearity. The means show that with a more severe flaw like the 100% gap flaw the onset of nonlinearity is reached at a lower stress. But, in Figure 5.3.30 most of the data falls into the grey scatter band that makes up the non-flawed family. Because the non-flawed family has such a large amount of scatter there is no conclusive evidence to support that the flaws reduce the point at which nonlinearity begins for the tow families

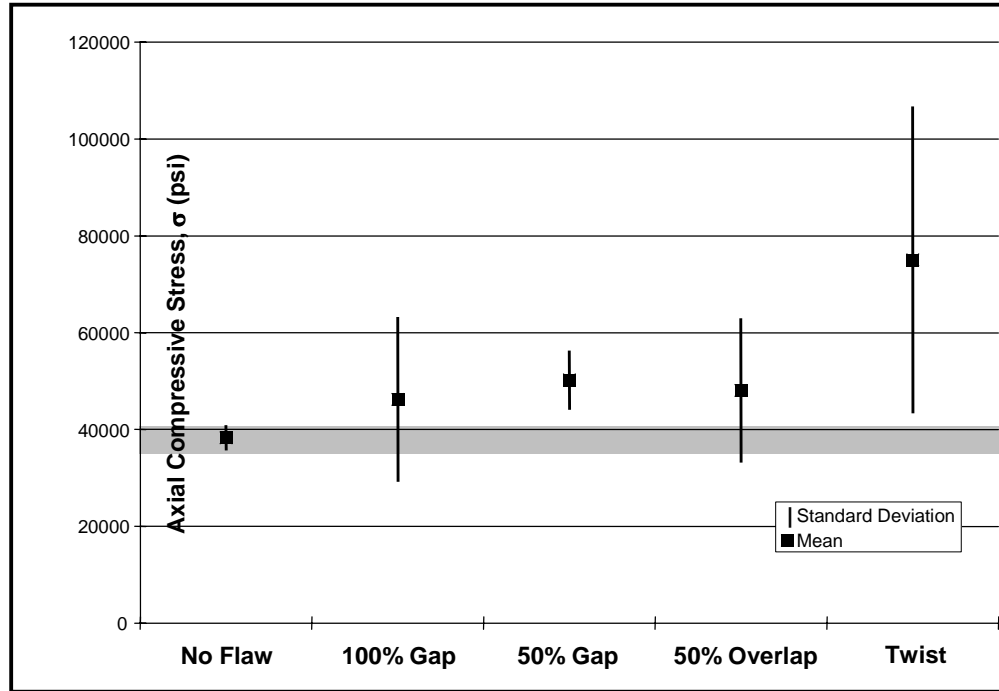


Figure 5.3.31 Nonlinearity Onset Comparison Between the Tape Families

The tape families show a different situation, as seen in Figure 5.3.31. In this case the standard deviation band for the non-flawed family is small but the family means do not show an effect from the flaws. In fact the unflawed family has the lowest stress for the onset of nonlinearity. The reasoning for this trend is that the tape families each experienced a different amount of bending. Bending is the main contributing factor in the onset of nonlinearity. The unflawed family experience a larger bending moment due to the bond line in the tab section being uneven. Thus the unflawed family has a lower stress at which the onset of nonlinearity begins.

5.3.4.4 Strength Results

The property most likely to be effected by the introduction of flaws is the strength. Introducing flaws will change the local fiber volume of the laminate. This will cause a local change in stiffness and could create a stress concentration at the boundaries of the flaw. The tests were designed to be taken to failure but in many cases a specimen was not loaded to failure because the two strain gages were diverging. Due to incomplete tests the data collected is incomplete and accurate statistical data cannot be drawn from the values. Table 5.3.10 and Table 5.3.11 list the mean strength values for each specimen and the mean and standard deviation for the family.

Table 5.3.10 Mean Tape Values for Laminate Strength

Specimen #	Non-Flawed	100% Gap	50% Gap	50% Overlap	Twist
	psi				
1	234672	307390	358259	--	--
2	--	--	--	--	--
3	371840	363238	363978	381716	341832
4	--	342986	280047	351543	361087
5	400623	--	--	358203	--
6	--	--	313095	353334	--
7	376458	--	--	300097	302334
Mean	345898	337871	328845	348979	335084
% St Dev	21.7	8.4	12.1	8.6	8.9

The values in Table 5.3.10 and Table 5.3.11 are normalized to fiber volume and bending the same all data. In this case the stress at failure does not take into account the bending. This stress is simply the load at failure divided by the cross-sectional area. The moment from the bending normalization has to be factored back into the failure stress measured during the test.

Table 5.3.11 Mean Tow Values for Laminate Strength

Specimen #	Non-Flawed	100% Gap	50% Gap	50% Overlap	Twist
	psi				
1	325986	--	--	373348	--
2	330241	--	--	294331	--
3	334081	--	--	304721	--
4	--	--	--	274201	--
5	--	--	--	258852	220979
6	--	--	--	305032	--
7	--	298521	--	340611	251522
Mean	330103	298521	--	307299	236251
St Dev	1.2	--	--	12.7	9.1

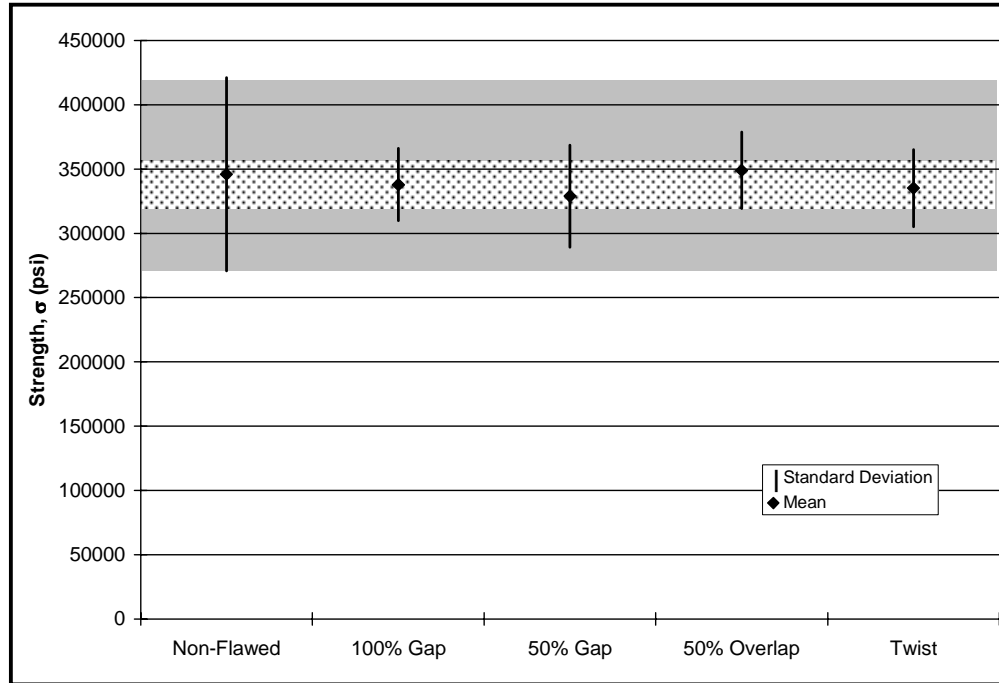


Figure 5.3.32 Strength Comparison Between the Tape Families

Figure 5.3.32 is a summary of the strength values for the five families in the tape group. It is seen that the mean values for each family all fall within a narrow scatter band (dotted region) of about 17,000 psi wide, or 5% of the mean. This would seem to be very conclusive for no change in strength due to induced flaws is evident since the band is so small compared to the mean values. But, the standard deviation data must also be taken into consideration. The standard deviation of the non-flawed family is large and overlaps the data from the other families. Since the non-flawed family has a large amount of scatter the effect of flaws on the strength of the laminate is small or nonexistent. But this data is incomplete, and therefore not accurate. Though the statistical data shows that there is no effect from the flaws, there are not enough values to get a good statistical average to make a definitive conclusion. The data could be skewed from the use of two different testing machines. Data from the initial stiffness and onset of nonlinearity indicate that the unflawed families have lower mean values.

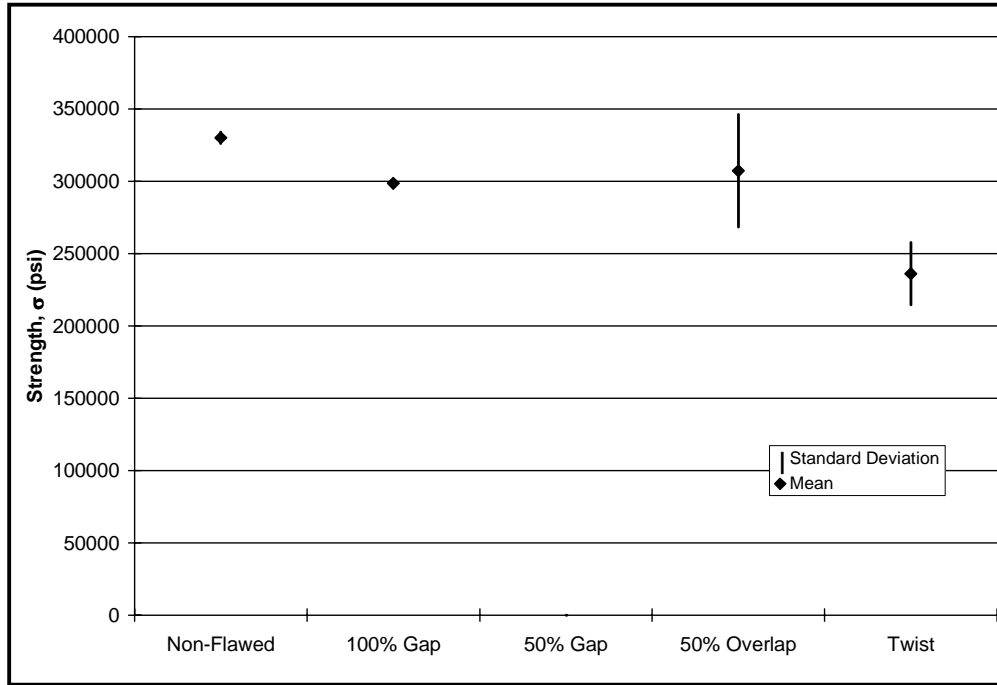


Figure 5.3.33 Strength Comparison Between the Tow Families

For the tow families, even fewer specimens were failed in the tow families, shown in Table 5.3.11 and Figure 5.3.33. The mean values from the testing show that there is a reductions in the laminate strength due to the flaws, but there is not enough data to make a definitive statement to that effect.

5.4 General Conclusions

5.4.1 Conclusions

The effect of using two machines is shown to be insignificant, and not responsible for variations in unflawed and flawed samples. Nonetheless, the practice of using multiple test machines is admittedly poor. Additional unflawed samples could be tested to remove any question of variability in this data, but the results will not vary from the documented scatter bands.

5.4.1.1 Effect on Initial Stiffness

The reduced fiber volume in the specimens with gaps, in theory, should have reduced the initial stiffness of the laminate. In actuality the stiffness did not have a noticeable change. The lack of change in stiffness is contributed to the lack of a defined flaw within the laminate. The gaps became filled in with the fibers of the adjacent plies. The overlaps, on the other hand, became distributed throughout the neighboring plies. Had there been a non-0° ply above and below the flaw this may have been different. The use of two testing machines does not indicate that the data was skewed from their use. Nonetheless, there does not seem to be an explanation for the lower stiffness. Even though, the comparison of the families clearly show that there the flaws had no effect on the initial stiffness of the laminate.

5.4.1.2 Effect on the Point of Nonlinearity

The point at which the laminate compressive stress-strain response becomes nonlinear was examined because of the bending occurring during testing. It was believed that the flaws would have an effect on the point at which the laminate properties exhibited nonlinear behavior. There was no conclusive microscopy evidence to prove that premature fiber failure was causing the nonlinearity. But, the scatter in the data was so great in most cases that all data overlapped. Thus no conclusive evidence to this affect is present that the flaws had any effect on this point.

5.4.1.3 Effect on the Axial strength

The axial strength of the laminate is dependent on the number of fibers within. Since the addition of flaws changes the number of fibers in the laminate, it would seem that there would be a change in the strength. Nastran analyses and mechanical testing both show that there is little or no effect on the axial strength of the laminate due to flaws examined in this study.

5.4.2 Recommendations for Future Research

5.4.2.1 Fabrication -- Lay-up of tape and tow

The fabrication of panels, from which the specimens are taken, introduced much of the error experienced in testing. The location of the flaw within a specimen was not guaranteed. This came about because the method of placing the flaws in the laminate was inaccurate. The

paper used to space the flaws, in the tape panels, had to be measured and cut out and then placed by hand. The paper also was easily damaged. A solution to this problem would be a more permanent spacer. Also an automated cutting system would reduce discrepancies in the prepreg strips used in the tape panels.

The tow panels, also, had to be laid up by hand. This meant laying down individual tows. Industry does not lay-up prepreg tow in this manner because of time and labor issues. The amount of time is inversely proportional to the amount of control exercised in tow placement. Even then, the quality of the tow lay-up is only as good as the attention taken in performing the task. An automated tow laying machine would greatly increase the accuracy and decrease the time to lay-up a panel. Also, any errors that occur with the tow laying machine should be repeatable. Where as the error with hand lay-up is most often not.

5.4.2.2 Fabrication -- Tab Thickness and Placement

The bending that occurred in testing was mostly caused by the thickness difference in the installed tabs. The largest culprit was the bond line between the specimen and tabs. There was not enough control over thickness of the tab's bond line. The process used for this research involved using two pieces of thin wire stretched across the panels to provide a thickness constant for the bond line. The problem that occurred was that there was not enough pressure over the tabs to push the excess epoxy out from in between the tab and the panel. More pressure is obviously what is needed to fix this.

To get more pressure over the tab a press or clamps must be used. This brings up another problem. The tabs slide independently of the panel and become out of position. A better way to fix this problem must be found. One suggestion is that holes be drilled in the corners of the panels and tabs once the tabs are in position. This will allow for an alignment rod, shorter than final the thickness of the combination of the tab and panel, to be placed through the panel and tab and minimize the amount of shift in the tab.

5.4.2.3 Finite Element Analysis

The finite element analyses performed in this study included unflawed as well as: 100% gap, 50% gap, and 50% overlap analyses. The test samples included one additional flaw type, a twist. This flaw was not included in the finite element analysis and should be included for future study. A possible way to model the flaw is shown in Figure 5.4.1. The black region is a gap area and the grey is an overlap area. The rest of the laminate is unflawed.

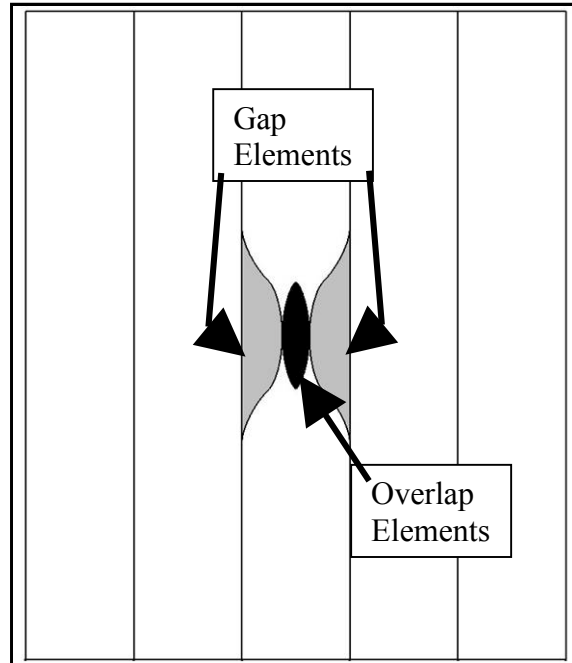


Figure 5.4.1 Finite element Twist

5.4.2.4 Testing

Bending was a problem during testing. The recommendations for out-of-plane bending were discussed in Section 5.4.2.2, but the alignment within the grips can cause in-plane bending. The problem was that there was no alignment spacer for the width of specimens tested. The test fixture only has alignment spacers for specimens of width, 0.25", 0.5", 0.75", and 1.0". Any specimen with a width that falls in-between these has to be aligned by sight. A spacer of the proper sized can be machined and the in-plane bending can be minimized.

Two testing machines were used for testing in this study. Not all of the specimens were tested on each machine and the data seems to show that samples tested on the MTS/Instron machine has results less than those on the Riehle machine. Therefore, error was introduced. For these test to be performed again, only one testing machine should be used.

5.5 Appendix A – NDE Scans

This Page Left Intentionally Blank

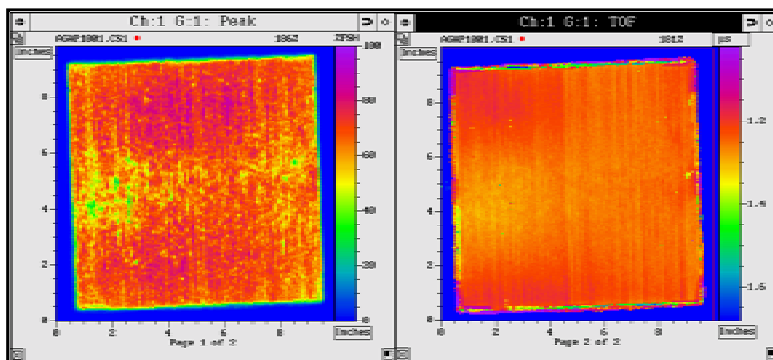


Figure 5.5.1 Peak Energy and TOF for Panel with 100% Tow Gap Flaws (Tape Panel)

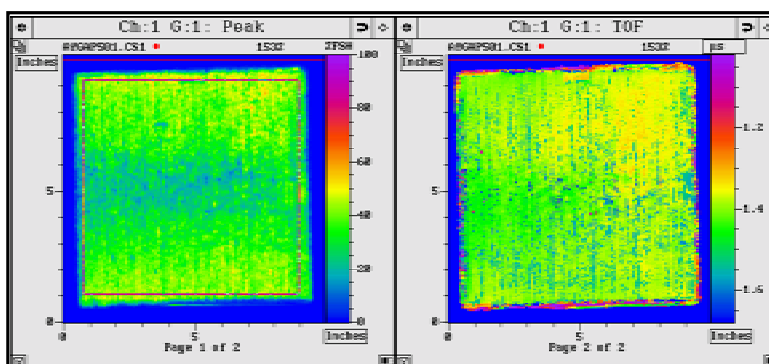


Figure 5.5.2 Peak Energy and TOF for Panel with 50% Tow Gap Flaws (Tape Panel)

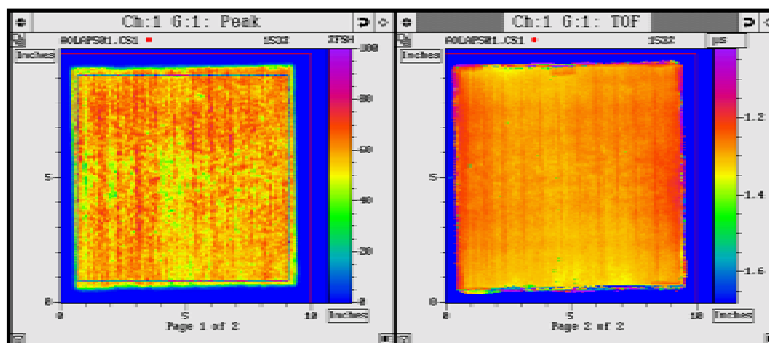


Figure 5.5.3 Peak Energy and TOF for Panel with 50% Tow Overlap Flaws (Tape Panel)

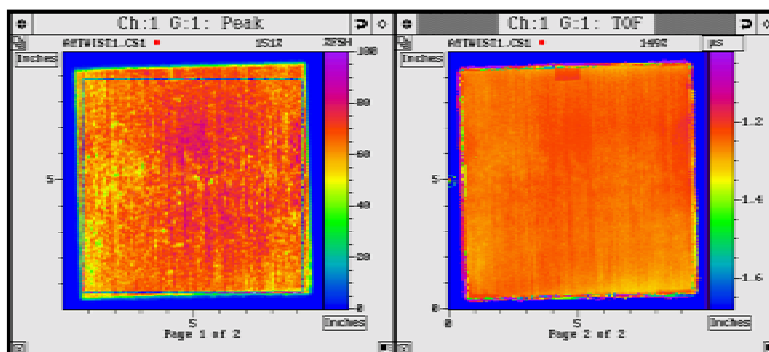


Figure 5.5.4 Peak Energy and TOF for Panel with Tow Twist Flaws (Tape Panel)

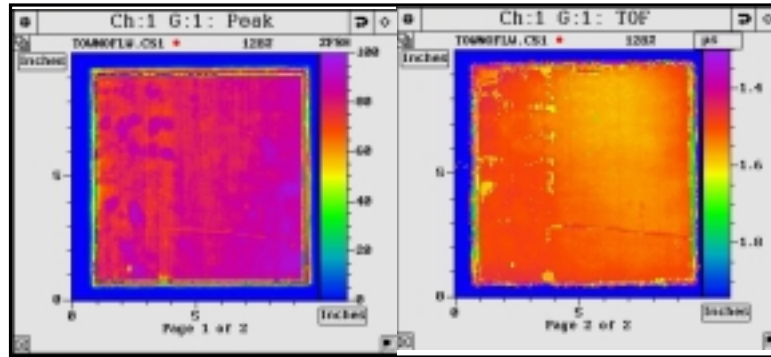


Figure 5.5.5 Peak Energy and TOF for Panel without Flaws (Tow Panel)

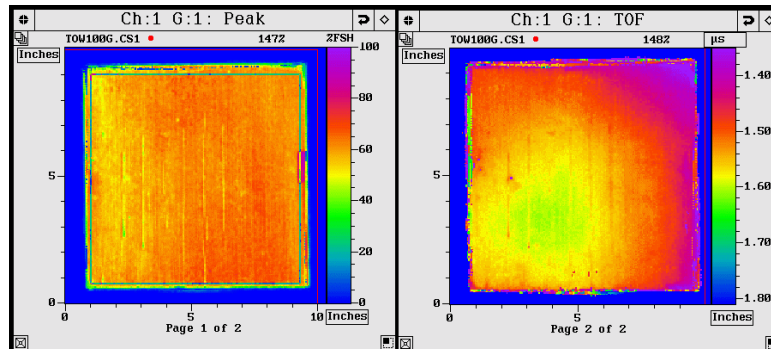


Figure 5.5.6 Peak Energy and TOF for Panel with 100% Tow Gap Flaws (Tow Panel)

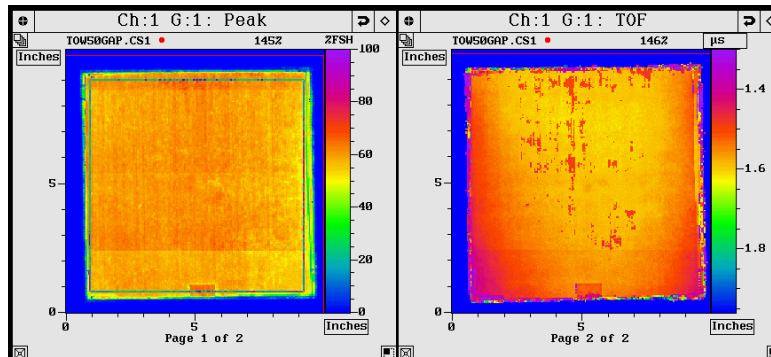


Figure 5.5.7 Peak Energy and TOF for Panel with 50% Tow Gap Flaws (Tow Panel)

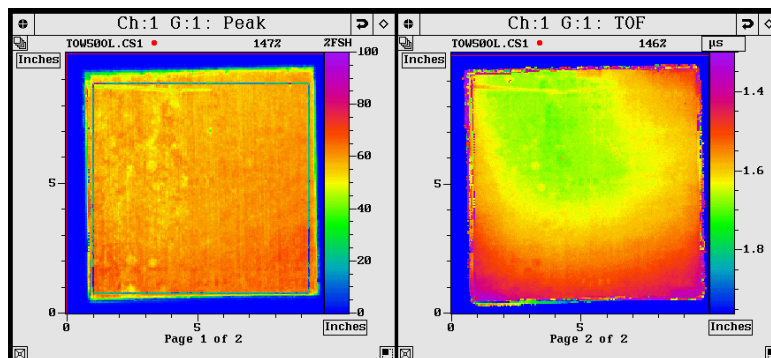


Figure 5.5.8 Peak Energy and TOF for Panel with 50% Tow Overlap Flaws (Tow Panel)

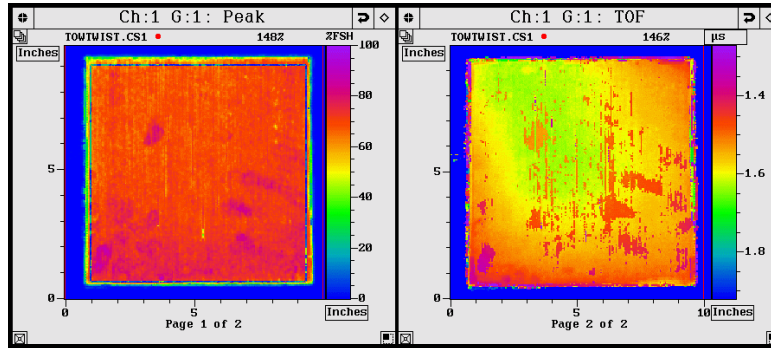


Figure 5.5.9 Peak Energy and TOF for Panel with Tow Twist Flaws (Tow Panel)

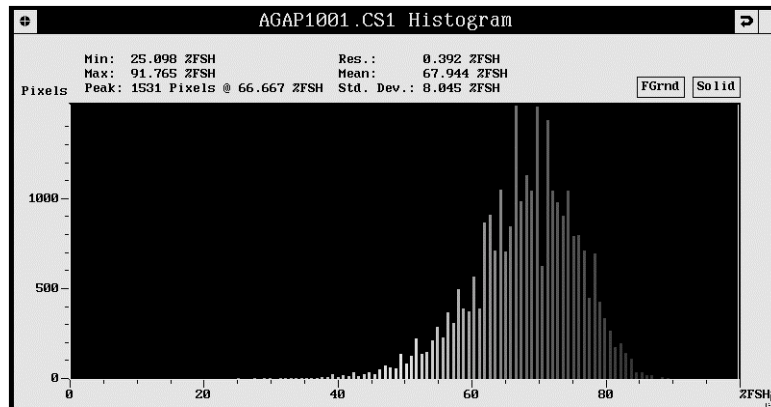


Figure 5.5.10 Histogram for Panel with 100% Tow Gap Flaws (Tape Panel)

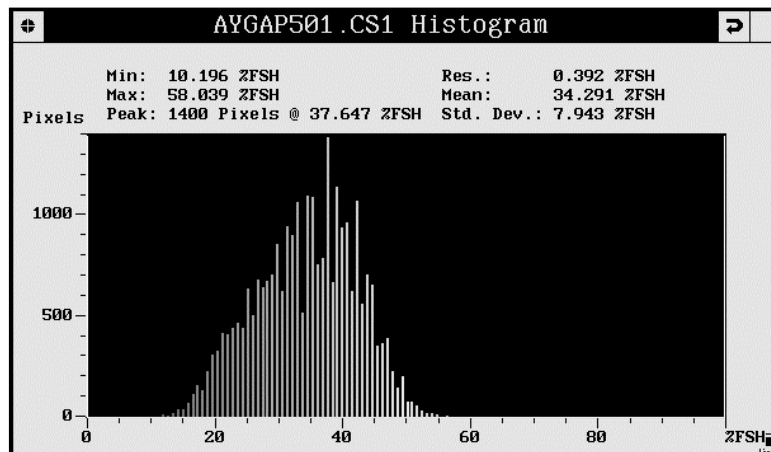


Figure 5.5.11 Histogram for Panel with 50% Tow Gap Flaws (Tape Panel)

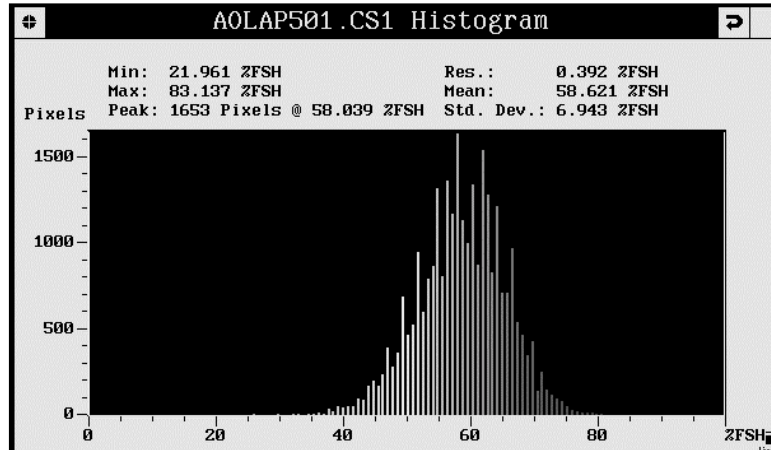


Figure 5.5.12 Histogram for Panel with 50% Tow Overlap Flaws (Tape Panel)

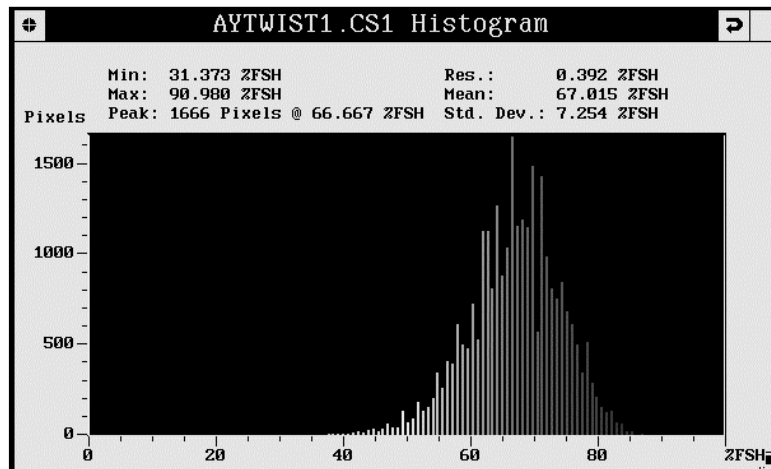


Figure 5.5.13 Histogram for Panel with Tow Twist Flaws (Tape Panel)

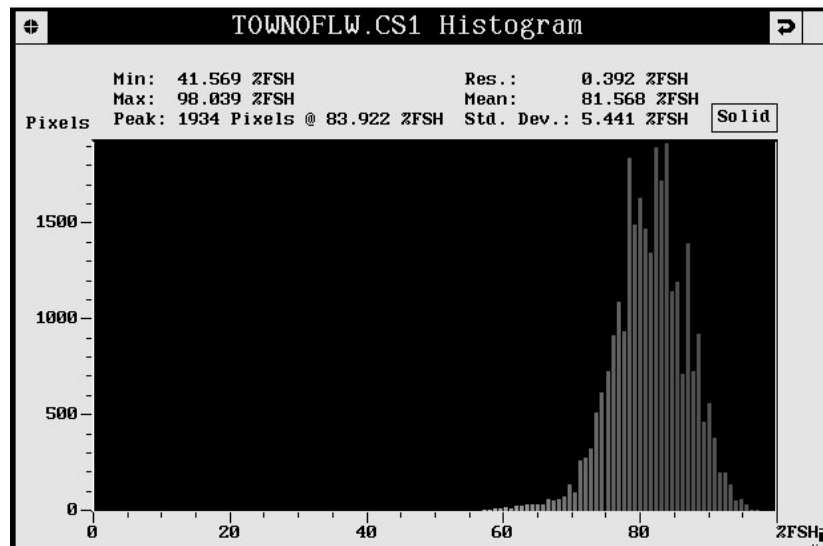


Figure 5.5.14 Histogram for Panel without Flaws (Tow Panel)

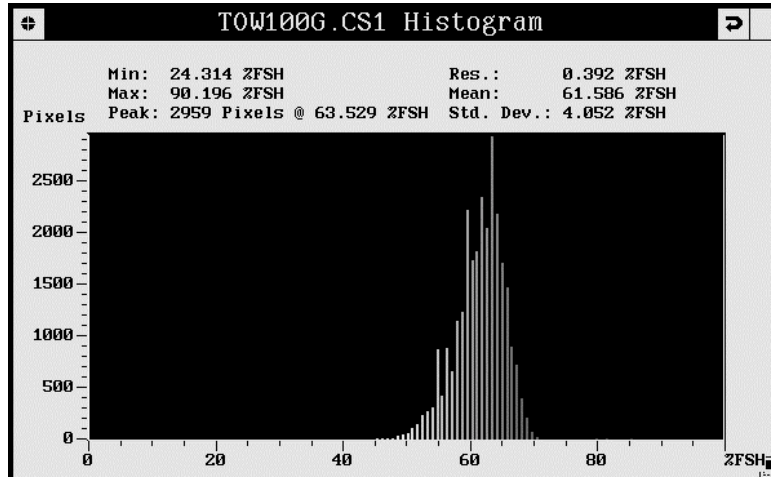


Figure 5.5.15 Histogram for Panel with 100% Tow Gap Flaws (Tow Panel)

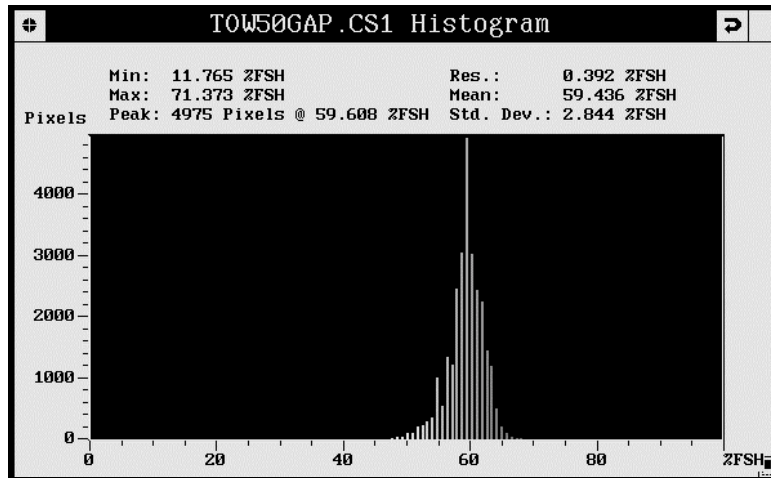


Figure 5.5.16 Histogram for Panel with 50% Tow Gap Flaws (Tow Panel)

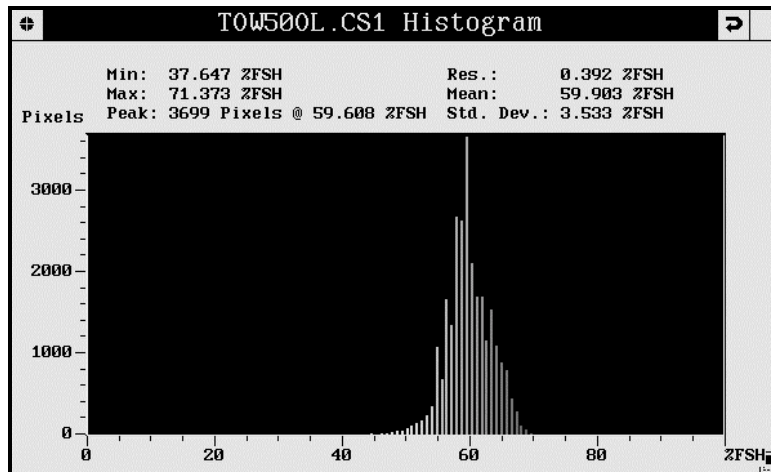


Figure 5.5.17 Histogram for Panel with 50% Overlap Flaws (Tow Panel)

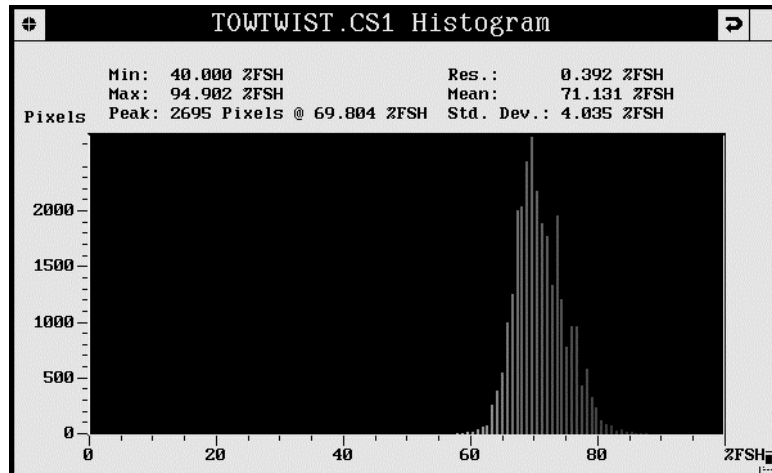


Figure 5.5.18 Histogram for Panel with Tow Twist Flaws (Tow Panel)

5.6 Appendix B – Initial Stiffness Plots

This Page Left Intentionally Blank

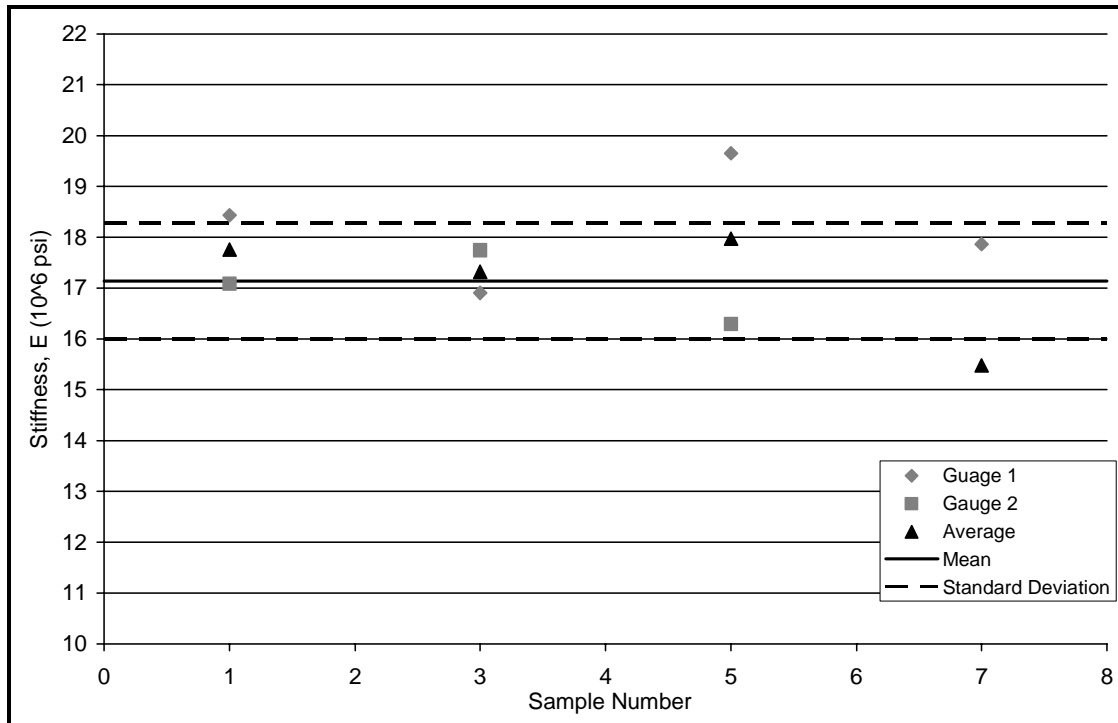


Figure 5.6.1 Initial Stiffness for Non-Flawed Tape Specimens

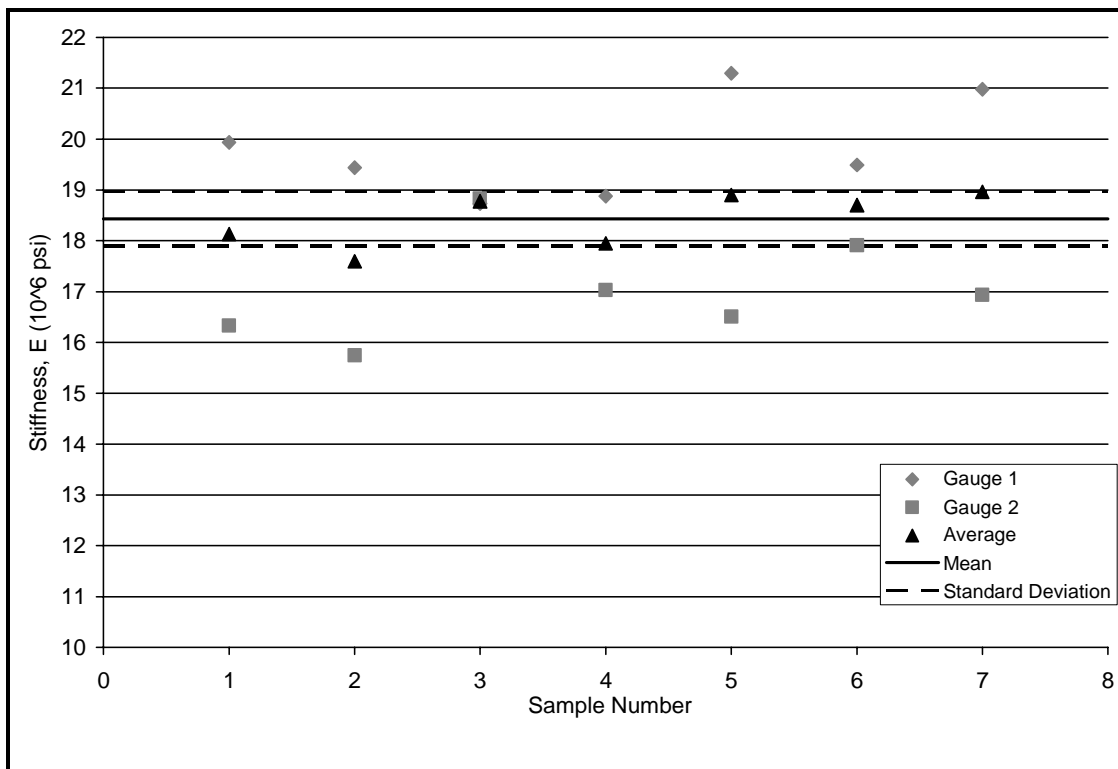


Figure 5.6.2 Initial Stiffness for 100% Gap Tape Specimens

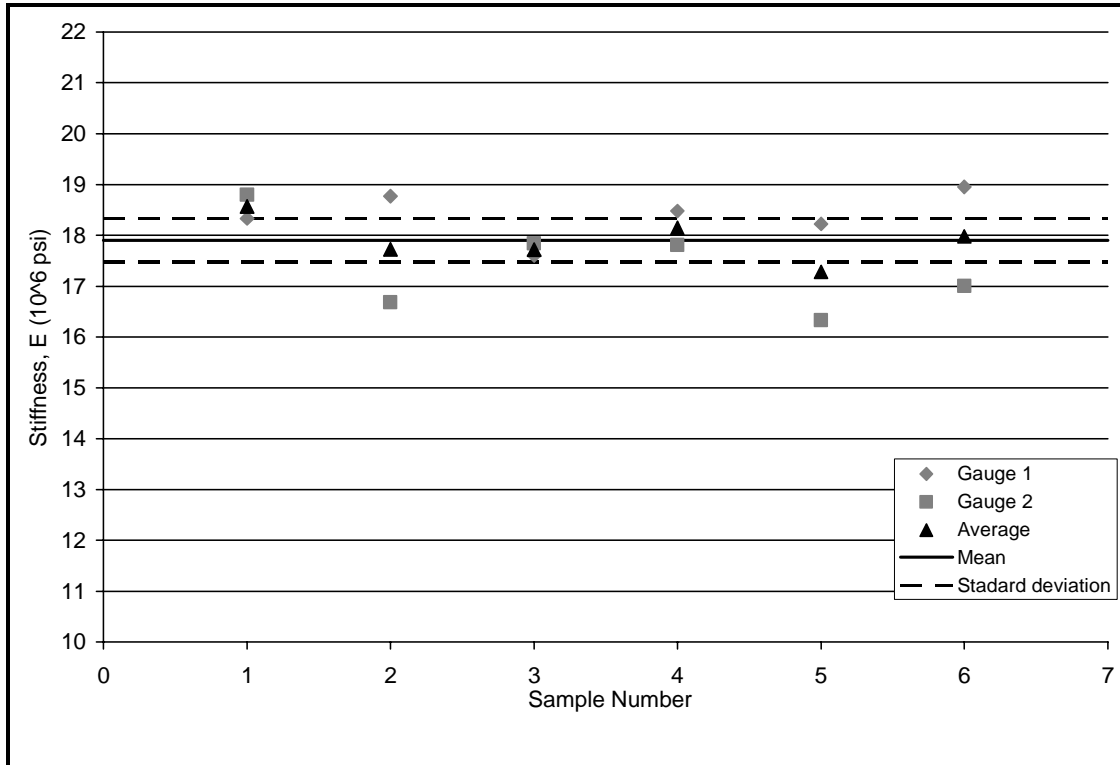


Figure 5.6.3 Initial Stiffness for 50% Gap Tape Specimens

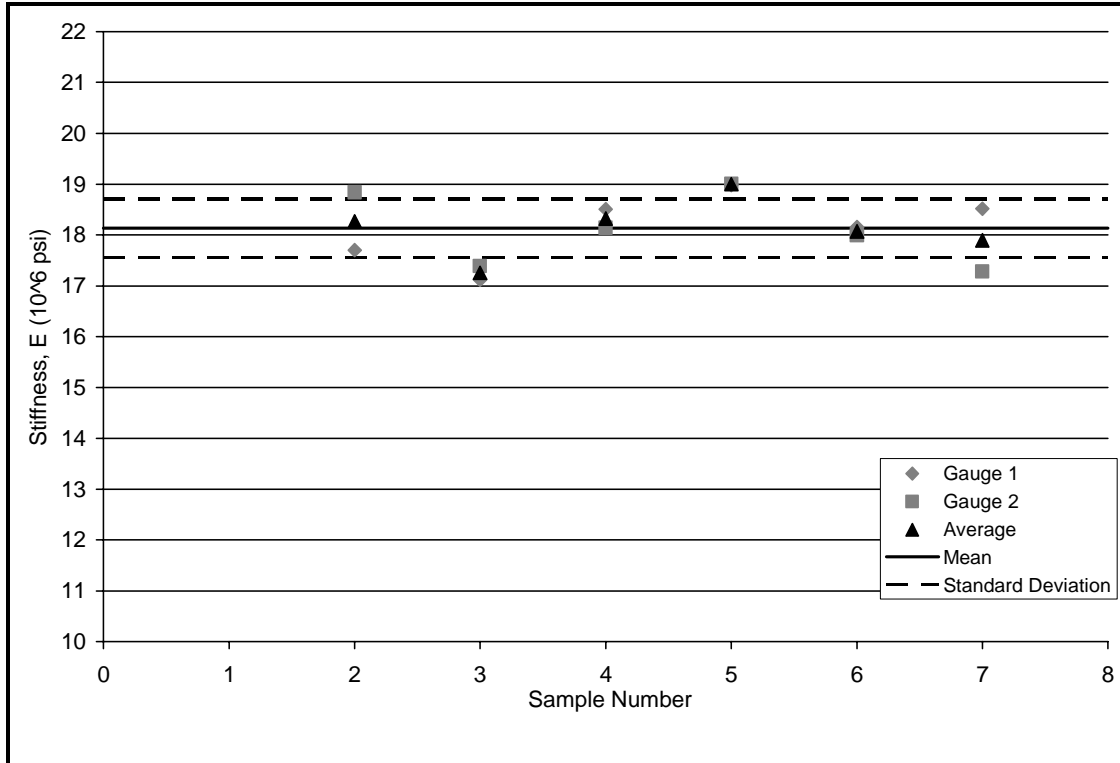


Figure 5.6.4 Initial Stiffness for 50% Overlap Tape Specimens

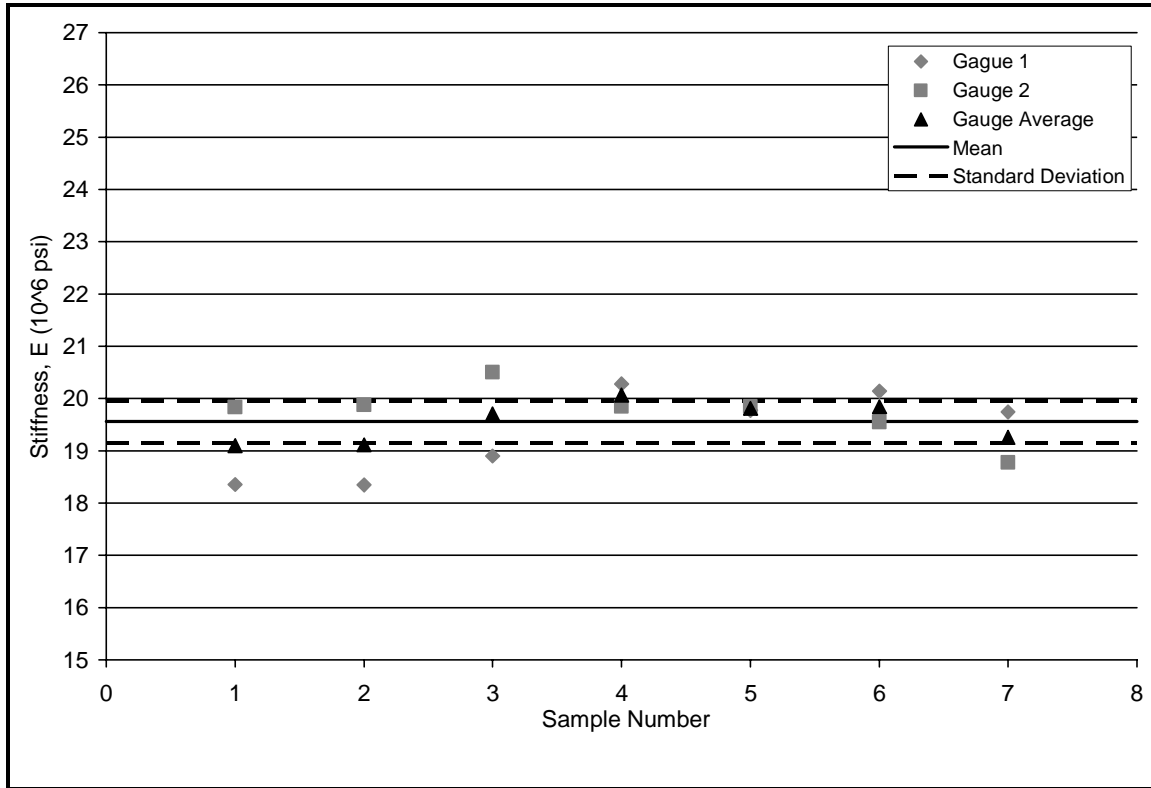


Figure 5.6.5 Initial Stiffness for Non-Flawed Tow Specimens

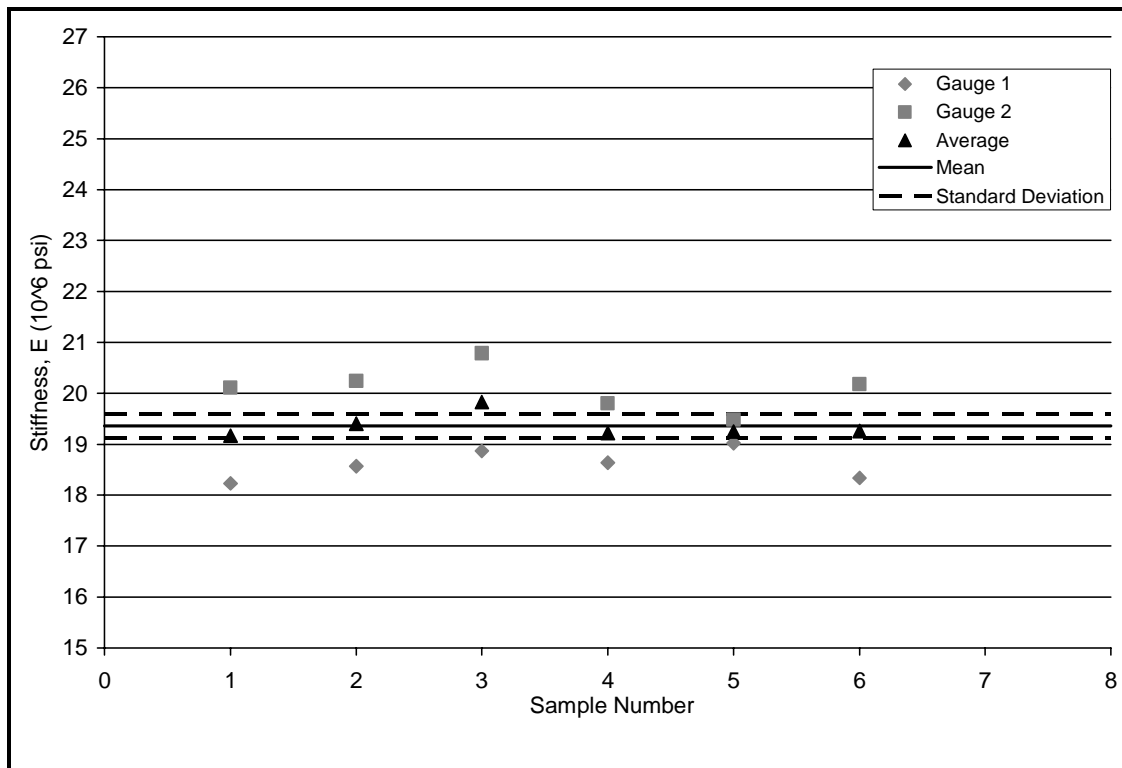


Figure 5.6.6 Initial Stiffness for 100% Gap Tow Specimens

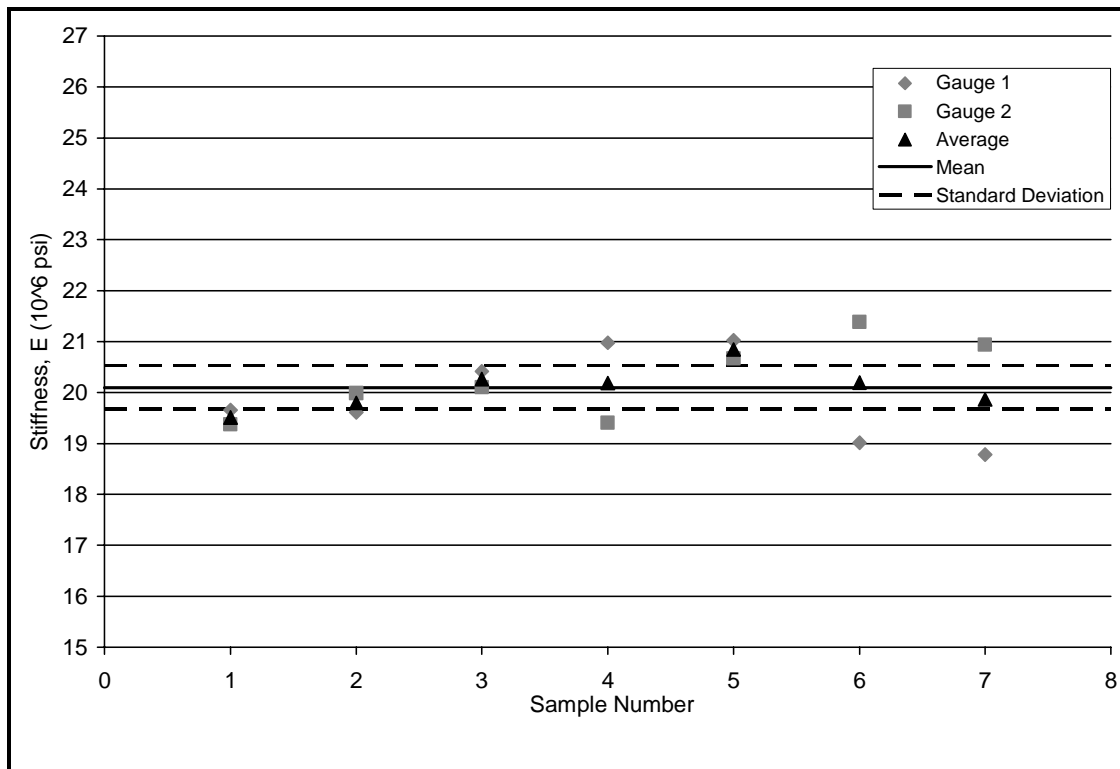


Figure 5.6.7 Initial Stiffness for 50% Gap Tow Specimens

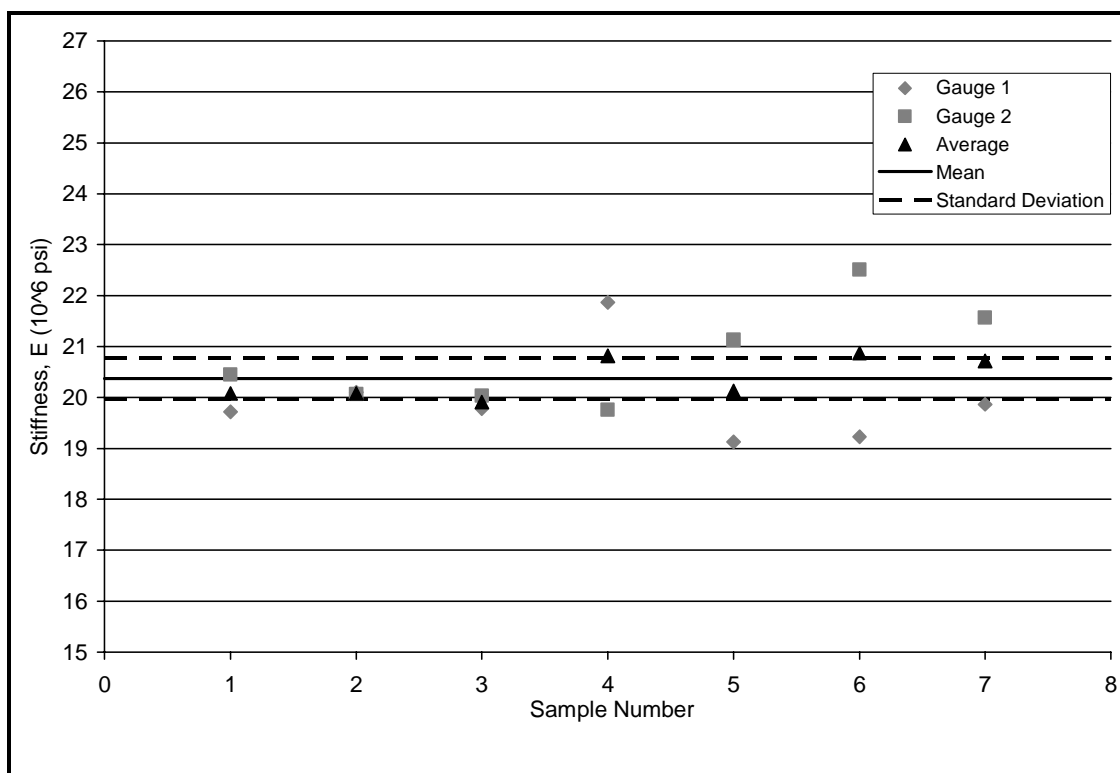


Figure 5.6.8 Initial Stiffness for 50% Overlap Tow Specimens

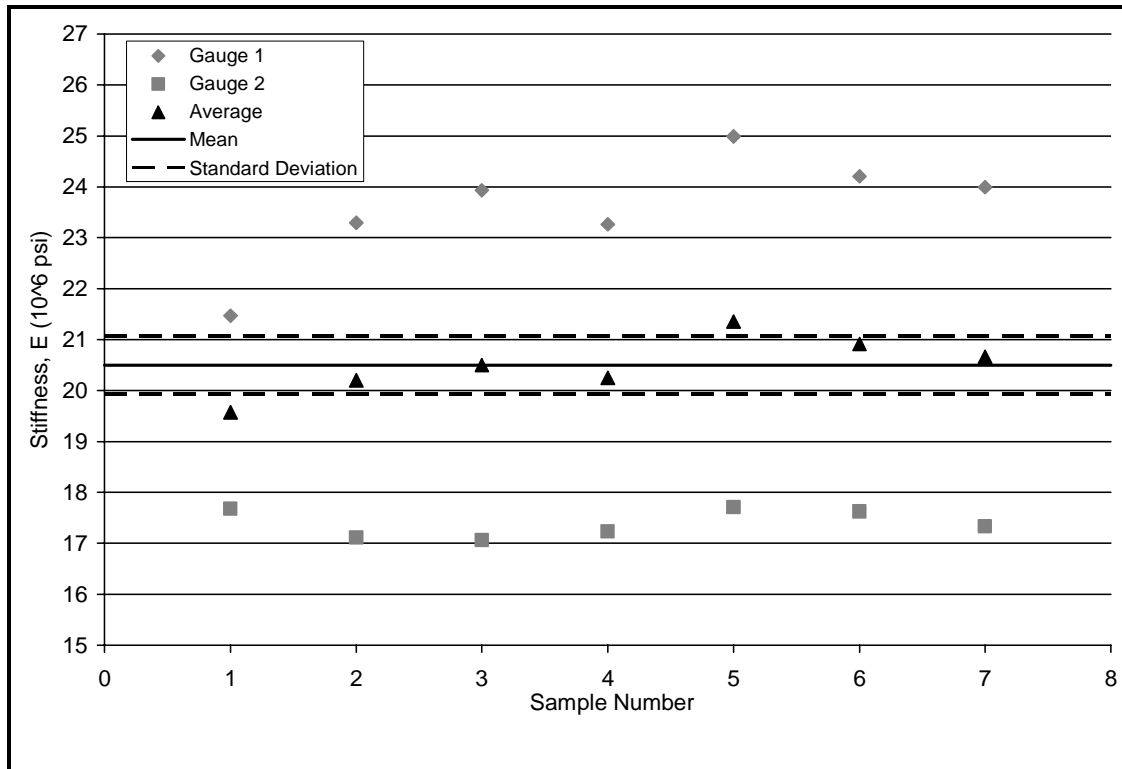


Figure 5.6.9 Initial Stiffness for Twist Tow Specimens

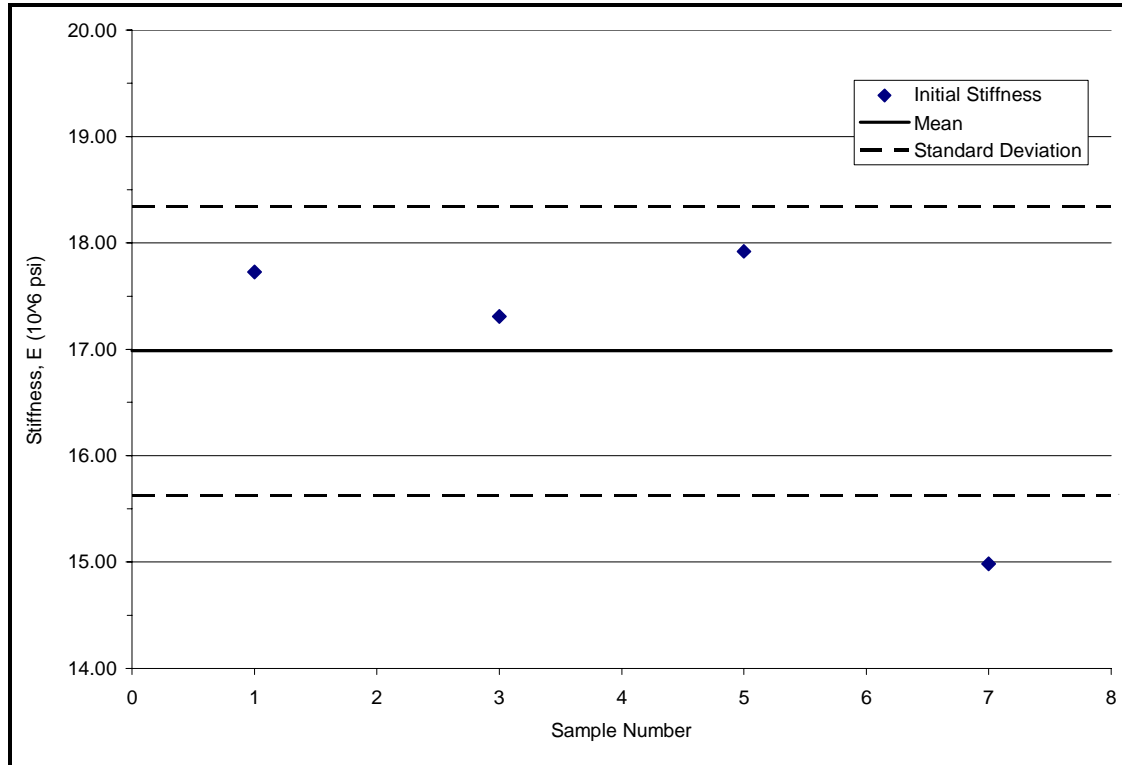


Figure 5.6.10 Initial Stiffness for Non-Flawed Tape Specimens Normalized to Bending

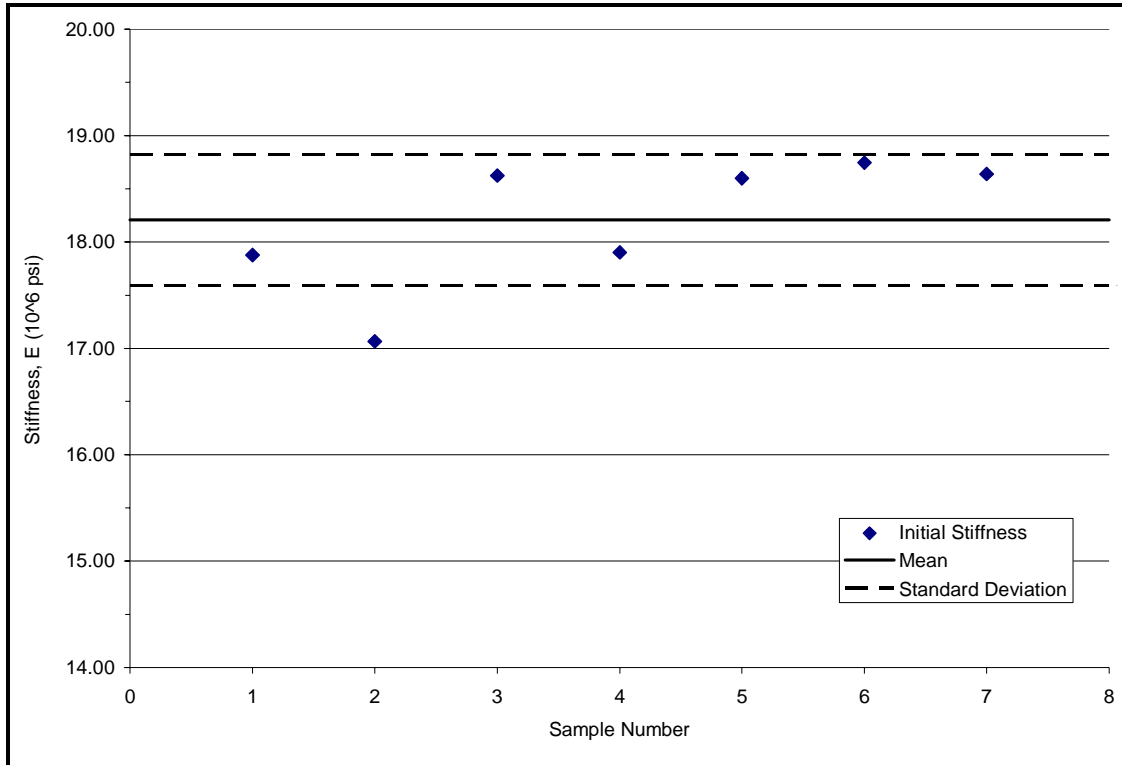


Figure 5.6.11 Initial Stiffness for 100% Gap Tape Specimens Normalized to Bending

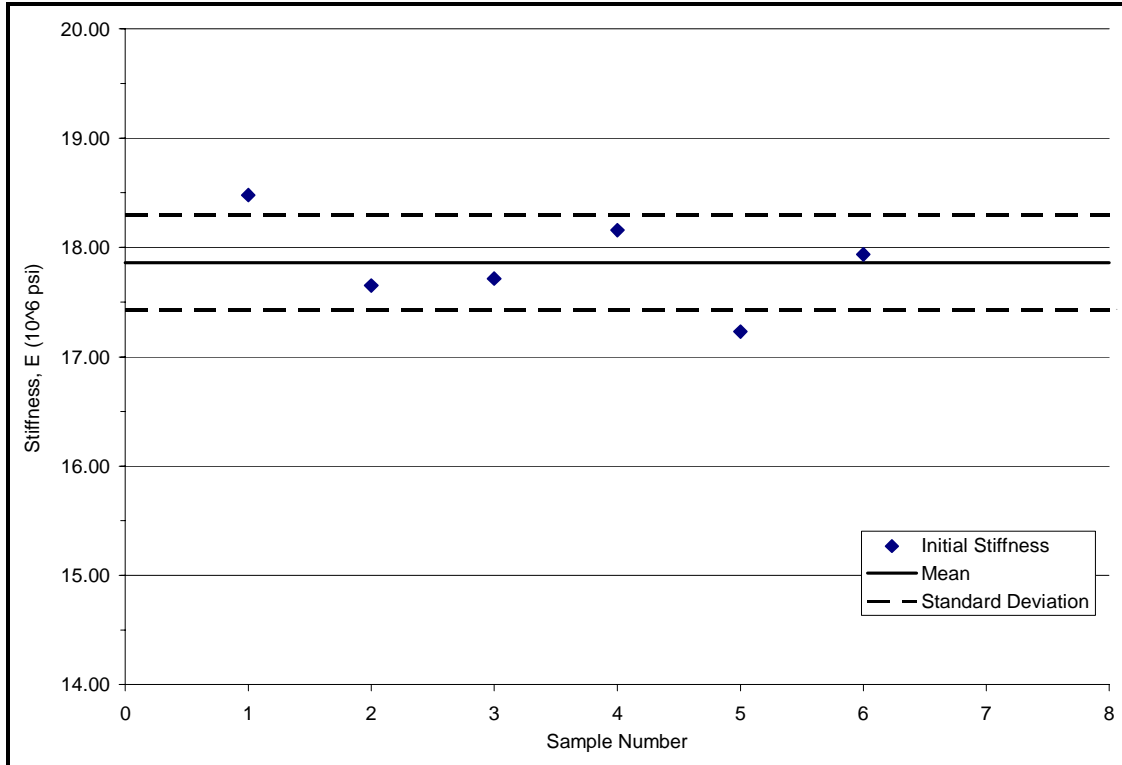


Figure 5.6.12 Initial Stiffness for 50% Gap Tape Specimens Normalized to Bending

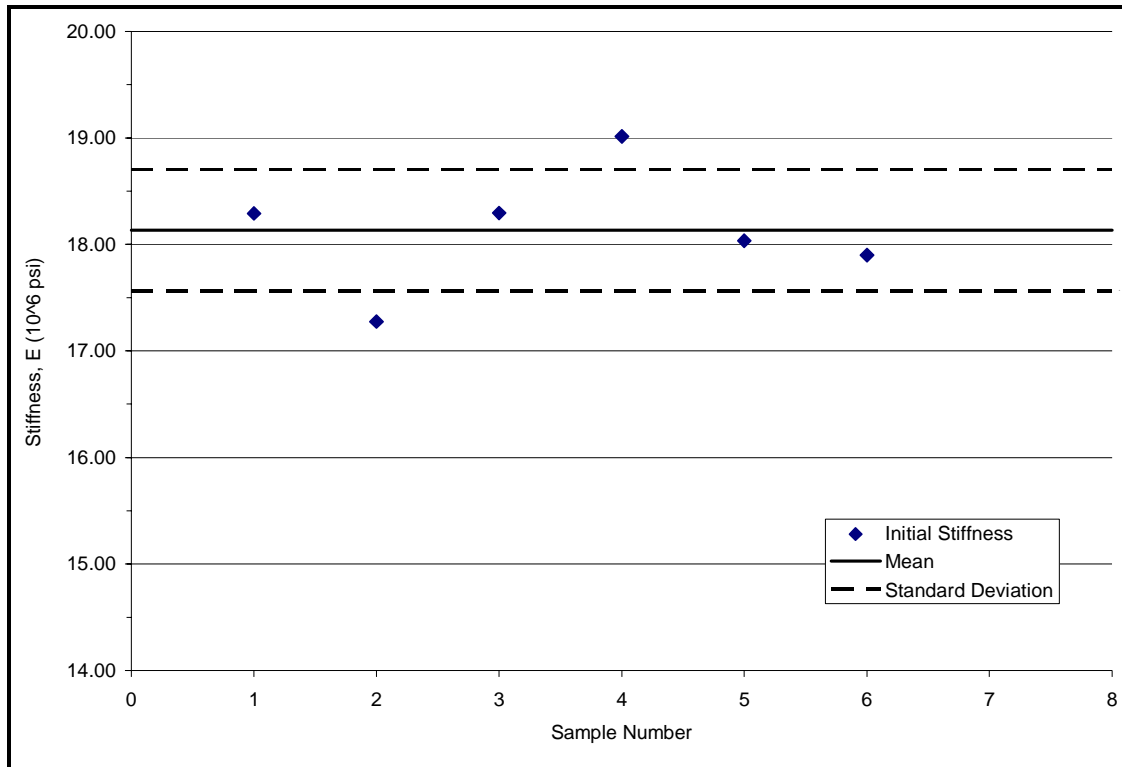


Figure 5.6.13 Initial Stiffness for 50% Overlap Tape Specimens Normalized to Bending

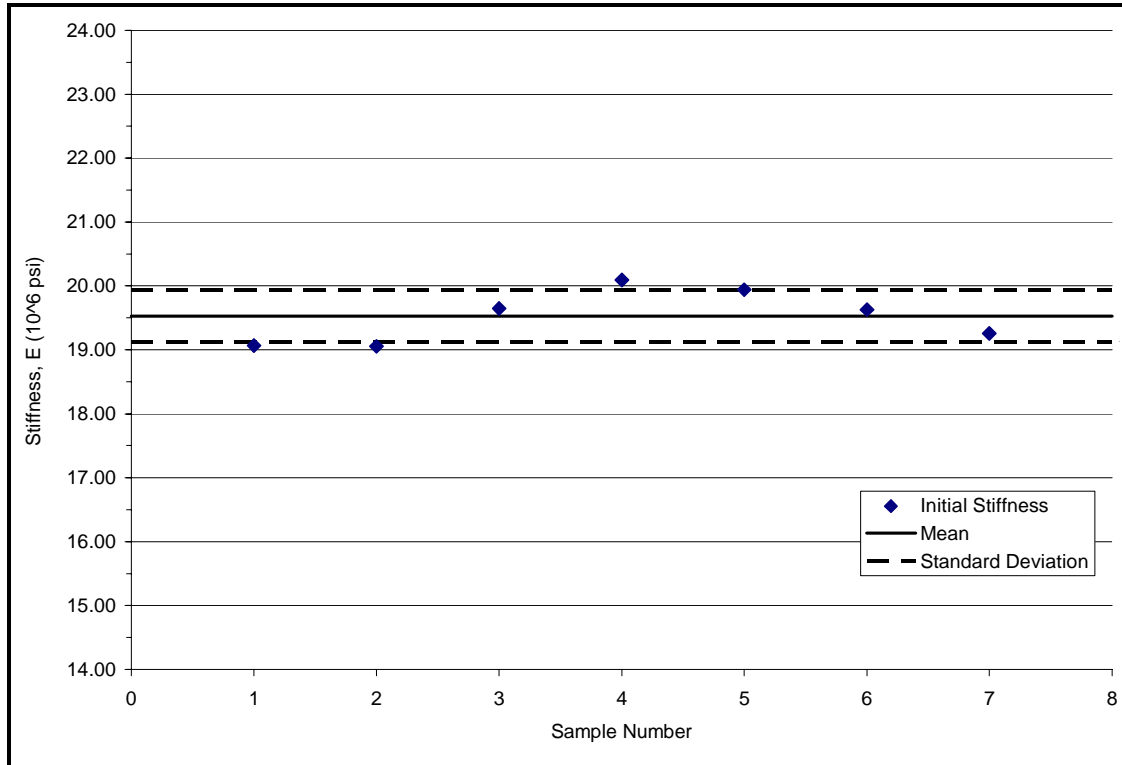


Figure 5.6.14 Initial Stiffness for Non-Flawed Tow Specimens Normalized to Bending

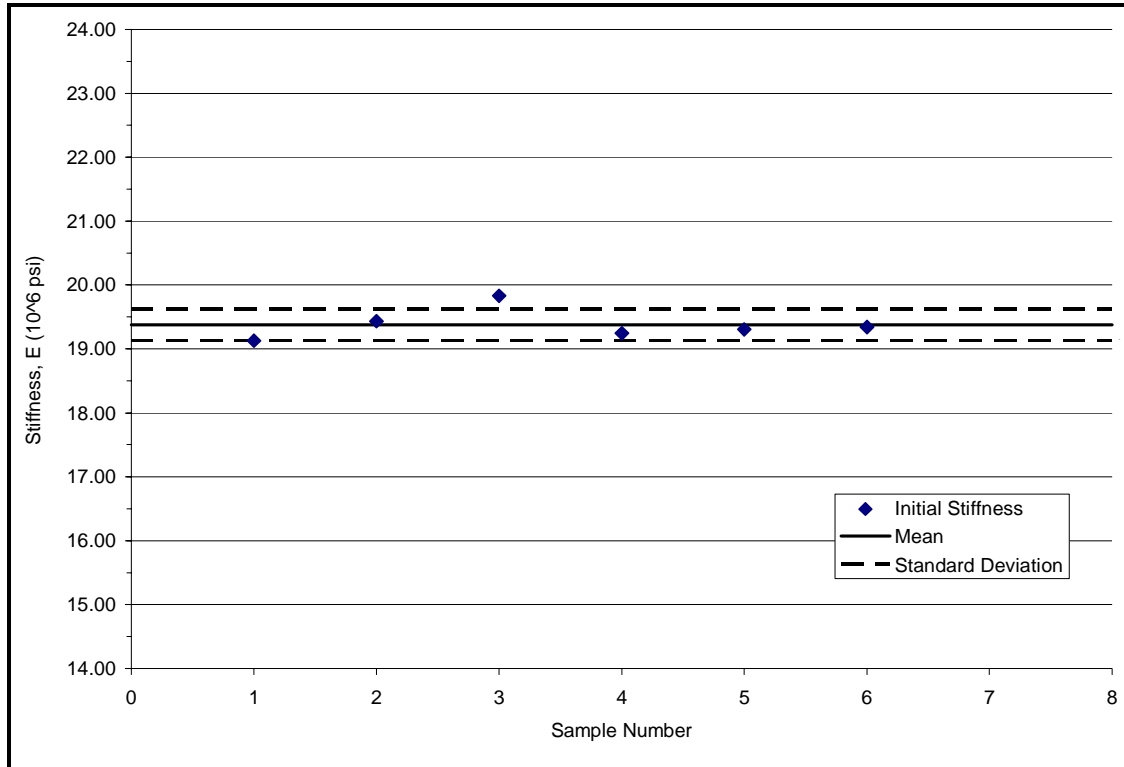


Figure 5.6.15 Initial Stiffness for 100% Gap Tow Specimens Normalized to Bending

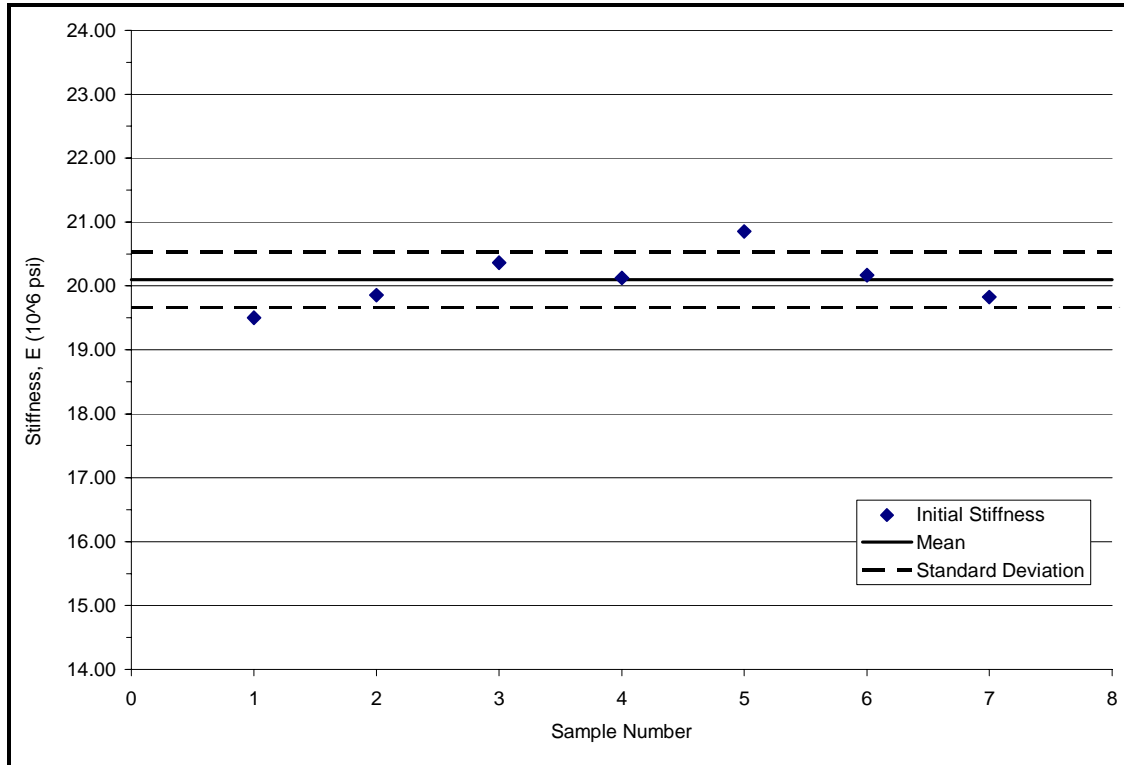


Figure 5.6.16 Initial Stiffness for 50% Gap Tow Specimens Normalized to Bending

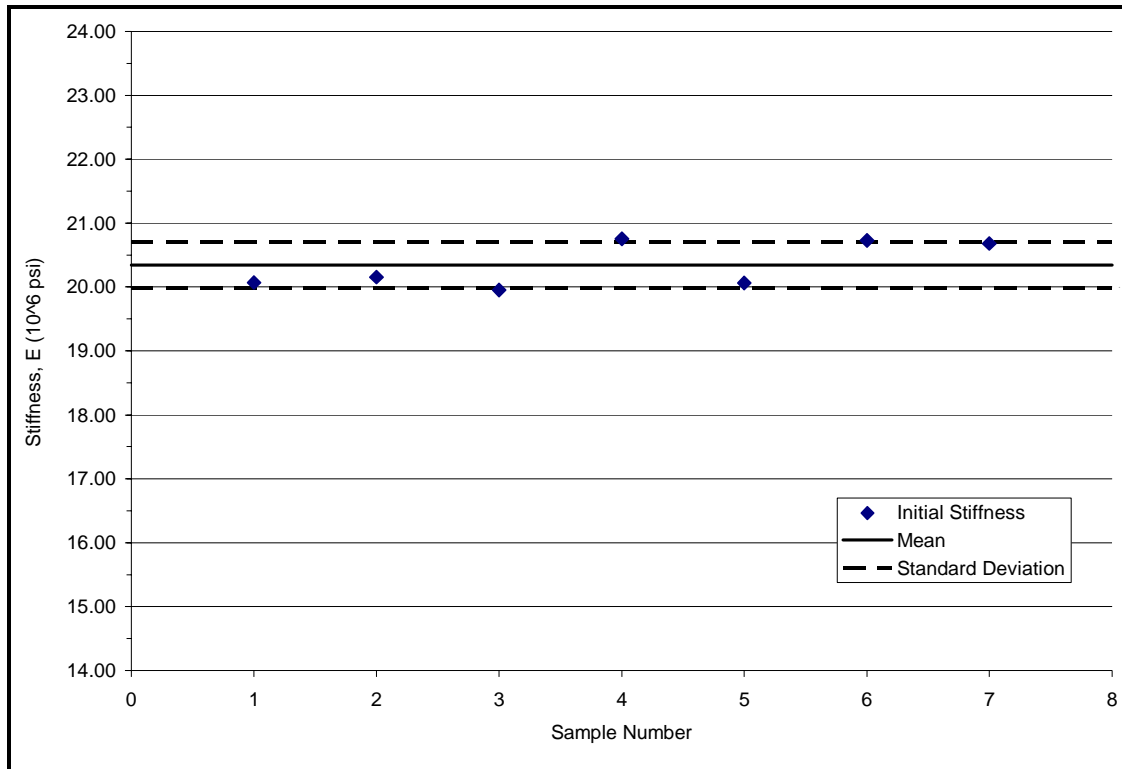


Figure 5.6.17 Initial Stiffness for 50% Overlap Tow Specimens Normalized to Bending

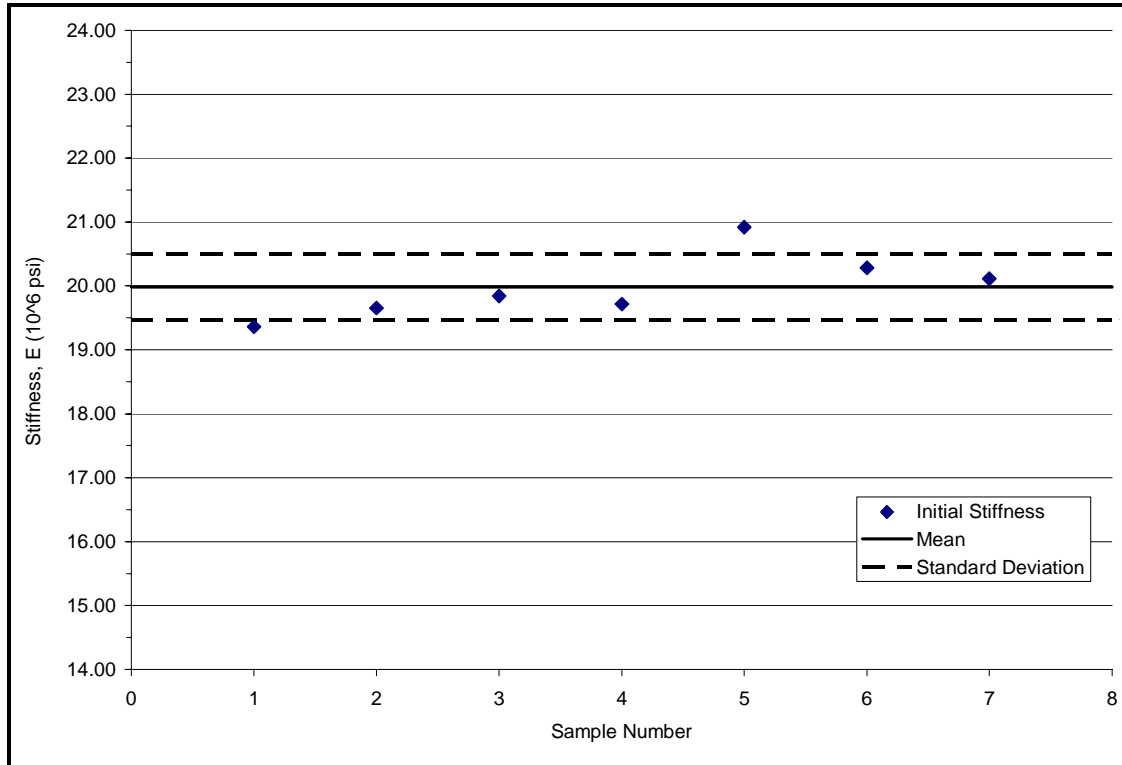


Figure 5.6.18 Initial Stiffness for Twist Tow Specimens Normalized to Bending

5.7 Appendix C – Onset of Nonlinearity Plots

This Page Left Intentionally Blank

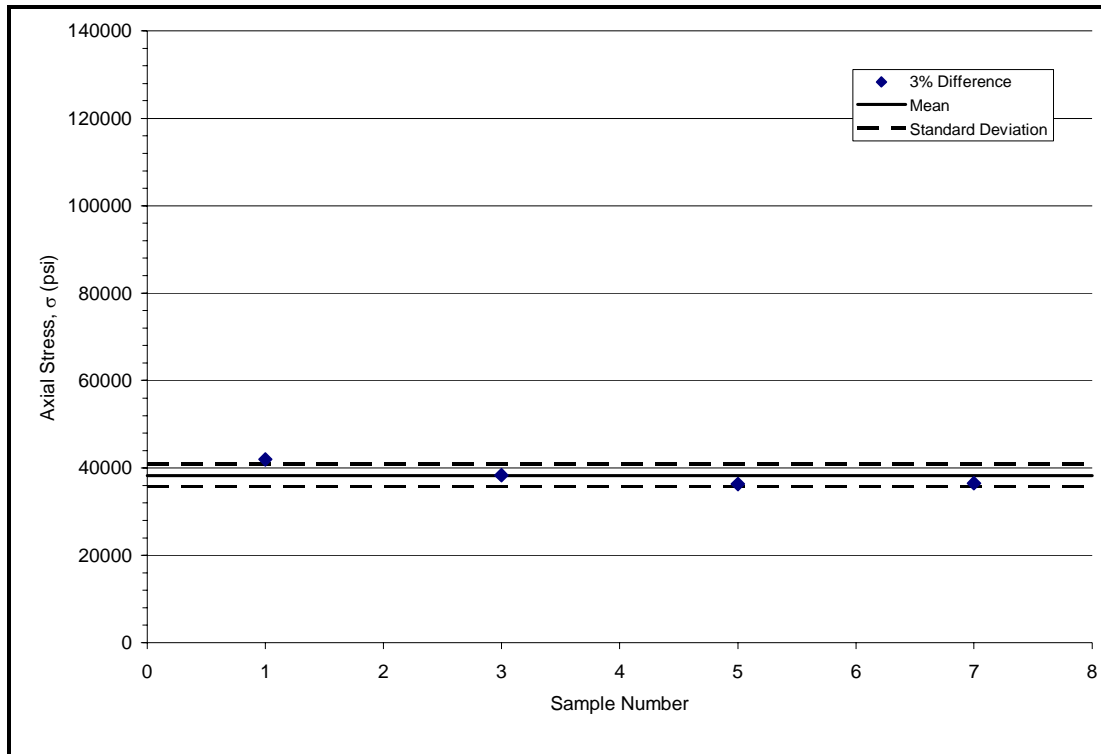


Figure 5.7.1 Onset of Nonlinearity for Non-Flawed Tape Specimens

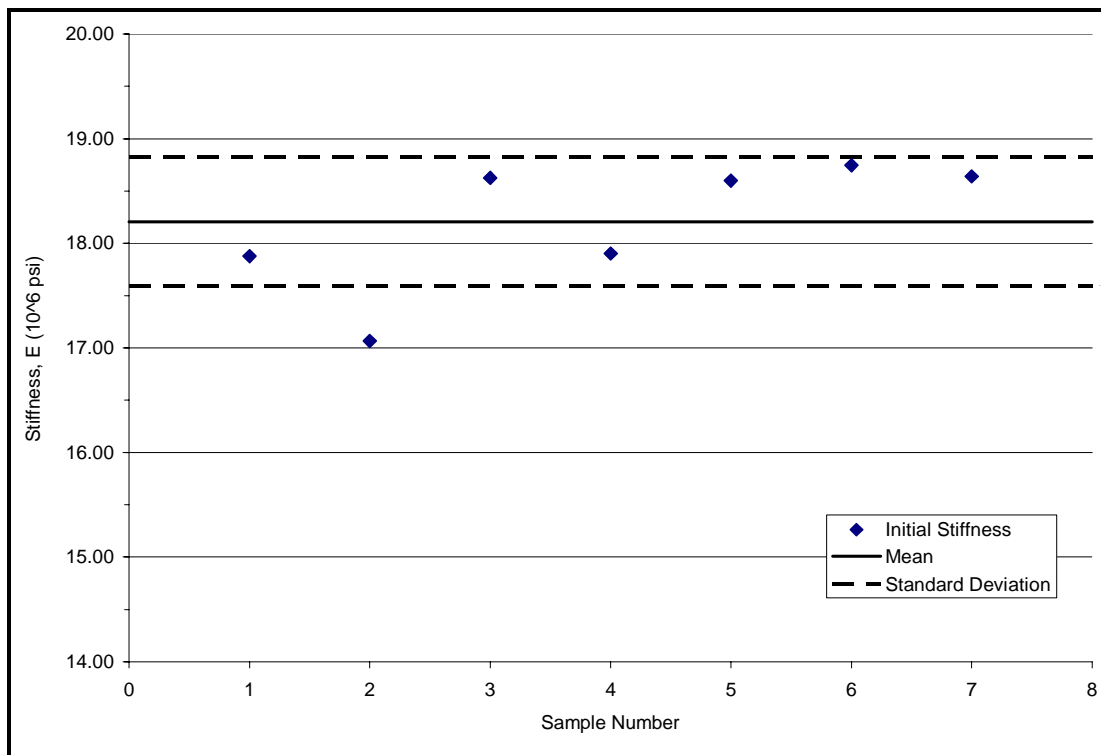


Figure 5.7.2 Onset of Nonlinearity for 100% Gap Tape Specimens

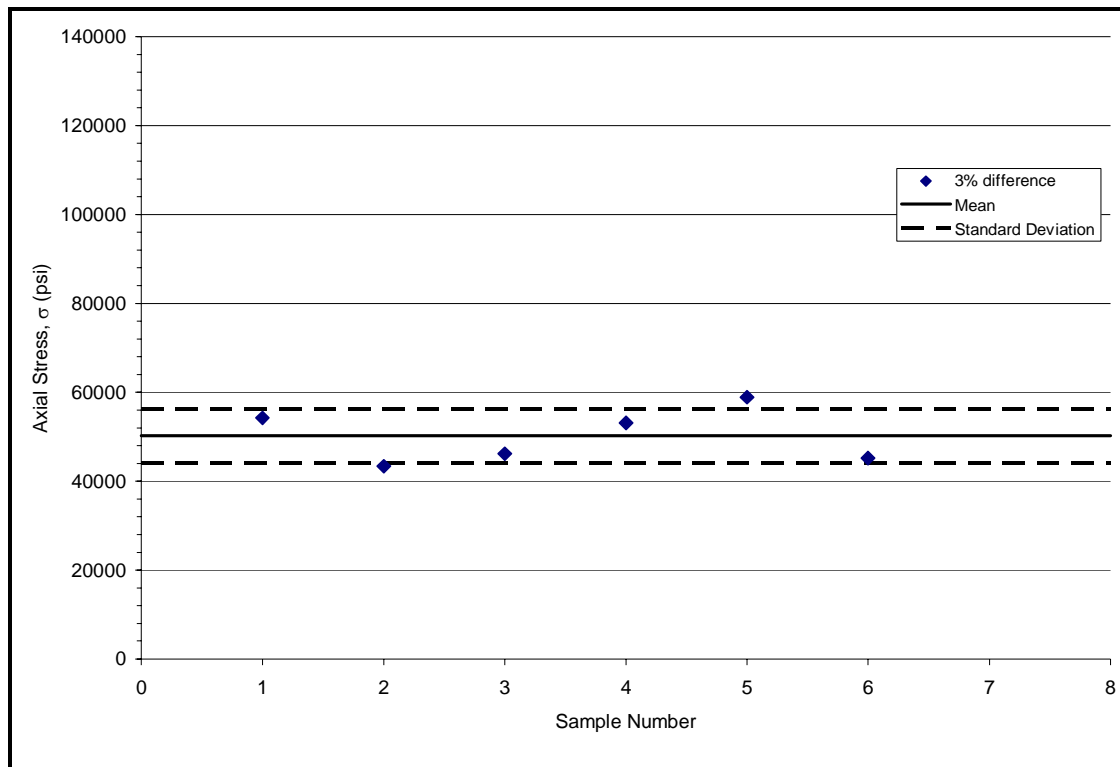


Figure 5.7.3 Onset of Nonlinearity for 50% Gap Tape Specimens

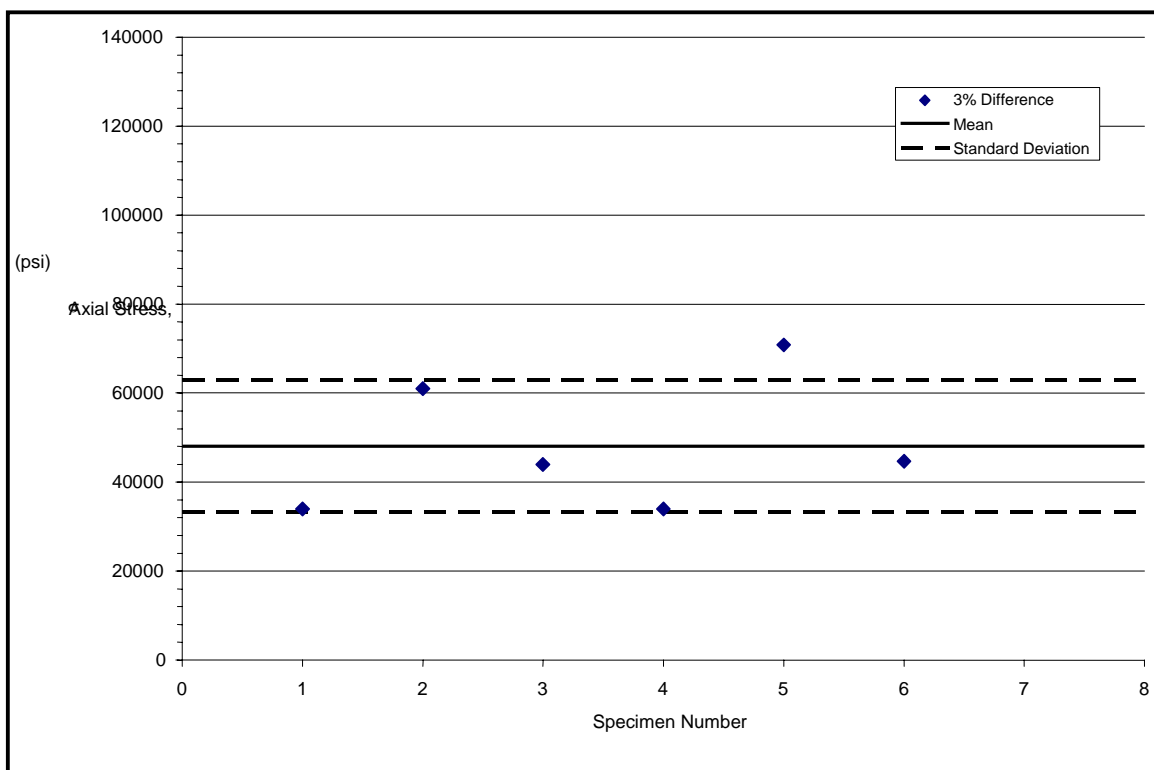


Figure 5.7.4 Onset of Nonlinearity for 50% Overlap Tape Specimens

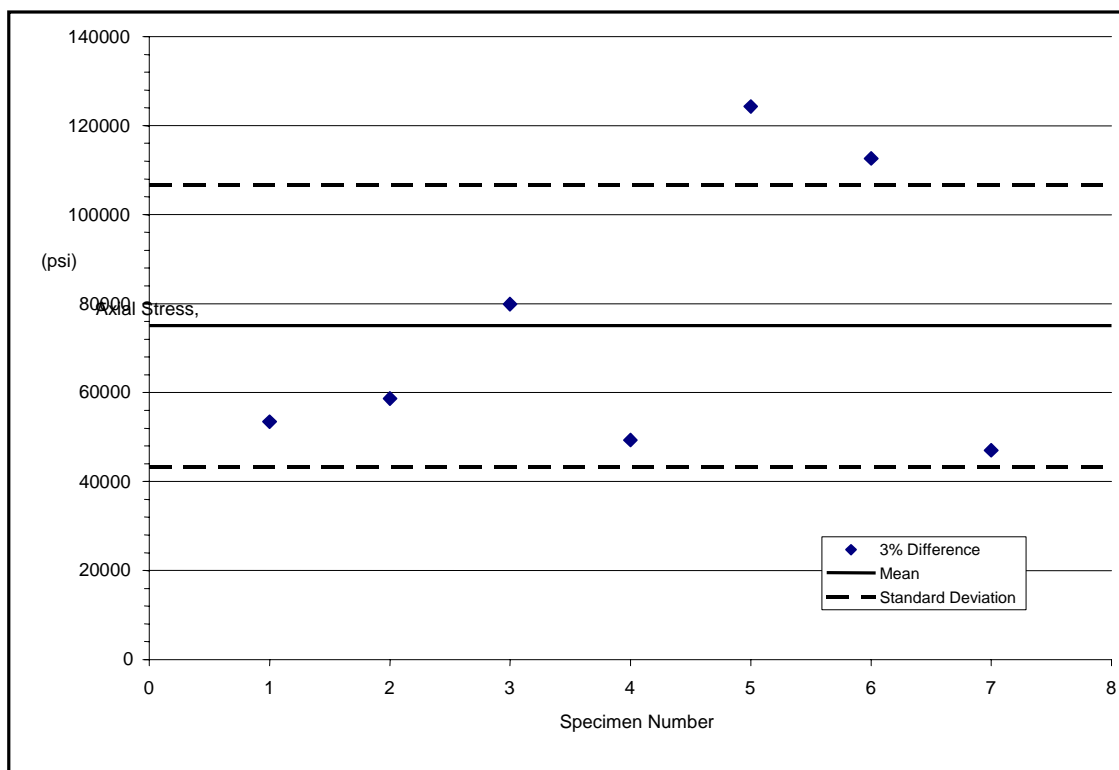


Figure 5.7.5 Onset of Nonlinearity for Twist Tape Specimens

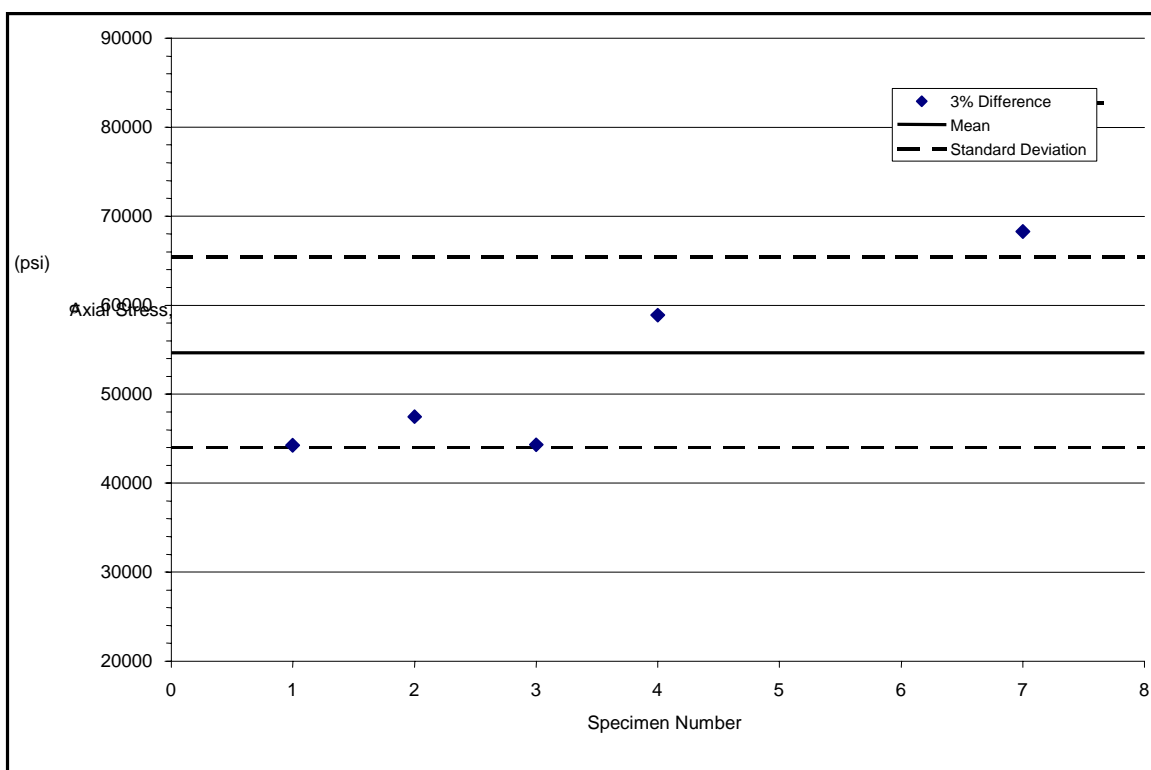


Figure 5.7.6 Onset of Nonlinearity for Non-Flawed Tow Specimens

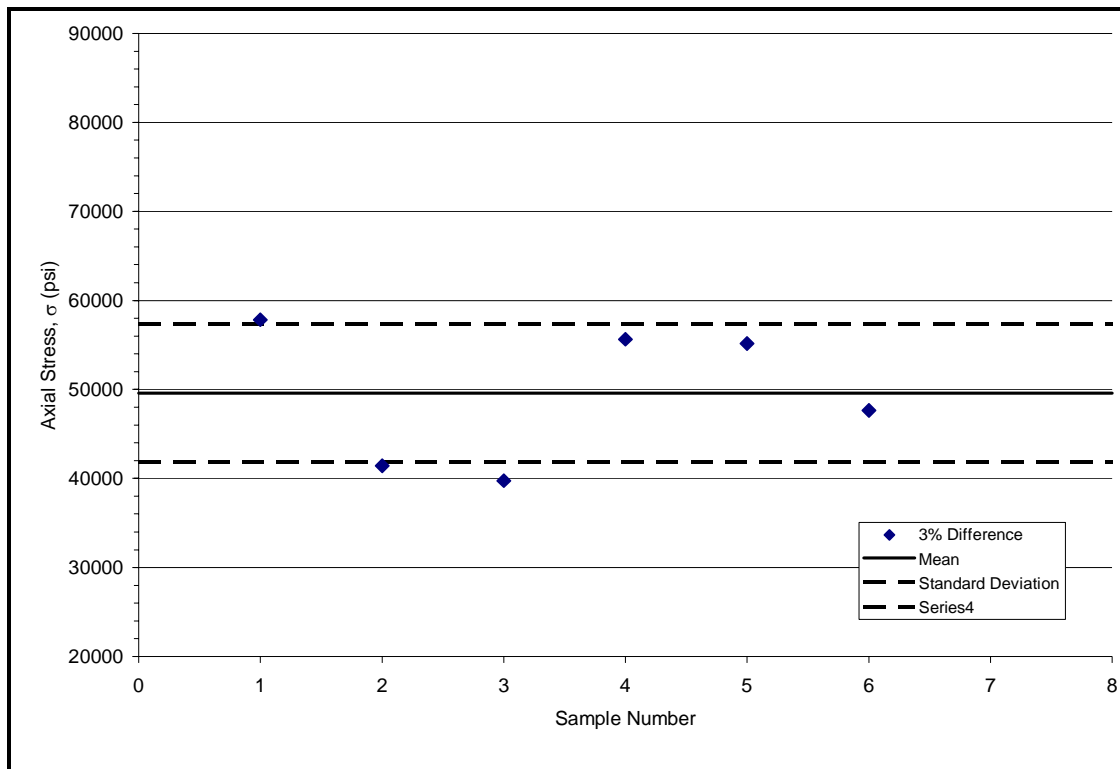


Figure 5.7.7 Onset of Nonlinearity for 100% Gap Tow Specimens

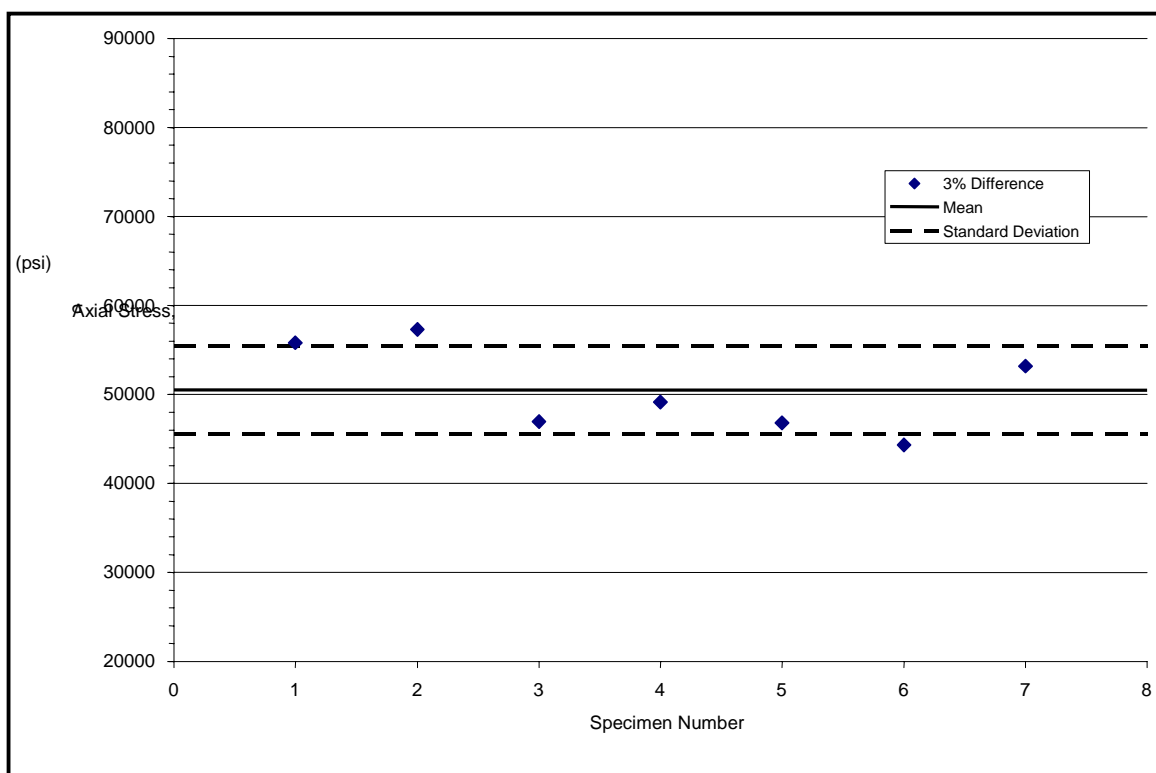


Figure 5.7.8 Onset of Nonlinearity for 50% Gap Tow Specimens

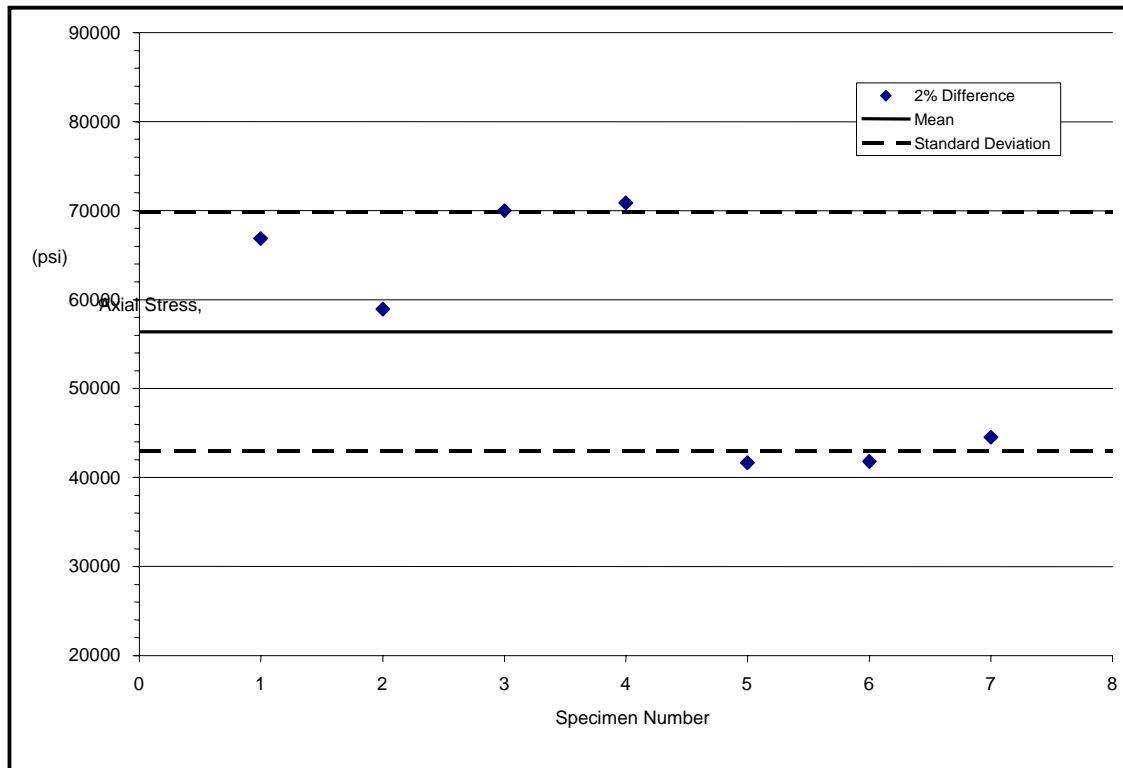


Figure 5.7.9 Onset of Nonlinearity for Twist Tow Specimens

5.8 Appendix D – Coupon Measurements

This Page Left Intentionally Blank

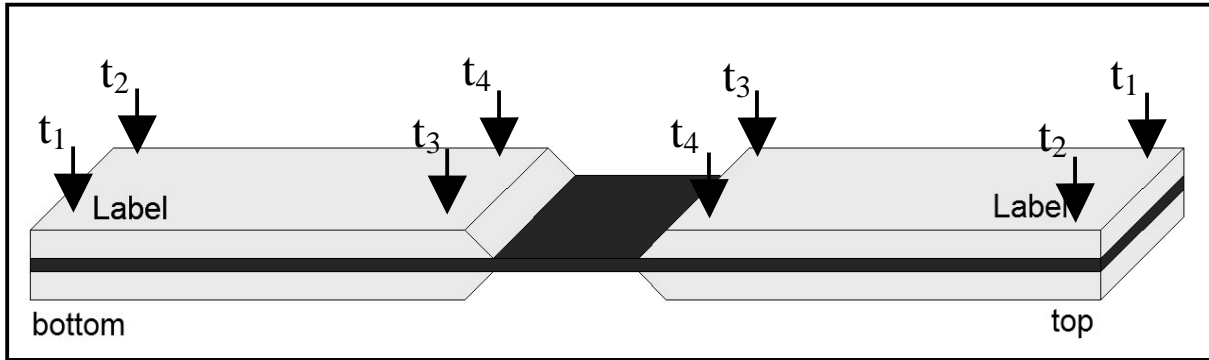


Figure 5.8.1 Location of Tab Section Thickness Measurements

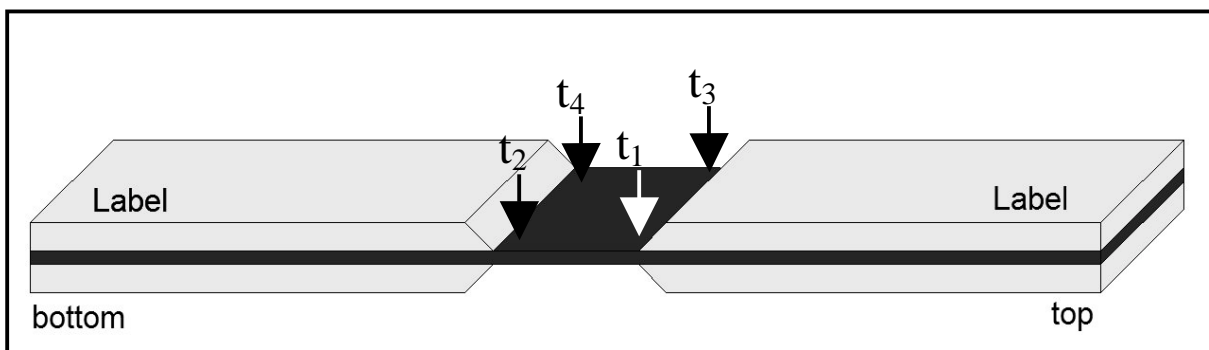


Figure 5.8.2 Location of Gage Section Thickness Measurements

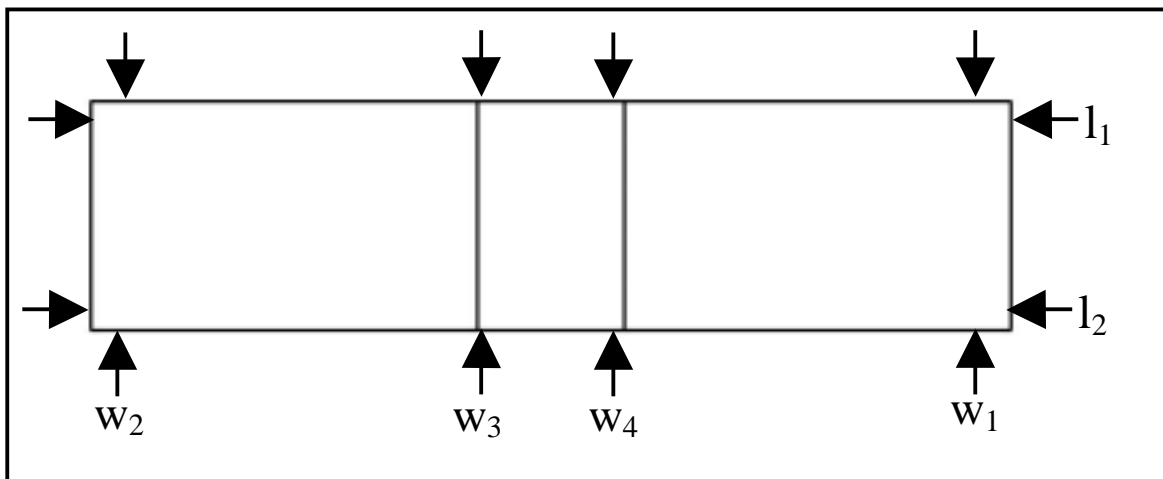


Figure 5.8.3 Location of Coupon Width and Length Measurements

Table 5.8.1 Tape Coupon's Gage Section Thickness Measurements

	Thick 1	Thick 2	Thick 3	Thick 4	ave. Thk
TP_xx0_NF_01	0.0725	0.0725	0.0730	0.0730	0.0728
TP_xx0_NF_02	0.0735	0.0735	0.0735	0.0730	0.0734
TP_xx0_NF_03	0.0735	0.0740	0.0740	0.0740	0.0739
TP_xx0_NF_04	0.0735	0.0735	0.0740	0.0735	0.0736
TP_xx0_NF_05	0.0735	0.0735	0.0730	0.0735	0.0734
TP_xx0_NF_06	0.0735	0.0735	0.0735	0.0735	0.0735
TP_xx0_NF_07	0.0735	0.0735	0.0735	0.0735	0.0735
TP_x50_OL_01	0.0725	0.0725	0.0730	0.0730	0.0728
TP_x50_OL_02	0.0740	0.0745	0.0735	0.0735	0.0739
TP_x50_OL_03	0.0750	0.0750	0.0745	0.0745	0.0748
TP_x50_OL_04	0.0750	0.0760	0.0750	0.0760	0.0755
TP_x50_OL_05	0.0750	0.0750	0.0750	0.0750	0.0750
TP_x50_OL_06	0.0750	0.0750	0.0745	0.0750	0.0749
TP_x50_OL_07	0.0745	0.0745	0.0750	0.0745	0.0746
TP_x50_OL_08	0.0745	0.0745	0.0740	0.0745	0.0744
TP_x50_OL_09	0.0735	0.0730	0.0735	0.0740	0.0735
TP_x50_OL_10	0.0730	0.0730	0.0725	0.0725	0.0728
TP_x50_GP_01	0.0790	0.0795	0.0795	0.0795	0.0794
TP_x50_GP_02	0.0805	0.0795	0.0805	0.0795	0.0800
TP_x50_GP_03	0.0800	0.0800	0.0800	0.0795	0.0799
TP_x50_GP_04	0.0795	0.0795	0.0800	0.0800	0.0798
TP_x50_GP_05	0.0790	0.0790	0.0795	0.0795	0.0793
TP_x50_GP_06	0.0785	0.0790	0.0790	0.0785	0.0788
TP_x50_GP_07	0.0780	0.0780	0.0780	0.0785	0.0781
TP_100_GP_01	0.0735	0.0730	0.0725	0.0730	0.0730
TP_100_GP_02	0.0730	0.0735	0.0735	0.0735	0.0734
TP_100_GP_03	0.0740	0.0735	0.0735	0.0730	0.0735
TP_100_GP_04	0.0735	0.0735	0.0735	0.0735	0.0735
TP_100_GP_05	0.0740	0.0740	0.0745	0.0745	0.0743
TP_100_GP_06	0.0745	0.0745	0.0745	0.0745	0.0745
TP_100_GP_07	0.0750	0.0750	0.0745	0.0740	0.0746
TP_xxT_TW_01	0.0730	0.0740	0.0740	0.0745	0.0739
TP_xxT_TW_02	0.0740	0.0735	0.0730	0.0735	0.0735
TP_xxT_TW_03	0.0725	0.0730	0.0730	0.0730	0.0729
TP_xxT_TW_04	0.0730	0.0730	0.0725	0.0730	0.0729
TP_xxT_TW_05	0.0730	0.0730	0.0735	0.0735	0.0733
TP_xxT_TW_06	0.0735	0.0735	0.0735	0.0735	0.0735
TP_xxT_TW_07	0.0740	0.0735	0.0740	0.0740	0.0739

Table 5.8.2 Tape Coupon's Width Measurements

	Width 1	Width 2	Width 3	Width 4	ave. wth @ Gage	ave. wth
TP_xx0_NF_01	0.6175	0.6180	0.6170	0.6170	0.6170	0.6174
TP_xx0_NF_02	0.5910	0.5985	0.5970	0.5975	0.5973	0.5960
TP_xx0_NF_03	0.5935	0.6005	0.5945	0.5955	0.5950	0.5960
TP_xx0_NF_04	0.6050	0.6065	0.6015	0.6015	0.6015	0.6036
TP_xx0_NF_05	0.6240	0.6210	0.6210	0.6215	0.6213	0.6219
TP_xx0_NF_06	0.5925	0.5930	0.5965	0.5965	0.5965	0.5946
TP_xx0_NF_07	0.6010	0.5930	0.5905	0.5865	0.5885	0.5928
TP_x50_OL_01	0.6270	0.6310	0.6310	0.6305	0.6308	0.6299
TP_x50_OL_02	0.6400	0.6410	0.6320	0.6340	0.6330	0.6368
TP_x50_OL_03	0.6260	0.6245	0.6235	0.6225	0.6230	0.6241
TP_x50_OL_04	0.6175	0.6200	0.6175	0.6180	0.6178	0.6183
TP_x50_OL_05	0.6175	0.6175	0.6180	0.6175	0.6178	0.6176
TP_x50_OL_06	0.6415	0.6440	0.6420	0.6425	0.6423	0.6425
TP_x50_OL_07	0.6310	0.6330	0.6295	0.6305	0.6300	0.6310
TP_x50_OL_08	0.6530	0.6555	0.6520	0.6535	0.6528	0.6535
TP_x50_OL_09	0.6270	0.6240	0.6270	0.6250	0.6260	0.6258
TP_x50_OL_10	0.6570	0.6545	0.6530	0.6530	0.6530	0.6544
TP_x50_GP_01	0.6115	0.6090	0.6055	0.6065	0.6060	0.6081
TP_x50_GP_02	0.6275	0.6255	0.6255	0.6255	0.6255	0.6260
TP_x50_GP_03	0.6600	0.6605	0.6600	0.6600	0.6600	0.6601
TP_x50_GP_04	0.6535	0.6535	0.6525	0.6530	0.6528	0.6531
TP_x50_GP_05	0.6060	0.6140	0.6065	0.6120	0.6093	0.6096
TP_x50_GP_06	0.6325	0.6375	0.6315	0.6325	0.6320	0.6335
TP_x50_GP_07	0.6390	0.6395	0.6370	0.6360	0.6365	0.6379
TP_100_GP_01	0.6245	0.6250	0.6240	0.6235	0.6238	0.6243
TP_100_GP_02	0.6205	0.6220	0.6235	0.6185	0.6210	0.6211
TP_100_GP_03	0.6465	0.6495	0.6500	0.6495	0.6498	0.6489
TP_100_GP_04	0.6530	0.6565	0.6575	0.6575	0.6575	0.6561
TP_100_GP_05	0.5975	0.5990	0.5925	0.5960	0.5943	0.5963
TP_100_GP_06	0.6165	0.6160	0.6130	0.6125	0.6128	0.6145
TP_100_GP_07	0.5915	0.5925	0.5920	0.5900	0.5910	0.5915
TP_xxT_TW_01	0.6085	0.6095	0.6045	0.6075	0.6060	0.6075
TP_xxT_TW_02	0.5845	0.5875	0.6855	0.5870	0.6363	0.6111
TP_xxT_TW_03	0.6310	0.6285	0.6250	0.6265	0.6258	0.6278
TP_xxT_TW_04	0.6360	0.6400	0.6370	0.6390	0.6380	0.6380
TP_xxT_TW_05	0.6305	0.6320	0.6300	0.6300	0.6300	0.6306
TP_xxT_TW_06	0.6010	0.5990	0.5965	0.5995	0.5980	0.5990
TP_xxT_TW_07	0.6135	0.6140	0.6100	0.6070	0.6085	0.6111

Table 5.8.3 Tape Coupon's Length Measurements

	Length 1	Length 2	ave. lgth
TP_xx0_NF_01	5.4840	5.4815	5.4828
TP_xx0_NF_02	5.4765	5.4805	5.4785
TP_xx0_NF_03	5.7870	5.4795	5.6333
TP_xx0_NF_04	5.4780	5.4790	5.4785
TP_xx0_NF_05	5.4790	5.4715	5.4753
TP_xx0_NF_06	5.4765	5.4780	5.4773
TP_xx0_NF_07	5.4750	5.4760	5.4755
TP_x50_OL_01	5.5175	5.5145	5.5160
TP_x50_OL_02	5.5125	5.5075	5.5100
TP_x50_OL_03	5.5045	5.5075	5.5060
TP_x50_OL_04	5.5010	5.5035	5.5023
TP_x50_OL_05	5.4960	5.4985	5.4973
TP_x50_OL_06	5.4910	5.4945	5.4928
TP_x50_OL_07	5.4895	5.4875	5.4885
TP_x50_OL_08	5.4850	5.4810	5.4830
TP_x50_OL_09	5.4800	5.4805	5.4803
TP_x50_OL_10	5.4775	5.4785	5.4780
TP_x50_GP_01	5.5040	5.5030	5.5035
TP_x50_GP_02	5.5030	5.5020	5.5025
TP_x50_GP_03	5.5020	5.5010	5.5015
TP_x50_GP_04	5.5005	5.5010	5.5008
TP_x50_GP_05	5.5010	5.5030	5.5020
TP_x50_GP_06	5.5035	5.5030	5.5033
TP_x50_GP_07	5.5035	5.5025	5.5030
TP_100_GP_01	5.5045	5.5055	5.5050
TP_100_GP_02	5.5035	5.5010	5.5023
TP_100_GP_03	5.5010	5.4985	5.4998
TP_100_GP_04	5.4990	5.4985	5.4988
TP_100_GP_05	5.4980	5.4965	5.4973
TP_100_GP_06	5.4950	5.4925	5.4938
TP_100_GP_07	5.4920	5.4920	5.4920
TP_xxT_TW_01	5.4955	5.4975	5.4965
TP_xxT_TW_02	5.4935	5.4940	5.4938
TP_xxT_TW_03	5.4920	5.4930	5.4925
TP_xxT_TW_04	5.4905	5.4880	5.4893
TP_xxT_TW_05	5.4880	5.4885	5.4883
TP_xxT_TW_06	5.4870	5.4835	5.4853
TP_xxT_TW_07	5.4820	5.4785	5.4803

Table 5.8.4 Tape Coupon's Top Tab Section Thickness Measurements

	tab top thick 1	tab top thick 2	tab top thick 3	tab top thick 4	ave. tab top
TP_xx0_NF_01	0.347	0.3455	0.3425	0.3365	0.3429
TP_xx0_NF_02	0.3485	0.3475	0.3455	0.3425	0.3460
TP_xx0_NF_03	0.348	0.348	0.3465	0.3475	0.3475
TP_xx0_NF_04	0.3475	0.3475	0.3485	0.3495	0.3483
TP_xx0_NF_05	0.3485	0.3475	0.35	0.349	0.3488
TP_xx0_NF_06	0.342	0.342	0.347	0.349	0.3450
TP_xx0_NF_07	0.348	0.3475	0.35	0.3485	0.3485
TP_x50_OL_01	0.3370	0.3330	0.3400	0.3365	0.3366
TP_x50_OL_02	0.3420	0.3400	0.3460	0.3430	0.3428
TP_x50_OL_03	0.3455	0.3440	0.3505	0.3490	0.3473
TP_x50_OL_04	0.3465	0.3460	0.3520	0.3515	0.3490
TP_x50_OL_05	0.3455	0.3470	0.3520	0.3525	0.3493
TP_x50_OL_06	0.3450	0.3455	0.3515	0.3515	0.3484
TP_x50_OL_07	0.3430	0.3435	0.3500	0.3505	0.3468
TP_x50_OL_08	0.3410	0.3420	0.3480	0.3495	0.3451
TP_x50_OL_09	0.3405	0.3410	0.3465	0.3475	0.3439
TP_x50_OL_10	0.3380	0.3390	0.3425	0.3445	0.3410
TP_x50_GP_01	0.3470	0.3475	0.3480	0.3515	0.3485
TP_x50_GP_02	0.3500	0.3515	0.3545	0.3570	0.3533
TP_x50_GP_03	0.3525	0.3535	0.3590	0.3610	0.3565
TP_x50_GP_04	0.3545	0.3545	0.3615	0.3630	0.3584
TP_x50_GP_05	0.3550	0.3550	0.3630	0.3630	0.3590
TP_x50_GP_06	0.3550	0.3555	0.3630	0.3630	0.3591
TP_x50_GP_07	0.3550	0.3540	0.3630	0.3625	0.3586
TP_100_GP_01	0.3345	0.3350	0.3340	0.3360	0.3349
TP_100_GP_02	0.3365	0.3370	0.3380	0.3405	0.3380
TP_100_GP_03	0.3395	0.3410	0.3435	0.3460	0.3425
TP_100_GP_04	0.3390	0.3400	0.3460	0.3470	0.3430
TP_100_GP_05	0.3405	0.3405	0.3495	0.3490	0.3449
TP_100_GP_06	0.3415	0.3415	0.3500	0.3500	0.3458
TP_100_GP_07	0.3410	0.3410	0.3495	0.3480	0.3449
TP_xxT_TW_01	0.3420	0.3405	0.3460	0.3420	0.3426
TP_xxT_TW_02	0.3460	0.3445	0.3515	0.3490	0.3478
TP_xxT_TW_03	0.3475	0.3460	0.3555	0.3530	0.3505
TP_xxT_TW_04	0.3475	0.3470	0.3575	0.3560	0.3520
TP_xxT_TW_05	0.3480	0.3480	0.3575	0.3575	0.3528
TP_xxT_TW_06	0.3475	0.3475	0.3575	0.3580	0.3526
TP_xxT_TW_07	0.3470	0.3470	0.3555	0.3580	0.3519

Table 5.8.5 Tape Coupon's Bottom Tab Section Thickness Measurements

	tab bot thick 1	tab bot thick 2	tab bot thick 3	tab bot thick 4	ave. tab bot
TP_xx0_NF_01	0.3320	0.3335	0.3305	0.3340	0.3325
TP_xx0_NF_02	0.3350	0.3360	0.3385	0.3360	0.3364
TP_xx0_NF_03	0.3375	0.3385	0.3420	0.3400	0.3395
TP_xx0_NF_04	0.3395	0.3390	0.3425	0.3440	0.3413
TP_xx0_NF_05	0.3395	0.3395	0.3440	0.3445	0.3419
TP_xx0_NF_06	0.3465	0.3465	0.3480	0.3485	0.3474
TP_xx0_NF_07	0.3395	0.3400	0.3460	0.3455	0.3428
TP_x50_OL_01	0.3370	0.3395	0.3380	0.3415	0.3390
TP_x50_OL_02	0.3420	0.3445	0.3450	0.3485	0.3450
TP_x50_OL_03	0.3470	0.3485	0.3505	0.3525	0.3496
TP_x50_OL_04	0.3500	0.3500	0.3540	0.3545	0.3521
TP_x50_OL_05	0.3515	0.3510	0.3545	0.3545	0.3529
TP_x50_OL_06	0.3520	0.3510	0.3550	0.3545	0.3531
TP_x50_OL_07	0.3505	0.3490	0.3530	0.3515	0.3510
TP_x50_OL_08	0.3485	0.3470	0.3505	0.3480	0.3485
TP_x50_OL_09	0.3455	0.3440	0.3470	0.3445	0.3453
TP_x50_OL_10	0.3425	0.3400	0.3425	0.3390	0.3410
TP_x50_GP_01	0.3490	0.3450	0.3510	0.3460	0.3478
TP_x50_GP_02	0.3515	0.3490	0.3570	0.3545	0.3530
TP_x50_GP_03	0.3540	0.3525	0.3605	0.3585	0.3564
TP_x50_GP_04	0.3550	0.3555	0.3630	0.3620	0.3589
TP_x50_GP_05	0.3550	0.3550	0.3640	0.3635	0.3594
TP_x50_GP_06	0.3545	0.3555	0.3635	0.3645	0.3595
TP_x50_GP_07	0.3545	0.3550	0.3620	0.3635	0.3588
TP_100_GP_01	0.3395	0.3375	0.3400	0.3335	0.3376
TP_100_GP_02	0.3420	0.3400	0.3455	0.3400	0.3419
TP_100_GP_03	0.3455	0.3465	0.3510	0.3460	0.3473
TP_100_GP_04	0.3450	0.3440	0.3520	0.3500	0.3478
TP_100_GP_05	0.3440	0.3440	0.3530	0.3500	0.3478
TP_100_GP_06	0.3440	0.3440	0.3510	0.3530	0.3480
TP_100_GP_07	0.3420	0.3430	0.3485	0.3500	0.3459
TP_xxT_TW_01	0.3395	0.3415	0.3405	0.3435	0.3413
TP_xxT_TW_02	0.3450	0.3455	0.3455	0.3485	0.3461
TP_xxT_TW_03	0.3470	0.3480	0.3500	0.3520	0.3493
TP_xxT_TW_04	0.3480	0.3480	0.3525	0.3525	0.3503
TP_xxT_TW_05	0.3490	0.3485	0.3535	0.3535	0.3511
TP_xxT_TW_06	0.3485	0.3480	0.3535	0.3530	0.3508
TP_xxT_TW_07	0.3485	0.3480	0.3525	0.3520	0.3503

Table 5.8.6 Tow Coupon's Gage Section Thickness Measurements

	Thick 1	Thick 2	Thick 3	Thick 4	ave. Thk
TOW_xx0_NF_01	0.0895	0.0890	0.0890	0.0895	0.0893
TOW_xx0_NF_02	0.0890	0.0890	0.0900	0.0890	0.0893
TOW_xx0_NF_03	0.09	0.0900	0.0900	0.0900	0.0900
TOW_xx0_NF_04	0.0900	0.0905	0.0905	0.0900	0.0903
TOW_xx0_NF_05	0.0905	0.0910	0.0915	0.0915	0.0911
TOW_xx0_NF_06	0.0915	0.0915	0.0925	0.0920	0.0919
TOW_xx0_NF_07	0.0930	0.0925	0.0930	0.0930	0.0929
TOW_x50_OL_01	0.0900	0.0905	0.0920	0.0915	0.0910
TOW_x50_OL_02	0.0930	0.0925	0.0915	0.0925	0.0924
TOW_x50_OL_03	0.0925	0.0935	0.0940	0.0940	0.0935
TOW_x50_OL_04	0.0935	0.0945	0.0945	0.0935	0.0940
TOW_x50_OL_05	0.0935	0.0940	0.0940	0.0935	0.0938
TOW_x50_OL_06	0.0935	0.0945	0.0940	0.0935	0.0939
TOW_x50_OL_07	0.0940	0.0940	0.0940	0.0935	0.0939
TOW_x50_GP_01	0.0860	0.0865	0.0875	0.0870	0.0868
TOW_x50_GP_02	0.0875	0.0880	0.0885	0.0880	0.0880
TOW_x50_GP_03	0.0890	0.0880	0.0880	0.0885	0.0884
TOW_x50_GP_04	0.0890	0.0890	0.0890	0.0895	0.0891
TOW_x50_GP_05	0.0890	0.0890	0.0890	0.0890	0.0890
TOW_x50_GP_06	0.0890	0.0890	0.0880	0.0885	0.0886
TOW_x50_GP_07	0.0890	0.0880	0.0880	0.0880	0.0883
TOW_100_GP_01	0.0880	0.0870	0.0885	0.0885	0.0880
TOW_100_GP_02	0.0885	0.0885	0.0885	0.0880	0.0884
TOW_100_GP_03	0.0890	0.0885	0.0895	0.0890	0.0890
TOW_100_GP_04	0.0895	0.0890	0.0890	0.0900	0.0894
TOW_100_GP_05	0.0895	0.0895	0.0890	0.0890	0.0893
TOW_100_GP_06	0.0890	0.0885	0.0880	0.0880	0.0884
TOW_100_GP_07	0.0875	0.0870	0.0875	0.0875	0.0874
TOW_xxT_TW_01	0.0880	0.0885	0.0870	0.0870	0.0876
TOW_xxT_TW_02	0.0885	0.0885	0.0900	0.0895	0.0891
TOW_xxT_TW_03	0.0900	0.0900	0.0900	0.0900	0.0900
TOW_xxT_TW_04	0.0905	0.0900	0.0900	0.0905	0.0903
TOW_xxT_TW_05	0.0905	0.0905	0.0910	0.0905	0.0906
TOW_xxT_TW_06	0.0900	0.0905	0.0905	0.0900	0.0903
TOW_xxT_TW_07	0.0905	0.0905	0.0900	0.0895	0.0901

Table 5.8.7 Tow Coupon's Width Measurements

	Width 1	Width 2	Width 3	Width 4	ave. wth @ gage	ave. wth
TOW_xx0_NF_01	0.6245	0.6250	0.6230	0.6235	0.6233	0.6240
TOW_xx0_NF_02	0.6045	0.6055	0.6045	0.6045	0.6045	0.6048
TOW_xx0_NF_03	0.6240	0.6250	0.6230	0.6225	0.6228	0.6236
TOW_xx0_NF_04	0.6460	0.6425	0.6390	0.6390	0.6390	0.6416
TOW_xx0_NF_05	0.6275	0.6295	0.6280	0.6285	0.6283	0.6284
TOW_xx0_NF_06	0.6415	0.6415	0.6400	0.6385	0.6393	0.6404
TOW_xx0_NF_07	0.6125	0.6180	0.6100	0.6110	0.6105	0.6129
TOW_x50_OL_01	0.6240	0.6270	0.6210	0.6205	0.6208	0.6231
TOW_x50_OL_02	0.6300	0.6280	0.6295	0.6285	0.6290	0.6290
TOW_x50_OL_03	0.6295	0.6255	0.6245	0.6245	0.6245	0.6260
TOW_x50_OL_04	0.6130	0.6120	0.6140	0.6120	0.6130	0.6128
TOW_x50_OL_05	0.6370	0.6350	0.6315	0.6320	0.6318	0.6339
TOW_x50_OL_06	0.6385	0.6370	0.6350	0.6360	0.6355	0.6366
TOW_x50_OL_07	0.5965	0.5905	0.5955	0.5920	0.5938	0.5936
TOW_x50_GP_01	0.6085	0.6325	0.6180	0.6200	0.6190	0.6198
TOW_x50_GP_02	0.6225	0.6250	0.6250	0.6260	0.6255	0.6246
TOW_x50_GP_03	0.6230	0.6230	0.6265	0.6260	0.6263	0.6246
TOW_x50_GP_04	0.6230	0.6275	0.6285	0.6280	0.6283	0.6268
TOW_x50_GP_05	0.6195	0.6265	0.6195	0.6220	0.6208	0.6219
TOW_x50_GP_06	0.6205	0.6220	0.6215	0.6200	0.6208	0.6210
TOW_x50_GP_07	0.6265	0.6235	0.6260	0.6240	0.6250	0.6250
TOW_100_GP_01	0.6280	0.6295	0.6270	0.6270	0.6270	0.6279
TOW_100_GP_02	0.6140	0.6125	0.6100	0.6100	0.6100	0.6116
TOW_100_GP_03	0.6100	0.6145	0.6100	0.6095	0.6098	0.6110
TOW_100_GP_04	0.6065	0.6070	0.6070	0.6070	0.6070	0.6069
TOW_100_GP_05	0.6075	0.6065	0.6055	0.6050	0.6053	0.6061
TOW_100_GP_06	0.6155	0.6160	0.6155	0.6150	0.6153	0.6155
TOW_100_GP_07	0.6240	0.6240	0.6235	0.6230	0.6233	0.6236
TOW_xxT_TW_01	0.6285	0.6290	0.6270	0.6270	0.6270	0.6279
TOW_xxT_TW_02	0.6245	0.6285	0.6270	0.6255	0.6263	0.6264
TOW_xxT_TW_03	0.6190	0.6190	0.5960	0.6060	0.6010	0.6100
TOW_xxT_TW_04	0.6275	0.6285	0.6255	0.6250	0.6253	0.6266
TOW_xxT_TW_05	0.6270	0.6265	0.6220	0.6215	0.6218	0.6243
TOW_xxT_TW_06	0.6120	0.6100	0.6120	0.6110	0.6115	0.6113
TOW_xxT_TW_07	0.6240	0.6235	0.6220	0.6225	0.6223	0.6230

Table 5.8.8 Tow Coupon's Length Measurements

	Length 1	Length 2	ave. lgth
TOW_xx0_NF_01	5.5045	5.5035	5.5040
TOW_xx0_NF_02	5.5040	5.5030	5.5035
TOW_xx0_NF_03	5.5010	5.4995	5.5003
TOW_xx0_NF_04	5.5045	5.5020	5.5033
TOW_xx0_NF_05	5.5055	5.5050	5.5053
TOW_xx0_NF_06	5.5070	5.5060	5.5065
TOW_xx0_NF_07	5.5075	5.5060	5.5068
TOW_x50_OL_01	5.5155	5.5190	5.5173
TOW_x50_OL_02	5.5125	5.5140	5.5133
TOW_x50_OL_03	5.5080	5.5110	5.5095
TOW_x50_OL_04	5.5050	5.5065	5.5058
TOW_x50_OL_05	5.5020	5.5025	5.5023
TOW_x50_OL_06	5.5010	5.4990	5.5000
TOW_x50_OL_07	5.4945	5.4965	5.4955
TOW_x50_GP_01	5.4900	5.4885	5.4893
TOW_x50_GP_02	5.4900	5.4910	5.4905
TOW_x50_GP_03	5.4915	5.4915	5.4915
TOW_x50_GP_04	5.4920	5.4920	5.4920
TOW_x50_GP_05	5.4915	5.4920	5.4918
TOW_x50_GP_06	5.4925	5.4935	5.4930
TOW_x50_GP_07	5.4935	5.4935	5.4935
TOW_100_GP_01	5.5120	5.5160	5.5140
TOW_100_GP_02	5.5140	5.5155	5.5148
TOW_100_GP_03	5.5175	5.5180	5.5178
TOW_100_GP_04	5.5185	5.5190	5.5188
TOW_100_GP_05	5.5185	5.5180	5.5183
TOW_100_GP_06	5.5180	5.5180	5.5180
TOW_100_GP_07	5.5185	5.5170	5.5178
TOW_xxT_TW_01	5.4520	5.4535	5.4528
TOW_xxT_TW_02	5.4535	5.4530	5.4533
TOW_xxT_TW_03	5.4545	5.4550	5.4548
TOW_xxT_TW_04	5.4550	5.4560	5.4555
TOW_xxT_TW_05	5.4565	5.4570	5.4568
TOW_xxT_TW_06	5.4565	5.4565	5.4565
TOW_xxT_TW_07	5.4570	5.4565	5.4568

Table 5.8.9 Tow Coupon's Top Tab Section Thickness Measurements

	tab top thick 1	tab top thick 2	tab top thick 3	tab top thick 4	ave. tab top
TOW_xx0_NF_01	0.3495	0.3520	0.3510	0.3535	0.3515
TOW_xx0_NF_02	0.3550	0.3565	0.3560	0.3580	0.3564
TOW_xx0_NF_03	0.3575	0.3590	0.3595	0.3615	0.3594
TOW_xx0_NF_04	0.3595	0.3600	0.3625	0.3635	0.3614
TOW_xx0_NF_05	0.3610	0.3605	0.3640	0.3645	0.3625
TOW_xx0_NF_06	0.3600	0.3600	0.3640	0.3645	0.3621
TOW_xx0_NF_07	0.3610	0.3600	0.3640	0.3640	0.3623
TOW_x50_OL_01	0.3550	0.3565	0.3530	0.3555	0.3550
TOW_x50_OL_02	0.3585	0.3595	0.3595	0.3610	0.3596
TOW_x50_OL_03	0.3605	0.3620	0.3630	0.3650	0.3626
TOW_x50_OL_04	0.3620	0.3620	0.3670	0.3685	0.3649
TOW_x50_OL_05	0.3625	0.3620	0.3690	0.3715	0.3663
TOW_x50_OL_06	0.3625	0.3625	0.3710	0.3720	0.3670
TOW_x50_OL_07	0.3620	0.3610	0.3720	0.3720	0.3668
TOW_x50_GP_01	0.3520	0.3540	0.3500	0.3530	0.3523
TOW_x50_GP_02	0.3555	0.3565	0.3540	0.3555	0.3554
TOW_x50_GP_03	0.3575	0.3565	0.3570	0.3565	0.3569
TOW_x50_GP_04	0.3575	0.3565	0.3575	0.3575	0.3573
TOW_x50_GP_05	0.3565	0.3560	0.3570	0.3565	0.3565
TOW_x50_GP_06	0.3565	0.3555	0.3565	0.3555	0.3560
TOW_x50_GP_07	0.3565	0.3555	0.3555	0.3535	0.3553
TOW_100_GP_01	0.3550	0.3555	0.3530	0.3555	0.3548
TOW_100_GP_02	0.3565	0.3570	0.3565	0.3590	0.3573
TOW_100_GP_03	0.3570	0.3575	0.3600	0.3610	0.3589
TOW_100_GP_04	0.3575	0.3570	0.3610	0.3625	0.3595
TOW_100_GP_05	0.3575	0.3570	0.3620	0.3625	0.3598
TOW_100_GP_06	0.3570	0.3555	0.3625	0.3620	0.3593
TOW_100_GP_07	0.3555	0.3545	0.3610	0.3600	0.3565
TOW_xxT_TW_01	0.3550	0.3560	0.3510	0.3530	0.3538
TOW_xxT_TW_02	0.3570	0.3585	0.3555	0.3580	0.3573
TOW_xxT_TW_03	0.3600	0.3610	0.3605	0.3630	0.3611
TOW_xxT_TW_04	0.3615	0.3630	0.3655	0.3675	0.3644
TOW_xxT_TW_05	0.3630	0.3635	0.3685	0.3705	0.3664
TOW_xxT_TW_06	0.3645	0.3635	0.3710	0.3710	0.3675
TOW_xxT_TW_07	0.3635	0.3620	0.3705	0.3690	0.3663

Table 5.8.10 Tow Coupon's Bottom Tab Section Thickness Measurements

	tab bot thick 1	tab bot thick 2	tab bot thick 3	tab bot thick 4	ave. tab bot
TOW_xx0_NF_01	0.3580	0.3575	0.3560	0.3555	0.3568
TOW_xx0_NF_02	0.3590	0.3580	0.3575	0.3565	0.3578
TOW_xx0_NF_03	0.3590	0.3585	0.3580	0.3570	0.3581
TOW_xx0_NF_04	0.3595	0.3595	0.3595	0.3595	0.3595
TOW_xx0_NF_05	0.3595	0.3590	0.3610	0.3505	0.3575
TOW_xx0_NF_06	0.3590	0.3590	0.3620	0.3615	0.3604
TOW_xx0_NF_07	0.3595	0.3590	0.3625	0.3630	0.3610
TOW_x50_OL_01	0.3585	0.3585	0.3600	0.3575	0.3586
TOW_x50_OL_02	0.3595	0.3585	0.3640	0.3620	0.3610
TOW_x50_OL_03	0.3605	0.3595	0.3675	0.3655	0.3633
TOW_x50_OL_04	0.3610	0.3605	0.3685	0.3680	0.3645
TOW_x50_OL_05	0.3620	0.3610	0.3685	0.3690	0.3651
TOW_x50_OL_06	0.3620	0.3610	0.3665	0.3675	0.3643
TOW_x50_OL_07	0.3605	0.3605	0.3635	0.3655	0.3625
TOW_x50_GP_01	0.3500	0.3475	0.3470	0.3450	0.3474
TOW_x50_GP_02	0.3525	0.3510	0.3500	0.3485	0.3505
TOW_x50_GP_03	0.3560	0.3540	0.3535	0.3510	0.3536
TOW_x50_GP_04	0.3585	0.3565	0.3575	0.3555	0.3570
TOW_x50_GP_05	0.3595	0.3585	0.3600	0.3575	0.3589
TOW_x50_GP_06	0.3600	0.3590	0.3610	0.3600	0.3600
TOW_x50_GP_07	0.3585	0.3590	0.3600	0.3605	0.3595
TOW_100_GP_01	0.3590	0.3585	0.3575	0.3560	0.3578
TOW_100_GP_02	0.3595	0.3595	0.3585	0.3580	0.3589
TOW_100_GP_03	0.3600	0.3595	0.3595	0.3590	0.3595
TOW_100_GP_04	0.3595	0.3595	0.3605	0.3600	0.3599
TOW_100_GP_05	0.3585	0.3590	0.3610	0.3605	0.3598
TOW_100_GP_06	0.3585	0.3585	0.3600	0.3610	0.3595
TOW_100_GP_07	0.3565	0.3575	0.3585	0.3600	0.3581
TOW_xxT_TW_01	0.3550	0.3525	0.3570	0.3535	0.3545
TOW_xxT_TW_02	0.3585	0.3560	0.3615	0.3590	0.3588
TOW_xxT_TW_03	0.3600	0.3590	0.3650	0.3630	0.3623
TOW_xxT_TW_04	0.3610	0.3605	0.3675	0.3660	0.3638
TOW_xxT_TW_05	0.3630	0.3615	0.3690	0.3675	0.3653
TOW_xxT_TW_06	0.3635	0.3630	0.3705	0.3705	0.3669
TOW_xxT_TW_07	0.3635	0.3635	0.3695	0.3695	0.3665

5.9 *Appendix E – Raw and Normalized Data*

This Page Left Intentionally Blank

Table 5.9.1 Data for Unflawed Tape Family

Run	Initial Axial Compressive Stiffness (10 ⁶ psi)								Stress at onset of nonlinearity (psi)		Ultimate failure (psi)	
	Gauge 1		Gauge 2		Average		Normalized to bending					
	Raw	Normalized	Raw	Normalized	Raw	Normalized	Raw	Normalized			Raw	Normalized
01-0	24.14	18.06	23.13	17.30	23.66	17.68	23.603	17.66	75058.71	56155.09		
01-1	24.33	18.20	22.83	17.08	23.58	17.64	23.506	17.59	50745.25	37965.00		
01-2	24.35	18.22	22.84	17.09	23.60	17.65	23.535	17.61	48700.26	36435.05		
01-3	24.28	18.16	22.82	17.07	23.55	17.62	23.47	17.56	54916.24	41085.53		
01-4	24.50	18.33	23.14	17.32	23.82	17.82	23.876	17.86	49262.65	36855.80		
01-5	25.01	18.71	22.88	17.12	23.94	17.91	23.891	17.87	60925.75	45581.53		
01-6	24.99	18.70	22.61	16.92	23.80	17.81	23.768	17.78	54304.26	40627.68		
01-7	25.03	18.73	23.02	17.22	24.02	17.97	24.005	17.96	62132.73	46484.53		
01-8	25.12	18.79	22.20	16.61	23.66	17.70	23.585	17.65	48170.33	36038.58	192047.63	234671.61
Average	24.64	18.43	22.83	17.08	23.74	17.76	23.69	17.73	56024.02	41914.31		
02-0												
03-0	22.17	16.84	24.03	18.25	23.10	17.55	23.026	17.49	54629.2	41502.80		
03-1	22.01	16.72	23.33	17.72	22.67	17.22	22.644	17.20	47064.54	35755.79		
03-2	22.18	16.85	23.27	17.68	22.73	17.27	22.711	17.25	61287.28	46561.07		
03-3	22.20	16.87	23.22	17.64	22.71	17.25	22.702	17.25	46405.43	35255.05		
03-4	22.37	17.00	23.19	17.62	22.78	17.31	22.782	17.31	46781.65	35540.87		
03-5	22.55	17.13	23.09	17.54	22.82	17.34	22.819	17.34	46679.61	35463.35	185982.96	371840.09
Average	22.25	16.90	23.35	17.74	22.80	17.32	22.78	17.31	50474.62	38346.49		
04-0												
05-0	26.05	19.65	21.59	16.29	23.82	17.97	23.75	17.92	48184.79	36359.10	200331.20	400622.68
06-0												
07-0	24.33	18.39	22.61	17.09	23.47	17.74	23.417	17.70	55538.48	41979.42		
07-1	23.62	17.86	14.68	11.10	19.15	14.48	18.215	13.77	62199.24	47014.03		
07-2	23.66	17.89	14.62	11.05	19.14	14.47	18.144	13.71	37123.68	28060.37		
07-3	23.63	17.86	14.61	11.04	19.12	14.45	18.134	13.71	45144.05	34122.66		
07-4	23.78	17.97	14.55	11.00	19.16	14.48	18.194	13.75	43256.26	32695.75		
07-5	22.80	17.23	22.82	17.25	22.81	17.24	22.823	17.25	46309.77	35003.79	188229.127	376458.25
Average	23.64	17.87	17.31	13.09	20.48	15.48	19.82	14.98	48261.91	36479.34		

Table 5.9.2 Data for 100% Tow Gap Flaw Tape Family

	Initial Axial Compressive Stiffness								Stress at onset of nonlinearity (psi)		Ultimate Failure (psi)	
	Gauge 1		Gauge 2		Average							
	Raw	Normalized	Raw	Normalized	Raw	Normalized	Raw	Normalized	Raw	Normalized	Raw	normalized
01-0	24.87	18.67	22.19	16.66	23.53	17.66	23.39	17.56	85713.93	64347.15		
01-1	27.48	20.63	21.53	16.17	24.51	18.40	24.05	18.06	70594.00	52996.32		
01-2	27.33	20.52	21.53	16.17	24.43	18.34	24.00	18.02	54015.80	40550.73	173497.68	307390.33
Average	26.56	19.94	21.75	16.33	24.16	18.13	23.81	17.88	70107.91	52631.40		
02-0	28.65	21.62	20.24	15.27	24.45	18.45	23.28	17.57				
02-1	28.65	21.62	19.71	14.87	24.18	18.25	23.27	17.56	146012.01	110177.20		
02-2	19.98	15.07	22.66	17.10	21.32	16.08	21.30	16.07	59315.82	44758.32	~	
Average	25.76	19.44	20.87	15.75	23.32	17.59	22.62	17.06	102663.92	77467.76		
03-0	24.78	18.73	24.91	18.83	24.85	18.78	24.64	18.62	75370.09	56969.37	174635.46	363237.59
04-0	25.10	18.97	22.42	16.95	23.76	17.96	23.49	17.76				
04-1	24.85	18.78	22.63	17.10	23.74	17.94	23.87	18.05	43546.42	32915.08	171749.31	342985.52
Average	24.97	18.88	22.52	17.03	23.75	17.95	23.68	17.90	43546.42	32915.08		
05-0	29.39	22.44	22.67	17.31	26.03	19.88	25.45	19.43	45312.57	34599.53		
05-1	27.49	20.99	21.00	16.04	24.25	18.51	23.95	18.29	54607.53	41696.93		
05-2	26.79	20.45	21.19	16.18	23.99	18.32	23.67	18.07	43699.12	33367.54	~	
Average	27.89	21.30	21.62	16.51	24.76	18.90	24.36	18.60	47873.07	36554.66		
06-0	25.44	19.49	23.37	17.91	24.41	18.70	24.47	18.74	43021.24	32960.54	~	
07-0	27.17	20.85	22.18	17.02	24.68	18.94	24.39	18.72	44565.67	34201.08		
07-1	27.52	21.12	21.94	16.84	24.73	18.98	24.19	18.56	43338.87	33259.60	~	
Average	27.34	20.98	22.06	16.93	24.70	18.96	24.29	18.64	43952.27	33730.34		

Table 5.9.3 Data for 50% Tow Gap Flaw Tape Family

Run	Initial Axial Compressive Stiffness								Stress at Onset of Nonlinearity		Ultimate Failure (psi)	
	Gauge 1		Gauge 2		Average		Normalized to bending		Nonlinearity		Ultimate Failure (psi)	
	Raw	Normalized	Raw	Normalized	Raw	Normalized	Raw	Normalized	Raw	Normalized	Raw	Normalized
01-0	22.46	18.33	23.03	18.80	22.75	18.57	22.64	18.48	66505.68	54287.21	179205.32	358258.62
02-0	23.22	19.11	20.61	16.95	21.91	18.03	21.82	17.95	50292.32	41375.83		
02-1	22.41	18.43	19.95	16.41	21.18	17.42	21.09	17.35	55150.08	45372.34	~	
Average	22.81	18.77	20.28	16.68	21.55	17.73	21.45	17.65	52721.20	43374.08		
03-0	21.43	17.60	21.72	17.84	21.57	17.72	21.57	17.72	56231.08	46189.41	183620.24	363977.56
04-0	22.53	18.48	21.72	17.81	22.13	18.15	22.14	18.16	64704.80	53066.72	140807.70	280047.12
05-0	22.56	18.39	20.14	16.42	21.35	17.40	21.19	17.27	87475.02	71291.60		
05-1	22.17	18.07	19.94	16.25	21.05	17.16	21.09	17.18	57135.96	46565.45	~	
Average	22.37	18.23	20.04	16.33	21.20	17.28	21.14	17.23	72305.49	58928.53		
06-0	23.45	18.99	20.44	16.55	21.94	17.77	21.83	17.68	67807.59	54914.10		
06-1	23.36	18.92	21.56	17.46	22.46	18.19	22.47	18.19	43903.46	35555.30	155113.52	313095.14
Average	23.40	18.95	21.00	17.01	22.20	17.98	22.15	17.94	55855.52	45234.70		

Table 5.9.4 Data for 50% Tow Overlap Flaw Tape Family

	Initial Axial Compressive Stiffness								Stress at Onset of Nonlinearity		Ultimate Failure (psi)	
	Gauge 1		Gauge 2		Average		Normalized to bending		Raw	Normalized	Raw	Normalized
	Raw	Normalized	Raw	Normalized	Raw	Normalized	Raw	Normalized				
01-0												
02-0	23.29	17.70	24.79	18.84	24.04	18.27	24.07	18.29	44766.31	34009.78	~	
03-0	22.26	17.12	22.61	17.39	22.43	17.26	22.47	17.28	79306.25	60964.03	171285.14	381715.64
04-0	24.23	18.82	21.64	16.80	22.94	17.81	22.83	17.72	70305.24	54587.06		
04-1	23.44	18.20	25.08	19.47	24.26	18.84	24.30	18.87	43005.10	33390.42	169680.04	351543.21
Average	23.84	18.51	23.36	18.14	23.60	18.32	23.56	18.30	56655.17	43988.74		
05-0	24.61	18.98	24.65	19.01	24.63	19.00	24.65	19.01	43996.97	33934.32	190149.99	358202.52
06-0	23.57	18.15	23.36	17.99	23.46	18.07	23.42	18.03	91993.66	70835.31	186199.85	353334.19
07-0	25.29	19.41	21.29	16.33	23.29	17.87	23.28	17.86	70380.62	54012.27		
07-1	22.98	17.63	23.76	18.23	23.37	17.93	23.37	17.93	46084.62	35366.77	170934.80	300097.45
Average	24.14	18.52	22.52	17.28	23.33	17.90	23.32	17.90	58232.62	44689.52		

Table 5.9.5 Data for Twisted Tow Flaw Tape Family

Run	Initial Axial Compressive Stiffness (10 ⁶ psi)								Stress at Onset of Nonlinearity		Ultimate Failure (psi)	
	Gauge 1		Gauge 2		Average		Normalized to bending		Nonlinearity		Ultimate Failure (psi)	
	Raw	Normalized	Raw	Normalized	Raw	Normalized	Raw	Normalized	Raw	Normalized	Raw	Normalized
01-0	25.70	19.53	21.78	16.55	23.74	18.04	23.56	17.90	81636.14	62020.46		
01-1	26.55	20.18	21.52	16.35	24.04	18.27	23.77	18.06	59067.23	44874.45	~	
Average	26.12	19.85	21.65	16.45	23.89	18.15	23.67	17.98	59067.23	53447.46		
02-0	24.67	18.65	20.90	15.80	22.79	17.22	22.73	17.18	77540.11	58609.61	~	
03-0	22.99	17.24	23.03	17.27	23.01	17.25	23.07	17.29	106557.57	79857.91	172801.21	341831.87
04-0	24.15	18.10	23.71	17.78	23.93	17.94	24.09	18.05	65796.84	49310.42	173818.58	361087.22
05-0	22.46	16.93	22.63	17.06	22.54	16.99	22.44	16.90	164943.82	124250.67		
06-0	28.52	21.56	19.53	14.77	24.03	18.16	23.28	17.60				
06-1	28.13	21.26	19.48	14.72	23.80	17.99	22.93	17.33	137031.89	103577.17		
06-2	27.21	20.57	19.37	14.64	23.29	17.60	22.57	17.06	160986.68	121683.68	~	
Average	27.67	20.91	19.42	14.68	23.54	17.80	22.75	17.19	149009.29	112630.43		
07-0	23.64	17.97	24.28	18.45	23.96	18.21	23.99	18.23	61921.06	47042.56	153048.95	302333.97

Table 5.9.6 Data for Unflawed Tow Family

Runs	Initial Axial Compressive Stiffness (10 ⁶ psi)								Stress at Onset of Nonlinearity		Ultimate Failure (psi)	
	Gauge 1		Gauge 2		Ave		Normalized to bending		Raw	Normalized	Raw	Normalized
	Raw	Normalized	Raw	Normalized	Raw	Normalized	Raw	Normalized				
01-0	17.42	18.51	18.73	19.90	18.07	19.20	18.05	19.18	41967.85	44601.46		
01-1	17.03	18.10	18.95	20.13	17.99	19.12	17.95	19.08	41650.46	44264.15		
01-2	16.89	17.95	18.72	19.89	17.80	18.92	17.76	18.88	44652.41	47454.48		
01-3	17.53	18.63	18.37	19.53	17.95	19.08	17.94	19.06	47334.45	50304.83		
01-4	17.30	18.39	18.72	19.89	18.01	19.14	17.99	19.12	37631.67	39993.17		
01-5	17.47	18.57	18.50	19.66	17.98	19.11	17.95	19.08	36628.67	38927.23	162536.59	325986.30
Average	17.27	18.36	18.66	19.83	17.97	19.10	17.94	19.07	41644.25	44257.56		
02-0	17.25	18.34	18.69	19.88	17.97	19.11	17.93	19.06	44677.69	47481.35	164664.11	330240.97
03-0	17.78	19.06	19.13	20.50	18.46	19.78	18.41	19.73	45307.90	48555.74		
03-1	17.53	18.78	19.18	20.55	18.35	19.67	18.30	19.61	41570.56	44550.50		
03-2	17.60	18.86	19.09	20.46	18.34	19.66	18.29	19.60	37159.86	39823.62	167040.38	334080.76
Average	17.63	18.90	19.13	20.50	18.38	19.70	18.33	19.65	41346.11	44309.95		
04-0	18.84	20.26	18.77	20.18	18.80	20.22	18.76	20.16	66074.59	71007.77		
04-1	18.92	20.34	18.68	20.09	18.80	20.21	18.90	20.31	45182.75	48556.12		
04-2	18.82	20.24	17.94	19.29	18.38	19.76	18.43	19.81	53096.35	57060.55	~	
Average	18.86	20.28	18.46	19.85	18.66	20.07	18.70	20.09	54784.56	58874.81		
05-0	18.40	19.96	18.55	20.13	18.48	20.04	18.60	20.18	80734.07	87602.91		
05-1	18.37	19.92	18.58	20.16	18.48	20.04	18.64	20.23	43142.24	46812.77		
05-2	17.81	19.31	18.26	19.81	18.03	19.56	18.11	19.65	62035.31	67313.26		
05-3	18.32	19.88	17.80	19.31	18.06	19.59	18.17	19.71	53117.57	57636.80	~	
Average	18.22	19.77	18.30	19.85	18.26	19.81	18.38	19.94	59757.30	64841.44		
06-0	18.04	19.74	18.34	20.07	18.19	19.91	17.82	19.50				
06-1	18.77	20.54	17.39	19.03	18.08	19.78	18.06	19.76			~	
Average	18.40	20.14	17.87	19.55	18.13	19.84	17.94	19.63				
07-0	18.38	20.33	17.07	18.88	17.72	19.61	17.73	19.61				
07-1	17.32	19.16	16.81	18.59	17.07	18.88	17.11	18.92	113349.65			
07-2												
07-3	17.84	19.73	16.68	18.45	17.26	19.09	17.26	19.09	83510.75	92356.05		
07-4	17.84	19.73	17.34	19.18	17.59	19.46	17.55	19.41	39955.36	44187.36	~	
Average	17.84	19.74	16.97	18.78	17.41	19.26	17.41	19.26	78938.59	68271.70		

Table 5.9.7 Data for 100% Gap Flaw Tow Family

	Initial Axial Compressiv Stiffness (10^6 psi)								Stress at Onset of		Ultimate Failure (psi)	
	Gauge 1		Gauge 2		Average		Normalized to bending		Nonlinearity (psi)			
	Raw	Normalized	Raw	Normalized	Raw	Normalized	Raw	Normalized	Raw	Normalized	Raw	Normalized
01-0	17.65	18.50	18.93	19.83	18.29	19.17	18.30	19.17	52442.81	54953.17	--	--
01-1	16.91	17.71	19.05	19.96	17.98	18.84	17.97	18.83	79099.55	82885.93	--	--
01-2	17.62	18.47	19.61	20.55	18.62	19.51	18.49	19.38	33999.45	35626.95	--	--
Average	17.39	18.23	19.19	20.11	18.29	19.17	18.25	19.13	55180.60	57822.02	--	--
02-0	18.79	19.78	19.84	20.88	19.32	20.33	19.33	20.34	35666.00	37532.54	--	--
02-1	17.03	17.93	18.45	19.42	17.74	18.67	17.85	18.79	38251.48	40253.33	--	--
02-2	17.09	17.99	19.39	20.41	18.24	19.20	18.22	19.18	44160.60	46471.70	--	--
Average	17.64	18.57	19.22	20.24	18.43	19.40	18.47	19.43	39359.36	41419.19	--	--
03-0	18.00	19.07	19.52	20.69	18.76	19.88	18.77	19.89	43064.42	45638.64	--	--
03-1	17.96	19.03	19.34	20.50	18.65	19.77	18.64	19.75	34786.49	36865.89	--	--
03-2	17.44	18.49	19.97	21.16	18.71	19.82	18.73	19.85	34721.06	36796.55	--	--
Average	17.80	18.87	19.61	20.78	18.71	19.82	18.71	19.83	37523.99	39767.03	--	--
04-0	17.85	19.00	18.36	19.54	18.10	19.27	18.14	19.30	56876.34	60530.16	--	--
04-1	17.31	18.43	18.49	19.69	17.90	19.06	17.91	19.06	49304.36	52471.74	--	--
04-2	17.36	18.48	18.94	20.17	18.15	19.33	18.19	19.36	50615.11	53866.70	--	--
Average	17.51	18.64	18.60	19.80	18.05	19.22	18.08	19.24	52265.27	55622.87	--	--
05-0	18.01	19.15	18.10	19.25	18.05	19.20	18.12	19.26	58173.09	61823.63	--	--
05-1	17.56	18.67	18.46	19.63	18.01	19.15	18.06	19.19	50019.05	53157.90	--	--
05-2	18.10	19.24	18.41	19.58	18.25	19.41	18.32	19.47	47511.54	50493.03	--	--
Average	17.89	19.02	18.32	19.48	18.10	19.25	18.17	19.31	51901.23	55158.19	--	--
06-0	17.63	18.56	19.39	20.41	18.51	19.49	18.77	19.75	34141.97	35928.75	--	--
06-1	17.15	18.05	19.05	20.05	18.10	19.05	18.09	19.04	45210.13	47576.16	--	--
06-2	17.49	18.41	19.07	20.07	18.28	19.24	18.27	19.23	56456.67	59411.27	--	--
Average	17.42	18.34	19.17	20.18	18.30	19.26	18.38	19.34	45269.59	47638.73	--	--

Table 5.9.8 Data for 50% Gap Flaw Tow Family

Runs	Initial Axial Compressive Stiffness (10 ⁶ psi)								Stress at Onset of Nonlinearity (psi)		Ultimate Failure (psi)	
	Gauge 1		Gauge 2		Average		Normalized to bending					
	Raw	Normalized	Raw	Normalized	Raw	Normalized	Raw	Normalized	Raw	Normalized	Raw	Normalized
01-0	18.99	19.62	19.01	19.65	19.00	19.64	19.02	19.64	58239.51	60160.48		
01-1	19.08	19.72	18.79	19.42	18.94	19.57	18.95	19.57	48155.74	49744.11		
01-2	18.99	19.63	18.42	19.04	18.70	19.33	18.67	19.28	55681.38	57517.98		
Average	19.02	19.66	18.74	19.37	18.88	19.51	18.88	19.50	54025.54	55807.52		
02-0	18.53	19.42	18.46	19.34	18.50	19.38	18.51	19.39	68770.21	72062.14		
02-1	18.71	19.61	19.14	20.05	18.93	19.83	18.98	19.89	47070.80	49324.01		
02-2	18.89	19.79	19.63	20.57	19.26	20.18	19.36	20.28	48212.37	50520.23		
Average	18.71	19.61	19.08	19.99	18.89	19.80	18.95	19.86	54684.46	57302.13		
03-0	19.51	20.53	18.71	19.69	19.11	20.11	19.18	20.18	56551.34	59510.90		
03-1	19.33	20.34	19.22	20.23	19.27	20.29	19.35	20.36	37123.76	39066.60		
03-2	19.36	20.38	19.37	20.39	19.37	20.39	19.52	20.54	40201.20	42305.08		
Average	19.40	20.42	19.10	20.11	19.25	20.26	19.35	20.36	44625.44	46960.86		
04-0	20.37	21.61	17.75	18.84	19.06	20.22	18.97	20.13	47993.21	50933.49		
04-1	19.54	20.74	18.78	19.92	19.16	20.33	19.14	20.32	51494.68	54649.49		
04-2	19.40	20.58	18.34	19.46	18.87	20.02	18.78	19.93	39368.75	41780.66		
Average	19.77	20.98	18.29	19.40	19.03	20.19	18.96	20.13	46285.55	49121.21		
05-0	20.56	21.79	19.68	20.86	20.12	21.32	20.15	21.35	36481.06	38661.76		
05-1	19.26	20.42	19.14	20.28	19.20	20.35	19.18	20.33	60607.46	64230.34		
05-2	19.70	20.87	19.70	20.87	19.70	20.87	19.70	20.87	35388.13	37503.50		
Average	19.84	21.03	19.51	20.67	19.67	20.85	19.67	20.85	44158.88	46798.53		
06-0	18.14	19.14	20.86	22.01	19.50	20.57	19.50	20.58	35537.88	37503.51		
06-1	17.98	18.97	20.18	21.29	19.08	20.13	19.00	20.05	42022.17	44346.45		
06-2	17.94	18.93	19.76	20.84	18.85	19.89	18.83	19.87	48444.82	51124.34		
Average	18.02	19.01	20.27	21.38	19.14	20.20	19.11	20.17	42001.62	44324.77		
07-0	18.31	19.25	20.32	21.36	19.31	20.30	19.27	20.25	35082.49	36866.28		
07-1	17.24	18.13	19.18	20.17	18.21	19.15	18.25	19.17	74519.19	78308.15	150118.98	298520.95
Average	17.77	18.69	19.75	20.77	18.76	19.73	18.76	19.71	54800.84	57587.21		

Table 5.9.9 Data for 50% Overlap Flaw Tow Family

Runs	Initial Axial Compressive Stiffness (10 ⁶ psi)								Stress at Onset of Nonlinearity		Ultimate Failure (psi)	
	Gauge 1		Gauge 2		Average		Normalized to bending		Raw	Normalized	Raw	Normalized
	Raw	Normalized	Raw	Normalized	Raw	Normalized	Raw	Normalized				
01-0	17.30	18.75	18.94	20.52	18.12	19.63	18.10	19.61	67839.58	73510.38		
01-1	19.10	20.70	18.79	20.36	18.95	20.53	18.95	20.53	48155.74	52181.14	142330.48	373347.73
Average	18.20	19.72	18.87	20.44	18.53	20.08	18.52	20.07	57997.66	62845.76		
02-0	17.72	19.49	18.17	20.00	17.95	19.74	17.96	19.75	58453.45	64296.71		
02-1	18.82	20.71	18.30	20.13	18.56	20.42	18.70	20.56	35200.53	38719.32	148010.78	294331.01
Average	18.27	20.10	18.24	20.06	18.25	20.08	18.33	20.16	46826.99	51508.02		
03-0	17.77	19.78	18.00	20.04	17.88	19.91	17.92	19.95	49462.85	55069.97	152935.18	304720.87
04-0	19.45	21.77	17.79	19.91	18.62	20.84	18.61	20.83	67237.23	75259.58		
04-1	19.62	21.96	17.52	19.61	18.57	20.78	18.48	20.68	45546.33	50980.65	138141.68	274200.83
Average	19.54	21.87	17.65	19.76	18.59	20.81	18.54	20.76	56391.78	63120.11		
05-0	17.08	19.08	19.24	21.49	17.12	19.13	18.09	20.19	68429.60	76390.51		
05-1	17.17	19.18	18.59	20.77	17.88	19.97	17.85	19.93	43500.77	48561.53	130684.61	258851.55
Average	17.12	19.13	18.92	21.13	18.02	20.13	17.97	20.06	55965.19	62476.02		
06-0	17.19	19.23	20.13	22.51	18.66	20.87	18.55	20.73	47912.17	53557.46	153606.30	305032.10
07-0	17.77	19.87	19.29	21.57	18.53	20.72	18.50	20.68	36534.50	40839.20	172628.68	340611.30

Table 5.9.10 Data for Twisted Tow Flaw Tow Family

Runs	Initial Axial Compressive Stiffness (10 ⁶ psi)								Stress at Onset of Nonlinearity		Ultimate Failure (psi)	
	Gauge 1		Gauge 2		Average		Normalized to bending		Nonlinearity		Ultimate Failure (psi)	
	Raw	Normalized	Raw	Normalized	Raw	Normalized	Raw	Normalized	Raw	Normalized	Raw	Normalized
01-0	20.82	21.72	16.97	17.70	18.89	19.71	18.52	19.32				
01-1	20.29	21.17	16.99	17.73	18.64	19.45	18.45	19.25	61396.33	64061.13		
01-2	20.63	21.52	16.88	17.61	18.76	19.56	18.70	19.52	66779.59	69678.04	~	
Average	20.58	21.47	16.95	17.68	18.76	19.57	18.56	19.36	64087.96	66869.58		
02-0	21.60	22.92	15.98	16.95	18.79	19.94	18.33	19.46				
02-1	22.31	23.67	16.27	17.26	19.29	20.47	18.70	19.85	55527.09	58928.93	~	
Average	21.95	23.29	16.13	17.11	19.04	20.20	18.52	19.65	55527.09	58928.93		
03-0	22.27	23.87	15.96	17.11	19.12	20.49	18.51	19.83	67712.03	72565.88		
03-1	22.40	24.00	15.88	17.02	19.14	20.51	18.53	19.85	62932.64	67443.89	~	
Average	22.33	23.93	15.92	17.06	19.13	20.50	18.52	19.84	65322.33	70004.88		
04-0	21.72	23.35	16.23	17.45	18.97	20.40	18.46	19.84	93644.92	100636.51		
04-1	21.56	23.18	15.83	17.02	18.69	20.10	18.23	19.59	38271.14	41128.48	~	
Average	21.64	23.27	16.03	17.24	18.83	20.25	18.35	19.72	65958.03	70882.50		
05-0	23.16	24.99	16.42	17.71	19.79	21.35	19.39	20.92	38613.86	41669.22	138430.18	220979.21
06-0	22.69	24.39	16.31	17.54	19.50	20.97	19.08	20.50	41685.82	44798.11		
06-1	21.62	23.24	16.39	17.62	19.00	20.43	18.67	20.07	36114.81	38811.16	~	
Average	22.49	24.21	16.37	17.62	19.43	20.92	18.88	20.29	38900.31	41804.64		
07-0	23.11	24.80	15.76	16.91	19.44	20.85	18.74	20.11	39789.82	42701.33		
07-1	22.18	23.79	16.51	17.71	19.34	20.75	18.93	20.32	34622.24	37155.62		
07-2	21.81	23.40	16.19	17.37	19.00	20.39	18.55	19.91	50070.11	53733.85	155304.19	251522.34
Average	22.37	24.00	16.15	17.33	19.26	20.66	18.74	20.11	41494.06	44530.27		

6.0. Design of a low cost tape placement head for Automated Fiber Steering (Low Cost Fiber Placement/Composite Panel Manufacturing)

In order to develop a set of criteria for quality control of the manufacture of composite parts, fiber steered panels will be fabricated at the University of Kansas. These panels will be fabricated to desired specifications with various degrees of fiber steering and with specific, intentional local flaws. Flaws to be studied include twisted tows, overlaps and gaps. Nondestructive evaluation techniques to quantify these flaws and the effect of these flaws on the mechanical properties of fiber placed parts will also be studied. To facilitate such trade studies requires access to fiber placement hardware.

The goal is to produce fiber placed parts at the University of Kansas. To accomplish this a fiber placement machine is being designed, built and tested. The fiber placement machine requires a number of parts, a motion control system and a fiber placement head with cut and re-feed capability.

The motion control system must be capable of at least four axes of motion. This motion will allow fabrication of flat plates for the testing required to develop robust quality control criteria. This motion control system must be accurate and repeatable. The fiber placement head also requires cut and re-feed capabilities, which will allow the start and stop of tows at desired locations on the part.

6.1. Motion Control

A number of different forms of motion control were investigated. Through these investigations it was discovered that robotic arms used in automated manufacturing could be fitted with a fiber placement head. Industrial robot arms with the required axes of motion were found to be readily available in the School of Engineering and were therefore chosen as the motion control systems for the fiber placement machine.

The Intelledex 605 robotic arm, Figure 6.1, was the first to be set up and to come online. The robot has a payload weight capacity of 2.27 kg. (5.00 lbs.), or 5.44 kg (12 lbs.) at a decreased speed and accuracy. This arm also allows for six axes of motion, and supports the addition of pneumatically operated mechanical devices. This allowed for the complete integration of the mechanisms needed to fabricate fiber steered panels.

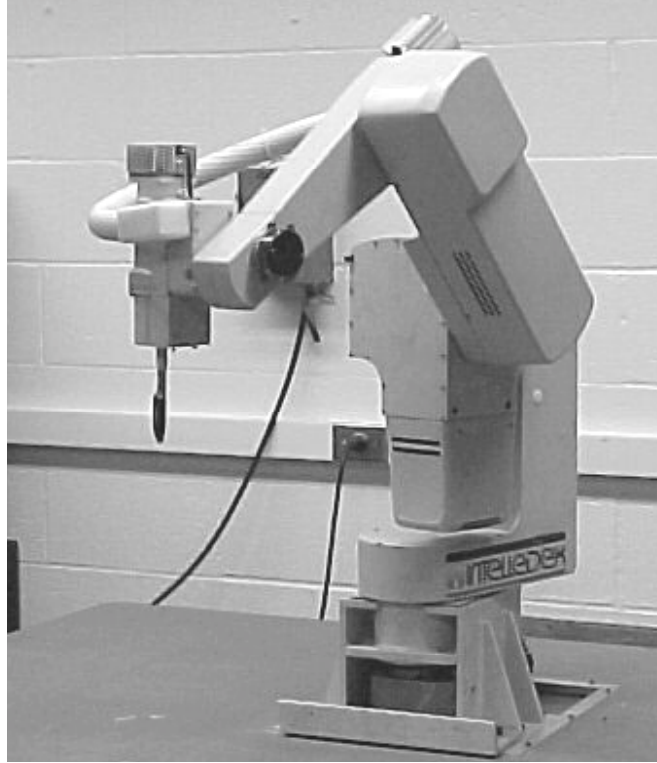


Figure 6.1 Intelledex 605 Robotic Arm

The other robotic arm to come online was the ASEA 6L. The ASEA has a payload weight capacity of 6.00 kg. (13.2 lbs) and five axes of motion. The ASEA robot (Figure 6.2) has been powered up but has not been tested for accuracy.

The Intelledex and the ASEA are both controlled via a host PC computer. This PC computer runs a ROBOT BASIC program that requires as input the defining points of a curve. The fiber placement design software (Section 2) is used to generate these points as well as the programs that teach the robot where these points are located on the curve. The interaction between the BASIC program and the robot provides the ability to create any parts within the reach of the robotic arm.

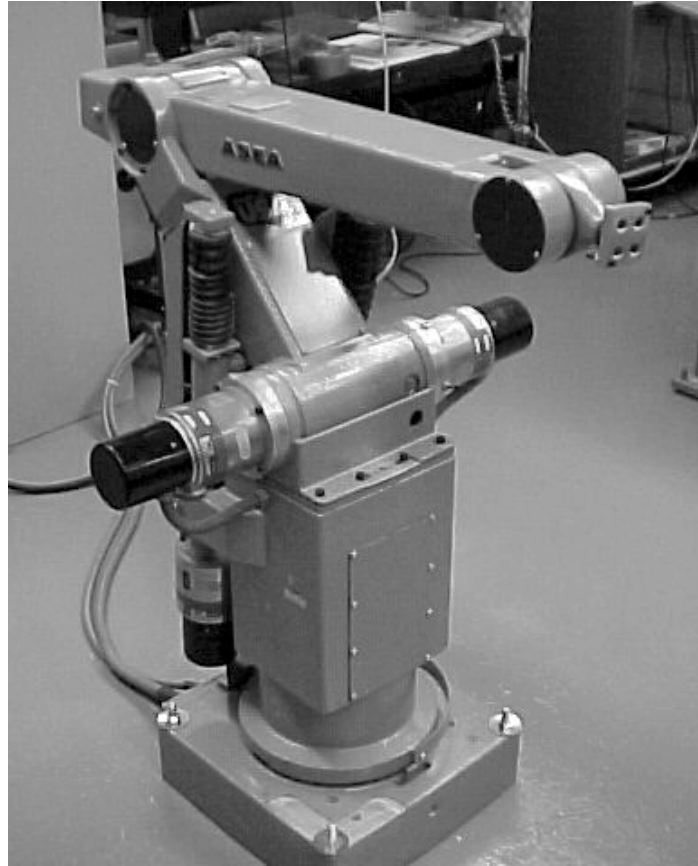


Figure 6.2 ASEA 6L Robotic Arm

6.2. Accuracy Tests

The Intelledex robotic arm was chosen to be the first to receive a fiber head and was therefore tested first for accuracy. These tests involve the use of the fiber placement design software to draw path curves that could be programmed into the robot and then redrawn by the robot while it held a pen, Figure 6.1

The fiber placement design software was used to create a path curve and to write the generated points into a program that the Intelledex robotic arm motion control system can understand. These programs are loaded into the robot and the actual path of the robotic arm is traced on paper using a pen held in the mechanical grip. Actual path curves drawn by the robot are then compared to theoretical path curves that were printed onto transparencies. The geometric difference between these curves drawn by the robot and the master transparencies is measured, and represents the absolute accuracy of the fiber placement head, Figure 6.3.

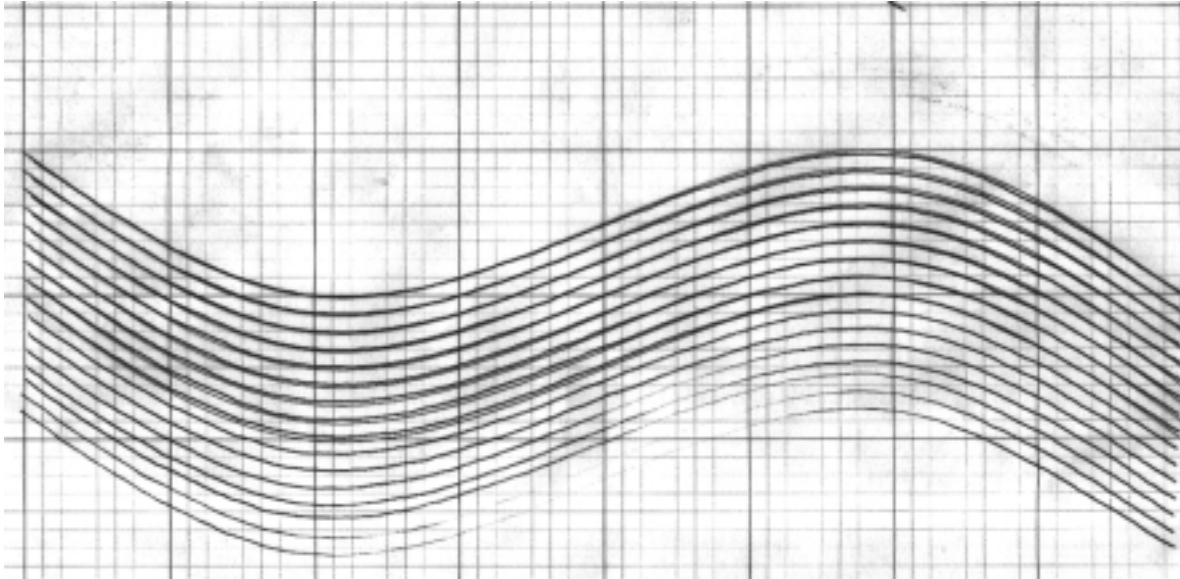


Figure 6.3 Accuracy Test Path Curves with Theoretical Curve Overlay

The distance between the path curves should remain constant. This distance was chosen to be 0.318 cm (0.125 in) for this set of tests. This value was determined because the width of the tow material that is going to be used is 0.318 cm (0.125 in), though this can be changed if a different material is used for composite manufacturing. The distance between these theoretical path curves and the robotically generated curves should be less than a $1/10^{\text{th}}$ of a tow width, 0.032cm (0.013 in). This distance would prevent the part from developing overlaps and gaps (no gaps or overlaps are desired in placing tow, but it is accepted that there is some flexure in the pen assembly that will not exist in the head assembly, thus a small error is accepted in these accuracy tests).

The tests that produced Figure 6.3, showed an error that was seen in both the concave and convex parts of the path curves. These errors were thought to have occurred because of test set up that was used. The pen was found to be susceptible to bending, which would cause the errors that were seen. The paper that was used was also found to be moving during the tests, which would cause the errors. Further tests could be performed using an available digitizing tablet. This would allow for the arm to work above the tablet and would remove the chance for the pen to bend or for the movement of the paper. However, the team is comfortable with the accuracy of the placement system, and will continue with more relevant accuracy tests placing ribbon and tow material.

Tests of this same nature were performed at different head heights to see if the accuracy would increase if the arm were not extending to the point of its maximum reach. These tests showed that placement accuracy was unaffected by tool head height. Tests were also performed using tool head rotation, Figure 6.4. This rotation allows the fiber tow to remain perpendicular to the path curve. This test showed a repeated error in the distance between the theoretical curves and the robotic path curves of 0.50 cm (0.20 in). This error was created because the pen that was used has a curve in it that moved it out of the middle of the tool head rotation. Since the error is repeatable and predictable, it can be corrected within the fiber placement software as it creates

the curves for the robot programs. Further tests using actual tow material and head rotation will help to find a workable solution for this error.

These tests proved that the Intelledex robot has sufficient accuracy to produce the required motions to fabricate composite test coupons. It was also discovered in the testing that the fiber placement head should be manufactured with the compaction roller in the center of the tool head rotation. This will help to minimize errors in the path curves and the intended path. The placement head design further ensures that it is not susceptible to vibrations and bending, which would create additional errors in part fabrication.

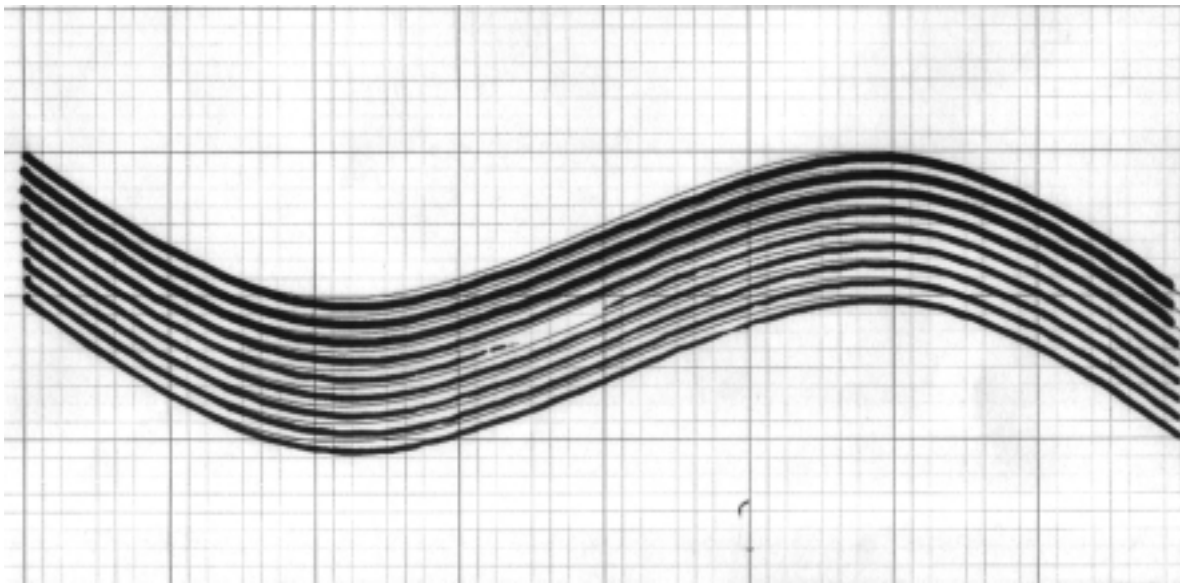


Figure 6.4 Accuracy Test with Head Rotation

6.3. Initial Head Design

The fiber placement head design incorporates ideas acquired from the University of Delaware's tape lay up head design [32]. The University of Delaware design employs a robotic arm, which makes it a good example for what has been successfully accomplished. The head design manufactured at the University of Kansas employs a cut and re-feed system that was integrated into the program of the robotic arm. This integration allows for complete automation with the need only for operator supervision. The cut and re-feed system allows the tow to be cut and re-fed through to the compaction roller. The head is then repositioned at the start of a new pass.

The fiber placement head design incorporates a set of three gas springs, Figure 6.5, to allow for compaction pressure. These springs will also be used to ensure that the head is always within proper contact of the part. The cutter is actuated using a linear actuator, Figure 6.5, which cuts the fiber tow against the cutting block, Figures 6.5 and 6.6.

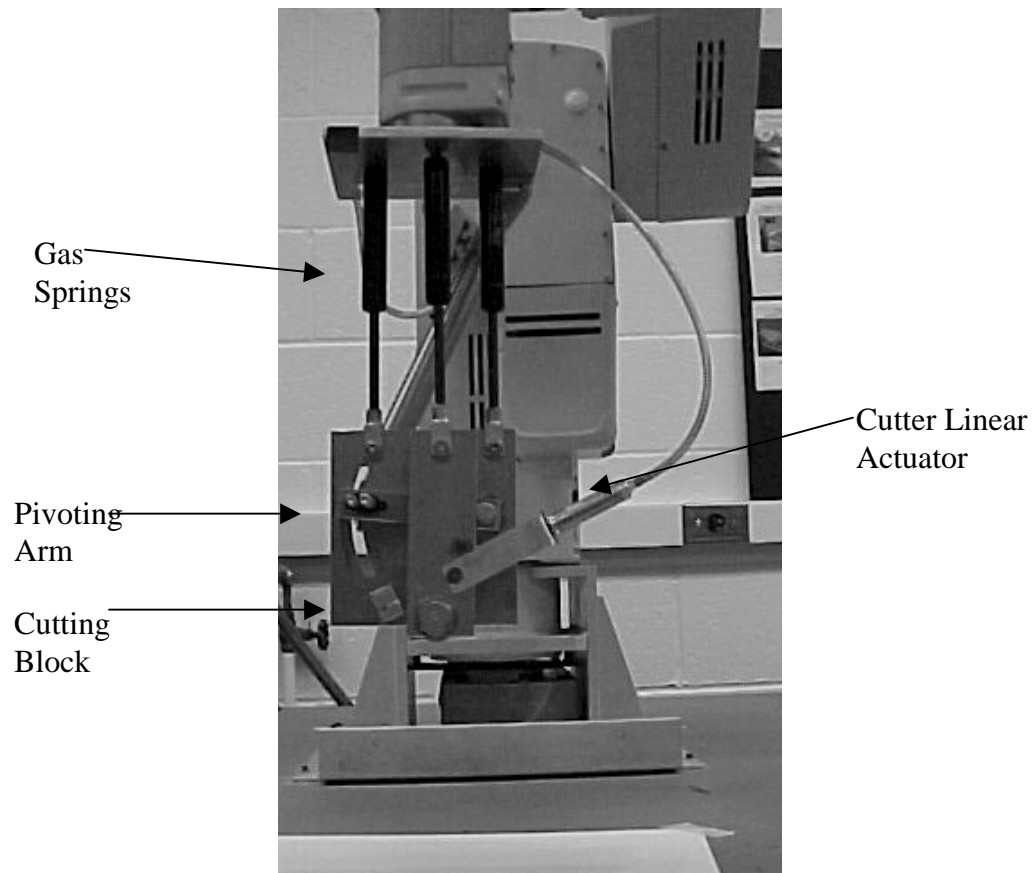


Figure 6.5 Fiber Placement Head (Front View)

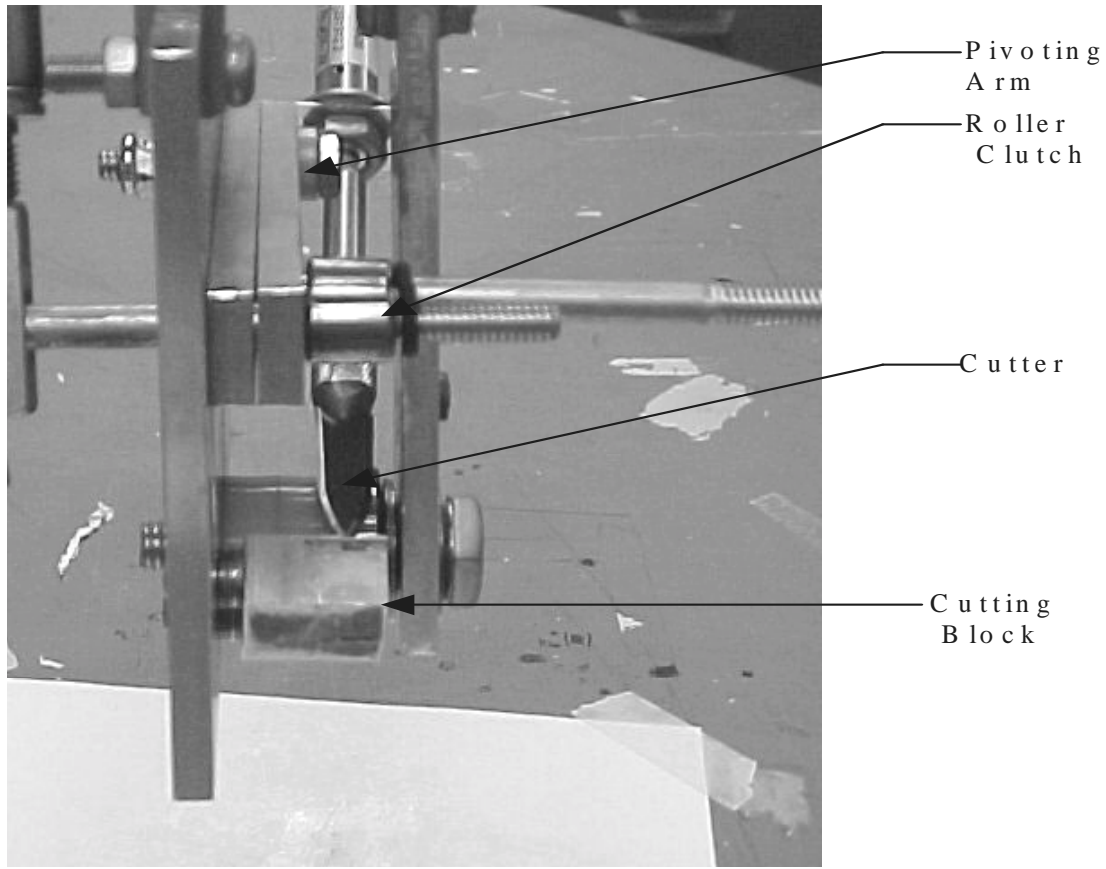


Figure 6.6 Fiber Placement Head (Side View)

The re-feed of the tow at the start of a new pass, after it has been cut, is accomplished using a pivoting arm, Figures 6.5 and 6.6. This arm has two roller clutches, which only allow motion in one direction. This keeps the fiber from pulling out of the cutting block. The roller clutches clamp the tow when the pivoting arm is actuated. This actuation moves the arm and therefore the tow down through the cutting block and into position to be laid down.

The cutting mechanism uses a linear actuator to quickly move an exacto blade through the fiber tow. A spear headed exacto blade, Figure 6.7, is used to pierce the middle of the tow and then cut the tow all the way across using the double-sided cutting surface. Tests involving this cutting blade have been very successful in providing a clean, straight cut.

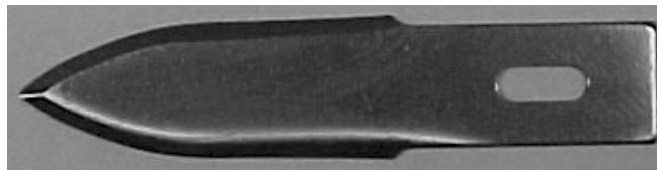


Figure 6.7 Spear Exacto Blade

The need for back tension along the fiber is the focus for our current design efforts. A slip clutch is used to provide a constant rotational tension in the system. The addition of tension to

the system has proven to help in the cutting process. Without this tension the tow material is found to bow and to move out of the cutting block while cutting.

The fiber placement head has been tested using a ribbon material of the same width as the composite tow material to be used, 0.318 cm (0.125 in). The fiber placement head was designed with the ability to increase the tow width to 0.475 cm (0.187 in) by changing the cutting block, but this tow width has not been used for testing. This ribbon material is being laid up using an adhesive on a piece of paper. The same programs used in the pen accuracy tests are being used in the testing of the fiber placement head and its cut and re-feed mechanisms. Tests for the fiber placement head also involve the placement of tow material onto paper printed with the theoretical curves and then taking a photograph of the actual tow location to measure overlaps and gaps. Once placement accuracy is verified using low-cost ribbon, placement tests will begin with available preimpregnated tow material. Initial test samples shall be flat plates with local, isolated gap and overlap flaws. These samples will allow NDE characterization and classification studies.

6.4. Design of a low cost placement head for Automated Fiber Steering

The main aim of this Project is to design a low-cost, automated placement head that is capable of laying down and steering Pre-preg carbon fiber tow onto a flat surfaces and curved surfaces. The Intelledex 605 robotic arm has been chosen to mount the fiber placement head the robot has a payload weight capacity of 2.27 kgs (5.00 lbs). This arm allows for six axes of motion and supports the addition of pneumatically operated mechanical devices.

6.4.1. Customer Requirements

The tow placement design has the following design requirements.

- 1) The head need to place a carbon fiber tow 3 mm (0.125”) to 5 mm (0.187”) in width
- 2) The placement width is parametric to 25 mm (1”).
- 3) The tow back tension should be equal to 0.25lb to avoid slack.
- 4) The head should be able to place the tow on the tool surface with an accuracy of 0.002”.
- 5) The active feed system should feed the tow from the spool with a rate of 50 inches/minute.
- 6) The application pressure should be 69 Kilo Pascal (10 psi) nominal , 689.4 Kilo Pascal (100 psi) maximum.
- 7) The head weight limitation is 2.27 kgs (5.00 lbs). (due to weight limitation on the Intelledex robot).
- 8) The head should be capable of being integrated with a larger robot for future use.

- 9) The head should incorporate independent cut and refeed capability.
- 10) The head design should minimize twist in tow, friction and edge fraying of feed tow.
- 11) Though machine limits placement initial samples are likely to be sizes of 254 mm (10") to 762 mm (30") radius.
- 12) The head along with robotic arm should be capable of being mounted on a truck and transported for remote access..

6.4.2. Head Configuration

The data obtained from the performance characteristics of the initial tow placement head design at University of Kansas, formed the basis for this head design. The main problem observed in the last head design was that there was a persistent vibration problem during the tow placement process, partly due to a large moment arm formed by the three gas springs used in the design and the multitude of fixtures and joints all of which adversely contributed to the vibrations which affected the ability of the head to place tow.

The second problem observed was the inability of the tow cut system to provide a clean cut while on the fly. The spear headed exacto blade used in cut- system had limited success in providing a clean straight cut to pre-preg tow.

All these factors along with an emphasis on simplicity of operation and manufacturing were taken into account while designing the present tow placement head. The foremost thing was to keep the head weight less than 2.27 kgs (5.00 lbs) due to weight limitation on the Intelledex 605 model robot.

The head design incorporates ideas taken from the thermoplastic tow placement head design of The Institut für Verbundwerkstoffe, Germany. This " Swing-Arm" design in theory should be light weight and reduce considerably the vibration levels while placing tow. This "Swing-Arm" design Concept was chosen to minimize the vibration thus increasing the tow placement accuracy. Also this design provides ease of manufacturability and simplicity in operation. As there is no complex machining operations involved during the fabrication of the individual parts, and as attachment components are readily formed sheet metal, our concept is affordable.

6.4.2.1 CAD Drawings

The conceptual design and the drawings of the tow placement head were drafted using the Pro-Engineer design package. Final assembly drawings with various views are shown in Figures 6.8-6.9.

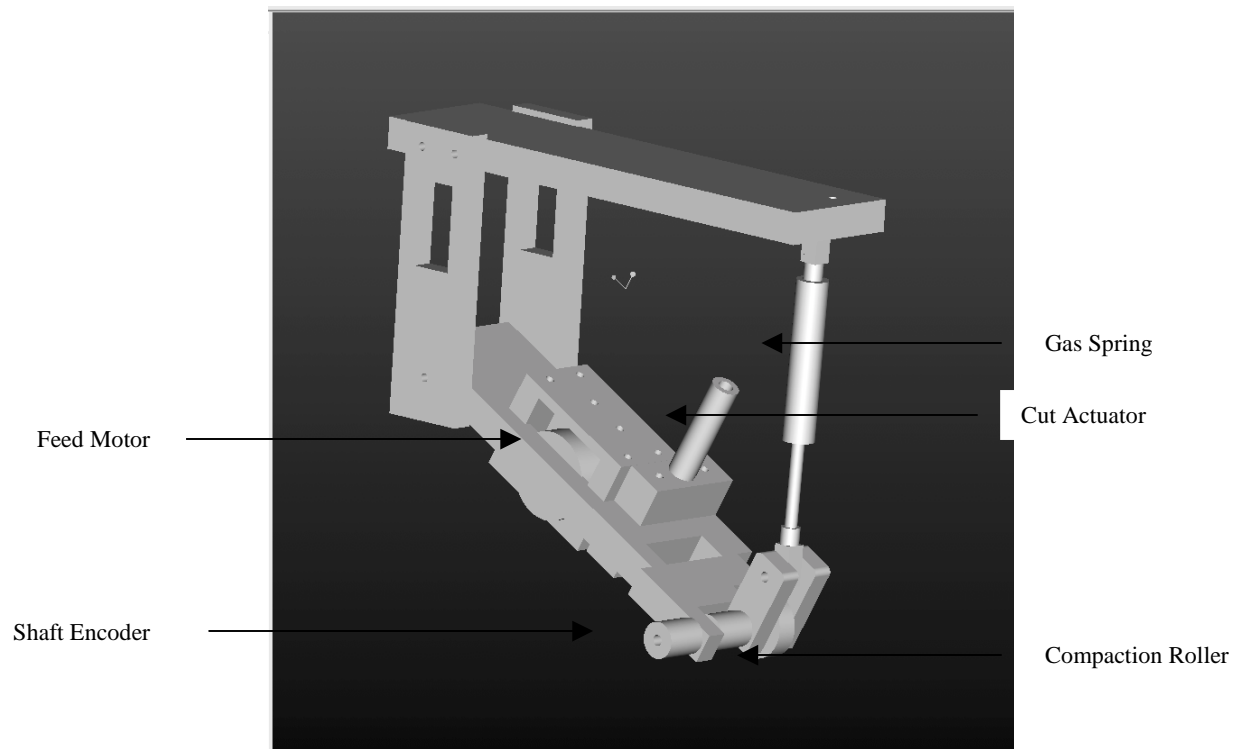


Figure 6.8 The Tow placement head configuration

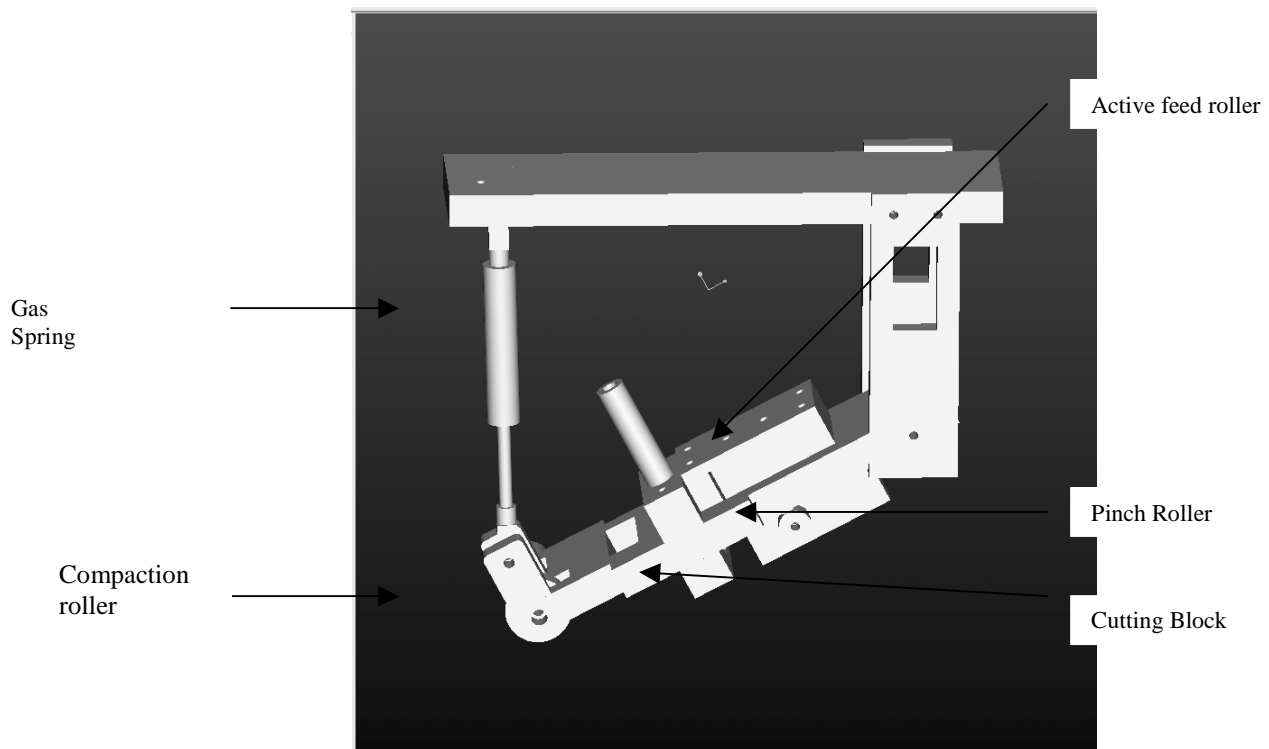


Figure 6.9 The Tow placement head side view

6.4.2.2 The control system

The fiber placement head design incorporates original ideas which tend to automate the process and introduce intelligent features into the tape placement head. The new head design has an active feed system driven by a stepper motor. The new thing about this system is that it does not depend upon any control system in the robot and is independent. This integration allows for complete automation with need for only operator supervision.

The original idea is to monitor the revolution rate of the compaction roller with an incremental shaft encoder and then transmit that rate to a Motorola HC-11 type micro-controller which in turn drives the stepper motor. The symbolic representation of the idea is shown in Figure 6.10.

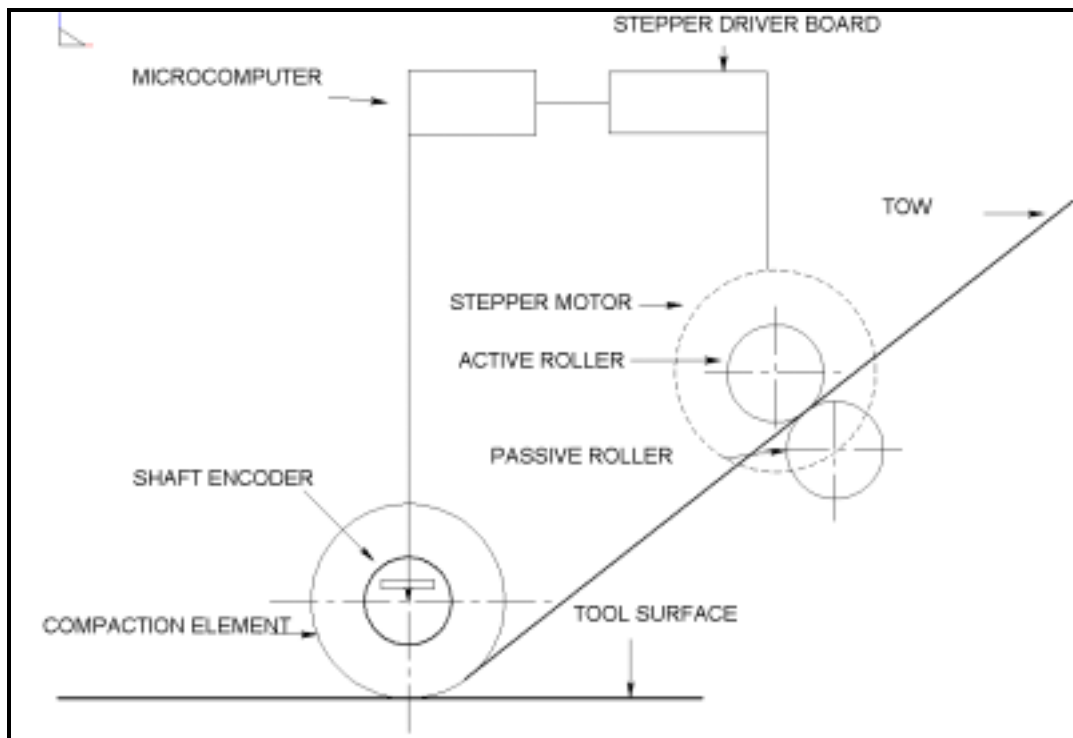


Figure 6.10 The symbolic representation of the Control System

The control system consists of the following components:

- 1) **Shaft encoder-** The shaft encoder selected is an Iwatsu optical encoder having a resolution of 200 cycles/revolution which has characteristics of long life and digital output.

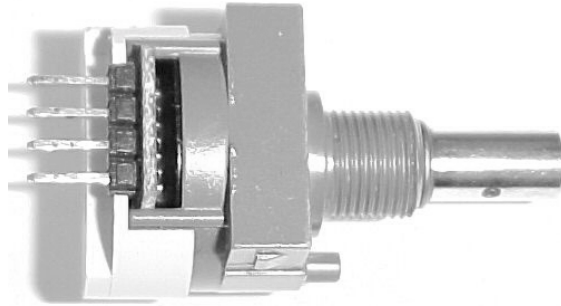


Figure 6.11 Iwatsu optical Encoder

- 2) **Microcontroller-** Extensive research was done in selecting a suitable microcontroller for the application. First attempts were made by combining a BASIC stamp type of micro-controller. The BASIC stamp was chosen taking into account the user-friendly interface and steep learning curve.



Figure 6.12 BASIC Stamp 2p 24-Pin Module

The stepper driver chosen in the first developmental attempt was a BistepA06 stepper controller Board. Extensive experiments were undertaken in the first phase by placing the Iwatsu optical encoder, the BASIC stamp and the BistepA06 stepper board driving the stepper motor. However, after the experimentation it was realized that BASIC stamp utilizes a higher level programming language, therefore the multitasking is not possible in this combination. Multitasking is absolutely imperative in this kind of “Master-Slave” design, where the encoder turn rate governs the speed of the stepper motor coupled to the feed rollers, thus controlling the feed rate of the tow from the spool. Hence a search was initiated for a micro-controller utilizing a lower level programming language such as assembly language and having software and hardware interrupt capabilities. The software and hardware interrupt capability enables a processor to perform multi-tasking operation hence making it suitable for this application. The search yielded that the Motorola HC-11 type of micro-controller is suitable for this task.

The HC11 is a powerful 8-bit data, 16-bit address micro-controller from Motorola. The M68HC11 is optimized for low power consumption and high-performance operation at bus frequencies up to 4 MHz.



Figure 6.13 Motorola HC-11 Micro-controller chip

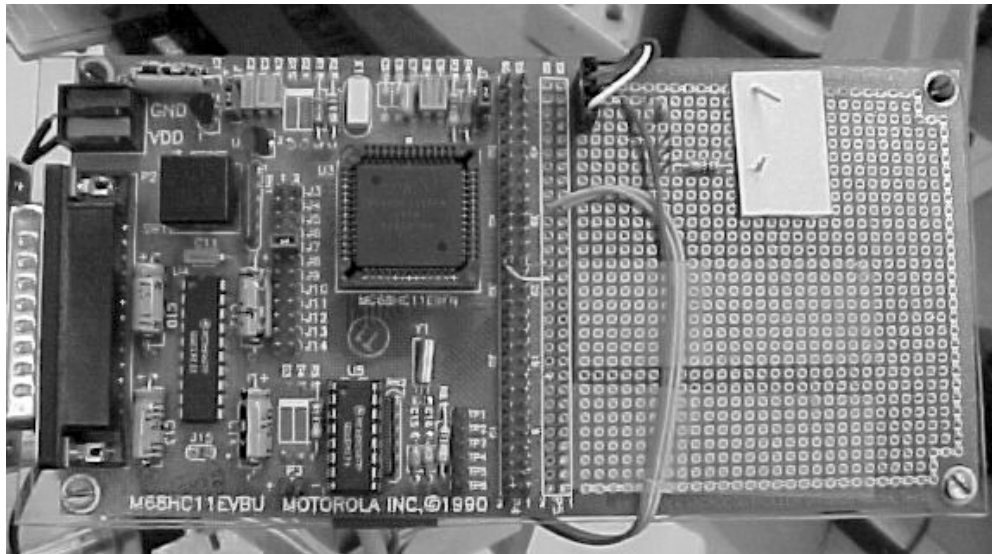


Figure 6.14 Motorola HC-11 Micro-controller chip mounted on board

The features include:

- Powerful bit-manipulation instructions
- Six powerful addressing modes (Immediate, Extended, Indexed, Inherent and Relative)
- Power saving STOP and WAIT modes
- Memory mapped I/O and special functions

The HC-11 micro controller has multi-tasking capabilities using the interrupt routines which is the reason why this controller was selected for this application, as the micro-controller needs to evaluate the pulses coming from the shaft encoder, process them and send the instructions to the stepper motor controller simultaneously. Given all these factors involved and the low cost of the unit the HC-11 was chosen.

3) NMB stepper motor:

The stepper motor was selected for this application because stepper motors are ideal for precision control, and may be easily operated in forward and reverse directions at varying speeds. This four-phase motor has a step angle of 3.6 degrees and requires 12 VDC for operation. Many kinds of stepper motors were analyzed for this application but the NMB stepper motor has lower vibration levels, lesser weight and ease of mounting as compared to other stepper motors such as Howard Industries steppers. Above all this motor offers low cost as compared to other brands.



Figure 6.15 12 Volt / 90 Ohm Unipolar Stepper Motor

4) Stepper board

The stepper driver board is intended to be the link between a microprocessor and a stepper motor. The stepper driver board amplifies a small voltage signal from micro-controller into high current for running the motor. The stepper driver receives two input signals from the micro-controller, namely step and direction. Every time the step line is pulsed the motor makes one step.

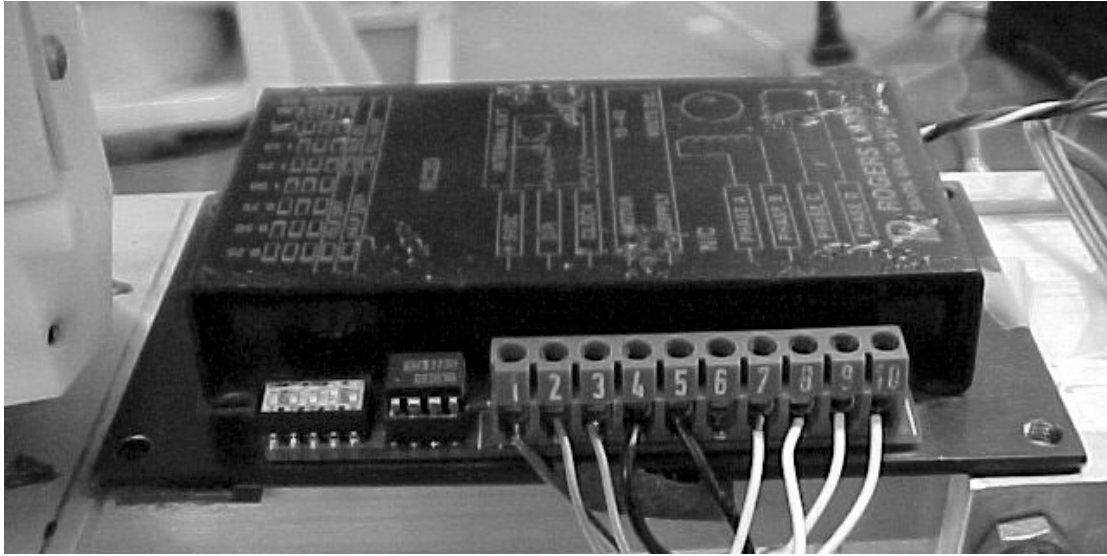


Figure 6.16 Stepper board mounted on the head

6.4.2.3 Compaction system

1) **Gas spring**- The fiber-placement head design incorporates a gas spring to allow for compaction pressure, This spring also ensures that head is always in proper contact with the part. The compaction pressure is readily varied by changing this one spring, and accuracy placement tests as a function of compaction pressure are currently underway.

6.4.2.4 Tape cut system

6.4.2.4.1 Tape cutting Mechanics

There are a number of ways of cutting pre-preg tow. Taking into account the costs involved and to keep the design as simple as possible only mechanical cutting methods were investigated. The aim was to select such a tow cutting method that minimizes tow edge damage in the cut zone and increases reproducibility of the cut profile. Three methods were investigated. Figure 6.17 shows the method in which a flat blade is penetrated through the tape into a support pad. The principal reason for not pursuing this solution any further is that the support pad might be worn out quickly by the penetrating cutter.

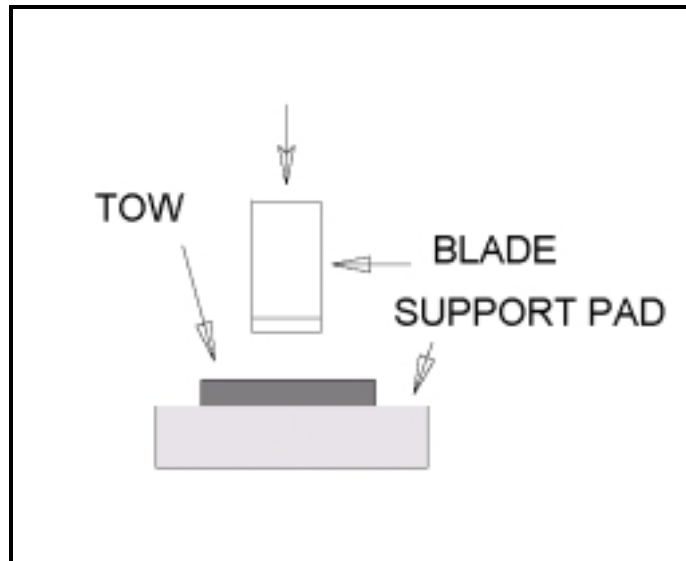


Figure 6.17 Tow cutting principle with a flat edged blade

The next option for tow cutting was a spear headed exacto blade, where the blade is used to pierce the middle of the tow and then cut the tow all the way across using the double-sided cutting surface. Experience with this kind of cutting system in the previous design reveals that this type of cutting method is not able to repeatedly provide a clean cut to the tow, hence a decision was made against using this kind of cut system.

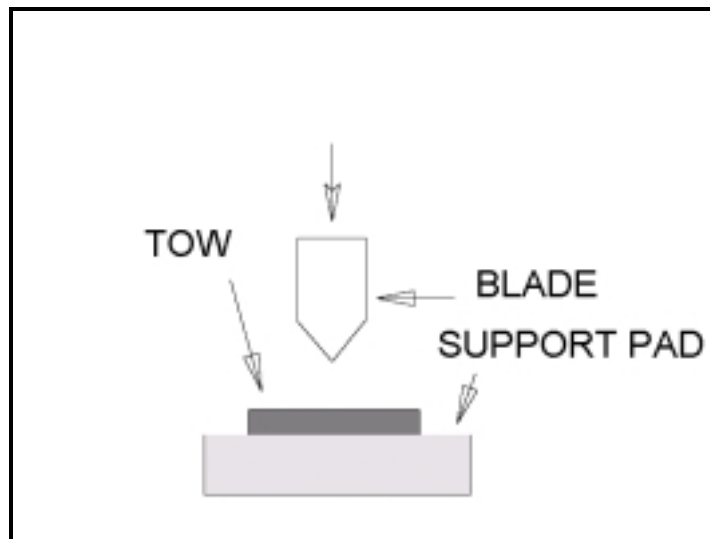


Figure 6.18 Tow cutting principle with a spear type blade

The third option analyzed for the tow cutting system was using an angled blade actuated sideways across a guide channel. This type of blade provided the cleanest and most effective cut with minimal end damage to the tow, hence this cut system was incorporated into the design. Also, this mode of tow cutting provides the ability for tow cut and reefed on the fly. As the tow is being fed through the guide channel the blade just cuts the tow and is retracted back by the double acting actuator hence the tow can be again reefed towards the compaction roller with ease.

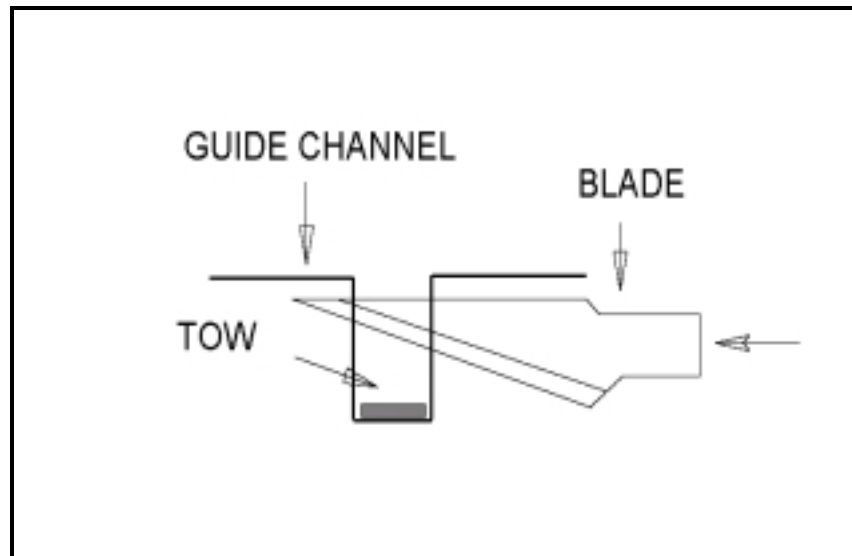


Figure 6.19 Tow cutting principle with angled blade

Cut system components

1) Cutting blades- The X-acto cutting blade with profile as shown in Figure 6.20 was chosen for its superior cutting characteristics and edge retention capabilities.

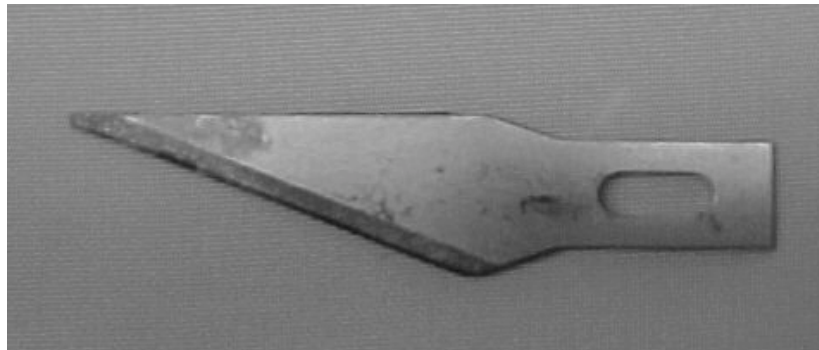


Figure 6.20 The Xacto cutting blade profile

2) Cut actuator: The cutter blade is actuated using a double acting linear actuator which cuts the fiber tow in the guide channel. The air pressure used for actuating is about 90 psi.



Figure 6.21 The cut system assembly

6.4.2.5 Feed and Re-feed system

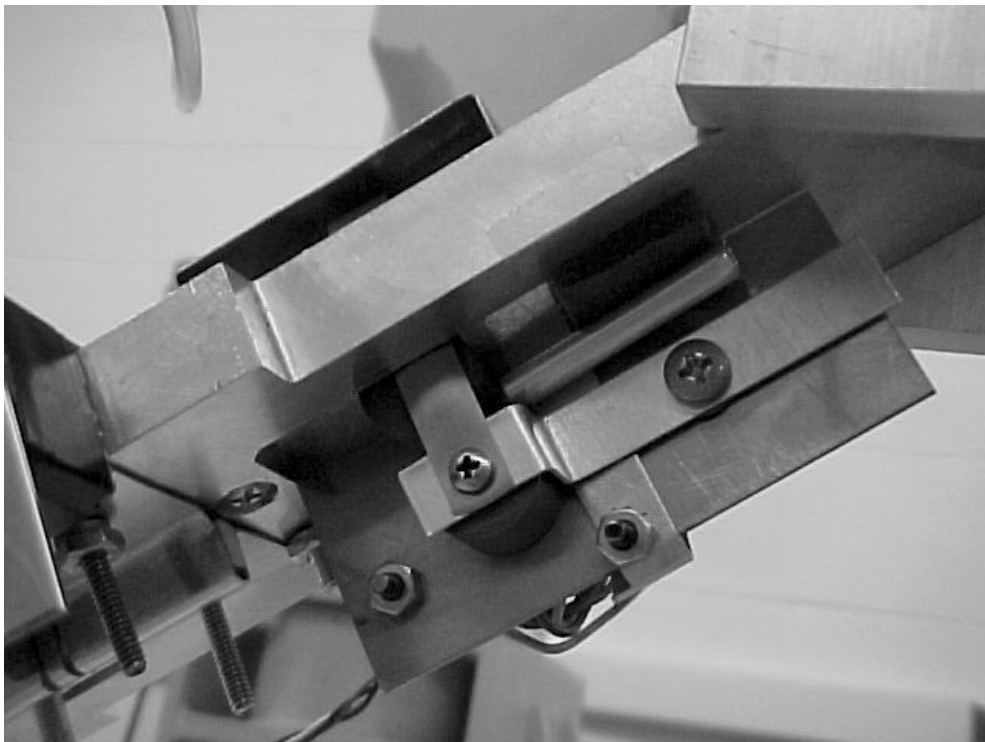


Figure 6.22 The feed system assembly

6.4.3 Integration with robotic facilities at University of Kansas, composites lab

Manufacture of the prototype placement head is complete, and the integration and verification of the control mechanism is in work. Placement tests continue in the laboratory, prior to investigating the portability of the concept.

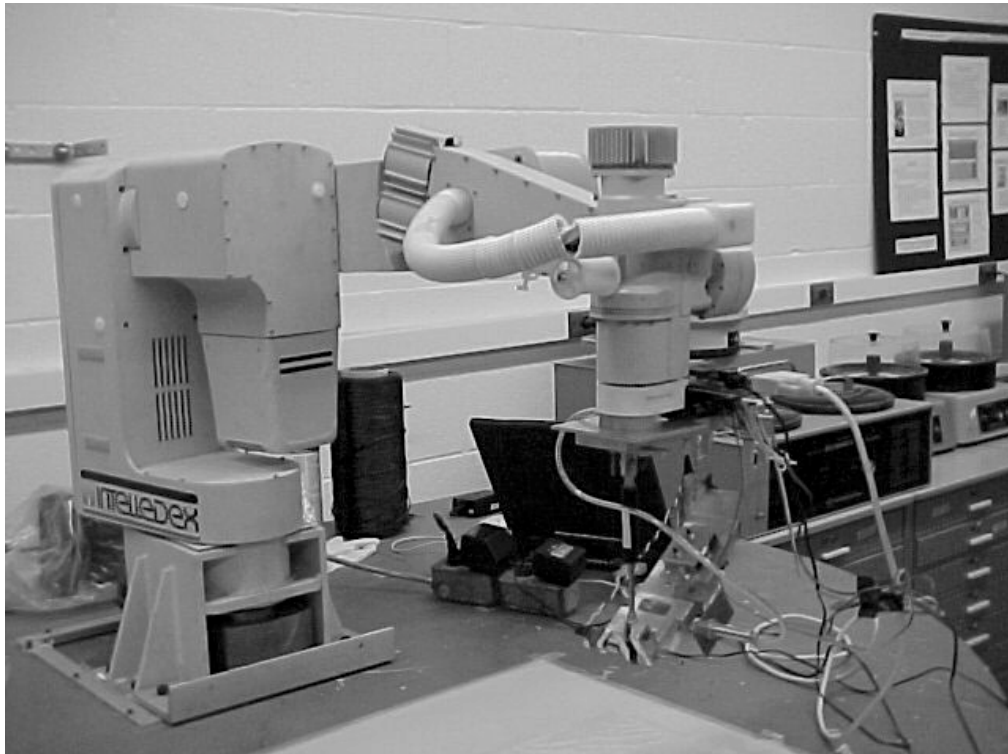


Figure 6.23 Prototype placement head mounted on KU Intelledex Robot

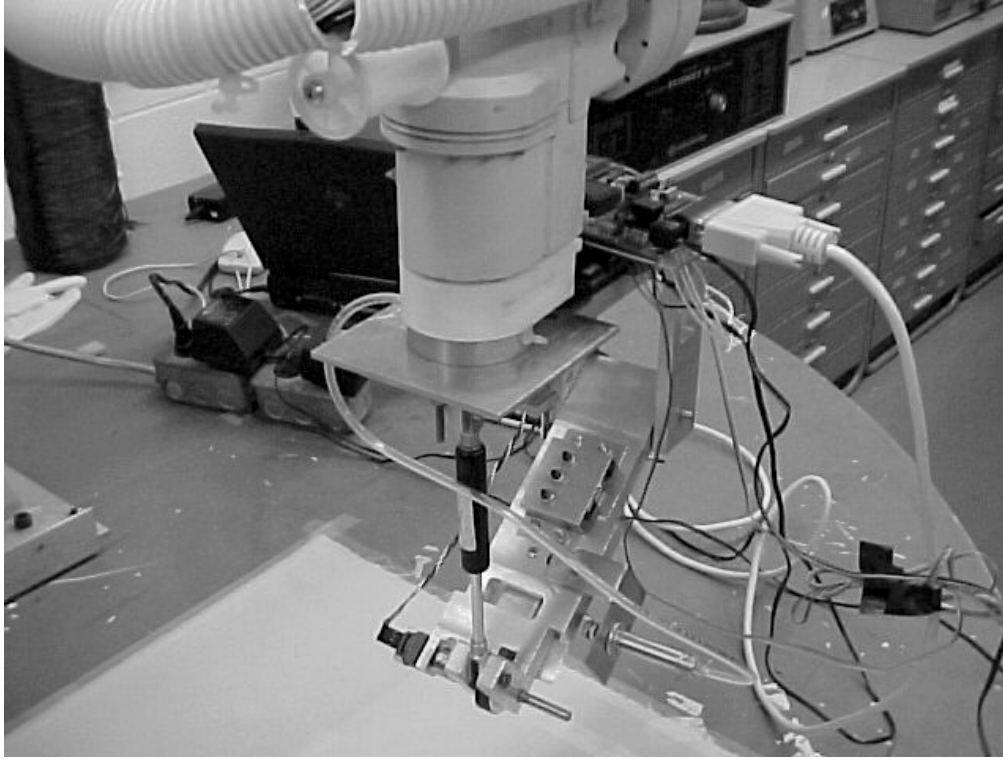


Figure 6.24 Prototype placement head – Roller and Linear Actuator

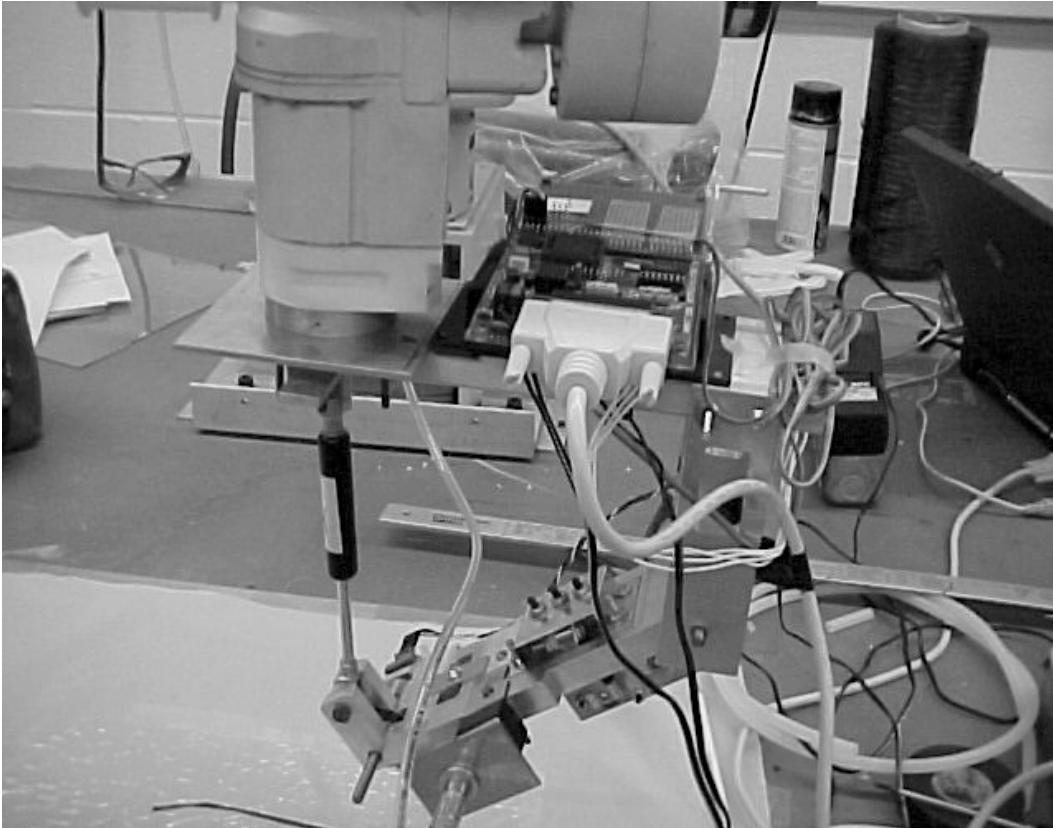


Figure 6.25 Prototype placement head – Controller Board and Swing Assembly

7.0 Summary and Conclusions

Research activities outlined offer significant increases in design and analysis capability for the fiber placement process, particularly with respect to steered fibers. This increased capability has the potential to offer significant weight savings in composite structural applications, at no additional cost. Weight savings of up to 30% have been demonstrated on simple geometry, and smaller but still significant weight savings are expected for representative modern aircraft structure. Results from specific research in this activity will serve the greater good by identifying a real potential for expected weight savings on representative aerospace structure, and by providing useful design and analysis tools and methodologies. Other industries will realize the benefits of this research program, as they explore the advantages of composite materials and begin to become involved with fiber placement. This and future reports will document

- an increased understanding of the mechanics of the behavior of laminates with steered fibers
- a thorough understanding of the limitations of existing analytical methods for evaluating behavior of steered fiber composites
- design and analysis tools and methodologies for preliminary and detailed design of fiber steered composites
- identified weight savings feasible with fiber steering on representative aerospace structures
- exploratory research in and recommendations for quality assurance of fiber steered composites
- specific recommendations for material and component test requirements for fiber steered composites
- specific recommendations for further research programs on steering patterns and on interaction effects of common local fiber architecture flaws such as gaps and overlaps.

Research activities outlined also offer significant advances in approaches for quality control and mechanical properties for steered fiber composites. These observations have the potential to develop guidelines in steered fiber composite manufacturing to define part quality. The presented NDE technique demonstrates a layer by layer inspection method for steered composite structures to quantify the flaws and aid in the selection of test specimens. Mechanical compression tests were performed to quantify the mechanical properties of steered fiber composites. The detail mechanical tests are addressed in the context of observed feature effect examinations:

- Radius variation effect test
- Width variation effect test
- Misalignment effect test
- Minimum steering radius test
- Family ply versus Unidirectional ply test

with misalignment effects critical in curvilinear or steered fiber composites.

Output of the mechanical compression tests have agreed well with finite element simulations for uniaxial steered composites, and family based laminates will ensue in Fall, 2004. The theoretical analysis was focused on the same feature effect investigations for direct comparison with the results of mechanical compression tests.

It is premature to make major conclusions regarding mechanical performance, but in general there is shown to be no influence of steering on compression mechanical performance, to 46cm steering radii (also shown for tension and shear in alternate programs). In addition, the following issues are raised:

- ❖ How does the curing process affect the mechanical properties?
- ❖ Is the current limitation of minimum fiber steering radius, 45.7 cm, reasonable?
- ❖ What is the minimum allowed steering radius?
- ❖ How can the fiber architecture variation be reduced?
- ❖ How much difference is there between the outputs of theoretical models and mechanical testing, and are they within reasonable tolerance?

Mechanical testing addressed in this paper is performed with conventional methods that assume the fiber axis is coincident with the longitudinal axis of the coupon, but steered fiber architectural structure will also have transverse and in-plane shear components as well as significant free-edge effects. A new mechanical test standard should be established to account for these effects.

7.1 Conclusions for Integrated Design and Analysis Tools

Fiber placement of composite structures promises reduced cost in the form of production waste savings, and increased structural strength-to-weight ratios that can be realized with tailored fiber orientations. To date, reduced production costs have been realized with fiber placement, but a lack of robust design and analysis tools prevents designers from fully exploring weight saving design solutions in the preliminary design phase. A design and analysis tool for fiber placed composites must be capable of modeling the part down to the level of the tow, in turn requiring a method to represent the position of individual tows on the design surface. In this thesis, we have formally defined two types of curves required to represent individual tows in a fiber placed part; the offset curve on a surface, and the laminate family curve; and present approximate methods to compute both types.

Offset curves on a surface are used to represent the positions of individual tows that lie next to one another with no gaps or overlaps of tow material. The curves are used to represent a group of tows laid by a single pass of the fiber placement machine head (a course), and can be used to orient multiple courses along the primary load path of the part. We present a method to calculate piecewise linear approximations of offset curves on the surface. We also present a closed form expression which bounds the error of our approximation when the cross section of our design surface is well approximated by a circular arc. We report no such closed form expression for a design surface with arbitrarily curved cross section. However, we propose an alternative method of bounding the error that does not involve additional geometric constructions or queries. It is verified that the results of this approximation are of the same order as a much more computationally intensive method involving the construction and length calculation of

additional curves on the surface. It is found that, in the domain of fiber placement, the cumulative error in offset distance after placing 10^3 to 10^4 curves is of the order of a single offset. This error is well within current allowable error for a manufactured part.

To handle loads that are offset from the primary load path of a part, a different fiber (curve) orientation method is needed. Such a curve must exhibit a constant angle of intersection with each curve in a series of offset curves. This curve is known as a laminate family curve. A method is presented that calculates a piecewise linear approximation of a laminate family curve, given a series of offset curves. We have shown that the approximate laminate family curve exhibits error (variation from the desired angle of intersection) that directly proportional to the offset distance and indirectly proportional to the local radius of curvature of the offset curves.

The approximation methods for offset curves and laminate family curves are implemented in the Steered Composites Analysis and Design System, SCADS. SCADS uses the approximation methods to model the tows, courses and plies of a fiber placed part. The analysis methods of a previously implemented system are incorporated into SCADS- allowing the quantification of gaps, overlaps, and tow level properties; and the generation of files for use by Finite Element Analysis packages.

7.2 Conclusions for Structural Optimizations of Steered-Fiber Composite Structures

This paper investigates the potential payoffs of composite structures using fiber steering (FS) conceptual design. It calls for the tailorability of curvilinear-family laminates to specific internal load paths, which involves simultaneous optimizations of both rangewise layer thickness and orientations. A curvilinear-family laminate consists of four layers or $[\pm\theta_1, \theta_2, \theta_3]_s$. Each layer is composed of a collective of several 0.0055-inch plies. Structures exhibiting steered-fiber architecture have been shown to improve load capability and ultimately weight reductions. The design concept has been successfully demonstrated on four preliminary and three representative aircraft models under various load cases:

Preliminary Studies

- ➔ **Plate with a hole:** three square plate-with-a-hole models with different width-to-diameter (W/D) parameters subjected to various loads (bi-axial tension, uniaxial tension, and in-plane shear). W/D are 5.0, 3.33, and 2.5.
- ➔ **Wing Torque Box:** An intermediate complexity wing (ICW) subjected to aerodynamic loads.
- ➔ **Cantilever panel:** a cantilever rectangular panel subjected to transverse loads
- ➔ **Cantilever tube:** A cantilever cylindrical tube subjected to combined loads (bending, compression and torsion)

Representative Primary and Secondary Aircraft Structural Components

- ➔ **Wing:** a representative of a regional jet's primary structural component or BGE wing

- ➔ **Aft pressure bulkhead:** a representative of a general aviation aircraft's secondary structural component or pb2 model
- ➔ **Horizontal Stabilator:** a representative of a tactical fighter's primary structural component or F22 model.

Using MBB-LAGRANGE as the main computational tool throughout the research, this gradient-based and finite-element structural optimization routine enables robust and efficient demonstrations of FS conceptual design. It is configured solely on $[A]$ matrix or composite-membrane computations with several mathematical programming algorithms available for structural optimization. Recursive Quadratic Programming by Powell (RQP2) is the primary optimization algorithm for FS-related problems.

Four design variable (DV) configurations, namely baseline, Steering I, II and III, have been proposed and defined for four preliminary models. All four configurations are composed of symmetric laminates, but each has different balance properties. The baseline configuration is a pure layer-thickness optimization design with $[\pm 45, 0, 90]_s$ and is balanced with respect to (w.r.t.) the principal material coordinate. The Steering I configuration has one angle DV per element with $[\pm \theta_1, \theta_2, \theta_3]_s$, where the θ_2° layer is the primary DV. $\pm \theta_1^\circ$ and θ_3° layers are linked to θ_2° DV with $\pm 45^\circ$ and 90° respectively. In this case, the laminate is balanced w.r.t. the local material coordinate. The Steering II configuration has three layer-angle DV per element or range of elements with $[\pm \theta_1, \theta_2, \theta_3]_s$. $\pm \theta_1^\circ$ layers, are linked as one DV each for layer thickness and orientation, respectively. However, Steering II laminate is unbalanced w.r.t. either the local or principal material coordinate. Finally, Steering III configuration takes only one DV by linking $\pm \theta_1^\circ$ layers in $[\pm \theta_1, 0, 90]$. As a result, Steering III is balanced w.r.t. the principal material coordinate.

The objective function for these models is minimum structural weight, while maximum strain failure criterion with only fiber-related failure modes (longitudinal tension and compression), upper and lower layer thickness, and $\pm 45^\circ$ angle thresholds are design constraints under different loading cases. Displacement or maximum wing-tip deflection and critical-buckling constraints are also included onto some of the models. Nevertheless, improvements in MBB-LAGRANGE buckling formulations are required to incorporate better layouts of steered-fiber architecture onto airframe structures. This is further explained in the Section 3.6.3.

Optimal results corresponding to FS conceptual design are presented in Section 3.4.3 and Appendix C for preliminary models, and Section 3.5.3 and Appendix E for preliminary and aircraft models respectively as layer-thickness contours and layer-angle mappings following the curvilinear laminate family (Section 3.1.2) definitions. Results of weight savings for each model are listed in Tables 3.4.4 and 3.5.7, where FS-related configurations (Steering I, II and III) are compared with the baseline design. From the studies, it is concluded that:

- ➔ **Weight savings of up to 27% for linear static analysis** is attainable, which is primarily based on **Steering II configuration**. However, further verifications and sound decisions must be made because the resultant laminate is unbalanced w.r.t. either the local or principal material coordinate. Computational efforts for Steering II configuration are

greater than Steering I and II because of the additional layer-angle DV per element or range of element.

- ➔ **Weight savings of up to 26% for linear static analysis** is achievable, which is associated with **Steering III configuration**. This configuration yields balanced results w.r.t. the primary material coordinate, which is more realistic and acceptable in composite laminate design.
- ➔ **Weight savings of up to 20% for linear static analysis** is reasonable, which corresponds to **Steering I configuration**. This resultant laminates are balanced w.r.t. the local material coordinate, but unbalanced w.r.t. the principal material coordinate. Steering I configuration is the best candidate of FS conceptual design because the primary or axial load trajectories are governed only by the primary layer angle, θ_2 . The off-axis and transverse load paths are contributed by $\pm\theta_1$ and θ_3 , respectively. Nevertheless, further investigations are required to verify the macroscopic behavior and response of the laminates.
- ➔ **Weight savings of up to 6% for linear buckling analysis** is observable, which is primarily based on Steering II configuration for ICW model. Again, the optimal results may not be realistic due to issues of unbalanced laminates. In addition, MBB-LAGRANGE buckling formulations must be revisited for FS-related optimizations.
- ➔ **“Smooth” or rangewise continuous layer-angle mappings and layer-thickness contours** are demonstrated in most of the studies.
- ➔ **Optimal layer-angle mappings and layer-thickness contours are very load-path-sensitive**. This is illustrated in the plate-with-a-hole models in Section 3.4.3, where layer orientations are tailored significantly w.r.t. the primary load paths under different load cases (bi-axial tension, uniaxial tension, and in-plane shear). However, the variations of steering patterns do not depend strongly on W/D parameter under identical load conditions. A larger W/D model may seem to have a greater propagation or variation in layer thickness near the hole vicinity due to stress concentrations. Also, with a greater W/D, layer orientations for Steering I configuration are discontinuous along the boundary due to the influence of stress concentrations. Nevertheless, the variation of steering patterns w.r.t. W/D parameter is generally insensitive.
- ➔ Careful **selections of rangewise DV-linking based on strain contours** yield satisfactory FS-related results, especially represented by BGE wing model in section 3.5.4.2.
- ➔ **Structures with minimum-gage solutions do not exhibit continuous layer-angle mappings and layer-thickness contours**. This is particularly true for pb2 and F22 models in Sections 3.5.4.3 and 3.5.4.4. It is recommended to impose a greater load factor so that FS conceptual design can be demonstrated.

All in all, **MBB-LAGRANGE** is a **robust and efficient tool** for fiber steering conceptual design.

7.3 Conclusions for Nondestructive Evaluation and Mechanical testing of Steered Fiber Composites

As a conclusion, analyzed results of the theoretical models are compared with the output of experimental compression tests. Both theoretical data and experimental data show the same trends as follows:

- The dominant feature effect in steered fiber composites is the sample misalignment, and initial misalignment brings significant changes in mechanical properties.
- The steering radius variation has little affect on compression properties (about 2-3 %).
- The specimen width variation is also found to be a minor effect.
- The minimum steering radius is proved 52cm or less of steering radius in this project.

Research activities outlined offer significant advances in approaches for quality control and mechanical properties for steered fiber composites. These observations have the potential to develop guidelines in steered fiber composite manufacturing to define part quality.

Mechanical testing addressed in this paper is performed with conventional methods that assume the fiber axis is coincident with the longitudinal axis of the coupon, but steered fiber architectural structure will also have transverse and in-plane shear components as well as significant free-edge effects. A new mechanical test standard should be established to account for these effects.

A limiting factor in this project was the availability of steered fiber panels. The expense of constructing steered fiber panels with existing fiber placement hardware limits the amount of testing that can be performed and the breadth of trade study parameters. A new low-cost fabrication method would enable more extensive testing to be performed.

Due to the limitation of test machine capacity, the ready-to-test Boeing coupons were in hold for further investigation. A new test machine is in place, and tests will commence in Fall 2004.

7.4 Conclusions for the Effect of Common Tow Features on Compressive Properties of Unidirectional Composite

The effect of using two machines is shown to be insignificant, and not responsible for variations in unflawed and flawed samples. Nonetheless, the practice of using multiple test machines is admittedly poor. Additional unflawed samples could be tested to remove any question of variability in this data, but the results will not vary from the documented scatter bands.

7.4.1 Effect on Initial Stiffness

The reduced fiber volume in the specimens with gaps, in theory, should have reduced the initial stiffness of the laminate. In actuality the stiffness did not have a noticeable change. The

lack of change in stiffness is contributed to the lack of a defined flaw within the laminate. The gaps became filled in with the fibers of the adjacent plies. The overlaps, on the other hand, became distributed throughout the neighboring plies. Had there been a non-0° ply above and below the flaw this may have been different. The use of two testing machines does not indicate that the data was skewed from their use. Nonetheless, there does not seem to be an explanation for the lower stiffness. Even though, the comparison of the families clearly show that there the flaws had no effect on the initial stiffness of the laminate.

7.4.2 Effect on the Point of Nonlinearity

The point at which the laminate compressive stress-strain response becomes nonlinear was examined because of the bending occurring during testing. It was believed that the flaws would have an effect on the point at which the laminate properties exhibited nonlinear behavior. There was no conclusive microscopy evidence to prove that premature fiber failure was causing the nonlinearity. But, the scatter in the data was so great in most cases that all data overlapped. Thus no conclusive evidence to this affect is present that the flaws had any effect on this point.

7.4.3 Effect on the Axial strength

The axial strength of the laminate is dependent on the number of fibers within. Since the addition of flaws changes the number of fibers in the laminate, it would seem that there would be a change in the strength. Nastran analyses and mechanical testing both show that there is little or no effect on the axial strength of the laminate due to flaws examined in this study.

7.5 Conclusions for the Design of a Low Cost Tape Placement Head for Automated Fiber Steering

A limiting factor in this project was the availability of steered fiber panels. The expense of constructing steered fiber panels with existing fiber placement hardware limits the amount of testing that can be performed and the breadth of trade study parameters. Manufacturing capability is strongly required to extend the mechanical testing. The University of Kansas is on its second iteration of a low cost fiber placement head, but we are far from the capability to accurately and repeatedly place tow.

8.0 References

Chapter 1:

- 1.1 C.G. Grant, V. M. Benson, “ Automated Fiber Placement – Evolution and Current Demonstrations.” Third NASA Advanced Composite Technology Conference, Long Beach, California, June 8-11, 1992, pp. 625-648.
- 1.9 R. Flory, and E. Bernardon,” Effect of Steering and Conformance Requirements on Automated Material Deposition Equipment.” Charles Stark Draper Laboratory, Inc., Subcontract No. CACDRA.001 issued by The Composites Automation Consortium, Inc.
- 1.36 R. Neddo and C. Kogstrom. “Automated Tow Placement of Fan Cowl Door Skins” 28th International SAMPE Technical Conference. November 4-7, 1996.
- 1.37 Cincinnati Milicron Viper Fiber Place Machine Brochure, Cincinnati Milicron.
- 1.38 K. Lim, “Structural Optimization for Fiber Steering Conceptual Design” The University of Kansas, Master Thesis, May 2002.

Chapter 2:

- 2.1. Hale, R. D. *Excerpts From the Technical Proposal for Integrated Design and Analysis Tools for Reduced Weight, Affordable Fiber Steered Composites*. University of Kansas Flight Research Laboratory, KU-FRL-22480-1. 1 September, 1999.
- 2.2. The Boeing Company. *Fiber Placement Benchmark and Technology Roadmap*. Report 99P0028. 15 July, 1999.
- 2.3. Broomhead, P. and Edkins, M. Generating NC Data at the Machine Tool for the Manufacture of Free-form surfaces. *International Journal of Production Research*. Vol 24. Jan/Feb, 1986. ns 1.1-14
- 2.4. Loney, G. C. and Ozsoy, T. M. NC machining of free form surfaces, *Computer Aided Design*. Vol 19, n 2. March, 1987. pp 85-90
- 2.5. Xia, J. and Ge, Q.J. An exact representation of effective cutting shapes of 5-axis CNC machining using rational Bezier and B-spline tool motions. *Proceedings - IEEE International Conference on Robotics and Automation*, v 1, 2001. 2001 IEEE International Conference on Robotics and Automation (ICRA), May 21-26 2001. Seoul. pp 342-347
- 2.6. Ge, Q. J. Kinematics-driven geometric modeling: a framework for simultaneous NC tool-path generation and sculptured surface design. *Proceedings - IEEE International Conference on Robotics and Automation*, v2, 1996, *Proceedings of the 1996 13th IEEE International Conference on Robotics and Automation. Part 2 (of 4)*. Apr 22-28 1996. Minneapolis, MN, USA. pp 1819-1824

- 2.7. Huang, Y. and Oliver, J. H. Non-constant parameter NC tool path generation on sculptured surfaces. *Computers in Engineering - 1992, Proceedings of the 1992 ASME International Computers in Engineering Conference and Exposition*. Aug 2-6 1992. San Francisco, CA, USA. pp 411-419
- 2.8. Suresh, K. and Yang, D.C.H. Constant scallop-height machining of free-form surfaces. *Journal of Engineering for Industry, Transactions of the ASME*. Vol 116, n 2. May, 1994. pp 253-259
- 2.9. Sarma, R. and Dutta, D. Geometry and generation of NC tool paths. *Journal of Mechanical Design, Transactions Of the ASME*. Vol 119, n 2. June, 1997. pp 253-258
- 2.10. Lee, Y. S. and Ji, H. Surface interrogation and machining strip evaluation for 5-axis CNC die and mold machining. *International Journal of Production Research*. v 35, n 1. Jan, 1997. pp 225-252.
- 2.11. Lee, Y.S. Adaptive tool path planning by machining strip evaluation for 5-axis complex surface machining. *Transactions of NAMRI/SME*. Vol 26. 1998. pp 141-146.
- 2.12. Chiou, C.J. and Lee, Y.S. A Machining Potential Field Approach to Tool Path Generation for Multi-Axis Sculptured Surface Machining. *Computer-Aided Design*. v 34, n 5. 15 April, 2002. pp 357-371
- 2.13. Hale, R.D. and Vasey-Glandon, V.M. PACKS: an Affordable Knowledge-driven Composite Design for Manufacturing Process. *Proceedings of the 46th International SAMPE Symposium and Exhibition - Science of Advanced Materials and Process Engineering Series, Vol. 46, Long Beach, CA, May 6-10, 2001*. Society for the Advancement of Material and Process Engineering, pp 1885-1899
- 2.14. Vasey-Glandon, V.M., Hale, R.D. et al. Knowledge Driven Composite Design Optimization Process and System Therefor. United States Patent 6,341,261. 22 January, 2002.
- 2.15. TechnoSoft, Inc. *Adaptive Modeling Language Reference Manual: AML Version 3.1.3*. Cincinnati, Ohio. 1999.
- 2.16. Guillermin, O. and Grape, J. Advanced CAD software tools for cost-effective composite engineering. *Proceedings of the 46th International SAMPE Symposium and Exhibition - Science of Advanced Materials and Process Engineering Series, Vol. 46, Long Beach, CA, May 6-10, 2001*. Society for the Advancement of Material and Process Engineering, pp 1899-1911
- 2.17. Vistagy, Inc. *FiberSIM Documentation*. Waltham, Massachusetts. 2001.
- 2.18. Vistagy, Inc. FiberSIM FiberPlacement Interface. Waltham, Massachusetts. May 1, 2001.
- 2.19. Goering, J. Integrated design and analysis tool for 3D woven structures. *AIAA/ASME/ASCE/AHS/ASC Structures, Structural Dynamics, and Materials Conference*

- and Exhibit, 41st*. Atlanta, GA. Apr. 3-6, 2000. AIAA Paper 2000-1376.
- 2.20. Hale, R.D. and Vasey-Glandon, V.M.. Fiber Placement and Fiber Steering Systems and Corresponding Software for Composite Structures. Boeing Attorney Docket 99-441, Submitted to U.S. Patent Office July, 2001.
 - 2.21. Miller, J.R. Vector Geometry for Computer Graphics. *IEEE Computer Graphics and Applications*. Vol. 19, No. 3. May/June 1999. pp 66-73.
 - 2.22. Beyer, W. H. (editor). *CRC Standard Mathematical Tables*. CRC Press, Inc. Boca Raton, Florida. 1984
 - 2.23. Farin, G. *Curves and Surfaces for Computer Aided Geometric Design- A Practical Guide*. Academic Press. San Diego, California. 1997
 - 2.24. Walter, M. and Fournier, A. Approximate Arc Length Parameterization. *Anios do IX SIBGRAPI*. Caxambu, MG, Brazil. 1996. pp. 143-150
 - 2.25. Jackson, P. Editor. *Jane's All the World's Aircraft 2001-2002*. Jane's Information Group, Ltd. Surrey, England. 2001
 - 2.26. Hale, R. D., et al. *Integrated Design and Analysis Tools for Reduced Weight Affordable Fiber Steered Composites, Year 1 Annual Summary Report*. University of Kansas Flight Research Laboratory, KU-FRL-22480-2. 15 September, 2001.
 - 2.27. Unigraphics Solutions, Inc. *Parasolid Online Documentation Web, Parasolid V11.1.167*. Maryland Heights, MO. November, 1999.
 - 2.28. MSC.Software Corporation. *MSC.Patran User's Guide, MSC.Patran 2001 r2a*. Santa Ana, CA. 2001.
 - 2.29. Ansys Incorporated. *ANSYS 6.0 Documentation*. Canonsburg, PA. 2001.
 - 2.30. Abbott, I. H. and Von Doenhoff, A. E. *Theory of Wing Sections*. Dover Publications, Inc. New York, New York. 1959.
 - 2.31. Tomblin, J. et al. *Material Qualification Methodology for Epoxy-Based Prepreg Composite Material Systems*. United States Department of Transportation, Federal Aviation Administration Report DOT/FAA/AR-00/47. Washington, DC. April, 2001.

Chapter 3:

- 3.1. Evans, D. O. "Design Considerations for Fiber Placement," Proceedings of the 1993 38th International SAMPE Symposium and Exhibition. Part 1 (of 2), Anaheim, CA, May 10-13, 1993, p. 170-181.
- 3.2. Barth, J. R. "Fabrication of Complex Composite Structures Using Advanced Fiber Placement Technology," 35th International SAMPE Symposium, April 2-5, 1990.

- 3.3. Enders, M. L.; and Hopkins, P. C. "Developments in the Fiber Placement Process," 36th International SAMPE Symposium, April 15-18, 1991.
- 3.4. R. L. Anderson, "Advantages of Fiber Placement Versus Conventional Filament Winding for a Marine Structure," Proceedings of the American Society of Composites 4th Technical Conference, edited by K. L. Reifsnider, Technomic, Lancaster, PA, 1989, p. 453-462.
- 3.5. Langone, R. J., Pasanen, M., Mondo, J., Martin, J. "Continued Development of Automated, In-Situ Processing for Thermoplastic Composite Structures and Components," Automated Dynamics Corp., Schenectady, NY.
- 3.6. Engineering Notebook, "Rivals Take Different Paths to JSF," Aerospace America, August 1998.
- 3.7. Grant, C. G. "Fiber Placement Process Utilization Within the Worldwide Aerospace Industry," SAMPE Journal, v36, no. 4, July/August 2000.
- 3.8. Flory, R.; and Bernardon, E. "Effect of Steering and Conformance Requirements on Automated Material Deposition Equipment," Charles Stark Draper Laboratory, Inc.
- 3.9. Kay, B. F. "RWSTD Airframe Technology – Foundation for the 21st Century," American Helicopter Society 57th Annual Forum, Washington, D.C., May 9-11, 2001.
- 3.10. Guillermin, O. and Grape, J. "Advanced CAD software tools for cost-effective composite engineering," Proceedings of the 46th International SAMPE Symposium and Exhibition - Science of Advanced Materials and Process Engineering Series, v 46, Long Beach, CA, May 6-10, 2001.
- 3.11. Inside Manufacturing, "Fiber Placement Enables Cost-Effective JSF Part Fabrication," High-Performance Composites, January 2002.
- 3.12. Mondo, J., Pasanen, M., Langone, R., Martin, J., "Advances in Automated Fiber Placement of Aircraft Structures," Automated Dynamics Corporation, NY, USA.
- 3.13. DiNardo, M. T., and Lagace, P. A. "Buckling and Postbuckling of Laminated Composites with Ply Dropoffs," AIAA Journal, v27 No. 10, October 1989, p. 1392-1398.
- 3.14. Leissa, A. W.; and Martin, A. F. "Vibration and buckling of rectangular composite plates with variable fiber spacing," Composite Structures, v14, n 4, 1990, p. 339-357.
- 3.15. Hale, R.D. and Vasey-Glandon, V.M. "PACKS: An Affordable Knowledge-Driven Composite Design for Manufacturing Process." SAMPE 2001, Long Beach, CA, May 6-10, 2001.

- 3.16. Hale, R. D., Moon, R., Lim, K., Schueler, K., and Wiehn, M., "Integrated Design and Analysis Tools for Reduced Weight, Affordable Fiber Steered Composites," Annual Summary Report, University of Kansas Flight Research Laboratory, September 15, 2001.
- 3.17. Makiyama, A. M.; and Platts, M. J. "Topology design for composite components of minimum weight," *Applied Composite Materials*, v3, n1, 1996, p. 29-41.
- 3.18. Cooper, A. A. G., "Trajectory Fiber Reinforcement of Composite Structures," Ph.D. Dissertation, Washington Univ., St. Louis, MO, 1972.
- 3.19. Katz, Y.; Haftka, R. T.; and Altus, E. "Optimization of Fiber Directions for Increasing the Failure Load of a Plate with a Hole," *Proceedings of the American Society of Composites 4th Technical Conference*, edited by K. L. Reifsnider, Technomic, Lancaster, PA, 1989, p. 62-71.
- 3.20. Hyer, M. W.; and Charette, R. F. "Use of Curvilinear Fiber Format in Composite Structure Design," *Proceedings of the 30th Structures, Structural Dynamics, and Materials (SDM) Conference*, Washington D.C., April 1989.
- 3.21. Hyer, M.W.; and Lee, H. H. "The Use of Curvilinear Fiber Format to Improve Buckling Resistance of Composite Plates with Central Holes," *Composites Structures*, v18, No. 3, 1991, p. 239-261.
- 3.22. Jones, S.E.; and Platts, M. J. "Using internal fiber geometry to improve the performance of pin-loaded holes in composite materials," *Applied Composite Materials*, v3, n2, 1996, p. 117-134.
- 3.23. Berchtold, G.; Klenner, J. "The Integrated Design and Manufacturing of Composite Structures for Aircraft Using An Advanced Tape Laying Technology." DASA/MBB Military Aircraft Division, Germany. DGLR-Jahrestagung, Bremen, Sept. 1992.
- 3.24. Tosh, M.W.; and Kelly, D. W. "On the design, manufacture and testing of trajectorial fiber steering for carbon fiber composite laminates," *Composites - Part A: Applied Science and Manufacturing*, v31, n10, Elsevier Science Ltd., England, 2000, p. 1047-1060.
- 3.25. Duvaut, G.; Terrel, G.; Lene, F.; Verijenko, V.E. "Optimization of fiber reinforced composites," *Composite Structures*, v48, n1, Elsevier Science Ltd., England, 2000, p. 83-89.
- 3.26. Reuschel, D.; and Mattheck, C. "Optimization of Fiber Arrangement with CAIO (computer aided internal optimization) and Application to Tensile Samples," *International Conference on Computer Aided Optimum Design of Structures*, v5, Ashurst, England, 1999, p. 247-255.

- 3.27. Eschenauer, H., Schuhmacher, G., and Krammer, J. "Constructive Design Models for Multidisciplinary Optimization of Fiber Composite Structures," AIAA-92-4684-CP.
- 3.28. Gurdal, Z.; and Olmedo, R. "In-plane Response of laminates with Spatially Varying Fiber Orientations: Variable Stiffness Concept," AIAA Journal, v31, 1993, p. 751-758.
- 3.29. Olmedo, R.; and Gurdal, Z. "Buckling Response of Laminates with Spatially Varying Fiber Orientations," Proceeding of the AIAA/ASME/ASCE/AHS/ASC Structures, Structural Dynamics, and Materials Conference, La Jolla, CA, April 19-21, 1993, p. 2261-2269.
- 3.30. Waldhart, C.; Gurdal, Z.; and Ribbens, C. "Analysis of tow placed, parallel fiber, variable stiffness laminates," Proceedings of the 1996 37th AIAA/ASME/ASCE/AHS/ASC Structures, Structural Dynamics, and Materials Conference. Part 4 (of 4), Salt Lake City, UT, Apr 15-17 1996, p. 2210-2220.
- 3.31. Nagendra, S.; Kodiyalam, S.; Davis, J. E.; and Parthasarathy, V. N. "Optimization of Tow Fiber Paths for Composite Design." Proceedings of the 36th Structures, Structural Dynamics, and Materials (SDM) Conference, 1995.
- 3.32. Pandey, M.D. "Effect of Fiber Waviness on Buckling Strength of Composite Plates," Journal of Engineering Mechanics, v125, no. 10, October 1999.
- 3.33. Pratt, W. F., Rotz, C. A., and Jensen, C. G. "Improved Damping and Stiffness in Composite Structures Using Geometric Fiber Wave Patterns," Proceedings of the ASME Noise Control and Acoustic Division, NCA 23, Advanced Material for Vibro-Acoustic Applications, v2, 1996, p. 37-43.
- 3.34. Steurer, K. A., and Jensen, D. W. "Enhanced Damping of Continuous Wave Fiber Composite Sandwich Panels," 41st AIAA/ASME/ASCE/AHS/ASC Structures, Structural Dynamics, and Materials Conference and Exhibit, Atlanta, GA, April 3-6, 2000.
- 3.35. Biggerstaff, J. M., and Kosmatka, J. B. "Directional Damping Materials for Integrally Damped Composite Plates," SPIE Smart Structures and Materials Conference, March 1, 1999.
- 3.36. Vanderplaats, G. N. "Numerical Optimization Techniques for Engineering Design with application," McGraw-Hill Book Company, NY, 1984.
- 3.37. Kumar, V., Acikgoz, M., Cakal, H., and Ari, O. "Multilevel Optimization with Multiple Objectives and Mixed Design Variables," 4th AIAA/USAF/NASA/OAI Symposium on Multidisciplinary Analysis and Optimizations, OH, September 21-23, 1992.
- 3.38. Venkataraman, S.; and Haftka, R. "Optimization of Composite Panels – A Review," Proceedings of the 14th Annual Technical Conference of the American Society of Composites, Dayton, OH, Sep. 27-29, 1999.

- 3.39. Soremekun, G.A. "Genetic Algorithms for Composite Laminate Design and Optimization," Master Thesis, Virginia Polytechnic Institute and State University, February 1997.
- 3.40. Gurdal, Z., Haftka, R. T., and Hajela, P. "Design and Optimization of Laminated Composite Materials," John Wiley & Sons Inc., NY, 1999.
- 3.41. Krammer, J. "Practical Architecture of Design Optimization Software for Aircraft Structures Taking the MBB-LAGRANGE Code as an Example," AGARD-lecture Series, no. 186, 1992.
- 3.42. Schweiger, J.; Krammer, J; and Hornlein, H. "Development and Application of the Integrated Structural Design Tool LAGRANGE," AIAA-96-4169-CP, 1996.
- 3.43. Hornlein, J.; and Simpson, J. "Performance of Integrated Structural Design Tools and Applications," ECCOMAS 96, John Wiley & Sons, Ltd., Paris, Sept. 9-13, 1996.
- 3.44. Hornlein, H.E.R.M., and Stettner, M. "Structural Design Process: Projects-Programs-Prospects," Optimization Industry, March 23-27, 1997.
- 3.45. Eschenauer, H., Schuhmacher, G., Hartzheim, W. "Multidisciplinary Design of Fiber Composite Aircraft Structures by LAGRANGE." Journal of Computers and Structures, 1992.
- 3.46. Sensburg, O. "Mathematical Optimization: A Powerful Tool for Aircraft Design," AGARD Lecture Series, no. 186, 1992.
- 3.47. Sensburg, O.; Schweiger, J.; Goedel, H.; and Lotze, A. "Integration of structural optimization in the general design process for aircraft," Journal of Aircraft, v 31, n 1, Jan-Feb, 1994, p 206-212.
- 3.48. Moore, G. J. "MSC/NASTRAN Design Sensitivity and Optimization: User's Guide, v67" MacNeal-Schwendler Corp., CA, 1992.
- 3.49. Yu, X., Johnson, E. H., and Zhang, S. "Discrete Optimization in MSC/NASTRAN," MSC. Software Corp., CA, 2001.
- 3.50. http://www.vrand.com/genesis_fact.htm, "GENESIS v.7.0 fact sheet," May 29, 2002.
- 3.51. <http://dt.fme.vutbr.cz/~cf/Cfdprodu.htm>, "VORSTAB fact sheet," May 29, 2002.
- 3.52. Reuschel, D.; and Mattheck, C. "Three-dimensional fiber optimization with computer aided internal optimization," Aeronautical Journal, London, v103, n1027, 1999, p. 415-420.

- 3.53. Tischler, V. A.; and Venkayya, V. B. "Ply Orientation as a Variable in Multidisciplinary Optimization," 4th AIAA/USAF/NASA/OAI Symposium on Multidisciplinary Analysis and Optimizations, Cleveland, OH, September 21-23, 1992.
- 3.54. Niu, M. C. "Airframe Structural Design," Conlimit Press LTD., CA, 1988.
- 3.55. http://www.vistagy.com/products/pdf/Raytheon_Premier_Customer_Success_Story.pdf, "Raytheon Aircraft Uses FIBERSIM to Reduce Shop Floor Changes by 5 to 1 on First Premier I Business Jet," May 29, 2002.
- 3.56. <http://www.atk.com/aerospace/descriptions/DataSheets/f-22shaf.htm>, "Advanced aircraft parts made possible through automated fiber placement technology," May 29, 2002.
- 3.57. Schueler, K. and Hale, R. "Object-oriented Implementation of an Integrated Design and Analysis Tool for Fiber-placed Structures," AIAA Paper AIAA-2002-1223, 43rd AIAA/ASME/ASCE/AHS/ASC Structures, Structural Dynamics, and Materials Conference. April 22-25, 2001. Denver, CO.

Chapter 4:

- 4.1. C.G. Grant, V. M. Benson, "Automated Fiber Placement – Evolution and Current Demonstrations." Third NASA Advanced Composite Technology Conference, Long Beach, California, June 8-11, 1992, pp. 625-648.
- 4.2. M. L. Enders, P. C. Hopkins, "Developments in the Fiber Placement Process." International SAMPE Symposium and Exhibition, 36th, San Diego, CA, April 15-18, 1991.
- 4.3. C. G. Grant, "Fiber Placement Process Utilization within Worldwide Aerospace Industries." SAMPE Journal, Vol. 36, No. 4, July/August, 2000.
- 4.4. M. J. Shuart, N. J. Johnson, H. B. Dexter, J. M. Marchello, and R. W. Grenoble, "Automated Fabrication Technologies for High Performance Polymer Composites." AGARD Spring '98, Workshop on Intelligent Processing of High Performance Materials, Brussels, Belgium, May 11-15, 1998.
- 4.5. D. A. Sandusky, J. M. Marchello, M. Baucom, and N. J. Johnston, "Customized ATP Towpreg." International SAMPE Technical Conference, 24th and International SAMPE Metals and Metals Processing Conference, 3rd, Toronto, Canada, Oct. 20-22, 1992. pp. T591-T605.
- 4.6. L. C. Dickinson and J. W. Deaton, "Mechanical Characterization of Two Thermoplastic Composites Fabricated by Automated Tow Placement." Third NASA Advanced Composites Technology Conference, Vol. 1, Part 2, Jan 01, 1993, pp. 665-687.
- 4.7. B. Hulcher, J. M. Marchello, J. A. Hinklet, N. J. Johnston, and M. A. Lamontia, "Dry Ribbon for Heated Head Automated Fiber Placement."

- 4.8. D. W. Kelly, R. Willgoss, R. Li and A. Crosky, "A Manufacturing Procedure for Composite Laminate Production with Precision Fiber Placement." ONR Grant N000140010583, Cooperative Research Centre for Advanced Composite Structures Ltd.
- 4.9. R. Flory, and E. Bernardon, "Effect of Steering and Conformance Requirements on Automated Material Deposition Equipment." Charles Stark Draper Laboratory, Inc., Subcontract No. CACDRA.001 issued by The Composites Automation Consortium, Inc.
- 4.10. M. Daniel, H M. Hsiao, S. C. Wooh, and J. Vittoser, "Processing and Compressive Behavior of Thick Composites." *Mechanics of Thick Composites*, ASTM AMD-Vol162, 1933, pp107-126.
- 4.11. Yu. M. Tarnopol'skii, G. G. Portnov, and I. G. Zhigun, "Effect of fiber curvature on the modulus of elasticity for uni-directional glass-reinforced plastics in tension." *Polym. Mech.*, 3, 1967, pp. 161-166.
- 4.12. T. W. Chou, and K. Takahashi; "Nonlinear elastic behavior of flexible fibre composites", *composites*, Vol. 18, 1987, pp. 25-34.
- 4.13. Mrse and M. R. Piggott, "Relation between Fibre Divagation and Compressive Properties of Fibre Composites." *Proceeding, 14th International SAMPE Symposium*, 1990, pp. 2236-2244.
- 4.14. E. T. Jr. Camponeschi, "Lamina Waviness Levels in Thick Composites and Its effect on Their Compression Strength," *Composites, Design, Manufacture, and Application*, 1991, pp. 30E1 – 30E13.
- 4.15. H.M. Hsiao and I. M. Daniel; "Effect of Fiber Waviness on Stiffness and Strength Reduction of Unidirectional Composites Under Compressive Loading," *Composite Science and Technology* 56, 1996, pp581-593
- 4.16. H.M. Hsiao and I. M. Daniel; "Elastic Properties of Composites with Fiber Waviness," *Composites Part A* 27A, 1996, pp. 931-941
- 4.17. P. J. Joyce and T. J. Moon; "Compression Strength Reduction in Composites with In-Plane Fiber Waviness," *Composite Materials; Fatigue and Fracture*, 7th Vol., ASTM STP 1330, R. B. Bucinell, Ed., ASTM, 1998, pp. 76-96.
- 4.18. H. G. Rai, C. W. Rogers, and D. A. Crane, "Mechanics of Curved Fiber Composites." *Proceedings, 47th Annual Forum of the American Helicopter Society*, 1991, pp.297-304.
- 4.19. T. Stecenko and M. R. Piggott; "Fiber Waviness and Other Mesostructures in Filament Wound Materials," *Journal of Reinforced Plastics and Composites*, Vol. 16, No. 18, 1997, pp. 1659-1674.

- 4.20. G. Andresen; "Prediction of Wave Nesting Effects on Composite Laminate Compressive Strength" Iowa State University of Science and Technology, Ames, IA 50011, March, 1996.
- 4.21. A.S. Argon in H. Herman ed., Fracture of Composites, in Treatise on Materials Science and Technology, Vol. 1, Academic Press, New York, 1972, pp. 78-114.
- 4.22. M. R. Piggott, "A Theoretical Framework for the compressive properties of aligned fibre Composites." *Journal of Material Science*, Vol. 16, 1981, P 2831.
- 4.23. H.T. Hahn and J. G. Williams, "Compression Failure Mechanisms in Unidirectional Composites." NASA Technical Memorandum 85834, 1984.
- 4.24. W. D. Claus, Jr., "Filament Misalignment and Composite Strength" *Composite Materials, Testing and Design*, Proceedings of the Second Conference, Anaheim, California, April, 1971. pp. 20-22.
- 4.25. S.W. Yurgartis, "Measurement of Small Angle Fiber Misalignments in Continuous Fiber Composites." *Composites Science and Technology*, Vol. 30, 1987, pp. 279-293
- 4.26. S. M. Haffner, J. N. Caron, K. V. Steiner, J. B. Mehl, and K. Friedrich, "Feasibility Study of a Laser-Ultrasonic System for Nondestructive Evaluation of Composite Structures." University of Delaware Center for Composite Materials, CCM-95-21, 1995.
- 4.27. S. C. Wooh, "Development of Ultrasonic Nondestructive Methods for Defect and Damage Characterization in Composite Materials", NASA Technical Reports, 90N21816, Jan. 01, 1989.
- 4.28. J. H. Williams, Jr., B. Doll, "Ultrasonic Attenuation as an Indicator of Fatigue Life of Graphite/Epoxy Fiber Composite", NASA Technical Report, NASA-CR-3179, Dec. 01, 1979.
- 4.29. D. K. Hsu, V. Dayal, Z. Liu, and D. Fei, "Detection and Characterization of Defects in Composites", Project 7, CNDE I/U Program Review Meeting, April 16-18, 2001.
- 4.30. Zweben, "Size Effect in Composite Materials and Structures: Basic Concept and Design Consideration." Workshop on Scaling Effects in Composite Materials and Structure, NASA Conference Publication 3271, LaRc, Jul. 1994, pp. 197-217.
- 4.31. Zweben, W. S. Smith and M. W. Wardle "Test Methods for Fiber Tensile Strength, Composite Flexural Modulus and Properties of Fabric-Reinforced Laminates." *Composite Materials; Testing and Design*, 5th Conference, ASTM STP 647, American Society for Testing and Materials, Philadelphia, 1979, pp. 228-262.
- 4.32. Zweben, "The Effect of Stress Nonuniformity and Size on the Strength of Composite Materials." *Composite Technology Review*, Vol. 3, No. 1, 1981, pp. 23-26.

- 4.33. G. Camponeschi; “The Effect of Specimen Scale on the Compression Strength of Composite Materials” Workshop on Scaling Effects in Composite Materials and Structure, NASA Conference Publication 3271, LaRc, Jul. 1994, pp. 81-99.
- 4.34. M. R. Wisnom; “The Effect of Specimen Size on the Bending Strength of Unidirectional Carbon Fibre-Epoxy.”, Composite Structure (ISSN 0263-8223), Vol. 18, No. 1, 1991, pp. 47-63.
- 4.35. Peter R. Scholtes, Brian L. Joiner, Barbara J. Streibel; “The Team Handbook”, second edition, Joiner Associate Inc., June 1996.
- 4.36. R. Neddo and C. Kogstrom. “Automated Tow Placement of Fan Cowl Door Skins” 28th International SAMPE Technical Conference. November 4-7, 1996.
- 4.37. Cincinnati Milicron Viper Fiber Place Machine Brochure, Cincinnati Milicron.
- 4.38. K. Lim, “Structural Optimization for Fiber Steering Conceptual Design” The University of Kansas, Master Thesis, May 2002.
- 4.39. K. Schueler and R.D. Hale, "Object-Oriented Implementation of an Integrated Design and Analysis Tool for Fiber Placed Structures," AIAA-2002-1223, Proceedings, 43rd AIAA/ASME/ASCE/AHS/ASC Structures, Structural Dynamics and Materials Conference, Denver, CO, April 22-25, 2002.
- 4.40. R.D. Hale and K. Schueler, "Knowledge-Based Software Systems for Composite Design, Analysis and Manufacturing," SAE-2002-01-1536, Proceedings, SAE General Aviation Technology Conference and Exposition, Wichita KS, April 16-18, 2002.
- 4.41. K.L. Schueler, J.R. Miller and R.D. Hale, "Approximate Geometric Methods in Application to the Modeling of Fiber Placed Composite Structures," submitted to *Journal of Computing and Information Science in Engineering*. The American Society of Mechanical Engineers. (2002).
- 4.42. The Boeing Company. “Fiber Steering for Reduced Weight Affordable Composite Structure.” Contract N00140-95-2-J044 awarded by the Office of Naval Research Center of Excellence for Composites Manufacturing Technology, April 1997 to April 1998.
- 4.43. A.L. Velocci, "R&D Unit Pressed to Save \$1 Billion," *Aviation Week and Space Technology*, 148/19 (1998) 75-76.
- 4.44. R.D. Hale et. al. "Integrated Design and Analysis Tools for Reduced Weight, Affordable Fiber Steered Composites, Year 1 Annual Summary Report, KUFRL22480-2” 15 September, 2000.
- 4.45. Wyoming Test Fixtures, Inc. “High Performance Test Fixture” Product Catalog No. 105

- 4.46. B. McIlroy, Machining of Fiber Steered Laminates, Request for Work, The Boeing Company. August, 1997.
- 4.47. A.S. Argon in H. Herman ed., Fracture of Composites, in Treatise on Materials Science and Technology, Vol. 1, Academic Press, New York, 1972, pp. 78-114.
- 4.48. R.D. Hale et. al. "Integrated Design and Analysis Tools for Reduced Weight, Affordable Fiber Steered Composites, Annual Summary Report, KUFRL22480-3" 15 September, 2001.
- 4.49. J. Krautkramer and H. Krautkramer, Ultrasonic Testing of Materials, 4th Edition, Springer-Verlag, Berlin New York, 1990.
- 4.50. Liu, Z. Fei, D. Dayal, V. Hsu D.K. and Hale, R.D. "Ultrasonic NDE and Mechanical Testing of Fiber Placement Composites," Review of Progress in Quantitative Nondestructive Evaluation, Volume 20, Plenum Publishing, 2001.
- 4.51. ASTM Designation: D-695-96, "Standard Test Method for Compressive Properties of Rigid Plastics." pp. 78-84.
- 4.52. ASTM Designation: D 3410/D 3410M-95," Standard Test Method for Compressive Properties of Polymer Matrix Composite Materials with Unsupported Gage Section by Shear Loading", pp. 129-144.
- 4.53. R. D. Hale and K. Schueler, " Object-Oriented Design and Analysis Tools for Fiber Placed and Fiber Steered Structure." Proceedings SAMPE 2002

Chapter 5:

- 5.1 M. P. Wiehn, R.D. Hale, "Low Cost Robotic Fabrication Methods For Tow Placement", *International SAMPE Symposium and Exhibition*, v 47 II, 2002, pp. 1842-1852.
- 5.2 B. D. Agarwal, L.J. Broutman, Analysis and Performance of Fiber Composites Second Edition, A Wiley-Interscience Publication, John Wiley & Sons, INC. 1990.
- 5.3 J. R. Vinson, R. L. Sierakowski, The Behavior of Structural Composite Materials, Marinus Nijhoff Publishers, 1987.
- 5.4 Annual Book of ASTM Standards – General Products, Chemical, specialties and End Use Products, Vol. 15.03, Space Simulation; Aerospace and Aircraft; Composite Materials. pp. 128-144.
- 5.5 D. J. Bradley, D. O. Adams, H. E. Gascoigne, "Interlaminar Strains and Compressive Strength Reductions Due to Nested Layer Waviness in Composite Laminates", *Journal of Reinforced Plastics and Composites*, Vol 17, No 11, 1998, pp.989-1011.
- 5.6 R. D. Hale, K. Schueler, "Object-Oriented Design and Analysis Tools for Fiber Placed and Fiber Steered Structures", *International SAMPE Symposium and Exhibition (Proceedings)*, v 47 II, 2002, p 1827-1841.

- 5.7 D. Evans, "Design Considerations for Cost Effective Fiber Placement", *38th International SAMPE Symposium*, May 10-13, 1993, pp. 170-181.
- 5.8 T. J. Moon, P. J. Joyce, D. Kugler, "A Technique for Characterizing process-induced Fiber Waviness in Unidirectional Composite Laminates – Using Optical Microscopy", *Journal of Composites Materials*, Vol. 31, No. 17, 1997, p 1694-1727.
- 5.9 T. J. Moon, P. J. Joyce, D. Kugler, "Investigation of the Effect of part Length on Process-Induced Fiber-Wrinkled Regions in Composite Laminates", *Journal of Composites Materials*, Vol. 31, No. 17, 1997, p 1728-1757.
- 5.10 N. A. Fleck, J. Y. Shu, "Microbuckle Initiation in Fibre Composites: A Finite Element Study", *Journal of the Mechanics and Physics of Solids*, Vol. 43, No. 12, 1995, pp. 1887-1918.
- 5.11 R. A. Raouf, "Effects of Layer Waviness on Interlaminar Stresses in Thick Composite Plates", *Journal of Thermoplastic Composite Materials*, Vol. 7, July 1994, pp. 261-269.
- 5.12 D. O'Hare Adams, S. J. Bell, "Compression Strength Reductions in Composite Laminates due to Multiple-Layer Waviness", *Composites Science and Technology*, Vol. 53, 1995, pp. 207-212.
- 5.13 H. M. Hsiao, I. M. Daniel, S. C. Wooh, "Effect of Fiber Waviness on the Compressive Behavior of Thick Composites", *Failure Mechanics in Advanced Polymeric Composites*, ASME, AMD-Vol. 196, 1994, pp.141-159.
- 5.14 D. O'Hare Adams, M. W. Hyer, "Effects of Layer Waviness on Compression-Loaded Thermoplastic Composite Laminates", Center for Composite Materials and Structures, Feb 1992.
- 5.15 A. J. Sawicki, P. J. Minguet, "Effect of intraply overlaps and gaps upon the compression strength of composite laminates", American Institutet5 of Aeronautics and Astronautics, Inc. pp. 744 – 754, 1998.
- 5.16 K. B. Breiling, "Effects of Nesting on Compression-Loaded 2-D Woven Textile Composites", Iowa State University Thesis, 1994.
- 5.17 M. A. Verhulst, "Layer nesting Effects on Compression-Loaded and Tension Loaded 2-D Textile Composites", Iowa State University Thesis, 1995.
- 5.18 A. L. Highsmith, J. L. Davis and K. L. Helms, "The Influence of Fiber Waviness on the Compressive Behavior of Unidirectional Continuous Fiber Composites," *Composite Materials: Testing and design*, ASTM STP 1120, Glenn C. Grimes, Ed., American Society for Testing and Materials, Philadelphia, 1992, pp. 20-36.
- 5.19 T. J. Moon, J. J. Peter, "Compression Strength reduction in Composites with In-plane Fiber Waviness," *Composite Materials: Fatigue and Fracture*, Seventh Volume, ASTM STP 1330, R. B. Bucinell, Ed., American Society for Testing and Materials, 1998, pp. 76-96.
- 5.20 R. D. Hale, M Villa. "Influence of Opposing Wave Nesting in Compression-Loaded Composites", *Journal of Composite Materials*, Sage Publications Ltd, Vol. 37, n. 13, 2003, pp. 1149-1166.

- 5.21 R. D. Hale, D. O . Adams. "Influence of In-Plane Misalignment on Moiré Interferometry Results", *Journal of Composite Materials*, Technomic Publishing Co. Inc. Lancaster, PA, USA, Vol. 31, n. 24, 1997, pp. 2444-2459
- 5.22 J. Krautkrämer, H. Krautkrämer. Ultrasonic Testing of Materials 4th, fully revised Edition. Springer-Verlag, Berlin, Germany, 1990
- 5.23 Personal correspondence. Dr. R. Hale. Associate Professor of Aerospace Engineering, The University of Kansas. August 5 2004.
- 5.24 R. C. Hibeler, Mechanics of Materials, Third Edition, Prentice Hall, Upper Saddle River, New Jersey, 1997.